frontiers | Research Topics

Advanced imaging in breast cancer: New hopes, new horizons!

Edited by
Abhishek Mahajan

Published in
Frontiers in Oncology

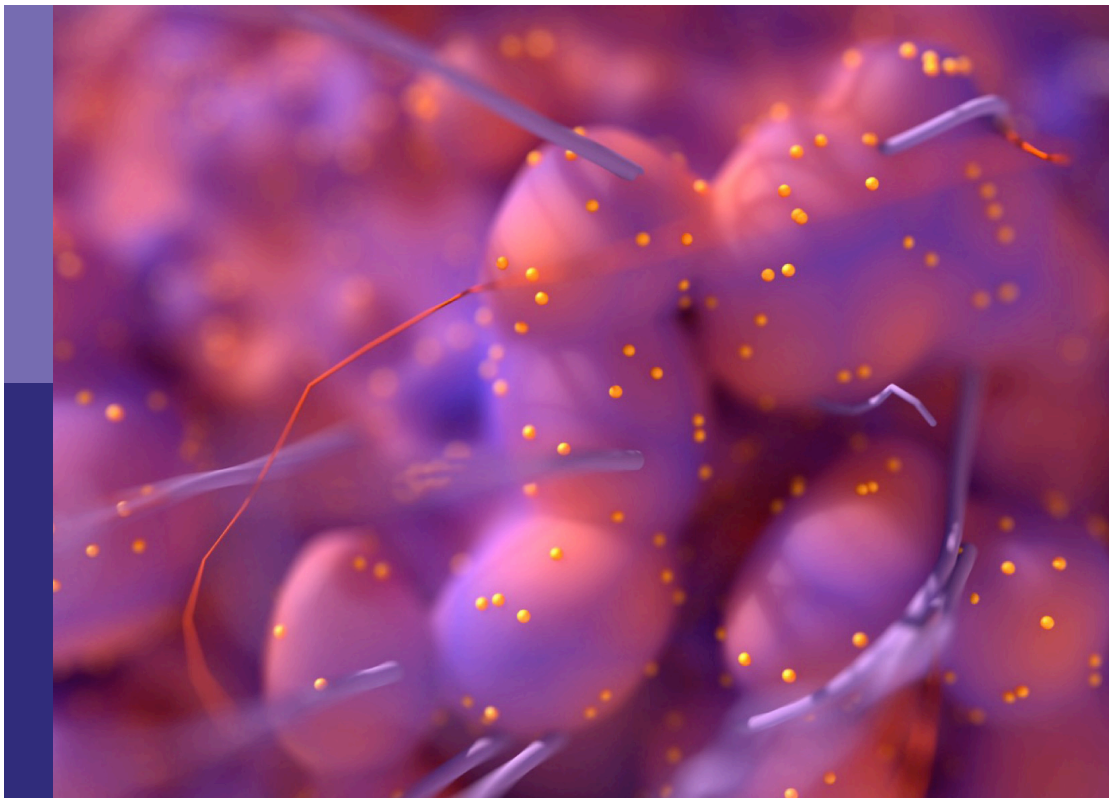

ISSN 1664-8714
ISBN 978-2-83251-845-8
DOI 10.3389/978-2-83251-845-8

About Frontiers

Frontiers is more than just an open access publisher of scholarly articles: it is a pioneering approach to the world of academia, radically improving the way scholarly research is managed. The grand vision of Frontiers is a world where all people have an equal opportunity to seek, share and generate knowledge. Frontiers provides immediate and permanent online open access to all its publications, but this alone is not enough to realize our grand goals.

Frontiers journal series

The Frontiers journal series is a multi-tier and interdisciplinary set of open-access, online journals, promising a paradigm shift from the current review, selection and dissemination processes in academic publishing. All Frontiers journals are driven by researchers for researchers; therefore, they constitute a service to the scholarly community. At the same time, the *Frontiers journal series* operates on a revolutionary invention, the tiered publishing system, initially addressing specific communities of scholars, and gradually climbing up to broader public understanding, thus serving the interests of the lay society, too.

Dedication to quality

Each Frontiers article is a landmark of the highest quality, thanks to genuinely collaborative interactions between authors and review editors, who include some of the world's best academicians. Research must be certified by peers before entering a stream of knowledge that may eventually reach the public - and shape society; therefore, Frontiers only applies the most rigorous and unbiased reviews. Frontiers revolutionizes research publishing by freely delivering the most outstanding research, evaluated with no bias from both the academic and social point of view. By applying the most advanced information technologies, Frontiers is catapulting scholarly publishing into a new generation.

What are Frontiers Research Topics?

Frontiers Research Topics are very popular trademarks of the *Frontiers journals series*: they are collections of at least ten articles, all centered on a particular subject. With their unique mix of varied contributions from Original Research to Review Articles, Frontiers Research Topics unify the most influential researchers, the latest key findings and historical advances in a hot research area.

Find out more on how to host your own Frontiers Research Topic or contribute to one as an author by contacting the Frontiers editorial office: frontiersin.org/about/contact

Advanced imaging in breast cancer: New hopes, new horizons!

Topic editor
Abhishek Mahajan — The Clatterbridge Cancer Centre, United Kingdom

Citation
Mahajan, A., ed. (2023). *Advanced imaging in breast cancer: New hopes, new horizons!* Lausanne: Frontiers Media SA. doi: 10.3389/978-2-83251-845-8

The authors declare that the research was conducted in the absence of any commercial or financial relationships that could be construed as a potential conflict of interest

Table of contents

frontiers | Frontiers in Oncology

TYPE Editorial
PUBLISHED 21 February 2023
DOI 10.3389/fonc.2023.1155500

OPEN ACCESS

EDITED AND REVIEWED BY
Zaver Bhujwalla,
School of Medicine, Johns Hopkins University, United States

*CORRESPONDENCE
Abhishek Mahajan
drabhishek.mahajan@yahoo.in

SPECIALTY SECTION
This article was submitted to Cancer Imaging and Image-directed Interventions, a section of the journal Frontiers in Oncology

RECEIVED 31 January 2023
ACCEPTED 08 February 2023
PUBLISHED 21 February 2023

CITATION
Mahajan A and Majithia J (2023) Editorial: Advanced imaging in breast cancer: New hopes, new horizons!.
Front. Oncol. 13:1155500.
doi: 10.3389/fonc.2023.1155500

Editorial: Advanced imaging in breast cancer: New hopes, new horizons!

Abhishek Mahajan[1]* and Jinita Majithia[2]

[1]The Clatterbridge Cancer Centre, Liverpool, United Kingdom, [2]Tata Memorial Hospital, Mumbai, India

KEYWORDS

breast cancer, imaging, artificial intelligence, imaging biomarkers, functional imaging

Editorial on the Research Topic
Advanced imaging in breast cancer: New hopes, new horizons!

Frontier's in Oncology is a coveted journal encompassing technologies, fields and categories related to Cancer Research. An internationally recognized journal, Frontier's in Oncology is cited by more than 25,000 articles over the past few years. Under the dedicated leadership and guidance of Dr. Abhishek Mahajan, Consultant Radiologist at Clatterbridge Cancer Centre, Liverpool, UK, and ex-Consultant Radiologist at Tata Memorial Hospital, Mumbai, India, having more than 15 years of experience in Oncoimaging, the Research Topic of "Advanced Imaging in Breast Cancer" hopes to present high quality articles with a goal to continuously strive towards advancing the knowledge and understanding of Breast Cancer.

Introduction

Breast cancer is the most commonly diagnosed cancer worldwide with more than 2 million new cases in 2020. The incidence of breast cancer has increased over the past few decades and this can be attributed to change in the risk factor profiles, better cancer registration and advances in cancer detection. Breast cancer is the fifth most common cause of cancer-related deaths globally, with a disturbing estimated number of 2.3 million new cases, as per the GLOBOCAN 2020 data (1), and the global burden is only expected to increase. The breast cancer morbidity and mortality rates have significantly increased over the past few decades (2). There are more lost disability-adjusted life years (DALYs) by women to breast cancer globally than any other type of cancer. Breast cancer also represents a large social and economic burden to the society. The increase in the fiscal costs borne by the Government and Insurance companies as well as the emotional and physical costs borne by the patient and their families is unparalleled.

In order to maintain a good survival rate there have been constant efforts by scientists, researchers and the medical fraternity to not only introduce effective screening programs for early detection, but also for updating their knowledge database about evolving risk factors and epidemiology and recent advances in imaging for monitoring and surveillance of breast cancer in order to provide insights into new treatment strategies and patient

stratifications that can impact management and eventual outcome of a patient with breast cancer.

Various new breast imaging tools have been identified and are being constantly developed to further improve our current ability to identify and treat early-stage breast cancer. This include advances in current technologies as well as introduction and implementation of new breast imaging platforms. Mammography is the gold standard first line imaging technique in preliminary diagnosis. Advances like Digital breast Tomosynthesis (DBT) as well as Volumetric Breast Density add incremental value in characterising normal and abnormal findings in the clinical setting of primary evaluation as well as post operative follow up in breast cancer (3). However, breast lesions identified on mammography usually require further investigation by ultrasonography. Ultrasonography (USG) has a useful role in characterizing the tumor as well as guiding interventions. There are recent advances in fusion based approach of mammography and ultrasonography, developing algorithms which improve the accuracy of computer-aided diagnosis (CAD) for analyzing breast lesion on ipsilateral mammography views (4). Recently, Contrast enhanced Mammography (CEM), a novel imaging modality, was developed as an adjunct to mammography to provide additional physiologic information about local breast perfusion in order to characterize enhancing lesions of the breast. Magnetic Resonance Imaging (MRI), however has been a game changer in breast imaging owing to its high soft tissue resolution and its use is becoming more prevalent, providing detailed three dimensional and cross-sectional models which are highly useful in diagnosis and monitoring. Diffusion weighted imaging (DWI) particularly has revolutionized oncological imaging, by giving vital qualitative and quantitative information regarding tumor biology that helps in detection, characterization and post treatment surveillance of lesions (5). Over the past years, Positron Emission Tomography (PET) has seen progress from being solely a research tool to replacing conventional imaging in various types of cancers (6). In breast imaging, there is strong supporting evidence that PET-CT is more rigorous than CT alone for revelation of breast lesions and distant metastases (7).

Current challenges and opportunities in advanced breast imaging

1. Lack of awareness, delay in seeking healthcare, delay from the healthcare provider's side, shortage of resources and high attrition rate have been few of the largest roadblocks. The emphasis of early diagnosis of breast cancer cannot be stressed upon enough in an era where there is evidence that newer emerging imaging techniques have facilitated improved outcome upon timely treatment. Beginning with education of women for self-breast examination to effective government policies for screening, one can ensure prompt diagnosis.
2. Requirement of large and homogeneous data representation across the globe has been another challenge. The varying demographics of breast cancer in different populations coupled with different socio-economic backgrounds and disorganized policies has not allowed for formulation and implementation of uniform and universally accepted protocols for screening programs. Encouraging and promoting incentives for research as well as providing support and funding from influential agencies and national and international health-care departments can positively impact and motivate the medical fraternity for continued research and development.
3. The controversies surrounding the appropriate techniques for imaging of breast cancer has been an on-going and ever-growing debate among radiologists. The acceptance of newer imaging modalities has been a serious challenge especially in developing nations, where the resistance towards use of these advanced techniques is not only because of the lack of awareness and training of the health care provider but also the lack of availability and funding. Acceptance and adequate penetration of newer health-care technologies can significantly improve the greater good of precision medicine.
4. Lack of expertise among health care providers regarding revolution in cancer research that has ushered in following the introduction of Artificial Intelligence (AI). There is an existing gap between the acceptance and implementation of AI in healthcare worldwide. Adoption of AI in clinical workflow applications can enable doctors and hospitals to offer new healthcare services. Government initiatives, ethical considerations and joint public private sector collaborations will ease the progress of AI, especially in developing countries (8).
5. Adding fuel to fire was the COVID pandemic. Besides the socio-economic and financial crisis to humankind, the pandemic also negatively impacted health-care by delaying research, which was on one of its fastest tracks in centuries (9). As the world continues to be at war and grapples with the aftermath of this disaster, health care providers and radiologists began realize the challenges of the large number of advanced breast cancer cases. There is always a silver lining though. The thrust towards setting up newer and more advanced health-care technologies came from the pressing need of the large number of backlog cases of breast cancer and also for providing remote health-care.

Articles in the Research Topic

The aim of this Research Topic is to provide a diverse selection of stimulating research in the field of breast cancer by respected authors who have sacrificed countless hours in trying to bring forth well-researched and eloquent articles.This Research Topic aims to identify new ways researchers are refining and optimizing techniques in order to improve patient outcomes in diagnosed cases of breast cancer and to enable better monitoring and follow up throughout the course of treatment.

In this Research Topic, we present 21 topics, 16 of which are original research articles, 3 are systematic reviews and 2 are case reports.

The two unique case reports presented include one by Wei et al., who discuss a rare case of Inflammatory MyofibroblasticTumor (IMT) of the Breast with insights in the clinical, imaging and pathological findings. The other is by Jiang et al., discussing the imaging features (especially highlighting the MRI characteristics), pathology and clinical management of Mucocele-Like Tumor of the Breast Associated With Ductal Carcinoma In Situ.

One of the review articles, by Lei et al. discusses the challenges and future perspectives of the application of Artificial Intelligence in Medical Imaging of the Breast. A systemic review and meta-analysis, by Jiang et al., highlights the accuracy and feasibility of Sentinel Lymph Node Biopsy Mapped With Carbon Nanoparticle Suspensions in Patients With Breast Cancer. A systemic review article by Majithia et al., discuss the comprehensive literature on the various imaging appearances of fat necrosis in the breast.

Gao et al. conducted a study to assess the Screening Efficiency of Breast Cancer by Combining Conventional Medical Imaging Examinations With Circulating Tumor Cells.Amongst original research work done in the field of Artificial Intelligence, Zhang et al. discuss the clinical application of Ultrasound Image Deep Learning Model in Evaluating the Accuracy of Breast Cancer and Molecular Subtype Diagnosis. Song et al. evaluated the use of Texture Analysis, Using Semiquantitative Kinetic Parameter Maps from Dynamic Contrast Enhanced MRI, an imaging biomarker for pre-operative prediction of HER2 status in Breast Cancer. Similarly, Zhang et al. discuss the use of Texture Analysis of Dynamic Contrast Enhanced MRI Intra-tumoral Subregions to Identify Benign and Malignant Breast Tumors. A multi-centre prospective study by Zhao et al., elaborate on the enhancing diagnostic performance of breast ultrasound for patients with opportunistic screening-detected breast lesions by a Deep Learning-Based System.

Wang et al. evaluated the Combined Use of Shear Wave Elastography, Microvascular Doppler Ultrasound Technique and BI-RADS for the Differentiation of Benign and Malignant Breast Masses. With their retrospective multicentre study, Zhang et al., aimed at developing and validating and interpretable and simple-to-use ultrasound nomogram that is based on quantitative morphometric features for the prediction of breast malignancy. In a prospective study, Zhang et al., studied the association between vascular index (in Doppler evaluation) measured *via* Superb Microvascular Imaging and molecular subtype of invasive breast cancer and concluded that there was certain degree of correlation between the two and that vascular index has a limited role in predicting the luminal type A with high sensitivity and triple-negative subtype with high specificity. Zhao et al. investigated the diagnostic value of contrast-enhanced cone-beam breast computed tomography (CE-CBBCT) in predicting breast lesion with rim enhancement for malignancy. There were three studies on MRI, particularly centred around the use of Diffusion Weighted sequence. One was by He et al., exploring the Applications of Diffusion Weighted Imaging Techniques for Differentiating Benign and Malignant Breast Lesions. Another was a study by Lv et al. to evaluate the role of apparent diffusion coefficient (ADC) values obtained from diffusion-weighted imaging (DWI) in the differentiation of malignant from benign papillary breast lesions. A retrospective study by Yang et al. evaluated the performance of readout-segmented echo-planar imaging DWI (rs-EPI DWI) in detecting and characterizing breast cancers in a large Chinese cohort in comparison to dynamic contrast-enhanced MRI.

Bourgeois et al., evaluated the distribution of free indocyanine green following intravenous injection, in Near-Infrared Fluorescence imaging of breast cancer and axillary lymph nodes. Li et al. developed a comprehensive model for diagnosis and differentiation of primary breast lymphoma from breast cancer.

In a non-imaging based study, He et al. studied the Feasibility and Clinical Value of CT-Guided ^{125}I Brachytherapy for Pain Palliation in Patients With Breast Cancer and Bone Metastases After External Beam Radiotherapy Failure. Another non-imaging based original article based on Animal model, Wang et al., envisioned that intraoperative real-time fluorescence imaging with a human serum albumin decorated indocyanine green probe could enable complete surgical removal of breast cancer in a mouse model.

Conclusion

The field of breast imaging is always evolving with significant advances. There is always a learning curve in the interpretation of new technologies, and as medical practitioners we owe it to the vast global community to constantly advance ourselves in order to come up with more advanced technologies that can serve humanity. This will further aid the development of novel approaches for precision medicine in breast cancer. This issue aims to provide a comprehensive summary of recent advances and possibilities in the field of clinical breast imaging. The support of our esteemed authors, expertise of our panel of reviewers, round-the-clock hard work of the editorial and production staff and the keen interest of our beloved readers keeps the motivation going for Frontier's in Oncology to continue to contribute to the ever-expanding field of breast oncology and to strive better each time.

Author contributions

All authors listed have made a substantial, direct, and intellectual contribution to the work and approved it for publication.

Conflict of interest

The authors declare that the research was conducted in the absence of any commercial or financial relationships that could be construed as a potential conflict of interest.

Publisher's note

References

1. Sung H, Ferlay J, Siegel RL, Laversanne M, Soerjomataram I, Jemal A, et al. Global cancer statistics 2020: GLOBOCAN estimates of incidence and mortality worldwide for 36 cancers in 185 countries. *CA Cancer J Clin* (2021) 71:209–49. doi: 10.3322/caac.21660

2. Azamjah N, Soltan-Zadeh Y, Zayeri F. Global trend of breast cancer mortality rate: A 25-year study. *Asian Pac J Cancer Prev* (2019) 20(7):2015–20. doi: 10.31557/APJCP.2019.20.7.2015

3. Ramani SK, Rastogi A, Mahajan A, Nair N, Shet T, Thakur MH, et al. Imaging of the treated breast post breast conservation surgery/oncoplasty: Pictorial review. *World J Radiol* (2017) 9(8):321–9. doi: 10.4329/wjr.v9.i8.321

4. Sapate S, Talbar S, Mahajan A, Sable N, Desai S, Thakur M. Breast cancer diagnosis using abnormalities on ipsilateral views of digital mammograms. *Biocybernetics Biomed Engineering*. (2020) 40(1):290–305. doi: 10.1016/j.bbe.2019.04.008

5. Mahajan A, Deshpande SS, Thakur MH. Diffusion magnetic resonance imaging: A molecular imaging tool caught between hope, hype and the real world of" personalized oncology". *World J Radiol* (2017) 9(6):253–68. doi: 10.4329/wjr.v9.i6.253

6. Mahajan A, Cook G. Physiologic and molecular basis of PET in cancer imaging. *Basic Sci PET Imaging* (2017), 399–427. doi: 10.1007/978-3-319-40070-9_17

7. Shawky M, Ali ZAE, Hashem DH, Houseni M. Role of positron-emission tomography/computed tomography (PET/CT) in breast cancer. *Egypt J Radiol Nucl Med* (2020) 51:125. doi: 10.1186/s43055-020-00244-9

8. Mahajan A, Vaidya T, Gupta A, Rane S, Gupta S. Artificial intelligence in healthcare in developing nations: The beginning of a transformative journey. *Cancer Res Statistics Treat* (2019) 2(2):182. doi: 10.4103/CRST.CRST_50_19

9. Mahajan A. COVID-19 and its socioeconomic impact. *Cancer Res Statistics Treat* (2021) 4(1):12–8. doi: 10.4103/crst.crst_29_21

frontiers in Oncology

ORIGINAL RESEARCH
published: 05 March 2021
doi: 10.3389/fonc.2021.623506

Evaluating the Accuracy of Breast Cancer and Molecular Subtype Diagnosis by Ultrasound Image Deep Learning Model

Xianyu Zhang[1†], Hui Li[1†], Chaoyun Wang[2†], Wen Cheng[3†], Yuntao Zhu[2], Dapeng Li[4], Hui Jing[3], Shu Li[5], Jiahui Hou[3], Jiaying Li[1], Yingpu Li[1], Yashuang Zhao[4], Hongwei Mo[2*] and Da Pang[1*]*

[1] Department of Breast Surgery, Harbin Medical University Cancer Hospital, Harbin, China, [2] Harbin Engineering University Automation College, Harbin, China, [3] Department of Ultrasound, Harbin Medical University Cancer Hospital, Harbin, China, [4] Department of Epidemiology, Harbin Medical University, Harbin, China, [5] Prenatal Diagnosis Center, The First Affiliated Hospital of Harbin Medical University, Harbin, China

Background: Breast ultrasound is the first choice for breast tumor diagnosis in China, but the Breast Imaging Reporting and Data System (BI-RADS) categorization routinely used in the clinic often leads to unnecessary biopsy. Radiologists have no ability to predict molecular subtypes with important pathological information that can guide clinical treatment.

Materials and Methods: This retrospective study collected breast ultrasound images from two hospitals and formed training, test and external test sets after strict selection, which included 2,822, 707, and 210 ultrasound images, respectively. An optimized deep learning model (DLM) was constructed with the training set, and the performance was verified in both the test set and the external test set. Diagnostic results were compared with the BI-RADS categorization determined by radiologists. We divided breast cancer into different molecular subtypes according to hormone receptor (HR) and human epidermal growth factor receptor 2 (HER2) expression. The ability to predict molecular subtypes using the DLM was confirmed in the test set.

Results: In the test set, with pathological results as the gold standard, the accuracy, sensitivity and specificity were 85.6, 98.7, and 63.1%, respectively, according to the BI-RADS categorization. The same set achieved an accuracy, sensitivity, and specificity of 89.7, 91.3, and 86.9%, respectively, when using the DLM. For the test set, the area under the curve (AUC) was 0.96. For the external test set, the AUC was 0.90. The diagnostic accuracy was 92.86% with the DLM in BI-RADS 4a patients. Approximately 70.76% of the cases were judged as benign tumors. Unnecessary biopsy was theoretically reduced by 67.86%. However, the false negative rate was 10.4%. A good prediction effect was shown for the molecular subtypes of breast cancer with the DLM. The AUC were 0.864, 0.811, and 0.837 for the triple-negative subtype, HER2 (+) subtype and HR (+) subtype predictions, respectively.

OPEN ACCESS

Edited by:
Fu Wang,
Xi'an Jiaotong University, China

Reviewed by:
Montserrat Muñoz,
Hospital Clínic de Barcelona, Spain
Guowu Yang,
University of Electronic Science and Technology of China, China

***Correspondence:**
Da Pang
pangda@ems.hrbmu.edu.cn
Hongwei Mo
honwei2004@126.com
Yashuang Zhao
zhao_yashuang@163.com

[†]These authors have contributed equally to this work

Specialty section:
This article was submitted to Cancer Imaging and Image-directed Interventions, a section of the journal Frontiers in Oncology

Received: *30 October 2020*
Accepted: *15 February 2021*
Published: *05 March 2021*

Citation:
Zhang X, Li H, Wang C, Cheng W, Zhu Y, Li D, Jing H, Li S, Hou J, Li J, Li Y, Zhao Y, Mo H and Pang D (2021) Evaluating the Accuracy of Breast Cancer and Molecular Subtype Diagnosis by Ultrasound Image Deep Learning Model. Front. Oncol. 11:623506. doi: 10.3389/fonc.2021.623506

Conclusion: This study showed that the DLM was highly accurate in recognizing breast tumors from ultrasound images. Thus, the DLM can greatly reduce the incidence of unnecessary biopsy, especially for patients with BI-RADS 4a. In addition, the predictive ability of this model for molecular subtypes was satisfactory,which has specific clinical application value.

Keywords: breast cancer, deep learning, ultrasound, cancer diagnosis, molecular subtype

INTRODUCTION

Breast cancer is the most common malignant tumor in women in China (1, 2). Breast ultrasound is more suitable for tumor discovery in Asian women considering the higher breast density (3, 4) and the younger age at diagnosis (5, 6). Patients with Breast Imaging Reporting and Data System (BI-RADS) 4a or higher findings are usually recommended to undergo core needle biopsy or surgery. BI-RADS has a wide range of possibilities to predict the presence of malignancies, but its false positive findings lead to unnecessary biopsies in a large number of individuals without breast cancer (7).

The combination of deep learning (8) and large datasets has shown good performance in the diagnosis of many diseases, including cancer (9–12). The deep learning model (DLM) takes the original image pixels and corresponding category labels in medical image data as inputs and does not require manual design features required by traditional methods but automatically learns features related to category classification (13).

Based on receptor status, breast cancers are divided into five subtypes (14). If the molecular subtype is identified before surgery, we can determine whether the patient is suitable for neoadjuvant treatment and which scheme should be more efficient. However, currently, we cannot obtain subtype information through traditional ultrasound examinations.

In addition to the differentiation of benign and malignant breast tumors from ultrasound images, previous studies have focused on the correlation between imaging features and molecular subtypes. Breast cancers with the triple-negative subtype were more likely to be associated with circumscribed margins and were less associated with calcifications (15–18). Human epidermal growth factor receptor 2 (HER2) (+) breast cancers usually show enhanced posterior acoustics on ultrasound images (15, 17). Tumors with posterior shadowing are often found in hormone receptor (HR) (+) HER2 (–) breast cancers (16, 19, 20). In addition, echogenic halos were frequently present in the HR (+) HER2 (–) subtype (17, 20). Due to the various imaging features of different subtypes, there is potential to predict molecular subtypes with DLM by analyzing only the ultrasound images.

In this study, we constructed a DLM based on ultrasound images. We obtained a higher accuracy for breast tumor diagnosis with the DLM than with radiologists. We obtained a good prediction for tumor molecular subtypes, which may provide more choices for therapy.

MATERIALS AND METHODS

This study was approved by the Institutional Review Board of Harbin Medical University Cancer Hospital. Because of its retrospective nature, the study was exempt from obtaining informed consent from patients.

Datasets

We obtained original ultrasound images for the training and testing datasets from the breast image database of Harbin Medical University Cancer Hospital (a total of 17,226 images from 2,542 patients). All patients underwent surgical treatment with definitive pathological results. The cohort selection flowchart is shown in **Figure 1**. Patients in the external test set were enrolled from The First Affiliated Hospital of Harbin Medical University and were selected with the same criteria as those for the training and test sets. Exclusion criteria for the datasets are described in the **Supplementary Material**.

We selected ultrasound images of breast cancer patients with corresponding pathological results. We excluded tumors with incomplete immunohistochemistry results and then separated the tumors into molecular subtypes. Data on estrogen receptor (ER) and progesterone receptor (PR) expression were collected. Patients with positivity for either or both receptors were defined as being HR positive. According to the expression of two indicators, HR and HER2, we regrouped patients into three molecular subtypes: HER2 (+) subtype, HR (+) subtype and triple-negative subtype. HER2 (+) subtype = HR (+) HER2 (+) or HR (–) HER2 (+); HR (+) subtype = HR (+) HER2 (–); triple-negative subtype = HR (–) HER2 (–).

In **Figure 2**, we listed some samples of breast ultrasound images from the datasets, which were presented by classification of benign and malignant tumors and molecular subtypes.

The training and test sets were formed by a random sampling method at a ratio of 4:1. The compositions of these sets are shown in **Figure 1**. It is noteworthy that within the training set, we redivided it into a new training set and a validation set for model tuning and training at a ratio of 4:1. The optimal model obtained was tested with the test set and the external test set.

Development of the DLM

All images in the datasets were 8-bit and 3-channel images, so they could be used as training set and test set images to fine-tune the deep convolutional neural network (DCNN) directly. **Supplementary Figure 1** shows the whole process of breast ultrasound image analysis.

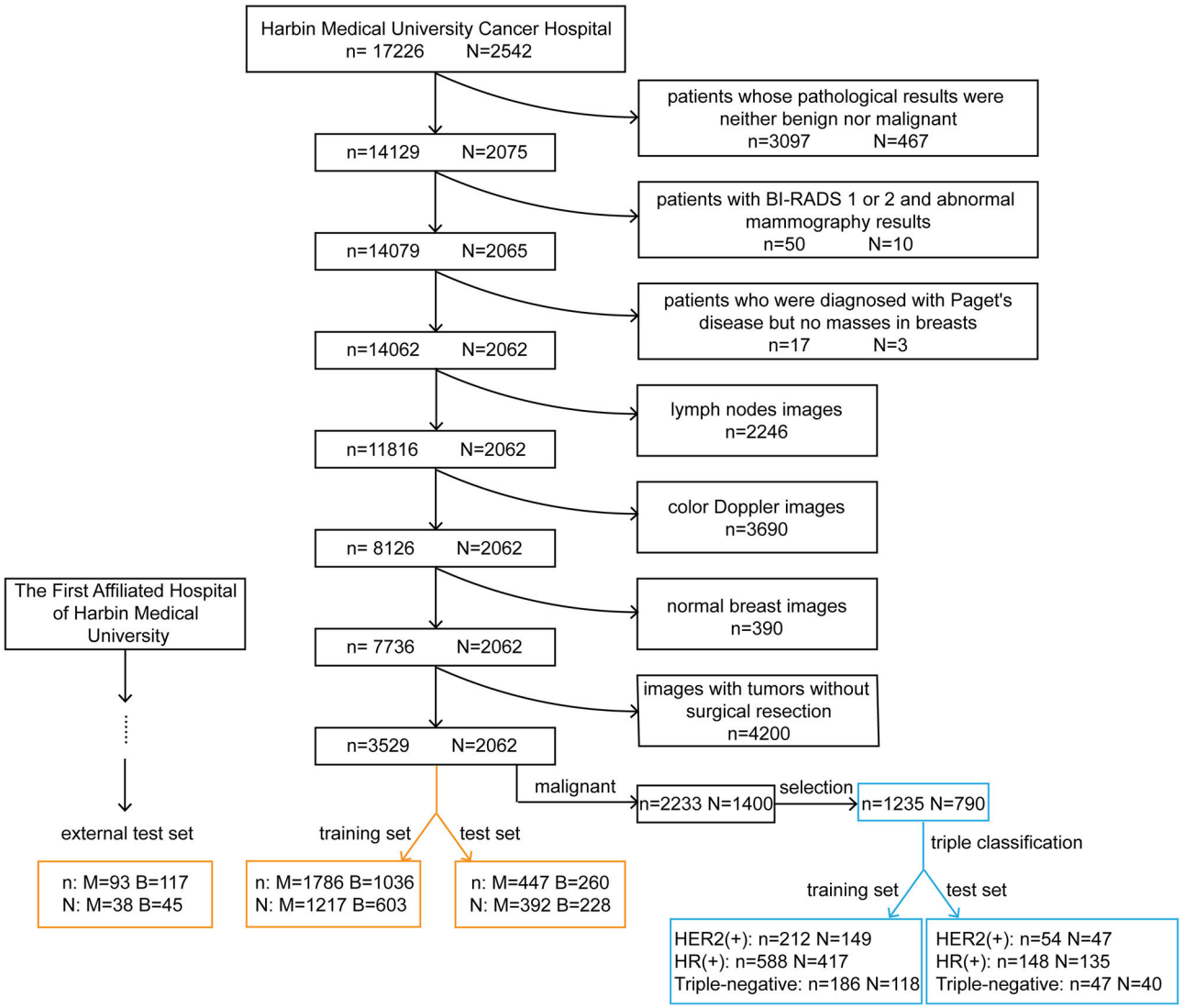

FIGURE 1 | Cohort selection flowchart and the composition of the training, test and external test sets. The black rectangles represent the process of data selection. The orange rectangles represent the composition of datasets for the diagnosis of breast tumors. The blue rectangles represent the composition of datasets used to predict the molecular classification of breast cancer. *n*, the number of images; *N*, the number of patients; M, malignant; B, benign; HER2, human epidermal growth factor receptor 2; HR, hormone receptor.

To obtain a better deep learning effect, the necessary image preprocessing algorithm was used to improve the image quality. In the image preprocessing of the **Supplementary Material**, we specifically described how to carry out preprocessing of breast ultrasound images.

Considering the amount of data compared with the depth of deep learning, we used data enhancement to enhance the diversity and generalization of the data. We used data enhancement in the Keras model, which could enhance the real-time data with the help of a central processing unit (CPU) during training. Due to the particularity of the ultrasound image data, we used four kinds of random operations to enhance the data: vertical rotation, horizontal rotation, center rotation, and scale reduction.

Because the data had enough high-quality samples after preprocessing and expansion, we used the deep learning Keras framework to transfer and fine-tune the Xception network, making it a network that could extract features for breast ultrasound images (21). The Xception convolution neural network (CNN) has trained more than 1.2 million images from the ImageNet large-scale vision recognition challenge (ILSVRC) knowledge base.

The structure of the Xception model mainly consisted of a convolutional layer and a fully connected classification layer. **Figure 3** shows the structure diagram of our model training,

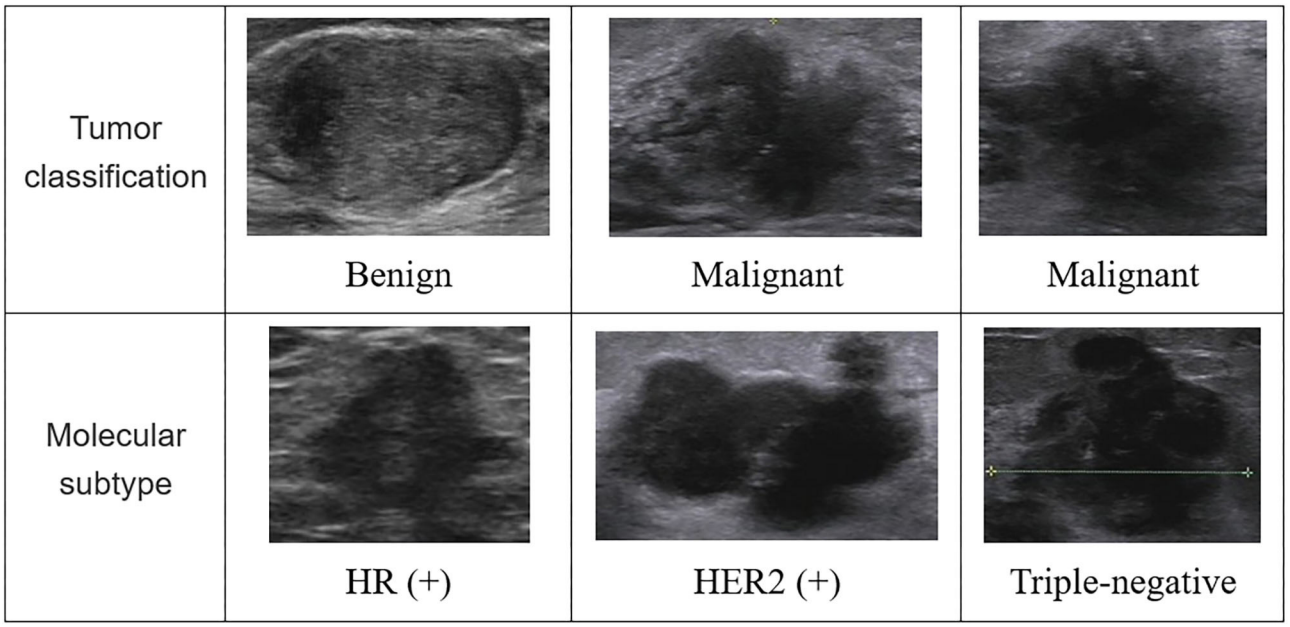

FIGURE 2 | Some samples of breast ultrasound images from the datasets. In the first column, the samples were divided according to the diagnosis results of the tumor, which were benign and malignant; in the second column, the samples were classified according to molecular subtypes, which were divided into images of HR (+) subtype, HER2 (+) subtype, and triple-negative subtype. HR, hormone receptor; HER2, human epidermal growth factor receptor 2.

which mainly adopted the transfer learning method to train the model. CNN-1 represented the training model on the ImageNet dataset and outputted 1,000 classification results. The CNN-2 model was obtained through transfer learning of the CNN-1 model and used for the classification of benign and malignant breast tumors by ultrasound images. The specific model training method was to freeze the convolutional layer parameters of CNN-2 and then train the fully connected layer of the CNN-2 model. After the training was stable, we defrosted the convolutional layer for retraining to achieve the best effect. CNN-3 was a classification model of molecular subtypes, which was acquired from the transfer learning of the CNN-2 model. Two specific training parameters are shown in the **Supplementary Material**.

Statistical Analysis

Evaluation of the DLM was performed with R version 3.5.1. For binary classification in discriminating breast cancer patients from controls, a classification matrix (caret version 6.0–80) and the receiver operating characteristic (ROC) curve (pROC version 1.13.0) were generated to visualize the diagnostic ability of the DLM. For the triple classification of the three molecular subtypes, a classification matrix and the ROC curve using a one-vs-all approach (multiROC version 1.1.1) were generated. The area under the curve (AUC), accuracy, sensitivity, and specificity were calculated to compare the predictive performance between the DLM and BI-RADS classification systems in the test and external test sets. $P < 0.05$ was considered to indicate a statistically significant difference. Moreover, the calculation of sample size is shown in the **Supplementary Material**.

RESULTS

Cohort Composition

We divided the ultrasound images collected from Harbin Medical University Cancer Hospital into two sets (**Figure 1**). The training set was composed of 2,822 images, including 1,786 images from 1,217 patients with malignant tumors and 1,036 images from 603 patients with benign tumors. The test set was composed of 707 images, including 447 images from 392 patients with malignant tumors and 260 images from 228 patients with benign tumors. After applying the same exclusion criteria, external test set images were collected from The First Affiliated Hospital of Harbin Medical University, including 93 images from 38 patients with malignant tumors and 117 images from 45 patients with benign tumors.

Two datasets were used for molecular subtype prediction (**Figure 1**). The training set consisted of 212 images from 149 HER2 (+) subtype patients, 588 images from 417 HR (+) subtype patients and 186 images from 118 triple-negative subtype patients. The test set comprised 54 images from 47 HER2 (+) subtype patients, 148 images from 135 HR (+) subtype patients and 47 images from 40 triple-negative subtype patients.

Performance in Diagnosis

The DLM was more accurate (0.897, 95% CI: 0.872–0.918) than ultrasound doctors (0.856, 95% CI: 0.828–0.881) ($P = 0.024$) (**Tables 1**, **2**). The doctors used the malignant probability and BI-RADS system to determine positive ultrasound findings. For sensitivities, 91.3 and 98.7% ($P < 0.001$) were achieved for the DLM and BI-RADS systems, respectively. However, the

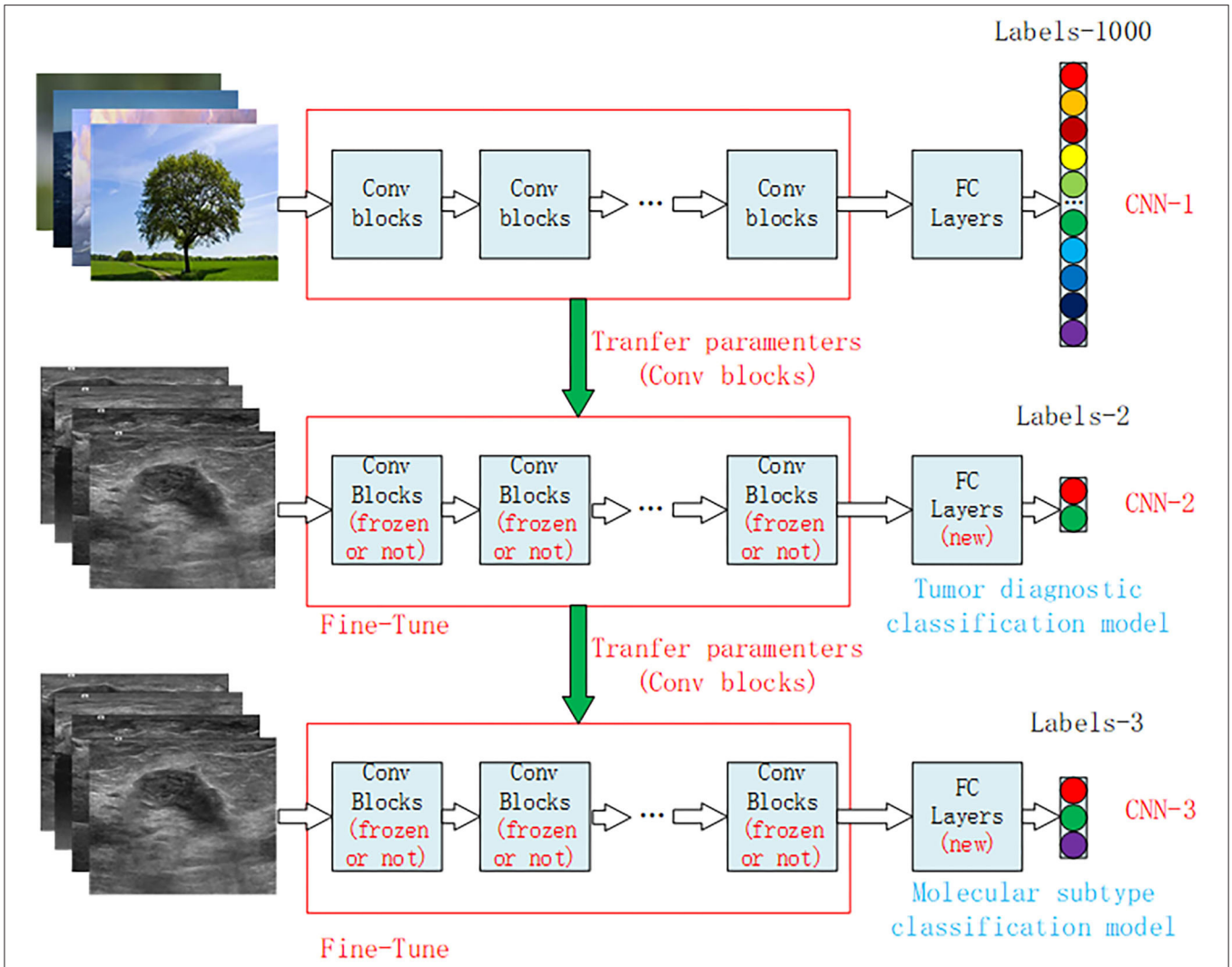

FIGURE 3 | Structural diagram of the transfer learning model for breast cancer ultrasound images. CNN-1 represents the classification model trained on the ImageNet dataset, which is divided into 1,000 categories of natural images. CNN-2 is the benign and malignant tumor diagnostic model obtained by model transfer and retraining on the basis of the CNN-1 model, and CNN-3 is the classification model of tumor molecular subtypes obtained by model transfer and retraining on the basis of the CNN-2 model. CNN, convolution neural network.

specificity of the DLM (86.9%) was significantly higher than that of BI-RADS (63.1%) ($P < 0.001$). This result indicates that the DLM may reduce the unnecessary biopsy of false positive findings with the BI-RADS system. For the test set, the AUC was 0.96. For the external test set, the AUC was 0.90 (**Figure 4**). These results suggest that the DLM has good performance in breast cancer diagnosis.

Reducing Unnecessary Biopsy

Each ultrasound image had corresponding BI-RADS, DLM, and pathological results. The proportion of all patients with BI-RADS 4a judged as benign (70.76%) by the DLM was greater than that judged as malignant (29.24%) (**Figure 5A**). This result indicated that 70.76% of BI-RADS 4a patients did not need surgery when diagnosed using the DLM. The diagnostic accuracy for BI-RADS 4a patients reached 92.86%, and unnecessary biopsy was reduced by 67.86%, with a false negative rate of 10.4% for the DLM (**Figure 5B**). These findings suggest that the DLM can greatly reduce the incidence of unnecessary

TABLE 1 | Confusion matrices of the test set and external test set.

		Pathology			
		Test set		External test set	
		+	–	+	–
BI-RADS	+	441	96	–	–
	–	6	164	–	–
DLM	+	408	34	76	18
	–	39	226	17	99

+, malignant; –, benign; BI-RADS, Breast Imaging Reporting and Data System; DLM, deep learning model.

biopsy, especially for BI-RADS 4a patients with a low false negative rate.

Molecular Subtype Prediction

The DLM can be used not only in the diagnosis of breast cancer but also in the prediction of molecular subtypes. From the results of the triple classification, the triple-negative subtype reached the highest AUC of 0.864. The AUC of the HER2 (+) subtype was 0.811, and the AUC of the HR (+) subtype was 0.837 (**Figure 6**). Accuracy of the HR (+) subtype (85.14%) was significantly higher than that of the HER2 (+) subtype (50%) and triple-negative subtype (53.19%) (**Supplementary Table 1**).

TABLE 2 | Identification performance of BI-RADS and the DLM on the test set and external test set.

	Test set			External test set	
	BI-RADS	**DLM**	***P*-value***	**BI-RADS**	**DLM**
Accuracy	0.856	0.897	0.024	–	0.833
Sensitivity	0.987	0.913	<0.001	–	0.817
Specificity	0.631	0.869	<0.001	–	0.846
Positive predictive value	0.821	0.923	<0.001	–	0.809
Negative predictive value	0.965	0.853	<0.001	–	0.853
Kappa	0.666	0.779	–	–	0.663

*BI-RADS, Breast Imaging Reporting and Data System; DLM, deep learning model; *chi-square test.*

DISCUSSION

We successfully established a DLM for breast cancer diagnosis and molecular subtype prediction based on ultrasound images. The accuracy of the DLM in the diagnosis of breast cancer was higher than that of BI-RADS, and the DLM performed well in both the test set and external test set. The DLM can apparently reduce unnecessary biopsy for patients with BI-RADS 4a. In the predictive results of the DLM for the molecular subtypes of breast cancer, we could see that its performance for various subtypes was ideal, and there were no significant disparities among them.

In many studies of cancer diagnosis, the accuracy of DLMs is higher than that of radiologists. Li et al. successfully developed a DCNN model for the diagnosis of thyroid cancer with ultrasound images. The accuracy was 89.8% with the DCNN model vs. 78.8% with radiologists (22). To classify invasive adenocarcinomas from preinvasive lesions, Wang et al. (23) developed a CNN model. The accuracy of the model (84%) was higher than that of three radiologists (radiologist 1: 80.2%; radiologist 2: 80.7%; and radiologist 3: 81.7%). He et al. used a CNN to predict the local recurrence of giant cell bone tumors. The accuracy of the CNN model was 75.0%, while the accuracy of radiologists was 64.3% (24). Our study had similar results. The DLM was more accurate (0.897, 95% CI: 0.872–0.918) than radiologists (0.856, 95% CI: 0.828–0.881) ($P = 0.024$). In summary, the DLM performed well and has the potential to provide better diagnostic results than radiologists.

At present, there are few studies on the diagnosis of breast cancer with DLMs based on ultrasound images. In recent studies, researchers used different DLMs to diagnose breast tumors on ultrasound images, and the one that performed best was selected

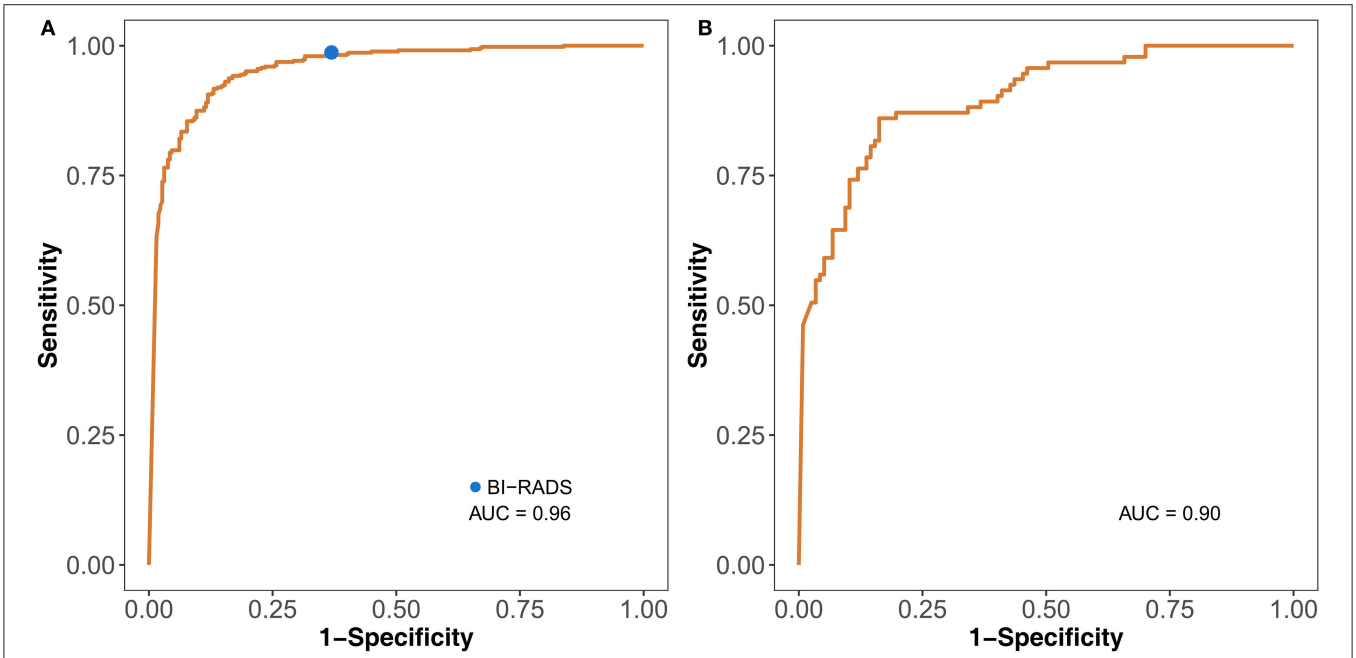

FIGURE 4 | Identification performance of the DLM on the test set **(A)** and external test set **(B)**. The blue dot on the left ROC curve indicates the performance of BI-RADS. DLM, deep learning model; ROC, receiver operating characteristic; BI-RADS, Breast Imaging Reporting and Data System; AUC, area under the curve.

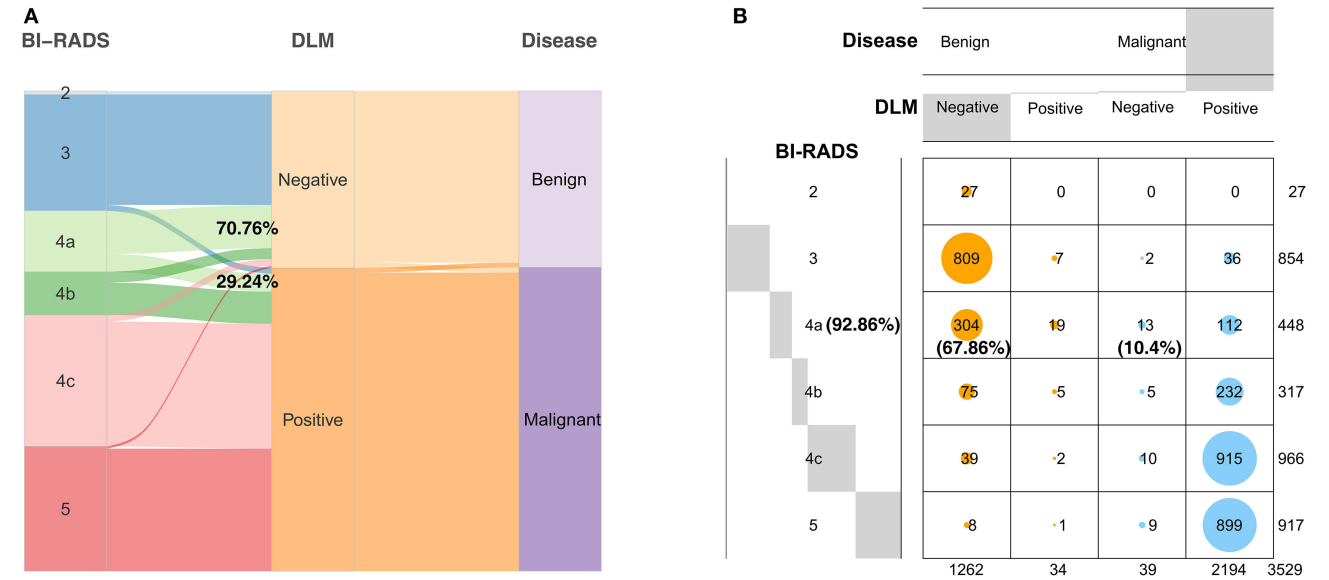

FIGURE 5 | Diagnostic results of the DLM for breast tumors with different BI-RADS categorizations compared with the definitive pathological results. **(A)** The width of the extended branches corresponds to the size of the data; 70.76% represents the percentage of BI-RADS 4a patients diagnosed as benign by the DLM; 29.24% represents the percentage of BI-RADS 4a patients diagnosed as malignant by the DLM. **(B)** The numbers in this graph represent the number of images; 92.86% represents the diagnostic accuracy of BI-RADS 4a patients with the DLM; 67.86% represents the reduction rate of unnecessary biopsy in BI-RADS 4a patients with the DLM; 10.4% represents the false negative rate of BI-RADS 4a patients with the DLM. Negative means the diagnosis of the DLM is benign. Positive means the diagnosis of the DLM is malignant. DLM, deep learning model; BI-RADS, Breast Imaging Reporting and Data System.

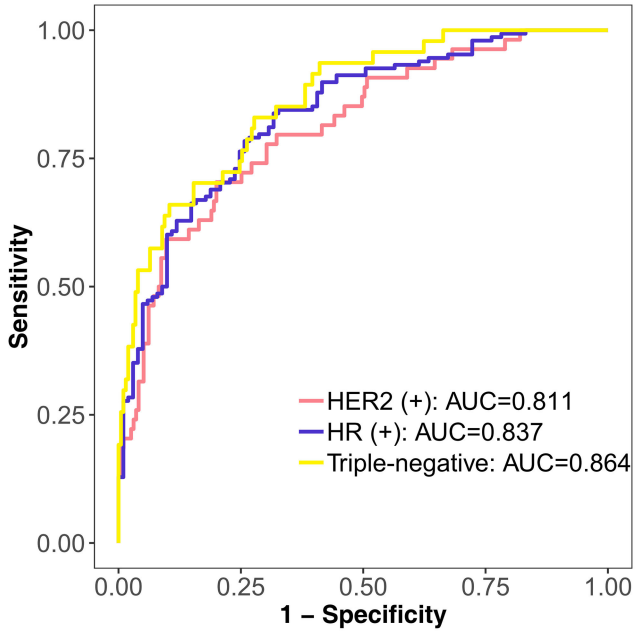

FIGURE 6 | Performance of the DLM in identifying different molecular subtypes with triple classification on the test set. HER2 (+) subtype = HR (+) HER2 (+) or HR (–) HER2 (+); HR (+) subtype = HR (+) HER2 (–); triple-negative subtype = HR (–) HER2 (–). DLM, deep learning model; HER2, human epidermal growth factor receptor 2; HR, hormone receptor.

after comparison. The purpose of these studies was to develop only a DLM for the classification of malignant and benign masses (25–29). In our study, we sought to develop a DLM not only for classifying masses but also for reducing unnecessary biopsy. Unnecessary biopsy was theoretically reduced by 67.86% with the DLM in BI-RADS 4a patients. Zhu et al. (30) developed a DLM based on breast MRIs that showed some predictive value for molecular subtypes. However, these researchers only considered the distinction between the luminal A subtype and all other subtypes. Unlike their model, our model can differentiate each molecular subtype and guide individualized treatment. To the best of our knowledge, this is the first study to apply a DLM to the prediction of molecular subtypes using ultrasound images.

The DLM is better than traditional methods in identifying benign and malignant breast tumors. It performs well with high AUC values and other indicators and reduces the burden of radiologists (31). DLMs do not require time-consuming tumor boundary labeling, which is a necessary step for traditional methods. In addition, the DLM can make better use of the hidden information around the tumor, which is ignored by traditional methods.

Currently, most studies use statistical analysis to obtain low-dimensional features of breast ultrasound images for molecular classification. These low-dimensional features are easily affected by the number and quality of the samples collected, making it difficult to mine and quantify the relationships between images and subtypes (32). However, deep learning methods can extract

abstract features. All extracted features are high-dimensional features related to molecular classification. Although difficult to visualize, molecular classification is important and can greatly improve recognition accuracy.

There are limitations in our study. First, the training set data came from one hospital, and we did not summarize the basic information on patients and tumors. Second, regardless of the training, test or external test sets, the sample size was small. Thus, these results need to be validated with a larger cohort to determine the value of our model in clinical practice. Third, because the study was retrospective, all patients underwent surgical treatment. However, there are many women who have a BI-RADS categorization with certain malignant potential who choose observation instead of surgical treatment. This factor may be one of the reasons why our study did not achieve a better result.

CONCLUSION

We demonstrated that our DLM can recognize breast tumors and predict molecular subtypes with high accuracy based solely on ultrasound images, which may make DLM an effective alternative to clinical biopsy. It is necessary to cooperate with other institutions to expand the dataset to better confirm our model and make it an important decision-making tool with great potential in clinical application.

DATA AVAILABILITY STATEMENT

The original contributions presented in the study are included in the article/**Supplementary Material**, further inquiries can be directed to the corresponding author/s.

ETHICS STATEMENT

This study was approved by the Institutional Review Board of Harbin Medical University Cancer Hospital. Because of its retrospective nature, the written informed consent of patients was exempted.

AUTHOR CONTRIBUTIONS

XZ, YaZ, HM, and DP conceived and designed the study. WC, HJ, SL, and JH collected the clinical and imaging data. HL, JL, and YL performed image preprocessing. XZ, CW, YuZ, DL, YaZ, HM, and DP performed the data interpretation and the statistical analysis. All authors approved the final manuscript.

FUNDING

This work was supported by the National Natural Science Foundation of China (82073410), Heilongjiang Province Applied Technology Research and Development (GA20C016), and the Haiyan Research Foundation (JJZD2020-08).

SUPPLEMENTARY MATERIAL

The Supplementary Material for this article can be found online at: https://www.frontiersin.org/articles/10.3389/fonc.2021.623506/full#supplementary-material

REFERENCES

1. Fan L, Strasser-Weippl K, Li JJ, St Louis J, Finkelstein DM, Yu KD, et al. Breast cancer in China. *Lancet Oncol.* (2014) 15:e279–89. doi: 10.1016/S1470-2045(13)70567-9
2. Bray F, Ferlay J, Soerjomataram I, Siegel RL, Torre LA, Jemal A. Global cancer statistics 2018: GLOBOCAN estimates of incidence and mortality worldwide for 36 cancers in 185 countries. *CA Cancer J Clin.* (2018) 68:394–424. doi: 10.3322/caac.21492
3. Nie K, Su MY, Chau MK, Chan S, Nguyen H, Tseng T, et al. Age- and race-dependence of the fibroglandular breast density analyzed on 3D MRI. *Med Phys.* (2010) 37:2770–6. doi: 10.1118/1.3426317
4. Li E, Guida JL, Tian Y, Sung H, Koka H, Li M, et al. Associations between mammographic density and tumor characteristics in Chinese women with breast cancer. *Breast Cancer Res Treat.* (2019) 177:527–36. doi: 10.1007/s10549-019-05325-6
5. Zhou C, He J, Li J, Fan J, Zhang B, Yang H, et al. A nation-wide multicenter 10-year (1999-2008) retrospective clinical study of endocrine therapy for Chinese females with breast cancer. *PLoS One.* (2014) 9:e100159. doi: 10.1371/journal.pone.0100159
6. Leong SP, Shen ZZ, Liu TJ, Agarwal G, Tajima T, Paik NS, et al. Is breast cancer the same disease in Asian and Western countries? *World J Surg.* (2010) 34:2308–24. doi: 10.1007/s00268-010-0683-1
7. Zhang X, Zhao W, Wei W, You Z, Ou X, Sun M, et al. Parallel analyses of somatic mutations in plasma circulating tumor DNA (ctDNA) and matched tumor tissues in early-stage breast cancer. *Clin Cancer Res.* (2019) 25:6546–53. doi: 10.1158/1078-0432.CCR-18-4055
8. LeCun Y, Bengio Y, Hinton G. Deep learning. *Nature.* (2015) 521:436–44. doi: 10.1038/nature14539
9. Zhou D, Tian F, Tian X, Sun L, Huang X, Zhao F, et al. Diagnostic evaluation of a deep learning model for optical diagnosis of colorectal cancer. *Nat Commun.* (2020) 11:2961. doi: 10.1038/s41467-020-16777-6
10. Song Y, Zhang YD, Yan X, Liu H, Zhou M, Hu B, et al. Computer-aided diagnosis of prostate cancer using a deep convolutional neural network from multiparametric MRI. *J Magn Reson Imaging.* (2018) 48:1570–7. doi: 10.1002/jmri.26047
11. Wang CJ, Hamm CA, Savic LJ, Ferrante M, Schobert I, Schlachter T, et al. Deep learning for liver tumor diagnosis part II: convolutional neural network interpretation using radiologic imaging features. *Eur Radiol.* (2019) 29:3348–57. doi: 10.1007/s00330-019-06214-8
12. Xiong H, Lin P, Yu JG, Ye J, Xiao L, Tao Y, et al. Computer-aided diagnosis of laryngeal cancer via deep learning based on laryngoscopic images. *EBioMedicine.* (2019) 48:92–9. doi: 10.1016/j.ebiom.2019.08.075
13. Pang S, Yu Z, Orgun MA. A novel end-to-end classifier using domain transferred deep convolutional neural networks for biomedical images. *Comput Methods Programs Biomed.* (2017) 140:283–93. doi: 10.1016/j.cmpb.2016.12.019
14. Perou CM, Sorlie T, Eisen MB, van de Rijn M, Jeffrey SS, Rees CA, et al. Molecular portraits of human breast tumours. *Nature.* (2000) 406:747–52. doi: 10.1038/35021093
15. Wu T, Li J, Wang D, Leng X, Zhang L, Li Z, et al. Identification of a correlation between the sonographic appearance and molecular subtype of invasive breast cancer: a review of 311 cases. *Clin Imaging.* (2019) 53:179–85. doi: 10.1016/j.clinimag.2018.10.020

16. Celebi F, Pilanci KN, Ordu C, Agacayak F, Alco G, Ilgun S, et al. The role of ultrasonographic findings to predict molecular subtype, histologic grade, and hormone receptor status of breast cancer. *Diagn Interv Radiol.* (2015) 21:448–53. doi: 10.5152/dir.2015.14515
17. Zhang L, Li J, Xiao Y, Cui H, Du G, Wang Y, et al. Identifying ultrasound and clinical features of breast cancer molecular subtypes by ensemble decision. *Sci Rep.* (2015) 5:11085. doi: 10.1038/srep11085
18. Ko ES, Lee BH, Kim HA, Noh WC, Kim MS, Lee SA. Triple-negative breast cancer: correlation between imaging and pathological findings. *Eur Radiol.* (2010) 20:1111–17. doi: 10.1007/s00330-009-1656-3
19. Irshad A, Leddy R, Pisano E, Baker N, Lewis M, Ackerman S, et al. Assessing the role of ultrasound in predicting the biological behavior of breast cancer. *AJR Am J Roentgenol.* (2013) 200:284–90. doi: 10.2214/AJR.12.8781
20. Boisserie-Lacroix M, Macgrogan G, Debled M, Ferron S, Asad-Syed M, McKelvie-Sebileau P, et al. Triple-negative breast cancers: associations between imaging and pathological findings for triple-negative tumors compared with hormone receptor-positive/human epidermal growth factor receptor-2-negative breast cancers. *Oncologist.* (2013) 18:802–11. doi: 10.1634/theoncologist.2013-0380
21. Chollet F. Xception: deep learning with depthwise separable convolutions. In: *2017 IEEE Conference on Computer Vision and Pattern Recognition (CVPR).* Honolulu, HI (2017).
22. Li X, Zhang S, Zhang Q, Wei X, Pan Y, Zhao J, et al. Diagnosis of thyroid cancer using deep convolutional neural network models applied to sonographic images: a retrospective, multicohort, diagnostic study. *Lancet Oncol.* (2019) 20:193–201. doi: 10.1016/S1470-2045(18)30762-9
23. Wang S, Wang R, Zhang S, Li R, Fu Y, Sun X, et al. 3D convolutional neural network for differentiating pre-invasive lesions from invasive adenocarcinomas appearing as ground-glass nodules with diameters </=3 cm using HRCT. *Quant Imaging Med Surg.* (2018) 8:491–9. doi: 10.21037/qims.2018.06.03
24. He Y, Guo J, Ding X, van Ooijen PMA, Zhang Y, Chen A, et al. Convolutional neural network to predict the local recurrence of giant cell tumor of bone after curettage based on pre-surgery magnetic resonance images. *Eur Radiol.* (2019) 29:5441–51. doi: 10.1007/s00330-019-06082-2
25. Moon WK, Lee YW, Ke HH, Lee SH, Huang CS, Chang RF. Computer-aided diagnosis of breast ultrasound images using ensemble learning from convolutional neural networks. *Comput Methods Programs Biomed.* (2020) 190:105361. doi: 10.1016/j.cmpb.2020.105361
26. Tanaka H, Chiu SW, Watanabe T, Kaoku S, Yamaguchi T. Computer-aided diagnosis system for breast ultrasound images using deep learning. *Phys Med Biol.* (2019) 64:235013. doi: 10.1088/1361-6560/ab5093
27. Cao Z, Yang G, Chen Q, Chen X, Lv F. Breast tumor classification through learning from noisy labeled ultrasound images. *Med Phys.* (2020) 47:1048–7. doi: 10.1002/mp.13966
28. Zhou Y, Xu J, Liu Q, Li C, Liu Z, Wang M, et al. A radiomics approach with CNN for shear-wave elastography breast tumor classification. *IEEE Trans Biomed Eng.* (2018) 65:1935–42. doi: 10.1109/TBME.2018.2844188
29. Weiss N, Kost H, Homeyer A. Towards interactive breast tumor classification using transfer learning. In: *International Conference Image Analysis and Recognition*. Cham: Springer (2018). p. 727–36.
30. Zhu Z, Albadawy E, Saha A, Zhang J, Harowicz MR, Mazurowski MA. Deep learning for identifying radiogenomic associations in breast cancer. *Comput Biol Med.* (2019) 109:85–90. doi: 10.1016/j.compbiomed.2019.04.018
31. Xiao T, Liu L, Li K, Qin W, Yu S, Li Z. Comparison of transferred deep neural networks in ultrasonic breast masses discrimination. *Biomed Res Int.* (2018) 2018:4605191. doi: 10.1155/2018/4605191
32. Boisserie-Lacroix M, Bullier B, Hurtevent-Labrot G, Ferron S, Lippa N, Mac Grogan G. Correlation between imaging and prognostic factors: molecular classification of breast cancers. *Diagn Interv Imaging.* (2014) 95:227–33. doi: 10.1016/j.diii.2013.12.013

Conflict of Interest: The authors declare that the research was conducted in the absence of any commercial or financial relationships that could be construed as a potential conflict of interest.

frontiers in Oncology

ORIGINAL RESEARCH
published: 05 March 2021
doi: 10.3389/fonc.2021.627158

Feasibility and Clinical Value of CT-Guided ^{125}I Brachytherapy for Pain Palliation in Patients With Breast Cancer and Bone Metastases After External Beam Radiotherapy Failure

Jian He[1†], Qicong Mai[1†], Fangfang Yang[2], Wenhang Zhuang[1], Qing Gou[1], Zejian Zhou[1], Rongde Xu[1], Xiaoming Chen[1] and Zhiqiang Mo[1*]*

[1] Department of Interventional Radiology, Guangdong Provincial People's Hospital, Guangdong Academy of Medical Sciences, Guangzhou, China, [2] Department of Medical Simulation Center, Guangdong Provincial People's Hospital, Guangdong Academy of Medical Sciences, Guangzhou, China

Objectives: To evaluate the feasibility and clinical value of CT-guided iodine-125 (^{125}I) brachytherapy for pain palliation in patients with breast cancer and bone metastases after external beam radiotherapy failure.

Methods: From January 2014 to July 2016, a total of 90 patients, who had received the standard therapies for bone metastases but still suffered moderate-to-severe pain, were retrospectively studied. About 42 patients were treated with both ^{125}I brachytherapy and bisphosphonates (Group A), and 48 patients were treated with bisphosphonates alone (Group B).

Results: In Group A, 45 ^{125}I brachytherapy procedures were performed in 42 patients with 69 bone metastases; the primary success rate of ^{125}I seed implantation was 92.9%, without severe complications. Regarding pain progression of the two groups, Group A exhibited significant relief in "worst pain," "least pain," "average pain," and "present pain" 3-day after treatment and could achieve a 12-week-remission for "worst pain," "least pain," "average pain," and "present pain." The morphine-equivalent 24-h analgesic dose at 3 days, 4 weeks, 8 weeks, and 12 weeks was 91 ± 27, 53 ± 13, 31 ± 17, and 34 ± 12 mg for Group A, and 129 ± 21, 61 ± 16, 53 ± 15, and 105 ± 23 mg for Group B. Group A experienced a lower incidence of analgesic-related adverse events and better quality of life than Group B.

Conclusion: The CT-guided ^{125}I brachytherapy is a feasible and an effective treatment for the palliation of pain caused by bone metastases from breast cancer after external beam radiotherapy failure.

Keywords: iodine-125, brachytherapy, palliative medicine, bone neoplasms, breast neoplasms

OPEN ACCESS

Edited by:
Fu Wang,
Xi'an Jiaotong University, China

Reviewed by:
Zhanwang Xiang,
Third Affiliated Hospital of Sun Yat-sen University, China
Athanasios G. Zafeirakis,
Army Share Fund Hospital (NIMTS), Greece
Rui Gao,
The First Affiliated Hospital of Xi'an Jiaotong University, China

***Correspondence:**
Xiaoming Chen
chenxiaoming@gdph.rog.cn
Zhiqiang Mo
mozhiqiang@gdph.org.cn

[†] These authors have contributed equally to this work

Specialty section:
This article was submitted to Cancer Imaging and Image-directed Interventions, a section of the journal Frontiers in Oncology

Received: *08 November 2020*
Accepted: *04 February 2021*
Published: *05 March 2021*

Citation:
He J, Mai Q, Yang F, Zhuang W, Gou Q, Zhou Z, Xu R, Chen X and Mo Z (2021) Feasibility and Clinical Value of CT-Guided ^{125}I Brachytherapy for Pain Palliation in Patients With Breast Cancer and Bone Metastases After External Beam Radiotherapy Failure. Front. Oncol. 11:627158. doi: 10.3389/fonc.2021.627158

INTRODUCTION

Approximately 65–75% of patients with advanced breast cancer develop bone metastases (1), which may cause skeletal-related events (SREs), such as bone pain, pathological fracture, and hypercalcemia (2). Of these events, bone pain is the earliest symptom that conspicuously decreases the quality of life of patients (1). Thus, pain palliation is the primary therapeutic goal in the management of bone metastases.

Chemotherapy and endocrine therapy are the currently used common baseline treatments for patients with advanced breast cancer and bone metastases (3). Nevertheless, previous studies have shown that such systemic therapies achieve limited long-term bone pain relief (4). Consequently, the loco-regional treatment is used to supplement systemic therapies. The external beam radiation therapy (EBRT) is the most effective local treatment for pain palliation, reportedly achieving remission in up to 60% of patients (2). In some patients, the prescribed the EBRT dose is limited when the bone metastases are adjacent to vital organs such as the spinal cord (5); therefore, the pain relief effect could be compromised. For patients with relapsing pain, bisphosphonates in combination with analgesics are needed to manage the response of the body to the pain. However, when patients receive high dosages of analgesics for pain control, dose-related adverse effects increase significantly, and the quality of life of patients is not improved (1). Radiofrequency ablation effectively and promptly achieves pain palliation in patients with bone tumors (6). However, the ablation has a critical limitation: The ablation margin cannot be visualized or monitored by CT. Thus, the ablation of vertebral bone tumors can cause intra- or post-procedural injury to the spinal cord within the ablation zone (7).

Previous studies have confirmed that iodine-125 (^{125}I) brachytherapy has advantages in regard to disease control in patients with solid tumors (8, 9). Thus, ^{125}I brachytherapy might be effective in bone pain palliation in patients with breast cancer after the failure of EBRT; however, few reports have evaluated ^{125}I brachytherapy in these patients. The purpose of our study was to evaluate the feasibility and clinical value of CT-guided ^{125}I brachytherapy for pain palliation in patients with bone metastases from breast cancer.

MATERIALS AND METHODS

Cohort and Sample Selection

In this retrospective study, we used data from patients with breast cancer and bone metastases who experienced moderate-to-severe pain. The radiological assessment of bone metastases includes enhanced CT, PET/CT, and radionuclide bone imaging. There were two groups in this study. Group A ($n = 42$) was treated with both ^{125}I brachytherapy and bisphosphonates, and Group B ($n = 48$) was treated with bisphosphonates alone. This study was approved by The Ethics Committee of the Guangdong Provincial People's Hospital.

All patients in the study underwent attempts to manage their pain using chemotherapy, endocrine therapy, molecular-targeted therapy, or EBRT but did not achieve satisfactory pain relief. All enrolled patients met the following criteria: (a) underwent resection of primary tumors, which had been histologically diagnosed as breast cancer; (b) bone metastases were the only possible cause of pain; (c) score of at least four points on the "worst pain" item of the Brief Pain Inventory (BPI) in the 24 h prior to completing the inventory (10); (d) four or fewer metastatic lesions with diameter $\leq$5 cm; (e) expected lifespan $\geq$3 months; (f) the Karnofsky Performance Status Scale $\geq$50 (11); (g) no severe coagulation disorder [prothrombin activity <40% or platelet count $<5 \times 10(9)/L$]; and (h) the absence of spinal cord compression or impending fracture. Additionally, all patients had received high doses of analgesics for a period of more than 1 month.

^{125}I Seed

The radioactive ^{125}I seeds (Yunke Pharmaceutical, Sichuan, China) were cylindrical titanium packages being 0.8 mm in diameter and 4.5 mm in length. The central source of the particle was an ^{125}I radionuclide silver rod with a diameter of 0.5 mm and length of 3.0 mm. The matched peripheral dose was 100–140 Gy, and the average energy was 27–35 KeV. The radius of effective antitumor activity was 1.7 cm. Each seed had an initial activity of 0.0296 Gbq and a half-life of 59.6 days; about 93–97% of the brachytherapy dose was delivered within 3–5 months.

^{125}I Brachytherapy

Before ^{125}I seed implantation, 5-mm thick CT sections were obtained for all patients. A computerized treatment planning system (TPS) (BT-RSI; Beijing Atom and High Technique Industries) was used to create a treatment plan for each patient. The gross tumor volume, planned target volume (PTV), and the surrounding vital organs were carefully delineated in every CT slice. PTV was defined as a 0.5–1.0 cm extension around the gross tumor volume. According to the three orthogonal diameters within the targeted tumor site and a prescribed matched peripheral dose, the TPS calculated the position of the brachytherapy applicator and the number of seeds to be implanted (**Figures 1A,B**); then, the TPS generated a dose-volume histogram that includes the isodose curves of different targets. According to the guideline of American Brachytherapy Society, the prescribed dose of the planned target was an average of 120 Gy (100–140 Gy) (12). The dose received by the surrounding organs was based on normal tissue constraint guidelines. The PTV edge accounted for 70–90% of the isodose curve; thus, 95% of the prescribed dose covered the PTV.

On the day of the procedure, patients were positioned on the CT gantry and were evaluated to locate the lesion site(s). Several 5-mm axial slices were obtained to delineate the upper and lower borders of the tumors. After achieving anesthesia with local infiltration of 5–15 ml of 1% lidocaine (Liduokayin; Yimin), an 18 G spinal needle (Yunke Pharmaceutical, Sichuan, China) was inserted into the farthest tumor edge, ∼5 mm

Abbreviations: ^{125}I, iodine-125; BPI-SF, brief pain inventory-short form; CT, computed tomography; PTV, planned target volume; SREs, skeletal-related events; TPS, treatment planning system; PET/CT, positron emission tomography-computed tomography.

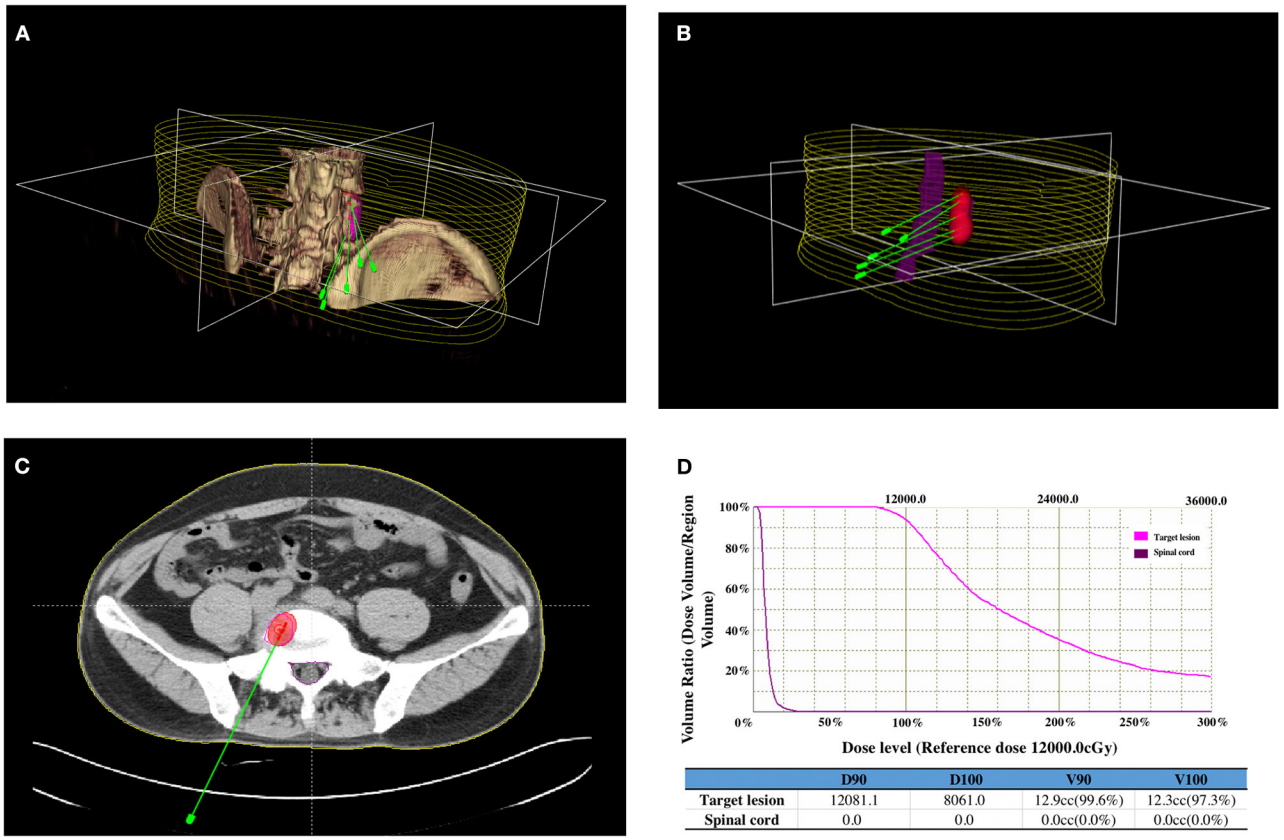

	D90	D100	V90	V100
Target lesion	12081.1	8061.0	12.9cc(99.6%)	12.3cc(97.3%)
Spinal cord	0.0	0.0	0.0cc(0.0%)	0.0cc(0.0%)

FIGURE 1 | Iodine-125 (^{125}I) brachytherapy treatment plan for bone metastases from breast cancer: **(A)** CT images of the lesion were reconstructed using a computerized treatment planning system (TPS), and the position of the brachytherapy applicators was calculated. **(B)** Three-dimensional image showing the relationship between the positions of the applicators, lesions, and spinal cord. **(C)** Two-dimensional image showing the irradiation dose (red area) of the ^{125}I brachytherapy field, tumor contour (purple line), and spinal cord (green line). **(D)** Dose-volume histogram indicating the prescribed dose to the lesion and the dose received by the spinal cord.

or less from the tumor border. A clip implant gun (Yunke Pharmaceutical, Sichuan, China) was then attached to the applicator for implantation. The ^{125}I seeds were released from deep to superficial while retracting the needle and keeping adjacent ^{125}I seeds at a distance of 5–15 mm. CT was performed after completing the implantation to identify any post-procedural complications and to verify that the position and intensity of the ^{125}I seeds were in accordance with the TPS (**Figures 1C,D**). If the lesion showed insufficient radioactivity, the procedure was repeated to implant additional ^{125}I seeds.

Follow-Up and Evaluation Criteria

The BPI short-form (BPI-SF) (a validated visual analog scale with the score ranging from 0 to 10) was completed by each patient to obtain a measure of pain intensity (worst pain, least pain, average pain, and present pain) and pain interference (with the seven health-related quality of life dimensions: general activity, mood, walking, normal work, social activities, sleep quality, and life satisfaction). Patients completed the BPI- SF by the assistance of a study coordinator who was familiar with focal painful metastases. When multiple metastases were treated in one patient, the response was recorded for the painful area that was mostly treated. The BPI-SF was administered pre- and post-procedure. All patients underwent dynamic enhanced CT and clinical hematological examinations within 3–5 weeks after the procedure to evaluate the safety and efficacy of the therapy. The percentage of intra- and post-procedural complications was recorded according to the Toxicity Criteria of the Radiation Therapy Oncology Group (13).

Statistical Analysis

Statistical analyses were performed using SPSS version 25.0 statistical software (IBM Corp.). Values are presented as the mean ± SD. We compared the characteristics of patients using the Pearson's chi-squared test. Statistical significance was set at $p < 0.05$. For pain palliation analyses, patients were analyzed according to their groups. Changes from baseline in the BPI-SF score were analyzed using the analysis of covariance with the treatment group and randomization stratification parameters as factors and the baseline value as a covariate. Pain palliation endpoints were analyzed using a step-down approach, in which the primary and secondary endpoints were tested sequentially

TABLE 1 | Clinical characteristics of the patients and tumors.

Characteristic	Group A	Group B	*p*
	n = 42	*n* = 48	
Age, years			**0.517**
Mean age (y ± SD)	54 ± 7	51 ± 8	
Range	36–63	33–69	
Site of bone metastases			**0.770**
Thoracic/lumbar vertebra	27	31	
Iliac/ischium/pubic bones	7	9	
Rib/chest wall	5	3	
Other	3	5	
Lesion diameter			**0.846**
≤2	21	25	
>2, ≤4	17	20	
>4	4	3	
Metastases numbers			**0.969**
1	19	21	
2	20	24	
≥3	3	3	
Type of bone metastases			**0.970**
Osteolytic	21	23	
Osteoplastic	13	16	
Mixed	8	9	
Radiological assessment			**0.862**
Enhanced CT	30	33	
PET/CT	9	10	
Radionuclide bone imaging	3	5	
History of treatment			**0.714**
Chemotherapy alone	14	18	
Endocrine therapy alone	9	12	
Combination therapy	19	18	

p, p-value; SD, standard deviation; PET/CT, Positron Emission Tomography-Computed Tomography.

to preserve the family-wise type I error rate using the following order: 12 weeks, 8 weeks, 4 weeks, and 3 days with the BPI-SF score (worst pain, least pain, average pain, and present pain). The BPI-SF score of worst pain at 12 weeks was defined as a primary endpoint. Each hypothesis was tested at a significance level of 0.05 (two-sided). Statistical significance at each step was required to test the next hypothesis.

RESULTS

Characteristics of Patients

In Group A, a total of 45 ^{125}I brachytherapy procedures were performed by experienced radiologists in 42 patients with 69 bone metastases. Thirty-nine (92.9%) of the 42 patients met the TPS criteria after the first procedure. Three patients who did not meet the TPS criteria received additional implantations. The final ^{125}I brachytherapy achievement rate was 97.6% (41/42 patients), and the total number of implanted seeds was 1,410, with an average of 20 ± 6 seeds per lesion (range: 10–35). As shown in **Table 1**, Groups A and B did not significantly differ in any clinicopathological variables.

Palliation of Bone Pain

Pre-Therapy (T_0) Pain Evaluation

The BPI-SF score for pain intensity is summarized in **Table 2**. There was no statistical difference in the mean score for "worst pain," "least pain," "average pain," and "present pain" at T_0 between Groups A and B.

Pain Evaluation 3 Days (T_1) After Therapy

In Group A, the score for "worst pain," "least pain," "average pain," and "present pain" was decreased at 3 days after therapy. In Group B, there were no changes in the score for all pain intensities during T_0 and T_1. There was a significant difference in the score for "worst pain," "least pain," "average pain," and "present pain" between Groups A and B at T_1, as shown in **Table 2**.

Pain Evaluation 4 Weeks (T_2), 8 Weeks (T_3), and 12 Weeks (T_4) After Therapy

In comparison with T_0, the score for "worst pain," "present pain," "average pain," and "least pain" was falling from T_2 to T_4 in Groups A and B. Regarding the pattern of pain remission, Group A achieved a continuous decline in the score for all pain intensity indices from T_2 to T_4, whereas Group B showed a reduction in the score from T_2 to T_3 and then rebounded at T_4. There were statistical differences in the score for all pain intensity indices between Groups A and B at T_4, and no statistical differences in the score for all pain intensity indices between Groups A and B at T_2 and T_3, as shown in **Table 2**.

Prescribed Dose and Adverse Reactions to Analgesics

The prescribed dose (morphine-equivalent 24-h dose) of analgesics is shown in **Table 2**. At T_0, there was no significant difference in the baseline of mean morphine-equivalent 24-h dose between Groups A and B ($p = 0.261$). In addition to patients experiencing pain relief, the mean morphine-equivalent 24-h dose of Group A was decreased gradually from T_0 to T_4, whereas that of Group B was decreased from T_0 to T_3 and rebounded at T_4. In both groups, there were statistical differences in the mean morphine-equivalent 24-h dose at T_1 and T_4, but no statistical differences in the mean morphine-equivalent 24-h dose at T_2 and T_3.

The incidence of adverse reactions (AEs) to analgesics is summarized in **Table 3**. As patients in Groups A and B received different dosages of analgesics, the incidence of AE or serious AE (SAE) in Group A was significantly lower than that of in Group B.

Domains of Interference by Pain

The score for interference by bone pain in daily life is summarized in **Table 4**. In addition to patients experiencing pain relief, the score on general activity, mood, sleep, normal work, and enjoyment of life was increased in both groups. However, the score for all domains shows a significant greater improvement in Group A as compared to Group B.

TABLE 2 | Pain-related variables and score from different therapy strategies.

BPI-SF scores	T_0		*p*	T_1		*p*	T_2		*p*	T_3		*p*	T_4		*p*
	Group A	Group B		Group A	Group B		Group A	Group B		Group A	Group B		Group A	Group B	
Worst pain			**0.067**			**0.021**			**0.071**			**0.197**			**0.028**
Mean scores	7 ± 0.5	7 ± 0.8		5 ± 0.4	7 ± 0.5		3 ± 0.6	4 ± 0.4		3 ± 0.2	3 ± 0.6		3 ± 0.5	6 ± 0.7	
Range	6–8	5–8		3–6	5–8		3–5	3–6		2–5	2–6		2–5	5–7	
Least pain			**0.131**			**0.039**			**0.191**			**0.063**			**0.015**
Mean scores	4 ± 0.7	4 ± 0.9		3 ± 0.7	5 ± 0.2		2 ± 0.5	3 ± 0.3		2 ± 0.6	3 ± 0.6		2 ± 0.4	4 ± 0.2	
Range	3–5	3–6		2–5	3–6		1–3	2–4		1–3	2–4		1–3	3–5	
Average pain			**0.073**			**0.017**			**0.227**			**0.243**			**0.027**
Mean scores	6 ± 0.6	6 ± 0.4		4 ± 0.4	6 ± 0.4		3 ± 0.6	4 ± 0.3		3 ± 0.5	3 ± 0.5		3 ± 0.4	5 ± 0.8	
Range	5–7	5–7		5–7	5–7		2–4	3–6		2–4	2–4		2–5	4–7	
Present pain			**0.158**			**0.018**			**0.338**			**0.479**			**0.011**
Mean scores	6 ± 0.3	6±0.6		4 ± 0.8	6 ± 0.6		3 ± 0.3	4 ± 0.3		3 ± 0.5	3 ± 0.7		3 ± 0.5	5 ± 0.6	
Range	5–7	5–7		3–6	5–7		2–5	3–5		2–5	2–5		2–5	3–6	
Morphine-equivalent 24-h dose			**0.261**			**0.041**			**0.161**			**0.097**			**0.019**
Mean doses (mg)	136 ± 35	140 ± 29		91 ± 27	129 ± 21		53 ± 13	61 ± 16		31 ± 17	53 ± 15		34 ± 12	105 ± 23	
Range (mg)	100–180	100–180		65–120	95–160		35–70	40–75		30–65	35–75		30–65	75–135	

T_0, preoperatively; T_1, 3 days post-procedure; T_2, 4 weeks post-procedure; T_3, 8 weeks post-procedure; T_4, 12 weeks post-procedure; BPI-SF, brief pain inventory-short form, p, p-value.

Mean scores with standard deviation for points on "worst pain," "least pain," "average pain," and "present pain." The points were graded on a numeric scale ranging from 0 to 10.

TABLE 3 | Adverse reactions to analgesics from different therapy strategies.

Adverse reactions to analgesics	Group A		Group B	
	AE	SAE	AE	SAE
Fatigue	8 (19)	7 (17)	17 (35)	15 (31)
Nausea	9 (21)	6 (14)	15 (31)	13 (27)
Constipation	8 (19)	5 (12)	20 (42)	14 (29)
Vomiting	6 (14)	3 (7)	16 (33)	10 (21)
Dizzy	7 (17)	6 (14)	19 (40)	16 (33)

AE, adverse event; SAE, serious adverse event.

Data are shown as n (%).

Procedure-Related Complications

Procedure-related complications are summarized in **Table 5**. In Group A, the incidence of radiodermatitis, wound infection, and subcutaneous hematomas was 10, 5, and 14%, respectively. In four patients (10%), minor displacement of the ^{125}I seeds was found after tumor volume shrinkage. No severe complications, such as massive bleeding and vital organ radiation injury, occurred after ^{125}I brachytherapy.

DISCUSSION

Bone pain is the most common clinical symptom in patients with breast cancer and bone metastases (14). According to National Comprehensive Cancer Network guidelines, the aim of the treatment for these advanced stage patients is symptom relief rather than complete disease eradication (1).

Regional therapies for relieving pain are indicated. In clinical practice, radiotherapy due to its minimal invasion is preferred to surgical resection. A prospective clinical trial of 1,016 patients performed by the Radiation Therapy Oncology Group showed that single and multiple EBRT fractions provided equal palliation of bone pain caused by metastatic lesions and also showed that 53 and 83% of patients achieved complete pain relief and partial relief, respectively, with durable responses (ranging from 12 to 28 weeks) (15). Generally, the EBRT is promising in regard to pain palliation for most patients with breast cancer and bone metastases (16); however, in patients with a high burden of lesions and with unclear margins relative to vital organs, the role of EBRT in pain palliation might be compromised because of its less than optimal radiation dose to the lesion(s) (17). For patients with relapsing pain after receiving EBRT, bisphosphonates and personalized dosages of analgesics show the benefits in pain control, but the long-term effect was not satisfactory due to dose-related adverse effects.

In the present study, the main findings were that ^{125}I brachytherapy in combination with bisphosphonates provided more efficient pain control than bisphosphonates alone in patients with breast cancer and bone metastases after external beam radiotherapy failure. After 3 days of treatment, Group A showed a significant greater decrease in visual analog scale score for pain intensity as compared to Group B, especially for "worst pain," "worst on average," and "present pain." We suggest that this may be because ^{125}I seeds provide a cytocidal

TABLE 4 | Pain interference-related variables from different therapy strategies.

Domains of interference by pain	Group A			Group B			*p*
	BT	AT	IM	BT	AT	IM	
General activity	61 ± 15	79 ± 9	19 ± 10	59 ± 13	64 ± 11	7 ± 4	0.023
Mood	57 ± 9	80 ± 12	25 ± 7	61 ± 10	70 ± 9	8 ± 5	0.017
Sleep	51 ± 13	77 ± 15	28 ± 11	54 ± 7	69 ± 13	11 ± 7	0.039
Normal work	62 ± 7	85 ± 11	24 ± 7	59 ± 11	71 ± 9	9 ± 6	0.014
Enjoyment of life	59 ± 11	76 ± 13	19 ± 10	61 ± 12	69 ± 9	6 ± 3	0.027

BT, before treatment; AT, after treatment; IM, improvement; p, p-value.
Mean scores with standard deviation for pain interference as "general activity," "mood," "sleep," "normal work," and "enjoyment of life." Pain interference scores were graded on a numeric scale ranging from 0 to 100.

effect without causing radioedema by continuously emitting low doses of X- and γ-rays (18). During the study, we found that patients who received ^{125}I brachytherapy in combination with bisphosphonates achieved up to 12 weeks of pain control, even with lower doses of analgesics. This result may be related to the fact that ^{125}I seeds have a long half-life of 59.6 days and could deliver 110–160 Gy during decay (12). Because the irradiation diameter of the ^{125}I seeds is 1.7 cm, the surrounding vital organs received a less than lethal dose of irradiation, even when the prescribed dose of ^{125}I brachytherapy was up to 160 Gy (19). Our findings suggested that ^{125}I brachytherapy might play a good role as ablation therapy, analogous to stereotactic ablative radiotherapy (20), and our results showed that the incidence of analgesic-related adverse events of Group A were significantly lower than that of Group B. As a result, patients experienced a better quality of life and could be well-treated as close to home as possible. At the end of follow-up, we observed the pain recurrence mainly due to the attenuation of ^{125}I radiation. In this case, the second ^{125}I brachytherapy should be considered. ^{125}I brachytherapy was a feasible treatment modality for bone metastases in this study, with a success rate of up to 97.6%. According to disease progression, we could implant the ^{125}I seeds to the same or other lesions after the first treatment cycle without increasing the risk of complications (21). In this study, TPS was used to plan ^{125}I seed implantation in accordance with the American Brachytherapy Society guidelines (more than 95% of the tumor receives 100% of the prescribed dose) (12). During the procedure, CT guidance clearly showed the implant volume and location of vital organs, allowing ^{125}I seed implantation to be as accurate as planned. However, we found that it was not easy to manually puncture osteoplastic lesions with brachytherapy applicators, which decreased the accuracy of ^{125}I seed implantation and increased the intensity of intra-procedure pain. We believe that a robotic technique for ^{125}I seed implantation would improve the procedural performance.

How do our findings affect clinical practice? We found that ^{125}I brachytherapy could achieve 12-week pain control and a high quality of life in patients with breast cancer and bone metastases after the failure of the EBRT. When the pain recurrence due to the attenuation of ^{125}I radiation, we could repeat ^{125}I brachytherapy without technique difficulty, which implies that the currently available approaches probably have the cytocidal effect in bone metastases, leading to the regression of pain. To draw definite conclusions, the mechanism of ^{125}I seed on killing bone metastases cancer cell to relieve pain is needed. In addition, other reported studies on ^{125}I brachytherapy have an advantage in local control for different malignant tumors (8, 9). We did not observe a significant lesion progression after 12-week post-^{125}I brachytherapy (data not shown). This may be explained by the modality of radiation release of ^{125}I seed. We should argue the role of ^{125}I brachytherapy in the regional control of bone metastases and the prevention of SREs in a long-term follow-up study.

TABLE 5 | ^{125}I brachytherapy-related complications.

Complication	Group A (*n* = 42)	
	n	%
Radiodermatitis	4	10
Wound infection	2	5
Small amount of subcutaneous haematoma	6	14
Massive bleeding	0	0
Minor displacement of ^{125}I seed	4	10
Vital organ radiation injures	0	0

Our findings should be considered in the context of the limitations of this study. This was a retrospective study with a small sample size. Large sample sizes are needed to confirm our results. Further studies should also aim to study the optimal dose of ^{125}I brachytherapy and the clinical benefit of treatment in regard to the prevention of SRE, progression-free survival, and overall survival.

In conclusion, the results of our study demonstrated the effectiveness of CT-guided ^{125}I brachytherapy in pain palliation for patients with breast cancer and bone

metastases after the failure of the EBRT. After CT-guided ^{125}I brachytherapy, patients achieved a 12-week extension in pain palliation, which resulted in less analgesic consumption, shorter hospitalization, and a better quality of life.

CONCLUSION

CT-guided ^{125}I brachytherapy is a feasible and an effective treatment for the palliation of pain caused by bone metastases from breast cancer after external beam radiotherapy failure.

DATA AVAILABILITY STATEMENT

The raw data supporting the conclusions of this article will be made available by the authors, without undue reservation.

ETHICS STATEMENT

The Ethics Committee of the Guangdong Provincial People's Hospital approved our study.

AUTHOR CONTRIBUTIONS

JH, QM, and XC conceived and designed the study. JH, XC, and ZM performed all of the ^{125}I brachytherapy procedures. JH, FY, and QM analyzed the data and drafted the manuscript. WZ, QG, and ZZ were the study coordinators. RX and WZ constructed the ^{125}I brachytherapy treatment plans. All authors read and approved the final manuscript.

ACKNOWLEDGMENTS

We are grateful to all staff and patients who supported this clinical study.

REFERENCES

1. Dixmerias F, Palussiere J. [Management of painful bone metastases]. *J Radiol.* (2011) 92:796–800. doi: 10.1016/j.jradio.2011.07.012
2. Cleeland CS, Body JJ, Stopeck A, von Moos R, Fallowfield L, Mathias SD, et al. Pain outcomes in patients with advanced breast cancer and bone metastases: results from a randomized, double-blind study of denosumab and zoledronic acid. *Cancer.* (2013) 119:832–8. doi: 10.1002/cncr.27789
3. Wilcken N, Hornbuckle J, Ghersi D. Chemotherapy alone versus endocrine therapy alone for metastatic breast cancer. *Cochrane Database Syst Rev.* (2003) 2003:CD002747. doi: 10.1002/14651858.CD002747
4. Luftner D, Niepel D. Breast cancer and bone metastases: a call for appropriate treatment. *Support Care Cancer.* (2016) 24:4075–7. doi: 10.1007/s00520-016-3335-7
5. Falivene S, Pezzulla D, Di Franco R, Giugliano FM, Esposito E, Scoglio C, et al. Painful bone metastasis in elderly treated with radiation therapy: single- or multiple-fraction regimen? A multicentre retrospective observational analysis. *Aging Clin Exp Res.* (2017) 29(Suppl. 1):143–7. doi: 10.1007/s40520-016-0671-x
6. Di Staso M, Zugaro L, Gravina GL, Bonfili P, Marampon F, Di Nicola L, et al. A feasibility study of percutaneous radiofrequency ablation followed by radiotherapy in the management of painful osteolytic bone metastases. *Eur Radiol.* (2011) 21:2004–10. doi: 10.1007/s00330-011-2133-3
7. Kastler A, Krainik A, Sakhri L, Mousseau M, Kastler B. Feasibility of real-time intraprocedural temperature control during bone metastasis thermal microwave ablation: a bicentric retrospective study. *J Vasc Interv Radiol.* (2017) 28:366–71. doi: 10.1016/j.jvir.2016.09.030
8. Mo Z, Zhang T, Zhang Y, Xiang Z, Yan H, Zhong Z, et al. Feasibility and clinical value of CT-guided (125)I brachytherapy for metastatic soft tissue sarcoma after first-line chemotherapy failure. *Eur Radiol.* (2018) 28:1194–203. doi: 10.1007/s00330-017-5036-0
9. Xiang Z, Li G, Liu Z, Huang J, Zhong Z, Sun L, et al. 125I brachytherapy in locally advanced nonsmall cell lung cancer after progression of concurrent radiochemotherapy. *Medicine.* (2015). 94:e2249. doi: 10.1097/MD.0000000000002249
10. Majedi H, Dehghani SS, Soleyman-Jahi S, Emami Meibodi SA, Mireskandari SM, Hajiaghababaei M, et al. Validation of the Persian version of the brief pain inventory (BPI-P) in chronic pain patients. *J Pain Symptom Manage.* (2017) 54:132–8.e2. doi: 10.1016/j.jpainsymman.2017.02.017
11. de Kock I, Mirhosseini M, Lau F, Thai V, Downing M, Quan H, et al. Conversion of Karnofsky Performance Status (KPS) and Eastern Cooperative Oncology Group Performance Status (ECOG) to Palliative Performance Scale (PPS), and the interchangeability of PPS and KPS in prognostic tools. *J Palliat Care.* (2013) 29:163–9. doi: 10.1177/082585971302900305
12. Horwitz EM, American Brachytherapy S. ABS brachytherapy consensus guidelines. *Brachytherapy.* (2012) 11:4–5. doi: 10.1016/j.brachy.2011.12.006
13. Ladue T, Klein MK, Veterinary Radiation Therapy Oncology G. Toxicity criteria of the veterinary radiation therapy oncology group. *Vet Radiol Ultrasound.* (2001) 42:475–6. doi: 10.1111/j.1740-8261.2001.tb00973.x
14. Ibrahim T, Mercatali L, Amadori D. A new emergency in oncology: bone metastases in breast cancer patients (review). *Oncol Lett.* (2013) 6:306–310. doi: 10.3892/ol.2013.1372
15. Rordorf T, Hassan AA, Azim H, Alexandru E, Er O, Gokmen E, et al. Bone health in breast cancer patients: a comprehensive statement by CECOG/SAKK Intergroup. *Breast.* (2014) 23:511–25. doi: 10.1016/j.breast.2014.05.023
16. Cai B, Nickman NA, Gaffney DK. The role of palliative external beam radiation therapy in boney metastases pain management. *J Pain Palliat Care Pharmacother.* (2013) 27:28–34. doi: 10.3109/15360288.2012.757267
17. Andrade RS, Proctor JW, Slack R, Marlowe U, Ashby KR, Schenken LL. A simple and effective daily pain management method for patients receiving radiation therapy for painful bone metastases. *Int J Radiat Oncol Biol Phys.* (2010) 78:855–9. doi: 10.1016/j.ijrobp.2009.09.002
18. Saito S, Yagi Y, Nishiyama T, Nakamura K, Toya K, Yorozu A. Brachytherapy with permanent seed implantation. Int *J Clin Oncol.* (2007). 6:395–407. doi: 10.1007/s10147-007-0710-x
19. Chiu-Tsao ST, Schaart DR, Soares CG, Nath R, No ATPCTG. Dose calculation formalisms and consensus dosimetry parameters for intravascular brachytherapy dosimetry: recommendations of the AAPM Therapy Physics Committee Task Group No. 149. *Med Phys.* (2007). 34:4126–57. doi: 10.1118/1.2767184
20. Palma DA, Olson R, Harrow S, Gaede S, Louie AV, Haasbeek C, et al. Stereotactic ablative radiotherapy versus standard of care palliative treatment in patients with oligometastatic cancers (SABR-COMET): a randomised, phase 2, open-label trial. *Lancet.* (2019) 393:2051–8. doi: 10.1016/S0140-6736(18)32487-5
21. Gregory KJ, Pattison JE, Bibbo G. Measurement uncertainty analysis of low-dose-rate prostate seed brachytherapy: post-implant dosimetry. *Australas Phys Eng Sci Med.* (2015) 38:71–81. doi: 10.1007/s13246-014-0325-2

Conflict of Interest: The authors declare that the research was conducted in the absence of any commercial or financial relationships that could be construed as a potential conflict of interest.

frontiers in Oncology

ORIGINAL RESEARCH
published: 08 March 2021
doi: 10.3389/fonc.2021.614050

OPEN ACCESS

Edited by:
Jiefu Jin,
Johns Hopkins University, United States

Reviewed by:
Shanshan Tan,
Johns Hopkins University, United States
Nai-Kei Wong,
Shantou University, China
Yunmei Wang,
Shaanxi Provincial Cancer Hospital, China

***Correspondence:**
Guo-Jun Zhang
gjzhang@xah.xmu.edu.cn
Wen-He Huang
huangwenhe2009@163.com
Li-Ming Nie
limingnie@gmail.com

†Present address:
Zun Wang,
Department of Breast and Thyroid Surgery, Shenzhen Baoan Women's and Children's Hospital, Jinan University, Shenzhen, China
Li-Ming Nie,
Department of Radiology & Research Center of Medical Sciences, Guangdong Provincial People's Hospital, Guangdong Academy of Medical Sciences, Guangzhou, China

Specialty section:
This article was submitted to Cancer Imaging and Image-directed Interventions, a section of the journal Frontiers in Oncology

Received: *05 October 2020*
Accepted: *28 January 2021*
Published: *08 March 2021*

Citation:
Wang Z, Chen M, Liu J-J, Chen R-H, Yu Q, Wang G-M, Nie L-M, Huang W-H and Zhang G-J (2021) Human Serum Albumin Decorated Indocyanine Green Improves Fluorescence-Guided Resection of Residual Lesions of Breast Cancer in Mice. Front. Oncol. 11:614050. doi: 10.3389/fonc.2021.614050

Human Serum Albumin Decorated Indocyanine Green Improves Fluorescence-Guided Resection of Residual Lesions of Breast Cancer in Mice

Zun Wang[1†], Min Chen[2,3,4], Jing-Jing Liu[3,4,5], Rong-He Chen[6], Qian Yu[6], Gui-Mei Wang[7], Li-Ming Nie[6†], Wen-He Huang[5*] and Guo-Jun Zhang[1,3,4,5*]*

[1] ChangJiang Scholar's Laboratory, Medical College, Shantou University, Shantou, China, [2] Clinical Central Research Core, Xiang'an Hospital of Xiamen University, School of Medicine, Xiamen University, Xiamen, China, [3] Key Laboratory for Endocrine-Related Cancer Precision Medicine of Xiamen, Xiang'an Hospital of Xiamen University, Xiamen, China, [4] Cancer Research Center, School of Medicine, Xiamen University, Xiamen, China, [5] Cancer Center & Department of Breast and Thyroid Surgery, Xiang'an Hospital of Xiamen University, School of Medicine, Xiamen University, Xiamen, China, [6] State Key Laboratory of Molecular Vaccinology and Molecular Diagnosis & Center for Molecular Imaging and Translational Medicine, School of Public Health, Xiamen University, Xiamen, China, [7] Department of Pathology, Xiang'an Hospital of Xiamen University, School of Medicine, Xiamen University, Xiamen, China

Objective: Achieving negative resection margin is critical but challenging in breast-conserving surgery. Fluorescence-guided surgery allows the surgeon to visualize the tumor bed in real-time and to facilitate complete resection. We envisioned that intraoperative real-time fluorescence imaging with a human serum albumin decorated indocyanine green probe could enable complete surgical removal of breast cancer in a mouse model.

Methods: We prepared the probe by conjugating indocyanine green (ICG) with human serum albumin (HSA). *In vitro* uptake of the HSA-ICG probe was compared between human breast cancer cell line MDA-MB-231 and normal breast epithelial cell line MCF 10A. *In vivo* probe selectivity for tumors was examined in nude mice bearing MDA-MB-231-luc xenografts and the FVB/N-Tg (MMTV-PyMT) 634Mul/J mice model with spontaneous breast cancer. A positive-margin resection mice model bearing MDA-MB-231-luc xenograft was established and the performance of the probe in assisting surgical resection of residual lesions was examined.

Results: A significantly stronger fluorescence intensity was detected in MDA-MB-231 cells than MCF 10A cells incubated with HSA-ICG. *In vivo* fluorescence imaging showed that HSA-ICG had an obvious accumulation at tumor site at 24 h with tumor-to-normal tissue ratio of 8.19 ± 1.30. The same was true in the transgenic mice model. The fluorescence intensity of cancer tissues was higher than that of non-cancer tissues (58.53 ± 18.15 *vs* 32.88 ± 11.34). During the surgical scenarios, the residual tumors on the surgical bed were invisible with the naked eye, but were detected and resected with negative margin

under HSA-ICG guidance in all the mice (8/8). Recurrence rate among mice that underwent resection with HSA-ICG (0/8) was significantly lower than the rates among mice with ICG (4/8), as well as the control group under white light (7/7).

Conclusions: This study suggests that real-time *in vivo* visualization of breast cancer with an HSA-ICG fluorescent probe facilitates complete surgical resection of breast cancer in a mouse xenograft model.

Keywords: breast cancer, tumor margin, indocyanine green, fluorescence-guided surgery, human serum albumin

INTRODUCTION

Breast-conserving surgery (BCS) with adjuvant whole-breast radiation therapy is the standard care for early-stage breast cancer. Successful BCS involves removal of malignant tissues with enough surrounding normal breast tissues to ensure complete tumor excision (negative margin), while leaving enough normal tissues to preserve the breast and provide an aesthetically acceptable result. However, 20–40% patients show positive margins after BCS, leading to unwanted reoperation (1, 2). This causes patients' anxiety and suffering, which may also compromise aesthetic results and increase infection risks and healthcare costs. In addition, margin status is a key risk factor for local recurrence and a prognostic factor for overall survival after BCS (3). A meta-analysis based on 33 studies showed that positive margins were associated with a 2-fold higher risk of local recurrence than negative margins (4).

To identify the resection margins involved and perform immediate selective margin re-excision, intraoperative margin assessment techniques have been investigated. Established methods include frozen sectioning, imprint cytology, intraoperative ultrasound, and specimen mammography (5). However, all the above techniques have their own limitations to some extent. Frozen sectioning and imprint cytology often disrupt the surgical workflow and are labor-intensive and time-consuming (6). Anatomical imaging modalities such as intraoperative ultrasound and specimen mammography could provide instant feedback of margin status but lack diagnostic accuracy (7). So far, no technique has been universally adopted for intraoperative margin assessment to the best of our knowledge. Therefore, it is imperative to develop an ideal method to identify involved margins rapidly and accurately.

Molecular fluorescence imaging coupled with contrast agent introduces a promising technique to visualize the tumor lesion, which can delineate tumor margins against normal tissues. It could provide instant feedback during surgery and augment the visual range for surgeons. For example, fluorescence-guided surgery with 5-aminolevulinic acid could make more complete resections with malignant glioma, which also improves patient outcomes (8). Near-infrared fluorescence imaging, at wavelengths in the 700–900 nm range, is particularly promising because autofluorescence from native tissue is minimal in this range, allowing a high signal-to-background ratio (9). Indocyanine green (ICG) is the only near-infrared fluorescent dye approved by the U.S. Food and Drug Administration for intravenous injections in humans. Several studies reported that intraoperative ICG fluorescence could localize non-palpable or occult breast cancer lesion and guide its excision (10, 11). Studies in mouse models of breast cancer showed that ICG is superior to visual inspection and palpation for identifying retained tumor margins (12, 13). But in the clinical application for fluorescence-guided surgery, ICG seemed to be less reliable for identifying positive margins. The potential explanation is that ICG cannot bind to specific ligands within the target tumor but spread to peritumoral tissues (13).

It is desirable to engineer ICG that binds selectively to tumors by combining it with human serum albumin (HSA). HSA plays an active role in tumor nutrition and demonstrates an obvious increased uptake by solid tumors (14). The tumor targeting makes HSA a promising carrier for cancer bioimaging and drug delivery (15, 16). It has been reported that HSA-ICG nanoparticles can be successfully applied to photothermal and photodynamic therapy (17), and tumor diagnosis based on fluorescence imaging and photoacoustic imaging (18, 19) in the literature. In the present study, we focused on its performance in guiding surgical removal of breast cancer in a mouse model. ICG was conjugated with HSA as a contrast agent for fluorescence imaging of breast cancer. Then, we evaluated the tumor selectivity of the HSA-ICG probe *in vitro* and *in vivo*. We subsequently used a mice model of positive margin resection with MDA-MB-231-luc xenograft to investigate whether HSA-ICG fluorescence guidance could detect tumor deposits. Finally, we compared the local recurrence rate and overall survival rate after surgery with HSA-ICG fluorescence guidance or not.

MATERIALS AND METHODS

Preparation and Characterization of Human Serum Albumin-Indocyanine Green

ICG-NHS (Xinyan Bomei Bio, Xi'an, China) was conjugated to HSA (Solarbio, Beijing, China) using a previously published protocol with minor modifications (20). Briefly, HSA was incubated with ICG at a molar ratio of 1:5 in 0.1 M Na2HPO4 (pH 8.5) at room temperature for 2 h. The mixture was purified on a Sephadex G50 column (PD-10; GE Healthcare, Piscataway, USA). The morphology of the resulting HSA-ICG conjugate was observed by G2 F30 Twin transmission electron microscopy (FEI/TECNAI, Hillsboro, USA). The molecular weight of the conjugate was determined using SDS-PAGE and Coomassie Brilliant Blue

staining. Gels were scanned at 800 nm using the Odyssey CLx scanner (LI-COR Bio, Lincoln, USA) to determine the intactness of HSA-ICG. The absorption spectrum of the conjugate was measured using a spectrophotometer (Thermo Multiskan GO, Thermo Fisher Scientific, Waltham, USA). The fluorescence emission spectrum was obtained after excitation at 745 nm using a fluorimeter (TECAN SPARK, Mannedorf, Switzerland). Protein concentration of the samples was determined using bicinchoninic acid assay (Solarbio, Beijing, China). The concentration of ICG of the probe was also measured by absorption with the above spectrophotometer to calculate the number of fluorophores conjugated to HSA. The purified HSA-ICG probes were stored in 0.1M phosphate-buffered saline (PBS) at 4°C.

Cell Cultures

Human breast cancer cell line MDA-MB-231 and non-cancerous breast epithelial cell line MCF 10A were purchased from the American Type Culture Collection (Rockville, USA). The MDA-MB-231-luc cell line was purchased from ZQXZ Biotechnology (Shanghai, China). These cell lines were cultured according to the vendors' recommendations.

Uptake and Cytotoxicity of Human Serum Albumin-Indocyanine Green *In Vitro*

MDA-MB-231 cells were seeded in six-well plates at a density of 2×10^5 cells per well, and incubated overnight for cell attachment. Then the cells were treated with HSA-ICG (at a final ICG concentration of 10 μg/ml) alone or in the presence of excess HSA (10 mg/ml) for 8 h. Cells were collected at 1, 2, 4, and 8 h, washed with cold PBS (1–4°C). Then the signal intensity of HSA-ICG was measured by flow cytometry (BD, Franklin Lakes, USA).

To investigate whether HSA-ICG is selectively taken up by cancer cells, MDA-MB-231 cells or MCF 10A cells were seeded at a density of 1×10^5 cells per well and cultured for 24 h. Afterward, the cells were incubated in fresh medium containing HSA-ICG (10 μg/ml) at 37°C for 4 h. Cells were washed with cold PBS and then fixed in 4% paraformaldehyde and nuclei were stained with DAPI. The internalization of HSA-ICG was observed using a confocal laser scanning microscope (FV1000, Olympus, Tokyo, Japan).

Cytotoxicity of HSA-ICG against MDA-MB-231 cells was measured by incubating them for 24 h in the presence of the conjugate at concentrations of 1.25–40 μg/ml. The viability was measured using a standard CCK8 assay (Promega, Beijing, China).

Real-Time PCR Analysis of Secreted Protein, Acidic And Rich In Cysteine Expression

Total RNA of MDA-MB-231 cells and MCF 10A cells was extracted and reverse-transcribed using Takara kits (Takara, Beijing, China) according to the manufacturer's instructions. Real-time PCR was performed with SYBR Green qPCR Master Mix (Thermo Fisher Scientific, Waltham, USA) using a CFX96 Real-time PCR Detection System machine (Bio-Rad, Hercules, USA). SPARC primers were synthesized by Brogene Biotechnology (Xiamen, China). The primers for the amplification of SPARC were as follows: forward, 5'-TGAGGTATCTGTGGGAGCTAATC-3'; and reverse, 5'-CCTTGCCGTGTTTGCAGTG-3'. We normalized Ct values to those of beta-actin and calculated relative expression using the $2_{-\Delta\Delta Ct}$ method.

Xenograft Models and Fluorescence Imaging

Animal experiments were approved by the Institutional Animal Care and Use Committee of Xiamen University, which were conducted accordance to relevant guidelines. Female BALB/c nude mice (6 weeks old, Charles River Labs, Beijing, China) received subcutaneous injection of MDA-MB-231-luc cells (5×10^6) in the right hind limb. Tumor volume was calculated as $[\pi/6 \times \text{length} \times (\text{width})^2]$.

When tumor volume reached 80 mm^3, HSA-ICG at doses equivalent to 1 mg ICG per kg or free ICG at 1 mg/kg was injected through the tail vein (n = 3 for each group). Mice were anesthetized with 2% isoflurane and fluorescence was imaged *in vivo* using an IVIS Lumina II imaging system (Perkin Elmer, Waltham, USA) at different time points (0, 3, 6, 9, 12, 24, 36, 48, 72, 96, and 120 h) after injection. Blood samples were also collected to determine fluorescence signal using a fluorimeter (TECAN SPARK). *Ex vivo* imaging was conducted at 24 h to determine fluorescence in the heart, liver, spleen, lungs, kidneys, and tumor. Tumor-to-background ratio (TBR) was defined as the fluorescence intensity in the tumor divided by the intensity in the upper limb.

Fluorescence Imaging Using Human Serum Albumin-Indocyanine Green in a Mouse Model of Spontaneous Breast Cancer

FVB/N-Tg(MMTV-PyMT)634Mul/J mice (Jackson Laboratory) were used to model orthotopic breast cancer. These mice spontaneously developed invasive breast carcinoma at a mean age of 53 days (21). At 7–9 weeks old, 10 mice were injected with HSA-ICG (1 mg/kg) through the tail vein. Twenty-four hours later, the combined 4^{th} and 5^{th} mammary glands (n = 20) were divided into four quadrants, each quadrant of the gland was removed sequentially. Fluorescence images of the mice were obtained before and after removal of each quadrant of the gland. All resected tissues were also analyzed by fluorescence imaging and histology. The latter was performed by an experienced pathologist according to mammary pathology of genetically engineered mice as described (22). The gland tissues were diagnosed as malignant or not based on histology. At last we correlated the pathology results with the fluorescence images of the resected tissues.

Establishment of a Positive-Margin Resection Model

Mice bearing MDA-MB-231-luc tumors of 600–700 mm^3 underwent resection under 2% isoflurane anesthesia. To establish a positive-margin resection model, 95% of the tumor mass was resected using a blunt dissection technique under white light (23). Then all the surgical bed was examined independently by two investigators. The mice were excluded if residual tumor

was visible to the naked eye. At the same time, all the mice were examined to confirm the presence of residual tumor by bioluminescence imaging with 150 mg/kg D-luciferin (Perkin Elmer, Waltham, USA) *via* intraperitoneal administration. All the remaining animals thought to be disease-free were then scanned using the hand-held near-infrared imaging system.

Residual Breast Cancer Tissue Resection Under the Human Serum Albumin-Indocyanine Green Fluorescence Guidance

At 24 h prior to surgery, the mice were received an intravenous injection of HSA-ICG (1 mg/kg of ICG, n = 10). Fluorescence imaging of tumor was performed prior to surgery using a hand-held near-infrared imaging system (Mingde Biotech, Langfang, China) with filters of 760/30 nm for excitation and 820/20 nm for emission. When the positive-margin resection model was established, two mice were excluded because of the visible residual tumor and eight remaining mice were used for the next surgery. Tissues with high fluorescence signals in the tumor bed were removed. Then, standard pathological procedures were used to determine whether residual foci exist in the resected fluorescence tissues with free margin. In addition, a margin of remaining nonfluorescent tissue was also removed and processed as control. Margins were defined as positive if tumor cells extended to the outside surface of the resected tissue.

Fluorescence Imaging of Specimen

After excision of the specimen, *ex vivo* imaging was performed with the hand-held near-infrared imaging system. Then, all the specimen was fixed in formalin and embedded in paraffin blocks and made into10-μm-thick tissue sections. We scanned the slides using the Odyssey CLx scanner (LI-COR Bio, Lincoln, USA). Microscopic assessment of the slides derived from HSA-ICG fluorescence signal was made to demonstrate the tracer distribution at a cellular level.

Fluorescence Image Analysis Related to Fluorescence-Guided Surgery

Intraoperative fluorescence images were recorded at three predefined time points: before the operation, before and after removal of tissue with fluorescence signals. Fluorescence images of specimens and slides were also recorded. Heatmap were created based on gray-scaled fluorescence images using MATLAB (MathWorks, Natick, USA). Fluorescence images as well as the regions of interest representing different tissue components were imported into ImageJ (National Institutes of Health, USA). Mean fluorescence intensity (MFI) was measured in arbitrary units for tumor and normal tissue *in vivo*, *ex vivo* and at tissue slice. TBR was defined as the MFI of tumor tissues divided by the MFI of surrounding normal tissues.

In addition, tumor lysates from mice that underwent fluorescence-guided surgery were analyzed by SDS-PAGE to confirm the presence of HSA-ICG in the tumor. The gel was scanned using the Odyssey CLx scanner at 800 nm.

Local Recurrence and Survival After the Fluorescence-Guided Surgery

During the fluorescence-guided surgery, HSA-ICG or free ICG (1 mg/kg) or saline as control was injected 24 h before the operation (n = 10 per group). After the establishment of positive-margin resection model, all the residual tumor mice (eight in the HSA-ICG group, eight in the ICG group, seven in control group) undergone fluorescence-guided surgery. After the surgery, mice were returned to their home cages. Local recurrence was observed every 2 days for 2 weeks and survival for 5 weeks. Mice were euthanized if weight loss exceeded 20% or recurrence tumor volume reached 1,500 mm^3.

Evaluation on Biosafety of Human Serum Albumin-Indocyanine Green

Healthy female FVB/NCrl mice (4–6 weeks old, Xiamen University) were randomly divided into two groups (n = 15 for each group). Mice in the HSA-ICG group received the injection of HSA-ICG probe (6 mg ICG per kg), while mice in the control group received the injection of saline solution. The mice were sacrificed on days 1, 7, and 30 (n = 5 per time point) to collect blood samples and major organs (heart, liver, spleen, lung, and kidney). The blood samples were measured for serum biochemical markers, including aspartate aminotransferase, alanine aminotransferase, albumin, total protein, total bilirubin, creatinine, and blood urea nitrogen. The major organs were stained with hematoxylin and eosin for histological analysis. During the observation period, the weight of the mice (n = 5) in each group was recorded every other day.

Statistical Analysis

We used GraphPad Prism 7.0b (GraphPad Software Inc., San Diego, USA) for statistical analyses. Quantitative results were presented as mean ± standard deviation. Differences among more than two groups were assessed for significance using one-way ANOVA followed by the Duncan multiple comparisons test. Differences between two groups were assessed using the Student's *t* test. Inter-group differences in postoperative recurrence and overall survival were assessed using the log-rank test. A two-sided P value of less than 0.05 was considered to be statistically significant.

RESULTS

Human Serum Albumin-Indocyanine Green Characterization

Negative staining of transmission electron microscopy images revealed that the diameters of HSA and HSA-ICG were 5.38 ± 0.92 and 5.69 ± 0.82 nm, respectively (**Figure S1A**). Thus, the conjugation of ICG to HSA almost had no effect on the overall size. The apparent molecular weight of HSA-ICG was only slightly higher than that of HSA, and SDS-PAGE did not detect any substantial aggregates of HSA (**Figure S1B**). Furthermore, fluorescence scanning showed that the fluorescence signal coincided with the location of HSA-ICG on the gel, while free ICG was located at the bottom of the gel

(**Figure S1B**). This indicated that the HSA-ICG conjugate was stable and did not dissociate during SDS-PAGE. ICG alone and HSA-ICG showed similar absorption peaks (788 *vs* 795 nm) and fluorescence emission peaks (820–825 nm) (**Figures S1C, D**). The slight red shift in absorption (~7 nm) further suggest the successful conjugation of ICG to HSA. The purified HSA-ICG conjugate was estimated to contain 3.5 ICG per 1 HSA.

Uptake of Human Serum Albumin-Indocyanine Green *In Vitro*

Fluorescence signals in MDA-MB-231 cells detected increased when incubated with HSA-ICG probes for 1, 2, 4, or 8 h, while the signals decreased when excess HSA was added (**Figure 1A**). This suggested that MDA-MB-231 cells internalized HSA-ICG in a time-dependent manner, the process of which was weakened in the presence of excess HSA. Quantitatively, the mean fluorescence intensity was significantly higher in HSA-ICG treated cells than in HSA-ICG treated cells with HSA blocking at selected time points (**Figure 1B**, one-way ANOVA, $P < 0.05$). Moreover, the probe mainly localized in the cytoplasm of MDA-MB-231 cells. On the contrary, normal breast epithelial MCF 10A cells internalized little HSA-ICG (**Figure 1C**). Relative mRNA expression of SPARC was significantly higher in breast cancer MDA-MB-231 cells than in human breast epithelial cells (**Figure S2**, unpaired Student's *t* test, $P < 0.05$).

In Vivo and *Ex Vivo* Fluorescence Imaging

When mice received ICG alone, the fluorescence signal appeared primarily in liver 3 h post-injection, but it was detected mainly in liver and tumor at 48 h, albeit considerably weaker. In contrast, the HSA-ICG fluorescence signal retained in the body for a longer time, as shown by a gradual increase that finally peaked at the tumor site at about 24 h (**Figures 2A, B**). *Ex vivo* fluorescence images of dissected organs and tumors 24 h post-injection confirmed that most free ICG accumulated in the liver, whereas enhanced fluorescent signals could be detected in liver, kidney, and tumor of HSA-ICG treated mice (**Figures 2C, D**). Compared with ICG-treated mice, blood from HSA-ICG treated mice showed significantly higher fluorescence intensity within 72 h after injection (**Figure 2E**). Furthermore, TBR reached the peak at 24 h in HSA-ICG treated mice, significantly higher than in ICG-treated mice (8.19 ± 1.30 *vs* 3.87 ± 0.68, unpaired Student's *t* test, $P < 0.05$) (**Figure 2F**, **Figure S3**).

Human Serum Albumin-Indocyanine Green Imaging in a Mouse Model of Spontaneous Breast Cancer

Fluorescence imaging was performed before and after surgical resection of breast tissue in a mouse model of spontaneous breast cancer (**Figures 3A, B**). Resected samples (n = 80) were also examined histologically (**Figure 3C**) and classified as non-

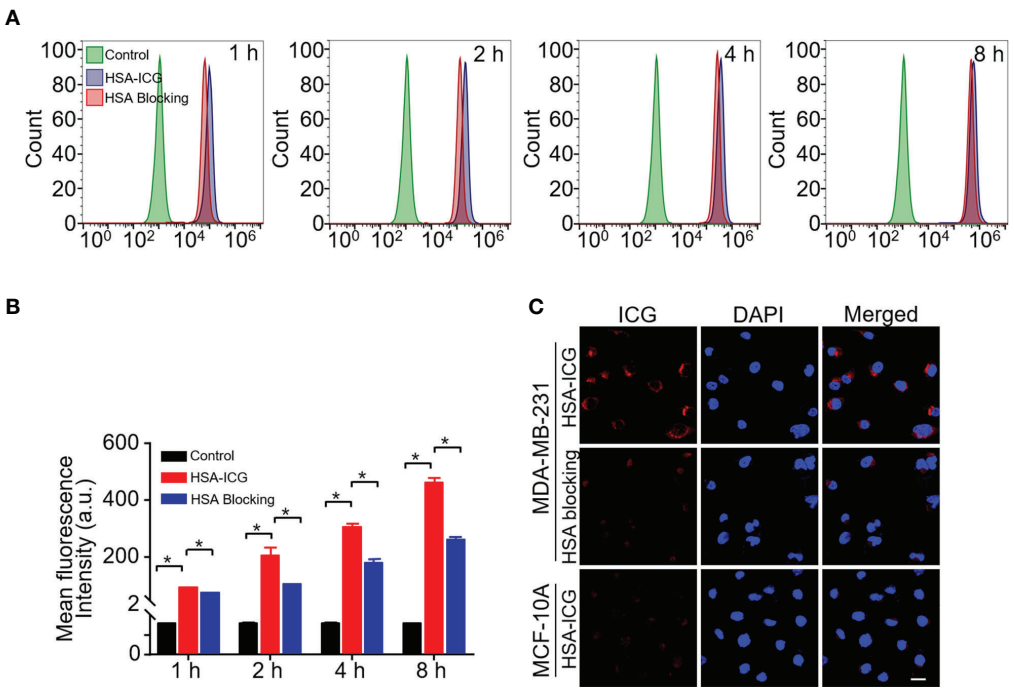

FIGURE 1 | Cell uptake of HSA-ICG. **(A)** Histogram showing flow cytometry based on fluorescence in MDA-MB-231 cells incubated for 1, 2, 4, or 8 h with HSA-ICG (10 μg/ml) alone or in the presence of excess HSA (10 mg/ml). **(B)** Mean fluorescence intensity from the flow cytometry in panel A at selected time points (n = 3, one-way ANOVA, *$P < 0.05$). **(C)** Confocal laser scanning micrographs of MDA-MB-231 and MCF 10A after 4 h incubation with HSA-ICG. Scale bar = 20 μm.

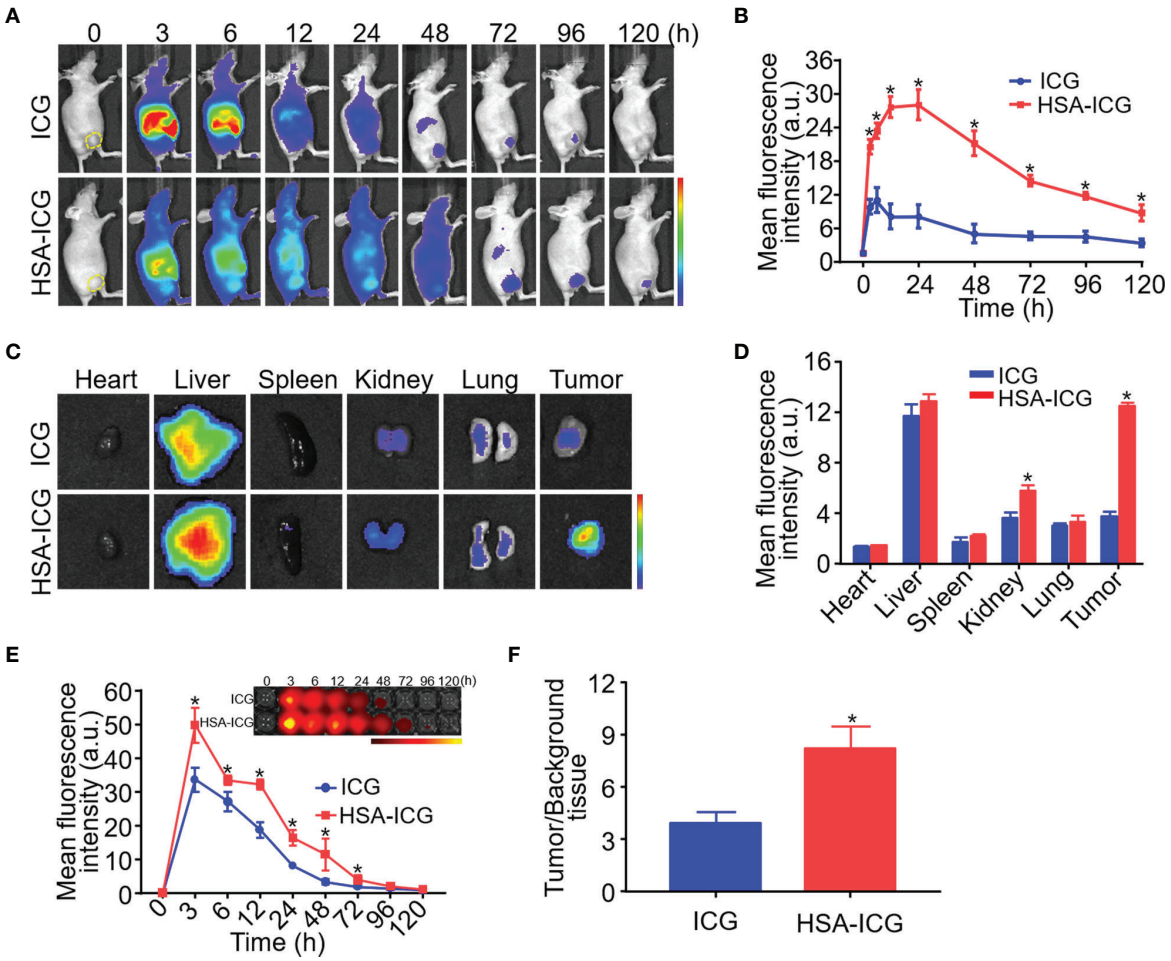

FIGURE 2 | *In vivo* and *ex vivo* fluorescence imaging of HSA-ICG in MDA-MB-231 tumor-bearing mice. **(A)** *In vivo* fluorescence images at indicated time points after intravenous injection of ICG or HSA-ICG (1 mg ICG per kg). Tumor tissue is delineated with a dashed line in the "0" images at far left. **(B)** Semi-quantitative analysis of *in vivo* fluorescence intensity of tumors. **(C)** Fluorescence images from organs and tumors excised 24 h after the injection of ICG or HSA-ICG. **(D)** Semiquantitative analysis of fluorescence signals from the samples in panel **(C)**. **(E)** Fluorescence images (inset) and semiquantitative analysis of fluorescence in blood sampled at different times after intravenous injection of the probe. **(F)** Tumor-to-background tissue ratios obtained at 24 h after injection of HSA-ICG or ICG. Background tissue was from the upper limb. Each group n = 3, (unpaired Student's *t* test, $^*P < 0.05$).

cancerous (n = 57) or cancerous (n = 23). The fluorescence intensity of all the samples were assessed in each mouse (**Figure 3D**). MFI of cancerous tissue was significantly higher than that of non-cancerous tissue (58.53 ± 18.15 *vs* 32.88 ± 11.34, unpaired Student's *t* test, $P < 0.05$) (**Figure 3E**).

Residual Breast Cancer Resection Guided by Human Serum Albumin-Indocyanine Green Fluorescence

We established a residual tumor model using MDA-MB-231-luc tumor-bearing mice whose xenografts were missed during surgery under white light alone. We confirmed the presence of tumor deposits in the tumor bed by bioluminescence (**Figure 4A**). Next, following the guidance of real-time fluorescence imaging, we observed the aggregated fluorescent signal in the tumor bed. Subsequently, the tissues with high fluorescence signal (**Figure 4B**) were resected and postoperative pathology examination validated the presence of cancer foci (**Figure 4C**). The fluorescence images obtained after the excision process indicated the removal of tissues with high fluorescence signal on the surgical bed (**Figure 4D**). Histology of tissues from the area confirmed the absence of residual tumors (**Figure 4E**).

Quantitative Analysis of Human Serum Albumin-Indocyanine Green Fluorescence Imaging During Surgery

Intraoperative and postoperative fluorescence images were analyzed to determine the ability of HSA-ICG in fluorescence-guided surgery for residual disease resection (**Figures 5A–J**) as recommended (24). The MFI were significantly higher for tumor tissues than surrounding normal tissues both *in vivo* (54.93 ± 13.37 *vs* 22.25 ± 3.32, paired Student's *t* test, $P < 0.05$, TBR 2.45 ± 0.36) and *ex vivo*

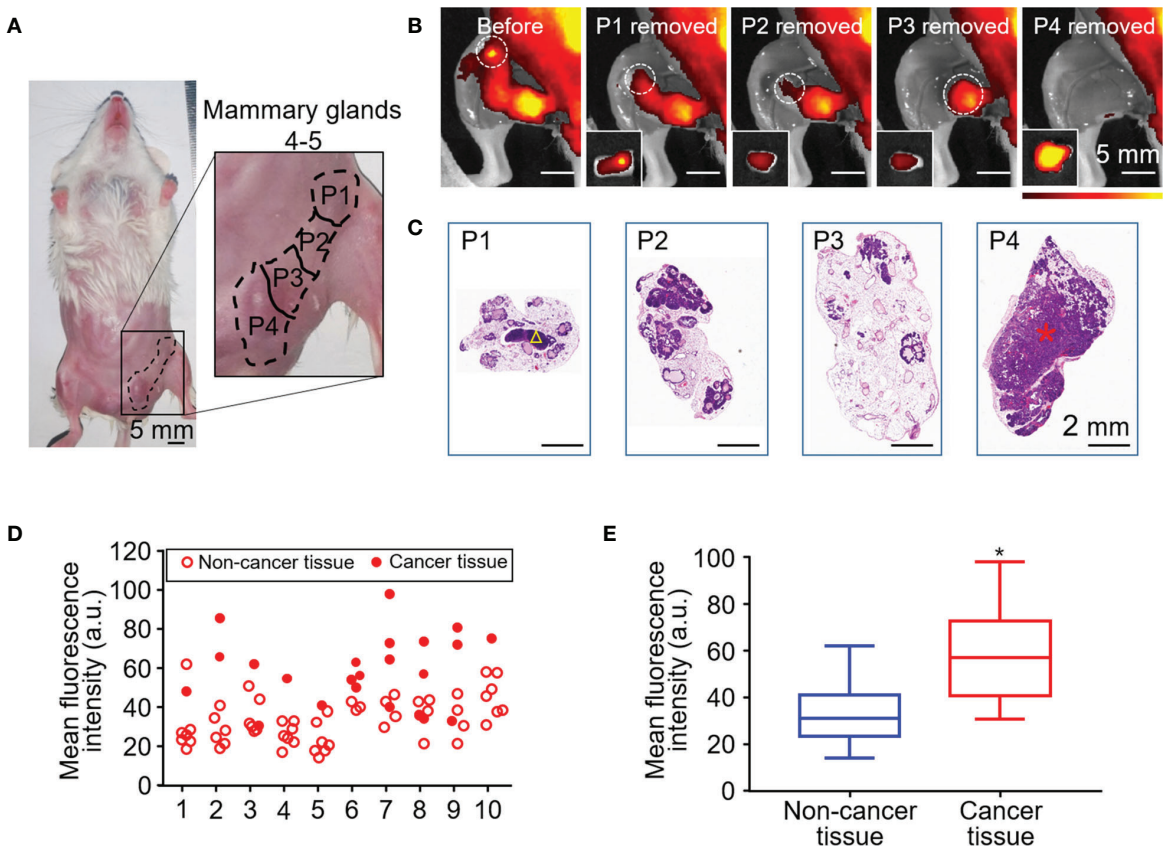

FIGURE 3 | HSA-ICG fluorescence imaging in a mouse model of spontaneous breast cancer. **(A)** Picture of mammary glands 4 and 5 divided into four approximately equal quadrants (P1–4), which were resected sequentially 24 h after the injection of HSA-ICG (1 mg/ml). **(B)** Representative fluorescence images before resection (leftmost) and after each sequential resection. Tissues resected (P1–4) are marked in white circles, and the corresponding *ex vivo* fluorescence images of excised tissues are shown as *insets* on the lower left. **(C)** Histological examination of resected pieces (P1–4), corresponding to the fluorescence images in panel **(B)** A yellow triangle in P1 marks a lymph node; a red asterisk in P4, a cancer lesion. **(D)** The fluorescence intensity distribution of the resected mammary gland tissues (P1–P4) in every case (n = 10). **(E)** Mean fluorescence intensity of 23 resected cancer tissues and 57 non-cancer tissues pooled from the 10 mice in panel **(D)** (unpaired Student's *t* test, $^*P < 0.05$).

(111.68 ± 12.59 *vs* 16.20 ± 2.54, paired Student's *t* test, $P < 0.05$, TBR 7.03 ± 1.27) (**Figures 5K, L**). This demonstrates that fluorescence imaging *ex vivo* can also be a useful diagnostic test to confirm successful removal. Histology of tissue sections confirmed significantly higher MFI in tumors than normal tissues (60.03 ± 20.88 *vs* 15.13 ± 7.94, paired Student's *t* test, $P < 0.05$, TBR 4.50 ± 1.45) (**Figure 5M**). Analysis of tumor lysates confirmed that the HSA-ICG conjugate was intact in tumor tissue (**Figure S4**).

Tumor-Free Surgical Margins Following Resection With Human Serum Albumin-Indocyanine Green Guidance

During the guidance of HSA-ICG fluorescent probes, there were multiple sites of fluorescence adjacent to a single tumor bed. A total of 12 such sites in eight animals were detected and resected, and confirmed by histology to be cancerous. Diameters of tumor foci on the slices of resected tissues (n = 12) ranged from 1.16 to 3.37 mm (mean, 2.19 mm). Histology showed that the margins of tissues resected under fluorescence guidance were tumor-free (**Figure 6A**), and that no residual tumor was detectable in the resected surgical bed in any of the eight animals (**Figure 6B**).

Decreased Local Recurrence and Improved Overall Survival With Human Serum Albumin-Indocyanine Green Guided Surgery

Next, local recurrence and overall survival was observed to assess the effectiveness of HSA-ICG fluorescence imaging. Until 2 weeks after surgery, none of the eight HSA-ICG-treated animals showed local recurrence, compared to 50% of the ICG-treated mice (4/8) and all seven control mice (**Figure 7A**). Overall survival differed in the same way across the three groups: 75% of the HSA-ICG-treated animals (6/8) survived within 5 weeks after operation, compared to only 25% of the ICG-treated animals (2/8) (**Figure 7B**). All control mice died from residual disease within 30 days after surgery. The HSA-ICG group showed significantly better overall survival than the control group (log-rank test, $^* P < 0.05$) and a trend of better survival compared with the ICG group.

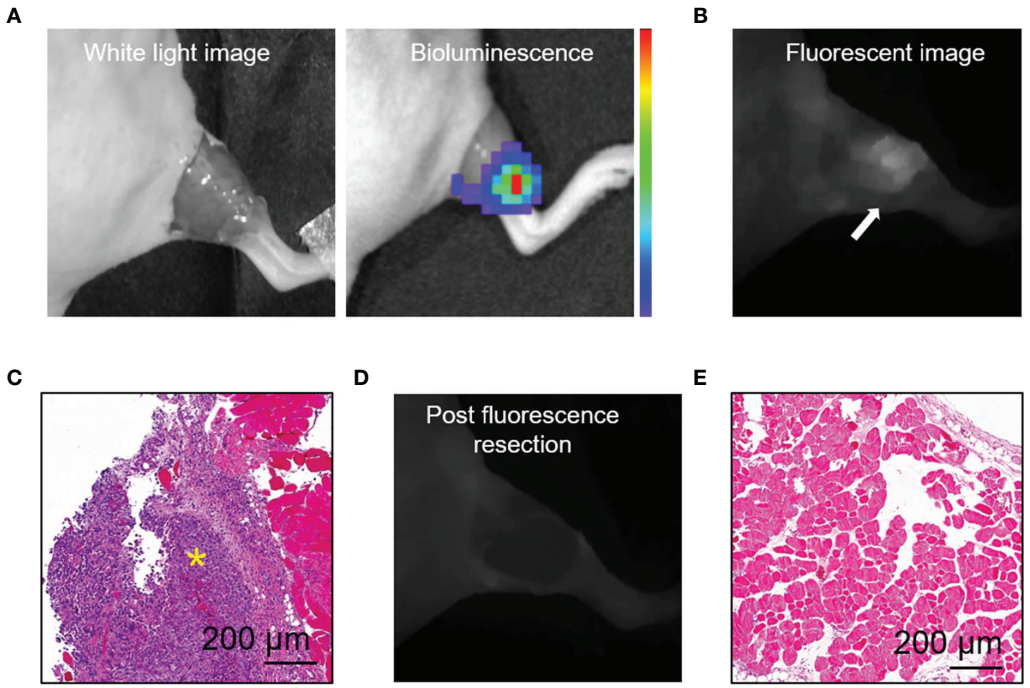

FIGURE 4 | HSA-ICG enabled fluorescence-guided resection of residual lesions in MDA-MB-231-luc tumor-bearing mice. **(A)** Establishment of the model of positive-margin resection. The residual cancer was not clearly seen by the unaided eye (left), and was confirmed by bioluminescence imaging (right). **(B)** Fluorescence image of the tumor bed showed residual cancer undetectable by white light. **(C)** Hematoxylin and eosin staining of the resected tissue from **(B)**. A yellow asterisk marks the tumor. **(D)** Fluorescent image of the tumor bed following fluorescence-guided resection, indicating the absence of fluorescence signal. **(E)** Tissues on the tumor bed from **(D)** were collected and examined histologically to confirm the absence of residual tumor.

Human Serum Albumin-Indocyanine Green Biosafety

The CCK8 assays revealed that HSA-ICG did not significantly decrease MDA-MB-231 cell viability for 24 h, even at concentrations up to 40 μg/ml (**Figure S5**). In the HSA-ICG-treated mice, there was neither obvious damage nor inflammation in the heart, liver, spleen, lung, and kidney on the 1st, 7th, and 30th days (**Figure S6A**). HSA-ICG also did not seem to substantially alter serum biomarkers of key organ function (**Figure S6B**). HSA-ICG-treated group and the control group showed similar trends in body weight during the 30 days after tracer injection (**Figure S6C**).

DISCUSSION

It is essential to determine the margin status accurately during breast-conserving surgery to avoid reoperation and reduce the risk of local recurrence. Fluorescence-guided surgery images the tumor and detects residual tumor in real-time, thus providing critical guidance to the surgeon. Here we show that conjugating ICG to HSA allows to selectively accumulate in MDA-MB-231-luc xenograft tumors, where it can guide tumor removal to ensure negative margins, leading to reduced recurrence and improved overall survival.

By conjugating HSA with ICG, we developed and validated an optical imaging probe (HSA-ICG) that could accumulate selectively in MDA-MB-231-luc xenografts and the FVB/N-Tg spontaneous breast cancer lesion of (MMTV-PyMT) 634Mul/J mouse model. The molecular weight of HSA-ICG is approximately 67 kDa after the conjunction, which subsequently results in an accumulation of macromolecules (>40 kDa) within the tumor interstitium known as the enhanced permeation and retention effect (14, 25). Moreover, it also has been reported that tumors uptake albumin as a source of energy actively for their accelerated growth, by breaking down albumin into its component amino acids in lysosomes (26). In addition, receptor-mediated albumin uptake pathways by albumin binding proteins were also involved, such as membrane-associated 60 kDa glycoprotein and "secreted protein, acidic and rich in cysteine" (SPARC) (27). In previous studies, the expression level of SPARC was found to be higher in human breast cancer tissue when compared with healthy breast tissue (28–30). In the present study, we also detected that SPARC was expressed at higher levels in breast cancer MDA-MB-231 cells than in normal breast epithelial MCF 10A cells. All the reasons above may elucidate the mechanism of selective accumulation of HSA-ICG in tumors.

In several previous studies, ICG with HSA premixing by the absorption of ICG to HSA was used for near-infrared fluorescence imaging of sentinel lymph nodes (SLN), but no

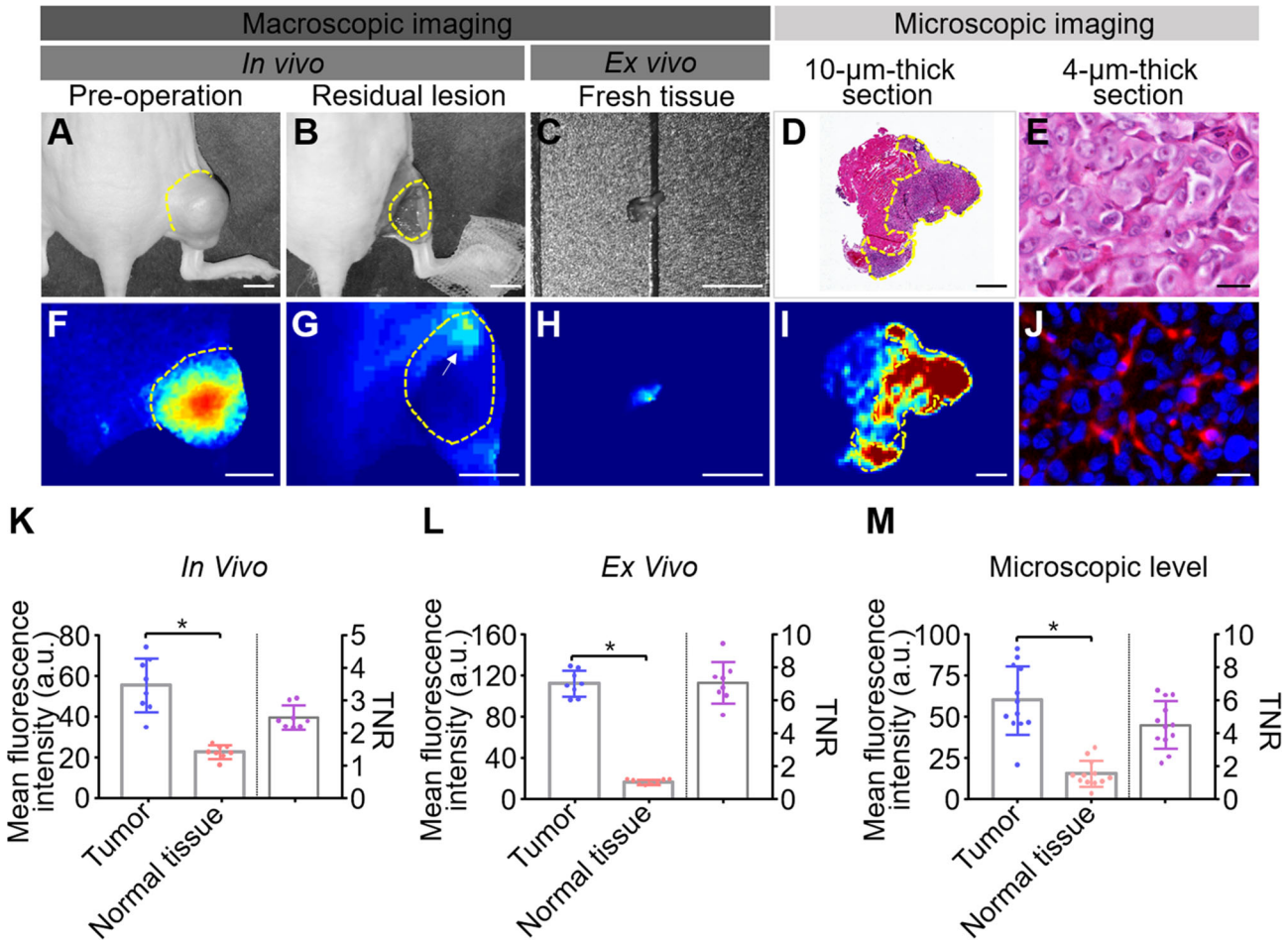

FIGURE 5 | Quantitative analysis of fluorescence images from fluorescence-guided surgery using HSA-ICG. **(A–J)** Correlation of fluorescence signals with pathology during fluorescence-guided surgery. **(A, F)** white-light images and corresponding fluorescence images of MDA-MB-231 tumors prior to surgery. **(B, G)** the corresponding images of the surgical bed of residual cancer model under HSA-ICG guidance. The yellow arrow in **(G)** points to the local aggregated fluorescence signal on the surgical bed. **(C, H)** *ex vivo* images of tissue resected from **(B)**. **(D)** hematoxylin and eosin staining of resected tissue, while **(I)** the corresponding fluorescence image. **(E, J)** the tracer at much higher cellular resolution. **(K–M)** Quantitative analysis of fluorescence signals of tumor and surrounding normal tissues *in vivo* **(K)**, *ex vivo* **(L)**, and in pathology slices **(M)**. Mean fluorescence intensity of normal tissues (red) and tumor tissues (blue) is depicted on the left y-axis, while the right y-axis shows the mean fluorescence intensity ratio of tumors to normal tissues. Tumors are outlined with a dashed line. Scale bars in all panels = 5 mm except **(D, I)**, where the scale bar = 500 μm; and **(E, J)**, where the scale bar = 25 μm. (paired Student's *t* test, * $P < 0.05$).

direct benefit was found with this probe for SLN mapping in preclinical and clinical trials (31, 32). It may be dissociated ICG from the complex due to low affinity of albumin compared with other serum protein, α1-lipoprotein, and γ-globulin (33). In the present study, HSA was conjugated with ICG derivatives (ICG-NHS ester), which could rapidly and high-specifically react to primary amine (-NH2) on HSA without altering the cyanine structure important for NIR absorption. Similar method was used with ICG derivatives (ICG-Sulfo-OSu) in previous study (19). Moreover, we confirmed that HSA-ICG was intact and present in tumor tissue by comparing the height of the band of the tumor lysates with the lane containing diluted HSA.

In the present study, we demonstrated that HSA-ICG fluorescence imaging was superior to ICG and naked eye for the detection of positive tumor margins in a surgical mice model for residual tumor. A mice model of MDA-MB-231-luc xenograft retained disease (12, 13, 23), in which the tumor deposits were not visible but could be detected by bioluminescence, was chosen to provide a scenario for examining the hypothesis that HSA-ICG can aid in identifying and completely resecting small foci of residual cancer. When using HSA-ICG to guide surgical resection, the signal on the surgical bed was sufficiently strong to be seen easily and to guide surgery in real-time with TNR approximately 2.5. During specimen imaging procedure, fluorescence imaging of the fresh surgical specimen and the pathology slides showed TNR with 7.03 and 4.50, which can provide the pathologist to outlines tumor tissue quickly and precisely. Most importantly, we confirmed the correlation of the

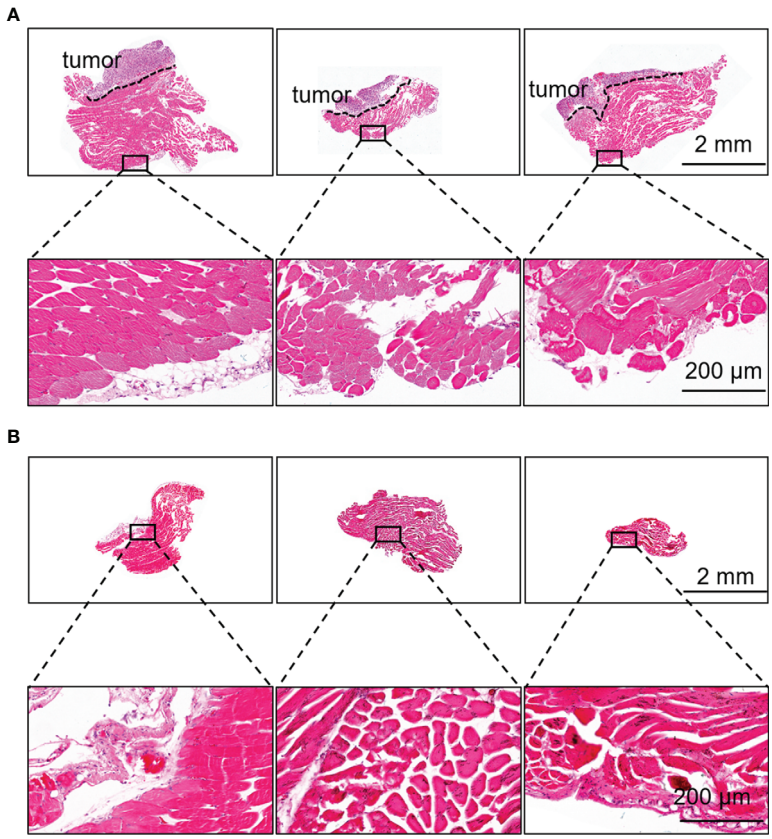

FIGURE 6 | Fluorescence-guided surgery based on HSA-ICG enabled complete removal of residual breast cancer lesions. **(A)** Representative hematoxylin and eosin staining of resected tissues that showed fluorescence signal during surgery and a negative margin. Dashed lines demarcate the tumor. Rectangles indicate the location of the higher-magnification views of the tissue margins, shown in the lower row. **(B)** Representative hematoxylin and eosin staining of the tissues on the surgical bed after surgery to confirm the absence of residual tumor.

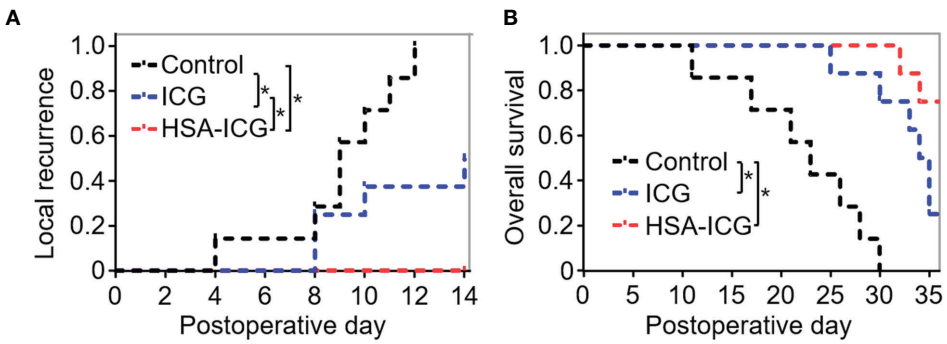

FIGURE 7 | Local recurrence and overall survival of MDA-MB-231-luc tumor-bearing mice after fluorescence-guided surgery. **(A)** Local recurrence within 2 weeks for mice that underwent resection under the guidance with HSA-ICG (n = 8 animals), ICG (8) or the control group (7). **(B)** Overall survival of the same mice as **(A)**. (log-rank test, $^*P < 0.05$).

fluorescence signal of the resected tissue with final histopathology. Furthermore, compared with surgery guided by ICG or visual inspection, HSA-ICG fluorescence-guided surgery resulted in significantly lower recurrence rate within14 days. The recurrence rate with ICG in our study (four of eight mice) was higher than the rate reported in a previous study (two of 22 mice) (12). It may be related with the usage dose of ICG, which was higher in previous study (7 *vs* 1 mg ICG per kg).

Our mice model suggests that fluorescence-guided surgery based on HSA-ICG provides a promising solution of negative margin and reduces local recurrence rates. however, small-animal models of tumor surgery could not fully reflect the complexities of human breast cancer therapy, it remains to be validated in patients. Interestingly, we found the lymph nodes surrounding the xenografts were highlighted during fluorescence-guided surgery (data not shown). Therefore, future work should also examine whether our approach can help map lymphatic metastasis, as suggested for HSA-ICG nanoprobes (18). However, specific labeling of such metastases must be established, since HSA in the tumor microenvironment is cleared *via* the lymphatic system through a natural recycling mechanism.

One limitation of our approach is that the relatively shallow penetration depth in fluorescence imaging may limit more complex resections, in which the target lesion lies behind other tissues or satellite lesions. We found that HSA-ICG can facilitate photoacoustic detection of tumors (data not shown), and this modality can penetrate down to several centimeters (34). We are exploring the use of photoacoustic imaging and HSA-ICG to detect residual lesions.

Despite these limitations, our study shows that fluorescence imaging by HSA-ICG can provide real-time imaging of tumors with high TBR, enable the surgeon to judge the completeness of resection of tumor lesion. With high biocompatibility and minimal toxicity, HSA-ICG fluorescence guidance is promising for further clinical translation in primary breast cancer patients.

DATA AVAILABILITY STATEMENT

The original contributions presented in the study are included in the article/**Supplementary Material**. Further inquiries can be directed to the corresponding authors.

ETHICS STATEMENT

The animal study was reviewed and approved by the Institutional Animal Care and Use Committee of Xiamen University.

AUTHOR CONTRIBUTIONS

G-JZ designed and directed the study and finalized the manuscript. L-MN directed the study. ZW coordinated and performed the study and drafted the manuscript. MC coordinated the study. J-JL cultured the cells, raised the mice, and conducted the experiments. R-HC conducted the statistical analysis for the data. QY performed the image processing. W-HH participated in the section of the surgery navigation. G-MW performed the pathological evaluation. All authors contributed to the article and approved the submitted version.

FUNDING

The present study was supported by the Natural Science Foundation of China (Grant No. 91859120), the Natural Science Foundation of Guangdong Province (Grant No. 2016A030312008), the Natural Science Foundation of Fujian Province of China (Grant No. 2020J01015), Fujian Major Scientific and Technological Special Project for Social Development (Grant No. 2020YZ016002), the Start-Up Fund for High-Talents from Xiamen University (G-JZ), and the Start-Up Fund for High-Talents from Xiang'an Hospital of Xiamen University (Grant No. PM201809170013), and the Science and Technology Plan Project of Shenzhen (No. JCYJ20160429172031572).

ACKNOWLEDGMENTS

The authors thank Fei Duan and Xiaobo Wang of the Molecular Imaging and Translational Medicine, School of Public Health, Xiamen University, Xiamen, China, for assisting in the image processing.

SUPPLEMENTARY MATERIAL

The Supplementary Material for this article can be found online at: https://www.frontiersin.org/articles/10.3389/fonc.2021.614050/full#supplementary-material

REFERENCES

1. Nag U, Hwang ES. Reoperation for Margins After Breast Conservation Surgery: What's Old Is New Again. *JAMA Surg* (2016) 151(7):656. doi: 10.1001/jamasurg.2015.5555
2. Valero MG, Mallory MA, Losk K, Tukenmez M, Hwang J, Camuso K, et al. Surgeon Variability and Factors Predicting for Reoperation Following Breast-Conserving Surgery. *Ann Surg Oncol* (2018) 25(9):2573–8. doi: 10.1245/s10434-018-6526-2
3. Kahlert S, Kolben TM, Schmoeckel E, Czogalla B, Hester A, Degenhardt T, et al. Prognostic impact of residual disease in simultaneous additional excision specimens after one-step breast conserving therapy with negative final margin status in primary breast cancer. *Eur J Surg Oncol* (2018) 44 (9):1318–23. doi: 10.1016/j.ejso.2018.06.014
4. Houssami N, Macaskill P, Marinovich ML, Morrow M. The association of surgical margins and local recurrence in women with early-stage invasive breast cancer treated with breast-conserving therapy: a meta-analysis. *Ann Surg Oncol* (2014) 21(3):717–30. doi: 10.1245/s10434-014-3480-5
5. Angarita FA, Nadler A, Zerhouni S, Escallon J. Perioperative measures to optimize margin clearance in breast conserving surgery. *Surg Oncol* (2014) 23 (2):81–91. doi: 10.1016/j.suronc.2014.03.002
6. Osako T, Nishimura R, Nishiyama Y, Okumura Y, Tashima R, Nakano M, et al. Efficacy of intraoperative entire-circumferential frozen section analysis of lumpectomy margins during breast-conserving surgery for breast cancer. *Int J Clin Oncol* (2015) 20(6):1093–101. doi: 10.1007/s10147-015-0827-2
7. St John ER, Al-Khudairi R, Ashrafian H, Athanasiou T, Takats Z, Hadjiminas DJ, et al. Diagnostic Accuracy of Intraoperative Techniques for Margin Assessment in Breast Cancer Surgery: A Meta-analysis. *Ann Surg* (2017) 265(2):300–10. doi: 10.1097/SLA.0000000000001897
8. Stummer W, Pichlmeier U, Meinel T, Wiestler OD, Zanella F, Reulen H-J. Fluorescence-guided surgery with 5-aminolevulinic acid for resection of

malignant glioma: a randomised controlled multicentre phase III trial. *Lancet Oncol* (2006) 7(5):392–401. doi: 10.1016/s1470-2045(06)70665-9
9. Frangioni J. In vivo near-infrared fluorescence imaging. *Curr Opin Chem Biol* (2003) 7(5):626–34. doi: 10.1016/j.cbpa.2003.08.007
10. Aydogan F, Ozben V, Aytac E, Yilmaz H, Cercel A, Celik V. Excision of Nonpalpable Breast Cancer with Indocyanine Green Fluorescence-Guided Occult Lesion Localization (IFOLL). *Breast Care (Basel)* (2012) 7(1):48–51. doi: 10.1159/000336497
11. Liu J, Guo W, Tong M. Intraoperative indocyanine green fluorescence guidance for excision of nonpalpable breast cancer. *World J Surg Oncol* (2016) 14(1):266. doi: 10.1186/s12957-016-1014-2
12. Madajewski B, Judy BF, Mouchli A, Kapoor V, Holt D, Wang MD, et al. Intraoperative near-infrared imaging of surgical wounds after tumor resections can detect residual disease. *Clin Cancer Res* (2012) 18(20):5741–51. doi: 10.1158/1078-0432.CCR-12-1188
13. Keating J, Tchou J, Okusanya O, Fisher C, Batiste R, Jiang J, et al. Identification of breast cancer margins using intraoperative near-infrared imaging. *J Surg Oncol* (2016) 113(5):508–14. doi: 10.1002/jso.24167
14. Daum S, Magnusson JP, Pes L, Garcia Fernandez J, Chercheja S, Medda F, et al. Development of a Novel Imaging Agent for Determining Albumin Uptake in Solid Tumors. *Nucl Med Mol Imaging* (2019) 53(3):189–98. doi: 10.1007/s13139-019-00587-w
15. Kudarha RR, Sawant KK. Albumin based versatile multifunctional nanocarriers for cancer therapy: Fabrication, surface modification, multimodal therapeutics and imaging approaches. *Mater Sci Eng C Mater Biol Appl* (2017) 81:607–26. doi: 10.1016/j.msec.2017.08.004
16. An F-F, Zhang X-H. Strategies for Preparing Albumin-based Nanoparticles for Multifunctional Bioimaging and Drug Delivery. *Theranostics* (2017) 7 (15):3667–89. doi: 10.7150/thno.19365
17. Sheng Z, Hu D, Zheng M, Zhao P, Liu H, Gao D, et al. Smart human serum albumin-indocyanine green nanoparticles generated by programmed assembly for dual-modal imaging-guided cancer synergistic phototherapy. *ACS Nano* (2014) 8(12):12310–22. doi: 10.1021/nn5062386
18. Lin X, Liu C, Sheng Z, Gong X, Song L, Zhang R, et al. Highly Sensitive Fluorescence and Photoacoustic Detection of Metastatic Breast Cancer in Mice Using Dual-Modal Nanoprobes. *ACS Appl Mater Interfaces* (2018) 10 (31):26064–74. doi: 10.1021/acsami.8b09142
19. Kanazaki K, Sano K, Makino A, Takahashi A, Deguchi J, Ohashi M, et al. Development of human serum albumin conjugated with near-infrared dye for photoacoustic tumor imaging. *J BioMed Opt* (2014) 19(9):96002. doi: 10.1117/1.JBO.19.9.096002
20. Ogawa M, Kosaka N, Choyke PL, Kobayashi H. In vivo molecular imaging of cancer with a quenching near-infrared fluorescent probe using conjugates of monoclonal antibodies and indocyanine green. *Cancer Res* (2009) 69(4):1268–72. doi: 10.1158/0008-5472.CAN-08-3116
21. Guy CT, Cardiff RD, Muller WJ. Induction of mammary tumors by expression of polyomavirus middle T oncogene: a transgenic mouse model for metastatic disease. *Mol Cell Biol* (1992) 12(3):954–61. doi: 10.1128/mcb.12.3.954
22. Cardiff RD, Anver MR, Gusterson BA, Hennighausen L, Jensen RA, Merino MJ, et al. The mammary pathology of genetically engineered mice: the consensus report and recommendations from the Annapolis meeting. *Oncogene* (2000) 19(8):968–88. doi: 10.1038/sj.onc.1203277
23. Predina JD, Judy B, Fridlender ZG, Aliperti LA, Madajewski B, Kapoor V, et al. A positive-margin resection model recreates the postsurgical tumor microenvironment and is a reliable model for adjuvant therapy evaluation. *Cancer Biol Ther* (2012) 13(9):745–55. doi: 10.4161/cbt.20557
24. Tummers WS, Warram JM, van den Berg NS, Miller SE, Swijnenburg RJ, Vahrmeijer AL, et al. Recommendations for reporting on emerging optical imaging agents to promote clinical approval. *Theranostics* (2018) 8(19):5336–47. doi: 10.7150/thno.27384
25. Hoogenboezem EN, Duvall CL. Harnessing albumin as a carrier for cancer therapies. *Adv Drug Deliv Rev* (2018) 130:73–89. doi: 10.1016/j.addr.2018.07.011
26. Merlot AM, Kalinowski DS, Richardson DR. Unraveling the mysteries of serum albumin-more than just a serum protein. *Front Physiol* (2014) 5:299. doi: 10.3389/fphys.2014.00299
27. Loureiro A, Azoia NG, Gomes AC, Cavaco-Paulo A. Albumin-Based Nanodevices as Drug Carriers. *Curr Pharm Design* (2016) 22(10):1371–90. doi: 10.2174/1381612822666160125114900
28. Watkins G, Douglas-Jones A, Bryce R, Mansel RE, Jiang WG. Increased levels of SPARC (osteonectin) in human breast cancer tissues and its association with clinical outcomes. *Prostaglandins Leukot Essent Fatty Acids* (2005) 72 (4):267–72. doi: 10.1016/j.plefa.2004.12.003
29. Lindner JL, Loibl S, Denkert C, Ataseven B, Fasching PA, Pfitzner BM, et al. Expression of secreted protein acidic and rich in cysteine (SPARC) in breast cancer and response to neoadjuvant chemotherapy. *Ann Oncol* (2015) 26 (1):95–100. doi: 10.1093/annonc/mdu487
30. Bellahcene A, Castronovo V. Increased expression of osteonectin and osteopontin, two bone matrix proteins, in human breast cancer. *Am J Pathol* (1995) 146(1):95–100. doi: 10.1021/j100152a036
31. Hutteman M, Mieog JS, van der Vorst JR, Liefers GJ, Putter H, Lowik CW, et al. Randomized, double-blind comparison of indocyanine green with or without albumin premixing for near-infrared fluorescence imaging of sentinel lymph nodes in breast cancer patients. *Breast Cancer Res Treat* (2011) 127 (1):163–70. doi: 10.1007/s10549-011-1419-0
32. Oh Y, Quan YH, Choi Y, Kim CK, Kim H, Kim HK, et al. Intraoperative combined color and fluorescent images-based sentinel node mapping in the porcine lung: comparison of indocyanine green with or without albumin premixing. *J Thorac Cardiovasc Surg* (2013) 146(6):1509–15. doi: 10.1016/j.jtcvs.2013.02.044
33. Ohnishi S, Lomnes SJ, Laurence RG, Gogbashian A, Mariani G, Frangioni JV. Organic Alternatives to Quantum Dots for Intraoperative Near-Infrared Fluorescent Sentinel Lymph Node Mapping. *Mol Imaging* (2005) 4(3):172–81. doi: 10.1162/15353500200505127
34. Lin L, Hu P, Shi J, Appleton CM, Maslov K, Li L, et al. Single-breath-hold photoacoustic computed tomography of the breast. *Nat Commun* (2018) 9 (1):2352. doi: 10.1038/s41467-018-04576-z

Conflict of Interest: The authors declare that the research was conducted in the absence of any commercial or financial relationships that could be construed as a potential conflict of interest.

The reviewer NW declared a shared affiliation with one of the authors, ZW to the handling editor at time of review.

frontiers in Oncology

ORIGINAL RESEARCH
published: 09 March 2021
doi: 10.3389/fonc.2021.602906

Near-Infrared Fluorescence Imaging of Breast Cancer and Axillary Lymph Nodes After Intravenous Injection of Free Indocyanine Green

Pierre Bourgeois[1]*, *Isabelle Veys*[2], *Danielle Noterman*[2], *Filip De Neubourg*[2], *Marie Chintinne*[3], *Sophie Vankerckhove*[1] and *Jean-Marie Nogaret*[2]

[1] Nuclear Medicine Service, Institut Jules Bordet, Université Libre de Bruxelles, Brussels, Belgium, [2] Surgery Service, Institut Jules Bordet, Université Libre de Bruxelles, Brussels, Belgium, [3] Department of Anatomo-Pathology, Institut Jules Bordet, Université Libre de Bruxelles, Brussels, Belgium

OPEN ACCESS

Edited by:
Marie-France Penet,
Johns Hopkins University,
United States

Reviewed by:
Tomoharu Sugie,
Kansai Medical University Hospital,
Japan
John Russell Benson,
Cambridge University Hospitals NHS
Foundation Trust, United Kingdom

***Correspondence:**
Pierre Bourgeois
pierre.bourgeois@erasme.ulb.ac.be

Specialty section:
This article was submitted to
Cancer Imaging and
Image-directed Interventions,
a section of the journal
Frontiers in Oncology

Received: 04 September 2020
Accepted: 28 January 2021
Published: 09 March 2021

Citation:
Bourgeois P, Veys I, Noterman D,
De Neubourg F, Chintinne M,
Vankerckhove S and Nogaret J-M
(2021) Near-Infrared Fluorescence
Imaging of Breast Cancer and Axillary
Lymph Nodes After Intravenous
Injection of Free Indocyanine Green.
Front. Oncol. 11:602906.
doi: 10.3389/fonc.2021.602906

Background: Near-infrared fluorescence imaging (NIRFI) of breast cancer (BC) after the intravenous (IV) injection of free indocyanine green (fICG) has been reported to be feasible. However, some questions remained unclarified.

Objective: To evaluate the distribution of fICG in BC and the axillary lymph nodes (LNs) of women undergoing surgery with complete axillary LN dissection (CALND) and/or selective lymphadenectomy (SLN) of sentinel LNs (NCT no. 01993576 and NCT no. 02027818).

Methods: An intravenous injection of fICG (0.25 mg/kg) was administered to one series of 20 women undergoing treatment with mastectomy, the day before surgery in 5 (group 1) and immediately before surgery in 15 (group 2: tumor localization, 25; and pN+ CALND, 4) as well as to another series of 20 women undergoing treatment with tumorectomy (group 3). A dedicated NIR camera was used for *ex vivo* fluorescence imaging of the 45 BC lesions and the LNs.

Results: In group 1, two of the four BC lesions and one large pN+ LN exhibited fluorescence. In contrast, 24 of the 25 tumors in group 2 and all of the tumors in group 3 were fluorescent. The sentinel LNs were all fluorescent, as well as some of the LNs in all CALND specimens. Metastatic cells were found in the fluorescent LNs of the pN+ cases. Fluorescent BC lesions could be identified *ex vivo* on the surface of the lumpectomy specimen in 14 of 19 cases.

Conclusions: When fICG is injected intravenously just before surgery, BC can be detected using NIRFI with high sensitivity, with metastatic axillary LNs also showing fluorescence. Such a technical approach seems promising in the management of BC and merits further investigation.

Keywords: breast cancer, axillary lymph nodes, indocyanine green, fluorescence imaging, sentinel lymph nodes

INTRODUCTION

Indocyanine green (ICG) is a fluorescent cyanine dye used in medical diagnostics and approved by the Food and Drugs Administration and European Medicines Agency for several indications (1). Using near-infrared fluorescence imaging (NIRFI)-dedicated cameras, the intravenous (IV) injection of ICG enables imaging of the vascularization of the eye and transplants (2, 3). More recently, its use after intradermal and/or subcutaneous injection has been emphasized for lymphatic imaging in the evaluation of lymphedema (4, 5) and the detection of sentinel lymph nodes (LNs) (6–15). The ability of ICG to reveal various tumors after IV injection had also been demonstrated in both animals and humans (16–23).

In breast cancers (BC), its potential to enable their imaging in human patients was recognized as early as 2000 (24). Different subsequent studies (25–30) have shown that the kinetics of the accumulation and clearance of free ICG (fICG) allow the mammary cancerous tissues to be differentiated from healthy tissues. However, these data were obtained from a limited number of patients and at varying time points after fICG injection.

Because cancerous cells are found by pathologists near or in the surgical margins in 5.6 to 66% of cases after conservative surgery (31), a technical approach that would allow the visualization of tumor tissues and identification of tumor remnants after lumpectomy is of major interest. Currently, cryosection analysis represents the reference technique, but various techniques have been proposed for the evaluation and identification of tumor margins (32). Preliminary data of intraoperative NIRFI after the IV injection of methylene blue (MB) (33) or fluorescent molecules such as bevacizumab-IRDye800CW (34–39), among others, have been published. The injection of MB represents a simple approach but carries the risk of an allergic reaction (40), and fluorescent molecules such as bevacizumab-IRDye800CW present the main drawbacks of imaging agents in development, with all the limitations of such products.

This situation led us to launch the present studies in 2013 to evaluate the following in women undergoing surgery for histologically proven BC: 1) the best timing for fICG to be injected (the day before or just before the operation); 2) the accumulation of intravenously injected fICG in mammary tumors and in their respective axillary LNs; 3) the sensitivity of the approach in identifying these malignant lesions; and the potential contributions of such imaging methods in patients undergoing lumpectomy.

MATERIAL AND METHODS

Patients

The first study was approved by the Investigational Review Board (IRB) of the Jules Bordet Institute (CE2075) and was registered at ClinicalTrial.gov (NCT no. 01993576; https://clinicaltrials.gov/ct2/home) and the European Clinical Trials Database (EudraCT number 2013-000100-41; http://eudract.emea.europa.eu/). Between May 2013 and April 2014, twenty women (mean age, 60.3 years; range, 32 to 89 years) who were scheduled to undergo mastectomy (n = 19) or lumpectomy (n = 1) with selective lymphadenectomy (SLN) of axillary sentinel LNs (n = 5) and/or complete axillary LN dissection (CALND) (n = 15) for a histologically proven mammary tumor were enrolled in the study after providing written informed consent (see **Table S1** and **Table S2** for their characteristics). One patient (no. 8) was enrolled after neoadjuvant hormone therapy, and two (nos. 16 and 17) were enrolled in the framework of a relapse at the site of a previous lumpectomy.

The second study was also approved by the IRB of the Jules Bordet Institute (CE2200) and was registered at the ClinicalTrial.gov (NCT no. 02027818; https://clinicaltrials.gov/ct2/home) and the European Clinical Trials Database (EudraCT number 2013-005178-23; http://eudract.emea.europa.eu/). Between February and June 2014, twenty women (mean age, 60.1 years; range, 37 to 81 years) who were scheduled to undergo a lumpectomy with selective lymphadenectomy of axillary sentinel SLNs for a histologically proven mammary tumor were enrolled in the study after providing written informed consent (group 3: see **Table S3** for their characteristics).

The exclusion criteria were pregnancy, significant renal failure (creatinine >400 μmol/L), severe cardiac or pulmonary disease (ASA III-IV), a history of iodine allergy or anaphylactic reactions to insect bites or medication, and the presence or a history of hyperthyroidism. Patients were not limited in their normal behavior, diet, or medication intake before the study.

Surgery and Specimen Preparation

A total of 0.25 mg of fICG/kg patient weight was intravenously injected in the first five patients (nos. 1–5) the day before the operation (group 1). Because fluorescence was detected in only two of the four tumors, the subsequent 15 patients (group 2) of our first study and every patient of our 2nd study were injected immediately after anesthesia and before surgery.

The surgeons performed mastectomy or lumpectomy as usual, either preceded by the selective lymphadenectomy of the axillary sentinel LNs demonstrated by the pre-operative intra-mammary and peri-tumoral injections of radio-colloids (SLN; n = 25 patients) or followed by CALND (n = 15 patients). The delay between ICG injection and SLN dissection was 12–25 min, and that between ICG injection and CALND was 55–120 min.

The fresh specimens were always thereafter processed by the pathologist as usual. After dying the resection margins with India ink, each mastectomy and lumpectomy specimen was sliced at a thickness of 5–7 mm (see **Figure 1**) and 2–3 mm (see **Figure 2**), respectively, before being immersed in 4% buffered formalin overnight for fixation. For the mastectomy specimens, the area of interest, the tumor, and other areas after gross examination were also sliced thinner and processed as usual (dehydration and paraffin-embedding). Each LN was sliced at a thickness of 2 mm and fixed overnight in 4% buffered formalin before dehydration and paraffin-embedding.

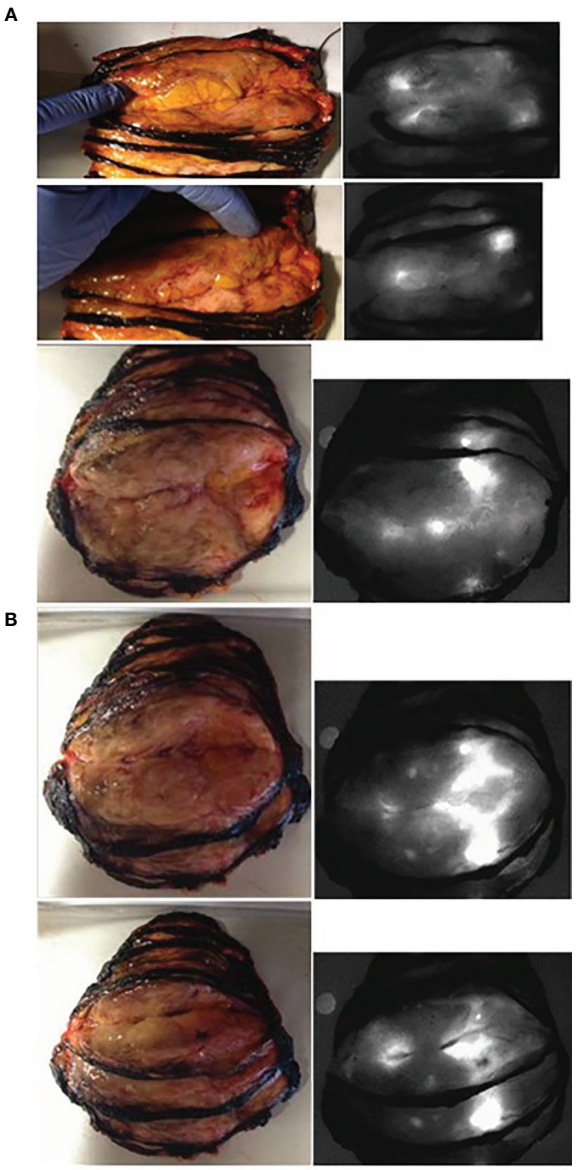

FIGURE 1 | Normal and fluorescent images of the freshly sliced specimen from patient n° 20 in group 2 (panel **A**: the two ductal lesions—shown by the author's finger—are fluorescent: the smallest was only 3 mm large) and from patient n° 19 in group 2 (panel **B**: with one lobular invasive).

Fluorescence Imaging

Fluorescence images of the freshly sliced specimens (see **Figures 1A, B**), specimens after incubation in formalin (see **Figures 2A, B**), mammary lesions isolated by the pathologists, and all sentinel LNs and/or non-sentinel LNs before (see **Figures 2C, D**) and after embedding in paraffin (see **Figures 3** and **4**) were obtained under standard conditions in the department of anatomo-pathology using a dedicated NIR camera system (Photodynamic Eye, PDE; Hamamatsu Photonics, Hamamatsu, Japan).

Fresh lumpectomy specimens were also imaged in the operating room (see **Figure 5**) using a dedicated NIR camera system (Photodynamic Eye, PDE; Hamamatsu Photonics, Hamamatsu, Japan).

Semiquantitative Analysis of Fluorescence Images

Videos were recorded and converted to AVI format still images for semiquantitative image analysis. Based on white-light images, regions of interest (ROIs) were drawn over the tumor tissues and the adjacent healthy mammary tissue (considered "background"), and the fluorescence intensity (expressed in arbitrary units, AU) was measured using IC-CALC software. Finally, the tumor-to-background fluorescence ratio (fTBR) was calculated for each tumor at different steps: when fresh, after fixation in formalin, and after embedding in paraffin. Dissected LNs were processed the same way.

RESULTS

Fluorescence of Mammary Tumors in Mastectomy and Lumpectomy Specimens

The first five patients in our 1st study were injected the day before surgery (group 1). In patient no. 1, the mammary lesion (one large *in situ* lesion limited to one-half of the breast) appeared faint but definitely more fluorescent than the normal mammary tissue. The largest LN, which was also fluorescent, was invaded by one ductal carcinoma. In the next four patients, who were also injected the day before surgery, only two mammary tumors fluoresced (**Table 1**).

In the subsequent five patients, who received an ICG injection immediately before the operation (following anesthesia), fluorescent mammary lesions were observed (**Table 1**). Thus, the last 10 patients were also injected immediately after anesthesia and before the operation.

In the 15 patients in group 2 who were injected just after anesthesia and before surgery (**Table 1**), 24 of the 25 clinically identified invasive cancerous lesions (14 ductal, 9 lobular, and 1 mucinous) were fluorescent, yielding a sensitivity of 96% in the mastectomy group. One tumor was not visualized well when examined as a fresh specimen (patient 18), and this was considered a false negative for fluorescence imaging because the lesion had been diagnosed on a biopsy performed the day before the mastectomy. No benign lesions were found in the mastectomy specimens and specificity of such ICG accumulation could not be established.

With regard to the possible influence of tumor size, one focus as small as 2 mm was detected in the multifocal lesion of one patient (no. 11), and small groups of cancerous cells dispersed on one surface 6 mm in diameter on the slide analyzed by the pathologist were reported in patient 17, who had mammary relapse.

Histological validation of ICG-positive tumors revealed a clear overlap between the fluorescence signals and tumor tissue (**Figure 2E**). In the last patient (no. 20), one tumor site was fluorescent, but no residual tumor was found after microscopic analysis. However, granulation tissue and inflammatory cells were observed.

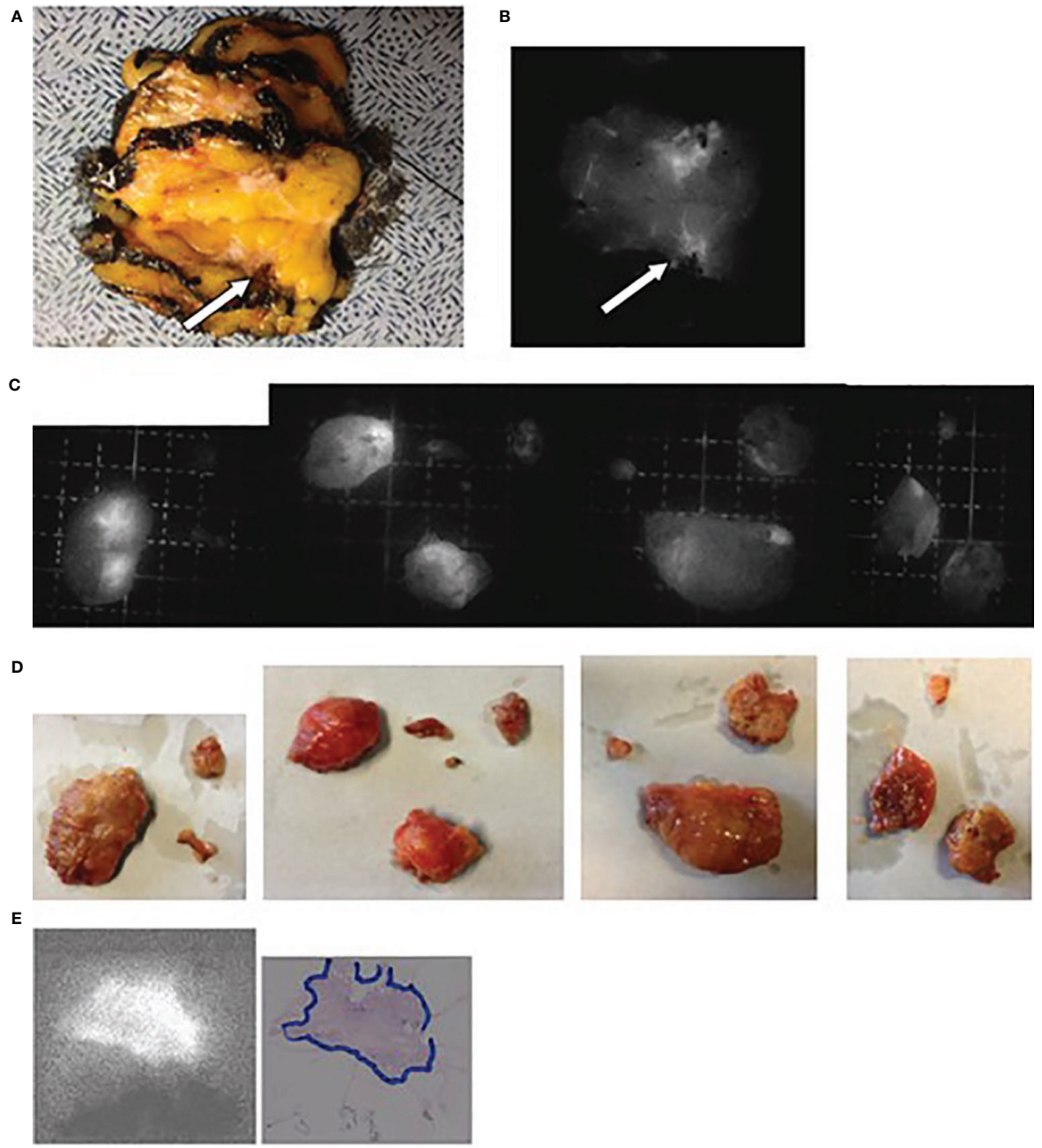

FIGURE 2 | Images obtained for patient N° 8 who underwent a tumorectomy with CALND after neoadjuvant hormone therapy. **(A)** Lesion (arrow) on the freshly sliced specimen. **(B)** NIR fluorescence image of the same slices with the arrow showing the tumor. **(C, D)** Fluorescent and optical images of the axillary LNs. **(E)** Fluorescent images of the tumor embedded in paraffin and the corresponding H&E-stained pathological slices with delineation of the tumor tissues.

When the lumpectomy specimens were imaged in the department of pathology after slicing, all the tumors were fluorescent, with no difference among the histopathological subtypes of tumors, giving an overall sensitivity of 100% in the lumpectomy group.

The mean maximum fTBR for the tumors (see **Table 1**) was 3.43 (standard deviation, ± 0.9) in the mastectomy specimens and 2.54 in the lumpectomy specimens (standard deviation, +/-0.73), and this metric did not seem to be influenced by the size (pT) of the tumors. However, this mean ratio in the

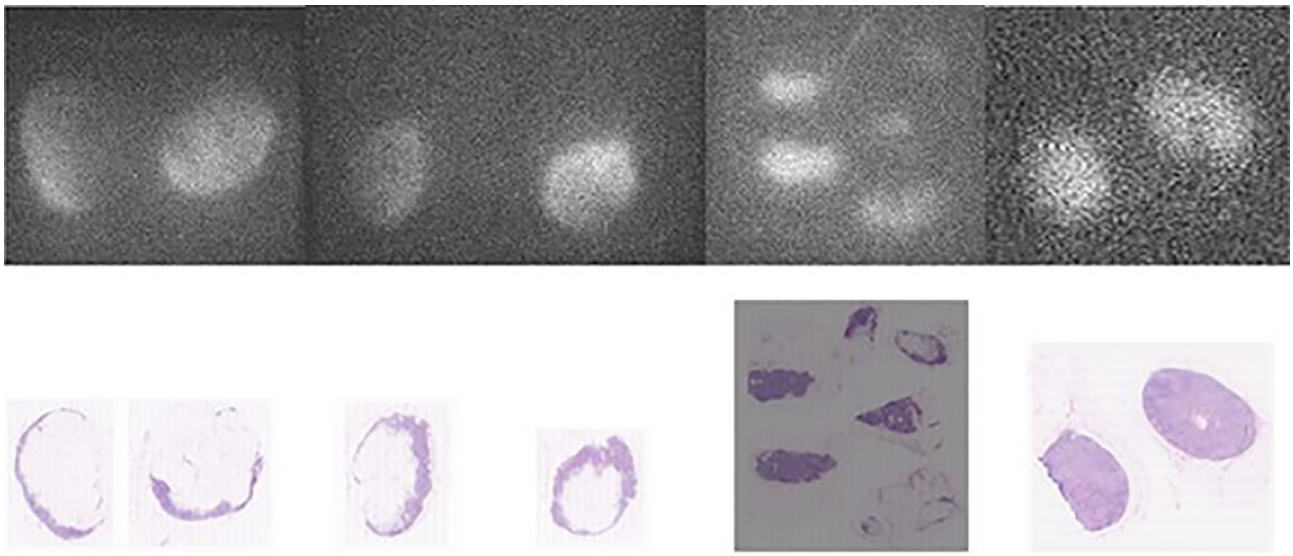

FIGURE 3 | Comparison between fluorescence images of the lymph node embedded in paraffin (upper pictures) and the corresponding AP slices (lower pictures) obtained from pN- patients. From left to right, the first three sets of pictures correspond to lymph nodes from patient n° 8 (of group 2) and the last right-sided set of pictures are lymph nodes from patient n° 9 (of group 2).

lumpectomy group was significantly higher ($2p < 0.05$ using the Kruskal-Wallis test) for the 12 patients (of Group 3) with histological grade 2 or 3 tumors (2.83 +/− 0.67; range = 2.0–4.0, with four cases of fTBR = 2.0) than for the eight patients with grade 1 tumors (1.84 +/− 0.2; range = 1.5–2.0).

Perioperative *Ex Vivo* Detection of Tumor Fluorescence in Lumpectomy Specimens

Tumor fluorescence was detected *ex vivo* in the operating room by NIR imaging of the whole lumpectomy specimens in 14 out of the 19 patients who were evaluated (Group 3: see **Figure 4**).

Tumor fluorescence could be detected in eleven out of thirteen lumpectomy specimens when the tumor size was larger than 10 mm but only three out of six lumpectomy specimens when the tumor size was less than 10 mm.

Among the 11 patients for whom we had the distance between the "closest" margins (n° 1, 4, 5, 7, 8, 10, 13, and 16–20: patient n° 8 was not evaluated in the operating room) and those for whom at least one surface of the tumor was fluorescent *ex vivo* (two surfaces were fluorescent for n° 5, 13, and 16), the tumor, except in one (patient n° 10), was not deeper than 5 mm ("final distance from invasive tumor to margin") under (one of) the corresponding *ex vivo* fluorescent walls of the specimen. In other words, if the margin was defined as "close" when the tumor was within 5 mm from the resection margin, the corresponding surface was fluorescent in the operating room in 100% out of 10 patients, but fluorescence was observed in only one (patient n° 10) out of the three in whom the distance from the tumor to the margin was greater than 5 mm.

Ex Vivo Free Indocyanine Green-FI of Axillary LNs

Patients Treated With Selective Lymphadenectomy

All the sentinel LNs were fluorescent in the 20 patients of Group 3 and in the four patients of Group 2 who underwent selective SLN guided by the preoperative peritumoral injection of radiocolloids.

Patients Treated With Complete Axillary Lymph Node Dissection

Among the 11 patients in group 2 who underwent CALND (**Table 2**), at least one of the dissected LNs was fluorescent in each patient. If the whole series is considered, a mean of 4.54 LNs per patient (from 1 to 8) were fluorescent, or 22.2% of all LNs found by the pathologist (from 10 to 60% if the number of fluorescent LNs is analyzed per patient).

The fluorescence in the normal LNs was localized and/or diffuse (**Figures 2C**, **3**, and **4**), sometimes with a (small or large) center that was not fluorescent (**Figure 3**). Histological validation of ICG-positive LNs showed a clear overlap between fluorescence and normal nodal tissues (**Figure 3**), with the hilum of the LNs not showing fluorescence.

In the four patients in group 2 who presented with LN metastases, 13 LNs harbored metastases, 10 (77%) of which were fluorescent. On the other hand, 17 (22%) of the 78 lymph nodes were fluorescent, and 10 (82%) of these 17 fluorescent LNs harbored metastases. In contrast, metastases were found in only 3 of the 61 non-fluorescent LNs, representing a false-negative rate (FNR) of 5%. The distribution of ICG in the metastatic LNs appeared somewhat different from what was observed in the normal LNs and in metastatic tumor areas.

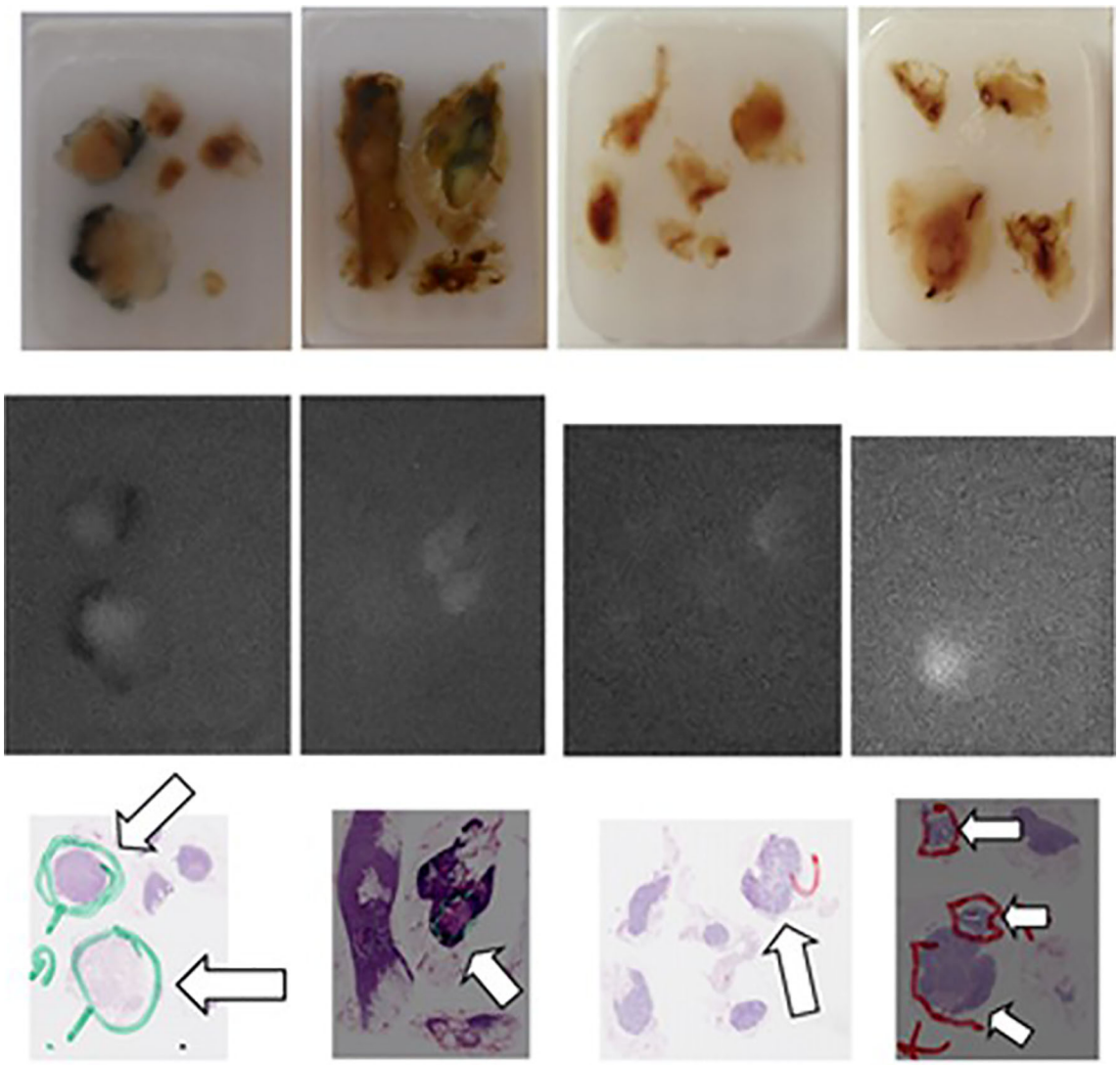

FIGURE 4 | Comparison of the "real" images (upper panel), of the fluorescence images (mid panel) and of the corresponding AP slices of pN+ lymph nodes (arrows) embedded in paraffin obtained, from left to right, in patient n° 11 (two first series), in patient n° 18 (third series), and in patient n° 19 (fourth series) from Group 2.

DISCUSSION

Indocyanine Green in Mammary Tumors

After IV injection, unbound fICG demonstrates rapid clearance from the blood circulation through the hepatobiliary system, with a half-life of 150 to 180 s (41). Because ICG has both lipophilic and hydrophilic properties, it also exhibits reversible binding to albumin and serum globulins, such as alpha1-lipoproteins. Unlike fICG, the complex formed by ICG and these proteins behaves like a macromolecule in the circulation.

With regard to our field of application in patients with tumors, the imaging of tumors immediately after the injection of ICG depends on their relative hypervascularization. In 2008, Wall et al. (42) demonstrated the correlation between the intensity of fluorescence and tumor vascularization in mammary tumor graft-bearing animals (MCF7 cell line).

Cancer tissues also exhibit "vascular fenestrations," which allow the extravasation of molecules over 50 kDa in molecular weight (MW) (43). In contrast, normal tissues have smaller vascular fenestrations that prevent the extravasation of molecules over 20 kDa in MW (44).

Two mechanisms, hypervascularization and the enhanced permeability retention (EPR) effect, can thus explain the ICG fluorescence of mammary tumors, but theoretically with potential differences in terms of sensitivity (and of specificity) over time.

Our observation that the mean maximum fTBR was higher in histological grade 2 and 3 tumors than in grade 1 tumors

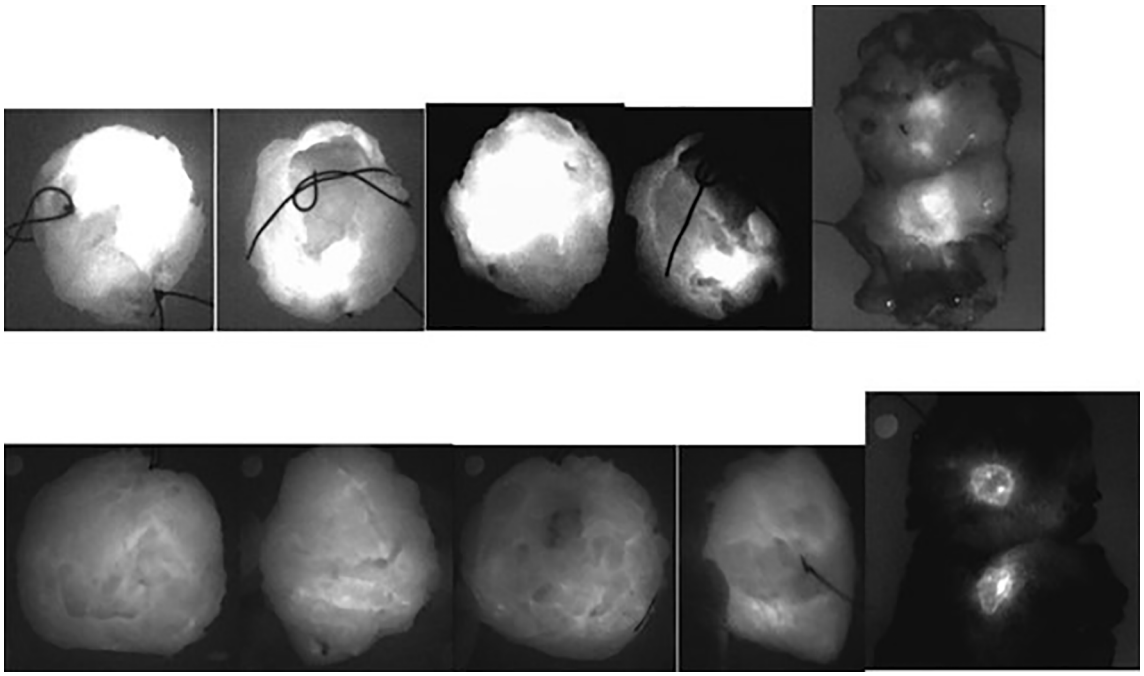

FIGURE 5 | *Ex vivo* NIR fluorescence imagings of lumpectomy specimens (in the operating room) and of their slicings (in the department of Pathology) obtained: Upper panel: in patient n° 5 of Group 3 with a lobular invasive carcinoma, 19 × 10 × 11 mm large, close to the posterior margin (<1 mm) and to the anterior margin (4 mm) within a tumorectomy specimen sized 35 mm × 27 mm × 20 mm, histologically graded 1, with a maximum tumor to background fluorescence ratio equal to 2.0: the corresponding views of the whole specimen showed clear fluorescence at the surface of the specimen- Lower panel: in patient n° 6 of Group 3 with a canalar invasive carcinoma, 14 mm large within a tumorectomy specimen sized 62 mm × 75 mm × 35 mm, histologically graded 2 and with a maximum tumor to background fluorescence ratio equal to 4.0: the tumor was well centered and the corresponding views of the whole specimen showed no clear fluorescence at the surface of the specimen.

supports the hypothesis of fluorescence related to the EPR effect. Daldrup et al. (45) showed in mammary tumor-bearing animals that capillary hyperpermeability to proteins with a high MW (i.e., the EPR effect) increases with the histological grade of tumors.

Sensitivity and Specificity of Indocyanine Green Near-Infrared Fluorescence Imaging for the Detection of Mammary Tumor Tissues

In the present series (with the injection of 0.25 mg per kg of patient weight), the accumulation of ICG as observed *ex vivo* in sliced specimens appears highly sensitive, with 44 of the 45 tumors showing fluorescence. The "falsely negative" non-fluorescent tumor had been biopsied the day before surgery, and the hematoma observed on pathology could explain its negative fluorescence. However, no benign lesions were found in the mastectomy specimens, and the specificity of such ICG accumulation could not be evaluated in our study.

Using *ex vivo* optical breast imaging after the IV injection of fICG (25 mg as a bolus), Schneider et al. (29) reported a sensitivity of 85.7% based on the positive detection of ***in vivo*** fluorescence in 12 out of 14 malignant lesions and a specificity of 87.5%, with no *in vivo* fluorescence detected in seven of eight benign lesions. A false-negative result was found in one patient for a micropapillary carcinoma (although the pT was 16 mm) and in another patient due to the presence of necrotic tissue at the center of the lesion.

Using intraoperative NIR imaging in 12 patients with BC but with fICG being injected 24 h before the operation and at a relatively high concentration (5 mg/kg), Keating et al. (46) reported fluorescence in all tumors, while in the department of pathology, we identified fluorescence in only two out of four tumor specimens when ICG was injected the day before the operation at a concentration of 0.25 mg/kg.

In the article published recently by our group (47), the sensitivity of ICG (injection unchanged) for detecting the fluorescent tumor in lumpectomy specimen was lower (31/35 or 87%). However, this result was obtained with a different NIRFI camera-device (and other parameters) and this difference stresses the importance of defining the optimal acquisition parameters for each imaging system. Interestingly, the false negatives were four of the (32) ductal carcinomas, which also showed the lowest fTBR in two of our patients with ductal cancer.

TABLE 1 | Fluorescence or not (and maximum fTBR) of tumors found in patients.

		Patient n°.	Inj ICG	BC1 fluo?	BC2 fluo?	BC3 fluo?	fTBR
1st study	**Group 1**						
		1	D-1	(Yes)			(2.0)
		2	D-1	No			Neg
		3	D-1	Yes	Data lost		Data lost
		4	D-1	No			Neg
		5	D-1	Yes			3.5
	Group 2						
		6	Preop	Yes	Yes		5.0
		7	Preop	Yes	Yes		2.5
		8	Preop	Yes			3.0
		9	Preop	Yes	Yes		3.0
		10	Preop	Yes			ND
		11	Preop	Yes	Yes	Yes	4.0
		12	Preop	Yes			4.0
		13	Preop	Yes			2.5
		14	Preop	Yes	Yes		5.0
		15	Preop	Yes			4.5
		16	Preop	Yes			2.5
		17	Preop	Yes			2.0
		18	Preop	Yes	**No**		2.5
		19	Preop	Yes	Yes	Yes	3.0
		20	Preop	Yes	Yes		4.5
2nd study	**Group 3**						
		1	Preop	Yes			3
		2	Preop	Yes			2
		3	Preop	Yes			2
		4	Preop	Yes			3
		5	Preop	Yes			2
		6	Preop	Yes			4
		7	Preop	Yes			4
		8	Preop	Yes			1.7
		9	Preop	Yes			2
		10	Preop	Yes			2
		11	Preop	Yes			1.5
		12	Preop	Yes			2
		13	Preop	Yes			4
		14	Preop	Yes			2
		15	Preop	Yes			4
		16	Preop	Yes			1.5
		17	Preop	Yes			2.5
		18	Preop	Yes			2
		19	Preop	Yes			2.5
		20	Preop	Yes			3

(Inj ICG D-1, patients injected the day before surgery; Inj ICG Preop, patients injected immediately after anesthesia and before surgery.

TABLE 2 | Number of LNs found by the pathologist in axillary specimens from patients in group 2.

Patient N°	Total LNs	pN+ LNs	Fluo LNs	pN + fluo LNs
6	16	0	2	0
7	22	0	5	0
8	34	0	8	0
9	7	0	4	0
11	35	4	7	4
14	21	3	5	3
15	29	0	5	0
16	10	0	6	0
18	9	1	1	1
19	13	5	4	2
20	29	0	3	0

total number, number of fluorescent LNs (fluo), pathologically positive LNs (pN+) and fluorescent and pN+ LNs (pN+ fluo).

Timing of Imaging After IV Indocyanine Green Injection

Not only the amount of ICG injected but also the timing of the injection thus appears to influence the fluorescence of mammary tumors. In addition, when the studies were initiated, the data were somewhat confusing. In animals, Reynold et al. (19) reported that spontaneous mammary tumors (in two female dogs) remained fluorescent for up to 120 min after the injection of ICG (which corresponds to the "vascular" phase of the tracer), and Gurfinkel et al. (18) found that, in one female dog operated on for a spontaneous mammary tumor, fluorescence remained detectable for 72 h after ICG injection (which is in agreement with the hypothesis of the extravasation and retention of ICG-labeled proteins). In patients and on ***ex vivo*** optical breast imaging after the IV injection of fICG (25 mg as a bolus), Poellinger et al. (30) reported the results of an analysis by two different readers of images recorded for during the IV administration of ICG (early imaging) and approximately 25 min after the IV injection of ICG (delayed imaging). The sensitivity of early imaging was low (~50 and 67%), but the corresponding specificity was high (88 and 75%). The sensitivity of delayed imaging was 85 and 92%, and the corresponding specificity was 75 and 62%. A higher mean contrast value was also reported for delayed imaging than for early imaging (0.64 *vs.* 0.25).

Potential Clinical Applications of Free Indocyanine Green Fluorescence Imaging in Breast Cancer

Although fICG is not tumor-specific, our data show that when ICG is injected at a concentration of 0.25 mg/kg just before the operation, it allows visualization of the tumor and not of the surrounding healthy tissues, which may have practical implications. For the purpose of intra- and postoperative diagnostic imaging, the identification of any abnormal tissues (sensitivity) is more important than specificity for tumor detection. Several new optical imaging agents targeting specific cell surface markers, such as HER2 receptor (48), have been reported, but these specific cellular markers may or may not be expressed on all cancer cells and are only related to tumors expressing these biomarkers on the cell surface (only 15–20% for HER2). Furthermore, these markers will have to be approved by the relevant authorities before use in clinical applications. Such agents could demonstrate superior sensitivity and specificity to ICG and merit consideration. However, none of these agents are as easy to apply in humans as ICG.

We identified four fields of clinical applications for the IV injection of fICG in the management of BC.

First, the detection of such fluorescence may be used by pathologists to look for the limits of mammary lesions and may represent an easy way to determine the tumor margin status. This approach could be particularly useful in cases where gross examination cannot allow clear mapping of the tumor limits (e.g., extensive fibrosis) and/or in cases of special patterns of infiltration without a fibrotic reaction of the stroma (e.g., lobular growth pattern with tumor cells infiltrating the tissue in single file or as single cells); these pathological situations can be anticipated on the basis of biopsies and/or radiological investigations.

Second, the perioperative detection of fluorescent lesions while the surgeon is performing lumpectomy represents another possible application of such fluorescence imaging. When the surgeon has cut the skin above the tumor location, the fluorescence emitted by the tumor may be detected and used to guide lumpectomy. Keating et al. (46) reported that the IV injection of 5.0 mg/kg of fICG 24 h before the operation allowed the positive identification of all 12 patients' breast tumors by intraoperative NIR imaging *in situ*; in the present study, with the injection of a lower concentration when the patient was anesthetized, we were able to observe tumor fluorescence in only 15 out of 19 cases ***ex vivo*** and mainly in the lumpectomy specimens of patients in which the tumor was close to the margin of the specimen. Our ability to visualize tumors is thus dependent on not only the concentration of ICG (injected and finally located in the tumor) but also the attenuation of the fluorescence by surrounding tissues.

This 2nd result may represent an advantage but also a drawback with regard to the third field of application: the detection of remnants by imaging of the surgical margins. Here, we feel it is important to stress the work reported by Madajewski et al. (49). These authors demonstrated the ability of fICG to show the limits of tumor areas (grafts in animals derived from cells of pleural, breast, lung, and esophageal cancer) and more precisely to identify the presence of malignant fluorescent remnants in surgical margins previously considered negative at first glance by the surgeon. The survival in the group in which these fluorescent remnants were removed was better than the survival in the control group, in which no such additional ICG-guided resection was performed. In a similar approach, Jiang et al. (50) confirmed the interest in NIR-guided surgery and reported the results of a series of 60 mice bearing 4TI BC tumors in their flank that traditional margin assessment identified 30% of positive margins, while NIR imaging identified 90% of positive margins.

Using NIR imaging after the injection of ICG, the problem of tumor remnants can be approached in two complementary ways. First, the tumor specimen, once *ex vivo*, can be examined for fluorescence emitted by the tumor. In the present series, fluorescence emitted by the tumor could be detected *ex vivo* on the surface of the lumpectomy specimen in 14 of the 19 evaluated cases but in only three out of six with a diameter <11 mm and in 11 out of 13 with a diameter >10 mm. The fact that the fluorescent tumors were also frequently close to the margin (12 being reported by the pathologist with a distance from the tumor to the margin of the lumpectomy specimen of 5 mm or less) also explains the detection of tumor fluorescence and might represent the most important factor allowing detectability when observing fresh specimens *ex vivo*, even for small tumors (<10 mm). However, such an approach would only allow (at the present stage of our developments) fluorescent areas at risk (of being positive) to be observed *ex vivo* and to be controlled *in vivo*. The second approach is more direct and consists of controlling the surgical bed and searching for and removing any remaining fluorescent tissue.

The feasibility of such NIR imaging, perioperatively and in the framework of conservative surgery, to observe fluorescence from BC tissue (and remnants) was reported by Tummers et al. (33), but after the IV injection of MB, another NIR fluorophore. Their overall identification rate was 18/21 for invasive carcinomas. This slightly lower sensitivity than that of ICG (at least 96% in the present study) might be explained by the greater attenuation with MB (penetration depth = approximately 5 mm) than with ICG (penetration depth = around 10 mm). Another hypothetical explanation might be that the cationic structure of MB would render MB the substrate of multidrug-resistant proteins known to be present in several types of BC (51) and that MB would thus be cleared from the tumor in such cases, with no or low fluorescence. Finally, Tummers et al. also reported (33) that they did not detect one mucinous adenocarcinoma, whereas such a lesion was detected by ICG fluorescence in our first series of patients treated with mastectomy. Of utmost interest, they also detailed that, in two patients with pathologically positive resection margins, fluorescent tumor tissues could be identified perioperatively on the surface of the resected specimen and/or in the wound bed.

Keating et al. also found (46) that ICG fluorescence could be detected in six cases in the surgical bed following lumpectomy, although all their patients had clear margins. With the high concentration of ICG they administered (also injected the day before), the fluorescence seems to no longer be limited to the tumor (as in our series) but to diffuse into the surrounding healthy tissues (Keating et al. mention in the discussion of their article that smears of fluid from the specimen were fluorescent) (46), which thus limits the value and potential of their approach in the detection of tumor remnants.

In a previous study, we had reported that the negative predictive value was 100% for the *ex vivo* ICG-FI detection of viable BCs tissues after neoadjuvant chemotherapy (52) as well as for the *in vivo* detection of ICG fluorescence in the tumoral bed after lumpectomy (47). The major contribution of the technique seems thus to be its excellent NPV, allowing the surgeon confidence that resection margins are clean if no residual fluorescence is visualized in the tumoral bed.

Fluorescence Imaging of Axillary Lymph Nodess After IV Indocyanine Green Injection

When our study was launched, the systematic presence of ICG fluorescence in the sentinel LNs and some LNs collected by CALND was unexpected despite some preliminary observations in the literature. Reynold et al. (19) reported in 1999 that the IV injection of ICG allowed the detection of fluorescence in draining

reactive LNs of spontaneous mammary tumors in two female dogs and that these structures remained fluorescent for up to 120 min after the injection of ICG. In humans, such visualization of fluorescence in LNs after the IV injection of fICG was reported in 2013 by Yokoyama et al. in patients who underwent lymphadenectomy for the nodal relapse of head and neck cancer (53). Our group confirmed their observation in 2016 in a series of 11 patients who had undergone cervical lymphadenectomy for primary and relapsing head and neck cancer (54) but also reported such accumulation of ICG in metastatic LNs in cases of colorectal and ovarian cancer (55–57).

In our patients who underwent SLN after peri-tumoral injection of radio-colloids, fluorescence was observed in all sentinel LNs. Due to the short delay between the excision of the sentinel LNs and the injection of ICG (<15 min), the fluorescence may be related to vascularization.

In patients who underwent CALND 50 to 120 min after the IV injection of ICG, no definitive explanations can be proposed regarding why some LNs remained fluorescent. At this stage of our analysis, we can propose two explanatory hypotheses: one consists of ICG accumulation *via* metastatic tumor tissues for pN + nodes, and the other consists of ICG accumulation by normal nodal tissues in an inflammatory state, stimulated by factors arising from the tumoral bed.

These results might be interesting for pathologists. The simple categorization of fluorescent LNs gives the following values (diagnosing one LN as pN+ on pathological examination): sensitivity and specificity of 77 and 81%, respectively, with a low positive predictive value of 20% but a high negative predictive value of 98.2%. In our limited series of 11 patients, pathologists have also isolated and analyzed 225 LNs but found only 13 pN+ LNs (in four patients) on histological examination, for an efficiency rate of only 5.5%; however, if they had isolated and analyzed the 50 fluorescent LNs, they would have found 10 pN+ LNs, for a higher efficiency rate of 20%. However, analysis of only the fluorescent LNs would have led to underestimation of the prognostic risk (related to the number of pN+ LNs) in one of the four pN+ patients, for whom only two of the pN+ LNs were fluorescent. The sensitivity of our ICG imaging (to show the lymph nodes at risk) may appear "low" and is based on *ex vivo* imaging. However, the aim of our study was not to evaluate the per-operative detection of fluorescent sentinel lymph nodes after the IV injection of ICG and we think that the lymphatic approaches after sub-cutaneous and/or intra-mammary injection of a dye and/or radio-tracer will remain the standard methods. HowH

These observations also concern a limited number of pN+ patients, and the next challenge will be to determine whether this technique can be used more specifically by pathologists to detect LNs at risk and with metastatic deposits without a loss of sensitivity or prognostic value.

CONCLUSION

Injecting fICG at a concentration of 0.25 mg/kg just before surgery seems to be an approach of interest in the management of patients with BC. In all, 44 out of 45 tumors were fluorescent. Fluorescent tumor tissues could also be identified perioperatively on the surface of the resected lumpectomy specimen in 14 of 19 cases. The fluorescence depended on the depth and location of the tumor in the specimen and on the histological grade of the tumor. The approach might be of interest in the management of patients with BC in order to perioperatively observe fluorescent tumor tissue and/or, more importantly, the persistent fluorescence of tumor remnants in the surgical bed. The unexpected detection of ICG fluorescence in some LNs obtained by CALND after IV injection of the dye and the presence of metastatic cells in these fluorescent LNs merit further investigations.

DATA AVAILABILITY STATEMENT

The raw data supporting the conclusions of this article will be made available by the authors, without undue reservation.

ETHICS STATEMENT

The studies involving human participants were reviewed and approved by the Investigational Review Board (IRB) of the Jules Bordet Institute (CE2075 and CE2200), 1, rue Heger-Bordet, 1000, Brussels, Belgium. The patients/participants provided their written informed consent to participate in this study.

AUTHORS CONTRIBUTIONS

PB, IV, and DN conceptualized the study. PB acquired the funding and developed the methodology. IV, DN, J-MN, FDN, MC, and PB provided the resources. PB and J-MN supervised the study. PB conducted the project administration. SV was in charge of the data curation. SV, MC, and PB conducted the investigation. PB prepared the original draft. J-MN, IV, DN, MC, and PB reviewed and edited the manuscript. All authors contributed to the article and approved the submitted version.

FUNDING

The studies were supported by a grant from « Les Amis de l'Institut Bordet ». The funders played no role in the study design, data collection or analysis, decision to publish, or preparation of the manuscript.

ACKNOWLEDGMENTS

We thank Mrs. Verheyden Brigitte and Dzhamalova Guzel for their kind help and patience during our imaging sessions in the Anatomo-Pathology Service.

SUPPLEMENTARY MATERIAL

The Supplementary Material for this article can be found online at: https://www.frontiersin.org/articles/10.3389/fonc.2021.602906/full#supplementary-material

REFERENCES

1. Vahrmeijer AL, Hutteman M, van der Vorst JR, van de Velde CJ, Frangioni JV. Image-guided cancer surgery using near-infrared fluorescence. *Nat Rev Clin Oncol* (2013) 10:507–18. doi: 10.1038/nrclinonc.2013.123
2. Liu DZ, Mathes DW, Zenn MR, Neligan PC. The application of indocyanine green fluorescence angiography in plastic surgery. *J Reconstr Microsurg* (2011) 27:355–64. doi: 10.1055/s-0031-1281515
3. Stanga PE, Lim JI, Hamilton P. Indocyanine green angiography in chorioretinal diseases: indications and interpretation: an evidence-based update. *Ophthalmology* (2003) 110:15–21. doi: 10.1016/S0161-6420(02)01563-4
4. Unno N, Inuzuka K, Suzuki M, Yamamoto N, Sagara D, Nishiyama M, et al. Preliminary experience with a novel fluorescence lymphography using indocyanine green in patients with secondary lymphedema. *J Vasc Surg* (2007) 45(5):1016–21. doi: 10.1016/j.jvs.2007.01.023
5. Yamamoto T, Narushima M, Yoshimatsu H, Yamamoto N, Kikuchi K, Todokoro T, et al. Dynamic Indocyanine Green (ICG) Lymphography for Breast Cancer-Related Arm Lymphedema. *Ann Plast Surg* (2013) 73(6):706–9. doi: 10.1097/SAP.0b013e318285875f
6. Nimura H, Narimiya N, Mitsumori N, Yamazaki Y, Yanaga K, Urashima M. Infrared ray electronic endoscopy combined with indocyanine green injection for detection of sentinel nodes of patients with gastric cancer. *Br J Surg* (2004) 91:575–9. doi: 10.1002/bjs.4470
7. Xiong L, Gazyakan E, Yang W, Engel H, Hünerbein M, Kneser U, et al. Indocyanine green fluorescence-guided sentinel node biopsy: a meta-analysis on detection rate and diagnostic performance. *Eur J Surg Oncol* (2014) 40:843–9. doi: 10.1016/j.ejso.2014.02.228
8. Wishart GC, Loh SW, Jones L, Benson JR. A feasibility study (ICG-10) of indocyanine green (ICG) fluorescence mapping for sentinel lymph node detection in early breast cancer. *Eur J Surg Oncol* (2012) 38(8):651–6. doi: 10.1016/j.ejso.2012.05.007
9. Ballardini B, Santoro L, Sangalli C, Gentilini O, Renne G, Lissidini G, et al. The indocyanine green method is equivalent to the 99mTc-labeled radiotracer method for identifying the sentinel node in breast cancer: a concordance and validation study. *Eur J Surg Oncol* (2013) 39(12):1332–6. doi: 10.1016/j.ejso.2013.10.004
10. Sugie T, Ikeda T, Kawaguchi A, Shimizu A, Toi M. Sentinel lymph node biopsy using indocyanine green fluorescence in early-stage breast cancer: a meta-analysis. *Int J Clin Oncol* (2017) 22(1):11–7. doi: 10.1007/s10147-016-1064-z
11. Sun WYL, Dang JT, Modasi A, Nasralla A, Switzer NJ, Birch D, et al. Diagnostic accuracy of sentinel lymph node biopsy using indocyanine green in lung cancer: a systematic review and meta-analysis. *Gen Thorac Cardiovasc Surg* (2020) 68(9):905–13. doi: 10.1007/s11748-020-01400-8
12. Liberale G, Bohlok A, Bormans A, Bouazza F, Galdon MG, El Nakadi I, et al. Indocyanine green fluorescence imaging for sentinel lymph node detection in colorectal cancer: A systematic review. *Eur J Surg Oncol* (2018) 44(9):1301–6. doi: 10.1016/j.ejso.2018.05.034
13. Jeremiasse B, van den Bosch CH, Wijnen MWHA, Terwisscha van Scheltinga CEJ, Fiocco MF, van der Steeg AFW. Systematic review and meta-analysis concerning near-infrared imaging with fluorescent agents to identify the sentinel lymph node in oncology patients. *Eur J Surg Oncol* (2020) 46(11):2011–22. doi: 10.1016/j.ejso.2020.07.012
14. Rocha A, Domínguez AM, Lécuru F, Bourdel N. Indocyanine green and infrared fluorescence in detection of sentinel lymph nodes in endometrial and cervical cancer staging - a systematic review. *Eur J Obstet Gynecol Reprod Biol* (2016) 206:213–9. doi: 10.1016/j.ejogrb.2016.09.027
15. Aoun F, Albisinni S, Zanaty M, Hassan T, Janetschek G, van Velthoven R. Indocyanine green fluorescence-guided sentinel lymph node identification in urologic cancers: a systematic review and meta-analysis. *Minerva Urol Nefrol* (2018) 70(4):361–9. doi: 10.23736/S0393-2249.17.02932-0
16. Itoshima T, Ito T, Ukida M, Ogawa H, Kitadai M, Hattori S, et al. Lack of uptake of indocyanine green and trypan blue by hepatocellular carcinoma. *Acta Med Okayama* (1984) 38:65–9. doi: 10.18926/AMO/30366
17. Hansen DA, Spence AM, Carski T, Berger MS. Indocyanine green (ICG) staining and demarcation of tumor margins in a rat glioma model. *Surg Neurol* (1993) 40:451–6. doi: 10.1016/0090-3019(93)90046-4
18. Gurfinkel M, Thompson AB, Ralston W, Troy TL, Moore AL, Moore TA, et al. Pharmacokinetics of ICG and HPPH-car for the detection of normal and tumor tissue using fluorescence, near-infrared reflectance imaging: a case study. *Photochem Photobiol* (2000) 72:94–102. doi: 10.1562/0031-8655(2000)072<0094:POIAHC>2.0.CO;2
19. Reynolds JS, Troy TL, Mayer RH, Thompson AB, Waters DJ, Cornell KK, et al. Imaging of spontaneous canine mammary tumors using fluorescent contrast agents. *Photochem Photobiol* (1999) 70:87–94. doi: 10.1111/j.1751-1097.1999.tb01953.x
20. Sallet G, Amoaku WM, Lafaut BA, Brabant P, De Laey JJ. Indocyanine green angiography of choroidal tumors. *Graefes Arch Clin Exp Ophthalmol* (1995) 233:677–89. doi: 10.1007/BF00164669
21. Kim HK, Quan YH, Choi BH, Park JH, Han KN, Choi Y, et al. Intraoperative pulmonary neoplasm identification using near-infrared fluorescence imaging. *Eur J Cardiothorac Surg* (2016) 49(5):1497–502. doi: 10.1093/ejcts/ezv367
22. Holt D, Okusanya O, Judy R, Venegas O, Jiang J, DeJesus E, et al. Intraoperative near-infrared imaging can distinguish cancer from normal tissue but not inflammation. *PloS One* (2014) 9(7):e103342. doi: 10.1371/journal.pone.0103342 eCollection 2014.
23. Predina JD, Newton AD, Corbett C, Shin M, Sulfyok LF, Okusanya OT, et al. Near-infrared intraoperative imaging for minimally invasive pulmonary metastasectomy for sarcomas. *J Thorac Cardiovasc Surg* (2019) 157(5):2061–9. doi: 10.1016/j.jtcvs.2018.10.169
24. Ntziachristos V, Yodh AG, Schnall M, Chance B, Concurrent MRI. and diffuse optical tomography of breast after indocyanine green enhancement. *Proc Natl Acad Sci U S A* (2000) 97:2767–72. doi: 10.1073/pnas.040570597
25. Intes X, Ripoll J, Chen Y, Nioka S, Yodh AG, Chance B. In vivo continuous-wave optical breast imaging enhanced with Indocyanine Green. *Med Phys* (2003) 30:1039–47. doi: 10.1118/1.1573791
26. Corlu A, Choe R, Durduran T, Rosen MA, Schweiger M, Arridge SR, et al. Three-dimensional in vivo fluorescence diffuse optical tomography of breast cancer in humans. *Opt Express* (2007) 15:6696–716. doi: 10.1364/OE.15.006696
27. Alacam B, Yazici B, Intes X, Nioka S, Chance B. Pharmacokinetic-rate images of indocyanine green for breast tumors using near-infrared optical methods. *Phys Med Biol* (2008) 53:837–59. doi: 10.1088/0031-9155/53/4/002
28. Hagen A, Grosenick D, Macdonald R, Rinneberg H, Burock S, Warnick P, et al. Late-fluorescence mammography assesses tumor capillary permeability and differentiates malignant from benign lesions. *Opt Express* (2009) 17:17016–33. doi: 10.1364/OE.17.017016
29. Schneider P, Piper S, Schmitz CH, Schreiter NF, Volkwein N, Lüdemann L, et al. Fast 3D Near-infrared breast imaging using indocyanine green for detection and characterization of breast lesions. *Rofo* (2011) 183:956–63. doi: 10.1055/s-0031-1281726
30. Poellinger A, Burock S, Grosenick D, Hagen A, Ludemann L, Diekmann F, et al. Breast Cancer: Early- and Late-Fluorescence Near-Infrared Imaging with Indocyanine Green—A Preliminary Study. *Radiology* (2011) 258:409–16. doi: 10.1148/radiol.10100258
31. Barrio AV, Morrow M. Appropriate Margin for Lumpectomy Excision of Invasive Breast Cancer. *Chin Clin Oncol* (2016) 5:35. doi: 10.21037/cco.2016.03.22
32. Butler-Henderson K, Lee AH, Price RI, Waring K. Intraoperative assessment of margins in breast conserving therapy: a systematic review. *Breast* (2014) 23:112–9. doi: 10.1016/j.breast.2014.01.002
33. Tummers QR, Verbeek FP, Schaafsma BE, Boonstra MC, van der Vorst JR, Liefers GJ, et al. Real-time intraoperative detection of breast cancer using near-infrared fluorescence imaging and Methylene Blue. *Eur J Surg Oncol* (2014) 40:850–8. doi: 10.1016/j.ejso.2014.02.225
34. Terwisscha van Scheltinga AG, van Dam GM, Nagengast WB, Ntziachristos V, Hollema H, Herek JL, et al. Intraoperative near-infrared fluorescence tumor imaging with vascular endothelial growth factor and human epidermal growth factor receptor 2 targeting antibodies. *J Nuclear Med* (2011) 52:1778–85. doi: 10.2967/jnumed.111.092833
35. Koch M, Ntziachristos V. Advancing Surgical Vision with Fluorescence Imaging. *Annu Rev Med* (2016) 67:153–64. doi: 10.1146/annurev-med-051914-022043
36. Lamberts LE, Koch M, de Jong JS, Adams ALL, Glatz J, Kranendonk MEG, et al. Tumor-Specific Uptake of Fluorescent Bevacizumab-IRDye800CW Microdosing in Patients with Primary Breast Cancer: A Phase I Feasibility

Study. *Clin Cancer Res* (2017) 23:2730–41. doi: 10.1158/1078-0432.CCR-16-0437
37. Koch M, de Jong JS, Glatz J, Symvoulidis P, Lamberts LE, Adams AL, et al. Threshold Analysis and Biodistribution of Fluorescently Labeled Bevacizumab in Human Breast Cancer. *Cancer Res* (2017) 77:623–31. doi: 10.1158/0008-5472.CAN-16-1773
38. Wilson KE, Bachawal SV, Willmann JK. Intraoperative Resection Guidance with Photoacoustic and Fluorescence Molecular Imaging Using an Anti-B7-H3 Antibody-Indocyanine Green Dual Contrast Agent. *Clin Cancer Res* (2018) 24(15):3572–82. doi: 10.1158/1078-0432.CCR-18-0417
39. Wojtynek NE, Olson MT, Bielecki TA, An W, Bhat AM, Band H, et al. Nanoparticle Formulation of Indocyanine Green Improves Image-Guided Surgery in a Murine Model of Breast Cancer. *Mol Imaging Biol* (2019) 22 (4):891–903. doi: 10.1007/s11307-019-01462-y
40. Bézu C, Coutant C, Salengro A, Daraï E, Rouzier R, Uzan S. Anaphylactic response to blue dye during sentinel lymph node biopsy. *Surg Oncol* (2011) 20:55–9. doi: 10.1016/j.suronc.2010.10.002
41. Desmettre T, Devoisselle JM, Mordon S. Fluorescence properties and metabolic features of indocyanine green (ICG) as related to angiography. *Surv Ophthalmol* (2000) 45:15–27. doi: 10.1016/S0039-6257(00)00123-5
42. Wall A, Persigehl T, Hauff P, Licha K, Schirner M, Müller S, et al. Differentiation of angiogenic burden in human cancer xenografts using a perfusion-type optical contrast agent (SIDAG). *Breast Cancer Res* (2008) 10: R23. doi: 10.1186/bcr1875
43. Maeda H, Matsumura Y. Tumoritropic and lymphotropic principles of macromolecular drugs. *Crit Rev Ther Drug Carrier Syst* (1989) 6:193–210.
44. Desser TS, Rubin DL, Muller HH, Qing F, Khodor S, Zanazzi G, et al. Dynamics of tumor imaging with Gd-DTPA-polyethylene glycol polymers: dependence on molecular weight. *J Magn Reson Imaging* (1994) 4:467–72. doi: 10.1002/jmri.1880040337
45. Daldrup H, Shames DM, Wendland M, Okuhata Y, Link TM, Rosenau W, et al. Correlation of dynamic contrast-enhanced MR imaging with histologic tumor grade:comparison of macromolecular and small-molecular contrast media. *AJR Am J Roentgenol* (1998) 171:941–9. doi: 10.2214/ajr.171.4.9762973
46. Keating J, Tchou J, Okusanya O, Fisher C, Batiste R, Jiang J, et al. Identification of breast cancer margins using intraoperative near-infrared imaging. *J Surg Oncol* (2016) 113(5):508–14. doi: 10.1002/jso.24167
47. Pop CF, Veys I, Vankerckhove S, Barbieux R, Chintinne M, Moreau M, et al. Absence of residual fluorescence in the surgical bed at near-infrared fluorescence imaging predicts negative margins at final pathology in patients treated with breast-conserving surgery for breast cancer. *Eur J Surg Oncol* (2020) 13:S0748–7983(20)30808-8. doi: 10.1016/j.ejso.2020.09.036
48. Maeda A, Bu J, Chen J, Zheng G, Ra S. DaCosta. Dual In Vivo Photoacoustic and Fluorescence Imaging of HER2 Expression in Breast Tumors for Diagnosis, Margin Assessment, and Surgical Guidance. *Mol Imaging* (2014) 2015(14):1–9. doi: 10.2310/7290.2014.00043
49. Madajewski B, Judy BF, Mouchli A, Kapoor V, Holt D, Wang MD, et al. Intraoperative near-infrared imaging of surgical wounds after tumor resections can detect residual disease. *Clin Cancer Res* (2012) 18:5741–51. doi: 10.1158/1078-0432.CCR-12-1188
50. Jiang JX, Keating JJ, Jesus EM, Judy RP, Madajewski B, Venegas O, et al. Optimization of the enhanced permeability and retention effect for near-infrared imaging of solid tumors with indocyanine green. *Am J Nucl Med Mol Imaging* (2015) 5(4):390–400.
51. Diddens HC. Role of multidrug resistance in photodynamic therapy. *Proc. SPIE* 1645, Optical Methods for Tumor Treatment and Detection: Mechanisms and Techniques in Photodynamic Therapy. (1992) 115:. doi: 10.1117/12.60934
52. Veys I, Pop CF, Barbieux R, Moreau M, Noterman D, Neubourg F, et al. ICG fluorescence imaging as a new tool for optimization of pathological evaluation in breast cancer tumors after neoadjuvant chemotherapy. *PloS One* (2018) 13 (5):e0197857. doi: 10.1371/journal.pone.0197857
53. Yokoyama J, Fujimaki M, Ohba S, Anzai T, Yoshii R, Ito S, et al. A feasibility study of NIR fluorescent image-guided surgery in head and neck cancer based on the assessment of optimum surgical time as revealed through dynamic imaging. *Onco Targets Ther* (2013) 6:325–30. doi: 10.2147/OTT.S42006
54. Digonnet A, van Kerckhove S, Moreau M, Willemse E, Quiriny M, Ahmed B, et al. Near infrared fluorescent imaging after intravenous injection of indocyanine green during neck dissection in patients with head and neck cancer: A feasibility study. *Head Neck* (2016) 38(Suppl 1):E1833–7. doi: 10.1002/hed.24331
55. Liberale G, Galdon MG, Moreau M, Vankerckhove S, El Nakadi I, Larsimont, et al. Ex vivo detection of tumoral lymph nodes of colorectal origin with fluorescence imaging after intraoperative intravenous injection of indocyanine green. *J Surg Oncol* (2016) 114:348–53. doi: 10.1002/jso.24318
56. Liberale G, Vankerckhove S, Galdon MG, Donckier V, Larsimont D, Bourgeois P. Fluorescence imaging after intraoperative intravenous injection of indocyanine green for detection of lymph node metastases in colorectal cancer. *Eur J Surg Oncol* (2015) 41:1256–60. doi: 10.1016/j.ejso.2015.05.011
57. Pop CF, Veys I, Gomez Galdon M, Moreau M, Larsimont D, Donckier V, et al. Ex vivo indocyanine green fluorescence imaging for the detection of lymph node involvement in advanced-stage ovarian cancer. *J Surg Oncol* (2018) 118 (7):1163–9. doi: 10.1002/jso.25263

Conflict of Interest: The authors declare that the research was conducted in the absence of any commercial or financial relationships that could be construed as a potential conflict of interest.

frontiers in Oncology

ORIGINAL RESEARCH
published: 22 March 2021
doi: 10.3389/fonc.2021.636471

Detection and Classification of Breast Lesions With Readout-Segmented Diffusion-Weighted Imaging in a Large Chinese Cohort

Zhen Lu Yang[1], Yi Qi Hu[1], Jia Huang[1], Chen Ao Zhan[1], Min Xiong Zhou[2], Xiao Yong Zhang[3], Hui Ting Zhang[4], Li Ming Xia[1] and Tao Ai[1]**

[1] Department of Radiology, Tongji Hospital, Tongji Medical College, Huazhong University of Science and Technology, Wuhan, China, [2] College of Medical Imaging, Shanghai University of Medicine & Health Sciences, Shanghai, China, [3] MR Scientific Marketing, Siemens Healthcare, Wuhan, China, [4] MR Collaborations, Siemens Healthcare, Shenzhen, China

OPEN ACCESS

Edited by:
Pilar López-Larrubia, Consejo Superior de Investigaciones Científicas (CSIC), Spain

Reviewed by:
Sunitha B. Thakur, Memorial Sloan Kettering Cancer Center, United States
Tristan Anselm Kuder, German Cancer Research Center (DKFZ), Germany

***Correspondence:**
Li Ming Xia
lmxia@tjh.tjmu.edu.cn
Tao Ai
aitao007@hotmail.com

Specialty section:
This article was submitted to Cancer Imaging and Image-directed Interventions, a section of the journal Frontiers in Oncology

Received: 01 December 2020
Accepted: 08 February 2021
Published: 22 March 2021

Citation:
Yang ZL, Hu YQ, Huang J, Zhan CA, Zhou MX, Zhang XY, Zhang HT, Xia LM and Ai T (2021) Detection and Classification of Breast Lesions With Readout-Segmented Diffusion-Weighted Imaging in a Large Chinese Cohort. Front. Oncol. 11:636471. doi: 10.3389/fonc.2021.636471

Objectives: To evaluate the performance of readout-segmented echo-planar imaging DWI (rs-EPI DWI) in detecting and characterizing breast cancers in a large Chinese cohort with comparison to dynamic contrast-enhanced MRI (DCE-MRI).

Methods: The institutional review board approved this retrospective study with waived written informed consent. A total of 520 women (mean age, 43.1- ± 10.5-years) were included from July 2013 to October 2019. First, the ability of rs-EPI DWI in detecting breast lesions identified by DCE-MRI was evaluated. The lesion conspicuity of rs-EPI-DWI and DCE-MRI was compared using the Wilcoxon signed rank test. With pathology as a reference, the performance of rs-EPI DWI and DCE-MRI in distinguishing breast cancers was evaluated and compared using the Chi-square test.

Results: Of 520 women, 327/520 (62.9%) patients had 423 lesions confirmed by pathology with 203 benign and 220 malignant lesions. The rs-EPI DWI can detect 90.8% (659/726) (reader 1) and 90.6% (663/732) (reader 2) of lesions identified by DCE-MRI. The lesion visibility was superior for DCE-MRI than rs-EPI-DWI (all $p < 0.05$). With pathology as a reference, the sensitivities and specificities of rs-EPI DWI in diagnosing breast cancers were 95.9% (211/220) and 85.7% (174/203) for reader 1 and 97.7% (215/220) and 86.2% (175/203) for reader 2. No significant differences were found for the performance of DCE-MRI and rs-EPI DWI in discriminating breast cancers (all $p > 0.05$).

Conclusions: Although with an inferior lesion visibility, rs-EPI DWI can detect about 90% of breast lesions identified by DCE-MRI and has comparable diagnostic capacity to that of DCE-MRI in identifying breast cancer.

Keywords: breast neoplasms, magnetic resonance imaging, diffusion weighted MRI, sensitivity, specificity

KEY POINTS

- Readout-segmented echo-planar imaging DWI (rs-EPI DWI) can detect about 90% of breast lesions identified by dynamic contrast-enhanced MRI (DCE-MRI).
- With pathology as reference, the sensitivity and specificity of rs-EPI DWI in characterizing breast cancers were 95.9% (211/220) and 85.7% (174/203) for reader 1 and 97.7% (215/220) and 86.2% (175/203) for reader 2.
- No significant differences were found between rs-EPI DWI and DCE-MRI for the sensitivity, specificity, accuracy, positive predictive value, and negative predictive value in distinguishing breast cancers (all $p > 0.05$).

INTRODUCTION

Breast cancer is the most common cancer for women worldwide and has become the leading cause of cancer-related death in Chinese women younger than 45-years old (1, 2). Chinese patients contribute significantly to the global burden of breast cancer and related deaths given the large population (1, 3). Miller et al. (4) reported that the 5-year relative survival rates for patients with breast cancer at stage I and stage IV were 100 and 26%, respectively. Early detection and treatment are crucial for improving the prognosis of patients with breast cancer.

Currently, mammography is recommended by clinical guidelines for breast cancer screening in many Western countries for women older than 40-years (5–7). However, Asian women usually have relatively dense and small breasts, making it difficult to effectively detect lesions in these women with mammography alone (7). Dynamic contrast-enhanced MRI (DCE-MRI) is so far the most sensitive imaging modality for identifying breast cancers, and it is therefore recommended for cancer screening of high-risk women as a supplement to mammography and/or breast ultrasound (8, 9). However, several disadvantages prevent its widespread use in screening average-risk women, including intravenous injection of gadolinium-based contrast agents (GBCAs), higher cost, longer acquisition time, and lower availability (10, 11). Abbreviated breast MRI protocols have been proposed to overcome some of these limitations and show feasibility in MRI breast cancer screening (12, 13). However, the gadolinium deposition in the body due to repeated injection of GBCAs has attracted broad attention over the world (14), which makes DCE-MRI unreasonable for breast cancer screening in the general population.

In order to identify a safe and effective screening tool, many studies have considered using non-contrast MRI protocols based on diffusion-weighted imaging (DWI) (10, 11, 15–17). In early studies, conventional single-shot echo-planar imaging DWI (ss-EPI DWI) sequences were used offering an advantage of speed and no requirement for GBCA contrast. However, it suffered from susceptibility artifacts, geometric distortions, and spatial blurring (18–21), which partly contributed to the discrepant and unsatisfactory sensitivities and specificities of DWI for breast cancer detection (17, 22, 23). Pinker et al. concluded that conventional ss-EPI DWI was not sufficient as a stand-alone modality for breast cancer detection (11). DWI based on readout-segmented technique (a multi-shot strategy) may improve spatial resolution for superior sensitivity and/or specificity and provide more potential when combined with a new technique (24, 25). During diffusion encoding in readout-segmented echo-planar imaging (rs-EPI), each shot involves only a limited transversal of k-space in the readout direction, but full resolution along the phase encoding direction (26). rs-EPI DWI should improve the visualization of anatomic structures with less image distortion and superior spatial resolution (19, 27, 28). Recently, the consensus recommendations of the European Society of Breast Radiology (EUSOBI) breast DWI working group stated that breast DWI had high specificity and may improve lesion classification in cancer screening. However, evidence supporting the use of DWI for screening as a stand-alone test or as a part of an unenhanced MRI protocol is currently insufficient (29).

The purpose of this study was to evaluate the ability of rs-EPI DWI in detecting breast lesions identified by DCE-MRI and the performance of rs-EPI DWI in distinguishing breast cancers with comparison to DCE-MRI in a large Chinese cohort by using pathology as the reference standard.

MATERIALS AND METHODS

Patients

The institutional review board of our hospital approved this single-institution retrospective study. The written informed consents of patients were waived. From July 2013 to October 2019, 956 women (mean age, 43.2- ± 10.5-years) were referred for breast MRI in our hospital due to one of the following conditions (inclusion criteria): (a) suspicious lesions on mammography and/or ultrasonography; (b) clinical symptoms/signs, such as breast pain, mass, and abnormal changes of skin and nipple; (c) high risk of breast cancer; and (d) presurgical evaluation or baseline assessment for monitoring therapeutic response.

The exclusion criteria included: (a) previous treatments including surgery, radiotherapy, and chemotherapy (patients underwent MRI for the assessment of therapy response or recurrence, $n = 247$); (b) needle biopsy performed prior to the breast MRI ($n = 148$); (c) patients with breast implants ($n = 28$); (d) poor image quality due to marked motion artifacts and/or insufficient field of view ($n = 3$); (e) only nipple lesions without involving breast parenchyma ($n = 3$); (f) pregnancy or lactation ($n = 7$); and (g) simple cysts (as a per-lesion exclusion). Finally, a total of 520 women (mean age, 43.1- ± 10.5-years) were included in this study.

Medical records were reviewed to record corresponding pathology results and status of estrogen receptor (ER), progesterone receptor (PR), human epidermal growth factor

Abbreviations: DWI, diffusion-weighted imaging; rs-EPI, readout-segmented echo-planar imaging; DCE-MRI, dynamic contrast-enhanced MRI; BI-RADS, Breast Imaging Reporting and Data System; ADC, apparent diffusion coefficient; PPV, positive predictive value; NPV, negative predictive value; GBCAs, gadolinium-based contrast agents; FGT, fibroglandular tissue; BPE, background parenchymal enhancement; TIC, time-signal intensity curve; ER, estrogen receptor; PR, progesterone receptor; HER2, human epidermal growth factor receptor-2; ROI, region of interest.

receptor-2 (HER2), and Ki-67 if available. The flowchart of this study is depicted in **Figure 1**.

Imaging Protocols

All breast MR images were obtained using a 3T MRI scanner (MAGNETOM Skyra, Siemens Healthcare, Erlangen, Germany) with bilateral, dedicated 4- or 16-channel phased-array breast coil with patients in the prone position. The scanning protocol mainly included T2-weighted imaging, rs-EPI DWI, and DCE-MRI. For DWI scanning in this study, 4 b values (0, 50, 1,000, and 2,000 s/mm^2) were used. The imaging parameters of each sequence are described in **Table 1**. For all DCE-MRI protocols, the gadodiamide contrast medium (Omniscan, GE Healthcare, Milwaukee, WI, USA) was intravenously injected at the end of the third dynamic acquisition phase, with a dose of 0.1 mmol/kg body weight at 2.5 ml/s. Contrast administration was followed with a 20 ml saline flush.

Image Assessment

All image datasets were reviewed using software RadiAnt DICOM-Viewer (version 5.0.2, Medixant, Poznán, Poland) by two readers (TA and ZLY with 10 and 3-years of experience in the breast MRI interpretation, respectively). Each reviewer was blinded to the corresponding clinical information, other imaging results, and pathology reports.

For DCE-MRI, the two readers independently evaluated images and determined the lesion types (mass or non-mass), lesion locations (by clock position), the distance of the lesions from the nipple, and maximal trans-axial diameters (only for mass lesions). For multiple lesions of the ipsilateral breast, a "separate" lesion was identified if the lesion location was relatively separate, and its boundary was disconnected/not continuous with other lesions. The amount of fibroglandular tissue (FGT) and background parenchymal enhancement (BPE) was also recorded by two readers by consensus according to the fifth edition of the Breast Imaging Reporting and Data System (BI-RADS® 5th edition) (30). The mean signal intensity of a region of interest (ROI) in each phase from 35/28/60 phases (all phases were involved) was used to generate a time-signal intensity curve (TIC) for each lesion by using a dedicated Syngo MR Workstation (Siemens Healthcare, Erlangen, Germany) with software program "Mean Curve." (Siemens Healthcare, Erlangen, Germany) An ROI for each lesion was manually drawn with an area of 0.2–0.4 cm^2 by avoiding vessels and necrotic regions. The BI-RADS categories of lesions on DCE-MRI were performed by referring criteria described in **Supplementary Table 1**, and reasonable adjustment was allowed according to the experience of readers. In brief, lesions were categorized as BI-RADS 2 or 5 when meeting all benign suspicious or malignant suspicious criteria, respectively. In case of fulfilling only one or more than one malignant suspicious criteria, BI-RADS 3 or 4 were given, respectively. The lesions with BI-RADS 2 or 3 were regarded as benign lesions; and the lesions with BI-RADS 4 or 5 were regarded as malignant lesions.

For rs-EPI DWI, the two readers independently analyzed the DWI images with different b-values and apparent diffusion coefficient (ADC) maps to record the lesion types (mass or non-mass), lesion locations (by clock position), the distance of the lesions from the nipple, and BI-RADS categories. The criteria of identifying lesion type on rs-EPI DWI was similar to that on DCE-MRI according to BI-RADS® 5th edition (30). T2-weighted MR images were included in DWI-based evaluation to exclude simple cysts. Mean ADC values were calculated using an in-house developed software called body diffusion laboratory on basis of a computing language and interactive environment (BoDiLab, Siemens Healthineers, Erlangen, Germany) as described in prior studies (31). All b-value data (0, 50, 1,000, and 2,000 s/mm^2) were used for generating ADC maps by using the following equation: $S(b) = S0 \times \exp(-b \times ADC)$, where $S(b)$ is the DWI signal intensity at a certain b-value, $S(0)$ is the baseline signal at $b = 0$, and b is the applied diffusion sensitization. For these measurements, an ROI for each lesion (0.2–0.4 cm^2) was drawn manually on the darkest portion of the ADC map by avoiding fatty and necrotic tissues by referring to corresponding T2-weighted images (29). The previously reported ADC cutoff values of 1.25×10^{-3} mm^2/s, which produced an excellent diagnostic accuracy (16), were used to distinguish malignant from benign lesions. The BI-RADS categories of lesions on rs-EPI DWI were referred to the criteria in **Supplementary Table 1** with the same rules mentioned in DCE-MRI assessment's subsection.

Reader 2 (ZLY) was responsible for matching lesions on DCE-MRI and rs-EPI DWI according to lesion size, location, and distance of the lesion from the nipple. The lesions on rs-EPI DWI or DCE-MRI were also correlated with the corresponding pathological findings according to the lesion locations described in the surgery/needle biopsy records and detailed pathology reports.

Additionally, the lesion visualization (lesion conspicuity) on DCE-MRI and on rs-EPI DWI with b-value of 1,000 s/mm^2 was evaluated independently by two readers using a 3-point scale: 3-excellent (clearly showing lesions and its detailed morphological features); 2-good (clearly showing lesions, but with loss of anatomic details); and 1-poor (barely showing lesions with unsatisfactory contrast).

Statistical Analysis

Statistical Package for the Social Sciences (SPSS) version 21.0 (IBM, Armonk, NY, USA) was applied for statistical analysis. The continuous variable was shown as mean ± SD, and categorical variable was displayed as percentage.

For summarizing lesion characteristics between benign and malignant lesions, data recorded by reader 2 (TA, who was more experienced in interpreting the breast MRI) was used for analysis, including lesion size, shape, margin, internal enhancement, distribution of non-mass-like lesions, TIC, and mean ADC value. Those characteristics were compared using the Student's t-test or the Chi-square test between benign and malignant lesions groups.

The ability of rs-EPI DWI in detecting breast lesions identified by DCE-MRI was evaluated on a per-patient and per-lesion level, respectively. Then, with pathology results as a reference, the performance of rs-EPI DWI and DCE MRI in distinguishing

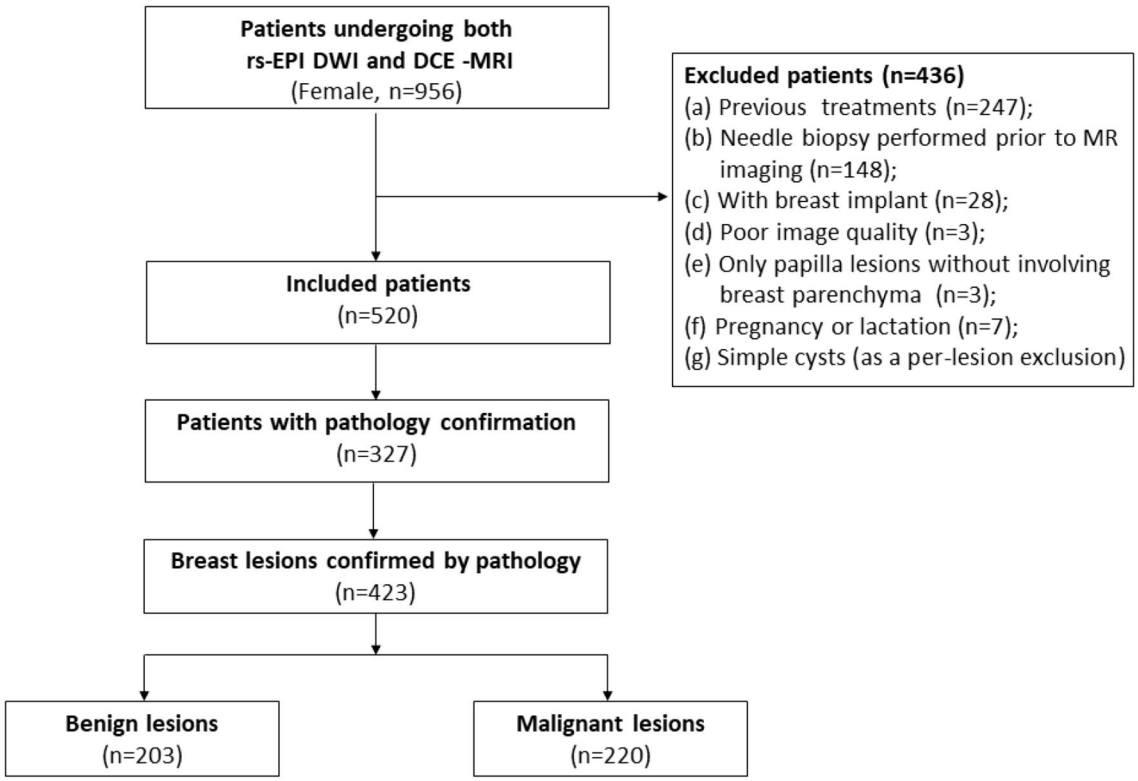

FIGURE 1 | Flowchart of this study. DCE-MRI, dynamic contrast material-enhanced MRI; rs-EPI DWI, readout-segmented echo-planar imaging diffusion-weighted imaging.

TABLE 1 | Sequence parameters for T2-weighted imaging, diffusion-weighted imaging, and dynamic contrast-enhanced MRI.

Parameters	T2-weighted sequence	Readout-segmented echo-planar imaging diffusion-weighted sequence (RESOLVE)	Dynamic contrast-enhanced MRI		
			TWIST-VIBE with 35 phases (n = 61, from Jul. 2013 to Jun. 2015)	TWIST-VIBE with 28 phases (n = 184, from Jul. 2015 to Oct. 2017)	TWIST-VIBE with 60 phases (n = 275, from Nov. 2017 to Oct. 2019)
Repetition time (ms)	3,700	5,000	5.40	5.91	5.24
Echo time (ms)	101	70	2.46	2.46	2.46
Field of view (mm^2)	320 × 320	169 × 280	270 × 320	290 × 320	260 × 320
Matrix	224 × 320	114 × 188	243 × 320	203 × 320	182 × 320
Flip angle (°)	137	180	9	10	10
Slice thickness (mm)	4.0	5.0	1.5, no gap	1.5, no gap	1.5, no gap
Pixel bandwidth (Hz/Px)	347	887	980	780	780
Parallel imaging	GRAPPA (x2)	GRAPPA (x2)	CAIPIRINHA (x4)	CAIPIRINHA (x4)	CAIPIRINHA (x4)
b-values (sec/mm^2)		0, 50, 1,000, 2,000			
Diffusion acquisition		5 readout segments, 1 average			
Diffusion gradient mode		3-scan-trace			
Temporal resolution (sec/phase)			11.24	7.96 (12 s of time interval for the late 10 phases)	5.74
Acquisition time (min:s)	2:06	4:27	6:48	5:51	5:57

TWIST, time-resolved angiography with stochastic trajectories; VIBE, volume-interpolated breath-hold examination.

breast lesions was assessed on per-patient and per-lesion basis and was compared by using the Chi-square test. The inter-reader agreement for lesion visualization on rs-EPI DWI (readers 1 and 2) and DCE-MRI (readers 1 and 2) was, respectively, assessed by the Cohen's Kappa analysis: $\kappa = 0.81–1.00$, excellent agreement; $\kappa = 0.61–0.80$, good agreement; $\kappa = 0.41–0.60$, moderate agreement; $\kappa = 0.21–0.40$, fair agreement; $\kappa = 0.01–0.20$, slight agreement; and $\kappa = 0$, no agreement (32). Additionally, the lesion conspicuity between rs-EPI-DWI and DCE-MRI was compared using the Wilcoxon signed rank test. When a $p < 0.05$, a statistical significance was considered. Based on available data, mean ADC values of invasive breast cancers with different molecular subtypes were compared by the one-way ANOVA test or by the Student *t*-test. The molecular subtypes of breast cancers include luminal A (ER or PR positive, or both, HER2 negative, and low expression of Ki-67), luminal B (ER or PR positive, or both, HER2 negative, and high expression of Ki-67), HER2-enriched (HER2 positive), and triple-negative tumors (ER, PR, and HER2 negative) (33).

RESULTS

General Characteristics

Of 520 women (mean age, 43.1- ± 10.5-years), FGT was observed in 21.7% (113/520) patients with low density (a and b) and 78.3% (407/520) patients with high density (c and d). Of patients with high density, 58.2% (237/407) were older than 40-years. Minimal or mild BPE was observed in 61.9% of patients (322/520), and moderate or marked BPE was observed in 38.1% of patients (198/520) (**Table 2**). Of 520 patients, 327/520 (62.9%) patients had 423 breast lesions confirmed by pathology with 203 benign lesions and 220 malignant lesions (**Table 2**). The lesion characteristics of benign and malignant lesions are shown in **Supplementary Table 2**.

TABLE 2 | Characteristics of 520 women study cohort.

Characteristic	Result
Mean age (years)	43.1 ± 10.5, Range of 12–83
Amount of FGT	
Almost entirely fat (a)	14 (2.7%)
Scattered fibroglandular tissue (b)	99 (19.0%)
Heterogeneous fibroglandular tissue (c)	324 (62.3%)
Extreme fibroglandular tissue (d)	83 (16.0%)
BPE level	
Minimal	60 (11.5%)
Mild	262 (50.4%)
Moderate	164 (31.5%)
Marked	34 (6.5%)
Available pathology results	
Patients	327
Benign	120/327 (36.7%)
Malignant	207/327 (63.3%)
Breast lesions	423
Benign	203/423 (48.0%)
Mass-like	192/423 (45.4%)
Non-mass-like	11/423 (2.6%)
Malignant	220/423 (52.0%)
Mass-like	181/423 (42.8%)
Non-mass-like	39/423 (9.2%)

Data percentages in parentheses. Mean age is mean ± SD.
DCE-MRI, dynamic contrast-enhanced MRI; FGT, fibroglandular tissue; BPE, background parenchymal enhancement.

Detection Ability of rs-EPI DWI for Breast Lesions Identified by DCE-MRI

On DCE-MRI, reader 1 detected 726 breast lesions (<10 mm, $n = 293$; ≥10 mm, $n = 368$; non-mass-like, $n = 65$) in 433 patients (low breast density, $n = 93$; high breast density, $n = 340$). The reader 2 diagnosed 732 breast lesions (<10 mm, $n = 299$; ≥10 mm, $n = 368$; non-mass-like lesions, $n = 65$) in 437 patients (low breast density, $n = 93$; high breast density, $n = 344$). The rs-EPI DWI can detect 95.4% (413/433) of patients and 90.8% (659/726) of lesions identified by DCE-MRI by reader 1, and 95.4% (417/437) of patients and 90.6% (663/732) of lesions depicted by DCE-MRI by reader 2. Of lesions ≥10 mm on DCE-MRI, 96.2% (354/368) and 96.2% (354/368) can be detected on rs-EPI DWI by reader 1 and reader 2, respectively. For lesions <10 mm on DCE-MRI, rs-EPI DWI can depict 82.6% (242/293) and 82.3% (246/299) of lesions by reader 1 and reader 2, respectively. **Figure 2** shows lesions delineated by rs-EPI DWI with good visualization of morphological details.

A good or excellent lesion visualization (2 or 3 score) was given in 94.0% (640/681) of lesions by reader 1 and 92.7% (636/686) by reader 2 on rs-EPI DWI, and 97.4% (707/726) of lesions by reader 1 and 97.0% (710/732) by reader 2 on DCE-MRI. The inter-reader agreement of the lesion visualization evaluation was good on rs-EPI-DWI ($k = 0.780$) and on DCE-MRI ($k = 0.683$). The lesion visibility was superior for DCE-MRI than rs-EPI-DWI (all $p < 0.05$).

Discrepant Findings of DCE-MRI and rs-EPI DWI in Detecting Breast Lesions

The details of discrepant findings of DCE-MRI and rs-EPI DWI in detecting breast lesions by two readers are shown in **Table 3**. A total of 22 lesions in 16 patients (reader 1) and 23 lesions in 17 patients (reader 2) were positive detection on rs-EPI DWI, whereas negative on DCE-MRI. A majority of those lesions were rated as BI-RADS 2 or 3 on rs-EPI DWI by the two readers and without any malignant pathology reports (**Table 3**, **Figures 3a–c**).

A total of 67 lesions in 56 patients (reader 1) and 69 lesions in 57 patients (reader 2) were positive on DCE-MRI, whereas negative on rs-EPI DWI (**Table 3**). Among those lesions, 76.1% (51/67) (reader 1) and 76.8% (53/69) (reader 2) had maximal diameter smaller than 10 mm, and more than 90% were categorized as BI-RADS 2 or 3 on DCE-MRI. According to the available pathological results, 34.3% (23/67) (reader 1) and 33.3% (23/69) (reader 2) of lesions missed by rs-EPI DWI were benign

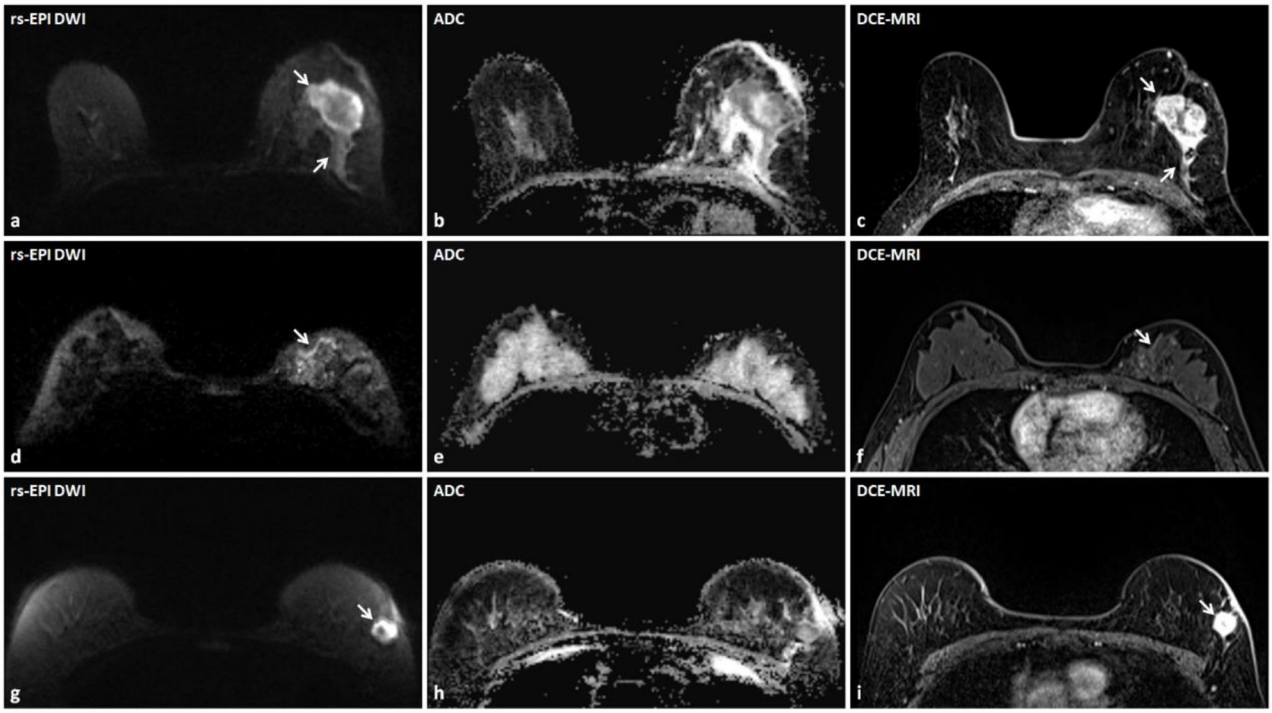

FIGURE 2 | Three lesions accurately detected by rs-EPI DWI with detailed morphology characteristics in three patients. **(a–c)** rs-EPI DWI (*b*-value, 1,000 s/mm^2), ADC map, and DCE-MRI of a 60-year-old woman with the left breast invasive carcinoma. **(a)** rs-EPI DWI shows an irregular mass (arrow) with markedly low signal on ADC map **(b)**, and the lesion shape and extent are consistent with that delineated on DCE-MRI (arrow) **(c)**. **(d–f)** rs-EPI DWI (*b*-value, 1,000 s/mm^2), ADC map, and DCE-MRI of a 50-year-old woman with the left breast ductal carcinoma *in situ*. **(d)** rs-EPI DWI shows abnormal linear hyper-intensity distributed along the duct (arrow) with superior visualization than observed on DCE-MRI (arrow) **(f)**, which may reflect the distribution of ductal carcinoma *in situ*. **(g–i)** rs-EPI DWI (*b*-value, 1,000 s/mm^2), ADC map, and DCE-MRI of a 57-year-old woman with the left breast invasive carcinoma. **(g)** rs-EPI DWI shows a mass with the heterogeneous internal structure (arrow) and low signal in the rim on ADC map **(h)**. **(i)** DCE-MRI shows an irregular mass (arrow) with heterogeneous enhancement.

TABLE 3 | Discrepant findings of DCE-MRI and rs-EPI DWI in detecting breast lesions.

Findings	Age (y) (Mean ± SD)	Size (mm) (Mean ± SD)	Mass (*n*)	Non-mass (*n*)	BI-RADS ratings (DCE-MRI)		BI-RADS ratings (rs-EPI DWI)		Histopathological results		
					2 or 3 (*n*)	4 or 5 (*n*)	2 or 3 (*n*)	4 or 5 (*n*)	Malignant (*n*)	Benign (*n*)	NA (*n*)
DCE-MRI (-) and rs-EPI DWI (+)											
R1 ($n = 22$)	43.6 ± 6.8	6.9 ± 2.5	21	1			19	3	0	5	17
R2 ($n = 23$)	43.8 ± 6.6	6.8 ± 2.4	22	1			18	5	0	5	18
DCE-MRI (+) and rs-EPI DWI (–)											
R1 ($n = 67$)	42.1 ± 10.3	8.0 ± 4.6	65	2	62	5			2	23	42
R2 ($n = 69$)	42.1 ± 10.3	7.9 ± 4.5	67	2	64	5			2	23	44

SD, standard deviation; BI-RADS, Breast Imaging Reporting and Data System; rs-EPI DWI, readout-segmented echo-planar imaging diffusion-weighted imaging; DCE-MRI, dynamic contrast-enhanced MRI; NA, not applicable; R1, reader 1; R2, reader 2.

diseases (**Figures 3d–f**), and only two lesions were confirmed as malignant (**Figure 4**).

Performance of rs-EPI DWI and DCE-MRI for Diagnosing Breast Cancers

With pathology as a standard reference, the performances of DCE-MRI and rs-EPI DWI for identifying breast cancers on per-patient basis and per-lesion basis are shown in **Supplementary Table 3** and **Table 4**, respectively.

The sensitivity, specificity, and accuracy of rs-EPI DWI in distinguishing breast cancers on per-lesion level were 95.9% (211/220), 85.7% (174/203), and 91.0% (385/423) for reader 1, and 97.7% (215/220), 86.2% (175/203), and 92.2% (390/423) for reader 2. The sensitivity, specificity, and accuracy of DCE-MRI in diagnosing breast cancers on per-lesion level were 98.2%

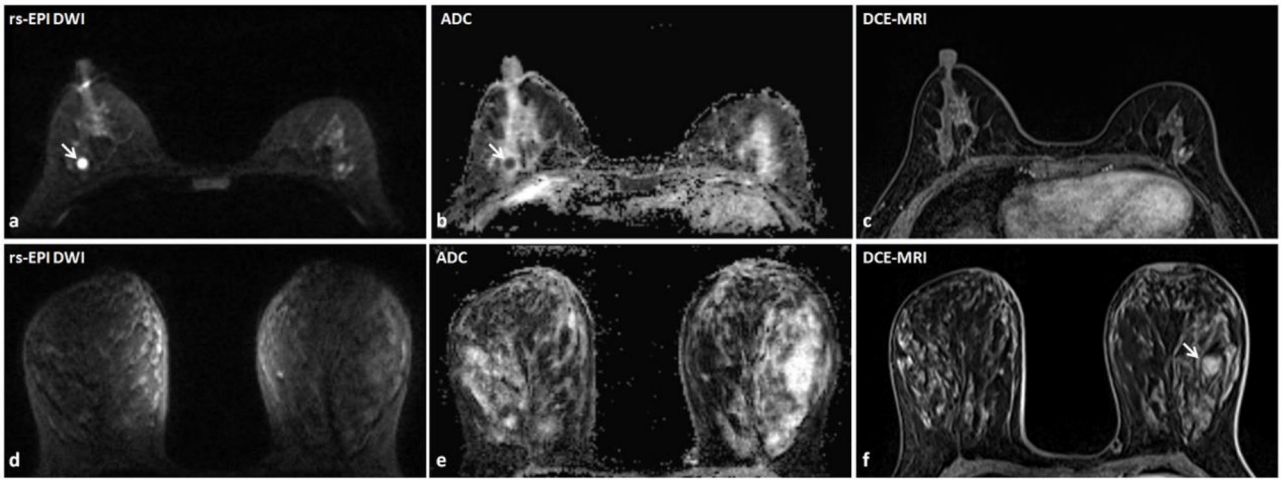

FIGURE 3 | Discrepant findings of DCE-MRI and rs-EPI DWI for detecting breast lesions. **(a)** rs-EPI DWI (*b*-value, 1,000 s/mm^2) shows a round, well-defined, and homogeneous nodule (6.7 mm) (arrow) with markedly low signal on ADC map **(b)** (mean ADC value, 0.47 × 10^{-3} mm^2/s) (arrow) in the right breast of a 43-year-old woman, whereas **(c)** DCE-MRI shows no abnormal enhancement at that location. This lesion was pathologically verified as the right breast fibroadenosis. **(d–f)** rs-EPI DWI (*b*-value, 1,000 s/mm^2), ADC map, and DCE-MRI of a 47-year-old woman with the left breast adenosis. **(f)** DCE-MRI depicts a well-defined lesion (14.6 mm) (arrow), whereas there is no abnormal signal on rs-EPI DWI **(d)** and ADC map **(e)**.

(216/220), 84.7% (172/203), and 91.7% (388/423) for reader 1 and 99.1% (218/220), 80.8% (164/203), and 90.3% (382/423) for reader 2. There were no significant differences for the overall performance in distinguishing breast cancers from benign lesions between DCE-MRI and rs-EPI DWI, and also for the analysis of the subgroups with different lesion types (all $p > 0.05$).

Based on the available data, the mean ADC values of the invasive breast cancers with different molecular subtypes are shown in **Supplementary Table 4**. A higher ADC value was found for non-luminal tumors when compared with luminal tumors.

False Findings Depicted by rs-EPI DWI During Diagnosing Breast Cancers

Several malignant tumors were classified as benign diseases based upon rs-EPI DWI including invasive carcinoma ($n = 5$ and 3 for readers 1 and 2, respectively), ductal carcinoma *in situ* ($n = 3$ and 2), and mucinous carcinoma ($n = 1$ and 0) (**Figures 5a–d**). A total of 29 (reader 1) and 28 (reader 2) benign lesions were classified as malignancies on rs-EPI DWI, including: intraductal papilloma ($n = 10$ and 8 for reader 1 and reader 2, respectively), fibroadenoma/fibroadenomatous hyperplasia ($n =$ 5 and 6), inflammatory change ($n = 5$ and 7) (**Figures 5e–h**), adenosis ($n = 7$ and 6), fibromatosis ($n = 1$ and 1), and phyllodes tumor ($n = 1$ and 0).

DISCUSSION

Readout-segmented echo-planar imaging DWI shows potential in breast cancer screening and diagnosis. In our study, rs-EPI DWI can detect about 90% of breast lesions identified by DCE-MRI. The sensitivity, specificity, and negative predictive value (NPV) of rs-EPI DWI for distinguishing breast lesions are comparable to those of DCE-MRI.

Non-contrast DWI has shown the potential to detect and differentiate breast lesions without the long-term toxicities potentially associated with contrast dosing. However, reported sensitivities (from 45 to 94%) and specificities (from 79 to 95.7%) varied greatly in earlier studies (34–37). Recently, several studies demonstrated improved diagnostic performance when using the readout-segmented technique (10, 19, 38).

In this study, we intended to explore the feasibility of rs-EPI DWI as an imaging tool for breast cancer screening, in particular in women with high breast density. For this purpose, rs-EPI DWI should firstly achieve the ability to detect lesions as many as possible, in particular for non-cystic lesions, which are of higher risk of malignancy. DCE-MRI is the most sensitive imaging modality for breast cancer detection and has an excellent spatial resolution. Based on our results, rs-EPI DWI can detect about 90% of the breast lesions identified by DCE-MRI, even with a slice thickness of 5.0 mm. The detection ability was slightly lower than the result reported by Telegrafo et al. (37) using an unenhanced-MRI protocol of short TI inversion recovery (STIR), T2-weighted and DWI (90% vs. 96%), which may be due to the thicker slice thickness of DWI in our study (5.0 mm vs. 3.0 mm). Small and benign lesions on DCE-MRI may be more easily overlooked by rs-EPI DWI. Of those missed lesions, however, most were rated as BI-RADS 2 or 3 on DCE-MRI, and only two of these lesions were finally verified as malignancies based upon histopathological examination. Therefore, although rs-EPI DWI may overlook some breast lesions identified by DCE-MRI, the probability of missing breast malignancies was quite low.

The second ability that rs-EPI DWI should reach is to pick up suspiciously malignant lesions. Thus, we included pathological results as a reference to evaluate the performance of DCE-MRI

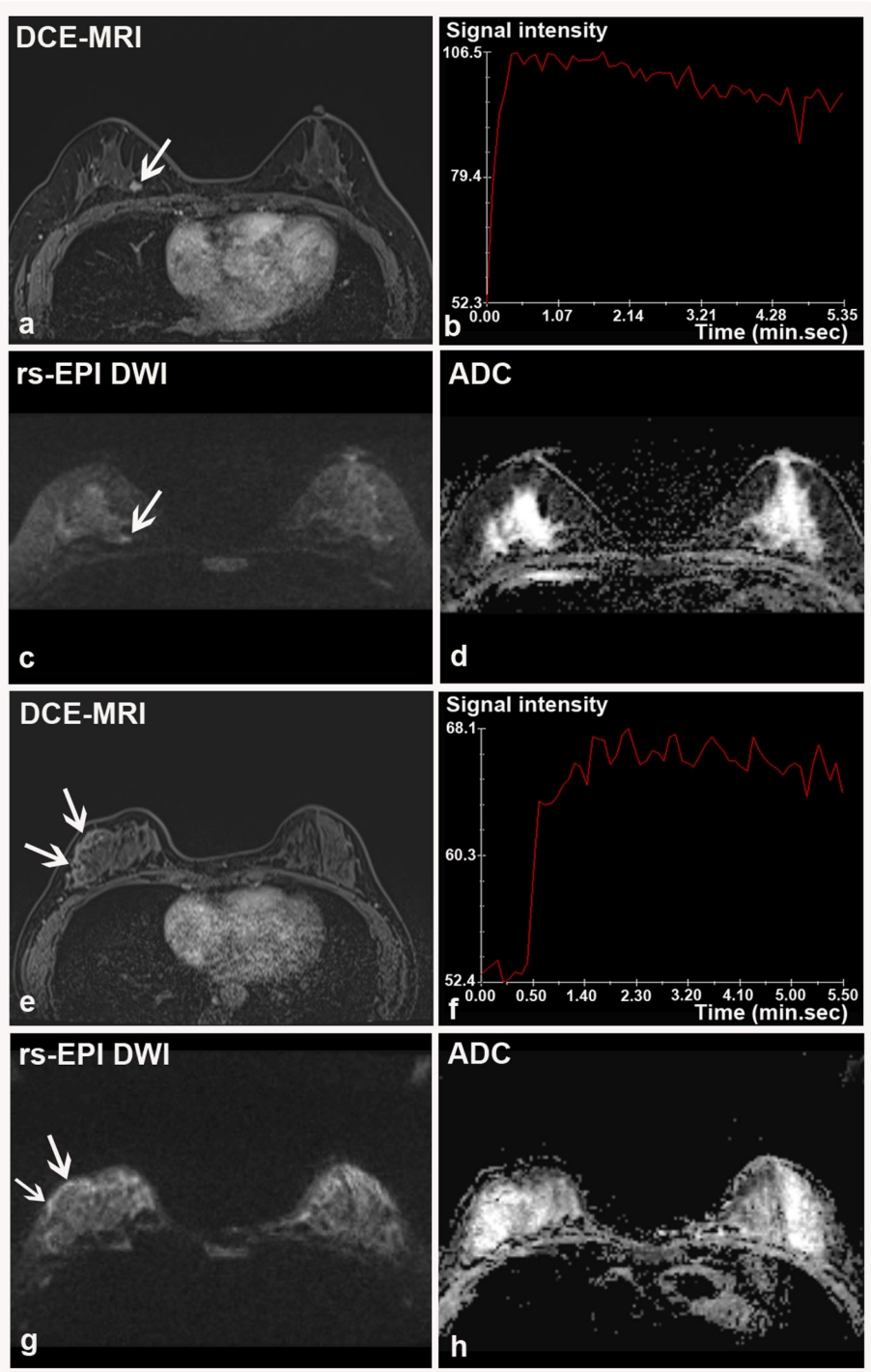

FIGURE 4 | Two breast malignancies missed by rs-EPI DWI in two patients. **(a–d)** DCE-MRI, time-signal intensity curve (TIC), rs-EPI DWI (*b*-value, 1,000 s/mm^2), and ADC map of a 55-year-old woman with the right breast ductal carcinoma *in situ*. **(a)** DCE-MRI shows a lobulated and spiculated nodule (8.7 mm) (arrow) with initial fast enhancement followed by a washout **(b)** classified as BI-RADS 4. No lesion was found on corresponding rs-EPI DWI **(c)** and ADC map **(d)**. **(e–h)** DCE-MRI, TIC, rs-EPI DWI (*b*-value, 1,000 s/mm^2), and ADC map of a 42-year-old woman with the right breast ductal carcinoma *in situ*. **(e)** DCE-MRI shows non-mass-like enhancement along the parenchyma surface (arrow) with initial fast enhancement followed by plateau **(f)** classified as BI-RADS 4. No lesion can be identified on corresponding rs-EPI DWI **(g)** and ADC map **(h)**. Slight high signal can be retrospectively observed for both cases on rs-EPI DWI (**c,g**, respectively) (arrow), but it was not considered sufficient to confirm the presence of lesions. The latter finding may be attributable to the inferior spatial resolution (5 mm) of our rs-EPI DWI protocol relative to DCE-MRI protocol.

TABLE 4 | Diagnostic performance of rs-EPI DWI and DCE-MRI for characterizing the breast cancers with pathology as reference standard.

	Results (*n*)				Test performance (%)				
Imaging modality	**TP**	**TN**	**FP**	**FN**	**Sens.**	**Spec.**	**PPV**	**NPV**	**Acc.**
rs-EPI DWI									
Overall									
R1	211	174	29	9	95.9 (211/220) [92.4–97.8]	85.7 (174/203) [80.2–89.9]	87.9 (211/240) [83.2–91.5]	95.1 (174/183) [90.9–97.4]	91.0 (385/423) [87.9–93.4]
R2	215	175	28	5	97.7 (215/220) [94.8–99.0]	86.2 (175/203) [80.8–90.3]	88.5 (215/243) [83.9–91.9]	97.2 (175/180) [93.7–98.8]	92.2 (390/423) [89.3–94.5]
Mass-like lesion									
R1	174	170	22	7	96.1 (174/181) [92.2–98.1]	88.5 (170/192) [83.3–92.3]	88.8 (174/196) [83.6–92.5]	96.0 (170/177) [92.1–98.1]	92.2 (344/373) [89.1–94.5]
R2	177	172	20	4	97.8 (177/181) [94.5–99.1]	89.6 (172/192) [84.5–93.2]	89.8 (177/197) [84.8–93.3]	97.7 (172/176) [94.3–99.1]	93.6 (349/373) [90.6–95.6]
Non-mass-like lesion									
R1	37	4	7	2	94.9 (37/39) [83.1–98.6]	36.4 (4/11) [15.2–64.6]	84.1 (37/44) [70.6–92.1]	66.7 (4/6) [30.0–90.3]	82.0 (41/50) [69.2–90.2]
R2	38	3	8	1	97.4 (38/39) [86.8–99.6]	27.3 (3/11) [9.7–56.6]	82.6 (38/46) [69.3–90.9]	75.0 (3/4) [30.1–95.4]	82.0 (41/50) [69.2–90.2]
DCE-MRI									
Overall									
R1	216	172	31	4	98.2 (216/220) [95.4–99.3]	84.7 (172/203) [79.1–89.0]	87.4 (216/247) [82.7–91.0]	97.7 (172/176) [94.3–99.1]	91.7 (388/423) [88.7–94.0]
R2	218	164	39	2	99.1 (218/220) [96.8–99.8]	80.8 (164/203) [74.8–85.6]	84.8 (218/257) [79.9–88.7]	98.8 (164/166) [95.7–99.7]	90.3 (382/423) [87.1–92.8]
Mass-like lesion									
R1	177	167	25	4	97.8 (177/181) [94.5–99.1]	87.0 (167/192) [81.5–91.0]	87.6 (177/202) [82.4–91.5]	97.7 (167/171) [94.1–99.1]	92.2 (344/373) [89.1–94.5]
R2	179	161	31	2	98.9 (179/181) [96.1–99.7]	83.9 (161/192) [78.0–88.4]	85.2 (179/210) [79.8–89.4]	98.8 (161/163) [95.6–99.7]	91.2 (340/373) [87.8–93.6]
Non-mass-like lesion									
R1	39	5	6	0	100 (39/39) [91.0–100]	45.5 (5/11) [21.3–72.0]	86.7 (39/45) [73.8–93.7]	100 (5/5) [56.6–100]	88.0 (44/50) [76.2–94.4]
R2	39	3	8	0	100 (39/39) [91.0–100]	27.3 (3/11) [9.7–56.6]	83.0 (39/47) [69.9–91.1]	100 (3/3) [43.9–100]	84.0 (42/50) [71.5–91.7]

TP, true positive; TN, true negative; FP, false positive; FN, false negative; Sens., sensitivity; Spec., specificity; PPV, positive predictive value; NPV, negative predictive value; Acc., Accuracy; R1, reader 1; R2, reader 2; rs-EPI DWI, readout-segmented echo-planar imaging diffusion-weighted imaging; DCE-MRI, dynamic contrast-enhanced MRI.

Data in parentheses are the numerator and denominator. Data in brackets are 95% CIs.

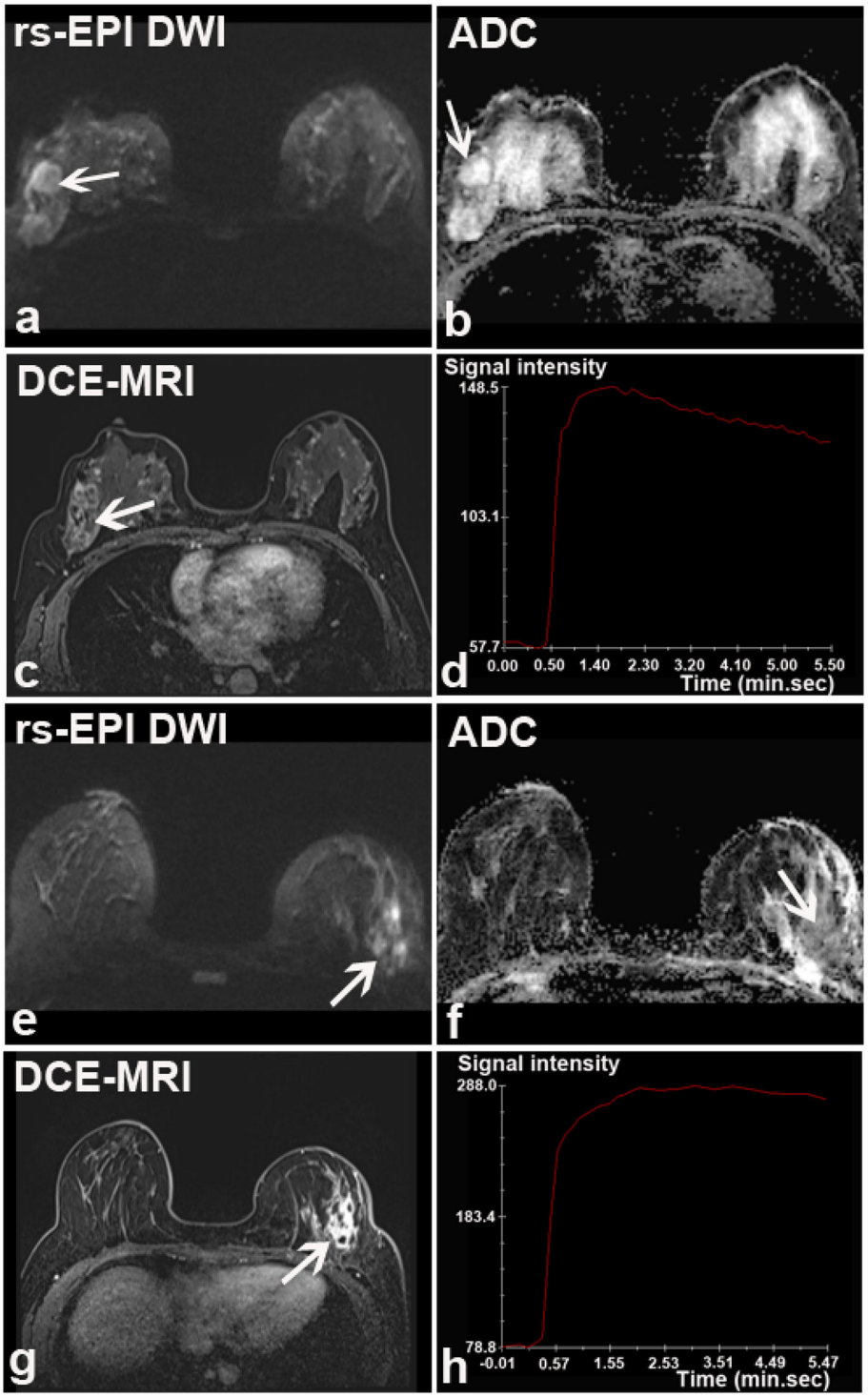

FIGURE 5 | Two breast lesions falsely classified by rs-EPI DWI in two patients. **(a–d)** rs-EPI DWI (*b*-value, 1,000 s/mm^2), ADC map, DCE-MRI, and time-signal intensity curve (TIC) from a 46-year-old woman with the right breast mucinous carcinoma. **(a)** rs-EPI DWI shows a lesion with an irregular shape and heterogeneous internal structure, but high signal on ADC map (arrow) **(b)**. The lesion was considered as fibrocystic hyperplasia and rated as BI-RADS 3. **(c)** DCE-MRI shows that this lesion has an irregular shape and heterogeneous signal enhancement (arrow) with initial fast enhancement followed by washout **(d)**. Thus, lesion was categorized as BI-RADS 4. **(e–h)** rs-EPI DWI (*b*-value, 1,000 s/mm^2), ADC map, DCE-MRI, and TIC from a 33-year-old woman with the left breast granulomatous mastitis accompanying a small abscess. **(e)** rs-EPI DWI shows irregular high signals with markedly low signal on ADC map (arrow) **(f)**. Lesion was categorized as malignancy based upon rs-EPI DWI. **(g)** DCE-MRI shows non-mass-like enhancement with segmental distribution (arrow) and initial fast enhancement followed by plateau **(h)**, thus categorized as BI-RADS 4.

and rs-EPI DWI in distinguishing breast cancers from benign diseases. During identifying breast cancers, rs-EPI DWI not only provided quantitative parameters (ADC values) but also detailed visualization of lesion morphological characteristics. By integrating each of these parameters together into a comprehensive diagnostic protocol, the performance of rs-EPI DWI for distinguishing breast lesions was actually equivalent to that of DCE-MRI, which was also provided by previous studies (10, 37). The sensitivity of DWI in our study was a little higher than that reported by Bickelhaupt et al. (17) (95.9%−97.7% vs. 92.0%), which may be partly due to the larger mean lesion size of our study. There were different causes for the inclusion into our study, such as clinical symptoms, which may explain the larger lesion size compared to the study using only patients with suspicious x-ray mammography (17).

Although encouraging results were found, several malignancies were still diagnosed as benign diseases according to rs-EPI DWI alone. Some small breast cancers (<10 mm) showed a relatively well-defined margin and homogeneous internal structures, and ROI of those lesions for quantitative measurements may be inaccurate due to partial volume effects. These factors may have led to the false classification of some small malignant lesions by rs-EPI-DWI. Some difficulties were also found when attempting to distinguish between the breast fibrocystic hyperplasia and breast cancers. In this study, a pathologically proven breast mucinous carcinoma was characterized as fibrocystic hyperplasia in a 46-year-old woman by an experienced radiologist (**Figures 5a–d**). This lesion had an irregular shape and heterogeneously increased T2 signal intensity with a high ADC value, thus resembling a manifestation of the breast fibrocystic hyperplasia. Conversely, some cases of the benign disease were wrongly interpreted as malignancies by the readers when only rs-EPI DWI data were used for the diagnosis. For example, a granulomatous mastitis, presenting as a large lesion with an irregular shape, heterogeneous internal structures, and decreased ADC value, was misdiagnosed as breast cancer (**Figures 5e–h**). It was also difficult to accurately identify non-mass-like lesions due to irregular distribution and inaccurate measurements of the ADC value. In this context, clinical symptoms and signs, and enhancement characteristics on DCE-MRI may provide additional information for the differential diagnosis.

Several limitations existed in our study. First, this study was conducted retrospectively at a single center. Second, the spatial resolution for the breast DWI in our study (5.0 mm) was lower than that of DCE-MRI (1.5 mm), which may result in missing some small lesions. In order to act as a reliable screening tool, the spatial resolution of the breast DWI needs to be further improved. Newly explored simultaneous multi-slice (SMS) acquisition based on the blipped controlled aliasing in parallel imaging results in the higher acceleration (blipped CAIPIRINHA) technique (39). The latter method has the potential to substantially reduce acquisition time and make it possible to improve the spatial resolution (smaller than 5.0 mm), without requiring additional scan time. Lastly, MR examinations in this study were performed using two types of the breast coils because of a system update and different scanning protocols were used for DCE-MRI, which may have introduced some variations in the results. Thus, a future multi-center clinical study using optimized standard MR sequences should be performed to further validate these results for rs-EPI DWI in the breast cancer screening and diagnosis.

In conclusion, rs-EPI DWI can detect about 90% of breast lesions identified with DCE-MRI, and provides comparable diagnostic performance to that of DCE-MRI for characterizing breast cancers. These findings suggest that rs-EPI DWI may provide a safe and reliable supplemental imaging modality for breast cancer screening, particularly for patients with dense breasts and contraindication for GBCA.

DATA AVAILABILITY STATEMENT

The raw data supporting the conclusions of this article will be made available by the authors, without undue reservation.

ETHICS STATEMENT

The studies involving human participants were reviewed and approved by The institutional review board of Tongji Hospital, Tongji Medical College, Huazhong University of Science and Technology. Written informed consent for participation was not provided by the participants' legal guardians/next of kin because: This is a retrospective study and no extra imaging scans and intervention were performed for participants. A waived written informed consent was approved by Our institutional review board.

AUTHOR CONTRIBUTIONS

ZLY and YQH performed study design, information collection, statistical analysis, and manuscript editing. LMX and TA guided study design, reviewed images, and revised manuscript. MXZ, XYZ, and HTZ provided technical support and software for measuring ADC values. JH and CAZ collected images and clinical information. All authors contributed to the article and approved the submitted version.

SUPPLEMENTARY MATERIAL

The Supplementary Material for this article can be found online at: https://www.frontiersin.org/articles/10.3389/fonc.2021.636471/full#supplementary-material

REFERENCES

1. Chen W, Zheng R, Baade PD, Zhang S, Zeng H, Bray F, et al. Cancer statistics in China, 2015. *CA Cancer J Clin.* (2016) 66:115–32. doi: 10.3322/caac.21338

2. Bray F, Ferlay J, Soerjomataram I, Siegel RL, Torre LA, Jemal A. Global cancer statistics 2018: GLOBOCAN estimates of incidence and mortality worldwide for 36 cancers in 185 countries. *CA Cancer J Clin.* (2018) 68:394–424. doi: 10.3322/caac.21492

3. Fan L, Strasser-Weippl K, Li JJ, St Louis J, Finkelstein DM, Yu KD, et al. Breast cancer in China. *Lancet Oncol.* (2014) 15:e279–89. doi: 10.1016/S1470-2045(13)70567-9
4. Miller KD, Nogueira L, Mariotto AB, Rowland JH, Yabroff KR, Alfano CM, et al. Cancer treatment and survivorship statistics, 2019. *CA Cancer J Clin.* (2019) 69:363–85. doi: 10.3322/caac.21565
5. Smith RA, Andrews KS, Brooks D, Fedewa SA, Manassaram-Baptiste D, Saslow D, et al. Cancer screening in the United States, 2017: a review of current American Cancer Society guidelines and current issues in cancer screening. *CA Cancer J Clin.* (2017) 67:100–21. doi: 10.3322/caac.21392
6. Schunemann HJ, Lerda D, Quinn C, Follmann M, Alonso-Coello P, Rossi PG, et al. Breast cancer screening and diagnosis: a synopsis of the European breast guidelines. *Ann Intern Med.* (2020) 172:46–56. doi: 10.7326/M19-2125
7. Uematsu T. The need for supplemental breast cancer screening modalities: a perspective of population-based breast cancer screening programs in Japan. *Breast Cancer.* (2017) 24:26–31. doi: 10.1007/s12282-016-0707-2
8. Amornsiripanitch N, Bickelhaupt S, Shin HJ, Dang M, Rahbar H, Pinker K, et al. Diffusion-weighted MRI for unenhanced breast cancer screening. *Radiology.* (2019) 293:504–20. doi: 10.1148/radiol.2019182789
9. Bennani-Baiti B, Krug B, Giese D, Hellmich M, Bartsch S, Helbich TH, et al. Evaluation of 3.0-T MRI brain signal after exposure to gadoterate meglumine in women with high breast cancer risk and screening breast MRI. *Radiology.* (2019) 293:523–30. doi: 10.1148/radiol.2019190847
10. Baltzer PAT, Bickel H, Spick C, Wengert G, Woitek R, Kapetas P, et al. Potential of noncontrast magnetic resonance imaging with diffusion-weighted imaging in characterization of breast lesions: intraindividual comparison with dynamic contrast-enhanced magnetic resonance imaging. *Invest Radiol.* (2018) 53:229–35. doi: 10.1097/RLI.0000000000000433
11. Pinker K, Moy L, Sutton EJ, Mann RM, Weber M, Thakur SB, et al. Diffusion-weighted imaging with apparent diffusion coefficient mapping for breast cancer detection as a stand-alone parameter: comparison with dynamic contrast-enhanced and multiparametric magnetic resonance imaging. *Invest Radiol.* (2018) 53:587–95. doi: 10.1097/RLI.0000000000000465
12. Petrillo A, Fusco R, Sansone M, Cerbone M, Filice S, Porto A, et al. Abbreviated breast dynamic contrast-enhanced MR imaging for lesion detection and characterization: the experience of an Italian oncologic center. *Breast Cancer Res Treat.* (2017) 164:401–10. doi: 10.1007/s10549-017-4264-y
13. Kuhl CK, Schrading S, Strobel K, Schild HH, Hilgers RD, Bieling HB. Abbreviated breast magnetic resonance imaging (MRI): first postcontrast subtracted images and maximum-intensity projection-a novel approach to breast cancer screening with MRI. *J Clin Oncol.* (2014) 32:2304–10. doi: 10.1200/JCO.2013.52.5386
14. Guo BJ, Yang ZL, Zhang LJ. Gadolinium deposition in brain: current scientific evidence and future perspectives. *Front Mol Neurosci.* (2018) 11:335. doi: 10.3389/fnmol.2018.00335
15. Ei Khouli RH, Jacobs MA, Mezban SD, Huang P, Kamel IR, Macura KJ, et al. Diffusion-weighted imaging improves the diagnostic accuracy of conventional 3.0-T breast MR imaging. *Radiology.* (2010) 256:64–73. doi: 10.1148/radiol.10091367
16. Bogner W, Gruber S, Pinker K, Grabner G, Stadlbauer A, Weber M, et al. Diffusion-weighted MR for differentiation of breast lesions at 3.0 T: how does selection of diffusion protocols affect diagnosis? *Radiology.* (2009) 253:341–51. doi: 10.1148/radiol.2532081718
17. Bickelhaupt S, Laun FB, Tesdorff J, Lederer W, Daniel H, Stieber A, et al. Fast and noninvasive characterization of suspicious lesions detected at breast cancer X-Ray screening: capability of diffusion-weighted MR imaging with MIPs. *Radiology.* (2016) 278:689–97. doi: 10.1148/radiol.2015150425
18. Bogner W, Pinker K, Zaric O, Baltzer P, Minarikova L, Porter D, et al. Bilateral diffusion-weighted MR imaging of breast tumors with submillimeter resolution using readout-segmented echo-planar imaging at 7 T. *Radiology.* (2015) 274:74–84. doi: 10.1148/radiol.14132340
19. Bogner W, Pinker-Domenig K, Bickel H, Chmelik M, Weber M, Helbich TH, et al. Readout-segmented echo-planar imaging improves the diagnostic performance of diffusion-weighted MR breast examinations at 3.0 T. *Radiology.* (2012) 263:64–76. doi: 10.1148/radiol.12111494
20. McKay JA, Church AL, Rubin N, Emory TH, Hoven NF, Kuehn-Hajder JE, et al. A comparison of methods for high-spatial-resolution diffusion-weighted imaging in breast MRI. *Radiology.* (2020) 297:304–12. doi: 10.1148/radiol.2020200221
21. Kishimoto AO, Kataoka M, Iima M, Honda M, Miyake KK, Ohashi A, et al. Evaluation of malignant breast lesions using high-resolution readout-segmented diffusion-weighted echo-planar imaging: comparison with pathology. *Magn Reson Med Sci.* (2020) doi: 10.2463/mrms.mp.2020-0021. [Epub ahead of print].
22. Baltzer PA, Benndorf M, Dietzel M, Gajda M, Camara O, Kaiser WA. Sensitivity and specificity of unenhanced MR mammography (DWI combined with T2-weighted TSE imaging, ueMRM) for the differentiation of mass lesions. *Eur Radiol.* (2010) 20:1101–10. doi: 10.1007/s00330-009-1654-5
23. Yabuuchi H, Matsuo Y, Sunami S, Kamitani T, Kawanami S, Setoguchi T, et al. Detection of non-palpable breast cancer in asymptomatic women by using unenhanced diffusion-weighted and T2-weighted MR imaging: comparison with mammography and dynamic contrast-enhanced MR imaging. *Eur Radiol.* (2011) 21:11–7. doi: 10.1007/s00330-010-1890-8
24. Bickelhaupt S, Jaeger PF, Laun FB, Lederer W, Daniel H, Kuder TA, et al. Radiomics based on adapted diffusion kurtosis imaging helps to clarify most mammographic findings suspicious for cancer. *Radiology.* (2018) 287:761–70. doi: 10.1148/radiol.2017170273
25. Mlynarska-Bujny A, Bickelhaupt S, Laun FB, Konig F, Lederer W, Daniel H, et al. Influence of residual fat signal on diffusion kurtosis MRI of suspicious mammography findings. *Sci Rep.* (2020) 10:13286. doi: 10.1038/s41598-020-70154-3
26. Porter DA, Heidemann RM. High resolution diffusion-weighted imaging using readout-segmented echo-planar imaging, parallel imaging and a two-dimensional navigator-based reacquisition. *Magn Reson Med.* (2009) 62:468–75. doi: 10.1002/mrm.22024
27. Kim YJ, Kim SH, Kang BJ, Park CS, Kim HS, Son YH, et al. Readout-segmented echo-planar imaging in diffusion-weighted MR imaging in breast cancer: comparison with single-shot echo-planar imaging in image quality. *Korean J Radiol.* (2014) 15:403–10. doi: 10.3348/kjr.2014.15.4.403
28. Kishimoto AO, Kataoka M, Iima M, Honda M, Miyake KK, Ohashi A, et al. The comparison of high-resolution diffusion weighted imaging (DWI) with high-resolution contrast-enhanced MRI in the evaluation of breast cancers. *Magn Reson Imaging.* (2020) 71:161–9. doi: 10.1016/j.mri.2020.03.007
29. Baltzer P, Mann RM, Iima M, Sigmund EE, Clauser P, Gilbert FJ, et al. Diffusion-weighted imaging of the breast-a consensus and mission statement from the EUSOBI International Breast Diffusion-Weighted Imaging working group. *Eur Radiol.* (2020) 30:1436–50. doi: 10.1007/s00330-019-06510-3
30. D'Orsi CJ, Sickles EA, Mendelson EB, Morris EA, Creech WE, Butler PF, et al. *ACR BI-RADS® Atlas, Breast Imaging Reporting and Data System*. Reston, VA: American College of Radiology (2013).
31. Sun K, Chen X, Chai W, Fei X, Fu C, Yan X, et al. Breast cancer: diffusion kurtosis MR imaging-diagnostic accuracy and correlation with clinical-pathologic factors. *Radiology.* (2015) 277:46–55. doi: 10.1148/radiol.15141625
32. Lu L, Zhang LJ, Poon CS, Wu SY, Zhou CS, Luo S, et al. Digital subtraction CT angiography for detection of intracranial aneurysms: comparison with three-dimensional digital subtraction angiography. *Radiology.* (2012) 262:605–12. doi: 10.1148/radiol.11110486
33. Harbeck N, Gnant M. Breast cancer. *Lancet.* (2017) 389:1134–50. doi: 10.1016/S0140-6736(16)31891-8
34. Horvat JV, Durando M, Milans S, Patil S, Massler J, Gibbons G, et al. Apparent diffusion coefficient mapping using diffusion-weighted MRI: impact of background parenchymal enhancement, amount of fibroglandular tissue and menopausal status on breast cancer diagnosis. *Eur Radiol.* (2018) 28:2516–24. doi: 10.1007/s00330-017-5202-4
35. McDonald ES, Hammersley JA, Chou SH, Rahbar H, Scheel JR, Lee CI, et al. Performance of DWI as a rapid unenhanced technique for detecting mammographically occult breast cancer in elevated-risk women

with dense breasts. *Am J Roentgenol.* (2016) 207:205–16. doi: 10.2214/AJR.15.15873
36. Belli P, Bufi E, Bonatesta A, Patrolecco F, Padovano F, Giuliani M, et al. Unenhanced breast magnetic resonance imaging: detection of breast cancer. *Eur Rev Med Pharmacol Sci.* (2016) 20:4220–9.
37. Telegrafo M, Rella L, Stabile Ianora AA, Angelelli G, Moschetta M. Unenhanced breast MRI (STIR, T2-weighted TSE, DWIBS): an accurate and alternative strategy for detecting and differentiating breast lesions. *Magn Reson Imaging.* (2015) 33:951–5. doi: 10.1016/j.mri.2015.06.002
38. Pinker K, Baltzer P, Bogner W, Leithner D, Trattnig S, Zaric O, et al. Multiparametric MR imaging with high-resolution dynamic contrast-enhanced and diffusion-weighted imaging at 7 T improves the assessment of breast tumors: a feasibility study. *Radiology.* (2015) 276:360–70. doi: 10.1148/radiol.15141905
39. Frost R, Jezzard P, Douaud G, Clare S, Porter DA, Miller KL. Scan time reduction for readout-segmented EPI using simultaneous multislice acceleration: diffusion-weighted imaging at 3 and 7 Tesla. *Magn Reson Med.* (2015) 74:136–49. doi: 10.1002/mrm.25391

Conflict of Interest: XYZ and HTZ were employed by the company Siemens Healthcare.

The remaining authors declare that the research was conducted in the absence of any commercial or financial relationships that could be construed as a potential conflict of interest.

frontiers in Oncology

ORIGINAL RESEARCH
published: 19 May 2021
doi: 10.3389/fonc.2021.643003

Enhancing the Screening Efficiency of Breast Cancer by Combining Conventional Medical Imaging Examinations With Circulating Tumor Cells

*Yang Gao[1,2], Wan-Hung Fan[3], Chaohui Duan[4], Wenhe Zhao[5], Jun Zhang[6] and Xixiong Kang[1,2]**

[1] Key Laboratory for Biomechanics and Mechanobiology of Ministry of Education, School of Biological Science and Medical Engineering, Beihang University, Beijing, China, [2] Beijing Advanced Innovation Center for Biomedical Engineering, Beihang University, Beijing, China, [3] Department of Clinical Medical Affairs, Hangzhou Watson Biotech, Hangzhou, China, [4] Department of Clinical Laboratory, Sun Yat-Sen Memorial Hospital, Sun Yat-Sen University, Guangzhou, China, [5] Department of Oncology, Sir Run Run Shaw Hospital, Zhejiang University School of Medicine, Hangzhou, China, [6] Department of Clinical Laboratory, Sir Run Run Shaw Hospital, Zhejiang University School of Medicine, Hangzhou, China

OPEN ACCESS

Edited by:
Pilar López-Larrubia,
Consejo Superior de Investigaciones Científicas (CSIC), Spain

Reviewed by:
Robert Vierkant,
Mayo Clinic, United States
Dawei Yang,
Liaocheng People's Hospital, China

***Correspondence:**
Xixiong Kang
kangxxtt@sina.com

Specialty section:
This article was submitted to Cancer Imaging and Image-directed Interventions, a section of the journal Frontiers in Oncology

Received: 16 February 2021
Accepted: 22 April 2021
Published: 19 May 2021

Citation:
Gao Y, Fan W-H, Duan C, Zhao W, Zhang J and Kang X (2021) Enhancing the Screening Efficiency of Breast Cancer by Combining Conventional Medical Imaging Examinations With Circulating Tumor Cells. Front. Oncol. 11:643003. doi: 10.3389/fonc.2021.643003

Purpose: Ultrasound (US) and mammogram (MMG) are the two most common breast cancer (BC) screening tools. This study aimed to assess how the combination of circulating tumor cells (CTC) with US and MMG would improve the diagnostic performance.

Methods: CTC detection and imaging examinations, US and MMG, were performed in 238 treatment-naive BC patients, 217 patients with benign breast diseases (BBD), and 20 healthy females. Correlations of CTC, US and MMG with patients' clinicopathological characteristics were evaluated. Diagnostic performances of CTC, US and MMG were estimated by the receiver operating characteristic curves.

Results: CTC, US and MMG could all distinguish BC patients from the control ($p < 0.0001$). Area under curve (AUC) of CTC, US and MMG are 0.855, 0.861 and 0.759, respectively. While US has the highest sensitivity of 0.79, CTC and MMG have the same specificity of 0.92. Notably, CTC has the highest accuracy of 0.83. Combination with CTC increases the AUC of US and MMG to 0.922 and 0.899, respectively. Combining MMG with CTC or US increases the sensitivity of MMG to 0.87, however "CTC + MMG" has a higher specificity of 0.85. "CTC + US" performs the best in BC diagnosis, followed by "CTC + MMG" and then "US + MMG".

Conclusion: CTC can be used as a diagnostic aid for BC screening. Combination with CTC increases the diagnostic potency of conventional BC screening imaging examinations, US and MMG, in BC diagnosis, especially for MMG.

Keywords: breast cancer, circulating tumor cells, mammogram, ultrasound, screening

INTRODUCTION

Breast cancer (BC) is the most frequently diagnosed cancer and the leading cause of cancer-related death in women worldwide (1). Every year there are more than 2 million of newly diagnosed cases and more than 630,000 people died of BC globally (1). About 12.4% of women (1 in 8) will develop BC at some point in their lives (1, 2). Although the incidence and mortality rates of BC are ranked 120 and 163 respectively in the world, BC is still the most common cancer among females in China (2, 3). It is estimated that 304,000 BC cases were newly diagnosed and approximately 69,900 women died of BC in China in 2015 (3). BC mortality rates have declined over the passing decades in developed countries such as the United States and United Kingdom, but death from BC in China is still slowly increasing (2). BC is generally diagnosed through either screening or a symptom (breast swelling or a palpable mass) that leads to a medical examination (4). The decline in BC mortality is mainly attributed to a combination of advances in prevention or screening and improved treatment methods (4). The aims of cancer prevention and screening are to reduce cancer incidence by removing carcinogenic factors from the daily-life and to identify asymptomatic patients at very early stage of tumor. Patients with smaller tumors have a higher chance to be cured. Recent innovations in cancer prevention and detection have come to the molecular level to allow for a more accurate identification of at-risk individuals (4). Introduction of new drugs and treatment regimens, such as adjuvant chemotherapy, hormonal therapy and immunotherapy, prolongs the survival of BC patients, especially for the patients at advanced cancer stage. BC screening is not yet a common routine practice in each province in China. Most BC patients have already reached the middle or late stage at the time of diagnosis, which may explain why the mortality of BC is still increasing and why 5-year-survival rate of BC in China is lower than that in the United States (82% VS 90%) (5).

Common screening modalities for BC include palpation, blood-based assay and medical imaging methods (6). Palpation can be further divided into self-breast examinations (SBE) and clinical breast examinations (CBE) (6). SBE was used to be considered as the first line of BC screening, but results of two clinical trials failed to show a BC mortality benefit due to SBE (7, 8). On the contrary, SBE usually leads to self-panic and unnecessary testing or biopsies, which turns out to be harmful for the subject (6). CBE is a palpation performed by trained clinic staff. CBE has a high specificity of 0.94-0.99, but a very low sensitivity of 0.21-0.54 (6). Therefore, CBE cannot exclude the presence of BC. Blood-based assay is a non-invasive method to detect serum BC specific biomarkers. Suggested biomarkers, such as carcinoembryonic antigen (CEA) and cancer antigen 15-3 or 27-29 (CA15-3, CA27-29), usually lack sensitivity and/or specificity, and thus not suitable for early disease detection (9).

Diagnostic imaging modalities recommended by American Joint Committee on Cancer (AJCC) for BC screening include mammography (MMG), ultrasound (US) and magnetic resonance imaging (MRI). MMG uses low dose X-rays to examine lesions in the breast, allowing the examinations of small calcification points, tumor *in situ* (Tis), and structure of the breast. MMG sensitivity for BC declines significantly with increasing breast density (10). Breast US is a non-invasive examination that uses high-frequency acoustic reflection to reveal tissue inside the breast. Breast US is often used in conjunction with MMG to increase the sensitivity of BC detection for women at average risk. US can help to identify whether the lumps found in MMG is solid or filled with fluid. Although US is more accurate than MMG in differentiating breast masses or cysts, it cannot detect the small calcification points, the sign of early stage lesion, and is less sensitive to tumors with size less than 5 mm or deep in the breast. US also generates more false-positive examinations. MRI is often used in conjunction with MMG for high-risk women BC screening. MRI has no radiation exposure and can provide excellent images with high contrast and resolution under appropriate conditions. MRI is the most sensitive diagnostic tool for breast diseases because it can be performed in any direction without the influence of tissue overlap or breast composition. In the cost-effective aspect, MRI is more used in the diagnosing and staging process rather than BC screening. Aforementioned imaging methods can all detect early stage BC, however, these conventional imaging methods still have some limitations that would affect image quality and thus the diagnostic accuracy of the breast examination. Therefore, it is still in an urgent need to find a reliable biomarker allowing better screening and early diagnosis of BC.

Circulating tumor cells (CTC) are tumor cells shed from the primary tumor or metastatic sites into circulation. The 7th edition of AJCC Staging Manual for BC has introduced a new cancer stage, cM0(i+), at which no clinical or radiographic evidence of distant metastases is found, but tumors cells are still detected in the bone marrow, blood or distant non-regional lymph nodes. Therefore, CTC represent the process of tumor metastasis. CTC has been proven to be a prognostic factor in BC to predict patients' survival outcomes (11, 12). Patients with metastatic BC (MBC) usually have more CTC and BC patients with more CTC usually have shorter progression free survival and overall survival (11). In addition, studies show as well that CTC can reflect the tumor burden and can be used as a monitoring biomarker to assess patients' response to treatment and tumor recurrences (13). CTC are rare cells in the bloodstream. The most common strategy to enrich and identify CTC from the surrounding blood cells is based on the epithelial cell biomarkers. CellSearch® (Menarini Silicon Biosystems, Huntingdon Valley, US), the only U.S. Food and Drug Administration (FDA) approved CTC system, use epithelial cell adhesion molecule (EpCAM) and cytokeratin (CK) antibody to enrich and identify CTC. Blood cells would not express EpCAM or CK, while most of the epithelial cells found in the circulation are tumor cells detaching from the solid tumors of epithelial origin. Therefore, it is common to use epithelial markers to detect CTC.

Previous studies showed CTC could reflect tumor burden in BC and can distinguish diseased patients from the healthy control (14). Overall CTC detection rate with CytoSorter® (Hangzhou

Watson Biotech, Hangzhou, China), a microfluidic-based immuno-capture CTC platform, in BC is 85.16%, and detection rates in early stage (stage I-II) BC are still more than 80%, suggesting that CTC could be used a diagnostic tool for BC screening (14). US and MMG are the two most common methods for BC screening in Chinese clinic. 238 BC patients, 217 patients with benign breast diseases (BBD), and 20 healthy females from 2 hospitals were enrolled in this study. We aimed to compare the performances of CTC, US and MMG in BC diagnosis and to assess whether the combination with CTC would enhance the diagnostic potency of US and MMG.

MATERIAL AND METHODS

Patients

In total, 238 female BC patients, including 17 ductal carcinoma *in situ* (DCIS), 82 stage I, 106 stage II, 31 stage III and 2 stage IV, 217 patients with BBD and 20 healthy females from Zhejiang University Medical College Affiliated Sir Run Shaw Hospital and Sun Yat-Sen University Sun Yat-Sen Memorial Hospital were enrolled in this study between December 2017 and December 2018. Control referred to patients with BBDs and healthy volunteers. Stage I-II BC patients were considered as patients at early stage. Inclusion criteria were as follows: (1) female patients age between 18 to 75 years; (2) patients had negative history of malignancy and were treatment-naive before enrollment; (3) patients received US and MMG examinations before diagnosis. (4) healthy females had no medical history of any malignant disease and no findings in breast by palpation, US and/or MMG. Exclusion criteria were as follows: (1) patients were pregnant or breast-feeding; (2) patients were currently undergoing or had prior cancer treatment; (3) patients had other malignant tumors or other malignant diseases within 5 years prior to enrollment; (4) patients had other conditions which investigators thought not suitable for the study. Patients' clinicopathological characteristics, including age, menstrual state, histological type, grade, hormone receptors, human epidermal growth factor receptor 2 (HER2) and the clinical stage at diagnosis were collected.

Blood Collection and CTC Detection

CTC were enriched by CytoSorter® epithelial cells detection kit. CTC detection procedure was following CytoSorter® manufacturer protocol and was described in the previous study (14, 15). In brief, the CytoChipNano was first coated with EpCAM antibody before placing onto CytoSorter®. The first 2 mL of peripheral blood was discarded to avoid potential skin epithelial cell contamination from venipuncture and 4 mL of blood was proceed to gradient-centrifuge within 6 hours after collection to collect the peripheral blood mononuclear cells (PBMC) layer. PBMC sample solution was then transferred into the spiral sample tube. Once the CTC enrichment was finished, the CytoChipNano was removed from CytoSorter® and proceed to the immunofluorescence staining of PanCK-FITC (pan-cytokeratin-fluorescein isothiocyanate), CD45-PE (cluster of differentiation 45-phycoerythrin) and DAPI (4,6-diamidino-2-phenylindole). An OPPNO immunofluorescence microscopy (DSY5000X, OPPNO, Chongqing, China) was used to identify CTC by searching for PanCK-FITC+, CD45-PE-, and DAPI+ cells.

Medical Imaging Examinations

US examination was performed with IU Elite® (Philips Healthcare, Best, Netherlands). MMG examination was performed using Selenia® (Hologic, Santiago, USA). Examination results were evaluated by experienced radiologists according to American College of Radiology (ACR) Breast Imaging-Reporting and Data System (BI-RADS) assessment categories.

Statistical Analysis

Statistical analyses were performed using Prism 5.0 (Graphpad, La Jolla, CA, USA) and SPSS 20 (IBM, Armonk, NY, USA). Student t test was used for continuous variables, as appropriate. The x^2 test and Fisher's exact test were used for the comparison of categorical parameters. One-way analysis of variance (ANOVA) was performed to calculate the differences among multiple groups. The receiver operating characteristic (ROC) curves were plotted to evaluate the sensitivity, specificity and area under the curve (AUC) value of the diagnostic methods. CTC, US and MMG cut-off values were determined by the highest Youden index (sensitivity + specificity - 1). A two-sided p value less than 0.05 was considered statistically significant.

Combinational ROC Model

Combinational ROC analyses were performed using SPSS 20. The multiple variable were combined using logistic regression. In brief, the BI-RADS categories, 1, 2, 3, 4a, 4b, 4c, 5 and 6, were first convert into scores, 1, 2, 3, 4, 5, 6, 7 and 8, respectively. Binary logistic regression analysis was used to calculate the correlation coefficient of each variable in the combination with respect to diagnosis. Combination score would be obtained based on the variables and correlation coefficients. ROC of combination scores was drawn. The point closest to the left upper corner of the combinational ROC would be used as the combination score cut-off to calculate the sensitivity and specificity.

RESULTS

CTC Can Reflect BC Patients' Tumor Burden and Can Be Used as a Diagnostic Aid for BC Screening

CTC were identified as PanCK positive, CD45 negative and DAPI positive cells as shown in **Figure 1A**. Correlation of CTC with patients' clinicopathological features are listed in **Table 1**. CTC are detected in 199 out of 238 BC patients, 71 out of 217 patients with BBD and 5 out of 20 healthy females. The average CTC counts (maximum CTC count) are 2.38 (15), 0.43 (4) and

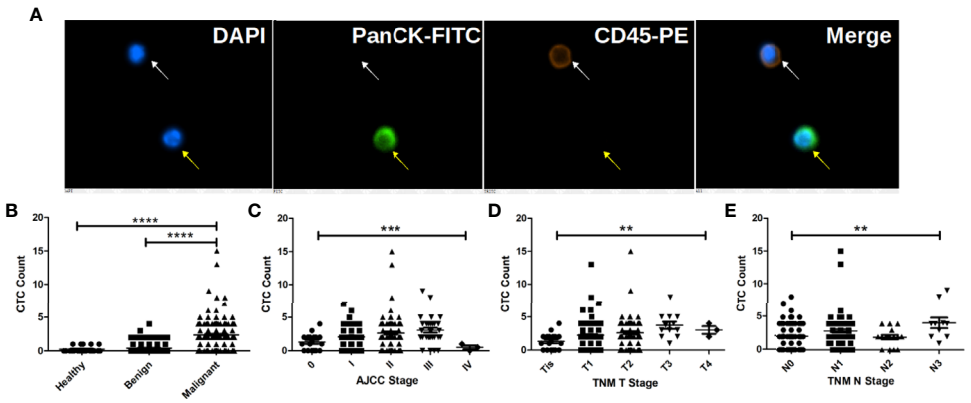

FIGURE 1 | CTC are correlated with BC patients' cancer stage, tumor size and lymph node involvement and can be used to distinguish BC patients from patients with benign tumors and healthy female. **(A)** Immunofluorescent staining of a captured CTC, indicated by the yellow arrow. CTC is defined as a DAPI (blue) positive, PanCK-FITC (green) positive and CD45-PE (orange) negative cell, while a white blood cell is indicated by the white arrow as a DAPI positive, CD45-PE positive and PanCK-FITC negative cell. **(B)** CTC enumeration can differentiate BC patients from patients with benign tumors and healthy females (both $p < 0.0001$). **(C)** CTC enumerations are correlated with BC patients' cancer stage ($p = 0.0007$), tumor size ($p = 0.0015$) and lymph node involvement ($p = 0.0034$). More CTC are found in patient with bigger tumors and more lymph node involvement as shown in **(D, E)**. **** indicates $P < 0.0001$, *** indicates $0.0001 < P < 0.001$, while ** indicates $0.001 < P < 0.01$.

TABLE 1 | Correlations of CTC with patients' pathoclinical characteristics.

Group	n	Average Age (Median, Range) (years)	CTC detected in	CTC Detection Rate (%)	Average CTC Count (Range) (/4 mL)	p Value*
BC Patients	238	52.34 (51, 29-75)	199	83.61	2.38 (0-15)	**<0.0001**
Patients with BBD	217	46.97 (45, 20-73)	71	32.72	0.43 (0-4)	
Healthy volunteers	20	50.58 (49, 29-67)	5	25	0.25 (0-1)	
(All BC patients number = 238)						
AJCC Stage						**0.0007**
0	17	51.75 (46, 40-67)	11	64.71	1.29 (0-4)	
I	82	54.6 (55, 31-73)	68	82.93	2.06 (0-7)	
II	106	51.91 (51, 29-73)	92	86.79	2.63 (0-15)	
III	31	48.37 (46, 29-75)	27	87.1	3.06 (0-9)	
IV	2	48.5 (48.5, 34-63)	1	50	0.5 (0-1)	
TNM Stage						
Tumor Size						**0.0015**
Tis	17	51.75 (46, 40-67)	11	64.71	1.29 (0-4)	
T1	117	53.49 (54, 31-73)	98	83.76	2.23 (0-13)	
T2	91	51.52 (50, 29-75)	77	84.62	2.59 (0-15)	
T3	11	50.28 (54, 29-64)	11	100	3.73 (1-8)	
T4	2	38 (38, 37-39)	2	100	3 (2-4)	
Lymph Node Involvement						**0.0034**
N0	142	53.76 (53, 29-73)	111	78.17	2.06 (0-8)	
N1	72	50.99 (50.5, 29-69)	66	91.67	2.86 (0-15)	
N2	15	46.49 (45, 33-75)	11	73.33	1.93 (0-4)	
N3	9	50.52 (54, 34-64)	9	100	4.11 (1-9)	

CTC, circulating tumor cell; n, number of patients; BC, breast cancer; BBD, benign breast diseases; AJCC, American Joint Committee on Cancer; TNM, tumor-node-metastasis; Tis, tumor in situ.

**The p value of comparisons is based on the CTC enumeration of each group.*

Bold values mean statistical significances.

0.25 (1), respectively. Most control (patients with BBD and healthy females) have less than 2 CTC. Statistical results show that CTC enumeration could be able to differentiate BC patients from patients with BBD and healthy females as shown in **Figure 1B** (both $p < 0.0001$). Statistical results show as well that CTC are correlated with AJCC stage ($p = 0.0007$), tumor size ($p = 0.0015$) and lymph node involvement ($p = 0.0034$) as shown in **Figures 1C–E**. Patients at advanced cancer stage or with bigger tumors or more lymph node involvement tend to have more CTC. CTC detection rates in early stages (stage I & II) BC patients are 82.93% and 86.79%, respectively. Furthermore, CTC are detected in 11 out of 17 Tis (DCIS) patients. Overall CTC detection in BC patients is 83.61%. Taken together, the results suggest that CTC could be used as a diagnostic tool for BC screening.

Comparison of Diagnostic Potency of CTC, US and MMG in BC Diagnosis

The most common methods for BC screening in clinic are MMG and US. Therefore, we compared the performances of CTC, US and MMG in BC diagnosis. First, ROC curves were plotted separately as shown in **Figure 2**. When CTC cut-off value was set to 2, and both US BI-RADS and MMG BI-RADS cut-off scores were set to 4b, the highest Youden index of 0.65, 0.65 and 0.5 would be generated for CTC, US, and MMG, respectively. Detailed diagnostic performances of CTC, US and MMG are listed in **Table 2**. Among these three methods, US shows the highest sensitivity of 0.79. CTC and MMG have the same specificity of 0.92, while CTC

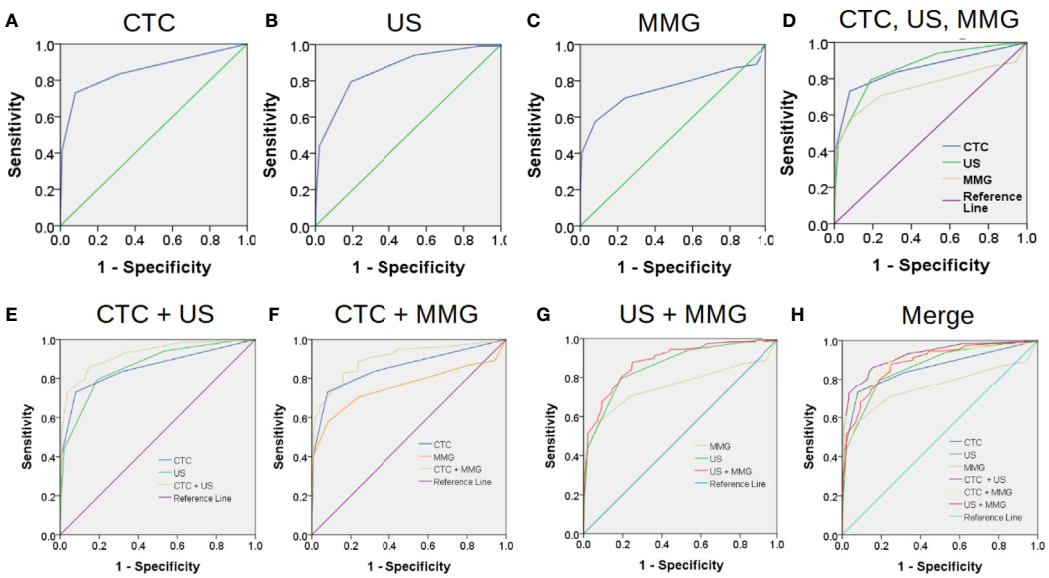

FIGURE 2 | Combination of conventional medical imaging examinations with CTC enhances the diagnostic efficiency for BC. The performances of CTC, US and MMG in BC diagnosis are shown in **(A–C)** by the receiver operating characteristic (ROC) curves. Area under the curve (AUC) of CTC, US and MMG are 0.855, 0.861 and 0.759, respectively. CTC exhibits a similar diagnostic performance as US as shown in **(D)**. Combination of CTC enhances the performances of US and MMG in BC diagnosis as shown in **(E, F)** with AUC increasing from 0.855 to 0.922 and 0.759 to 0.899, respectively. However, combination of MMG with US does not improve the diagnostic performance of US much as shown in **(F)** with AUC increasing slightly from 0.855 to 0.884. "CTC + US" gives the best diagnostic performance, while "CTC + MMG" and "US + MMG" have similar improved diagnostic performances as shown in **(H)**.

TABLE 2 | Diagnostic power of CTC, US and MMG in breast cancer diagnosis*.

	CTC	95% CI	US	95% CI	MMG	95% CI
Sensitivity	0.73	0.67 - 0.79	0.79	0.74 - 0.84	0.58	0.51 - 0.64
Specificity	0.92	0.88 - 0.95	0.81	0.75 - 0.86	0.92	0.88 - 0.95
Accuracy	0.83	0.79 - 0.86	0.80	0.76 - 0.84	0.75	0.71 - 0.79
Positive Likelihood Ratio (LR+)	9.12	5.88 - 14.13	4.18	3.19 - 5.48	7.18	4.60 - 11.20
Negative Likelihood Ratio (LR-)	0.29	0.24 -0.36	0.25	0.20 - 0.33	0.46	0.40 - 0.54
Youden Index	0.65	N/A	0.65	N/A	0.50	N/A
Area Under Curve (AUC)[#]	0.855	0.819 - 0.890	0.861	0.828 - 0.894	0.759	0.712 - 0.805
	CTC + US	**95% CI**	**CTC + MMG**	**95% CI**	**US + MMG**	**95% CI**
Sensitivity	0.90	0.86 - 0.94	0.87	0.82 - 0.91	0.87	0.82 - 0.91
Specificity	0.76	0.70 - 0.81	0.85	0.80 - 0.89	0.79	0.73 - 0.84
Accuracy	0.83	0.79 - 0.86	0.86	0.83 - 0.89	0.83	0.79 - 0.86
Positive Likelihood Ratio (LR+)	3.69	2.94 - 4.63	5.89	4.32 - 8.03	4.12	3.21 - 5.30
Negative Likelihood Ratio (LR-)	0.13	0.09 - 0.19	0.15	0.11 - 0.21	0.17	0.12 - 0.23
Youden Index	0.66	N/A	0.72	N/A	0.66	N/A
Area Under Curve (AUC)[#]	0.922	0.898 - 0.946	0.899	0.870 - 0.928	0.884	0.855 - 0.914

CTC, circulating tumor cell; CI, confidence interval; US, ultrasound; MMG, mammogram; N/A,. not applicable.

Confidence intervals for sensitivity, specificity and accuracy are "exact" Clopper-Pearson confidence intervals. Confidence intervals for the likelihood ratios are calculated using the "Log method".

**CTC, US and MMG cut-off values were determined by the highest Youden index (sensitivity + specificity - 1). When CTC cut-off value was set to 2, and both US BI-RADS and MMG BI-RADS cut-off scores were set to 4b, the highest Youden index of 0.65, 0.65 and 0.5 would be generated for CTC, US, and MMG, respectively. Subjects with more than 2 CTC, or with US or MMG BI-RADS score higher than 4b are classified as CTC, US and MMG positive for diagnosis, respectively. As long as any measurement of composing parameter was higher than its cut-off value, the combination result would be considered as positive for diagnosis.*

[#]AUC was determined by the ROC.

shows the highest accuracy of 0.83. Based on the AUC, CTC exhibits a similar diagnostic potency as US.

Subjects with more than 2 CTC, or with US or MMG BI-RADS score higher than 4b are classified as CTC, US and MMG positive for diagnosis, respectively. Correlation of CTC, US and MMG positive rates with patients' clinicopathological characteristics are listed in **Table 3** and shown in **Figure 3**. CTC, US and MMG positive rates show significant differences among BC patients, patients with BBD and healthy females (all $p < 0.0001$). CTC and US positive rates are associated with cancer stage ($p = 0.0021$ and 0.0034, respectively), tumor size ($p = 0.0444$ and 0.0054, respectively) and lymph node metastases ($p = 0.0086$ and 0.0271, respectively), while MMG positive rate is only associated with lymph node metastases ($p = 0.0195$). For early stage BC diagnosis, US has the highest sensitivity of 0.80, followed by CTC (0.74) and then MMG (0.57). Taken together, CTC and US have similar performances in BC diagnosis, and MMG shows the least diagnostic potency.

Combination With CTC Improves the Performances of US and MMG in BC Diagnosis

Next, we investigated whether the combination with CTC would enhance the performances of US and MMG in BC diagnosis. As shown in **Table 2** and **Figure 2**, combining with CTC increases the AUC of US and MMG from 0.861 to 0.922 and 0.759 to 0.899, respectively, while combining with MMG increases only slightly the AUC of US from 0.861 to 0.884. Although US has a slightly higher AUC of 0.861 than CTC (0.855), the combination of CTC with MMG generates a higher AUC of 0.899 than the conjugation of US with MMG (0.884). As long as any measurement of composing parameter was equal to or higher than its cut-off value, the combination result would be considered as positive for diagnosis. Combination with CTC increases the diagnostic sensitivity of US and MMG from 0.79 to 0.90 and 0.58 to 0.87, respectively. But at the same time, the specificity decreases from 0.81 to 0.76 and 0.92 to 0.85, respectively. Among these three combinations, "CTC + US" has the highest AUC of 0.922, followed by "CTC + MMG" (0.899) and then "US +MMG" (0.884). However, "CTC + MMG" has the highest accuracy of 0.86, followed by "CTC +US" (0.83) and "US + MMG" (0.83). Combination with CTC or US increases the sensitivity of MMG both to 0.87, but "CTC + MMG" has a higher specificity of 0.85.

As shown in **Table 4**, due to decreased specificity caused by the combinations, "CTC + US", "CTC + MMG" and "US +MMG" all show less statistical correlation with the patients' clinicopathological features. As for early stage BC diagnosis, "CTC + US", "CTC + MMG" and"US +MMG" have sensitivities of 0.91, 0.87 and 0.88, respectively. Taken together, combining with CTC would improve the performances of US and MMG in BC diagnosis, especially for MMG. Regarding improved diagnostic performance, the combination of CTC with either of US or MMG is better than the combination of US and MMG together.

DISCUSSIONS

Although our results confirmed the previous findings that CTC could be used to distinguish BC patients from the healthy females or patients with BBD (both $p < 0.0001$) and CTC could reflect

TABLE 3 | Clinicopathological characteristics of BC patients with ≥ 2 or < 2 CTC, with US BI-RADS score ≥ 4b or < 4b, and with MMG BI-RADS score ≥ 4b or < 4b.

Groups	n	CTC		p Value*	US BI-RADS		p Value*	MMG BI-RADS		p Value*
		≥ 2	< 2		≥ 4b	< 4b		≥ 4b	< 4b	
BC Patients	238	174	64	**<0.0001**	189	49	**<0.0001**	137	101	**<0.0001**
Patients with BBD	217	19	198		45	172		19	198	
Healthy volunteers	20	0	20		0	20		0	20	
(All BC patients number = 238)										
AJCC Stage				**0.0021**			**0.0034**			0.1573
0	17	8	9		8	9		7	10	
I	82	56	26		62	20		42	40	
II	106	83	23		89	17		65	41	
III	31	27	4		28	3		21	10	
IV	2	0	2		2	0		2	0	
Tumor Size				**0.0444**			**0.0054**			0.1857
Tis	17	8	9		8	9		7	10	
T1	117	83	34		91	26		63	54	
T2	91	71	20		78	13		57	34	
T3	11	10	1		10	1		9	2	
T4	2	2	0		2	0		1	1	
Lymph Node Metastasis				**0.0086**			**0.0271**			**0.0195**
Yes	96	79	17		83	13		64	32	
No	142	95	47		106	36		73	69	

BC, breast cancer; CTC, circulating tumor cell; US, ultrasound; BI-RADS, breast imaging-reporting and data system; MMG, mammogram; n, number of patients; BBD, benign breast diseases; AJCC, American Joint Committee on Cancer; Tis, tumor in situ.

**Based on the Youden index analysis, CTC, US and MMG cut-off values were 2, 4b, and 4b, respectively. Subjects with more than 2 CTC, or with US or MMG BI-RADS score higher than 4b are classified as CTC, US and MMG positive for diagnosis, respectively. The p value of comparisons is based on the positive proportion among groups.*

Bold values mean statistical significances.

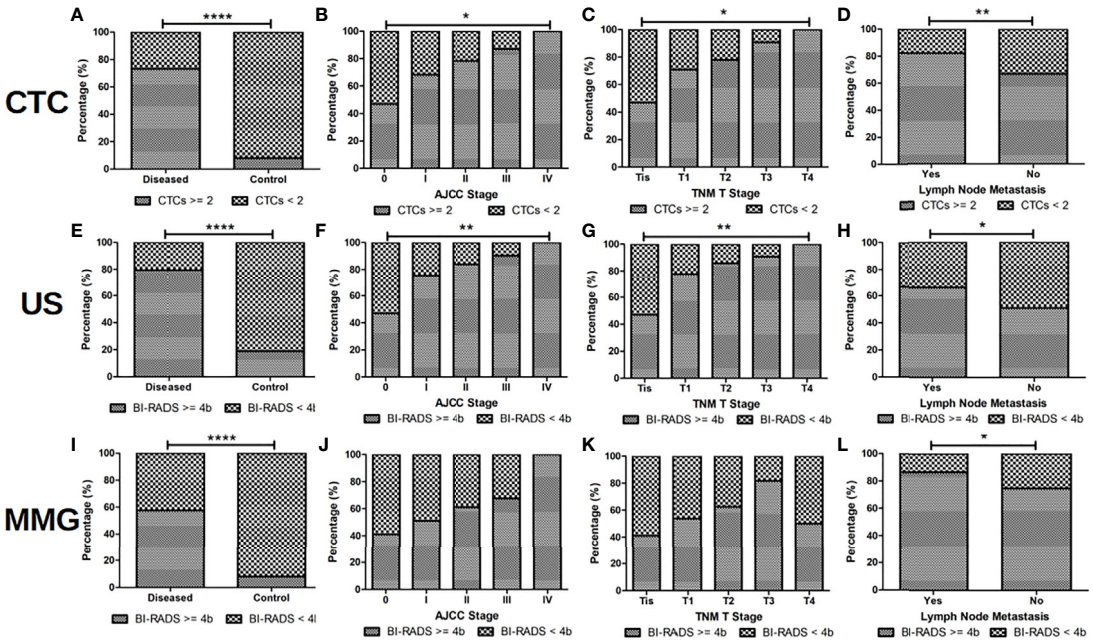

FIGURE 3 | CTC and US are more sensitive than MMG for BC diagnosis. When CTC cut-off value of 2, US and MMG BI-RADS cut-off score of 4b were set, positive rates of CTC, US and MMG show significant differences between BC patients and controls (patients with BBDs and healthy volunteers) as shown in **(A, E, I)**, respectively (all $p < 0.0001$). US should be slightly more sensitive than CTC in BC diagnosis, for positive rates of US are more correlated with BC patients' cancer stage and tumor size than CTC as shown in **(B, C, F, G)**. No statistical significance is found between positive rate of MMG and BC patients' cancer stage and tumor size as shown in **(J)** and **(K)**. Positive rates of CTC, US and MMG showed significant differences between BC patients with and without lymph node metastases as shown in **(D)**, **(H)** and **(L)** ($p = 0.0086$, 0.0271 and 0.0195, respectively). **** indicates $P < 0.0001$, ** indicates $0.001 < P < 0.01$, while * indicates $0.01 < P < 0.05$.

tumor burden (14), still 71 out of 217 patients with BBD had CTC detected. We used epithelial markers to detect CTC and the identified cells were not further validated by any tumor specific marker. Therefore, the CTC found in patients with BBD were not truly tumor cells but circulating epithelial cells. A study with CellSearch® system showed as well that positive events that met the criteria for "CTC" were detected in 11.3% of patients with benign colon diseases (16). Our results showed that CTC are correlated with tumor stage, tumor size and lymph node involvement ($p= 0.0007$, 0.0015 and 0.0034, respectively. Clinical value of CTC in BC has started to be recognized gradually by most BC experts worldwide. In the 8th edition of the AJCC BC guidelines published in 2018, it is written that CTC can be used as a prognostic biomarker to predict patients' survival outcomes. In the 2019 Chinese Society of Clinical Oncology (CSCO) BC clinical guidelines, it is written that CTC can reflect the condition of tumor tissue and can be used as a replacement of biopsy samples for pathological diagnosis, disease monitoring and molecular sequencing. CTC can be used to monitor treatment response and to predict prognosis (11–13). CTC has been proposed as a screening tool for lung cancer in high-risk groups of people (17). Based on the reviews of CTC in BC published in 2013 and 2016, maximum CTC detection rates in early stage and metastatic BC are 55% and 54%, respectively (11, 18). The detection rate varied depending on which CTC enrichment method was used (11, 18). CellSearch® system has CTC detection rates in BC less than 40% (18). Metastasis is an inevitable process during tumor progression. According to the recent study on ex vivo colorectal tumor model, a CTC can be released into circulation even when the tumor is smaller than 0.01 cm^3 (19). CTC represents the process of metastasis. Just due to the heterogeneous tumor nature, some patients would have less CTC in the circulation. In theory, as long as a detection method is sensitive, CTC should be detected in every cancer patient. Thus, CTC should be a reliable method for cancer screening. The reason why CTC has not been suggested as a screening tool for BC in practice might be due to the low detection rates. However, with the improvements of the CTC enrichment techniques recently, CTC detection is getting more sensitive. Liang et al. used CanPatrol™ system to detect CTC in early stage BC, and the detection rate is 81% (20). We used CytoSorter® to detect CTC in BC, and the overall CTC detection rate is 83.61% and the detection rate in early stage is 84.86%. With such a high detection rate, CTC can no doubt be used as a screening tool for BC. But a breast cancer specific marker might be required to be ascertained that the captured CTC originate from breast lesions and to reduce the false positive results in patients with BBD and healthy people.

Our results suggest that CTC can reflect tumor burden. BC patients at advanced stage, with bigger tumor and more lymph node involvement have usually more CTC. But in fact, less CTC were detected and a lower CTC detection rate was found in stage

TABLE 4 | Clinicopathological characteristics of BC patients diagnosed by CTC combined with US, CTC combined with MMG, or US combined with MMG.

Groups	n	CTC + US		p Value#	CTC + MMG		p Value#	US + MMG		p Value#
		Positive*	Negative		Positive*	Negative		Positive*	Negative	
BC Patients	238	215	23	**<0.0001**	207	31	**<0.0001**	207	31	**<0.0001**
Patients with BBD	217	58	159		35	182		50	167	
Healthy volunteers	20	0	20		0	20		0	20	
(All BC patients number = 238)										
AJCC Stage				**0.0137**			0.0951			**0.03**
0	17	12	5		12	5		11	6	
I	82	71	11		68	14		69	13	
II	106	100	6		96	10		96	10	
III	31	30	1		29	2		29	2	
IV	2	2	0		2	0		2	0	
TNM Stage										
Tumor Size				0.0662			0.119			0.0695
Tis	17	12	5		12	5		11	6	
T1	117	106	11		99	18		102	15	
T2	91	85	6		84	7		82	9	
T3	11	10	1		10	1		10	1	
T4	2	2	0		2	0		2	0	
Lymph Node Involvement				**0.0115**			0.0596			0.1872
N0	142	121	21		118	24		118	24	
N1	72	71	1		68	4		67	5	
N2	15	14	1		12	3		14	1	
N3	9	9	0		9	0		8	1	
Lymph Node Metastasis				**0.0011**			**0.0307**			**0.0307**
Yes	96	94	2		89	7		89	7	
No	142	121	21		118	24		118	24	

BC, breast cancer; CTC, circulating tumor cell; US, ultrasound; MMG, mammogram; n, number of patients; BBD, benign breast diseases; AJCC, American Joint Committee on Cancer; TNM, tumor-node-metastasis; Tis, tumor in situ.

**Based on the Youden index analysis, CTC, US and MMG cut-off values were 2, 4b, and 4b, respectively. As long as any measurement of composing parameter was higher than its cut-off value, the combination result would be considered as positive for diagnosis.*

#The p value of comparisons is based on the positive proportion among groups.

Bold values mean statistical significances.

IV patients. It could be due to that the sample size is too small (n = 2) or we used the wrong antibody to capture CTC. EpCAM antibody is supposed to capture the epithelial type of CTC. According to the AJCC BC staging guidelines, any TxNx patient with distant metastasis is classified as a stage IV patient. Epithelial-mesenchymal transition (EMT) plays an important role during tumor metastasis (21, 22). An epithelial type of CTC must transform into a migratory mesenchymal CTC before it settles down to a distant site. During EMT, cells lose expression of epithelial markers, such as EpCAM or CK, which might explain why less CTC were detected in stage IV BC patients with EpCAM antibody (22). Studies have shown patients with more mesenchymal type of CTC usually have worse survival outcomes (22, 23). However, further studies need to be conducted to confirm whether BC patients at advanced stage, with bigger tumors, or more lymph node involvement would have more mesenchymal type of CTC.

US and MMG are the two most common screening tools for BC in China. Next, we compared the diagnostic potency of CTC, US and MMG for diagnosing BC, especially in the detection of early stage BC. As shown in **Tables 2** and **3**, US has the highest sensitivity of 0.79, followed by CTC (0.73) and then MMG (0.58). CTC and MMG have the same specificity of 0.92, followed by US (0.81). The AUC of CTC, US and MMG are 0.855, 0.861 and 0.759, respectively. CTC has the highest accuracy of 0.83, followed by US (0.80) and then MMG (0.75). As for early stage tumor diagnosis, US has the highest sensitivity of 0.80, followed by CTC (0.74) and then MMG (0.57). Based on the AUC, CTC and US have similar diagnostic potency. Although the sensitivity of US is higher, it generates more false-positives as well, which might lead to over-diagnosis and panic in patients with BBD. The specificity and accuracy of CTC are slightly higher than those of US. Taken together, in our study, CTC performs the best in BC diagnosis, followed by US and then MMG. There are two limitations that restrain the use of CTC in routine practice as a diagnostic aid. First, a standard for CTC is still lacking. Many techniques have been developed to enrich CTC. Methodologies with low sensitivities are not suitable for clinical use. But for the ones with high sensitivities, results of different methods are sometimes not comparable with each other. Thus, a standard must be established before CTC can be used as a common diagnostic tool. Second, comparing to other diagnostic tools in clinic, CTC is pricey and usually not covered by the health insurances. High cost limits the clinical use of CTC in practice.

MMG is in fact the gold standard for BC screening, and is the only screening modality that has shown to lead to a reduction in BC mortality (24). Screening MMG leads to a 19% overall reduction in BC mortality (25). However, the sensitivity of MMG depends on the patients' age and breast composition

(26). MMG is more sensitive in women over 50 than in younger women, and in women with fatty breasts than ones with dense breasts (27). Regarding BC mortality, screening MMG is less beneficial for women in their 40s (15%) and more useful for women in their 60s (32%) (25). Sensitivity of MMG was 0.82 among women with predominantly fatty breast, but 0.24 in women with heterogeneous dense breasts (28). As older women tend to have fatty breasts, we analyzed the diagnostic potency of MMG in BC diagnosis among different BC patients grouped by age and found that sensitivity and AUC of MMG increased in older women (data not shown). Furthermore, Chinese women usually have dense breasts (29). Taken together, the dense breast should be the reason why MMG has the lowest diagnostic sensitivity in our study. The sensitivity of US depends on the patient's age and breast composition as well (28). US usually has a higher sensitivity than MMG in women younger than 45 years, whereas MMG has a higher sensitivity than US in women older than 60 years (28). But in our study, US showed higher sensitivities of BC detection in both women younger than 45 years and older than 60 years (data not shown). Sensitivity of US was 0.71 among women with predominantly fatty breast and 0.57 for heterogeneous dense breasts (28). In a cohort study of 30-39 years old women, US showed a better sensitivity of 0.96 compared to MMG (0.61) (30). However, MMG had a better specificity of 0.94 compared to 0.89 for US (30). The use of US in conjugation with MMG increase both sensitivity and specificity for BC screening (28). In another single-center, prospective, non-randomized comparison study, Cortesi et al. found that MRI, MMG and US had different diagnostic sensitivity in different group of people (31). In BRCA mutated patients, MRI alone with annual US could be offered. In high risk patients, MMG plus biannual US provide the most sensitive diagnosis and for intermediate risk group an annual MMG could be sufficient (31). Overall, the most sensitive technique was MRI (0.94) followed by MMG (0.55) and US (0.29) (31). Berg et al. shows that US is comparable with MMG for BC screening, and US is more sensitive for invasive and node-negative cancers (32). Common limitation for US and MMG is the false positives. In our study, US has a higher false positive rate of 19% than MMG (8%), which is consistent with previous study showing that false positive are more common with US screening (32).

MMG is the gold standard for BC screening recommended by American Cancer Society, but MMG shows the lowest sensitivity of 0.58 in our study. Lastly, we investigated whether combination with CTC would increase the sensitivity of MMG and at the same time maintain the specificity in an acceptable level. As shown in **Table 2**, the combination with CTC enhances the diagnostic performances of US and MMG indicated by the increased AUC. Among these three combinations, "CTC + US" has the highest AUC and sensitivity of 0.922 and 0.90, respectively. "CTC + MMG" has the highest specificity and accuracy of 0.85 and 0.86, respectively. The combination with CTC or US increases the sensitivity of MMG by 50% to 0.87, but "CTC + MMG" has a higher specificity of 0.85 than "US + MMG" of 0.79. Therefore, "CTC + MMG" performs better than "US + MMG" in BC diagnosis. Based on the AUC, combination improves the diagnostic performance. "CTC + US" has the best performance, followed by "CTC + MMG" and then "US + CTC". Based on the specificity and accuracy, "CTC + MMG" is the best combination. Theoretically, we should use the point closest to the left upper corner of the combinational ROC as the combination score cut-off to calculate the sensitivity and specificity. However, this model would be too complicated to be used in practice. In practice, the combinational results would be considered as positive as long as either one of composing measurements is higher than its cut-off or all of the composing measurements are higher than cut-off. We used the former definition in our study. When CTC is more than 2 or US/MG BI-RADS is higher than 4b, the combination result would be considered as positive. The sensitivity would usually increase while specificity would decrease in this model. However, it still fit the combinational ROC as shown in **Figures 2E–G**. The points closest to the upper left corners of the curves had higher sensitivities and slightly lower specificity. Since previous study (32) and our results showed US generated falser positive, it would be more logic to define the positive result for "CTC + US" as CTC $\geqq$ 2 and BI-RADS $\geqq$ 4b at the same time. In this definition, "CTC + US" has a sensitivity, specificity and accuracy of 0.62, 0.97 and 0.80, respectively. The specificity of US is much improved in this model. Thus, in practice, we can choose which model to be used depending on sensitivity or specificity we want to improve. MMG usually has a low sensitivity for BC diagnosis, therefore, it would be better to use the definition of positive result for "CTC + MMG" as CTC $\geqq$ 2 or BI-RADS $\geqq$ 4b. Our results indicate "CTC + US" or "CTC + MMG" performs better than "US + MMG" in BC diagnosis.

Our study is the first study comparing the diagnostic performances of CTC, US and MMG in the same cohort. Results of this work show that CTC detected by CytoSorter® can be used as a diagnostic aid to assist in early diagnosis and screening of BC. Combination of CTC enhances the diagnostic efficiency of US and MMG for BC screening, especially for MMG in Chinese women. Still more studies on larger patient population should be conducted to confirm our findings.

DATA AVAILABILITY STATEMENT

The raw data supporting the conclusions of this article will be provided by the authors on request.

ETHICS STATEMENT

The studies involving human participants were reviewed and approved by the ethics committees of Zhejiang University Medical College Affiliated, Sir Run Run Shaw Hospital, and Sun Yat-Sen University, Sun Yat-Sen Memorial Hospital, with IRB number, Qi Xie Lin Chuang Shi Yan 20180427-1 and [2018]

kuaishendi(75)Hao, respectively. The patients/participants provided their written informed consent to participate in this study.

AUTHOR CONTRIBUTIONS

Conception and design: YG and XK. Acquisition of data: WZ, JZ, and CD. Analysis and interpretation of data: YG and W-HF. Writing of the manuscript: YG and W-HF. Review of the manuscript: All authors. All authors contributed to the article and approved the submitted version.

ACKNOWLEDGMENTS

We would like to thank all the members of clinical laboratory of Watson Biotech for the help in CTC detection. Special thanks to Dr. NG for reading this manuscript and valuable opinions.

REFERENCES

1. Siegel RL, Miller KD, Jemal A. Cancer Statistics, 2019. *CA Cancer J Clin* (2019) 69(1):7–34.
2. Bray F, Ferlay J, Soerjomataram I, Siegel RL, Torre LA, Jemal A. Global Cancer Statistics 2018: GLOBOCAN Estimates of Incidence and Mortality Worldwide for 36 Cancers in 185 Countries. *CA Cancer J Clin* (2018) 68 (6):394–424.
3. Zheng R, Sun K, Zhang S, Zeng HM, Zou XN, Chen R, et al. Report of Cancer Epidemiology in China, 2015. *Chin J Oncol* (2019) 41(1):19–28.
4. McDonald ES, Clark AS, Tchou J, Zhang P, Freedman GM. Clinical Diagnosis and Management of Breast Cancer. *J Nucl Med* (2016) 57 Suppl 1:9S–16S.
5. Sivasubramaniam PG, Zhang BL, Zhang Q, Smith JS, Zhang B, Tang ZH, et al. Breast Cancer Disparities: A Multicenter Comparison of Tumor Diagnosis, Characteristics, and Surgical Treatment in China and the U.S. *Oncologist* (2015) 20(9):1044–50.
6. Jordan V, Khan M, Prill D. Breast Cancer Screening: Why Can't Everyone Agree? *Prim Care* (2019) 46(1):97–115.
7. Thomas DB, Gao DL, Ray RM, Wang WW, Allison CJ, Chen FL, et al. Randomized Trial of Breast Self-Examination in Shanghai: Final Results. *J Natl Cancer Inst* (2002) 94(19):1445–57.
8. Semiglazov VF, Sagaidak VN, Moiseyenko VM, Mikhailov EA. Study of the Role of Breast Self-Examination in the Reduction of Mortality From Breast Cancer. The Russian Federation/World Health Organization Study. *Eur J Cancer* (1993) 29A(14):2039–46.
9. Brooks M. Breast Cancer Screening and Biomarkers. *Methods Mol Biol* (2009) 472:307–21.
10. Kolb TM, Lichy J, Newhouse JH. Comparison of the Performance of Screening Mammography, Physical Examination, and Breast US and Evaluation of Factors That Influence Them: An Analysis of 27,825 Patient Evaluations. *Radiology* (2002) 225(1):165–75.
11. Bidard FC, Proudhon C, Pierga JY. Circulating Tumor Cells in Breast Cancer. *Mol Oncol* (2016) 10(3):418–30.
12. Hayes DF, Cristofanilli M, Budd GT, Ellis MJ, Stopeck A, Miller MC, et al. Circulating Tumor Cells At Each Follow-Up Time Point During Therapy of Metastatic Breast Cancer Patients Predict Progression-Free and Overall Survival. *Clin Cancer Res* (2006) 12(14 Pt 1):4218–24.
13. Yan WT, Cui X, Chen Q, Li YF, Cui YH, Wang Y, et al. Circulating Tumor Cell Status Monitors the Treatment Responses in Breast Cancer Patients: A Meta-Analysis. *Sci Rep* (2017) 7:43464.
14. Jin L, Zhao W, Zhang J, Chen W, Xie T, Wang L, et al. Evaluation of the Diagnostic Value of Circulating Tumor Cells With CytoSorter(®) CTC Capture System in Patients With Breast Cancer. *Cancer Med* (2020) 9 (5):1638–47.
15. Zheng W, Zhang Y, Guo L, Wang S, Fang M, Mao W, et al. Evaluation of Therapeutic Efficacy With CytoSorter(®) Circulating Tumor Cell-Capture System in Patients With Locally Advanced Head and Neck Squamous Cell Carcinoma. *Cancer Manag Res* (2019) 11:5857–69.
16. Pantel K, Denève E, Nocca D, Coffy A, Vendrell JP, Maudelonde T, et al. Circulating Epithelial Cells in Patients With Benign Colon Diseases. *Clin Chem* (2012) 58(5):936–40.
17. Castro J, Sanchez L, Nuñez MT, Lu M, Castro T, Sharifi HR, et al. Screening Circulating Tumor Cells as a Noninvasive Cancer Test in 3388 Individuals From High-Risk Groups (ICELLATE2). *Dis Markers* (2018) 2018:4653109.
18. Eroglu Z, Fielder O, Somlo G. Analysis of Circulating Tumor Cells in Breast Cancer. *J Natl Compr Canc Netw* (2013) 11(8):977–85.
19. Hu Z, Ding J, Ma Z, Sun R, Seoane JA, Scott Shaffer J, et al. Quantitative Evidence for Early Metastatic Seeding in Colorectal Cancer. *Nat Genet* (2019) 51(7):1113–22.
20. Liang B, Luo M, Yang D, Su K, Yuan H, Kong Z, et al. Phenotypes of Circulating Tumor Cells Predict Lymph Node Involvement in Patients With Early Breast Cancer. *Int J Clin Exp Pathol* (2017) 10(3):3401–8.
21. Yu M, Bardia A, Wittner BS, Stott SL, Smas ME, Ting DT, et al. Circulating Breast Tumor Cells Exhibit Dynamic Changes in Epithelial and Mesenchymal Composition. *Science* (2013) 339(6119):580–4.
22. Lowes LE, Goodale D, Xia Y, Postenka C, Piaseczny MM, Paczkowski F, et al. Epithelial to-Mesenchymal Transition Leads to Disease-Stage Differences in Circulating Tumor Cell Detection and Metastasis in Pre-Clinical Models of Prostate Cancer. *Oncotarget* (2016) 7(46):76125–39.
23. Zhang S, Wu T, Peng X, Liu J, Liu F, Wu S, et al. Mesenchymal Phenotype of Circulating Tumor Cells is Associated With Distant Metastasis in Breast Cancer Patients. *Cancer Manag Res* (2017) 9:691–700.
24. Berry DA, Cronin KA, Plevritis SK, Fryback DG, Clarke L, Zelen M, et al. Effect of Screening and Adjuvant Therapy on Mortality From Breast Cancer. *N Engl J Med* (2005) 353(17):1784–92.
25. Pace LE, Keating NL. A Systematic Assessment of Benefits and Risks to Guide Breast Cancer Screening Decisions. *JAMA* (2014) 311(13):1327–35.
26. von Euler-Chelpin M, Lillholm M, Vejborg I, Nielsen M, Lynge E. Sensitivity of Screening Mammography by Density and Texture: a Cohort Study From a Population-Based Screening Program in Denmark. *Breast Cancer Res* (2019) 21(1):111.
27. Siu ALon behalf of the U.S. Preventive Services Task Force. Screening for Breast Cancer: U.S. Preventive Services Task Force Recommendation Statement. *Ann Intern Med* (2016) 164(4):279–96.
28. Devolli-Disha E, Manxhuka-Kërliu S, Ymeri H, Kutllovci A. Comparative Accuracy of Mammography and Ultrasound in Women With Breast Symptoms According to Age and Breast Density. *Bosn J Basic Med Sci* (2009) 9(2):131–6.
29. Bae JM, Kim EH. Breast Density and Risk of Breast Cancer in Asian Women: A Meta-Analysis of Observational Studies. *J Prev Med Public Health* (2016) 49(6):367–75.
30. Hardy K. Early Ultrasound - Breast Cancer Diagnosis in Younger Women. *Radiol Today* (2013) 14(1):26.
31. Cortesi L, Canossi B, Battista R, Pecchi A, Drago A, Dal Molin C, et al. Breast Ultrasonography (BU) in the Screening Protocol for Women At Hereditary-Familial Risk of Breast Cancer: has the Time Come to Rethink the Role of BU According to Different Risk Categories? *Int J Cancer* (2019) 144(5):1001–9.
32. Berg WA, Bandos AI, Mendelson EB, Lehrer D, Jong RA, Pisano ED. Ultrasound as the Primary Screening Test for Breast Cancer: Analysis From ACRIN 6666. *J Natl Cancer Inst* (2015) 108(4):djv367.

Conflict of Interest: The authors declare that the research was conducted in the absence of any commercial or financial relationships that could be construed as a potential conflict of interest.

frontiers in Oncology

CASE REPORT
published: 01 June 2021
doi: 10.3389/fonc.2021.646336

Inflammatory Myofibroblastoma of the Breast: A Case Report

*Ling Wei†, Guoyuan Jiang†, Lala Bai, Tingchao Li, Xuejin Ma, Lin Jiang, Jie Wang and Shiguang Li**

Department of Radiology, The Third Affiliated Hospital of Zunyi Medical University, The First People's Hospital of Zunyi, Zunyi, China

Inflammatory myofibroblastic tumor (IMT) is a rare tumor with low-grade malignant risk mainly occurring in soft tissues and lungs, and it is extremely rare in the breast. Meanwhile, imaging findings of the tumor often present with non-specific features that lead to misdiagnosis and delayed treatment. Here, we report a case of inflammatory myofibroblastic tumor in the breast with the imaging findings of mammography, magnetic resonance imaging (MRI), and pathologic findings to improve the understanding of the disease. The patient was treated by surgical operation, and was followed up for 44 months, no local recurrence and distant metastasis.

Keywords: inflammatory myofibroblastoma, breast, mammography, MRI, case report

OPEN ACCESS

Edited by:
Abhishek Mahajan, Tata Memorial Hospital, India

Reviewed by:
Subathra Adithan, Jawaharlal Institute of Postgraduate Medical Education and Research (JIPMER), India
Sikandar Shaikh, Shadan Hospital and Institute of Medical Sciences, India
Arpita Sahu, Tata Memorial Hospital, India

***Correspondence:**
Shiguang Li
imaging_shiguangli@163.com

†These authors have contributed equally to this work and share first authorship

Specialty section:
This article was submitted to Cancer Imaging and Image-directed Interventions, a section of the journal Frontiers in Oncology

Received: *26 December 2020*
Accepted: *19 April 2021*
Published: *01 June 2021*

Citation:
Wei L, Jiang G, Bai L, Li T, Ma X, Jiang L, Wang J and Li S (2021) Inflammatory Myofibroblastoma of the Breast: A Case Report. Front. Oncol. 11:646336. doi: 10.3389/fonc.2021.646336

INTRODUCTION

Inflammatory myofibroblastic tumor (IMT) of the breast, first reported at 1988 (1), is now considered as a true low-grade neoplasm and mixture of spindle cells and chronic inflammatory cells, such as lymphocytes, plasma cells, and eosinophils according to the 2013 World Health Organization classification of tumors of soft tissue (2). Although it is more often seen in the lung, soft tissue, and viscera in children and young adults, broad age range has been documented in recent years (3). The incidence of breast IMT is unknown, to our knowledge, approximately 30 cases have been described in the literature, one of which is reported to appear near a previous surgical site. The case we reported also occurred at the site of a previous operation. Breast IMTs are easily misdiagnosed and confused with other breast disorders like cancer or fibroadenoma due to lack of typical clinical and imaging characteristics. The purpose of this report is to shed new understanding on this rare tumor-like disorder by analyzing the complete pathological and imaging documentation of one breast IMT in our hospital.

CASE REPORT

A 50-year-old woman presented with a gradually increasing mass in the right breast, accompanied by progressive pain and slight redness of the localized skin. Two months ago, a quail egg-like mass was detected in the inner upper quadrant of the right breast when she underwent a physical examination, but she did not take any diagnostic and treatment measures. The woman had a history of surgery for fibroadenoma of the right breast two years ago, so it is worthy of being mentioned that the mass is just located right at the site of the previous surgery. Physical examination revealed a 5-cm old postoperative scar at the inner upper quadrant of the right breast, and a well-circumscribed mass measuring 4.5 cm in

diameter was identified here with regular shape and slightly mobility. She had no family history of breast cancer. Ultrasonography (US) revealed an irregular shaped, hypoechoic mass with well-defined margins at the 2 o'clock position in the right breast, while septum and punctate blood flow signals were detected in the lesion. The lesion was classified as Breast Imaging Reporting and Data System (BI-RADS) category 4A.

Mammography obtained before fibroadenoma surgery showed a well-defined high-density mass in the inner upper quadrant of the right breast (**Figures 1A, B**). Mammography, performed two years after the initial operation, showed a high density, irregular mass with spiculated margins, accompanied by an incomplete halo sign (**Figures 1C** arrow, **D**) in the inner upper quadrant of the right breast. In addition, the skin adjacent to the areola had thickened. We classified the mass as BI-RADS category 4B according to imaging findings in mammography, including irregular shape, ill-defined margins, and incomplete halo sign around the mass.

MRI of the breast performed during a prior hospital admission, including traditional MRI and gadolinium-enhanced breast MRI, revealed an irregular mass, accompanied by architectural distortion, measuring 4.5 × 3.5 × 3.0 cm in size under the scar area of the inner upper quadrant of the right breast (**Figure 2**). The lesion had iso/hyper-intensity on axial fat-suppressed T2-weighted imaging (**Figure 2A**) and iso/hypo-intensity on axial T1-weighted imaging (**Figure 2B**), which showed heterogeneous high signal intensity on DWI (b = 1000 s/mm2) with low signal intensity ADC map (**Figures 2C, D**) that suggested restricted diffusion. Dynamic-contrast enhanced MRI showed a rapid heterogeneous rim enhancement mass with dark internal septation (**Figure 2E**, arrow), accompanied by non-mass enhancement in the initial period (**Figure 2E**), increased blood flow around the lesion in the maximal intensity projection (**Figure 2F**), and 201% of the early enhanced rate and a plateau in the delayed period and in the time intensity curve of the lesion (**Figure 3**). The lesion was assessed as BI-RADS category 4B by the readers, which suggested the likelihood of a malignant lesion. However, there was a history of surgery at the site of the mass two years ago and the clinical picture was characterized by progressive pain and mild skin redness. So a suspicion of inflammatory lesion was raised. After multidisciplinary discussion between breast surgeons and radiologists, the decision was made to proceed with surgical resection.

Gross examination of the surgical specimen revealed a 5 × 4 × 4 cm mass that was solid and greyish-white and yellowish. Pathologic analysis of the mass showed proliferating spindle cells interwoven within inflammatory cells, including plasma cells and lymphocytes (**Figure 4A**). On immunohistochemical examination (**Figure 4**), the mass was positive for smooth muscle actin (SMA) (**Figure 4B**), vimentin (**Figure 4D**), and Ki-67 in about 30% of the spindle tumor cells (**Figure 4C**) while negative for CD34. Meanwhile, no ALK gene rearrangement was detected by fluorescence *in situ* hybridization (**Figure 5**). The diagnosis of inflammatory myofibroblastic tumor (IMT) was established by the pathological findings.

DISCUSSION

Inflammatory myofibroblastic tumor of the breast is an extremely rare entity that can recur, with a recurrence rate of 25% (4). So far, the pathogenesis of IMT is still unclear, and it was initially thought to be related to trauma, infection, surgery, and other stimuli, which

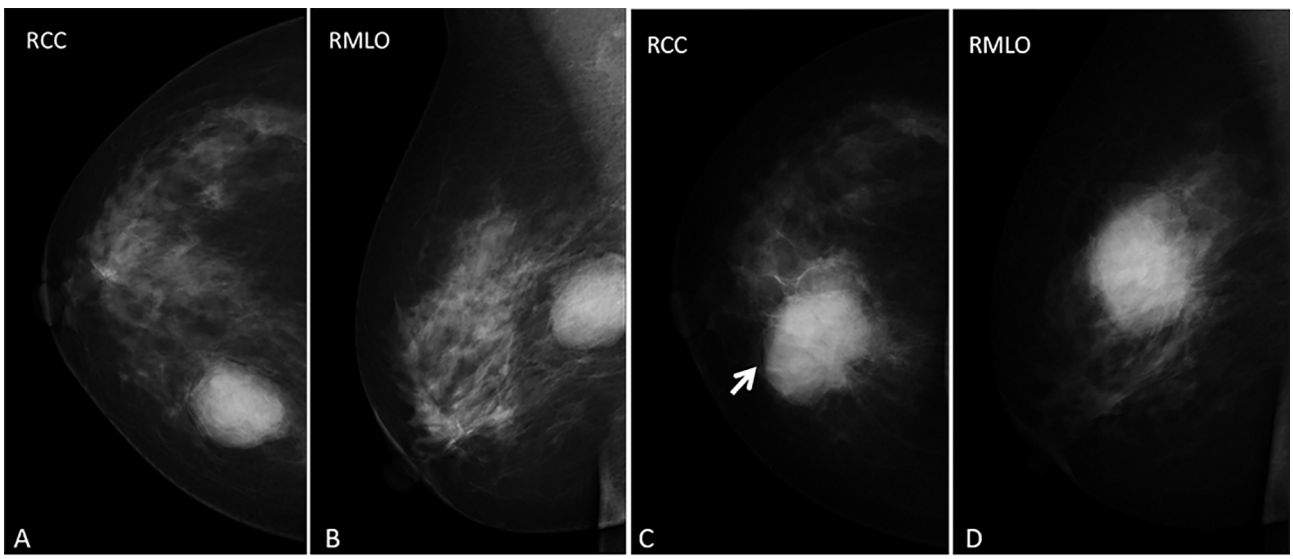

FIGURE 1 | **(A–D)** images represent RCC and RMLO views before the first fibroadenoma surgery and in the current presentation (the inflammatory myofibroblastic tumor), respectively. Mammography obtained before fibroadenoma surgery showed **(A, B)** an oval-shaped, circumscribed mass and mammography performed two years after the operation showed **(C, D)** a slight hyperdense mass with an ill-defined, spiculated margin, accompanied by an incomplete halo sign (arrow) and thickened the skin adjacent to the areolar in the inner upper quadrant of the right breast.

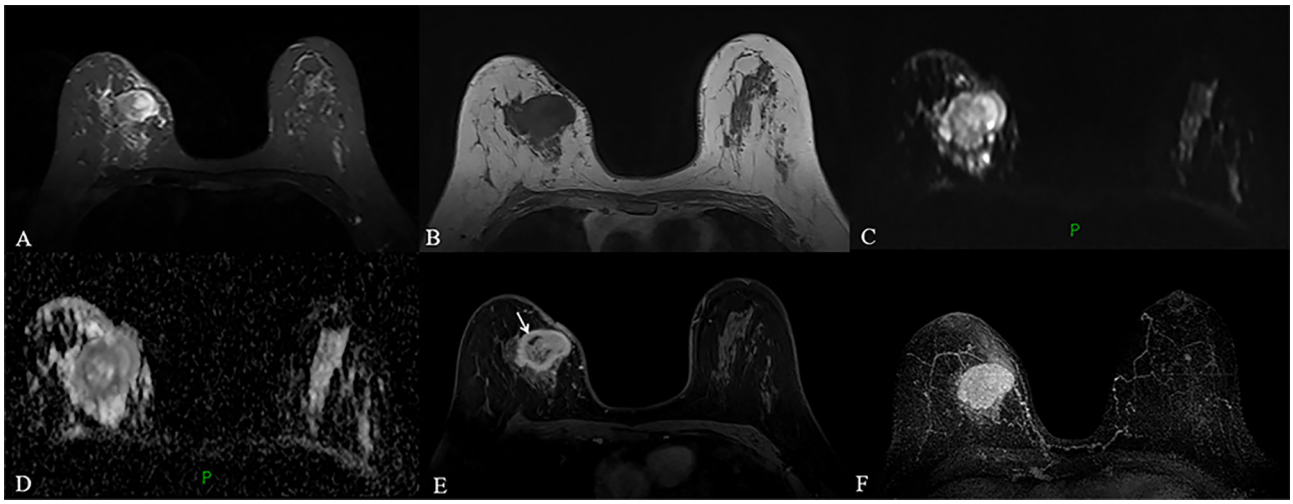

FIGURE 2 | **(A–F)** MRI obtained two years after the operation revealed a circumscribed mass with irregular shape and slightly distorted structure, accompanied by thickening of adjacent skin in the inner upper quadrant of the right breast, a mass showed heterogeneous high signal intensity on fat-suppressed T2-weighted images and low signal intensity on T1-weighted images **(A, B)**. The lesion with high signal intensity on DWI **(C)** had low signal intensity on ADC map **(D)**, which indicated restricted diffusion. Dynamic contrast-enhanced MRI revealed a fast, heterogeneous enhanced mass in the initial phase **(E)**. Maximum intensity projection (MIP) revealed a mass with increased blood supply **(F)**.

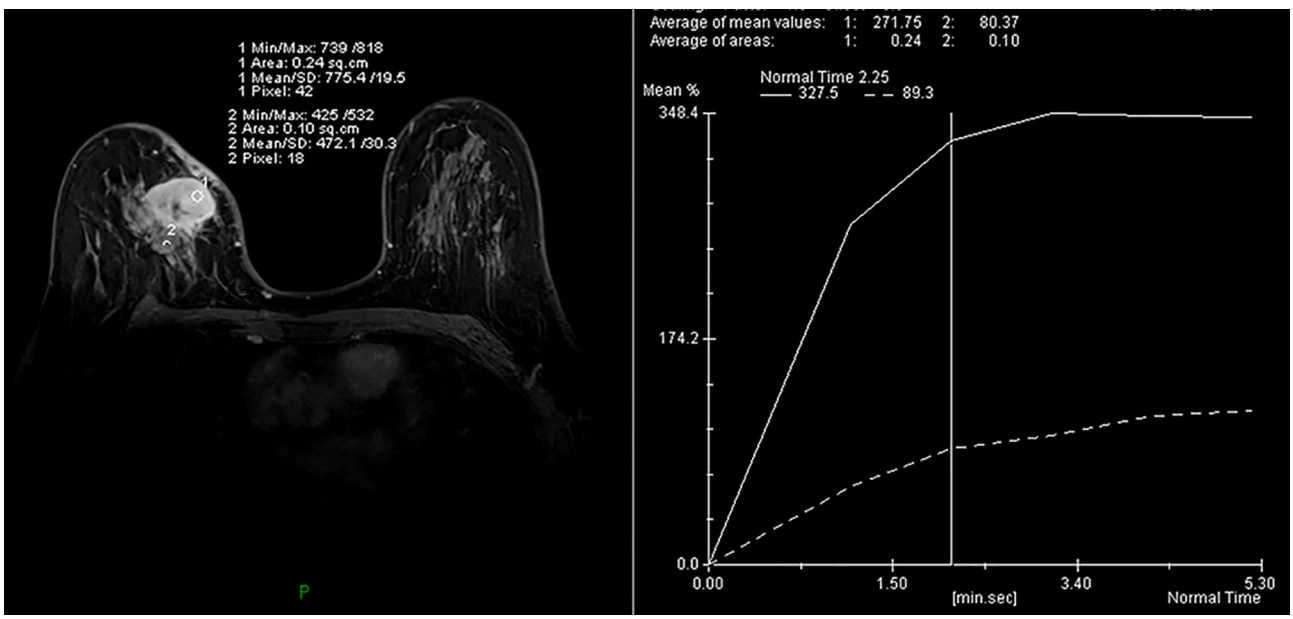

FIGURE 3 | A time intensity curve of the mass showed a plateau (TIC II) in the delayed period.

finally activated myofibroblasts with proliferative potential to proliferate and form tumors, and were called inflammatory pseudotumors. However, recent studies have shown that both intrapulmonary and extrapulmonary IMT are abnormal with chromosomes 2 and 9. Approximately 50% ~ 75% of IMT showed the fusion of ALK, TPM3, and TPM4 genes on 2P23, leading to the overexpression of the ALK protein (5, 6). Some groups reported that IMT was related to the expression of p53 and MDM2 genes (7). ALK gene fusion caused by a non-classical pathway was also found in IMT, suggesting that the ALK signaling pathway plays an important role in the majority of IMT tumors (8, 9). These findings suggest that IMT is a true tumor and not an inflammatory lesion, and that genetics and molecular studies confirm that IMT is a monoclonal proliferation.

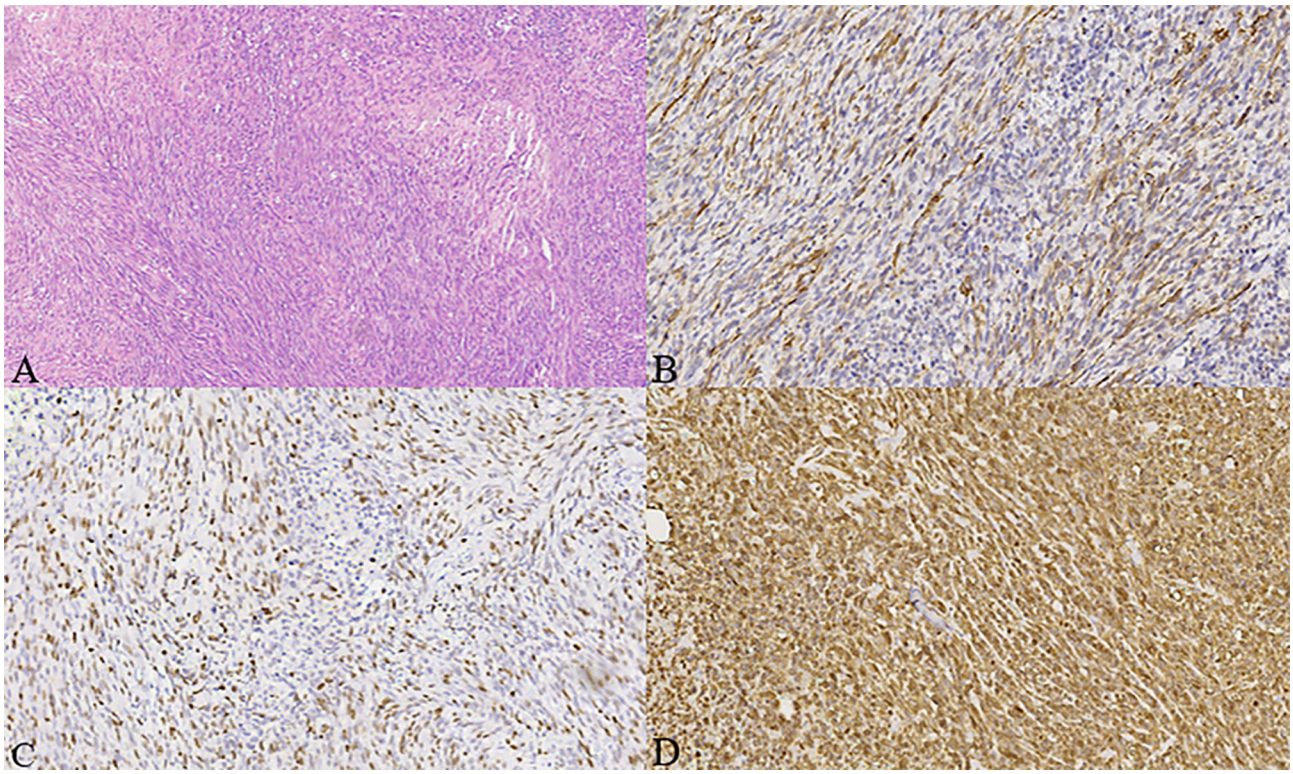

FIGURE 4 | **(A–D)** Histologic, immunohistochemical staining of inflammatory myofibroblastic tumor (IMT). The mass showed spindle cells admixed with inflammatory cells (H&E stain, × 100) **(A)**. Immunohistochemical staining showed positive staining for smooth muscle actin (SMA) in the spindle tumor cells (SMA, × 200) **(B)**, positive staining for Ki-67 in about 30% of the spindle tumor cells (Ki-67, × 200) **(C)**, as well as positive staining for vimentin in the spindle tumor cells (vimentin, × 200) **(D)**.

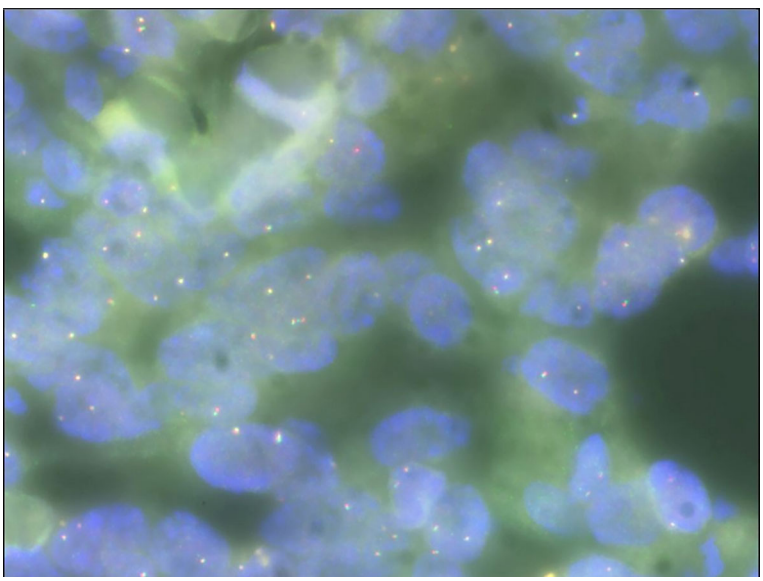

FIGURE 5 | Fluorescence *in situ* hybridization analysis showing no ALK gene rearrangement (× 100).

At present, the diagnosis of the disease is challenging. In this regard, we make some differential diagnoses of some breast diseases according to the imaging and pathology of the case to improve the understanding of the disease. Based on this case, many other causes of breast mass may be considered in differential diagnoses.

Fibroadenoma and phyllodes tumor should firstly be included in the differential diagnosis due to the black septum and lobulated shape of the mass shown on contrast-enhanced MRI. Duman L et al. (10) reported that fibroadenoma tended to be homogeneously enhanced and had a hypointense internal septum, while in this case, even with a hypointense septum, the mass showed rapid heterogeneous enhancement which made a fibroadenoma unlikely. Although phyllode tumors are frequently lobulated in shape–this is similar to the MRI findings in this case–the internal cystic areas were detected in the former. Imaging findings of the two diseases are non-specific, hence final diagnoses are based on histopathological findings. A phyllode tumor is a tumor in which epithelial cells and stromal cells grow simultaneously. It is diagnosed when the fibroepithelial architecture shows an inflated intracanalicular pattern with leaf-like fronds protruding into cystically dilated spaces accompanied by hypercellularity (11). So, a phyllode tumor was excluded from the differential diagnosis.

Meanwhile, the differential diagnosis may secondly include spindle cell lesions, either benign or malignant. Myofibroblastomas of the breast (MFB) are common in men, and their clinical manifestations are a steady and slow-growing mass with the duration of months to years. Imaging manifestations of MFB are usually benign, showing high signal and internal septum on T2WI without restricted diffusion, but malignancy cannot be ruled out safely just with MRI. The diagnosis is mainly based on immunohistochemical analysis including positive results for SMA, CD34, CD10, and desmin whereas CD117 is usually negative (12, 13).

Nodular fasciitis (NF) of the breast is a benign, pseudomyofibroblastic proliferative lesion. Rapid growth and spontaneous dissipation may be the characteristics of NF. The typical imaging findings of NF include low or iso-signal intensity on T1WI and hyperintensity on T2WI with enhancement after contrast injection (14). These features are not specific, however, its diagnosis often depends on pathology. It is reported in the literature that SMA and CD38 are positive, vimentin is positive, and AE1/AE3 are negative (15).

Breast fibromatosis is a locally invasive benign tumor with a high recurrence tendency and no metastasis potential, which can occur in the breast parenchyma, or originate from the pectoral fascia and extend into the breast. The typical manifestation of breast fibromatosis is a mass with unclear boundary and irregular shape, which sometimes may be accompanied by stretching and binding of the Cooper ligament. Fascia involvement may be the feature of breast fibromatosis (16). Although the imaging findings of breast fibromatosis are unspecific, MRI can be used to evaluate the location and degree of lesion before operation, and to evaluate residual lesions and detect recurrence after operation. The typical immunohistochemical features of fibromatosis are localized expression of SMA and calcium protein, but no cytokeratin CD34 or S100. Almost all reported cases had focal expression of beta catenin (17).

Spindle cell carcinoma to the breast (SpCC) usually manifests as a rapidly growing mass, however, their prominent clinical manifestations remain unclear. A high density ill-defined mass is seen on mammography whereas an irregular mass with microlobulated margin, complex echogenicity, and posterior acoustic enhancement on ultrasound imaging are common features in the diagnostic images of SpCC (18). The evidence of diffuse cytokeratin or p63 immunoreactivity in the malignant spindle cells suggests a diagnosis of spindle cell breast carcinoma (19, 20).

We present a rare case of inflammatory myofibroblastoma that may be associated with trauma of the breast, similar cases have been reported where the lesion occurred near the postoperative site of fibroadenoma in the literature (21), which may provide some instruction for future clinical work: if a patient with a history of surgery has lesions in the surgical site, inflammatory myofibroblastic tumor may be included in the diagnosis. The patient was followed for 44 months without recurrence or metastasis.

In conclusion, IMT of the breast is a very rare condition. Its clinical findings are mostly related to inflammatory conditions but some of the features are more similar to the lines of the tumor pathology. Even if it is a low grade malignant tumor, recurrence and metastasis may be picked up by systematic follow-up and for this reason it is treated usually by surgical resection. Therefore, it is so important to determine the correct diagnosis and treatment of this condition.

DATA AVAILABILITY STATEMENT

The original contributions presented in the study are included in the article/supplementary material. Further inquiries can be directed to the corresponding author.

ETHICS STATEMENT

Written informed consent was obtained from the individual(s) for the publication of any potentially identifiable images or data included in this article.

AUTHOR CONTRIBUTIONS

LW and GJ: manuscript writing. TL: pathological review. LB, LJ, XM, and JW: manuscript revision. SL: conception and critical review. All authors contributed to the article and approved the submitted version.

ACKNOWLEDGMENTS

The authors thank the members of their research group for useful discussions.

REFERENCES

1. Pettinato G, Manivel J, Insabato L, De Chiara A, Petrella G. Plasma Cell Granuloma (Inflammatory Pseudotumor) of the Breast. *Am J Clin Pathol* (1988) 90(5):627–32. doi: 10.1093/ajcp/90.5.627
2. Karanian M, Coindre JM. Fourth Edition of WHO Classification Tumours of Soft Tissue. *Ann Pathol* (2015) 35(1):71–85. doi: 10.1016/j.annpat.2014.11.003
3. Inoue M, Ohta T, Shioya H, Sato S, Takahashi H, Nakata N, et al. Inflammatory Myofibroblastic Tumors of the Breast With Simultaneous Intracranial, Lung, and Pancreas Involvement: Ultrasonographic Findings and a Review of the Literature. *J Med Ultrason (2001)* (2018) 45(2):331–5. doi: 10.1007/s10396-017-0829-y
4. Choi EJ, Jin GY, Chung MJ, Moon WS, Youn HJ. Primary Inflammatory Myofibroblastic Tumors of the Breast With Metastasis: Radiographic and Histopathologic Predictive Factors. *J Breast Cancer* (2015) 18(2):200–5. doi: 10.4048/jbc.2015.18.2.200
5. Zen Y, Kasahara Y, Horita K. Inflammatory Pseudotumor of the Breast in a Patient With a High Serum IgG4 Level: Histologic Similarity to Sclerosing Pancreatitis. *Am J Surg Pathol* (2005) 29(2):275–8. doi: 10.1097/01.pas.0000147399.10639.f5
6. Vecchio GM, Amico P, Grasso G, Vasquez E, La Greca G, Magro G. Post-Traumatic Inflammatory Pseudotumor of the Breast With Atypical Morphological Features: A Potential Diagnostic Pitfall. Report of a Case and a Critical Review of the Literature. *Pathol Res Pract* (2011) 207(5):322–6. doi: 10.1016/j.prp.2011.01.009
7. Yamamoto H, Oda Y, Saito T, Sakamoto A, Tsuneyoshi M. p53 Mutation and MDM2 Amplification in Inflammatory Myofibroblastic Tumours. *Histopathology* (2010) 42(5):431–9. doi: 10.1046/j.1365-2559.2003.01611.x
8. Lovly CM, Gupta A, Lipson D. Inflammatory Myofibroblastic Tumors Harbor Multiple Potentially Actionable Kinase Fusions. *Cancer Discovery* (2014) 4(8):889–95. doi: 10.1158/2159-8290.CD-14-0377
9. Schaefer IM, Cote GM, Hornick JL. Contemporary Sarcoma Diagnosis, Genetics, and Genomics. *J Clin Oncol* (2017) 36(2):101–10. doi: 10.1200/JCO.2017.74.9374
10. Taliaferro AS, Fein-Zachary V, Venkataraman S, Mehta TS, Patel A, Slanetz PJ. Imaging Features of Spindle Cell Breast Lesions. *AJR Am J Roentgenol* (2017) 209(2):454–64. doi: 10.2214/AJR.16.17610
11. Tan BY, Acs G, Apple SK, Badve S, Bleiweiss IJ, Brogi E, et al. Phyllodes Tumours of the Breast: A Consensus Review. *Histopathology* (2016) 68(1):5–21. doi: 10.1111/his.12876
12. Yilmaz R, Akkavak G, Ozgur E, Onder S, Ozkurt E, Dursun M. Myofibroblastoma of the Breast: Ultrasonography, Mammography, and Magnetic Resonance Imaging Features With Pathologic Correlation. *Ultrasound Q* (2018) 34(2):99–102. doi: 10.1097/RUQ.0000000000000337
13. Lee EJ, Chang YW, Jin YM, Kim NW. Multimodality Images of Myofibroblastoma in the Male Breast: A Case Report and a Review of the Literature. *Clin Imaging* (2018) 51:300–6. doi: 10.1016/j.clinimag.2018.06.004
14. Rhee SJ, Kim JH, Lim S-J. Nodular Fasciitis of the Breast: Two Cases With a Review Ofimaging Findings. *Clin Imaging* (2014) 38(5):730–3. doi: 10.1016/j.clinimag.2014.04.006
15. Paliogiannis P, Cossu A, Palmieri G, Scognamillo F, Pala C, Nonnis R, et al. Breast Nodular Fasciitis: A Comprehensive Review. *Breast Care* (2016) 11(4):270–4. doi: 10.1159/000448185
16. Liu H, Zeng H, Zhang H, Wang H, Cheng Z, Hu Y, et al. Breast Fibromatosis: Imaging and Clinical Findings. *Breast J* (2020) 26(11):2217–22. doi: 10.1111/tbj.14008
17. Ebrahim L, Parry J, Taylor DB. Fibromatosis of the Breast: A Pictorial Review of the Imaging and Histopathology Findings. *Clin Radiol* (2014) 69(10):1077–83. doi: 10.1016/j.crad.2014.05.105
18. Choi BB, Shu KS. Metaplastic Carcinoma of the Breast: Multimodality Imaging and Histopathologic Assessment. *Acta Radiol* (2012) 53(1):5–11. doi: 10.1258/ar.2011.110341
19. Koker MM, Kleer CG. p63 Expression in Breast Cancer: A Highly Sensitive and Specific Marker of Metaplastic Carcinoma. *Am J Surg Pathol* (2004) 28(28):1506–12. doi: 10.1097/01.pas.0000138183.97366.fd
20. Tse GM, Tan PH, Chaiwun B, Putti TC, Lui PC, Tsang AK, et al. p63 is Useful in the Diagnosis of Mammary Metaplastic Carcinomas. *Pathology* (2006) 38(1):16–20. doi: 10.1080/00313020500444625
21. Mao X, Liu H, Du J, Yu N, Chen L, Zhang L. Imaging Findings of Inflammatory Myofibroblastic Tumor in Breast: A Case Report. *Med (Baltimore)* (2018) 97(32):e11804. doi: 10.1097/MD.0000000000011804

Conflict of Interest: The authors declare that the research was conducted in the absence of any commercial or financial relationships that could be construed as a potential conflict of interest.

frontiers in Oncology

ORIGINAL RESEARCH
published: 08 June 2021
doi: 10.3389/fonc.2021.675160

Texture Analysis Using Semiquantitative Kinetic Parameter Maps from DCE-MRI: Preoperative Prediction of HER2 Status in Breast Cancer

Lirong Song[1†], *Chunli Li*[2†] *and Jiandong Yin*[1*]

[1] Department of Radiology, Shengjing Hospital of China Medical University, Shenyang, China, [2] Department of Biomedical Engineering, School of Fundamental Sciences, China Medical University, Shenyang, China

OPEN ACCESS

Edited by:
Mario Sansone,
University of Naples Federico II, Italy

Reviewed by:
Roberta Fusco,
Istituto Nazionale Tumori Fondazione G. Pascale (IRCCS), Italy
Stefano Marrone,
University of Naples Federico II, Italy

***Correspondence:**
Jiandong Yin
jiandongyin@sina.com

[†]These authors have contributed equally to this work and share first authorship

Specialty section:
This article was submitted to Cancer Imaging and Image-directed Interventions, a section of the journal Frontiers in Oncology

Received: 02 March 2021
Accepted: 14 May 2021
Published: 08 June 2021

Citation:
Song L, Li C and Yin J (2021) Texture Analysis Using Semiquantitative Kinetic Parameter Maps from DCE-MRI: Preoperative Prediction of HER2 Status in Breast Cancer. Front. Oncol. 11:675160. doi: 10.3389/fonc.2021.675160

Objective: To evaluate whether texture features derived from semiquantitative kinetic parameter maps based on breast dynamic contrast-enhanced magnetic resonance imaging (DCE-MRI) can determine human epidermal growth factor receptor 2 (HER2) status of patients with breast cancer.

Materials and Methods: This study included 102 patients with histologically confirmed breast cancer, all of whom underwent preoperative breast DCE-MRI and were enrolled retrospectively. This cohort included 48 HER2-positive cases and 54 HER2-negative cases. Seven semiquantitative kinetic parameter maps were calculated on the lesion area. A total of 55 texture features were extracted from each kinetic parameter map. Patients were randomly divided into training (n = 72) and test (n = 30) sets. The least absolute shrinkage and selection operator (LASSO) was used to select features in the training set, and then, multivariate logistic regression analysis was conducted to establish the prediction models. The classification performance was evaluated by receiver operating characteristic (ROC) analysis.

Results: Among the seven prediction models, the model with features extracted from the early signal enhancement ratio (ESER) map yielded an area under the ROC curve (AUC) of 0.83 in the training set (sensitivity of 70.59%, specificity of 92.11%, and accuracy of 81.94%), and the highest AUC of 0.83 in the test set (sensitivity of 57.14%, specificity of 100.00%, and accuracy of 80.00%). The model with features extracted from the slope of signal intensity (SI_{slope}) map yielded the highest AUC of 0.92 in the training set (sensitivity of 82.35%, specificity of 97.37%, and accuracy of 90.28%), and an AUC of 0.79 in the test set (sensitivity of 92.86%, specificity of 68.75%, and accuracy of 80.00%).

Conclusions: Texture features derived from kinetic parameter maps, calculated based on breast DCE-MRI, have the potential to be used as imaging biomarkers to distinguish HER2-positive and HER2-negative breast cancer.

Keywords: breast cancer, HER2, dynamic contrast-enhanced magnetic resonance imaging, texture analysis, semiquantitative kinetic parameter map

INTRODUCTION

Breast cancer is one of the most common cancers in women, and breast cancer alone accounts for 30% of new cancer cases in females (1). The status of human epidermal growth factor receptor 2 (HER2) is a biological factor that influences breast cancer survival. The 5-year relative survival rate has increased to 91% largely due to improvements in treatment, such as aromatase inhibitors for hormone receptor-positive tumors and trastuzumab for HER2-positive tumors. Of patients with hormone receptor-positive tumors, 81% receive hormonal therapy (2). With the development of new therapeutic drugs, better responses are seen with more specific pharmaceutical treatment options based on different molecular markers (3, 4). Therefore, it is very important to accurately identify HER2 status to individualize treatment. At present, HER2 amplification status is determined by immunohistochemistry (IHC); tumors are considered to be HER2-positive if the IHC analysis is scored as 3, whereas tumors are considered to be HER2-negative if scored as 0 or 1. For tumors with IHC scores of 2, further analysis by fluorescence *in situ* hybridization (FISH) is needed to detect the amplification status of the HER2 gene. However, these methods require invasive biopsies, and are also subject to sampling errors due to intratumoral heterogeneity (5). Moreover, FISH examination is costly and time-consuming. Thus, it would be clinically beneficial to develop a cost- and time-effective, accurate, noninvasive method to detect HER2 status.

Breast dynamic contrast-enhanced magnetic resonance imaging (DCE-MRI) is the most widely used and clinically proven imaging technique in breast cancer, and it has high sensitivity for detecting breast lesions. It provides anatomical information as well as hemodynamic information of the tumor with a high spatial resolution (6). Previous studies on breast DCE-MRI have indicated that morphological and kinetic characteristics were associated with benign and malignant tumors, response to neoadjuvant chemotherapy, and histopathological factors of breast cancer (7–11).

Texture analysis has been widely applied to characterize the spatial distribution of gray level intensities in images, capturing image patterns which are usually unrecognizable or unresolved by the human eye (12–14). This approach aims to extract high-throughput information to characterize image heterogeneity in specific target regions (15, 16). The most commonly used texture features can be layered by the statistical order of the voxel information encoded within the target regions, including first-order (also called histogram), second-order (gray level co-occurrence matrix and run-length matrix), and high-order (structural and transformed) texture features, proving to be helpful in assessing tumors. Earlier studies on rectal cancer revealed that texture features were useful for prediction of pathological complete response after neoadjuvant chemotherapy (17–19). Moreover, histogram features have been shown to be useful in evaluating tumor heterogeneity in glioma and cervical cancers (20, 21).

In previous studies, texture features derived from mammography and multidetector computed tomography images have been applied and shown to potentially identify HER2 status in patients with breast cancer (22, 23). However, DCE-MRI is recognized as the most common and effective method in breast cancer imaging. Montemurro et al. (10) showed that Fischer's score, which included three morphological, two functional, and five DCE-MRI features, was inversely associated with HER2-overexpression. Another study demonstrated that texture features from DCE-MRI were predictive of HER2 status (24). Semiquantitative kinetic parameter maps provide a technique for leveraging the pre- and post-contrast acquisitions, and can reflect kinetic information for breast cancer. A recent study demonstrated that the model based on texture features from semiquantitative kinetic parameter maps was able to discriminate sentinel lymph node status (25). To the best of our knowledge, no previous study has investigated the association between HER2 status in breast cancer and texture features extracted from semiquantitative kinetic parameter maps calculated from breast DCE-MRI.

Thus, the aim of this study was to evaluate whether features derived from semiquantitative kinetic parameter maps could be used to identify HER2 status in patients with breast cancer.

MATERIALS AND METHODS

Study Population

This retrospective study was approved by our institutional review board (NO.2019PS175K) and the requirement for informed consent was waived. From January 2019 to January 2020, female patients with histologically confirmed breast cancer who underwent breast DCE-MRI were reviewed with our picture archiving and communication system (PACS). The inclusion criteria were as follows: (1) visible breast lesion on DCE-MRI; (2) histologically confirmed breast cancer; and (3) exact HER2 amplification status determined by IHC/FISH examination. The exclusion criteria were: (1) patients who underwent a biopsy before MRI examination; (2) patients who received neoadjuvant chemotherapy before MRI; and (3) insufficient MRI quality due to obvious motion artifacts.

Finally, a total of 102 patients were enrolled in this study retrospectively. Of these patients, 48 were HER2-positive and 54 were HER2-negative. The clinical characteristics collected using the PACS included age, maximum tumor diameter, estrogen receptor status, progesterone receptor status, Ki-67 status, histological grade, and histological type. Patients were randomly divided into a training set (n = 72, 34 HER2-positive and 38 HER2-negative) and a test set (n = 30, 14 HER2-positive and 16 HER2-negative) at a proportion of 70% and 30%, respectively. **Figure 1** shows the workflow of this study.

MRI Acquisition

All patients received a pretreatment breast DCE-MRI at our institution using a 3.0 Tesla MR scanner (Ingenia, Philips Medical System, Best, Netherlands) equipped with a dedicated 7-channel bilateral breast coil with patient in a prone position. First, an axial fat-saturated T1-weighted precontrast scan based on the VIBRANT-VX technique was acquired. Then, eight axial contrast-enhanced fat-saturated T1-weighted scans were acquired after the intravenous bolus injection of a contrast agent (Magnevist, Bayer Healthcare Pharmaceuticals, Berlin, Germany) with a dose of 0.15 mmol per kg body weight. The imaging parameters were as follow: repetition time, 4.14 ms; echo time, 2.10 ms; flip angle, 12°; slice thickness, 2.00 mm; spacing between slices, 1.00 mm; field of view, 340 × 340 mm^2; matrix, 380 × 380. Eight subtraction sequences were obtained by subtracting the precontrast scan from each of the eight postcontrast scans.

Image Processing and Semiquantitative Kinetic Parameter Calculation

Two breast radiologists, each with over 6 years of experience, were blinded to HER2 status of patients and invited to help review the images. Slices with the maximum tumor diameter were chosen in consensus. The third-phase subtraction image, the eight phases of

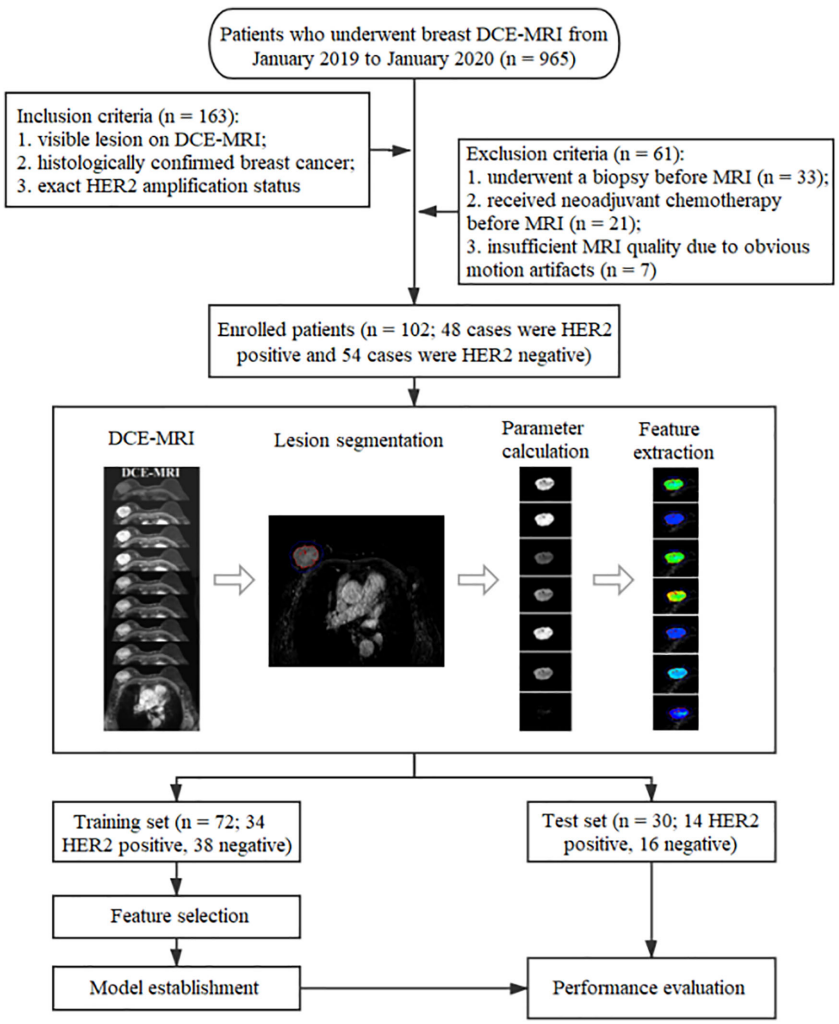

FIGURE 1 | The workflow of this study.

postcontrast images, and the precontrast image of the slice were downloaded and used for subsequent processing.

The lesion area was first delineated automatically on the third-phase subtraction image using an in-house software programmed with MATLAB 2018a (Mathworks, Natick, MA, USA). Seven semiquantitative kinetic parameter maps were calculated on the lesion area, respectively. The seven kinetic parameters included the initial percentage of enhancement ($E_{initial}$), the percentage of peak enhancement (E_{peak}), the early signal enhancement ratio (ESER), the maximum slope of increase (MSI), the second enhancement percentage (SEP), the signal enhancement ratio (SER), and the slope of signal intensity (SI_{slope}). The calculation formulas of the parameters are as follows:

$$E_{initial} = (SI_1 - SI_0)/SI_0 \times 100\,\% \quad (1)$$

where SI_1 and SI_0 represent the signal intensities of the first postcontrast image and the precontrast image, respectively.

$$E_{peak} = (SI_{peak} - SI_0)/SI_0 \times 100\,\% \quad (2)$$

where SI_{peak} represents the peak signal intensity value of the contrast enhancement.

$$ESER = (SI_1 - SI_0)/(SI_2 - SI_0) \times 100\,\% \quad (3)$$

where SI_2 represents the signal intensity at the second postcontrast time point.

$$MSI = \max(SI_{i+1} - SI_i) \quad (4)$$

where SI_i and SI_{i+1} stand for the signal intensity of a certain phase and the following phase respectively, with i ranges from 0 to 7.

$$SEP = (SI_2 - SI_0)/SI_0 \times 100\,\% \quad (5)$$

$$SER = (SI_{peak} - SI_0)/(SI_8 - SI_0) \times 100\,\% \quad (6)$$

where SI_8 is the signal intensity at the eighth postcontrast time point.

$$SI_{slope} = [(SI_8 - SI_{mean})/SI_{mean}] \times 100\,\% \quad (7)$$

where SI_{mean} is the mean value of the signal intensity at the first two postcontrast time points.

Texture Feature Extraction

All texture feature extraction was performed using an in-house software developed in MATLAB 2018a. Fifty-five texture features were derived from each kinetic parameter map, including histogram features, gray level co-occurrence matrix (GLCM) features, gray level run-length matrix (GRLM) features, and discrete wavelet transformation (DWT) features. The details of these features are provided in **Table 1**. GLCM parameters were calculated from four GLCMs corresponding to a distance of one pixel and four angles (0°, 45°, 90°, 135°), and the mean value of each feature over the four GLCMs was utilized. GRLM parameters were calculated from four GRLMs corresponding to four angles (0°, 45°, 90°, 135°), and the mean value of each feature over the four GRLMs was utilized. DWT parameters were calculated for two layers and three directions (horizontal, vertical, diagonal) to produce low and high frequency components. For example, harr_L represented the low frequency component using harr wavelet, and harr_DH2 represented the diagonal high frequency component of the second layer using harr wavelet.

Model Construction and Statistical Analysis

The clinical characteristics and kinetic parameters of the patients were statistically analyzed using SPSS 22.0 (IBM, Corp). Categorical variables included estrogen receptor status, progesterone receptor status, Ki-67 status, histological grade, and histological type, and these variables were compared between HER2-positive and -negative groups using the chi-square test or Fisher's exact test. For quantitative data including age, maximum tumor diameter, kinetic parameters, and texture features, the independent sample *t*-test was utilized when the data was normally distributed with homogeneous variance, and the Mann-Whitney *U* test was used when the

TABLE 1 | Details of extracted texture features.

Methods	Texture features	Quantity
Histogram	Mean, Variance, Skewness, Kurtosis	4
GLCM	Autocorrelation, Contrast, Correlation, Cluster Prominence, Cluster Shade, Dissimilarity, Energy, Entropy, Homogeneity, Maximum Probability, Variance, Sum Average, Sum Variance, Sum Entropy, Difference Variance, Difference Entropy, Information Measure of Correlation 1, Information Measure of Correlation 2, Inverse Difference Normalized	19
GRLM	Short Run Emphasis, Long Run Emphasis, Gray Level Nonuniformity, Run-Length Nonuniformity, Run Percentage, Low Gray Level Run Emphasis, High Gray Level Run Emphasis, Short Run Low Gray Level Emphasis, Short Run High Gray Level Emphasis, Long Run Low Gray Level Emphasis, Long Run High Gray Level Emphasis	11
DWT	Harr parameters	7
	Deubechies2 parameters	7
	Symlet4 parameters	7
Total		55

GLCM, gray level co-occurrence matrix; GRLM, gray level run-length matrix; DWT, discrete wavelet transformation.

data was not normally distributed. A two-sided *P* value less than 0.05 was considered statistically significant.

The data from 72 patients in the training set were used for feature selection and model construction. Feature selection was performed using MATLAB 2018a. Separately for each kinetic map, Pearson's correlation analysis was first performed among features in the training set. Highly correlated features with coefficients greater than 0.95 were marked, and the ones with higher correlations with other features were removed. Then, the least absolute shrinkage and selection operator (LASSO) was used to select features with nonzero coefficients among the remaining features by 10-fold cross-validation. After removal, the features were randomly divided into 10 groups. At each feature selection loop, one group of features was chosen as the validation set and the remaining groups were used as the training set. The optimal subset of features for prediction was generated after each loop, and this process was repeated for all ten folds. All selected features were recorded for further analysis.

The multivariate logistic regression analysis using forward stepwise selection was applied with entry of the selected features to establish the prediction model. Spearman's correlation analysis was performed to evaluate the correlation between texture features contained in the model and HER2 status. The performance of the trained model was assessed through the area under the receiver operating characteristic (ROC) curve (AUC). The sensitivity, specificity, and accuracy were calculated correspondingly. The optimal threshold was chosen according to the maximum Youden index. The established prediction model was further tested on the test set using the same threshold determined on the training set. The corresponding AUC, sensitivity, specificity, and accuracy were also calculated. The above analysis was performed on MedCalc (version 14.10.20, http://www.medcalc.org/).

RESULTS

Characteristics of the Study Population

A total of 102 patients (51.60 ± 10.10 years) were included in this study. The detailed clinical and histopathological characteristics between HER2-positive and -negative groups are listed in **Table 2**. There was no statistical difference between the two groups with respect to age ($P = 0.57$), maximum tumor diameter ($P = 0.26$), histological grade ($P = 0.17$), or histological type ($P = 0.91$). The two groups showed significant differences in terms of estrogen receptor status ($P < 0.01$), progesterone receptor status ($P = 0.02$), and Ki-67 status ($P = 0.04$). **Figure 2** shows two randomly selected cases used to display the results of lesion segmentation along with seven semiquantitative DCE maps and corresponding pathological results.

Performance of the Prediction Model

The comparison results of the average value of seven kinetic parameters in the lesion area between HER2-positive and -negative groups is provided in **Table 3**. There were no significant differences in the average value of seven kinetic parameters between the two groups. **Table 4** presents the logistic regression models obtained from the training set. **Table 5** shows comparison results of texture features included in models in the training set between HER2-positive and -negative groups. Short Run Emphasis derived from $E_{initial}$,

TABLE 2 | Clinical and histopathological characteristics of all patients.

Characteristics	HER2 status		*P*-value
	Positive (n = 48)	Negative (n = 54)	
Age (mean ± SD)	50.96 ± 10.59	52.09 ± 9.69	0.57[a]
Maximum tumor diameter (mm)	20.79 ± 5.13	19.69 ± 4.79	0.26[a]
Estrogen receptor status			**<0.01**[b]
Positive	26 (54.20%)	43 (79.60%)	
Negative	22 (45.80%)	11 (20.40%)	
Progesterone receptor status			**0.02**[b]
Positive	21 (43.80%)	36 (66.70%)	
Negative	27 (56.20%)	18 (33.30%)	
Ki-67 status			**0.04**[c]
≥14%	44 (91.70%)	40 (74.10%)	
<14%	4 (8.30%)	14 (25.90%)	
Histological grade			0.17[c]
I	0	3 (5.60%)	
II	33 (68.80%)	39 (72.20%)	
III	15 (31.20%)	12 (22.20%)	
Histological type			0.91[c]
Invasive carcinoma of no special type	45 (93.80%)	50 (92.60%)	
Ductal carcinoma in situ	3 (6.20%)	2 (3.70%)	
Invasive lobular carcinoma	0	1 (1.75%)	
Invasive micropapillary carcinoma	0	1 (1.75%)	

[a]*Variables were tested using the independent sample t-test.*
[b]*Variables were tested using the χ^2 test.*
[c]*Variables were tested using Fisher's exact test.*
The bold P-values are considered statistically significant.

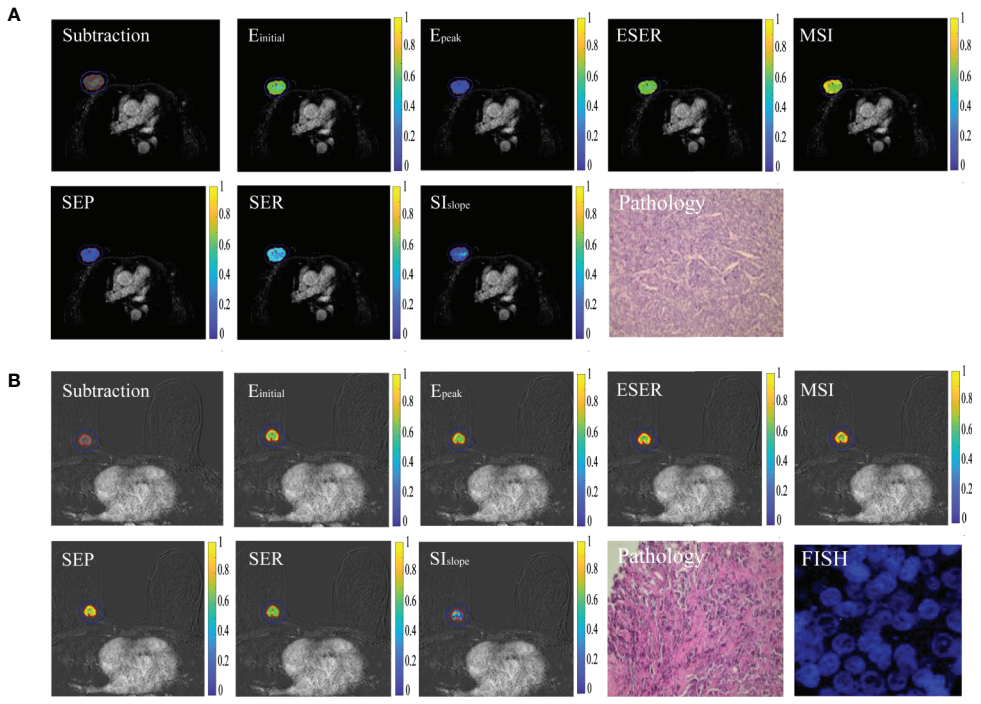

FIGURE 2 | Typical cases of HER2 positivity and negativity. **(A)** Sample images of HER2 positivity, including lesion segmentation, seven semiquantitative DCE maps, and corresponding pathological results. **(B)** Sample images of HER2 negativity.

ESER, MSI, and SER maps were significantly different between HER2-positive and -negative patients ($P < 0.01$, < 0.01, < 0.01, and < 0.01, respectively). Contrast ($P < 0.01$) and harr_HH2 ($P < 0.01$) from E_{peak} maps, autocorrelation ($P < 0.01$) from SEP maps, and gray level nonuniformity ($P < 0.01$) from SI_{slope} were also significantly different between the two groups.

TABLE 3 | Comparison results of the average value of seven kinetic parameters from the lesion area.

Parameters	HER2 Positive	HER2 Negative	*P*-value
$E_{initial}$	185.57 ± 10.95	173.52 ± 10.08	0.42
E_{peak}	269.21 ± 104.98	276.41 ± 87.37	0.71
ESER	80.80 ± 13.94	63.41 ± 75.78	0.12
MSI	110.45 ± 31.41	106.13 ± 33.13	0.50
SEP	227.19 ± 86.98	227.47 ± 82.95	0.99
SER	132.47 ± 23.23	131.13 ± 19.68	0.75
SI_{slope}	7.68 ± 17.26	12.26 ± 16.72	0.18

Variables were tested using the independent sample t-test.

TABLE 4 | Logistic regression models.

Parameter maps	Logistic regression model
$E_{initial}$	*Y* = 11.52-0.42*Kurtosis-15.89*Short Run Emphasis
E_{peak}	*Y* = 1.23 + 6.39*Contrast-1.02*harr_HH2
ESER	*Y* = 8.33-13.80*Short Run Emphasis
MSI	*Y* = 8.53-14.83*Short Run Emphasis
SEP	*Y* = -4.46+1.80*Autocorrelation
SER	*Y* = 7.90-12.60*Short Run Emphasis
SI_{slope}	*Y* = -24.22+0.34*harr_DH2+0.24*symlet4_HH1+0.12*Gray Level Nonuniformity-0.01*High Gray Level Run Emphasis-0.08*Mean

The performance of the prediction models is summarized in **Table 6**. Among the seven prediction models, models with features extracted from the ESER map yielded an AUC of 0.83 in the training set [95% confidence interval (CI), 0.72–0.91; sensitivity of 70.59%, specificity of 92.11%, and accuracy of 81.94%], and the highest AUC of 0.83 in the test set (95% CI, 0.64–0.94; sensitivity of 57.14%, specificity of 100.00%, and accuracy of 80.00%). The model with features extracted from the SI_{slope} map yielded the highest AUC of 0.92 in the training set (95% CI, 0.84–0.97; sensitivity of 82.35%, specificity of 97.37%, and accuracy of 90.28%), and an AUC of 0.79 in the test set (95% CI, 0.59–0.91; sensitivity of 92.86%, specificity of 68.75%, and accuracy of 80.00%). The corresponding ROC curves of the models with features extracted from the seven kinetic parameter maps are shown in **Figure 3**.

DISCUSSION

In this study, the correlation between texture features and HER2 status in breast cancer was investigated using a texture analysis of seven semiquantitative kinetic parameter maps based on breast DCE-MRI. The results demonstrated that texture analysis based on DCE-MRI images has the potential to discriminate HER2

TABLE 5 | Comparison of texture features included in the logistic regression models in the training set between HER2-positive and -negative groups.

Parameter maps	Texture features	HER2 Positive	HER2 Negative	*P*-value	Correlation with HER2 status (r_s)
$E_{initial}$	Kurtosis	4.53 ± 2.99	5.72 ± 3.28	0.12[a]	-0.30
	Short Run Emphasis	0.55 (0.45-0.62)	0.67 (0.62-0.71)	**<0.01**[b]	-0.52
E_{peak}	Contrast	0.34 (0.21-0.52)	0.19 (0.16-0.26)	**<0.01**[b]	0.44
	harr_HH2	2.07 (1.66-2.54)	2.40 (2.15-3.35)	**<0.01**[b]	-0.50
ESER	Short Run Emphasis	0.53 (0.43-0.64)	0.68 (0.62-0.73)	**<0.01**[b]	-0.57
MSI	Short Run Emphasis	0.49 (0.41-0.60)	0.65 (0.61-0.70)	**<0.01**[b]	-0.60
SEP	Autocorrelation	3.14 (2.14-3.61)	1.92 (1.56-2.42)	**<0.01**[b]	-0.37
SER	Short Run Emphasis	0.56 (0.47-0.67)	0.69 (0.64-0.74)	**<0.01**[b]	-0.54
SI_{slope}	harr_DH2	5.01 ± 1.84	4.79 ± 2.07	0.63[a]	0.08
	symlet4_HH1	10.31 ± 6.36	10.20 ± 4.48	0.93[a]	-0.07
	Gray Level Nonuniformity	263.25 (217.54-400.84)	215.25 (209.30-226.33)	**<0.01**[b]	0.43
	High Gray Level Run Emphasis	1.23E+5 (1.00E+5-1.66E+5)	1.44E+5 (1.27E+5-1.57E+5)	0.10[b]	-0.20
	Mean	9.60 ± 19.63	13.00 ± 17.87	0.44[a]	-0.08

[a]*Variables were tested using the independent sample t-test.*
[b]*Variables were tested using the Mann-Whitney U test.*
The bold P-values are considered statistically significant.

TABLE 6 | Performance of prediction models.

	AUC	95% CI	Sensitivity	Specificity	Accuracy
$E_{initial}$					
Training set	0.85	0.75-0.93	67.65%	94.74%	81.94%
Test set	0.71	0.52-0.86	71.43%	68.75%	70.00%
E_{peak}					
Training set	0.84	0.73-0.91	70.59%	89.47%	80.56%
Test set	0.61	0.42-0.78	35.71%	100.00%	70.00%
ESER					
Training set	0.83	0.72-0.91	70.59%	92.11%	81.94%
Test set	0.83	0.64-0.94	57.14%	100.00%	80.00%
MSI					
Training set	0.84	0.74-0.92	73.53%	84.21%	79.17%
Test set	0.81	0.63-0.93	57.14%	100.00%	80.00%
SEP					
Training set	0.81	0.70-0.89	58.82%	92.11%	76.39%
Test set	0.63	0.44-0.80	64.29%	75.00%	70.00%
SER					
Training set	0.81	0.71-0.90	67.65%	86.84%	77.78%
Test set	0.81	0.63-0.93	92.86%	56.25%	73.33%
SI_{slope}					
Training set	0.92	0.84-0.97	82.35%	97.37%	90.28%
Test set	0.79	0.59-0.91	92.86%	68.75%	80.00%

AUC, area under the receiver operating characteristic curve; CI, confidence interval.

status in breast cancer. HER2 is a cell surface receptor expressed in normal breast cells that controls growth, division, and repair of breast cells (26). HER2-positive breast cancer is considered an aggressive disease, because the amplification of the HER2 gene results in an abnormally high amount of HER2 gene expression and HER2 proteins per cancer cell. Therefore, HER2-positive cancers promote the rapid growth and division of cancer cells, and the prognosis is generally poor (27). Trastuzumab treatment can be beneficial for breast cancer with HER2 amplification and overexpression, and therefore the HER2 status serves as a guide for treatment and is a crucial indicator of prognosis (28).

In recent years, there have been some studies on the association between radiomic features and HER2 status (22–24, 26, 29–31). Several studies investigated the relationship between HER2 status and radiomic features in gastric cancer and colorectal cancer (29–31). Li et al. (29) built and validated a CT-based radiomics nomogram for HER2 status prediction, which showed good performance. Zhou et al. (22) reported that mammography radiomics features can effectively diagnose HER2 status of patients with breast cancer, most notably with a model built using a combination of features from cranial caudal and mediolateral oblique views. One study indicated that

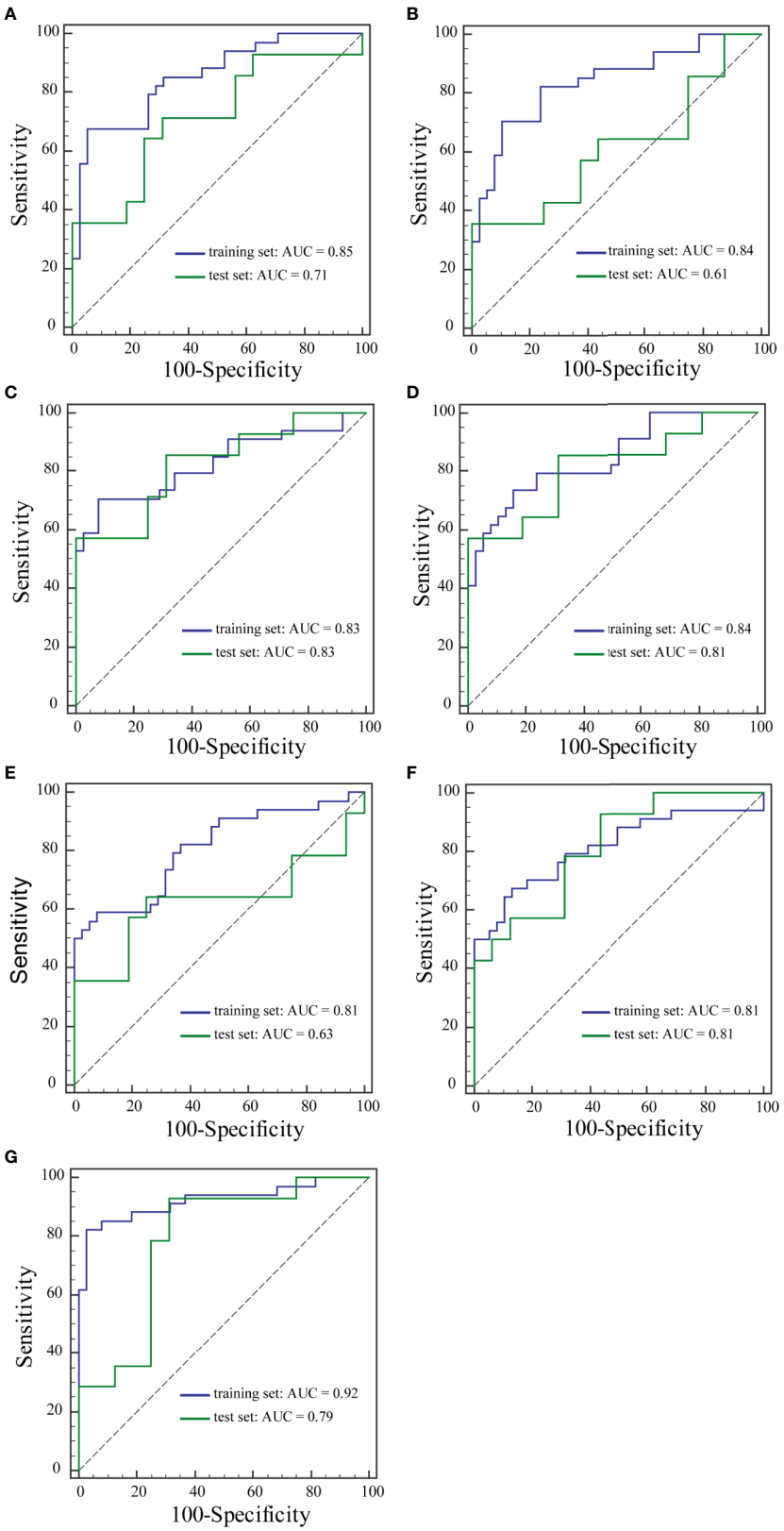

FIGURE 3 | ROC curves of the training set and the test set from Einitial **(A)**, Epeak **(B)**, ESER **(C)**, MSI **(D)**, SEP **(E)**, SER **(F)**, and SIslope **(G)** maps.

radiomics features from multidetector computed tomography images were associated with HER2 status in patients with breast cancer (23). Another study developed support vector machine models based on radiomic features from fat-suppressed T2-weighted images and DCE-MRI and, using a combination of these features, noninvasively evaluated the HER2 status of patients with breast cancer. The model based on the combination of fat-suppressed T2-weighted images and DCE-MRI exhibited the best performance for predicting the HER2 status of patients with an AUC of 0.86 and an accuracy of 79.5% in the primary cohort, and an AUC of 0.81 and an accuracy of 78.3% in the validation cohort (24). However, no previous studies have explored the relationship between HER2 status in breast cancer and radiomic features derived from semiquantitative kinetic parameter maps based on breast DCE-MRI.

In the present study, the association between texture features from semiquantitative kinetic parameter maps and HER2 status in breast cancer was investigated. Fifty-five texture features were extracted from each of the seven semiquantitative kinetic parameter maps for each patient. Logistic regression models using forward stepwise selection were developed and validated to predict different HER2 status in breast cancer. Among the seven prediction models based on texture features from $E_{initial}$, E_{peak}, ESER, MSI, SEP, SER, and SI_{slope} maps, two of the prediction models showed relatively good performance. The model built using features from the ESER map yielded an AUC of 0.83 in the training set, and the highest AUC of 0.83 in the test set. The model with features extracted from the SI_{slope} map yielded the highest AUC of 0.92 in the training set, and an AUC of 0.79 in the test set. The texture features selected in the seven models included mean, kurtosis, contrast, autocorrelation, gray level nonuniformity, short run emphasis, high gray level run emphasis, and three DWT features. Contrast represents local variations presented in maps. Autocorrelation detects repetitive patterns of texture elements. Gray level nonuniformity measures the similarity of the gray level throughout the lesion area. Short run emphasis reflects the distribution of short runs. Compared with HER2-negative breast cancer, semiquantitative kinetic parameter maps of HER2-positive breast cancer showed higher contrast, autocorrelation, and gray level nonuniformity, as well as lower short run emphasis in the training set. The manifestation of these features indicated that semiquantitative kinetic parameter maps of HER2-positive breast cancer may show more heterogeneity and higher texture complexity than HER2-negative breast cancer.

Fusco et al. (32) calculated 10 semiquantitative kinetic parameters, maximum signal difference (MSD), time to peak between wash-in and wash-out segments, wash-in slope (WIS), wash-out slope (WOS), wash-in intercept, wash-out intercept, area under the curve of wash-in, area under the curve of wash-out, area under the curve of wash-in and wash-out, and standardized index of shape (SIS) as well as 50 textural features to predict breast cancer therapy response. The results demonstrated that SIS achieved the highest AUC value (0.93), suggesting that the joint feature from semiquantitative parametric maps may obtain the best diagnostic performance. In our study, we evaluated the texture features based on seven independent semiquantitative kinetic parameter maps.

A recent study showed that deforming autoencoder convolutional neural networks based on 3TP (three-channel images representing a given slice at three different time points, uniquely identified by means of the three time points) slices of DCE-MRI could be developed to discriminate malignant from benign lesions, and good diagnostic performance was achieved (33). In comparison, the performance of deep learning features was not investigated in our research, as we focused solely on the feasibility of the texture features from semiquantitative kinetic parameter maps. In addition, MRI scans in our study included more phases for post-contrast acquisitions, based on which of the seven kinetic maps were obtained. To improve the performance of the prediction model, further work should be conducted to develop the classification models by combining texture and deep learning features from kinetic maps of DCE-MRI for preoperative prediction of HER2 status in patients with breast cancer.

This study had several limitations. First, the sample size in this study was relatively small and this may have impeded the generalizability of the findings. Second, our results may not be applicable in all other institutions as our study was performed in a single institution with uniform MRI parameters. Additional studies are needed to increase cohort size and consider various conditions. Third, only the texture features extracted from semiquantitative kinetic parameter maps were used to discriminate different HER2 status in breast cancer in this study. Other clinical and histopathological characteristics such as volume, tumor location, lymph-vascular invasion, and diffusion-weighted imaging radiomics may also be good signatures for distinguishing positive and negative status of hormone receptors in breast cancer (25, 34). Combining texture features and clinical characteristics in models may improve prediction performance. Fourth, the slices with maximum tumor diameter were selected and utilized in our study. Texture analysis was performed on two-dimensional images, and the representation of the entire volume of the tumor may have been limited compared with three-dimensional analysis. Finally, Piantadosi et al. (35) reported a U-shaped deep convolutional neural network that exploited the well-known 3TP approach for the automatic lesion segmentation task, which showed a good result in breast DCE-MRI segmentation. However, our study used the semi-automatic segmentation based on Otsu's algorithm, which was time-consuming. Thus, in our future research, automatic lesion segmentation will be performed using the U-shaped deep convolutional neural network.

CONCLUSION

In conclusion, our results indicated that texture features derived from kinetic parameter maps, calculated based on breast DCE-MRI, have the potential to be used as imaging biomarkers for distinguishing HER2-positive and HER2-negative breast cancer.

Further studies with larger sample sizes are necessary to verify the results of this study.

DATA AVAILABILITY STATEMENT

The original contributions presented in the study are included in the article/supplementary material/Further inquiries can be directed to the corresponding author.

ETHICS STATEMENT

Written informed consent was not obtained from the individual(s) for the publication of any potentially identifiable images or data included in this article.

AUTHOR CONTRIBUTIONS

LS performed the experiment and wrote the paper. CL revised the manuscript. JY designed the study. All authors contributed to the article and approved the submitted version.

FUNDING

This research was supported by grants from the Research and Development (R&D) Foundation for Major Science and Technology from Shenyang (No. 19-112-4-105), the Big Data Foundation for Health Care from China Medical University (No. HMB201902105), the Natural Fund Guidance Plan from Liaoning (No. 2019-ZD-0743), and the 345 Talent Project from Shengjing Hospital of China Medical University.

REFERENCES

1. Siegel RL, Miller KD, Jemal A. Cancer Statistics, 2020. *CA Cancer J Clin* (2020) 70:7–30. doi: 10.3322/caac.21590
2. Miller KD, Nogueira L, Mariotto AB, Rowland JH, Yabroff KR, Alfano CM, et al. Cancer Treatment and Survivorship Statistics, 2019. *CA Cancer J Clin* (2019) 69:363–85. doi: 10.3322/caac.21565
3. Collins DJ, Padhani AR. Dynamic Magnetic Resonance Imaging of Tumour Perfusion. *IEEE Eng Med Biol Mag* (2004) 23:65–83. doi: 10.1109/MEMB.2004.1360410
4. Siemann DW. The Unique Characteristics of Tumor Vasculature and Preclinical Evidence for its Selective Disruption by Tumor-Vascular Disrupting Agents. *Cancer Treat Rev* (2011) 37:63–74. doi: 10.1016/j.ctrv.2010.05.001
5. Davnall F, Yip CS, Ljungqvist G, Selmi M, Ng F, Sanghera B, et al. Assessment of Tumor Heterogeneity: An Emerging Imaging Tool for Clinical Practice? *Insights Imaging* (2012) 3:573–89. doi: 10.1007/s13244-012-0196-6
6. Liu Z, Feng B, Li C, Chen Y, Chen Q, Li X, et al. Preoperative Prediction of Lymphovascular Invasion in Invasive Breast Cancer With Dynamic contrast-enhanced-MRI-based Radiomics. *J Magn Reson Imaging* (2019) 50:847–57. doi: 10.1002/jmri.26688
7. Fusco R, Di Marzo M, Sansone C, Sansone M, Petrillo A. Breast DCE-MRI: Lesion Classification Using Dynamic and Morphological Features by Means of a Multiple Classifier System. *Eur Radiol Exp* (2017) 1:10. doi: 10.1186/s41747-017-0007-4
8. Wang C, Wei W, Santiago L, Whitman G, Dogan B. Can Imaging Kinetic Parameters of Dynamic Contrast-Enhanced Magnetic Resonance Imaging be Valuable in Predicting Clinicopathological Prognostic Factors of Invasive Breast Cancer? *Acta Radiol* (2018) 59:813–21. doi: 10.1177/0284185117740746
9. Li W, Arasu V, Newitt DC, Jones EF, Wilmes L, Gibbs J, et al. Effect of MR Imaging Contrast Thresholds on Prediction of Neoadjuvant Chemotherapy Response in Breast Cancer Subtypes: A Subgroup Analysis of the ACRIN 6657/I-SPY 1 Trial. *Tomography* (2016) 2:378–87. doi: 10.18383/j.tom.2016.00247
10. Montemurro F, Martincich L, Sarotto I, Bertotto I, Ponzone R, Cellini L, et al. Relationship Between DCE-MRI Morphological and Functional Features and Histopathological Characteristics of Breast Cancer. *Eur Radiol* (2007) 17:1490–7. doi: 10.1007/s00330-006-0505-x
11. Yamaguchi K, Abe H, Newstead GM, Egashira R, Nakazono T, Imaizumi T, et al. Intratumoral Heterogeneity of the Distribution of Kinetic Parameters in Breast Cancer: Comparison Based on the Molecular Subtypes of Invasive Breast Cancer. *Breast Cancer* (2015) 22:496–502. doi: 10.1007/s12282-013-0512-0
12. Chitalia RD, Kontos D. Role of Texture Analysis in Breast MRI as a Cancer Biomarker: A Review. *J Magn Reson Imaging* (2019) 49:927–38. doi: 10.1002/jmri.26556
13. Ma W, Ji Y, Qi L, Guo X, Jian X, Liu P. Breast Cancer Ki67 Expression Prediction by DCE-MRI Radiomics Features. *Clin Radiol* (2018) 73:909.e1–.e5. doi: 10.1016/j.crad.2018.05.027
14. Dong Y, Feng Q, Yang W, Lu Z, Deng C, Zhang L, et al. Preoperative Prediction of Sentinel Lymph Node Metastasis in Breast Cancer Based on Radiomics of T2-weighted Fat-Suppression and Diffusion-Weighted MRI. *Eur Radiol* (2018) 28:582–91. doi: 10.1007/s00330-017-5005-7
15. Yoon HJ, Kim Y, Kim BS. Intratumoral Metabolic Heterogeneity Predicts Invasive Components in Breast Ductal Carcinoma in Situ. *Eur Radiol* (2015) 25:3648–58. doi: 10.1007/s00330-015-3761-9
16. Gillies RJ, Kinahan PE, Hricak H. Radiomics: Images are More Than Pictures, They are Data. *Radiology* (2016) 278:563–77. doi: 10.1148/radiol.2015151169
17. Ahmed A, Gibbs P, Pickles M, Turnbull L. Texture Analysis in Assessment and Prediction of Chemotherapy Response in Breast Cancer. *J Magn Reson Imaging* (2013) 38:89–101. doi: 10.1002/jmri.23971
18. Aker M, Ganeshan B, Afaq A, Wan S, Groves AM, Arulampalam T. Magnetic Resonance Texture Analysis in Identifying Complete Pathological Response to Neoadjuvant Treatment in Locally Advanced Rectal Cancer. *Dis Colon Rectum* (2019) 62:163–70. doi: 10.1097/dcr.0000000000001224
19. Zou HH, Yu J, Wei Y, Wu JF, Xu Q. Response to Neoadjuvant Chemoradiotherapy for Locally Advanced Rectum Cancer: Texture Analysis of Dynamic Contrast-Enhanced MRI. *J Magn Reson Imaging* (2019) 49:885–93. doi: 10.1002/jmri.26254
20. Guan Y, Li W, Jiang Z, Chen Y, Liu S, He J, et al. Whole-Lesion Apparent Diffusion Coefficient-Based Entropy-Related Parameters for Characterizing Cervical Cancers: Initial Findings. *Acad Radiol* (2016) 23:1559–67. doi: 10.1016/j.acra.2016.08.010
21. Ryu YJ, Choi SH, Park SJ, Yun TJ, Kim JH, Sohn CH. Glioma: Application of Whole-Tumor Texture Analysis of Diffusion-Weighted Imaging for the Evaluation of Tumor Heterogeneity. *PloS One* (2014) 9:e108335. doi: 10.1371/journal.pone.0108335
22. Zhou J, Tan H, Bai Y, Li J, Lu Q, Chen R, et al. Evaluating the HER-2 Status of Breast Cancer Using Mammography Radiomics Features. *Eur J Radiol* (2019) 121:108718. doi: 10.1016/j.ejrad.2019.108718
23. Yang X, Wu L, Zhao K, Ye W, Liu W, Wang Y, et al. Evaluation of Human Epidermal Growth Factor Receptor 2 Status of Breast Cancer Using Preoperative Multidetector Computed Tomography With Deep Learning and Handcrafted Radiomics Features. *Chin J Cancer Res* (2020) 32:175–85. doi: 10.21147/j.issn.1000-9604.2020.02.05
24. Zhou J, Tan H, Li W, Liu Z, Wu Y, Bai Y, et al. Radiomics Signatures Based on Multiparametric MRI for the Preoperative Prediction of the HER2 Status of

Patients With Breast Cancer. *Acad Radiol [Preprint]* (2020). doi: 10.1016/j.acra.2020.05.040
25. Liu C, Ding J, Spuhler K, Gao Y, Serrano Sosa M, Moriarty M, et al. Preoperative Prediction of Sentinel Lymph Node Metastasis in Breast Cancer by Radiomic Signatures From Dynamic Contrast-Enhanced MRI. *J Magn Reson Imaging* (2019) 49:131–40. doi: 10.1002/jmri.26224
26. Chang RF, Chen HH, Chang YC, Huang CS, Chen JH, Lo CM. Quantification of Breast Tumor Heterogeneity for ER Status, HER2 Status, and TN Molecular Subtype Evaluation on DCE-MRI. *Magn Reson Imaging* (2016) 34:809–19. doi: 10.1016/j.mri.2016.03.001
27. Fleeman N, Bagust A, Boland A, Dickson R, Dundar Y, Moonan M, et al. Lapatinib and Trastuzumab in Combination With an Aromatase Inhibitor for the First-Line Treatment of Metastatic Hormone Receptor-Positive Breast Cancer Which Over-Expresses Human Epidermal Growth Factor 2 (HER2): A Systematic Review and Economic Analysis. *Health Technol Assess* (2011) 15:1–93, iii-iv. doi: 10.3310/hta15420
28. Goddard KA, Weinmann S, Richert-Boe K, Chen C, Bulkley J, Wax C. HER2 Evaluation and its Impact on Breast Cancer Treatment Decisions. *Public Health Genom* (2012) 15:1–10. doi: 10.1159/000325746
29. Li Y, Cheng Z, Gevaert O, He L, Huang Y, Chen X, et al. A CT-based Radiomics Nomogram for Prediction of Human Epidermal Growth Factor Receptor 2 Status in Patients with Gastric Cancer. *Chin J Cancer Res* (2020) 32:62–71. doi: 10.21147/j.issn.1000-9604.2020.01.08
30. Wang N, Wang X, Li W, Ye H, Bai H, Wu J, et al. Contrast-Enhanced CT Parameters of Gastric Adenocarcinoma: Can Radiomic Features be Surrogate Biomarkers for HER2 Over-Expression Status? *Cancer Manag Res* (2020) 12:1211–9. doi: 10.2147/cmar.S230138
31. Jeong JH, Kim J, Hong YS, Kim D, Kim JE, Kim SY, et al. Her2 Amplification and Cetuximab Efficacy in Patients with Metastatic Colorectal Cancer Harboring Wild-Type RAS and BRAF. *Clin Colorectal Cancer* (2017) 16: e147–e52. doi: 10.1016/j.clcc.2017.01.005
32. Fusco R, Granata V, Maio F, Sansone M, Petrillo A. Textural Radiomic Features and Time-Intensity Curve Data Analysis by Dynamic Contrast-Enhanced MRI for Early Prediction of Breast Cancer Therapy Response: Preliminary Data. *Eur Radiol Exp* (2020) 4:8. doi: 10.1186/s41747-019-0141-2
33. Gravina M, Marrone S, Sansone M, Sansone C. Dae-Cnn: Exploiting and Disentangling Contrast Agent Effects for Breast Lesions Classification in DCE-MRI. *Pattern Recogn Lett* (2021) 145:67–73. doi: 10.1016/j.patrec.2021.01.023
34. Fan M, Yuan W, Zhao W, Xu M, Wang S, Gao X, et al. Joint Prediction of Breast Cancer Histological Grade and Ki-67 Expression Level Based on DCE-MRI and DWI Radiomics. *IEEE J BioMed Health Inform* (2020) 24:1632–42. doi: 10.1109/jbhi.2019.2956351
35. Piantadosi G, Marrone S, Galli A, Sansone M, Sansone C. DCE-MRI Breast Lesions Segmentation With a 3TP U-Net Deep Convolutional Neural Network. In: *2019 IEEE 32nd International Symposium on Computer-Based Medical Systems (CBMS)* Cordoba, Spain, IEEE (2019). p. 628–33. doi: 10.1109/CBMS.2019.00130

Conflict of Interest: The authors declare that the research was conducted in the absence of any commercial or financial relationships that could be construed as a potential conflict of interest.

frontiers in Oncology

ORIGINAL RESEARCH
published: 21 June 2021
doi: 10.3389/fonc.2021.694634

Application of Diffusion Weighted Imaging Techniques for Differentiating Benign and Malignant Breast Lesions

Muzhen He[1,2†], *Huiping Ruan*[1,2†], *Mingping Ma*[1,2*] *and Zhongshuai Zhang*[3]

[1] Shengli Clinical Medical College of Fujian Medical University, Fuzhou, China, [2] Department of Radiology, Fujian Provincial Hospital, Fuzhou, China, [3] Siemens Healthcare Ltd., Shanghai, China

OPEN ACCESS

Edited by:
Pilar López-Larrubia,
Consejo Superior de Investigaciones Científicas (CSIC), Spain

Reviewed by:
Simona Marzi,
Istituti Fisioterapici Ospitalieri (IRCCS), Italy
Zebin Xiao,
Fudan University, China

***Correspondence:**
Mingping Ma
117788325@qq.com

[†]These authors have contributed equally to this work and share first authorship

Specialty section:
This article was submitted to Cancer Imaging and Image-directed Interventions, a section of the journal Frontiers in Oncology

Received: 23 April 2021
Accepted: 07 June 2021
Published: 21 June 2021

Citation:
He M, Ruan H, Ma M and Zhang Z (2021) Application of Diffusion Weighted Imaging Techniques for Differentiating Benign and Malignant Breast Lesions. Front. Oncol. 11:694634. doi: 10.3389/fonc.2021.694634

To explore the value of apparent diffusion coefficient (ADC), intravoxel incoherent motion (IVIM), and diffusional kurtosis imaging (DKI) based on diffusion weighted magnetic resonance imaging (DW-MRI) in differentiating benign and malignant breast lesions. A total of 215 patients with breast lesions were prospectively collected for breast MR examination. Single exponential, IVIM, and DKI models were calculated using a series of b values. Parameters including ADC, perfusion fraction (*f*), tissue diffusion coefficient (*D*), perfusion-related incoherent microcirculation (*D**), average kurtosis (MK), and average diffusivity (MD) were compared between benign and malignant lesions. ROC curves were used to analyze the optimal diagnostic threshold of each parameter, and to evaluate the diagnostic efficacy of single and combined parameters. ADC, *D*, MK, and MD values were significantly different between benign and malignant breast lesions (P<0.001). Among the single parameters, ADC had the highest diagnostic efficiency (sensitivity 91.45%, specificity 82.54%, accuracy 88.84%, AUC 0.915) and the best diagnostic threshold (0.983 μm^2/ms). The combination of ADC and MK offered high diagnostic performance (sensitivity 90.79%, specificity 85.71%, accuracy 89.30%, AUC 0.923), but no statistically significant difference in diagnostic performance as compared with single-parameter ADC (P=0.268). The ADC, *D*, MK, and MD parameters have high diagnostic value in differentiating benign and malignant breast lesions, and of these individual parameters the ADC has the best diagnostic performance. Therefore, our study revealed that the use of ADC alone should be useful for differentiating between benign and malignant breast lesions, whereas the combination of MK and ADC might improve the diagnostic performance to some extent.

Keywords: breast lesion, magnetic resonance imaging, apparent diffusion coefficient, intra-voxel incoherent motion, diffusion kurtosis imaging

INTRODUCTION

Breast cancer is the most common cancer in women. In 2018 there were approximately 2.1 million newly diagnosed female breast cancer cases worldwide, accounting for a quarter of female cancer cases (1). In China the incidence of breast cancer is relatively low, but since 1990 the incidence of breast cancer has increased rapidly, especially in urban areas (2, 3). Survival rates for breast cancer are greatly improved by early diagnosis. The main techniques used for identification of breast lesions are ultrasound, mammography, and magnetic resonance imaging (MRI). MRI offers better sensitivity and specificity than mammography and ultrasonography, especially for lesions in dense breasts (4, 5).

MRI can not only analyze the nature of the lesion through morphological features, but also obtain a variety of quantitative parameters using functional imaging sequences for more objective evaluation and diagnosis (6). Diffusion weighted MRI (DW-MRI), which indirectly reflects the degree of tissue differentiation and the integrity of cell membranes, is routinely used to improve the accuracy of differential breast lesion diagnoses (7–9).

The single exponential model is useful to distinguish benign from malignant breast lesions, and has been most widely used in clinical practice because of its short scanning time and simple post-processing (8, 10, 11). The ADC model requires two b-values to fit the curve. Many studies have shown that ADC has a certain significance in the identify of benign and malignant breast lesions (8, 9). The intravoxel incoherent motion (IVIM) model is first proposed by Bihan et al. (12) and has been reported to have good diagnostic performance for the diagnosis of pancreatic ductal adenocarcinoma (13). When b-value is low (≤200 s/mm^2), tissue diffusion is affected by microcirculation perfusion. As the b-value increases, the proportion of microcirculation perfusion is gradually reduced and it probably reflects the diffusion of water molecules in the tissue (14). However, the disadvantage of a high b-value is that it can reduce the signal-to-noise ratio. Therefore, in IVIM studies the b-value usually ranges from 0 to 1000 s/mm^2, and four to more than 10 different b-values are required to obtain perfusion fraction (*f*), tissue diffusion coefficient (*D*) and perfusion-related incoherent microcirculation (*D**) values (14, 15). Liu et al. (16) have shown that when b<200 s/mm^2, the attenuation speed of malignant lesions is significantly faster than that of normal breast tissue and benign lesions.

In the traditional DWI model, the diffusion of water molecules follows a Gaussian distribution, so the b-value affects the ADC value. In the diffusional kurtosis imaging (DKI) model first proposed by Jensen et al. (17), when the b-value is high (>1000 s/mm^2) the diffusion of water molecules follows a non-Gaussian distribution, the DKI model is more accurate at assessing the diffusion of water molecules in a lesion (17–19). In recent years, extended DWI models based on different b-values, including IVIM and DKI, have been used for the identification of tumors in liver (20), prostate (21, 22), thyroid (23) and brain (24). However, there have been few studies combining ADC, IVIM, and DKI values for use in the differentiation of benign and malignant breast lesions.

MATERIALS AND METHODS

Patients

The institutional ethics committee of our hospital approved this prospective study, and informed consent was provided by each patient. Patients with suspicious breast lesions from June 2019 to October 2020 were prospectively collected. Inclusion criteria: (1) No puncture, biopsy, radiotherapy, or chemotherapy were performed before MRI examination. (2) No contraindications to MRI examination. (3) All patients underwent plain MRI and multi-b-value DWI. (4) There was complete biopsy or surgical pathology. Exclusion criteria: (1) The solid part of the lesion was too small to delineate the ROI. (2) Image quality was poor and did not meet the post-processing requirements.

Scanning Method

All MR examinations were performed in a 3.0T MR (MAGNETOM Prisma, Siemens Healthcare, Erlangen, Germany) with 18-channel dual breast-dedicated phase-controlled surface coil. All patients were scanned in the prone position, with breasts naturally suspended in the coil. The sequences included T1WI (TR/TE=6.03/2.82 ms, thickness = 0.9 mm, number of slices = 160, bandwidth = 300 Hz/Px, FOV read = 340 mm, FOV phase = 100%, matrix size = 403×448), Fat saturation T2WI (TR/TE = 3730/69 ms, thickness = 4 mm, number of layers = 35, bandwidth = 246 Hz/Px, FOV read = 340 mm, FOV phase = 100%, matrix size = 384×384, averages = 2, concatenations = 2) and dynamic contrast enhanced MRI (DCE-MRI) (TR/TE = 4.03/1.33ms, thickness = 1.5 mm, number of slices = 112, bandwidth = 1120 Hz/Px, FOV read = 350 mm, FOV phase = 100%, matrix size = 259×320, Measurements 36, scan time = 343 s). The parameters of multiple b-value DWI sequences were TR/TE = 5700/62 ms, layer thickness = 4 mm, number of layers = 35, bandwidth = 2024 Hz/Px, FOV read = 340 mm, FOV phase = 60%, matrix size = 114×190; b-values = 0, 30, 50, 80, 120, 160, 200, 500, 1000, 1500, 2000 s/mm^2, averages = 1, 1, 1, 1, 1, 1, 1, 1, 2, 2, 3; scan time = 308 s.

Data Analysis

For each model, all DWI data were fitted pixel by pixel using a prototype software (Body Diffusion Toolbox, Siemens Healthcare, Erlangen, Germany), and the relevant parameter maps of ADC, IVIM, and DKI were obtained. Parameters including perfusion fraction (*f*), tissue diffusion coefficient (*D*), perfusion-related incoherent microcirculation (*D**), mean kurtosis (MK), and mean diffusivity (MD) were calculated. For the single exponential model, two b-values (0 and 1000 s/mm^2) were chosen with the equation. S(b)=S(0)×exp(-b× ADC) (1, 25). For the IVIM model, a total of nine b-values (0, 30, 50, 80, 120, 160, 200, 500, and 1000 s/mm^2) were used for data calculation using the classic two-step calculation method (26). The applied equation was: $S(b)/S(0) = (1-f) \times \exp(-b \cdot D) + f \times$

exp[-b·(D^* + D)] (2, 13). The parameter D was obtained using the data of b > 400 s/mm^2. D^* and f over all b values was calculated by a nonlinear regression algorithm, while keeping D constant (27). Five high b-values (0, 500, 1000, 1500, and 2000 s/mm^2) were selected for the DKI model, using the equation (17) S(b)=S (0) ×exp (-b× MD) + 1/6× b^2× MD^2× MK) (3). For all the formulas above, b is the diffusion-sensitive gradient factor, S(0) is the tissue signal intensity in the voxel when b=0 s/mm^2, and S(b) is the signal strength of the tissue within the element when b>0 s/mm^2. The mean value of signal intensity distribution within the region of interest (ROI) was calculated for each b value. Then, the mean signal intensities of b values in Eqs. (2) and (3) were fitted with the least square method using the Levenberg-Marquardt algorithm. The upper and lower limits of f and D* were 0%-40% and 0-50×10^{-3} mm^2/s respectively by referring to the range of each parameter in an earlier report (28). The goodness of fit in both the IVIM and DKI fittings was assessed by the coefficient of determination R2 (R2 = 1−ESS/TSS), where ESS and TSS is the sum of the squared errors between the data points and IVIM/DKI fitting curve, and the sum of the squared differences between the data points and the mean value of all data points, respectively. The pixel was excluded if its R2 value was < 0.8 (29).

ROI Delineation and Parameter Calculation

The ROI was measured by two radiologists with 10 years and 2 years of experience in breast imaging diagnosis. They read the images independently without knowing the pathological results and measured twice on the ADC image (b=1000 s/mm^2) at the largest level of the solid component of the lesion, avoiding obvious necrosis, cystic and liquefaction areas by referring to fat saturation T2WI and DCE-MRI imaging. The averaged ROI was then overlaid on the other parameter maps to obtain their corresponding parameters (**Figure 1**).

Statistical Methods

The Shapiro-Wilk normality test and the Levene variance homogeneity test were performed for all continuous variables. Values are described as mean ± standard deviation, and either a t-test or Mann-Whitney U test was used for comparisons between groups. The receiver operating characteristic (ROC) was used to

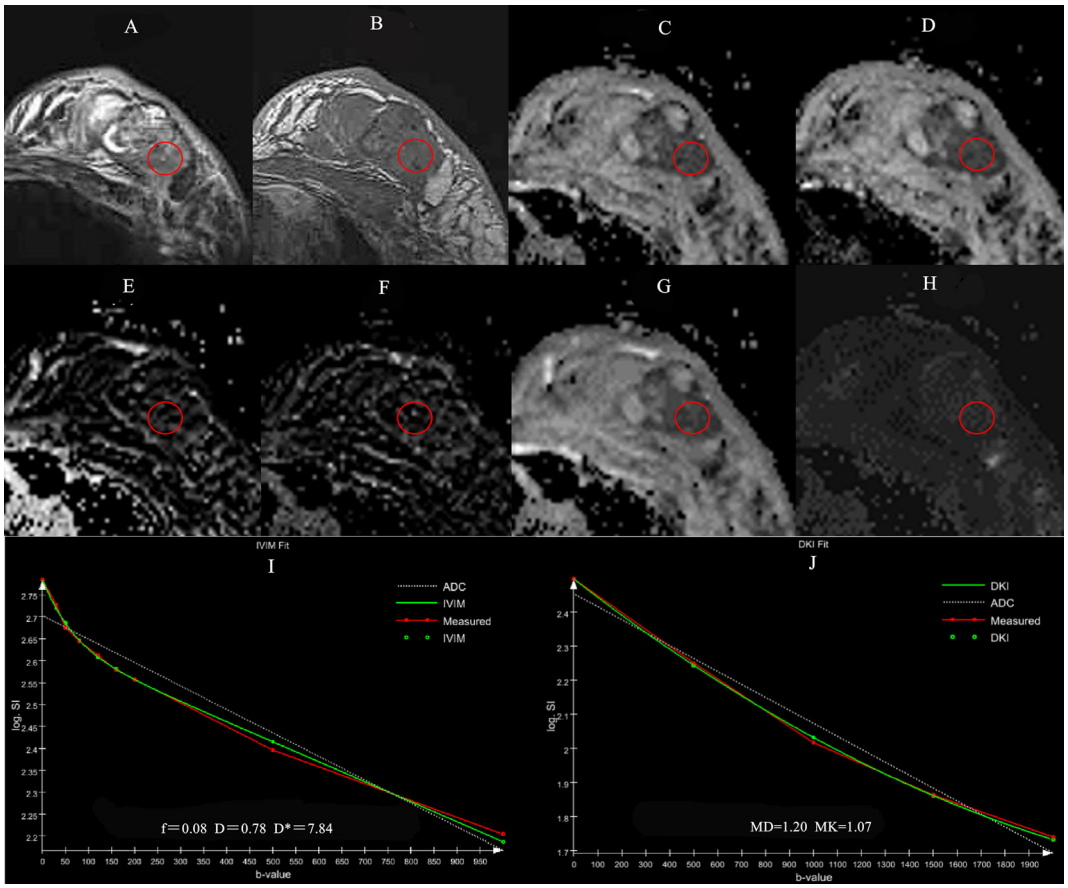

FIGURE 1 | A 56-year-old female patient with the left breast mass. The mass is located in outer quadrant of left breast (red round ROI), showing heterogeneous hyperintensity on TIRM **(A)**, hypointensity on T1WI **(B)**, ADC **(C)**, *D* **(D)** maps, isointensity on *f* **(E)**, *D** **(F)** maps, hypointensity on MD **(G)** and hyperintensity on MK **(H)** maps. Graphs show signal intensity *vs.* b value fits in single pixels of invasive ductal carcinoma of the breast with the IVIM **(I)** and DKI **(J)** models.

evaluate the diagnostic efficacy of each parameter. The stepwise backward logistic regression method was used to fit multiple parameters (P<0.1), and the parameters that were retained in the equation were combined to generate predicted probabilities for ROC curve evaluation. GraphPad Prism software (version 7.0) was used to draw the box plots, and SPSS (version 22.0) and R (version 3.6.0) software were used for statistical analysis. Significance was defined as p<0.05. The DeLong test was used to compare diagnostic efficiency across different parameters.

Consistency of the parameters was evaluated by comparing correlation factors within and between groups. Consistency within a group was evaluated by comparing two measurements by the same radiologist, and consistency between groups was evaluated by comparing the first measurement of each radiologist. When the interclass correlation coefficient (ICC) was greater than 0.75, consistency was considered good; between 0.50 and 0.75, fair; less than 0.50, very poor.

RESULTS

Clinical Data

A total of 202 female patients were enrolled. The average age of 54 patients in the benign group was 43.8 ± 9.2 years (range 28–62), and the average age of 148 patients in the malignant group was 52.1 ± 11.0 years (range 27–80). The age difference between the two groups was statistically significant (P<0.001).

Pathological Results

Among the 202 patients there were 215 lesions, 63 of which were benign (including 15 adenopathy, 45 fibroadenoma, and 3 abscesses), and 152 of which were malignant (including 16 carcinomas in situ, 135 invasive carcinomas, and 1 adenoid cystadenocarcinoma).

Quantitative Parameters

ADC, *D*, MK, and MD values were statistically significant in the identification of benign and malignant breast lesions (P<0.001), while *f* and *D** were not (P>0.05) (**Table 1**). The average values of ADC, *D*, and MD were greater in the benign lesion group than in the malignant lesion group, while the average MK value was smaller (**Table 1** and **Figure 2**).

Diagnostic Efficiency

Among the single-parameter indicators, ADC achieved the highest sensitivity (91.45%), specificity (82.54%), and accuracy (88.84%). The area under the ROC curve (AUC) was 0.915, and the critical value for diagnosis was 0.983 μm^2/ms. After logistic regression

TABLE 1 | Statistical result of various quantitative parameters in distinguishing benign and malignant breast lesions.

	Benign Lesions (n = 63)	Malignant Lesions (n = 152)	Z value	P value
ADC (μm^2/ms)	1.26 ± 0.21 (1.03-1.41)	0.80 ± 0.09 (0.70-0.90)	-9.570	<0.001
f (%)	6.85 ± 0.54 (5.03-9.45)	6.93 ± 0.71 (4.85-8.81)	-0.322	0.748
D (μm^2/ms)	1.15 ± 0.22 (0.99-1.39)	0.74 ± 0.17 (0.66-0.83)	-9.432	<0.001
*D** (μm^2/ms)	6.71 ± 0.41 (5.21-8.40)	7.73 ± 0.73 (5.25-10.31)	1.717	0.086
MK (μm^2/ms)	0.74 ± 0.19 (0.6-0.93)	1.05 ± 0.29 (0.92-1.17)	6.200	<0.001
MD (μm^2/ms)	1.55 ± 0.56 (1.34-1.78)	1.07 ± 0.23 (0.87-1.21)	-9.100	<0.001

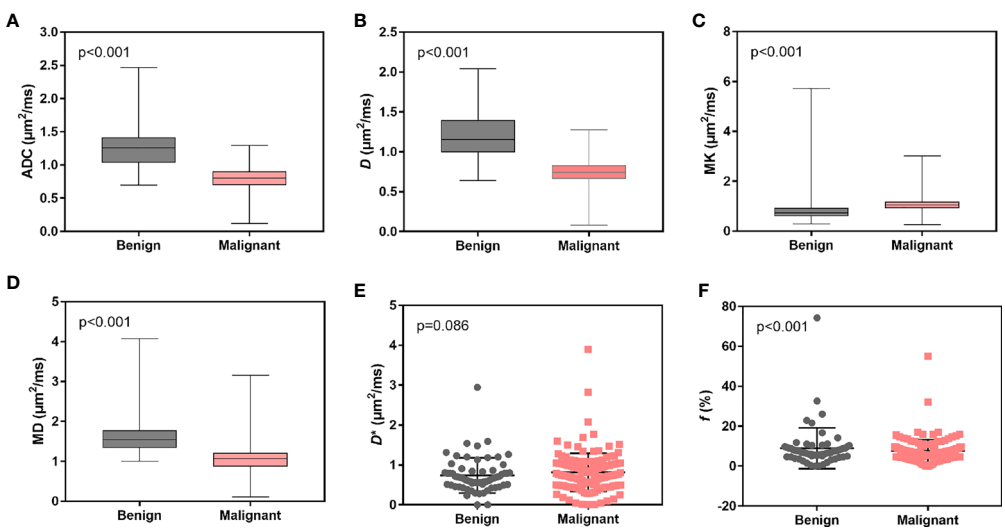

FIGURE 2 | Box and scatter plots for the average distribution of ADC, *D*, MK, MD, *D**, and *f* of benign *vs.* malignant breast lesions. **(A–D)** Average value of ADC, *D*, MK and MD. **(E, F)** Average values of *D** and *f*.

analysis, the combined application of ADC and MK outperformed ADC on most measures, demonstrating higher specificity (85.71%), accuracy (89.30%), and AUC (0.923) (**Table 2**). AUCs for all single parameters, as well as for ADC + MK, are shown in **Figure 3**.

The DeLong test showed that the diagnostic efficacy of ADC was better than that of MK and D^* (P<0.001), and there was no statistical difference between D and MD (P=0.524, 0.180). There was no significant difference in diagnostic efficacy between ADC alone as compared to ADC + MK (P=0.268).

Consistency Testing

ICC values for ADC, D, MK and MD measurements were all greater than 0.75, with good consistency of the inter- and intra-reader reproducibility. The ICC values for f measurement (inter-reader) was 0.675, and f and D^* measurements (intra-reader) was 0.724.

DISCUSSION

In this study, we find that the ADC, D, MK and MD values of different DWI techniques have high diagnostic value in differentiating benign and malignant breast lesions. Of these parameters, ADC had the best diagnostic performance, and the combined application of ADC and MK values achieved even higher diagnostic accuracy. A meta-analysis based on 13,847 lesions showed that ADC was meaningful in the differentiation of benign and malignant lesions, and recommended using an ADC value of 1.0 μm^2/ms as the threshold (9). In the present study, we found that if ADC <0.983 μm^2/ms was used as the threshold, the sensitivity was 91.45%, specificity was 82.54%, accuracy was 88.84%, and AUC was 0.915. Two b-values (0 and 1000 s/mm^2) were selected and the results showed that the average ADC of benign lesions of this group was significantly lower than that benign ones of meta-analysis, which is likely due to the mainly inclusion of fibroadenoma in the benign group of this study; fibrosis is known to reduce ADC values (25).

According to previous studies, the IVIM model should include b-values greater than 200 s/mm^2 (14). In the present study a total of nine b-values were selected, seven of which were less than 200 s/mm^2 to ensure accurate reflection of the diffusion of water molecules and blood microcirculation perfusion. In this analysis only D was able to reliably differentiate between benign and malignant breast lesions. D reflects the true diffusion of

TABLE 2 | The diagnostic performance of single and combined parameters.

	Threshold	AUC (95%CI)	Sensitivity	Specificity	Accuracy
ADC (μm^2/ms)	<0.983	0.915 (0.870-0.960)	91.45% (139/152)	82.54% (52/63)	88.84% (191/215)
D (μm^2/ms)	<0.952	0.909 (0.864-0.954)	90.13% (137/152)	80.95% (51/63)	87.44% (188/215)
D^* (μm^2/ms)	>0.873	0.574 (0.490-0.658)	42.76% (65/152)	77.78% (49/63)	53.02% (114/215)
MK (μm^2/ms)	>0.864	0.768 (0.688-0.849)	83.55% (127/152)	71.43% (45/63)	80.00% (172/215)
MD (μm^2/ms)	<1.297	0.895 (0.849-0.940)	88.82% (135/152)	79.37% (50/63)	86.05% (185/215)
ADC+MK	/	0.923 (0.881-0.964)	90.79% (138/152)	85.71% (54/63)	89.30% (192/215)

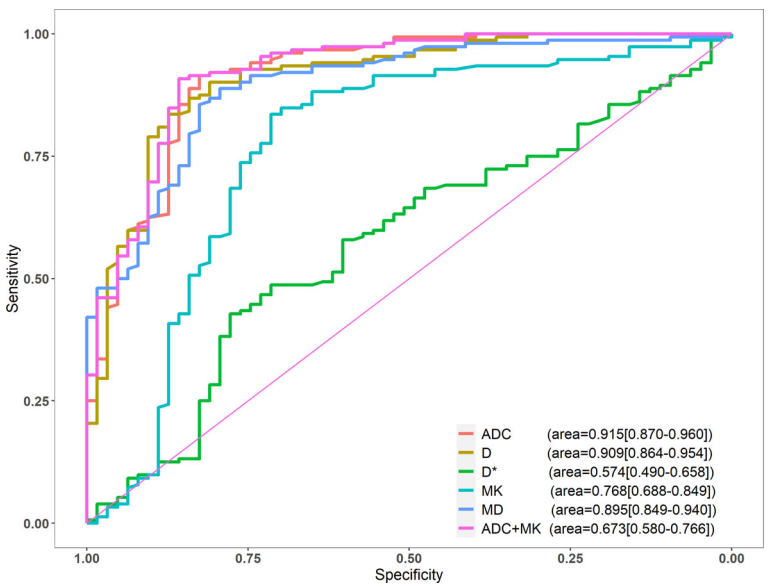

FIGURE 3 | ROC curves of ADC, D, D^*, MK, and MD.

water molecules after removing the effects of microcirculation perfusion, and the *D* value of malignant lesions is significantly lower than that of benign ones, as we and others have shown (16, 26, 30). *f* represents the ratio between microcirculation perfusion and overall diffusion. In a study by Liu et al. (16), the *f* value of malignant lesions was found to be significantly higher than that of benign lesions, which was thought to be related to the higher microcirculation blood volume of malignant tumors. In the present study, the average value of *f* was slightly higher in the malignant group, but the difference was not statistically significant. This may be due to the poor repeatability of *f* values between different observers and different machines (31). D^* represents the perfusion-related diffusion of microcirculation within the voxel, which is easily affected by neighboring structures and motion artifacts. As such, it is not known to be a good indicator of benign *vs.* malignant lesions (16, 30). Of the three IVIM parameters, we would recommend only *D* for use in differentiating benign and malignant breast lesions.

According to a preliminary study by Nogueira et al. (19), the DKI model needs to contain high (>200 s/mm^2) b-values. This study used five b-values (0, 500, 1000, 1500 and 2000 s/mm^2), and showed that MD of the malignant group was significantly lower than that of the benign group. This level of diagnostic efficiency is consistent with the results of other studies (18, 32). MK takes into account the heterogeneity and restriction of diffusion, and therefore reflects the complexity of biological tissues (24). Malignant lesions tend to have higher MK values than benign lesions due to structural heterogeneity, high cell density, interstitial vascular proliferation, and complex tissue structure, which was demonstrated in this and other studies (18, 32).

In this study, the diagnostic power of the ADC value was slightly higher than that of the DKI model. However, there was no significant difference between the two groups, which is consistent with the meta-analysis of Li et al. (32). The combined parameters of ADC and MK had the highest diagnostic efficiency, but there was no statistically significant difference between the combined parameters and single-parameter ADC. Taking into account the increased cost of combined parameter scanning and processing times, the single-parameter ADC value is more suitable for routine clinical applications.

There are limitations to this study. First, to ensure objectivity of data selection, ROIs were selected on an ADC map with b=1000 s/mm^2 and then copied to other parameter maps. However, this method may have allowed for the inclusion of images with poor signal-to-noise ratio, so the repeatability of IVIM and DKI parameters in this group is likely to be poor. Second, ROI measurements on one or even several selected sections of the tumor cannot reflect the tumor heterogeneity comprehensively. Therefore, the whole-tumor histogram analysis may be a more integrated method to investigate the histopathologic basis. Finally, some scholars believe that there is a correlation between IVIM or DKI parameters and prognostic factors of breast cancer, such as tumor size, nuclear grade, biological markers, and metastatic lymph nodes (26, 32, 33), but we did not investigate the correlation between them and need to be further improved in future research.

In conclusion, in the single parameter index of each DW-MRI model in this study, ADC was most valuable in the differential diagnosis of benign and malignant breast lesions. Although the combined application of ADC and MK values can achieve higher diagnostic efficacy than ADC alone, the difference is not statistically significant. Since the ADC image offers high signal-to-noise ratio, good data repeatability, and has the advantages of simple and quick detection, the single index model is worthy of further promotion in clinical applications.

DATA AVAILABILITY STATEMENT

The raw data supporting the conclusions of this article will be made available by the authors, without undue reservation.

ETHICS STATEMENT

The studies involving human participants were reviewed and approved by the institutional ethics committee of Fujian Provincial Hospital. The patients/participants provided their written informed consent to participate in this study.

AUTHOR CONTRIBUTIONS

MM and ZZ contributed to conception and design of the study. HR organized the database and wrote the first draft of the manuscript. MH performed the statistical analysis and wrote sections of the manuscript. All authors contributed to the article and approved the submitted version.

FUNDING

This work was supported by China International Medical Foundation (Grant number:Z-2014-07-1912-23), and the Natural Science Foundation of Fujian Province, China (Grant number:2020J011057).

REFERENCES

1. Bray F, Ferlay J, Soerjomataram I, Siegel RL, Torre LA, Jemal A. Global Cancer Statistics 2018: GLOBOCAN Estimates of Incidence and Mortality Worldwide for 36 Cancers in 185 Countries. *CA Cancer J Clin* (2018) 68 (6):394–424. doi: 10.3322/caac.21492
2. Fan L, Strasser-Weippl K, Li JJ, St Louis J, Finkelstein DM, Yu KD, et al. Breast Cancer in China. *Lancet Oncol* (2014) 15(7):e279–89. doi: 10.1016/s1470-2045(13)70567-9
3. Pan R, Zhu M, Yu C, Lv J, Guo Y, Bian Z, et al. Cancer Incidence and Mortality: A Cohort Study in China, 2008-2013. *Int J Cancer* (2017) 141 (7):1315–23. doi: 10.1002/ijc.30825

4. Barkhausen J, Bischof A, Haverstock D, Klemens M, Brueggenwerth G, Weber O, et al. Diagnostic Efficacy of Contrast-Enhanced Breast MRI Versus X-Ray Mammography in Women With Different Degrees of Breast Density. *Acta Radiol* (2021) 62(5):586–93. doi: 10.1177/0284185120936271
5. Zhang H, Guo LL, Tao WJ, Zhang JD, Bai GJ. Comparison of the Clinical Application Value of Mo-Targeted X-Ray, Color Doppler Ultrasound and MRI in Preoperative Comprehensive Evaluation of Breast Cancer. *Saudi J Biol Sci* (2019) 26(8):1973–77. doi: 10.1016/j.sjbs.2019.09.009
6. Rahbar H, Partridge SC. Multiparametric MR Imaging of Breast Cancer. *Magn Reson Imaging Clin N Am* (2016) 24(1):223–38. doi: 10.1016/j.mric.2015.08.012
7. Partridge SC, McDonald ES. Diffusion Weighted Magnetic Resonance Imaging of the Breast: Protocol Optimization, Interpretation, and Clinical Applications. *Magn Reson Imaging Clin N Am* (2013) 21(3):601–24. doi: 10.1016/j.mric.2013.04.007
8. Maric J, Boban J, Ivkovic-Kapicl T, Djilas D, Vucaj-Cirilovic V, Bogdanovic-Stojanovic D. Differentiation of Breast Lesions and Distinguishing Their Histological Subtypes Using Diffusion-Weighted Imaging and ADC Values. *Front Oncol* (2020) 10:332. doi: 10.3389/fonc.2020.00332
9. Surov A, Meyer HJ, Wienke A. Can Apparent Diffusion Coefficient (ADC) Distinguish Breast Cancer From Benign Breast Findings? A Meta-Analysis Based on 13 847 Lesions. *BMC Cancer* (2019) 19(1):955. doi: 10.1186/s12885-019-6201-4
10. Bozkurt Bostan T, Koç G, Sezgin G, Altay C, Fazıl Gelal M, Oyar O. Value of Apparent Diffusion Coefficient Values in Differentiating Malignant and Benign Breast Lesions. *Balkan Med J* (2016) 33(3):294–300. doi: 10.5152/balkanmedj.2016.141007
11. Chen X, Li WL, Zhang YL, Wu Q, Guo YM, Bai ZL. Meta-Analysis of Quantitative Diffusion-Weighted MR Imaging in the Differential Diagnosis of Breast Lesions. *BMC Cancer* (2010) 10:693. doi: 10.1186/1471-2407-10-693
12. Le Bihan D, Breton E, Lallemand D, Aubin ML, Vignaud J, Laval-Jeantet M. Separation of Diffusion and Perfusion in Intravoxel Incoherent Motion MR Imaging. *Radiology* (1988) 168(2):497–505. doi: 10.1148/radiology.168.2.3393671
13. Chen J, Liu S, Tang Y, Zhang X, Cao M, Xiao Z, et al. Diagnostic Performance of Diffusion MRI for Pancreatic Ductal Adenocarcinoma Characterisation: A Meta-Analysis. *Eur J Radiol* (2021) 139:109672. doi: 10.1016/j.ejrad.2021.109672
14. Koh DM, Collins DJ, Orton MR. Intravoxel Incoherent Motion in Body Diffusion-Weighted MRI: Reality and Challenges. *AJR Am J Roentgenol* (2011) 196(6):1351–61. doi: 10.2214/ajr.10.5515
15. Sigmund EE, Cho GY, Kim S, Finn M, Moccaldi M, Jensen JH, et al. Intravoxel Incoherent Motion Imaging of Tumor Microenvironment in Locally Advanced Breast Cancer. *Magn Reson Med* (2011) 65(5):1437–47. doi: 10.1002/mrm.22740
16. Liu C, Liang C, Liu Z, Zhang S, Huang B. Intravoxel Incoherent Motion (IVIM) in Evaluation of Breast Lesions: Comparison With Conventional DWI. *Eur J Radiol* (2013) 82(12):e782–9. doi: 10.1016/j.ejrad.2013.08.006
17. Jensen JH, Helpern JA, Ramani A, Lu H, Kaczynski K. Diffusional Kurtosis Imaging: The Quantification of Non-Gaussian Water Diffusion by Means of Magnetic Resonance Imaging. *Magn Reson Med* (2005) 53(6):1432–40. doi: 10.1002/mrm.20508
18. Sun K, Chen X, Chai W, Fei X, Fu C, Yan X, et al. Breast Cancer: Diffusion Kurtosis MR Imaging-Diagnostic Accuracy and Correlation With Clinical-Pathologic Factors. *Radiology* (2015) 277(1):46–55. doi: 10.1148/radiol.15141625
19. Nogueira L, Brandão S, Matos E, Nunes RG, Loureiro J, Ramos I, et al. Application of the Diffusion Kurtosis Model for the Study of Breast Lesions. *Eur Radiol* (2014) 24(6):1197–203. doi: 10.1007/s00330-014-3146-5
20. Ai Z, Han Q, Huang Z, Wu J, Xiang Z. The Value of Multiparametric Histogram Features Based on Intravoxel Incoherent Motion Diffusion-Weighted Imaging (DWI) for the Differential Diagnosis of Liver Lesions. *Ann Transl Med* (2020) 8(18):1128. doi: 10.21037/atm-20-5109
21. Liu Y, Wang X, Cui Y, Jiang Y, Yu L, Liu M, et al. Comparative Study of Monoexponential, Intravoxel Incoherent Motion, Kurtosis, and IVIM-Kurtosis Models for the Diagnosis and Aggressiveness Assessment of Prostate Cancer. *Front Oncol* (2020) 10:1763. doi: 10.3389/fonc.2020.01763
22. Shan Y, Chen X, Liu K, Zeng M, Zhou J. Prostate Cancer Aggressive Prediction: Preponderant Diagnostic Performances of Intravoxel Incoherent Motion (IVIM) Imaging and Diffusion Kurtosis Imaging (DKI) Beyond ADC at 3.0 T Scanner With Gleason Score at Final Pathology. *Abdom Radiol (NY)* (2019) 44(10):3441–52. doi: 10.1007/s00261-019-02075-3
23. Song SE, Cho KR, Seo BK, Woo OH, Park KH, Son YH, et al. Intravoxel Incoherent Motion Diffusion-Weighted MRI of Invasive Breast Cancer: Correlation With Prognostic Factors and Kinetic Features Acquired With Computer-Aided Diagnosis. *J Magn Reson Imaging* (2019) 49(1):118–30. doi: 10.1002/jmri.26221
24. Raab P, Hattingen E, Franz K, Zanella FE, Lanfermann H. Cerebral Gliomas: Diffusional Kurtosis Imaging Analysis of Microstructural Differences. *Radiology* (2010) 254(3):876–81. doi: 10.1148/radiol.09090819
25. Woodhams R, Matsunaga K, Iwabuchi K, Kan S, Hata H, Kuranami M, et al. Diffusion-Weighted Imaging of Malignant Breast Tumors: The Usefulness of Apparent Diffusion Coefficient (ADC) Value and ADC Map for the Detection of Malignant Breast Tumors and Evaluation of Cancer Extension. *J Comput Assist Tomogr* (2005) 29(5):644–9. doi: 10.1097/01.rct.0000171913.74086.1b
26. Liang J, Zeng S, Li Z, Kong Y, Meng T, Zhou C, et al. Intravoxel Incoherent Motion Diffusion-Weighted Imaging for Quantitative Differentiation of Breast Tumors: A Meta-Analysis. *Front Oncol* (2020) 10:585486. doi: 10.3389/fonc.2020.585486
27. Le Bihan D, Turner R, MacFall JR. Effects of Intravoxel Incoherent Motions (IVIM) in Steady-State Free Precession (SSFP) Imaging: Application to Molecular Diffusion Imaging. *Magn Reson Med* (1989) 10(3):324–37. doi: 10.1002/mrm.1910100305
28. Marzi S, Piludu F, Vidiri A. Assessment of Diffusion Parameters by Intravoxel Incoherent Motion MRI in Head and Neck Squamous Cell Carcinoma. *NMR BioMed* (2013) 26(12):1806–14. doi: 10.1002/nbm.3020
29. Fujima N, Yoshida D, Sakashita T, Homma A, Tsukahara A, Shimizu Y, et al. Prediction of the Treatment Outcome Using Intravoxel Incoherent Motion and Diffusional Kurtosis Imaging in Nasal or Sinonasal Squamous Cell Carcinoma Patients. *Eur Radiol* (2017) 27(3):956–65. doi: 10.1007/s00330-016-4440-1
30. Bokacheva L, Kaplan JB, Giri DD, Patil S, Gnanasigamani M, Nyman CG, et al. Intravoxel Incoherent Motion Diffusion-Weighted MRI at 3.0 T Differentiates Malignant Breast Lesions From Benign Lesions and Breast Parenchyma. *J Magn Reson Imaging* (2014) 40(4):813–23. doi: 10.1002/jmri.24462
31. Iima M, Kataoka M, Kanao S, Onishi N, Kawai M, Ohashi A, et al. Intravoxel Incoherent Motion and Quantitative non-Gaussian Diffusion MR Imaging: Evaluation of the Diagnostic and Prognostic Value of Several Markers of Malignant and Benign Breast Lesions. *Radiology* (2018) 287(2):432–41. doi: 10.1148/radiol.2017162853
32. Li Z, Li X, Peng C, Dai W, Huang H, Li X, et al. The Diagnostic Performance of Diffusion Kurtosis Imaging in the Characterization of Breast Tumors: A Meta-Analysis. *Front Oncol* (2020) 10:575272. doi: 10.3389/fonc.2020.575272
33. Jeh SK, Kim SH, Kim HS, Kang BJ, Jeong SH, Yim HW, et al. Correlation of the Apparent Diffusion Coefficient Value and Dynamic Magnetic Resonance Imaging Findings With Prognostic Factors in Invasive Ductal Carcinoma. *J Magn Reson Imaging* (2011) 33(1):102–9. doi: 10.1002/jmri.22400

Conflict of Interest: Author ZZ was employed by the company Siemens Healthcare Ltd.

The remaining authors declare that the research was conducted in the absence of any commercial or financial relationships that could be construed as a potential conflict of interest.

frontiers in Oncology

ORIGINAL RESEARCH
published: 08 July 2021
doi: 10.3389/fonc.2021.688182

Texture Analysis of DCE-MRI Intratumoral Subregions to Identify Benign and Malignant Breast Tumors

Bin Zhang[1], *Lirong Song*[2] *and Jiandong Yin*[2]*

[1] School of Medicine and Bioinformatics Engineering, Northeastern University, Shenyang, China, [2] Department of Radiology, Shengjing Hospital of China Medical University, Shenyang, China

Purpose: To evaluate the potential of the texture features extracted from dynamic contrast-enhanced magnetic resonance imaging (DCE-MRI) intratumoral subregions to distinguish benign from malignant breast tumors.

Materials and Methods: A total of 299 patients with pathologically verified breast tumors who underwent breast DCE-MRI examination were enrolled in this study, including 124 benign cases and 175 malignant cases. The whole tumor area was semi-automatically segmented on the basis of subtraction images of DCE-MRI in Matlab 2018b. According to the time to peak of the contrast agent, the whole tumor area was partitioned into three subregions: early, moderate, and late. A total of 467 texture features were extracted from the whole tumor area and the three subregions, respectively. Patients were divided into training (n = 209) and validation (n = 90) cohorts by different MRI scanners. The least absolute shrinkage and selection operator (LASSO) method was used to select the optimal feature subset in the training cohort. The Kolmogorov-Smirnov test was first performed on texture features selected by LASSO to test whether the samples followed a normal distribution. Two machine learning methods, decision tree (DT) and support vector machine (SVM), were used to establish classification models with a 10-fold cross-validation method. The performance of the classification models was evaluated with receiver operating characteristic (ROC) curves.

Results: In the training cohort, the areas under the ROC curve (AUCs) for the DT_Whole model and SVM_Whole model were 0.744 and 0.806, respectively. In contrast, the AUCs of the DT_Early model (P = 0.004), DT_Late model (P = 0.015), SVM_Early model (P = 0.002), and SVM_Late model (P = 0.002) were significantly higher: 0.863 (95% CI, 0.808–0.906), 0.860 (95% CI, 0.806–0.904), 0.934 (95% CI, 0.891–0.963), and 0.921 (95% CI, 0.876–0.954), respectively. The SVM_Early model and SVM_Late model achieved better performance than the DT_Early model and DT_Late model (P = 0.003, 0.034, 0.008, and 0.026, respectively). In the validation cohort, the AUCs for the DT_Whole model and SVM_Whole model were 0.670 and 0.708, respectively. In comparison, the AUCs of the DT_Early model (P = 0.006), DT_Late model (P = 0.043), SVM_Early model (P = 0.001), and SVM_Late model (P = 0.007) were significantly higher: 0.839 (95% CI, 0.747–0.908),

OPEN ACCESS

Edited by:
Chuanming Li,
Chongqing Medical University, China

Reviewed by:
Guolin Ma,
China-Japan Friendship Hospital, China
Huan Liu,
GE Healthcare, China

***Correspondence:**
Jiandong Yin
jiandongyin@sina.com

Specialty section:
This article was submitted to Cancer Imaging and Image-directed Interventions, a section of the journal Frontiers in Oncology

Received: *30 March 2021*
Accepted: *15 June 2021*
Published: *08 July 2021*

Citation:
Zhang B, Song L and Yin J (2021) Texture Analysis of DCE-MRI Intratumoral Subregions to Identify Benign and Malignant Breast Tumors. Front. Oncol. 11:688182. doi: 10.3389/fonc.2021.688182

0.784 (95% CI, 0.601–0.798), 0.890 (95% CI, 0.806–0.946), and 0.865 (95% CI, 0.777–0.928), respectively.

Conclusion: The texture features from intratumoral subregions of breast DCE-MRI showed potential in identifying benign and malignant breast tumors.

Keywords: breast tumors, magnetic resonance imaging, machine learning, texture analysis, DCE-MRI

INTRODUCTION

Breast cancer is one of the most common cancers and the main cause of cancer deaths in women, accounting for approximately 30% of new cancer cases in women and 14% of cancer deaths (1). Advances in medical technology have resulted in a relatively high cure rate for early breast cancer through radiotherapy, chemotherapy, and surgery (2, 3). The treatment options for benign and malignant breast tumors differ, as do the local recurrence and survival rates (4). Benign breast tumors are generally curable through active treatment, whereas malignant tumors are difficult to cure and usually require surgery after neoadjuvant therapy to suppress local recurrence (5–7). Therefore, distinguishing benign from malignant breast tumors quickly and accurately is important.

Magnetic resonance imaging (MRI) is a non-invasive imaging method increasingly being used to detect and diagnose breast cancer. MRI has a higher sensitivity for the detection of breast lesions than mammography or breast ultrasound (8, 9). Among the available MRI methods, dynamic contrast-enhanced MRI (DCE-MRI) can provide tumor anatomical information and hemodynamic information with high spatial resolution, and it plays an important role in the diagnosis, differential diagnosis, and treatment response assessment of breast cancer (10–13). However, many benign lesions show strong contrast enhancement, which can lead to false-positive diagnoses, unnecessary biopsies, or overtreatment (14). The rate of preoperative breast DCE-MRI examinations is increasing, and an effective method for characterizing enhanced lesions is crucial to improve the accuracy of diagnosis.

Texture analysis refers to the extraction of texture feature parameters through specific image processing technology to obtain a quantitative or qualitative description of the texture (15, 16). Texture analysis is applied to breast MRI through image processing methods, which can be used to quantify the heterogeneity of lesions (17, 18). Studies have shown that texture features that characterize intratumoral heterogeneity can help identify benign and malignant breast tumors and distinguish molecular subtypes of breast cancer (19–21).

Previous studies have mainly extracted texture features from the whole tumor area in MRI images. However, the texture features derived from subregions within the breast tumor may provide valuable information to aid in clinical diagnosis and help patients develop personal treatment plans (22–25). Fan et al. (26) have shown that the texture features extracted from intratumoral subregions of DCE-MRI can be used to predict Ki-67 status in estrogen receptor (ER)-positive breast cancer. To our knowledge, no research has been performed on the identification of benign and malignant breast tumors on the basis of texture features extracted from intratumoral subregions of breast DCE-MRI. The purpose of this study was to evaluate the potential of the texture features extracted from DCE-MRI of intratumoral subregions for distinguishing benign and malignant breast tumors.

MATERIALS AND METHODS

Study Cohort

This study was approved by the Ethics Review Committee at Shengjing Hospital of China Medical University (No. 2019PS175K), and the requirement for informed consent was waived because of the retrospective nature of the study. Between January 2017 and January 2020, patients who underwent breast DCE-MRI examinations were reviewed through the image archiving and communication system (PACS) at our institution. The study cohort initially included 378 patients. The inclusion criteria were as follows: (1) patients who underwent breast DCE-MRI and (2) patients with benign or malignant breast tumors confirmed by histopathology. The exclusion criteria were as follows: (1) patients treated with surgery, chemotherapy, or radiotherapy before DCE-MRI (n = 43); (2) patients diagnosed through excisional biopsy before DCE-MRI (n = 26); and (3) patients with insufficient image quality for subsequent processing because of obvious motion artifacts (n = 10). Consequently, 299 patients (mean age, 48.30 ± 9.74 years; range, 25–84 years) were divided into training (n = 209) and validation (n = 90) cohorts by different MRI scanners, including 124 benign and 175 malignant breast tumors. The clinical characteristics of the study cohort are summarized in **Table 1**. The flowchart of this study is shown in **Figure 1**.

Image Acquisition

In the training cohort, DCE-MRI examinations were performed with a GE 3.0T MRI scanner (Signa HDxt, GE Healthcare) equipped with a dedicated eight-channel bilateral breast coil on patients in a prone position. A transverse fat-suppression T1-weighted pre-contrast scan was first obtained with the VIBRANT-VX technique. Eight phases of fat-suppression T1-weighted post-contrast scans were acquired after intravenous injection of the contrast agent (Magnevist, Bayer-Schering Pharmaceuticals, Germany) at a dose of 0.15 mmol per kg body weight at 4 mlL/s and subsequent flushing with an equal volume of saline at the same injection speed. The following imaging parameters were used: repetition time (TR), 7.42 ms; echo time (TE), 4.25 ms; flip angle, 15°; slice thickness, 2.20 mm;

TABLE 1 | Clinical characteristics of the patients selected for this study.

Characteristic	Training cohort		Validation cohort	
	Number	%	Number	%
Total patients	209		90	
Benign (age range, 25–82 years)	84	40.2	40	44.4
Malignant (age range, 29–84 years)	125	59.8	50	55.6
BI-RADS				
3	18	8.6	7	7.8
4A	56	26.8	27	30
4B	43	20.6	16	17.8
4C	68	32.5	35	38.9
5	24	11.5	5	5.5
Histopathological Type				
Benign	84	40.2	40	44.4
Adenosis	48	23.0	23	25.5
Fibroadenoma	32	15.3	14	15.5
Papilloma	4	1.9	3	3.4
Malignant	125	59.8	50	55.6
Invasive carcinoma of no special type	116	55.5	41	45.6
Ductal carcinoma in situ	6	2.8	5	5.6
Invasive micropapillary carcinoma	2	1.0	3	3.3
Invasive lobular carcinoma	1	0.5	1	1.1

spacing between slices, 2.20 mm; field of view, 340 × 340 mm^2; image matrix, 1,024 × 1,024; slice number, 78. For each patient, eight phases of subtraction images were obtained by subtracting pre-contrast images from eight post-contrast images.

In the validation cohort, DCE-MRI examinations were performed with a Philips 3.0T MRI scanner (Ingenia, Philips Medical System, Best, Netherlands) equipped with a dedicated seven-channel bilateral breast coil with patient in a prone position. First, an axial fat-saturated T1-weighted pre-contrast scan was acquired. Then, eight axial contrast-enhanced fat-saturated T1-weighted scans were acquired after the intravenous bolus injection of the same contrast with the same dose. The imaging parameters were as follow: repetition time (TR), 4.14 ms; echo time (TE), 2.10 ms; flip angle, 12°; slice thickness, 2.00 mm; spacing between slices, 1.00 mm; field of view, 340 × 340 mm^2; matrix, 380 × 380; slice number, 78. Eight subtraction sequences were obtained by subtracting the pre-contrast scan from each of the eight post-contrast scans.

Image Processing and Lesion Segmentation

Two senior radiologists, with 10 and 15 years of experience in interpreting breast MRI were invited to review the subtraction images in the fourth phase and reached a consensus in selecting the slice image with the maximum tumor diameter for each patient for subsequent analysis (27). During the image review, the radiologists were blind to the patients' pathological results. The whole tumor area was segmented with a semi-automatic method in Matlab 2018b (Mathworks, Natick, MA, USA), as described below (28, 29). One of the two radiologists manually delineated a region of interest (ROI) with an arbitrary shape around the lesion area on the subtraction image. The pixel gray levels within the ROI were first normalized to $\mu \pm 3\sigma$ (μ: mean gray level of pixels within the ROI; σ: standard deviation), and the range was quantized to 8 bits/pixel to change the signal to noise ratio of the texture results (30–32). A spatial fuzzy C-means (FCM) algorithm was then used to delineate the contour boundary of the lesion according to the ROI, and the whole lesion area was refined through morphological processing methods (33–35). Another radiologist verified and proofread the results of the semi-automatic breast tumor segmentation.

Intratumoral Subregion Partition

To better understand the intratumoral heterogeneity of breast tumors, as in a previous study (26), we divided the lesion area into three subregions according to the variations in pixel signal intensity in different phases. The specific partition details are as follows:

The relative enhancement of the post-contrast image compared with the pre-contrast image on a pixel-by-pixel basis was calculated with the following formula:

$$H(m,n,t) = \frac{I(m,n,t) - I(m,n,t_0)}{I(m,n,t_0)} \quad (1)$$

where I(m, n, t) and I(m, n t_0) represent the signal intensity of the pixel (m, n) captured at times t and t_0 (the pre-contrast moment) (36). The time-signal intensity curve, H(m, n, t), was defined to describe the variation in the relative enhancement over time (37–39). The time to peak (TTP), which represents the arrival time of the peak relative enhancement, was calculated with the following formula:

$$TTP(m,n) = \arg\max_t H(m,n,t) \quad (2)$$

Then the pixels within the tumor region were divided into three subregions according to their TTP values. More specifically, pixel sets at the first four, fifth or sixth, and seventh or eighth phases to achieve peak enhancement values were defined as early, moderate, and late subregions, respectively; this method was similar to those described in previous studies

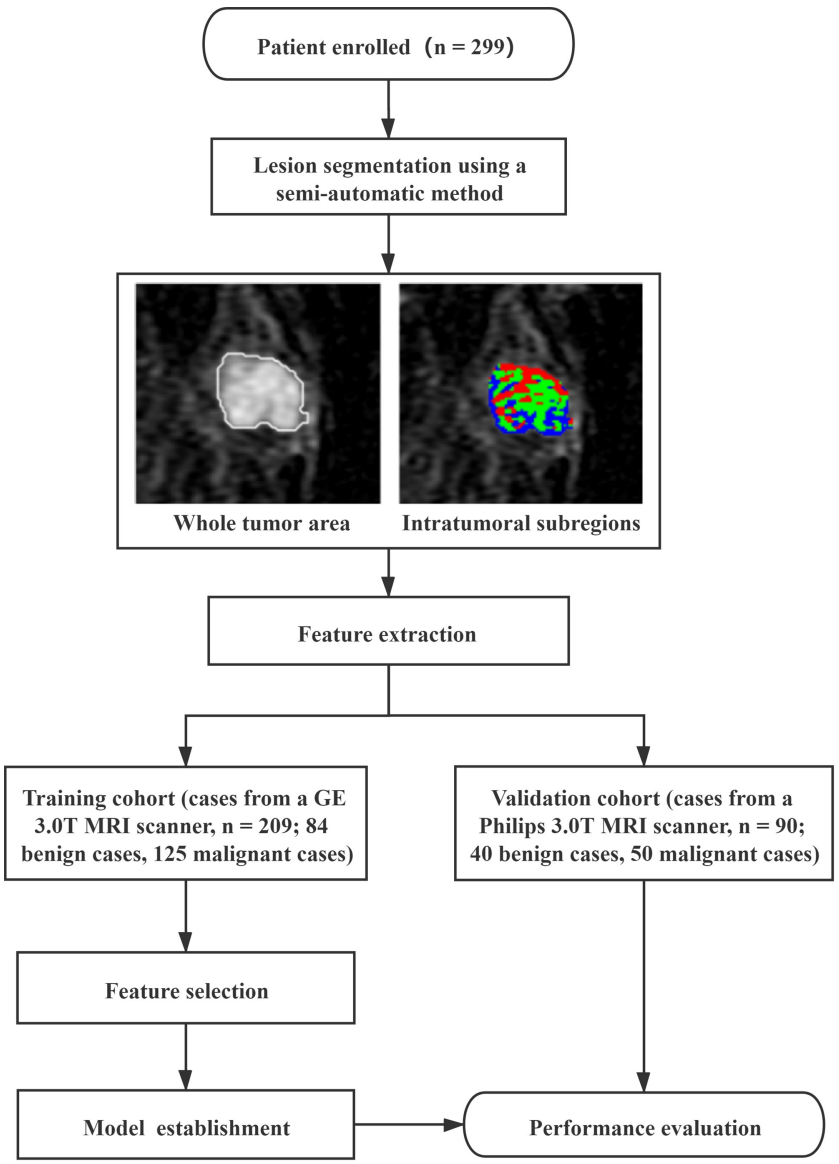

FIGURE 1 | The flowchart adopted in this study.

(26, 36). Therefore, the tumor was divided into three regions representing different sets of TTP values.

Texture Feature Extraction

A total of 467 texture features were extracted from the whole tumor area and the three subregions with Matlab 2018b. The feature extraction methods could be classified into the following four categories: histogram, gray-level co-occurrence matrix (GLCM), gray-level run length matrix (GRLM), and discrete wavelet transform (DWT). Detailed information on the features is shown in **Table 2**. Each GLCM feature was calculated by using four angles (0, 45, 90, and 135°) and four distances (1, 2, 3, and 4 pixels). Each GRLM feature was calculated by using four angles (0, 45, 90, and 135°) and a distance of 1 pixel. In the following, (d, 0), (d, d), (0, d), and (-d, -d) were used to represent 0, 45, 90, and 135°, respectively, where d is the distance. Each DWT feature was calculated with four scales and three directions (horizontal, vertical, and diagonal) to generate low and high frequency components. In the following content, for example, Haar_2HH was used to represent the horizontal high frequency component of the second scale with the Haar wavelet.

Feature Selection and Model Construction

To reduce the dimensionality of the features, the correlation between features was first tested with Pearson's correlation analysis, and features with correlation coefficients of >0.95 relative to other features were removed. The remaining features were filtered by the least absolute shrinkage and

TABLE 2 | Detailed information on the extracted features.

Methods	Texture features	Number
Histogram	Mean, Kurtosis, Skewness, Variance	4
GLCM	Autocorrelation, Contrast, Correlation, Cluster prominence, Cluster shadow, Dissimilarity, Energy, Entropy, Homogeneity, Maximum probability, Sum of square, Sum average, Sum variance, Sum entropy, Difference square, Difference entropy, Information measure of correlation, Inverse difference normalized, Inverse difference moment normalized	380
GRLM	Short run emphasis, Long run emphasis, Gray-level non-uniformity, Run length non-uniformity, Fraction of image in runs, Low gray-level run emphasis, High gray-level run emphasis, Short run low gray-level emphasis, Short run high gray-level emphasis, Long run low gray-level emphasis, Long run high gray-level emphasis	44
DWT	Harr parameters	13
	Deubechies2 parameters	13
	Symlet4 parameters	13
Total		467

GLCM, gray-level co-occurrence matrix; GRLM, gray-level run length matrix; DWT, discrete wavelet transform.

selection operator (LASSO) method to select the optimal feature subset (40). Two machine learning models, decision tree (DT) and support vector machine (SVM), were used to construct classification models based on the optimal feature subset in the training cohort with a 10-fold cross-validation method for identifying benign and malignant breast tumors. And the classification models were tested by using a independent validation cohort. The 10-fold cross-validation refers to random division of the data set into 10 sets, nine of which were used for training and the last of which was used for testing. This process was repeated 10 times, and the test data differed each time.

Statistical Analysis

All statistical analyses were performed in SPSS 22.0 (IBM, Armonk, NY, USA). The Kolmogorov-Smirnov test was first performed on texture features selected by LASSO to assess whether the samples followed a normal distribution (41); if so, the variables in the tables are represented by means ± standard deviation (SD), and if not, the variables in the tables are represented by medians ± interquartile range. Univariate logistic regression analysis was used to evaluate the performance of an independent feature in distinguishing benign from malignant breast tumors. The receiver operating characteristic (ROC) curve constructed in the professional statistics software MedCalc (version 14.10.20, http://www.medcalc.org/) was used to assess the classification performance by calculating the area under the ROC curve (AUC). The corresponding accuracy, sensitivity, and specificity were also determined. The DeLong test was used to determine the statistical significance of differences between AUCs. A two-tailed P value of <0.05 was considered statistically significant.

The intraobserver variability of texture features extracted by the two radiologists was evaluated by using intraclass correlation coefficients [ICC, (0, 0.4), poor agreement; (0.4, 0.6), moderate agreement; (0.6, 0.8), good agreement; and (0.8, 1), excellent agreement] (42, 43).

RESULTS

Study Cohort

A total of 299 patients were enrolled in this study. In the training cohort, the patients had 84 (40.2%) benign breast tumors classified into three histopathological types: adenosis (48), fibroadenoma (32), and papilloma (4). The 125 (59.8%) malignant breast tumors comprised 116 invasive carcinomas of no special type, 6 ductal carcinomas *in situ*, 2 invasive micropapillary carcinomas, and 1 invasive lobular carcinoma. In the validation cohort, the patients had 40 (44.4%) benign breast tumors classified into three histopathological types: adenosis (23), fibroadenoma (14), and papilloma (3). The 50 (55.6%) malignant breast tumors comprised 41 invasive carcinomas of no special type, 5 ductal carcinomas *in situ*, 3 invasive micropapillary carcinomas, and 1 invasive lobular carcinoma. The results of the whole tumor area segmentation and intratumoral subregion partition are displayed in **Figure 2**, which shows two randomly selected cases, one benign case and the other malignant case.

Univariate Analysis

The results of univariate logistic regression analysis for identifying benign and malignant breast tumors are displayed in **Table 3**, which shows the top six features with the best performance extracted from the three subregions and the whole tumor area. The AUCs of features derived from the whole tumor area ranged from 0.732 to 0.786. Features from the early subregion performed best among the three subregions, with AUC values ranging from 0.787 to 0.886. The AUCs of the run length non-uniformity (1, 0) ($P < 0.001$), difference square (0, 1) ($P = 0.004$), and short run emphasis (1, 0) ($P < 0.001$) from the early subregion were significantly higher than those from the whole tumor area. The AUCs from the moderate subregion ranged from 0.715 to 0.777, and the AUCs from the late subregion ranged from 0.685 to 0.884. Among all individual features, the run length nonuniformity (1, 0) extracted from the early region achieved the highest AUC of 0.886 [95% confidence interval (CI), 0.836–0.926].

Performance of Classification Models

Table 4 shows the performance of the classification models for distinguishing benign from malignant breast tumors in the training and validation cohorts, and the corresponding ROC curves are presented in **Figures 3** and **4**. In the training cohort, the AUCs of the DT_Whole model and SVM_Whole model were 0.744 and 0.806, respectively. In contrast, the AUCs of the DT_Early model ($P = 0.004$), DT_Late model ($P = 0.015$), SVM_Early model

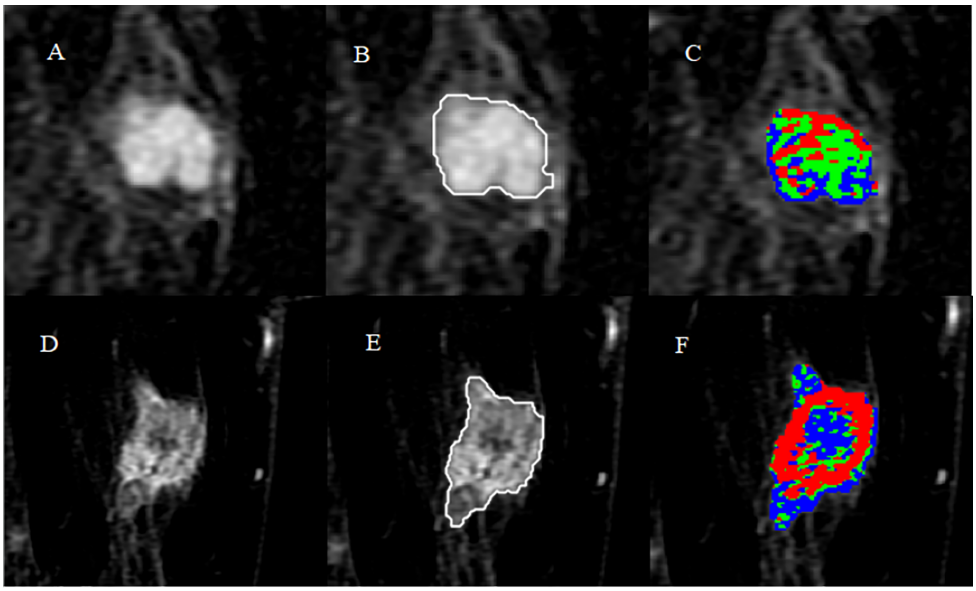

FIGURE 2 | Results of whole tumor segmentation and intratumoral subregion partition. The first row shows the results of a benign case: **(A)** subtraction image with the maximum tumor diameter; **(B)** result of the whole tumor area segmented with a semi-automatic method; **(C)** result of intratumoral subregion partition, in which red, green, and blue represent the early, moderate, and late subregions, respectively. The second row shows the results of a malignant case: **(D)** subtraction image; **(E)** result of the whole tumor area; **(F)** result of intratumoral subregion partition.

TABLE 3 | Univariate analysis for predicting benign and malignant breast tumors.

Methods	Subregions	Features	AUC	95% CI	*P*-value[a]
Intratumoral subregions	Early	Run length nonuniformity (1, 0)	0.886	0.836–0.926	<0.001
		Difference square (0, 1)	0.877	0.825–0.918	0.004
		Short run emphasis (1, 0)	0.870	0.817–0.913	<0.001
		Correlation (−1, 0)	0.836	0.779–0.884	0.081
		Information measure of correlation (−2, 0)	0.820	0.761–0.870	0.391
		Deubechies2_2HH	0.787	0.725–0.840	0.186
	Moderate	Gray-level non-uniformity (1, 0)	0.777	0.715–0.832	<0.001
		Deubechies2_1VH	0.740	0.675–0.798	0.357
		Haar_1DH	0.736	0.671–0.795	<0.001
		Symlet4_1DH	0.729	0.664–0.788	0.016
		Deubechies2_1DH	0.718	0.651–0.778	0.003
		Mean	0.715	0.648–0.775	0.238
	Late	Information measure of correlation (0,1)	0.884	0.833–0.924	0.002
		Information measure of correlation (−1,0)	0.853	0.798–0.898	0.059
		Deubechies2_2VH	0.849	0.797–0.898	0.001
		Haar_1HH	0.840	0.784–0.887	0.001
		Haar_4HH	0.724	0.658–0.783	<0.001
		Mean	0.685	0.617–0.747	0.157
Whole tumor area	/	Deubechies2_2DH	0.786	0.725–0.840	/
		Haar_2DH	0.779	0.717–0.833	/
		Symlet4_2VH	0.776	0.713–0.831	/
		Symlet4_2HH	0.747	0.682–0.804	/
		Deubechies2_3DH	0.734	0.669–0.793	/
		Mean	0.732	0.667–0.791	/

AUC, area under the receiver operating characteristic curve; CI, confidence interval.
[a]*P-value represents the comparison results of the features from the three intratumoral subregions and the same features from the whole tumor area.*
The symbol ("/") represents null.

(P = 0.002), and SVM_Late model (P = 0.002) were significantly higher: 0.863 (95% CI, 0.808–0.906), 0.860 (95% CI, 0.806–0.904), 0.934 (95% CI, 0.891–0.963), and 0.921 (95% CI, 0.876–0.954), respectively. The SVM_Early model and SVM_Late model achieved better performance than the DT_Early model and DT_Late model (P = 0.003, 0.034, 0.008, and 0.026, respectively), as shown in **Table 5**. In the validation cohort, the AUCs of the DT_Whole model and SVM_Whole model were 0.670 and 0.708, respectively.

TABLE 4 | Performance of classification models for identifying benign and malignant breast tumors.

Models		Cohort	AUC	95% CI	Sensitivity	Specificity	Accuracy	*P*-value[a]
DT	Early	Training	0.863	0.808–0.906	80.0%	91.7%	79.8%	0.004
		Validation	0.839	0.747–0.908	90.0%	80.0%	77.8%	0.006
	Moderate	Training	0.777	0.715–0.832	79.2%	76.2%	76.5%	0.473
		Validation	0.718	0.613–0.808	70.0%	75.0%	74.4%	0.406
	Late	Training	0.860	0.806–0.904	80.8%	84.5%	78.5%	0.015
		Validation	0.784	0.601–0.798	82.0%	77.5%	76.7%	0.043
	Whole	Training	0.744	0.679–0.802	86.4%	67.9%	74.2%	/
		Validation	0.670	0.563–0.766	74.0%	65.0%	67.8%	/
SVM	Early	Training	0.934	0.891–0.963	89.6%	86.9%	88.5%	0.002
		Validation	0.890	0.806–0.946	84.0%	85.0%	83.3%	0.001
	Moderate	Training	0.868	0.814–0.911	81.6%	84.5%	80.4%	0.078
		Validation	0.737	0.634–0.824	80.0%	73.5%	72.2%	0.664
	Late	Training	0.921	0.876–0.954	86.4%	85.7%	84.5%	0.002
		Validation	0.865	0.777–0.928	82.0%	80.0%	80.0%	0.007
	Whole	Training	0.806	0.746–0.857	69.6%	83.3%	65.5%	/
		Validation	0.708	0.602–0.799	88.0%	67.5%	61.1%	/

AUC, area under the receiver operating characteristic curve; CI, confidence interval; DT, decision tree; SVM, support vector machine.
[a]P-value represents the comparison results of the AUC value of the same model established by features from intratumoral subregions and the whole tumor area..
The symbol ("/") represents null.

In comparison, the AUCs of the DT_Early model (P = 0.006), DT_Late model (P = 0.043), SVM_Early model (P = 0.001), and SVM_Late model (P = 0.007) were significantly higher: 0.839 (95% CI, 0.747–0.908), 0.784 (95% CI, 0.601–0.798), 0.890 (95% CI, 0.806–0.946), and 0.865 (95% CI, 0.777–0.928), respectively. The SVM_Early model and SVM_Late model achieved better performance than the DT_Early model and DT_Late model (P = 0.018, 0.047, 0.035, and 0.029, respectively), as shown in **Table 6**. However, there was no significant difference between the SVM_Early model and the SVM_Late model in the training and validation cohorts (P = 0.524 and P = 0.523, respectively), and no significant difference between the DT_Early model and the DT_Late model (P = 0.945 and P = 0.332, respectively). Fifteen texture features extracted from the early subregion and 17 features extracted from the late subregion were selected by LASSO, as listed in **Table 7**.

Interobserver Agreement Evaluation

The texture features derived from the two groups of ROIs delineated independently by two radiologists showed excellent agreement [ICCs for whole lesion region, (0.875, 0.943); ICCs for early region, (0.853, 0.936); ICCs for moderate region, (0.837, 0.928); and ICCs for late region, (0.842, 0.931)].

DISCUSSION

This study investigated the relationship between texture features extracted from intratumoral subregions of breast DCE-MRI and the differential diagnosis of benign and malignant breast tumors. Features from subregions were able to distinguish benign from

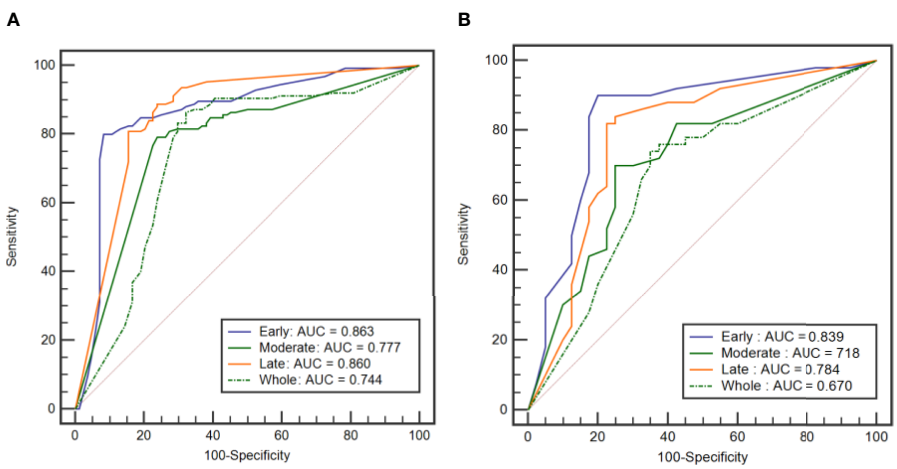

FIGURE 3 | ROC curves of the DT classification models established by using the features extracted from the three intratumoral subregions and the whole tumor area. **(A)** ROC curves from the training cohort. **(B)** ROC curve from the external validation cohort.

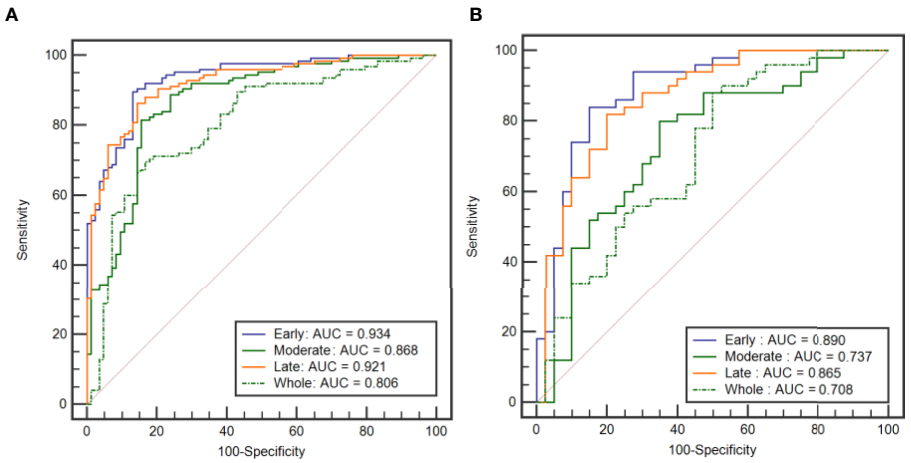

FIGURE 4 | ROC curves of the SVM classification models established by using the features extracted from the three intratumoral subregions and the whole tumor area. **(A)** ROC curves from the training cohort. **(B)** ROC curves from the external validation cohort.

TABLE 5 | *P*-values of DeLong tests between subregion models in the training cohort.

Classifier	DT_Early	DT_Moderate	DT_Late	SVM_Early	SVM_Moderate	SVM_Late
DT_Early	/	0.013	0.945	0.003	0.002	0.034
DT_Moderate	0.013	/	0.035	0.001	0.004	0.001
DT_Late	0.945	0.035	/	0.008	0.843	0.026
SVM_Early	0.003	0.001	0.008	/	0.020	0.524
SVM_Moderate	0.002	0.004	0.843	0.020	/	0.091
SVM_Late	0.034	0.001	0.026	0.524	0.091	/

DT, decision tree; SVM, support vector machine.
The symbol ("/") represents null.

TABLE 6 | *P*-values of DeLong tests between subregion models in the validation cohort.

Classifier	DT_Early	DT_Moderate	DT_Late	SVM_Early	SVM_Moderate	SVM_Late
DT_Early	/	0.068	0.332	0.018	0.111	0.047
DT_Moderate	0.068	/	0.370	0.006	0.760	0.012
DT_Late	0.332	0.370	/	0.035	0.511	0.029
SVM_Early	0.018	0.006	0.035	/	0.007	0.523
SVM_Moderate	0.111	0.760	0.511	0.007	/	0.032
SVM_Late	0.047	0.012	0.029	0.523	0.032	/

The symbol ("/") represents null.

malignant breast tumors, and features from subregions representing the early and late TTP values achieved better performance than those from the whole tumor area in the training and validation cohorts. The SVM_Early model, SVM_Moderate model, and SVM_Late model demonstrated higher performance than the DT_Early model, DT_Moderate model, and DT_Late model, respectively.

Texture analysis can characterize intratumoral heterogeneity on the basis of quantitative image features extracted from conventional medical imaging to help diagnose, stage, and predict the prognosis and response to treatment in multiple oncology fields (44–46). Intratumoral heterogeneity reflects differences in biological characteristics, such as gene expression, metabolism, and angiogenesis (23, 47). Texture features derived from intratumoral subregions that reflect the heterogeneity of breast tumors, rather than the whole tumor area, may play a more important role in the prognostic analysis and identification of hormone receptor status in breast cancer (26, 36). A previous study has shown that texture features extracted from subregions with rapid delayed washout can be used to assess ER status and lymph node classification in breast cancer (48). Chang et al. (49) have quantified intratumoral heterogeneity on breast DCE-MRI by using a subregion-based feature extraction method for predicting ER status, human epidermal growth factor receptor 2 (HER2) status, and triple-negative breast cancer, achieving accuracy of 73.53, 82.35, and 77.45%, respectively. In this study, an intratumoral subregion partition method was used to distinguish benign from malignant breast tumors. Texture

TABLE 7 | Texture features extracted from early and late subregions selected with LASSO.

Features	Benign	Malignant
Early subregion		
Mean[a]	133.642 ± 41.162	168.686 ± 42.720
Variance[a]	27.638 ± 10.281	33.551 ± 8.434
Difference square (0, 1)[b]	0.220 ± 0.104	0.991 ± 0.357
Correlation (–2, 0)[b]	0.654 ± 0.259	0.823 ± 0.0987
Information measure of correlation (0, 1)[b]	0.6131 ± 0.186	0.822 ± 0.0691
Short run emphasis (1, 0)[b]	0.897 ± 0.0944	0.622 ± 0.114
Run length non-uniformity (1, 0)[b]	560.054 ± 13.620	426.963 ± 52.547
Deubechies2_2HH[b]	7.810 ± 2.364	4.399 ± 1.231
Deubechies2_1VH[b]	9.040 ± 4.241	4.853 ± 1.680
Symlet4_1VH[b]	8.174 ± 3.807	4.359 ± 1.445
Haar_4HH[b]	3.231 ± 1.749	5.317 ± 1.992
Deubechies2_3HH[b]	4.963 ± 1.313	3.826 ± 0.831
Symlet4_4VH[b]	3.089 ± 1.469	4.938 ± 1.845
Symlet4_1DH[b]	5.212 ± 2.273	2.517 ± 0.964
Late subregion		
Mean[a]	117.859 ± 29.076	136.495 ± 29.933
Variance[a]	30.496 ± 7.022	35.016 ± 7.631
Contrast (0,1)[b]	0.384 ± 0.203	0.716 ± 0.252
Information measure of correlation (0, 1)[a]	–0.595 ± 0.099	–0.441 ± 0.0807
Information measure of correlation (–1, 0)[b]	–0.594 ± 0.0807	–0.462 ± 0.0492
Short run emphasis (1, 0)[b]	0.672 ± 0.117	0.810 ± 0.149
Haar_1HH[a]	7.709 ± 4.446	13.814 ± 4.073
Deubechies2_2VH[a]	5.455 ± 2.949	9.708 ± 2.897
Haar_2HH[a]	6.651 ± 4.085	8.691 ± 2.746
Haar_4HH[b]	5.029 ± 1.993	2.895 ± 0.978
Haar_3VH[b]	4.496 ± 1.049	5.425 ± 1.343
Haar_4DH[b]	2.048 ± 0.881	1.567 ± 0.569
Deubechies2_3VH[b]	4.640 ± 1.481	5.489 ± 1.427
Deubechies2_4VH[b]	4.287 ± 1.630	3.103 ± 1.293
Deubechies2_4DH[b]	1.292 ± 0.393	1.835 ± 0.720
Symlet4_3HH[b]	3.335 ± 1.161	4.755 ± 1.129
Symlet4_3VH[b]	3.722 ± 1.434	5.611 ± 1.262

[a]*The data are means ± SD.*
[b]*The data are medians ± interquartile range.*

features were derived from three subregions and the whole tumor area, and the corresponding classification models were established. The models built with features from the early and late subregions achieved better performance than models built with features from the whole tumor area. A possible explanation for this finding is that the intratumoral subregions reflect angiogenesis, which may be indicative of the aggressiveness of malignant breast tumors (50).

A previous study has investigated the diagnostic performance of mammography texture analysis in differentiating benign from malignant breast tumors (51). In the present study, the subtraction images of DCE-MRI were used for texture analysis. Previous studies have discussed the roles of histograms, GLCM, and GRLM-based texture features in the differential diagnosis or treatment response assessment in breast cancer (14, 44). In addition to the features used in these studies, DWT-based features were extracted in this study. DWT is used to modify the image from the spatial domain to the frequency domain and has been extensively applied to feature extraction from electroencephalogram signals (52, 53). In the present univariate analysis, the DWT-based features derived from the late subregion, including Deubechies2_2VH (P = 0.001), Haar_1HH (P = 0.001), and Haar_4HH (P < 0.001), performed better in distinguishing benign from malignant breast tumors than those derived from the whole tumor area.

Two prevalent machine learning methods, DT and SVM, were applied to establish classification models in this study. To prevent overfitting, a 10-fold cross-validation method was used. The models established with features from the early and late subregions achieved better performance than models from the whole tumor area in the training and validation cohorts. However, no significant differences were found between the performance of models from the moderate subregion and that of models from the whole tumor area in the training and validation cohorts (P = 0.473 and P = 0.078, P = 0.406 and P = 0.664, respectively). Furthermore, the SVM_Early model, SVM_Moderate model, and SVM_Late model had higher AUCs than the DT_Early model, DT_Moderate model, and DT_Late model. SVM initially maps the input vector to a higher-dimensional feature space and identifies the hyperplane that divides the data points into two categories; the resulting classifier can reliably classify new samples and achieve considerable versatility (54).

A previous study by Li et al. (55) has applied four methods to classify benign and malignant breast tumors, and reported that the DT model achieved the best performance, with an AUC of 0.781, a sensitivity of 0.6, and a specificity of 0.894. Another study has used

an SVM model for classifying benign and malignant breast tumors and obtained a sensitivity of 66.67% and a specificity of 93.55% (56). Wang et al. (20) have used logistic regression analysis to distinguish benign and malignant breast tumors, and achieved an accuracy of 79.5%, a sensitivity of 0.607, a specificity of 0.800, and an AUC of 0.802. In comparison, the best classification performance of our SVM_Early model achieved an AUC of 0.934, a sensitivity of 89.6%, a specificity of 86.9%, and an accuracy 88.5%. However, studies in which the classification model is based on deep learning methods have reported higher accuracy in distinguishing benign and malignant breast lesions (57, 58).

In addition, we separately evaluated the intraobserver variability of texture features extracted from the whole lesion region and from three different intratumoral subregions. The two radiologists showed high consistency in calculating texture features from the single-slice method, and all ICCs were greater than 0.8. The intraobserver variability was mainly related to slice selection and ROI delineation. Hence, standardized strategies for ROI determination are crucial.

This study has some limitations. First, the sample size was relatively small. Second, only a representative single-slice image was analyzed, and thus some useful information on the tumor might have been missed. Texture analysis based on three-dimensional breast tumor lesions may yield more useful information (59). Finally, the subtraction images of breast DCE-MRI were used to extract texture features. Features derived from post-contrast images or diffusion weighted imaging images may be helpful in distinguishing benign from malignant breast tumors (60).

CONCLUSION

The texture features extracted from intratumoral subregions of breast DCE-MRI can be used as imaging biomarkers for the differential diagnosis of benign from malignant breast tumors. Specifically, features derived from subregions representing the early and late TTP values achieved better performance than features from the whole tumor area. Further research with a larger sample size is needed to verify the results of this study.

DATA AVAILABILITY STATEMENT

The original contributions presented in the study are included in the article/supplementary material. Further inquiries can be directed to the corresponding author.

ETHICS STATEMENT

The studies involving human participants were reviewed and approved by Shengjing Hospital of China Medical University. Written informed consent for participation was not required for this study in accordance with the national legislation and the institutional requirements. Written informed consent was not obtained from the individual(s) for the publication of any potentially identifiable images or data included in this article.

AUTHOR CONTRIBUTIONS

Methodology, JY. Validation, LS. Investigation, BZ. Writing—original draft preparation, LS. Writing—review and editing, JY. Supervision, JY. Project administration, JY. Funding acquisition, JY. All authors contributed to the article and approved the submitted version.

FUNDING

This research was supported by grants from the Research and Development (R&D) Foundation for Major Science and Technology from Shenyang (No. 19-112-4-105), the Big Data Foundation for Health Care from China Medical University (No. HMB201902105), the Natural Fund Guidance Plan from Liaoning (No. 2019-ZD-0743), and the 345 Talent Project from Shengjing Hospital of China Medical University.

REFERENCES

1. Siegel RL, Miller KD, Jemal A. Cancer Statistics, 2020. *CA Cancer J Clin* (2020) 70(1):7–30. doi: 10.3322/caac.21590
2. Bayo J, Castaño MA, Rivera F, Navarro F. Analysis of Blood Markers for Early Breast Cancer Diagnosis. *Clin Transl Oncol* (2018) 20(4):467–75. doi: 10.1007/s12094-017-1731-1
3. Kunkler IH, Williams LJ, Jack WJ, Cameron DA, Dixon JM. Breast-Conserving Surgery With or Without Irradiation in Women Aged 65 Years or Older With Early Breast Cancer (PRIME II): A Randomised Controlled Trial. *Lancet Oncol* (2015) 16(3):266–73. doi: 10.1016/S1470-2045(14)71221-5
4. Lu Y, Chen Y, Zhu L, Cartwright P, Song E, Jacobs L, et al. Local Recurrence of Benign, Borderline, and Malignant Phyllodes Tumors of the Breast: A Systematic Review and Meta-Analysis. *Ann Surg Oncol* (2019) 26(5):1263–75. doi: 10.1245/s10434-018-07134-5
5. Grubstein A, Rapson Y, Stemmer SM, Allweis T, Wolff-Bar M, Borshtein S, et al. Timing to Imaging and Surgery After Neoadjuvant Therapy for Breast Cancer. *Clin Imaging* (2021) 71:24–8. doi: 10.1016/j.clinimag.2020.10.043
6. Heil J, Kuerer HM, Pfob A, Rauch G, Sinn HP, Golatta M, et al. Eliminating the Breast Cancer Surgery Paradigm After Neoadjuvant Systemic Therapy: Current Evidence and Future Challenges. *Ann Oncol* (2020) 31(1):61–71. doi: 10.1016/j.annonc.2019.10.012
7. Shien T, Iwata H. Adjuvant and Neoadjuvant Therapy for Breast Cancer. *Jpn J Clin Oncol* (2020) 50(3):225–9. doi: 10.1093/jjco/hyz213
8. Si L, Zhai R, Liu X, Yang K, Wang L, Jiang T. MRI in the Differential Diagnosis of Primary Architectural Distortion Detected by Mammography. *Diagn Interv Radiol* (2016) 22(2):141–50. doi: 10.5152/dir.2016.15017
9. Gubern-Mérida A, Vreemann S, Martí R, Melendez J, Lardenoije S, Mann RM, et al. Automated Detection of Breast Cancer in False-Negative Screening MRI Studies From Women at Increased Risk. *Eur J Radiol* (2016) 85(2):472–9. doi: 10.1016/j.ejrad.2015.11.031
10. Liu Z, Feng B, Li C, Chen Y, Chen Q, Li X, et al. Preoperative Prediction of Lymphovascular Invasion in Invasive Breast Cancer With Dynamic Contrast-Enhanced-MRI-Based Radiomics. *J Magn Reson Imaging* (2019) 50(3):847–57. doi: 10.1002/jmri.26688

11. Wang CH, Yin FF, Horton J, Chang Z. Review of Treatment Assessment Using DCE-MRI in Breast Cancer Radiation Therapy. *World J Methodol* (2014) 4(2):46–58. doi: 10.5662/wjm.v4.i2.46
12. Dalmış MU, Gubern-Mérida A, Vreemann S, Karssemeijer N, Mann R, Platel B. A Computer-Aided Diagnosis System for Breast DCE-MRI at High Spatiotemporal Resolution. *Med Phys* (2016) 43(1):84. doi: 10.1118/1.4937787
13. Pinker K, Helbich TH, Morris EA. The Potential of Multiparametric MRI of the Breast. *Br J Radiol* (2017) 90(1069):20160715. doi: 10.1259/bjr.20160715
14. Zhou J, Zhang Y, Chang KT, Lee KE, Wang O, Li J, et al. Diagnosis of Benign and Malignant Breast Lesions on DCE-MRI by Using Radiomics and Deep Learning With Consideration of Peritumor Tissue. *J Magn Reson Imaging* (2020) 51(3):798–809. doi: 10.1002/jmri.26981
15. Aker M, Ganeshan B, Afaq A, Wan S, Groves AM, Arulampalam T. Magnetic Resonance Texture Analysis in Identifying Complete Pathological Response to Neoadjuvant Treatment in Locally Advanced Rectal Cance. *Dis Colon Rectum* (2019) 62(2):163–70. doi: 10.1097/DCR.0000000000001224
16. Castellano G, Bonilha L, Li LM, Cendes F. Texture Analysis of Medical Images. *Clin Radiol* (2004) 59(12):1061–9. doi: 10.1016/j.crad.2004.07.008
17. Scalco E, Rizzo G. Texture Analysis of Medical Images for Radiotherapy Applications. *Br J Radiol* (2017) 90(1070):20160642. doi: 10.1259/bjr.20160642
18. Alobaidli S, McQuaid S, South C, Prakash V, Evans P, Nisbet A. The Role of Texture Analysis in Imaging as an Outcome Predictor and Potential Tool in Radiotherapy Treatment Planning. *Br J Radiol* (2014) 87(1042):20140369. doi: 10.1259/bjr.20140369
19. Mai H, Mao Y, Dong T, Tan Y, Huang X, Wu S, et al. The Utility of Texture Analysis Based on Breast Magnetic Resonance Imaging in Differentiating Phyllodes Tumors From Fibroadenomas. *Front Oncol* (2019) 9:1021. doi: 10.3389/fonc.2019.01021
20. Wang BT, Fan WP, Xu H, Li LH, Zhang XH, Wang K, et al. Value of Magnetic Resonance Imaging Texture Analysis in the Differential Diagnosis of Benign and Malignant Breast Tumors. *Chin Med Sci J* (2019) 34(1):33–7. doi: 10.24920/003516
21. Fan M, Zhang P, Wang Y, Peng W, Wang S, Gao X, et al. Radiomic Analysis of Imaging Heterogeneity in Tumours and the Surrounding Parenchyma Based on Unsupervised Decomposition of DCE-MRI for Predicting Molecular Subtypes of Breast Cancer. *Eur Radiol* (2019) 29(8):4456–67. doi: 10.1007/s00330-018-5891-3
22. Carvalho ED, Filho AOC, Silva RRV, Araújo FHD, Diniz JOB, Silva AC, et al. Breast Cancer Diagnosis From Histopathological Images Using Textural Features and CBI. *Artif Intell Med* (2020) 105:101845. doi: 10.1016/j.artmed.2020.101845
23. Marusyk A, Polyak K. Tumor Heterogeneity: Causes and Consequences. *Biochim Biophys Acta* (2010) 1805(1):105–17. doi: 10.1016/j.bbcan.2009.11.002
24. Kavya N, Sriraam N, Usha N, Bharathi H, Anusha S, Sharath D, et al. Breast Cancer Lesion Detection From Cranial-Caudal View of Mammogram Images Using Statistical and Texture Features Extractio. *Int J Biomed Clin Eng (IJBCE)* (2020) 9(1):16–32. doi: 10.4018/IJBCE.2020010102
25. Fujiwara T, Urata Y, Tanaka N. Telomerase-Specific Oncolytic Virotherapy for Human Cancer With the hTERT Promoter. *Curr Cancer Drug Targets* (2007) 7(2):191–201. doi: 10.2174/156800907780058835
26. Fan M, Cheng H, Zhang P, Gao X, Zhang J, Shao G, et al. DCE-MRI Texture Analysis With Tumor Subregion Partitioning for Predicting Ki-67 Status of Estrogen Receptor-Positive Breast Cancers. *J Magn Reson Imaging* (2018) 48(1):237–47. doi: 10.1002/jmri.25921
27. Wang TC, Huang YH, Huang CS, Chen JH, Huang GY, Chang RF. Computer-Aided Diagnosis of Breast DCE-MRI Using Pharmacokinetic Model and 3-D Morphology Analysis. *Magn Reson Imaging* (2014) 32(3):197–205. doi: 10.1016/j.mri.2013.12.002
28. Ren H, Zhou L, Liu G, Peng X, Shi W, Xu H, et al. An Unsupervised Semi-Automated Pulmonary Nodule Segmentation Method Based on Enhanced Region Growing. *Quant Imaging Med Surg* (2020) 10(1):233–42. doi: 10.21037/qims.2019.12.02
29. Liney GP, Gibbs P, Hayes C, Leach MO, Turnbull LW. Dynamic Contrast-Enhanced MRI in the Differentiation of Breast Tumors: User-Defined Versus Semi-Automated Region-of-Interest Analysis. *J Magn Reson Imaging* (1999) 10(6):945–9. doi: 10.1002/(sici)1522-2586(199912)10:6<945::aid-jmri6>3.0.co;2-i
30. Collewet G, Strzelecki M, Mariette F. Influence of MRI Acquisition Protocols and Image Intensity Normalization Methods on Texture Classification. *Magn Reson Imaging* (2004) 22:81–91. doi: 10.1016/j.mri.2003.09.001
31. Wang H, Nie P, Wang Y, Xu W, Duan S, Chen H, et al. Radiomics Nomogram for Differentiating Between Benign and Malignant Soft-Tissue Masses of the Extremities. *J Magn Reson Imaging* (2020) 51:155–63. doi: 10.1002/jmri.26818
32. Gibbs P, Turnbull LW. Textural Analysis of Contrast-Enhanced MR Images of the Breast. *Magn Reson Med* (2003) 50:92–8. doi: 10.1002/mrm.10496
33. Wang C, Pedrycz W, Yang J, Zhou M, Li Z. Wavelet Frame-Based Fuzzy C-Means Clustering for Segmenting Images on Graph. *IEEE Trans Cybern* (2020) 50(9):3938–49. doi: 10.1109/TCYB.2019.2921779
34. Boudraa AE, Champier J, Cinotti L, Bordet JC, Lavenne F, Mallet JJ. Delineation and Quantitation of Brain Lesions by Fuzzy Clustering in Positron Emission Tomography. *Comput Med Imaging Graph* (1996) 20(1):31–41. doi: 10.1016/0895-6111(96)00025-0
35. Khan SU, Ullah I, Ahmed I, Imran A, Ullah N. A Spatial Fuzzy C-Means Algorithm for Segmentation of Brain MRI Images. *J X-ray Sci Technol* (2019) 27(6):1087–99. doi: 10.3233/XST-190547
36. Ashraf A, Gaonkar B, Mies C, DeMichele A, Rosen M, Davatzikos C, et al. Breast DCE-MRI Kinetic Heterogeneity Tumor Markers: Preliminary Associations With Neoadjuvant Chemotherapy Response. *Transl Oncol* (2015) 8(3):154–62. doi: 10.1016/j.tranon.2015.03.005
37. Gu J, Polley EC, Denis M, Carter JM, Pruthi S, Gregory AV, et al. Early Assessment of Shear Wave Elastography Parameters Foresees the Response to Neoadjuvant Chemotherapy in Patients With Invasive Breast Cancer. *Breast Cancer Res* (2021) 23(1):52. doi: 10.1186/s13058-021-01429-4
38. Hylton N. MR Imaging for Assessment of Breast Cancer Response to Neoadjuvant Chemotherapy. *Magn Reson Imaging Clin N Am* (2006) 14(3):383–9, vii. doi: 10.1016/j.mric.2006.09.001
39. Lee SH, Kim JH, Cho N, Park JS, Yang Z, Jung YS, et al. Multilevel Analysis of Spatiotemporal Association Features for Differentiation of Tumor Enhancement Patterns in Breast DCE-MR. *Med Phys* (2010) 37(8):3940–56. doi: 10.1118/1.3446799
40. Yamada M, Jitkrittum W, Sigal L, Xing EP, Sugiyama M. High-Dimensional Feature Selection by Feature-Wise Kernelized Lass. *Neural Comput* (2014) 26(1):185–207. doi: 10.1162/NECO_a_00537
41. Field A. Discovering Statistics Using IBM SPSS Statistics.4th ed. New Delhi: Sage Publications Ltd (2013).
42. Liu L, Liu Y, Xu L, Li Z, Lv H, Dong N, et al. Application of Texture Analysis Based on Apparent Diffusion Coefficient Maps in Discriminating Different Stages of Rectal Cancer. *J Magn Reson Imaging* (2017) 45:1798–808. doi: 10.1002/jmri.25460
43. Yang L, Liu D, Fang X, Wang Z, Xing Y, Ma L, et al. Rectal Cancer: Can T2WI Histogram of the Primary Tumor Help Predict the Existence of Lymph Node Metastasis? *Eur Radiol* (2019) 29:6469–76. doi: 10.1007/s00330-019-06328-z
44. Ahmed A, Gibbs P, Pickles M, Turnbull L. Texture Analysis in Assessment and Prediction of Chemotherapy Response in Breast Cancer. *J Magn Reson Imaging* (2013) 38(1):89–101. doi: 10.1002/jmri.23971
45. Guan Y, Li W, Jiang Z, Chen Y, Liu S, He J, et al. Whole-Lesion Apparent Diffusion Coefficient-Based Entropy-Related Parameters for Characterizing Cervical Cancers: Initial Findings. *Acad Radiol* (2016) 23(12):1559–67. doi: 10.1016/j.acra.2016.08.010
46. Ryu YJ, Choi SH, Park SJ, Yun TJ, Kim JH, Sohn CH. Glioma: Application of Whole-Tumor Texture Analysis of Diffusion-Weighted Imaging for the Evaluation of Tumor Heterogeneity. *PloS One* (2014) 9(9):e108335. doi: 10.1371/journal.pone.0108335
47. Bedard PL, Hansen AR, Ratain MJ, Siu LL. Tumour Heterogeneity in the Clinic. *Nature* (2013) 501(7467):355–64. doi: 10.1038/nature12627
48. Chaudhury B, Zhou M, Goldgof DB, Hall LO, Gatenby RA, Gillies RJ, et al. Heterogeneity in Intratumoral Regions With Rapid Gadolinium Washout Correlates With Estrogen Receptor Status and Nodal Metastasis. *J Magn Reson Imaging* (2015) 42(5):1421–30. doi: 10.1002/jmri.24921
49. Chang RF, Chen HH, Chang YC, Huang CS, Chen JH, Lo CM. Quantification of Breast Tumor Heterogeneity for ER Status, HER2 Status, and TN Molecular Subtype Evaluation on DCE-MR. *Magn Reson Imaging* (2016) 34(6):809–19. doi: 10.1016/j.mri.2016.03.001
50. Li L, Wang K, Sun X, Wang K, Sun Y, Zhang G, et al. Parameters of Dynamic Contrast-Enhanced MRI as Imaging Markers for Angiogenesis and Proliferation in Human Breast Cancer. *Med Sci Monit* (2015) 21:376–82. doi: 10.12659/MSM.892534

51. Li Z, Yu L, Wang X, Yu H, Gao Y, Ren Y, et al. Diagnostic Performance of Mammographic Texture Analysis in the Differential Diagnosis of Benign and Malignant Breast Tumors. *Clin Breast Cancer* (2018) 18(4):e621–7. doi: 10.1016/j.clbc.2017.11.004
52. Ashraf R, Ahmed M, Jabbar S, Khalid S, Ahmad A, Din S, et al. Content Based Image Retrieval by Using Color Descriptor and Discrete Wavelet Transform. *J Med Syst* (2018) 42(3):44. doi: 10.1007/s10916-017-0880-7
53. Al-Fahoum AS, Al-Fraihat AA. Methods of EEG Signal Features Extraction Using Linear Analysis in Frequency and Time-Frequency Domains. *ISRN Neurosci* (2014) 2014:730218. doi: 10.1155/2014/730218
54. Kourou K, Exarchos TP, Exarchos KP, Karamouzis MV, Fotiadis DI. Machine Learning Applications in Cancer Prognosis and Prediction. *Comput Struct Biotechnol J* (2014) 13:8–17. doi: 10.1016/j.csbj.2014.11.005
55. Li K, Wang Q, Lu Y, Pan X, Liu L, Cheng S, et al. Machine Learning Based Tissue Analysis Reveals Brachyury has a Diagnosis Value in Breast Cancer. *Biosci Rep* (2021) 41(4):BSR20203391. doi: 10.1042/BSR20203391
56. Liu Y, Ren Li, Cao X, Tong Y. Breast Tumors Recognition Based on Edge Feature Extraction Using Support Vector Machine. *Biomed Biomed Signal Process Control [Preprint]* (2020) 58. doi: 10.1016/j.bspc.2019.101825
57. Krithiga R, Geetha P. Deep Learning Based Breast Cancer Detection and Classification Using Fuzzy Merging Techniques. *Mach Vision Appl* (2020) 31 (7):1–18. doi: 10.1007/s00138-020-01122-0
58. Aslam MA, Aslam, Daxiang C. Breast Cancer Classification Using Deep Convolutional Neural Networ. *J Phys: Conf Ser* (2020) 1584(1):012005–. doi: 10.1088/1742-6596/1584/1/012005
59. Zhou J, Luo LY, Dou Q, Chen H, Chen C, Li GJ, et al. Weakly Supervised 3D Deep Learning for Breast Cancer Classification and Localization of the Lesions in MR Images. *J Magn Reson Imaging* (2019) 50(4):1144–51. doi: 10.1002/jmri.26721
60. Mao N, Wang Q, Liu M, Dong J, Xiao C, Sun N, et al. Computerized Image Analysis to Differentiate Benign and Malignant Breast Tumors on Magnetic Resonance Diffusion Weighted Image: A Preliminary Study. *J Comput Assist Tomogr* (2019) 43(1):93–7. doi: 10.1097/RCT.0000000000000793

Conflict of Interest: The authors declare that the research was conducted in the absence of any commercial or financial relationships that could be construed as a potential conflict of interest.

frontiers in Oncology

REVIEW
published: 22 July 2021
doi: 10.3389/fonc.2021.600557

Artificial Intelligence in Medical Imaging of the Breast

Yu-Meng Lei[1], Miao Yin[1], Mei-Hui Yu[1], Jing Yu[1], Shu-E Zeng[2], Wen-Zhi Lv[3], Jun Li[4], Hua-Rong Ye[1], Xin-Wu Cui[5]* and Christoph F. Dietrich[6]*

[1] Department of Medical Ultrasound, China Resources & Wisco General Hospital, Academic Teaching Hospital of Wuhan University of Science and Technology, Wuhan, China, [2] Department of Medical Ultrasound, Hubei Cancer Hospital, Tongji Medical College, Huazhong University of Science and Technology, Wuhan, China, [3] Department of Artificial Intelligence, Julei Technology, Wuhan, China, [4] Department of Medical Ultrasound, The First Affiliated Hospital of Medical College, Shihezi University, Xinjiang, China, [5] Department of Medical Ultrasound, Tongji Hospital, Tongji Medical College, Huazhong University of Science and Technology, Wuhan, China, [6] Department Allgemeine Innere Medizin (DAIM), Kliniken Beau Site, Salem und Permanence, Bern, Switzerland

Artificial intelligence (AI) has invaded our daily lives, and in the last decade, there have been very promising applications of AI in the field of medicine, including medical imaging, *in vitro* diagnosis, intelligent rehabilitation, and prognosis. Breast cancer is one of the common malignant tumors in women and seriously threatens women's physical and mental health. Early screening for breast cancer *via* mammography, ultrasound and magnetic resonance imaging (MRI) can significantly improve the prognosis of patients. AI has shown excellent performance in image recognition tasks and has been widely studied in breast cancer screening. This paper introduces the background of AI and its application in breast medical imaging (mammography, ultrasound and MRI), such as in the identification, segmentation and classification of lesions; breast density assessment; and breast cancer risk assessment. In addition, we also discuss the challenges and future perspectives of the application of AI in medical imaging of the breast.

Keywords: artificial intelligence, machine learning, deep learning, breast, imaging

OPEN ACCESS

Edited by:
Emanuele Neri,
University of Pisa, Italy

Reviewed by:
Alberto Stefano Tagliafico,
University of Genoa, Italy
Subathra Adithan,
Jawaharlal Institute of Postgraduate Medical Education and Research (JIPMER), India

****Correspondence:***
Hua-Rong Ye
yehuarong@hotmail.com
Xin-Wu Cui
cuixinwu@live.cn

Specialty section:
This article was submitted to Cancer Imaging and Image-directed Interventions, a section of the journal Frontiers in Oncology

Received: *30 August 2020*
Accepted: *07 July 2021*
Published: *22 July 2021*

Citation:
Lei Y-M, Yin M, Yu M-H, Yu J, Zeng S-E, Lv W-Z, Li J, Ye H-R, Cui X-W and Dietrich CF (2021) Artificial Intelligence in Medical Imaging of the Breast. Front. Oncol. 11:600557. doi: 10.3389/fonc.2021.600557

INTRODUCTION

Artificial intelligence (AI) is commonly defined as "a system's ability to correctly interpret external data, to learn from such data, and to use those learnings to achieve specific goals and tasks through flexible adaptation". Over the past 50 years, the dramatic growth of computer functions related to big data intrusion has pushed AI applications into new areas (1). Currently, AI can be found in voice recognition, face recognition, driverless cars and other new technologies, and the application of AI in medical imaging has gradually become an important topic of research. AI algorithms, particularly deep learning (DL) algorithms, have demonstrated remarkable progress in image recognition tasks. Methods ranging from convolutional neural networks to variational autoencoders have been found in a myriad applications in the medical image analysis field and have promoted the rapid development of medical imaging (2). AI has made great contributions to early detection, disease evaluation and treatment response assessments in the field of medical image analysis for diseases such as pancreatic cancer (3), liver disease (4), breast cancer (5), chest disease (6), and neurological tumors (7).

Approximately 2.1 million newly diagnosed cases of breast cancer occurred in 2018 worldwide, accounting for almost 1 in 4 of all cases of cancer among women (8). Breast cancer is the most frequently diagnosed cancer in most countries (154 of 185) and is the leading cause of death due to cancer in over 100 countries (9). Breast cancer has a marked impact on women's physical and mental health, which seriously threatens women's lives and health. The early screening and treatment of breast diseases have become major health problems in the world. The correct diagnosis, especially the early detection and treatment of breast cancer, has a decisive impact on the prognosis. The clinical cure rate of early breast cancer can reach more than 90%; in the middle stage, it is 50 - 70%, and in the late stage, the treatment effect is very poor. Currently, Mammography, ultrasound and MRI are invaluable screening and supplemental diagnostic tool for breast cancer, they also have become important means of detection, staging and efficacy evaluations and follow-up examinations of breast cancer (10).

At present, breast images are mainly read, analyzed and diagnosed by radiologists. Under a large and long-term workload, radiologists are more likely to misjudge images due to fatigue, resulting in a misdiagnosis or missed diagnosis, which can be avoided with AI. To avoid human errors, computer-aided diagnosis (CAD) has been implemented. In CAD systems, a suitable algorithm completes the processing and analysis of an image (11). The latest breakthrough is DL, especially convolutional neural networks (CNNs), which has made significant progress in the field of medical imaging (12). This article briefly introduces the background of AI and mainly reviews its application in breast mammography, ultrasound and MRI image analysis. This paper also discusses the prospects for the application of AI in medical imaging.

BRIEF OVERVIEW OF AI

AI refers to the ability of application machines to imitate humans or human brain functions to learn and solve problems (13). It has been more than 60 years since John McCarthy put forward the concept of AI in 1956. Over the past ten years, AI technology has made explosive progress. As a branch of computer science, it attempts to produce a new kind of intelligent machine that responds like a human brain; its application field is very wide and includes robots, image recognition, language recognition, natural language processing, data mining, pattern recognition and expert system, etc. (14, 15). In the medical field, AI can be applied to health management, clinical decision support, medical imaging, disease screening and early disease prediction, medical records/literature analysis, and hospital management, etc. AI can analyze medical images and information for disease screening and prediction and assist doctors in making diagnosis. In breast imaging, Al-antari MA et al. studied a complete integrated CAD system that can be used for detection, segmentation, and classification of masses in mammography in 2018, and its accuracy was more than 92% in all aspects (16). Alejandro Rodriguez-Ruiz et al. gathered 2654 exams and readings by 101 radiologists, using a trained AI system to score the possibility of cancer between 1 and 10, they found that using an AI score of 2 as the threshold could reduce the workload by 17%, which proved that the AI automatic preselection can significantly reduce the workload of radiologists (17).

Machine learning (ML) is one of the most important ways to realize AI. ML is divided into unsupervised and supervised. Unsupervised ML classifies the radiomics features without using any information provided by or determined by an available historical set of imaging data of the same kind of the one under investigation. Supervised ML methods are first trained by means of an available data archive, i.e. all parameters in the algorithm are tuned until the method provides an optimal trade-off between its ability to fit the training set and its generalization power when a new data example arrives. In the world of supervised ML, sparsity-enhancing regularization networks are able to make the prediction while, at the same time, identifying the extracted features that mostly impact such prediction (18). ML indicates those computational algorithms that utilize as input the image features extracted by radiomics in order to provide as output predictions concerning disease outcomes on follow-up, such as linear regression, K-means, decision trees, random forest, PCA (principal component analysis), SVM (support vector machine), and ANNs (artificial neural networks).

DL, one of the AI systems based on neural networks, is structured by building models that imitate the human brain and is currently considered to be the latest technology for image classification. Neural networks first simulate nerve cells and then try to simulate the human brain using a simulation model called a perceptron. A neural network consists of continuous layers, including the input layer, the hidden layer, and the output layer. The input layer can process multi-dimensional data, and the hidden layer includes a convolutional layer, pooling layer and fully connected layer. The feature map created in the convolutional layer is initially passed through a non-linear activation function, and this is then transferred to the pooling layer to enable down-sampling of the feature map. The output is then passed into the fully connected layer to classify the overall outcome, and the output layer directly outputs data analysis results. A multilayer perceptron is constructed by making and arranging layers with perceptrons in which all nodes in the model are fully connected together, thus solving more complex problems (19). The learning paradigm of CNNs also involves supervised learning and unsupervised learning; supervised learning refers to the training procedure in which the observed training data and the associated ground truth labels for that data (or sometimes referred to as "targets") are both required for training the model. In contrast, unsupervised learning involves training data that has no diagnosis or normal/abnormal labels. Currently, supervised learning seems to be the most popular approach in image classification tasks (20).

APPLICATIONS OF AI IN MAMMOGRAPHY

Mammography is one of the most widely used methods for breast cancer screening (21, 22). Mammography is a non-invasive detection method associated with relatively decreased

pain, easy operation, high resolution, and good repeatability. The retained image can be compared before and after and is not limited by age or body shape. Mammography can detect breast masses that cannot be palpated by doctors and can reliably identify benign lesions and malignant tumors of the breast. Mammograms are currently acquired with full-field digital mammography (DM) systems and are provided in both for-processing (the raw imaging data) and for-presentation (a postprocessed version of the raw data) image formats (23, 24). To date, AI has been used to analyze mammography images in most studies mainly for the detection and classification of breast mass and microcalcifications, breast mass segmentation, breast density assessment, breast cancer risk assessment and image quality improvement.

Detection and Classification of Breast Masses

Among the different abnormalities seen on mammograms, masses are one of the most common symptoms of breast cancer. It is difficult to detect and diagnose masses because of variation in the shape, size, and margins, especially in the presence of dense breasts. Therefore, mass detection is an essential step in CAD. Some studies proposed a Crow search optimization based intuitionistic fuzzy clustering approach with neighborhood attraction (CrSA-IFCM-NA), and it has been proven that CrSA-IFCM-NA effectively separated the masses from mammogram images and had good results in terms of cluster validity indices, indicating the clear segmentation of the regions (24). Others developed a complete integrated CAD system, which included a regional DL approach You-Only-Look-Once (YOLO) and a new deep network model full resolution convolutional network (FrCN) and a deep CNN, to detect, segment, and classify masses in mammograms and used the INbreast dataset to verify that quality detection accuracy reached 98.96%, effectively assisting radiologists make an accurate diagnosis (16, 25, 26).

Detection and Classification of Microcalcifications

Breast calcifications are small spots of calcium salts in the breast tissue, and they appear as small white spots on mammography. There are two different types of calcifications: microcalcifications and macrocalcifications. Macrocalcifications are large and coarse and are mostly benign and age-related. Microcalcifications may be early signs of breast cancer, with sizes ranging from 0.1 mm to 1 mm, with or without visible masses (27). At present, several CAD systems have been developed to detect calcifications in mammography images. Cai H et al. developed a CNN model for the detection, analysis and classification of microcalcifications in mammography images and confirmed that the function of CNN model to extract images outperformed handcrafted features; they achieved a classification precision of 89.32% and a sensitivity of 86.89% by using filtered deep features that are fully utilized by the proposed CNN structure for traditional descriptors (28). Zobia Suhail et al. developed a novel method for the classification of benign and malignant microcalcifications using an improved Fisher linear discriminant analysis approach for the linear transformation of segmented microcalcification data in combination with a SVM variant to distinguish between the two classes; 288 region of interests (ROIs) (139 malignant and 149 benign) in the Digital Database for Screening Mammography (DDSM) were classified with an average accuracy of 96% (29). Jian W et al. developed a CAD system to detect breast microcalcifications based on dual-tree complex wavelet transform (DT-CWT) (30). To detect microcalcification in mammograms, Guo Y et al. proposed a new hybrid method *via* combining contourlet transform and non-linking simplified pulse-coupled neural network (31). An automatic neural network can automatically detect, segment and classify masses and microcalcifications in mammography, providing a reference for radiologists and significantly improving the work efficiency and accuracy of radiologists.

Breast Mass Segmentation

The true segmentation of masses is directly related to the effective treatment of the patient. Some researchers used the method of fuzzy contours to automatically segment breast masses from mammograms and evaluated the ROIs extracted from the mini-MIAS database. The results showed that the average true positive rate was 91.12%, and the precision was 88.08% (32). Global segmentation of masses on mammograms is a complex process due to low-contrast mammogram images, irregular shapes of masses, spiculated margins, and the presence of intensity variations in pixels. Some used the mesh-free based radial basis function collocation approach for the evolution of a level set function for segmentation of the breast as well as suspicious mass regions. Then, an SVM classifier was used to classify the suspicious areas into abnormal and normal areas. The results showed that the sensitivity and specificity for the DDSM dataset were 97.12% and 92.43% respectively (33). Plane fitting and dynamic programming were applied to detect and classify breast mass in mammography, the accuracy of segmentation of breast lesions got improved greatly (34). The correct segmentation of breast lesions provides a guarantee for accurate disease classification and diagnosis (35). The use of an automatic image segmentation algorithm shows the application and potential of DL in precision medical systems.

Breast Density Assessment

Breast density is a strong risk factor for breast cancer and is usually evaluated by two-dimensional (2D) mammograms. Women with higher breast density have a two- to six-fold higher risk of developing breast cancer than women with low breast density (36). Mammographic density has traditionally been assessed as the absolute or relative amount (as percentage of the total breast size) occupied by dense tissue, which appears on a mammographic images as white "cotton-like" patches (37). In the current context of breast density identification, accurate and consistent breast density assessment is highly desirable to provide clinicians and patients with more informed clinical decision-making support. Many studies have shown that AI technology can assist in the evaluation of mammographic breast density (BD). Mohamed AA et al. studied a CNN model based on the Breast Imaging Reporting and Data System

(BI-RADS) for BD categorization and classified the density of large (i.e., 22000 images) DM datasets (i.e., "scattered density" and "heterogeneous density"); they showed that with an increase in training samples could achieve the highest the area under the receiver operating characteristic curve (AUC) of 0.94-0.98 (38). They also used a CNN model to show that radiologists mostly used a medial oblique (MLO) view rather than a head-to-tail (CC) view to determine the category of BD (39). Le Boulc'h M and others evaluated the agreement between DenSeeMammo (an AI-based automatic BD assessment software approved by the Food and Drugs Administration) and visual assessment by a senior and a junior radiologist, and found that the BD assessment between the senior radiologist and the AI model was basically the same on DM (weighted=0.79; 95%CI:0.73-0.84) (40). Lehman CD et al. developed and tested a DL model to assess BD by using 58 894 randomly selected digital mammograms, and implemented the model by using a deep CNN, ResNet-18, with PyTorch. And it is concluded that the agreement between density assessments with the DL model and those of the original interpreting radiologist was good (k = 0.67; 95% CI: 0.66, 0.68), and in the four-way BI-RADS categorization, 9729 of 10763 (90%; 95% CI: 90%, 91%) DL assessments were accepted by the interpreting radiologist (41). The assessment of MBD by AI can reduce the variation between radiologists, better predict the risk of breast cancer and provide a basis for further detection and treatment.

Breast Cancer Risk Assessment

The high incidence and mortality of breast cancer are seriously threatening women's physical and mental health. At present, there are many known risk factors for breast cancer, as Sun YS et al. concluded in 2017, aging, family history, reproductive factors (early menarche, late menopause, late age at first pregnancy and low parity), estrogen (endogenous and exogenous estrogens), lifestyle (excessive alcohol consumption, too much dietary fat intake, smoking) are all risk factors for breast cancer (42), the early detection and prevention of breast cancer can be promoted by increasing the overall understanding and recognition of breast cancer risk.

Relevant literature shows that the research of AI in breast cancer risk prediction is also very extensive. Nindrea RD et al. conducted a systematic review of the published ML algorithms for breast cancer risk prediction between January 2000 and May 2018, summarized and compared five ML algorithms including SVM, ANN, decision tree (DT), naive Bayes, and K-nearest neighbor (KNN) algorithms, and confirmed that the SVM algorithm was able to calculate breast cancer risk with better accuracy than other ML algorithms (43). Some studies have shown that the mammography results, risk factors, and clinical findings were analyzed and learned through an ANN combined with cytopathological diagnosis to evaluate the risk of breast cancer for doctors to estimate the probability of malignancy and improve the positive predictive value (PPV) of the decision to perform biopsy (44). Yala A and his team also developed a hybrid DL model that operates on both the full-field mammogram and traditional risk factors, and found that it was more accurate than a current clinical standard, i.e. the Tyrer-Cusick model (45). As a result, AI predicts breast cancer risk with higher accuracy than other methods, which in turn helps physicians guide high-risk populations to conduct appropriate interventions to reduce the incidence of breast cancer.

Image Quality Improvement

Good image quality is the basis of accurate diagnoses of diseases. Image quality has a significant impact on the diagnosis rate and accuracy rate of AI for assessing breast diseases on mammography, and clear images are conducive to the detection and diagnosis of microscopic lesions. Computer algorithms for improving image quality have been proposed one after another. Because it provides more details on the data phase, directionality and shift invariance, multi-scale shearlet transform can yield multi-resolution results, which is helpful to detect cancer cells, particularly those with small contours. Shenbagavalli P and his colleagues enhanced mammogram image quality by using a shearlet transform image enhancement method and classified the DDSM database as benign and malignant with an accuracy of up to 93.45% (11). Teare P et al. used a novel form of a false color enhancement method to optimize the characteristics of mammography through contrast-limited adaptive histogram equalization (CLAHE) and utilized dual deep CNNs at different scales for classification of mammogram images and derivative patches combined with a random forest gating network, they achieved a sensitivity of 0.91 and a specificity of 0.80 (46). Image quality is the premise of an accurate diagnosis, therefore, strict image quality evaluation and improvement measures must be carried out to effectively assist radiologists and ANN systems for further analysis and diagnosis (**Table 1**).

APPLICATIONS OF AI IN BREAST ULTRASOUND

As a diagnostic method with a high utilization rate, ultrasound has many advantages, such as simple operation, no radiation, and real-time operation. Therefore, ultrasound imaging has gradually become a common imaging method for the detection and diagnosis of breast cancer. To avoid a missed diagnosis or misdiagnosis caused by lack of physician experience or subjective influence and to achieve the quantification and standardization of ultrasound diagnosis, an AI system was developed to detect and diagnose breast lesions in ultrasound images (47). Related studies (48, 49) have shown that the AI systems are mainly used for the identification and segmentation of ROIs, feature extraction and classification of benign and malignant lesions in breast ultrasound imaging.

Identification and Segmentation of ROIs

To accurately represent and diagnose the breast lesions, the lesions should first be segmented from the background. In the current clinical work, the manual segmentation of breast images was mainly carried out by ultrasound doctors, this process not only depends on the doctors' working experience but also takes time and effort. In addition, breast ultrasound images have low contrast, blurry boundaries, and a large amount of shadows,

TABLE 1 | Summary of key studies on the role of AI in mammography.

n	Task	Algorithms	No. of Cases	Results	Ref.
1	detect, segment, and classify the breast masses	a completely integrated CAD system (the You-Only-Look-Once to detect, the full resolution CNN to segment, the deep CNN to recognize and classify)	112	ACC= 95.64%	(16)
2	detect, analysis, and classify microcalcifications	a deep CNN with the same 5 convolutional layers	990	ACC=89.32% Sen = 86.89%	(28)
3	classify microcalcifications	an improved fisher linear discriminant analysis approach combined with a support vector machine variant	288	ACC=96%	(29)
4	segment breast masses	a hybrid method based on the active contours and fuzzy logic	57	ACC=88.08% Sen=91.12%	(32)
5	detect and segment breast masses	globally supported radial basis function based collocation method	300	AUC=98% Sen=97.12% Spe=92.43%	(33)
6	categorize breast density	a two-class CNN-based deep learning model	7000	AUC=94.21%	(38)
7	estimate breast cancer risk	a back-propagation learning algorithm	655	AUC=95.5% Sen=82% Spe=90%	(44)
8	enhance image quality	shearlet transform and neural network	300	ACC=93.45%	(11)

AI, artificial intelligence; CAD, computer aided diagnosis; CNN, convolutional neural network; ACC, accuracy; Sen, sensitivity; AUC, the area under the receiver operating characteristic curve; Spe, specificity.

therefore, an automatic segmentation method for breast ultrasound image lesions using AI is proposed. The segmentation process of breast ultrasound images mainly includes the detection of an ROI containing the lesion and delineation of its contours. Hu Y et al. proposed an automatic tumor segmentation method that combined a dilated fully convolutional network (DFCN) with a phase-based active contour (PBAC) model. After training, 170 breast ultrasound images were identified and segmented, and they achieved a mean DSC of 88.97%, which showed that the proposed segmentation method could partly replace the manual segmentation results in medical analysis (50). Kumar V. et al. proposed a multi-U-net algorithm and segmented masses from 258 women's breast ultrasound images, they achieved a mean Dice coefficient of 0.82, a true positive fraction (TPF) of 0.84, and a false positive fraction (FPF) of 0.01, which are obviously better than the results with the original U-net algorithm (51). Feng Y. et al. combined a Hausdorff-based fuzzy c-means (FCM) algorithm with an adaptive region selection scheme to segment ultrasound images of breast tumors. Based on the mutual information between regions, the neighborhood around each pixel is adaptively selected for Hausdorff distance measurement. The results showed that the adaptive Hausdorff-based FCM algorithm had a better performance than the Hausdorff-based and traditional FCM algorithms (52). The identification and segmentation of lesions in breast ultrasound images saves a considerable amount of time for ultrasound physicians to quickly identify and diagnose diseases and provide a foundation and guarantee for the development of AI for automatic diagnosis of breast diseases.

Feature Extraction

Ultrasound doctors usually identify and segment suspicious masses based on the morphological and texture features of the breast images. These features may be shape, orientation, edge, echo type, rear features, calcification location and hardness. Then, they classify suspicious masses according to the BI-RADS scale to quantify the degree of cancer suspicion in breast masses. The morphological features are very essential for the diagnosis of benign and malignant masses, and obtaining them correctly requires high demands on the ultrasound examiner. To reduce the dependence on the physician's experience, AI systems have been applied to the feature extraction of breast ultrasound images. According to the research by Hsu SM et al. morphological-feature parameters (e.g., standard deviation of the shortest distance), texture features (e.g., variance), and the Nakagami parameter are combined to extract the physical features of breast ultrasound images, they classified the data using FCM clustering and achieved an accuracy of 89.4%, a specificity of 86.3%, and a sensitivity of 92.5%. Compared with logistic regression and SVM classifiers, the maximum discrimination performance of the optimal feature collection was independent of the type of classifier, indicating that the combination of different feature parameters should be functionally complementary to improve the performance of breast cancer classification (53). Zhang et al. constructed a two-layer DL architecture to extract the shear-wave elastography (SWE) features by combining feature learning and feature selection. Compared with the statistical features of quantified image intensity and texture, the results showed that the DL features had better classification performance with an accuracy of 93.4%, a sensitivity of 88.6%, a specificity of 97.1%, and an area under the receiver operating characteristic curve of 0.947 (54). Relevant studies have shown that using CAD systems (S-Detect, Samsung RS80A ultrasound system) to analyze the ultrasound features of breast masses can significantly improve the diagnostic performance of experienced and inexperienced radiologists (**Figure 1**). CAD systems may be helpful in refining breast lesion descriptions and in making management decisions, and it improves the consistency of the characteristics of breast masses among observers (49, 55).

Benign and Malignant Classification

Breast cancer has a high incidence and mortality among women all over the world, therefore, many countries have carried out breast cancer screening for women of appropriate age. In breast

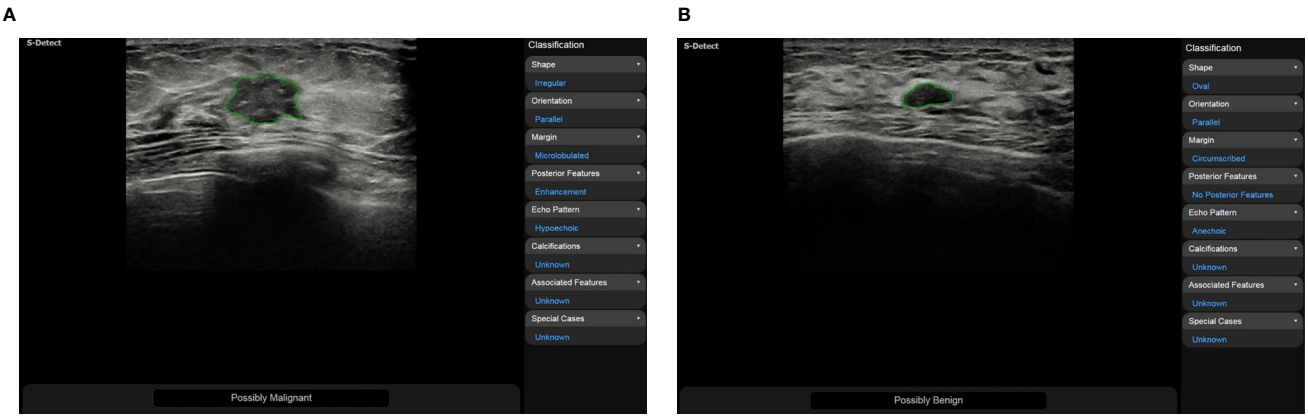

FIGURE 1 | **(A)** A 50-year-old woman was diagnosed with invasive cancer, and the results of CAD (S-Detect, Samsung RS80A ultrasound system) were "possibly malignant"; **(B)** A 48-year-old woman was diagnosed with adenosis, and the results of CAD were "possibly benign".

disease screening, the most important thing is to distinguish breast cancer from benign breast diseases. Physicians mainly classify the lesions in breast ultrasound images based on BI-RADS. To allow doctors with different experience to reach a consistent conclusion, AI systems with benign and malignant classification functions have been developed gradually. Cirtisis A et al. classified an internal data set and an external test data set by using a deep convolution neural network (dCNN) and classified breast ultrasound images into BI-RADS 2-3 and BI-RADS 4-5. The results showed that the dCNN reached a classification accuracy of 93.1% (external 95.3%), whereas the classification accuracy of radiologists was 91.6 ± 5.4% (external 94.1 ± 1.2%). This shows that dCNNs may be used to mimic human decision making (56). Becker AS et al. used DL software to analyze 637 breast ultrasound images (84 malignant and 553 benign lesions). A randomly chosen subset of the images (n=445, 70%) was used for the training of the software, and the remaining cases (n=192) were used to validate the resulting model in the training process. The results were compared with three readers with variable expertise (a radiologist, resident, and trained medical student), and the findings showed that the neural network, which was trained on only a few hundred cases, exhibited comparable accuracy to the reading of a radiologist. There was a tendency for the neural network to perform better than a medical student who was trained with the same training data set (57). This finding indicates that the classification and diagnosis of breast diseases assisted by AI can significantly shorten the diagnostic time of physicians and improve the diagnostic accuracy of inexperienced doctors (**Table 2**).

APPLICATIONS OF AI IN BREAST MRI

MRI is the most sensitive modality for breast cancer detection and is currently indicated as a supplement to mammography for patients at high risk (59). MRI can comprehensively evaluate the shape, size, scope and blood perfusion of breast masses through a variety of scanning sequences. However, it has disadvantages of low specificity, high cost, long examination time and selectivity for patients, therefore it is not as popularly used as mammography and ultrasound examinations. Most studies on breast imaging and DL have focused on mammography, less evidence is available concerning breast MRI (60). The study of DL in breast MRI mainly focuses on the detection, segmentation, characterization and classification of breast lesions (61–64). Ignacio Alvarez Illan et al. detected and segmented non-mass-enhanced lesions on dynamic contrast-enhanced magnetic resonance imaging (DCE-MRI) of the breast with a CAD system, and the optimized CAD system reduced and controlled the false positive rate and finally achieved satisfactory results (65). Herent P. et al. developed a DL model to detect, characterize and classify lesions on breast MRI (mammary glands, benign lesions, invasive ductal carcinoma and other malignant lesions) and achieved fine performance (60). Antropova N. et al. incorporated the dynamic and volumetric components of DCE-MRIs into breast lesion classification with DL methods using maximum intensity projection images. The results showed that incorporating both volumetric and dynamic DCE-MRI components can significantly improve CNN-based lesion classification (66). Jiang Y. et al. set up 19 breast imaging radiologists (eight academics and eleven private practices) to classify benign and malignant from DCE-MRI, and compared the classification results that only using conventionally available CAD evaluation software including kinetic maps and supplement using AI analytics through CAD software. It was found that the use of AI systems improved radiologists' performance in differentiating benign and malignant breast lesions on MRI (67). Breast MRI is still necessary to screen patients at high risk of breast cancer. The CAD system can improve the sensitivity of examination, decrease the false positive rate, and reduce unnecessary biopsy and psychological burden of patients (68) (**Table 3**).

TABLE 2 | Summary of key studies on the role of AI in breast ultrasound.

n	Task	Algorithms	No. of Cases	Results	Ref.
1	segment breast tumors	a dilated fully convolutional network combined with an active contour model	170	AUC=79.5% ACC=71.9% Sen=71.2% Spe=72.6%	(50)
2	segment breast masses	the underlying multi u-net algorithm based on CNN	433	Sen=84%	(51)
3	characterize breast tumors	fuzzy c-means clustering algorithm	160	AUC=96% ACC=89.4% Sen=92.5% Spe=86.3%	(53)
4	detect, highlight, and classify breast lesions	deep CNN	101	AUC=83.8%	(56)
5	classify breast tumors	an industrial grade image analysis software (ViDi Suite v. 2.0)	192	AUC=98% Sen=97.12% Spe=92.43%	(57)
6	classify breast tumors	a two-layer DL architecture comprised of the point-wise gated boltzmann machine and the restricted boltzmann machine	227	ACC=93.4% Sen=88.6% Spe=97.1% AUC=94.7%	(54)
7	identify ALN involvement	DL radiomics	584	AUC=90.2%	(58)

AI, artificial intelligence; AUC, the area under the receiver operating characteristic curve; ACC, accuracy; Sen, sensitivity; Spe, specificity; CNN, convolutional neural networks; DL, deep learning; ALN, axillary lymph node.

CONCLUSION

AI, particularly DL, is increasingly widely used in medical imaging and shows excellent performance in medical image analysis tasks. With its advantages of fast computing speed, good repeatability and no fatigue, AI can provide objective and effective information to doctors and reduce the workload of doctors and the rates of missed diagnosis and misdiagnosis (72). At present, the CAD system for breast cancer screening has been widely studied. In mammography, ultrasound, MRI and other imaging examinations, these systems can identify and segment breast lesions, extract features, classify them, estimate BD and the risk of breast cancer, and evaluate treatment effect and prognosis (39, 73–78). These systems show great advantages and potential in relieving pressure on doctors, optimizing resource allocation and improving accuracy.

CHALLENGES AND PROSPECTS

AI is still in the stage of "weak AI". Although it has made rapid developments in the medical field in the past decade, it is far from the goal of being fully integrated into the work of clinicians and large-scale application in the world. At present, there are many limitations in CAD systems for breast cancer screening, such as the lack of large-scale public datasets, the dependence on ROI annotation, high image quality requirements, regional differences, and overfitting and binary classification problems. In addition, AI mostly aims for one task

TABLE 3 | Summary of key studies on the role of AI in breast MRI.

n	Task	Algorithms	No. of Cases	Results	Ref.
1	detect, characterize and categorize lesions	a supervised-attention model with deep learning	335	AUC=81.6%	(60)
2	classify lesions	radiomic analysis and CNN	1294	AUC=98%	(62)
3	characterize and classify lesions	the combination of unsupervised dimensionality reduction and embedded space clustering followed by a supervised classifier	792	AUC=81%	(63)
4	classify breast tumors	QuantX	111	AUC=76%	(67)
5	assess and diagnose contralateral BI-RADS 4 lesions	MRI radiomics-based machine learning	178	AUC=77% ACC=74.1%	(69)
6	assess tumor extent and multifocality	CADstream software (version 5.2.8.591)	86	AUC = 88.8% Spe=92.1% PPV=90.0%	(70)
7	early predict pathological complete response to neoadjuvant chemotherapy and survival outcomes	linear support vector machine, linear discriminant analysis, logistic regression, random forests, stochastic gradient descent, decision tree, adaptive boosting and extreme gradient boosting	38	AUC=86%	(71)

AI, artificial intelligence; MRI, magnetic resonance imaging; AUC, the area under the receiver operating characteristic curve; CNN, convolutional neural network; BI-RADS, Breast Imaging Reporting and Data System; ACC, accuracy; CAD, computer-aided detection; Spe, specificity; PPV, positive predictive value.

training and cannot solve multiple tasks at the same time, which are the challenges and difficulties that DL faces in the development of breast imaging. Meanwhile, these also provide a new impetus for the development of breast imaging diagnostic disciplines and show the broad prospect of intelligent medical imaging in the future.

In addition to their application in traditional imaging methods, CAD systems based on DL are developing rapidly in the fields of digital breast tomosynthesis (79–81), ultrasound elastography (82), contrast-enhanced mammography, ultrasound and MRI et al. (83, 84). We believe that AI in breast imaging can not only be used for the detection, classification and prediction of breast diseases, but also further classify specific breast diseases (e.g. breast fibroplasia) and predict lymph node metastasis (85) and disease recurrence (86). It is believed that with the progress of AI technology, radiologists will achieve higher accuracy with higher efficiency and more accurate classification and determination of adjuvant treatment for breast diseases to achieve early detection, early diagnosis and early treatment of breast cancer and benefit the majority of patients.

AUTHOR CONTRIBUTIONS

MY, M-HY, JY, and W-ZL contributed to the collection of relevant literature. S-EZ, JL, and CFD contributed significantly to literature analysis and manuscript preparation. Y-ML sorted out the literature and wrote the manuscript. JY provided a lot of help in the revision of the manuscript. H-RY and X-WC were responsible for design of the review and provided data acquisition, analysis, and interpretation. All authors contributed to the article and approved the submitted version.

FUNDING

This work was supported by the key research and development project in Hubei Province(2020BCB022), the Joint Fund project of Hubei Provincial Health and Family Planning Commission (WJ2018H0104), the Natural Science Foundation of Hubei Province (2019CFB2876), and Science and Technology Bureau of Shihezi, China (No. 2019ZH11).

ACKNOWLEDGMENTS

I would like to extend my sincere gratitude to my colleagues for their help in the completion of this article and the reviewers for reviewing my article.

REFERENCES

1. Bouletreau P, Makaremi M, Ibrahim B, Louvrier A, Sigaux N. Artificial Intelligence: Applications in Orthognathic Surgery. *J Stomatol Oral Maxillofac Surg* (2019) 120(4):347–54. doi: 10.1016/j.jormas.2019.06.001
2. Hosny A, Parmar C, Quackenbush J, Schwartz LH, Aerts H. Artificial Intelligence in Radiology. *Nat Rev Cancer* (2018) 18(8):500–10. doi: 10.1038/s41568-018-0016-5
3. Korn RL, Rahmanuddin S, Borazanci E. Use of Precision Imaging in the Evaluation of Pancreas Cancer. *Cancer Treat Res* (2019) 178:209–36. doi: 10.1007/978-3-030-16391-4_8
4. Zhou LQ, Wang JY, Yu SY, Wu GG, Wei Q, Deng YB, et al. Artificial Intelligence in Medical Imaging of the Liver. *World J Gastroenterol* (2019) 25 (6):672–82. doi: 10.3748/wjg.v25.i6.672
5. Arieno A, Chan A, Destounis SV. A Review of the Role of Augmented Intelligence in Breast Imaging: From Automated Breast Density Assessment to Risk Stratification. *AJR Am J Roentgenol* (2019) 212(2):259–70. doi: 10.2214/AJR.18.20391
6. Qin C, Yao D, Shi Y, Song Z. Computer-Aided Detection in Chest Radiography Based on Artificial Intelligence: A Survey. *BioMed Eng Online* (2018) 17(1):113. doi: 10.1186/s12938-018-0544-y
7. Villanueva-Meyer JE, Chang P, Lupo JM, Hess CP, Flanders AE, Kohli M. Machine Learning in Neurooncology Imaging: From Study Request to Diagnosis and Treatment. *AJR Am J Roentgenol* (2019) 212(1):52–6. doi: 10.2214/AJR.18.20328
8. Cardoso F, Kyriakides S, Ohno S, Penault-Llorca F, Poortmans P, Rubio IT, et al. Early Breast Cancer: ESMO Clinical Practice Guidelines for Diagnosis, Treatment and Follow-Updagger. *Ann Oncol* (2019) 30(8):1194–220. doi: 10.1093/annonc/mdz173
9. Bray F, Ferlay J, Soerjomataram I, Siegel RL, Torre LA, Jemal A. Global Cancer Statistics 2018: GLOBOCAN Estimates of Incidence and Mortality Worldwide for 36 Cancers in 185 Countries. *CA Cancer J Clin* (2018) 68 (6):394–424. doi: 10.3322/caac.21492
10. Fiorica JV. Breast Cancer Screening, Mammography, and Other Modalities. *Clin Obstet Gynecol* (2016) 59(4):688–709. doi: 10.1097/GRF.0000000000000246
11. Shenbagavalli P, Thangarajan R. Aiding the Digital Mammogram for Detecting the Breast Cancer Using Shearlet Transform and Neural Network. *Asian Pac J Cancer Prev* (2018) 19(9):2665–71. doi: 10.22034/APJCP.2018.19.9.2665
12. Abdelhafiz D, Yang C, Ammar R, Nabavi S. Deep Convolutional Neural Networks for Mammography: Advances, Challenges and Applications. *BMC Bioinf* (2019) 20(Suppl 11):281. doi: 10.1186/s12859-019-2823-4
13. Hamet P, Tremblay J. Artificial Intelligence in Medicine. *Metabolism* (2017) 69S:S36–40. doi: 10.1016/j.metabol.2017.01.011
14. Viceconti M, Hunter P, Hose R. Big Data, Big Knowledge: Big Data for Personalized Healthcare. *IEEE J BioMed Health Inform* (2015) 19(4):1209–15. doi: 10.1109/JBHI.2015.2406883
15. Obermeyer Z, Emanuel EJ. Predicting the Future - Big Data, Machine Learning, and Clinical Medicine. *N Engl J Med* (2016) 375(13):1216–9. doi: 10.1056/NEJMp1606181
16. Al-Antari MA, Al-Masni MA, Choi MT, Han SM, Kim TS. A Fully Integrated Computer-Aided Diagnosis System for Digital X-Ray Mammograms *via* Deep Learning Detection, Segmentation, and Classification. *Int J Med Inform* (2018) 117:44–54. doi: 10.1016/j.ijmedinf.2018.06.003
17. Rodriguez-Ruiz A, Lang K, Gubern-Merida A, Teuwen J, Broeders M, Gennaro G, et al. Can We Reduce the Workload of Mammographic Screening by Automatic Identification of Normal Exams With Artificial Intelligence? A Feasibility Study. *Eur Radiol* (2019) 29(9):4825–32. doi: 10.1007/s00330-019-06186-9
18. Tagliafico AS, Piana M, Schenone D, Lai R, Massone AM, Houssami N. Overview of Radiomics in Breast Cancer Diagnosis and Prognostication. *Breast* (2020) 49:74–80. doi: 10.1016/j.breast.2019.10.018
19. Yanagawa M, Niioka H, Hata A, Kikuchi N, Honda O, Kurakami H, et al. Application of Deep Learning (3-Dimensional Convolutional Neural Network) for the Prediction of Pathological Invasiveness in Lung Adenocarcinoma: A Preliminary Study. *Med (Baltimore)* (2019) 98(25): e16119. doi: 10.1097/MD.0000000000016119
20. Le EPV, Wang Y, Huang Y, Hickman S, Gilbert FJ. Artificial Intelligence in Breast Imaging. *Clin Radiol* (2019) 74(5):357–66. doi: 10.1016/j.crad.2019.02.006
21. Welch HG, Prorok PC, O'Malley AJ, Kramer BS. Breast-Cancer Tumor Size, Overdiagnosis, and Mammography Screening Effectiveness. *N Engl J Med* (2016) 375(15):1438–47. doi: 10.1056/NEJMoa1600249

22. McDonald ES, Oustimov A, Weinstein SP, Synnestvedt MB, Schnall M, Conant EF. Effectiveness of Digital Breast Tomosynthesis Compared With Digital Mammography: Outcomes Analysis From 3 Years of Breast Cancer Screening. *JAMA Oncol* (2016) 2(6):737–43. doi: 10.1001/jamaoncol.2015.5536
23. Alsheh Ali M, Eriksson M, Czene K, Hall P, Humphreys K. Detection of Potential Microcalcification Clusters Using Multivendor for-Presentation Digital Mammograms for Short-Term Breast Cancer Risk Estimation. *Med Phys* (2019) 46(4):1938–46. doi: 10.1002/mp.13450
24. S P, NK V, S S. Breast Cancer Detection Using Crow Search Optimization Based Intuitionistic Fuzzy Clustering With Neighborhood Attraction. *Asian Pac J Cancer Prev* (2019) 20(1):157–65. doi: 10.31557/APJCP.2019.20.1.157
25. Jiang Y, Inciardi MF, Edwards AV, Papaioannou J. Interpretation Time Using a Concurrent-Read Computer-Aided Detection System for Automated Breast Ultrasound in Breast Cancer Screening of Women With Dense Breast Tissue. *AJR Am J Roentgenol* (2018) 211(2):452–61. doi: 10.2214/AJR.18.19516
26. Fan M, Li Y, Zheng S, Peng W, Tang W, Li L. Computer-Aided Detection of Mass in Digital Breast Tomosynthesis Using a Faster Region-Based Convolutional Neural Network. *Methods* (2019) 166:103–11. doi: 10.1016/j.ymeth.2019.02.010
27. Cruz-Bernal A, Flores-Barranco MM, Almanza-Ojeda DL, Ledesma S, Ibarra-Manzano MA. Analysis of the Cluster Prominence Feature for Detecting Calcifications in Mammograms. *J Healthc Eng* (2018) 2018:2849567. doi: 10.1155/2018/2849567
28. Cai H, Huang Q, Rong W, Song Y, Li J, Wang J, et al. Breast Microcalcification Diagnosis Using Deep Convolutional Neural Network From Digital Mammograms. *Comput Math Methods Med* (2019) 2019:2717454. doi: 10.1155/2019/2717454
29. Suhail Z, Denton ERE, Zwiggelaar R. Classification of Micro-Calcification in Mammograms Using Scalable Linear Fisher Discriminant Analysis. *Med Biol Eng Comput* (2018) 56(8):1475–85. doi: 10.1007/s11517-017-1774-z
30. Jian W, Sun X, Luo S. Computer-Aided Diagnosis of Breast Microcalcifications Based on Dual-Tree Complex Wavelet Transform. *BioMed Eng Online* (2012) 11:96. doi: 10.1186/1475-925X-11-96
31. Guo Y, Dong M, Yang Z, Gao X, Wang K, Luo C, et al. A New Method of Detecting Micro-Calcification Clusters in Mammograms Using Contourlet Transform and non-Linking Simplified PCNN. *Comput Methods Prog BioMed* (2016) 130:31–45. doi: 10.1016/j.cmpb.2016.02.019
32. Hmida M, Hamrouni K, Solaiman B, Boussetta S. Mammographic Mass Segmentation Using Fuzzy Contours. *Comput Methods Prog BioMed* (2018) 164:131–42. doi: 10.1016/j.cmpb.2018.07.005
33. Kashyap KL, Bajpai MK, Khanna P. Globally Supported Radial Basis Function Based Collocation Method for Evolution of Level Set in Mass Segmentation Using Mammograms. *Comput Biol Med* (2017) 87:22–37. doi: 10.1016/j.compbiomed.2017.05.015
34. Song E, Jiang L, Jin R, Zhang L, Yuan Y, Li Q. Breast Mass Segmentation in Mammography Using Plane Fitting and Dynamic Programming. *Acad Radiol* (2009) 16(7):826–35. doi: 10.1016/j.acra.2008.11.014
35. Anderson NH, Hamilton PW, Bartels PH, Thompson D, Montironi R, Sloan JM. Computerized Scene Segmentation for the Discrimination of Architectural Features in Ductal Proliferative Lesions of the Breast. *J Pathol* (1997) 181(4):374–80. doi: 10.1002/(SICI)1096-9896(199704)181:4<374::AID-PATH795>3.0.CO;2-N
36. Fowler EEE, Smallwood AM, Khan NZ, Kilpatrick K, Sellers TA, Heine J. Technical Challenges in Generalizing Calibration Techniques for Breast Density Measurements. *Med Phys* (2019) 46(2):679–88. doi: 10.1002/mp.13325
37. Hudson S, Vik Hjerkind K, Vinnicombe S, Allen S, Trewin C, Ursin G, et al. Adjusting for BMI in Analyses of Volumetric Mammographic Density and Breast Cancer Risk. *Breast Cancer Res* (2018) 20(1):156. doi: 10.1186/s13058-018-1078-8
38. Mohamed AA, Berg WA, Peng H, Luo Y, Jankowitz RC, Wu S. A Deep Learning Method for Classifying Mammographic Breast Density Categories. *Med Phys* (2018) 45(1):314–21. doi: 10.1002/mp.12683
39. Mohamed AA, Luo Y, Peng H, Jankowitz RC, Wu S. Understanding Clinical Mammographic Breast Density Assessment: A Deep Learning Perspective. *J Digit Imaging* (2018) 31(4):387–92. doi: 10.1007/s10278-017-0022-2
40. Le Boulc'h M, Bekhouche A, Kermarrec E, Milon A, Abdel Wahab C, Zilberman S, et al. Comparison of Breast Density Assessment Between Human Eye and Automated Software on Digital and Synthetic Mammography: Impact on Breast Cancer Risk. *Diagn Interv Imaging* (2020) 101(12):811–9. doi: 10.1016/j.diii.2020.07.004
41. Lehman CD, Yala A, Schuster T, Dontchos B, Bahl M, Swanson K, et al. Mammographic Breast Density Assessment Using Deep Learning: Clinical Implementation. *Radiology* (2019) 290(1):52–8. doi: 10.1148/radiol.2018180694
42. Sun YS, Zhao Z, Yang ZN, Xu F, Lu HJ, Zhu ZY, et al. Risk Factors and Preventions of Breast Cancer. *Int J Biol Sci* (2017) 13(11):1387–97. doi: 10.7150/ijbs.21635
43. Nindrea RD, Aryandono T, Lazuardi L, Dwiprahasto I. Diagnostic Accuracy of Different Machine Learning Algorithms for Breast Cancer Risk Calculation: A Meta-Analysis. *Asian Pac J Cancer Prev* (2018) 19(7):1747–52. doi: 10.22034/APJCP.2018.19.7.1747
44. Sepandi M, Taghdir M, Rezaianzadeh A, Rahimikazerooni S. Assessing Breast Cancer Risk With an Artificial Neural Network. *Asian Pac J Cancer Prev* (2018) 19(4):1017–9. doi: 10.31557/APJCP.2018.19.12.3571
45. Yala A, Lehman C, Schuster T, Portnoi T, Barzilay R. A Deep Learning Mammography-Based Model for Improved Breast Cancer Risk Prediction. *Radiology* (2019) 292(1):60–6. doi: 10.1148/radiol.2019182716
46. Teare P, Fishman M, Benzaquen O, Toledano E, Elnekave E. Malignancy Detection on Mammography Using Dual Deep Convolutional Neural Networks and Genetically Discovered False Color Input Enhancement. *J Digit Imaging* (2017) 30(4):499–505. doi: 10.1007/s10278-017-9993-2
47. Akkus Z, Cai J, Boonrod A, Zeinoddini A, Weston AD, Philbrick KA, et al. A Survey of Deep-Learning Applications in Ultrasound: Artificial Intelligence-Powered Ultrasound for Improving Clinical Workflow. *J Am Coll Radiol* (2019) 16(9 Pt B):1318–28. doi: 10.1016/j.jacr.2019.06.004
48. Wu GG, Zhou LQ, Xu JW, Wang JY, Wei Q, Deng YB, et al. Artificial Intelligence in Breast Ultrasound. *World J Radiol* (2019) 11(2):19–26. doi: 10.4329/wjr.v11.i2.19
49. Park HJ, Kim SM, La Yun B, Jang M, Kim B, Jang JY, et al. A Computer-Aided Diagnosis System Using Artificial Intelligence for the Diagnosis and Characterization of Breast Masses on Ultrasound: Added Value for the Inexperienced Breast Radiologist. *Med (Baltimore)* (2019) 98(3):e14146. doi: 10.1097/MD.0000000000014146
50. Hu Y, Guo Y, Wang Y, Yu J, Li J, Zhou S, et al. Automatic Tumor Segmentation in Breast Ultrasound Images Using a Dilated Fully Convolutional Network Combined With an Active Contour Model. *Med Phys* (2019) 46(1):215–28. doi: 10.1002/mp.13268
51. Kumar V, Webb JM, Gregory A, Denis M, Meixner DD, Bayat M, et al. Automated and Real-Time Segmentation of Suspicious Breast Masses Using Convolutional Neural Network. *PloS One* (2018) 13(5):e0195816. doi: 10.1371/journal.pone.0195816
52. Feng Y, Dong F, Xia X, Hu CH, Fan Q, Hu Y, et al. An Adaptive Fuzzy C-Means Method Utilizing Neighboring Information for Breast Tumor Segmentation in Ultrasound Images. *Med Phys* (2017) 44(7):3752–60. doi: 10.1002/mp.12350
53. Hsu SM, Kuo WH, Kuo FC, Liao YY. Breast Tumor Classification Using Different Features of Quantitative Ultrasound Parametric Images. *Int J Comput Assist Radiol Surg* (2019) 14(4):623–33. doi: 10.1007/s11548-018-01908-8
54. Zhang Q, Xiao Y, Dai W, Suo J, Wang C, Shi J, et al. Deep Learning Based Classification of Breast Tumors With Shear-Wave Elastography. *Ultrasonics* (2016) 72:150–7. doi: 10.1016/j.ultras.2016.08.004
55. Choi JH, Kang BJ, Baek JE, Lee HS, Kim SH. Application of Computer-Aided Diagnosis in Breast Ultrasound Interpretation: Improvements in Diagnostic Performance According to Reader Experience. *Ultrasonography* (2018) 37(3):217–25. doi: 10.14366/usg.17046
56. Ciritsis A, Rossi C, Eberhard M, Marcon M, Becker AS, Boss A. Automatic Classification of Ultrasound Breast Lesions Using a Deep Convolutional Neural Network Mimicking Human Decision-Making. *Eur Radiol* (2019) 29(10):5458–68. doi: 10.1007/s00330-019-06118-7
57. Becker AS, Mueller M, Stoffel E, Marcon M, Ghafoor S, Boss A. Classification of Breast Cancer in Ultrasound Imaging Using a Generic Deep Learning Analysis Software: A Pilot Study. *Br J Radiol* (2018) 91(1083):20170576. doi: 10.1259/bjr.20170576
58. Zheng X, Yao Z, Huang Y, Yu Y, Wang Y, Liu Y, et al. Deep learning radiomics can predict axillary lymph node status in early-stage breast cancer. *Nat Commun* (2020) 11(1):1236. doi: 10.1038/s41467-020-15027-z

59. Sheth D, Giger ML. Artificial Intelligence in the Interpretation of Breast Cancer on MRI. *J Magn Reson Imaging* (2020) 51(5):1310–24. doi: 10.1002/jmri.26878
60. Herent P, Schmauch B, Jehanno P, Dehaene O, Saillard C, Balleyguier C, et al. Detection and Characterization of MRI Breast Lesions Using Deep Learning. *Diagn Interv Imaging* (2019) 100(4):219–25. doi: 10.1016/j.diii.2019.02.008
61. Xu X, Fu L, Chen Y, Larsson R, Zhang D, Suo S, et al. Breast Region Segmentation Being Convolutional Neural Network in Dynamic Contrast Enhanced MRI. *Annu Int Conf IEEE Eng Med Biol Soc* (2018) 2018:750–3. doi: 10.1109/EMBC.2018.8512422
62. Truhn D, Schrading S, Haarburger C, Schneider H, Merhof D, Kuhl C. Radiomic Versus Convolutional Neural Networks Analysis for Classification of Contrast-Enhancing Lesions at Multiparametric Breast MRI. *Radiology* (2019) 290(2):290–7. doi: 10.1148/radiol.2018181352
63. Gallego-Ortiz C, Martel AL. A Graph-Based Lesion Characterization and Deep Embedding Approach for Improved Computer-Aided Diagnosis of Nonmass Breast MRI Lesions. *Med Image Anal* (2019) 51:116–24. doi: 10.1016/j.media.2018.10.011
64. Vidic I, Egnell L, Jerome NP, Teruel JR, Sjobakk TE, Ostlie A, et al. Support Vector Machine for Breast Cancer Classification Using Diffusion-Weighted MRI Histogram Features: Preliminary Study. *J Magn Reson Imaging* (2018) 47(5):1205–16. doi: 10.1002/jmri.25873
65. Illan IA, Ramirez J, Gorriz JM, Marino MA, Avendano D, Helbich T, et al. Automated Detection and Segmentation of Nonmass-Enhancing Breast Tumors With Dynamic Contrast-Enhanced Magnetic Resonance Imaging. *Contrast Media Mol Imaging* (2018) 2018:5308517. doi: 10.1155/2018/5308517
66. Antropova N, Abe H, Giger ML. Use of Clinical MRI Maximum Intensity Projections for Improved Breast Lesion Classification With Deep Convolutional Neural Networks. *J Med Imaging (Bellingham)* (2018) 5(1):014503. doi: 10.1117/1.JMI.5.1.014503
67. Jiang Y, Edwards AV, Newstead GM. Artificial Intelligence Applied to Breast MRI for Improved Diagnosis. *Radiology* (2021) 298(1):38–46. doi: 10.1148/radiol.2020200292
68. Meyer-Base A, Morra L, Meyer-Base U, Pinker K. Current Status and Future Perspectives of Artificial Intelligence in Magnetic Resonance Breast Imaging. *Contrast Media Mol Imaging* (2020) 2020:6805710. doi: 10.1155/2020/6805710
69. Hao W, Gong J, Wang S, Zhu H, Zhao B, Peng W. Application of MRI Radiomics-Based Machine Learning Model to Improve Contralateral BI-RADS 4 Lesion Assessment. *Front Oncol* (2020) 10:531476. doi: 10.3389/fonc.2020.531476
70. Song SE, Seo BK, Cho KR, Woo OH, Son GS, Kim C, et al. Computer-aided detection (CAD) system for breast MRI in assessment of local tumor extent, nodal status, and multifocality of invasive breast cancers: preliminary study. *Cancer Imaging* (2015) 15(1):1. doi: 10.1186/s40644-015-0036-2
71. Tahmassebi A, Wengert GJ, Helbich TH, Bago-Horvath Z, Alaei S, Bartsch R, et al. Impact of Machine Learning With Multiparametric Magnetic Resonance Imaging of the Breast for Early Prediction of Response to Neoadjuvant Chemotherapy and Survival Outcomes in Breast Cancer Patients. *Invest Radiol* (2019) 54(2):110-7. doi: 10.1097/RLI.0000000000000518
72. Morgan MB, Mates JL. Applications of Artificial Intelligence in Breast Imaging. *Radiol Clin North Am* (2021) 59(1):139–48. doi: 10.1016/j.rcl.2020.08.007
73. Hupse R, Samulski M, Lobbes MB, Mann RM, Mus R, den Heeten GJ, et al. Computer-Aided Detection of Masses at Mammography: Interactive Decision Support Versus Prompts. *Radiology* (2013) 266(1):123–9. doi: 10.1148/radiol.12120218
74. Quellec G, Lamard M, Cozic M, Coatrieux G, Cazuguel G. Multiple-Instance Learning for Anomaly Detection in Digital Mammography. *IEEE Trans Med Imaging* (2016) 35(7):1604–14. doi: 10.1109/TMI.2016.2521442
75. Mendelson EB. Artificial Intelligence in Breast Imaging: Potentials and Limitations. *AJR Am J Roentgenol* (2019) 212(2):293–9. doi: 10.2214/AJR.18.20532
76. Qi X, Zhang L, Chen Y, Pi Y, Chen Y, Lv Q, et al. Automated Diagnosis of Breast Ultrasonography Images Using Deep Neural Networks. *Med Image Anal* (2019) 52:185–98. doi: 10.1016/j.media.2018.12.006
77. Kooi T, Litjens G, van Ginneken B, Gubern-Merida A, Sanchez CI, Mann R, et al. Large Scale Deep Learning for Computer Aided Detection of Mammographic Lesions. *Med Image Anal* (2017) 35:303–12. doi: 10.1016/j.media.2016.07.007
78. Kim J, Kim HJ, Kim C, Kim WH. Artificial Intelligence in Breast Ultrasonography. *Ultrasonography* (2021) 40(2):183–90. doi: 10.14366/usg.20117
79. Sechopoulos I, Teuwen J, Mann R. Artificial Intelligence for Breast Cancer Detection in Mammography and Digital Breast Tomosynthesis: State of the Art. *Semin Cancer Biol* (2020) 72:214-25. doi: 10.1016/j.semcancer.2020.06.002
80. Skaane P, Bandos AI, Niklason LT, Sebuodegard S, Osteras BH, Gullien R, et al. Digital Mammography Versus Digital Mammography Plus Tomosynthesis in Breast Cancer Screening: The Oslo Tomosynthesis Screening Trial. *Radiology* (2019) 291(1):23–30. doi: 10.1148/radiol.2019182394
81. Lotter W, Diab AR, Haslam B, Kim JG, Grisot G, Wu E, et al. Robust Breast Cancer Detection in Mammography and Digital Breast Tomosynthesis Using an Annotation-Efficient Deep Learning Approach. *Nat Med* (2021) 27(2):244–9. doi: 10.1038/s41591-020-01174-9
82. Zhang Q, Song S, Xiao Y, Chen S, Shi J, Zheng H. Dual-Mode Artificially-Intelligent Diagnosis of Breast Tumors in Shear-Wave Elastography and B-Mode Ultrasound Using Deep Polynomial Networks. *Med Eng Phys* (2019) 64:1–6. doi: 10.1016/j.medengphy.2018.12.005
83. Adachi M, Fujioka T, Mori M, Kubota K, Kikuchi Y, Xiaotong W, et al. Detection and Diagnosis of Breast Cancer Using Artificial Intelligence Based Assessment of Maximum Intensity Projection Dynamic Contrast-Enhanced Magnetic Resonance Images. *Diag (Basel)* (2020) 10(5):330. doi: 10.3390/diagnostics10050330
84. Dalmis MU, Gubern-Merida A, Vreemann S, Bult P, Karssemeijer N, Mann R, et al. Artificial Intelligence-Based Classification of Breast Lesions Imaged With a Multiparametric Breast MRI Protocol With Ultrafast DCE-MRI, T2, and DWI. *Invest Radiol* (2019) 54(6):325–32. doi: 10.1097/RLI.0000000000000544
85. Zhou LQ, Wu XL, Huang SY, Wu GG, Ye HR, Wei Q, et al. Lymph Node Metastasis Prediction From Primary Breast Cancer US Images Using Deep Learning. *Radiology* (2020) 294(1):19–28. doi: 10.1148/radiol.2019190372
86. Chan HP, Samala RK, Hadjiiski LM. CAD and AI for Breast Cancer-Recent Development and Challenges. *Br J Radiol* (2020) 93(1108):20190580. doi: 10.1259/bjr.20190580

Conflict of Interest: The authors declare that the research was conducted in the absence of any commercial or financial relationships that could be construed as a potential conflict of interest.

frontiers in Oncology

ORIGINAL RESEARCH
published: 10 February 2022
doi: 10.3389/fonc.2022.804632

Enhancing Performance of Breast Ultrasound in Opportunistic Screening Women by a Deep Learning-Based System: A Multicenter Prospective Study

Chenyang Zhao[1], Mengsu Xiao[1], Li Ma[1], Xinhua Ye[2], Jing Deng[2], Ligang Cui[3], Fajin Guo[4], Min Wu[5], Baoming Luo[6], Qin Chen[7], Wu Chen[8], Jun Guo[9], Qian Li[10], Qing Zhang[1], Jianchu Li[1], Yuxin Jiang[1] and Qingli Zhu[1]**

[1] Department of Ultrasound, Chinese Academy of Medical Sciences and Peking Union Medical College Hospital, Chinese Academy of Medical Sciences and Peking Union Medical College, Beijing, China, [2] Department of Ultrasound, First Affiliated Hospital, Nanjing Medical University, Nanjing, China, [3] Department of Ultrasound, Peking University Third Hospital, Beijing, China, [4] Department of Ultrasound, Beijing Hospital, Beijing, China, [5] Department of Ultrasound, Nanjing Drum Tower Hospital, Nanjing, China, [6] Department of Ultrasound, Sun Yat-sen Memorial Hospital, Guangzhou, China, [7] Department of Ultrasound, Sichuan Provincial People's Hospital, University of Electronic Science and Technology of China, Chengdu, China, [8] Department of Ultrasound, First Hospital of Shanxi Medical University, Taiyuan, China, [9] Department of Ultrasound, Aero Space Central Hospital, Beijing, China, [10] Department of Ultrasound, Henan Provincial Cancer Hospital, Zhengzhou, China

OPEN ACCESS

Edited by:
Abhishek Mahajan, Tata Memorial Hospital, India

Reviewed by:
Fajin Dong, Jinan University, China
Ahmed Sayed, Helwan University, Egypt
Ahmet Veysel Polat, Ondokuz Mayıs University, Turkey
Li Ping Sun, Tongji University, China

***Correspondence:**
Qingli Zhu
zqlpumch@126.com
Yuxin Jiang
yuxinjiangxh@163.com

Specialty section:
This article was submitted to Cancer Imaging and Image-directed Interventions, a section of the journal Frontiers in Oncology

Received: *29 October 2021*
Accepted: *07 January 2022*
Published: *10 February 2022*

Citation:
Zhao C, Xiao M, Ma L, Ye X, Deng J, Cui L, Guo F, Wu M, Luo B, Chen Q, Chen W, Guo J, Li Q, Zhang Q, Li J, Jiang Y and Zhu Q (2022) Enhancing Performance of Breast Ultrasound in Opportunistic Screening Women by a Deep Learning-Based System: A Multicenter Prospective Study. Front. Oncol. 12:804632. doi: 10.3389/fonc.2022.804632

Purpose: To validate the feasibility of S-Detect, an ultrasound computer-aided diagnosis (CAD) system using deep learning, in enhancing the diagnostic performance of breast ultrasound (US) for patients with opportunistic screening-detected breast lesions.

Methods: Nine medical centers throughout China participated in this prospective study. Asymptomatic patients with US-detected breast masses were enrolled and received conventional US, S-Detect, and strain elastography subsequently. The final pathological results are referred to as the gold standard for classifying breast mass. The diagnostic performances of the three methods and the combination of S-Detect and elastography were evaluated and compared, including sensitivity, specificity, and area under the receiver operating characteristics (AUC) curve. We also compared the diagnostic performances of S-Detect among different study sites.

Results: A total of 757 patients were enrolled, including 460 benign and 297 malignant cases. S-Detect exhibited significantly higher AUC and specificity than conventional US (AUC, S-Detect 0.83 [0.80–0.85] vs. US 0.74 [0.70–0.77], $p < 0.0001$; specificity, S-Detect 74.35% [70.10%–78.28%] vs. US 54.13% [51.42%–60.29%], $p < 0.0001$), with no decrease in sensitivity. In comparison to that of S-Detect alone, the AUC value significantly was enhanced after combining elastography and S-Detect (0.87 [0.84–0.90]), without compromising specificity (73.93% [68.60%–78.78%]). Significant differences in the S-Detect's performance were also observed across different study

sites (AUC of S-Detect in Groups 1–4: 0.89 [0.84–0.93], 0.84 [0.77–0.89], 0.85 [0.76–0.92], 0.75 [0.69–0.80]; p [1 vs. 4] < 0.0001, p [2 vs. 4] = 0.0165, p [3 vs. 4] = 0.0157).

Conclusions: Compared with the conventional US, S-Detect presented higher overall accuracy and specificity. After S-Detect and strain elastography were combined, the performance could be further enhanced. The performances of S-Detect also varied among different centers.

Keywords: breast cancer, ultrasound, deep learning, computer-aided diagnosis, elastography

INTRODUCTION

A dramatic increase in breast cancer incidence was reported in China in recent years and early detection is essential to reduce the mortality of breast cancer (1). Different from western countries, in which mammography is the most used method for breast screening, in China, mammography is not so popular due to its relatively low accuracy for women with dense breasts, which accounts for more Chinese women than Caucasian women (2), as well as the inaccessibility of the equipment in some regions of the country. Ultrasound (US) has become the most common method for screening breast cancer in China, due to its high detection rate of breast cancers in dense breast tissue and convenience (3, 4). A multicenter study of the country revealed a better diagnostic performance and higher cost efficiency of US than that of mammography in breast screening, and US screening has been recommended for high-risk women by a nationwide guideline (5–7). To note, US screening is often opportunistic in China due to different economic statuses and the insurance policies of different areas.

Despite the good performance, there still exist several drawbacks of breast US. In consideration of its widespread use in China, it is imperative to enhance the diagnostic performance of US. Moreover, US tends to present a high sensitivity in detecting malignant lesions but a relatively low positive predictive value (PPV), causing unnecessary biopsies or repeated examinations in short intervals (8). Usually, the category 4 and 5 lesions of the Breast Imaging Reporting and Data System (BI-RADS) lexicon identified by screening US are strongly recommended for further evaluation. But in clinical practice, patients with screening-detected BI-RADS 3 lesions also tend to choose a second-time US examination or biopsies, resulting in a high recall rate and false-positive results (9). Moreover, the operator dependence of breast US also has an adverse impact on the screening results (10, 11). Hence, new imaging techniques that can overcome these defects of US can be of great clinical value.

Computer-aided diagnosis (CAD) systems, which are designed to help doctors in diagnosing diseases to provide automatic segmentation or diagnosis of medical images (12), has been intensively investigated in the field of breast imaging in recent years, especially the systems constructed on deep learning (DL) method (13–16). S-Detect™ is one of the DL-based CAD programs for classifying breast lesions through US images. It is an onboard software integrated on a commercial US machine. The software is composed of a DL algorithm, which has been trained by a large number of ultrasonic images of breast lesions. When provided with a static US figure showing a suspicious breast lesion, the software can give a dichotomic diagnosis of the lesion, as possibly benign or possibly malignant. Several studies from Europe and Asia have validated its excellent performance in enhancing the diagnostic accuracy of US by increasing the specificity, consequently assisting in reducing unnecessary biopsies of breast lesions (17–20). According to our preliminary single-center research, S-Detect™ can provide a reliable classification for the asymptomatic screening-detected breast lesions (21). In order to further investigate its benefit for those asymptomatic patients with US screening-detected breast lesions, we launched this nationwide multicenter study about the clinical use of S-Detect™ in China. In this study, patients with opportunistic screening-detected breast lesions who were going to receive a second-time breast US examination were enrolled and evaluated by the new CAD technique. As far as we know, this is the first multicenter study about S-Detect™, and none of the previous studies have investigated the feasibility of the software for US screening-detected breast lesions.

Apart from utilizing the CAD system alone, we also investigated the role of combining the CAD technique and elastography in promoting the diagnostic efficacy of US in re-evaluating opportunistic US screening-detected breast lesions. Elastography is applied as a complementary for US to characterize breast lesions by providing information about tissue stiffness (22–24). For strain elastography, compressive force is implemented on breast tissues, and the tissue stiffness is often expressed as pseudo-color mapping or fat-to-lesion strain ratio (SR), both of which have been verified as an effective method to present the elasticity of tumor tissues and help increase accuracy and specificity of diagnosing breast cancers (25, 26). Recently, a newly developed built-in software of strain elastography, E-breast™, has been put into clinical use and distinguished with its ability in providing a relative objective value of SR. Considering that both S-Detect™ and E-breast™ can provide relatively objective imaging parameters for breast US, it will be of interest to explore the potential value of

Abbreviations: US, ultrasound (US); BI-RADS, Breast Imaging Reporting, and Data System; PPV, positive predictive value; CAD, computer-aided diagnosis; DL, deep learning; SR, strain ratio; PLR, positive likelihood ratio; NLR, negative likelihood ratio; NPV, negative predictive value; ROC, receiver operating characteristic; AUC, area under the receiver operating characteristics curve; CNN, convolutional neural networks.

combining the use of the two novel imaging methods. Therefore, in this multicenter study, we also evaluated the diagnostic performance of the combination of S-Detect™ and E-breast™ in diagnosing breast lesions and investigate the clinical value of the combination. Therefore, in this multicenter study, we aim to investigate the feasibility of S-Detect™, a DL CAD tool for breast US, and its combination with elastography in diagnosing breast cancer for patients with opportunistic screening-detected breast lesions. We also compared the diagnostic performances of S-Detect™ among different centers.

MATERIALS AND METHODS

This study was designed as a prospective multicenter one, and it was approved by the institutional review board of all of the participating centers. Written informed consent was signed by each recruited patient. A total of 9 medical centers from six provinces and municipalities were involved in this study. All the centers are general hospitals and own large-scale breast imaging departments, where US is performed for patients with breast lesions as a clinical routine. Before the inception of the study, we enacted a protocol regulating standards for image and clinical data acquisition, operation method for the software, and classification criteria for enrolled patients and lesions. The investigators of these medical centers received training on the protocol and participated in the study after fully understanding the protocol and breast US knowledge. The study has also been registered at ClinicalTrials.gov (NCT03851497).

Patient Recruitment

From January 2019 to December 2019, a total of 757 patients from the medical centers were consecutively recruited in this study. Asymptomatic female patients with breast masses from the participated hospitals were enrolled in this study. Before participation, those patients were found to have BI-RADS 3–5 breast masses by bilateral breast US screening within 3 months and referred to the medical centers for further diagnostic imaging tests.

The definitions for asymptomatic individuals are listed as follows.

1. no self-palpable breast masses
2. no severe breast pain that could not be explained by physiological reason
3. no nipple discharge
4. no changes in breast appearance, including nipple inversion, skin redness, and skin retraction

Exclusion criteria included breast malignancy history, pregnancy, lactation, and refusal to participate in the study. When more than one lesion was found eligible in a patient, we selected the suspicious lesions or the largest ones. The patients received biopsies after US examinations within 2 weeks and had final pathological results referred to as the gold standard for classifying breast mass.

Imaging Analysis

Conventional Breast Ultrasound Examinations and Image Acquisition

The radiologists in this study who performed US examinations had at least 5-year experience in breast US. In all medical centers, the radiologists performed US examinations with a high-frequency linear transducer (L3-12), under the breast preset on the US machine (RS80A, Samsung Medison Co., Ltd., Korea) according to standard scanning protocol. For the grayscale US, the focal zone was adjusted with the lesion depth, and the gain was set at 25%–50%. For color Doppler, the imaging settings included a scale of 3 cm/s, a wall filter of 50–100 Hz, and a rectangular sampling box with no angulation. After detection of the target lesion, conventional grayscale US and color Doppler US were consecutively performed on two orthogonal planes. The radiologists assessed the lesions after the dynamic scanning. The image on the largest diameter of the lesion was recorded for further reading and CAD analysis by the radiologists.

Strain Elastography

The built-in software of strain elastography, E-breast™ (Samsung Healthcare, Seoul, South Korea), was utilized in this study. After the acquisition of elastographic imaging of a breast lesion, the SR between the mass and surrounding fat can be calculated using E-breast™. Elastography was performed by the same radiologist after completing a conventional breast US examination. Elastography imaging was acquired with freehand compression. Imaging methods have been previously described in detail (22, 26). Briefly, the radiologist put the probe perpendicular to the chest wall and parallel to the pectoralis muscle and applied the probe with only light pressure. The proper pressure was gauged under the guidance of a compression guide bar to acquire appropriate images for analysis. The compression guide bar was on the right side of the working interface of E-breast™ to guide the operators in applying compressive force. The compression guide bar displayed the degree of pressure in colors between 0 and 7 stages. 0 stage (all black) represented no movement of the probe; 1–2 stage (gray) represented not enough compression speed; and 3–7 stage (green) represented moderate compression speed, indicating a good-quality strain image. When the guide bar reached the 3–7 stage, the strain image was regarded as qualified for further analysis and selected for calculation subsequently.

For calculating SR, one elliptical frame for sampling region of interest (ROI) was placed on the target lesion on the elastographic image, and the straining value on the fat area was provided automatically by the software (22).

$$SR = \frac{\text{Average fat strain (automatically derived)}}{\text{Average lesion strain (lesion ROI)}}$$

Elastography was performed three times for each patient. The maximal SR was used for final analyses. The same depth, focus, and gain parameters were employed for elastography as were used for conventional imaging.

S-Detect™ Classifications for Breast Lesions

S-Detect™ (Samsung Healthcare, Seoul, South Korea) was embedded in the RS80A US system, and the radiologists opened the working interface of S-Detect™ after finishing giving a diagnosis of the lesions. The slice with the maximal size of the lesion was recorded by the radiologists performing US examinations for S-Detect™ analysis. The grouping for breast lesions of S-Detect™ was performed automatically after clicking the center of the lesion on a grayscale slice, presenting dichotomic results as possibly benign and possibly malignant by the software, along with automatically recognized ultrasonographic features, including shape, orientation, margins, pattern, and posterior acoustic features.

Image Interpretation

Before performing elastography and the CAD system, the radiologists gave a diagnosis of the lesion based on the BI-RADS lexicon on site (27). The lesions were classified into BI-RADS 3, 4, and 5 according to their ultrasonographic features, and the results of elastography and S-Detect had no impact on the diagnosis of radiologists. The BI-RADS classification of each lesion was decided by the US-operating radiologists after identifying the aforementioned US features. A cutoff value was set at category 4 to transform BI-RADS classification into a dichotomic form. Category 3 lesions were allocated to possibly benign, and categories 4 and 5 were put as possibly malignant.

Statistical Analysis

Previous studies showed that S-Detect could increase AUC from 0.76 to 0.83 (17–20). By applying that the disease prevalence of 10%, 90% power, 5% two-sided significance, and 10% missing data, a sample size of 768, including 192 malignancies and 576 benign, was figured out for this multicenter study.

A series of statistical parameters pertaining to the diagnostic performance of a test were calculated, including sensitivity, specificity, positive likelihood ratio (PLR), negative likelihood ratio (NLR), PPV, negative predictive value (NPV), receiver operating characteristic (ROC) curve, and area under the ROC curve (AUC) (28). The optimal cutoffs of SR were also calculated using ROC analysis, defined as the closest point on the ROC curve to the point (0, 1). We used 2 × 2 contingency tables, a chi-square test for comparing sensitivity and positivity, a generalized estimating equation for comparing PPV, and the method proposed by DeLong et al. for comparing AUC values (29). A p-value of <0.05 was considered statistically significant. A forward stepwise logistic regression method was applied to combine S-Detect™ and strain elastography. We regarded the result of S-Detect as categorical data and SR as continuous variables to construct the model. An equation was acquired subsequently after regression. We presented the equation representing the combination of the two methods determined by the multiple regression method in the form of a nomogram. The model underlying the nomogram was to classify breast lesions based on the results of S-Detect and strain elastography.

Then we divided the nine medical centers into four groups (Groups 1–4), on the basis of local economic and medical service resources of the geographical regions with different breast cancer incidence. Group 1 and Group 2 were the centers located in Beijing and the east area of China, respectively, both of which were highly developed regions of China. Group 3 and Group 4 were the centers in less-developed regions, including the west and central regions of China, respectively. Compared with Groups 3 and 4, Groups 1 and 2 are located in regions with better economic status and a higher level of medical care. In China, the incidence rate of breast cancer is higher in socioeconomically developed coastal cities, with the highest age-standardized rate (ASR) of 46.6 cases/100,000 women. In contrast, in less developed areas of the central and western regions, the ASR for breast cancer can be less than 7.94 cases per 100,000 women (30). In general, the incidence rates of breast cancer in the regions of Groups 1 and 2 were higher than those of Groups 3 and 4. The diagnostic performances of conventional US and S-Detect of the four groups were calculated and compared, respectively. The AUC values of the four groups, representing the overall accuracy, were compared. The AUC values of S-Detect in different regions or medical centers were also compared using the method described by Hanley and McNeil (31) for comparing the AUC of two independent ROC curves. We compared the sensitivity and specificity among different groups using the Mann–Whitney test of the Normal approximation in independent samples (32).

Statistical analysis was performed using Medcalc (MedCalc software, version 15, Ghent, Belgium), R (http://www.R-project.org), and EmpowerStats software (X&Y Solutions).

RESULTS

Basic Characteristics of Enrolled Patients

A total of 831 patients participated in the study from the nine medical centers, of which 768 were eligible. Among them, 757 patients (mean age 47.5 years; median age 47.5 [15–82] years) with satisfactory imaging and pathological results were finally enrolled for statistical analysis, including 297 malignant cases and 460 benign cases, of the medical centers (**Figure 1**). The clinical characteristics and pathological results of the patients are shown in **Table 1**.

Diagnostic Performances of S-Detect™

The diagnostic performances of S-Detect™ and conventional US are listed in **Table 2**. The ROC curves of the tests are illustrated in **Figure 2**. S-Detect™ was distinguished by its higher specificity and PPV than those of conventional US (specificity, 74.35% [70.10%–78.28%] vs. 54.13% [51.42%–60.29%], p [S-detect vs. conventional US] < 0.0001; PPV 69.59% [64.74%–74.13%] vs. 55.89% [51.42%–60.29%], p [S-detect vs. conventional US] < 0.0001). In the meantime, S-Detect™ possessed good sensitivity, which presented no statistical difference with that of the radiologist (91.91% [87.05%–93.92%] vs. 94.28% [90.99%–96.63%], p [S-Detect vs. conventional US] = 0.09). S-Detect™ also presented a high AUC value (0.83 [0.80–0.85] vs. 0.74 [0.70–0.77], p [S-Detect vs. conventional US] < 0.0001), suggesting its

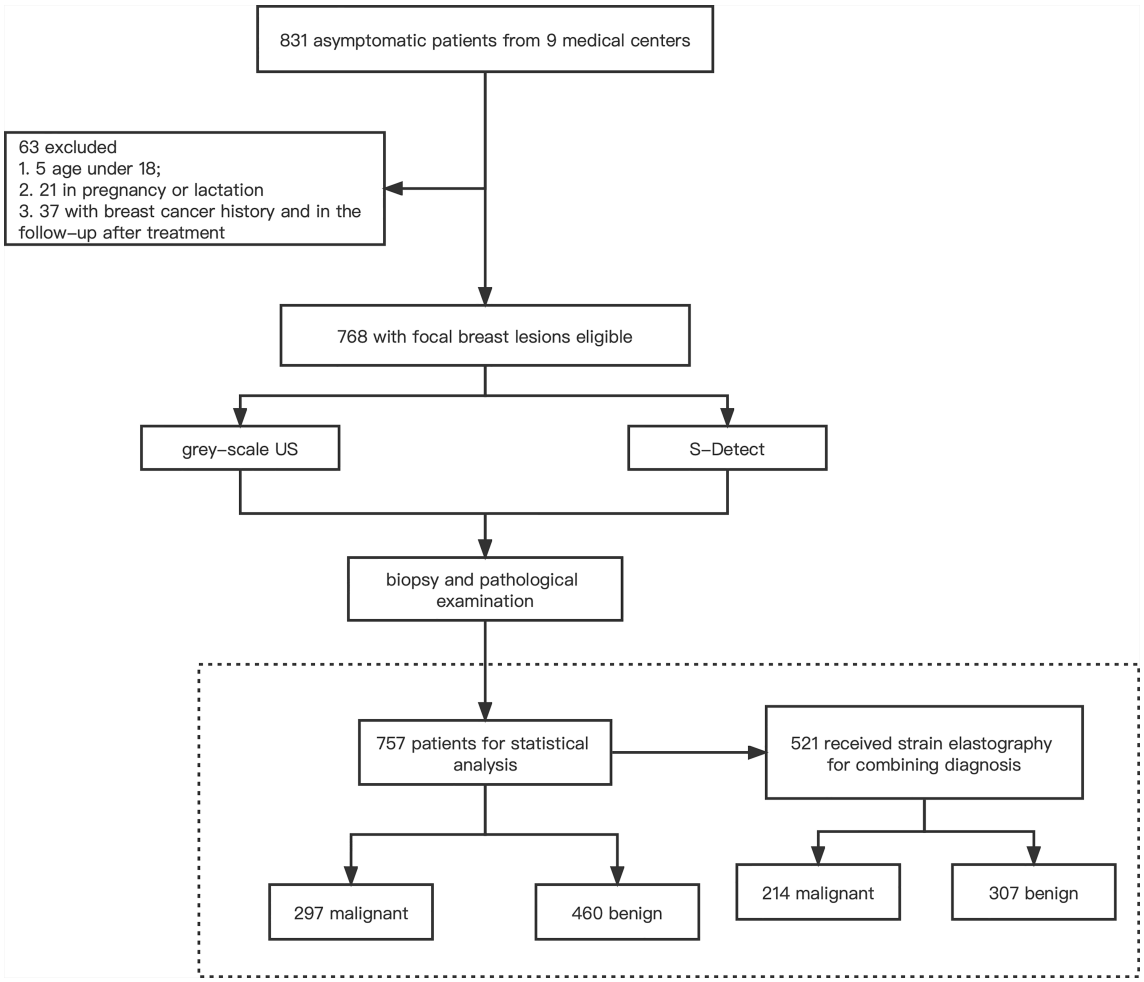

FIGURE 1 | The schematic of the study flow.

great diagnostic performance in dichotomic classification of breast lesion.

Combined Diagnosis of S-Detect™ and Strain Elastography

Among the 757 enrolled patients, 521 patients also received strain elastography and had SR values. The results of the 521 patients were further used for combining diagnosis of S-Detect™ and elastography. The results of S-Detect™ and strain elastography were combined through the multiple regression method. The equation for combining diagnosis was logit(Y) = −3.80213 + 0.72155 * SR + 2.78571 * S-Detect (0/1) (Y: predictive percentage), and it was illustrated as a nomogram (**Figure 3**). The best threshold of predictive percentage for the nomogram was 0.4304. As presented in **Table 1**, under the best threshold for the combined diagnosis, the diagnostic performance was significantly enhanced after combination with an AUC value of 0.860, higher than that of S-Detect ($p < 0.0001$). The combined diagnosis also presented higher specificity and PPV (specificity, 73.93% [68.60%–78.78%] vs. 69.31% [63.78%–74.45%], p [combination vs. E-breast] < 0.0001; PPV 70.96% vs. 67.71%, p [combination vs. S-Detect] = 0.005). The ROC curves for combining results, S-Detect, and the conventional US are presented in **Figure 4**. A typical case that was misdiagnosed by the conventional US and corrected by combining diagnosis is demonstrated in **Figure 5**.

The Differences in Diagnostic Performances Among Groups 1–4

As shown in **Table 3**, for Group 1, S-Detect presented higher specificity than the conventional US, but the sensitivity showed no difference (p[Sp] = 0.016; p[Se] = 0.25). The AUC value of S-Detect was significantly higher than the conventional US (0.89 [0.84–0.93] vs. 0.81 [0.75–0.86], p = 0.0013). For Group 2, S-Detect also had lower sensitivity and higher specificity than the conventional US (p[Sp] = 0.0001; p[Se] < 0.0001), and the AUC value showed no difference (0.79 [0.72–0.85] vs. 0.84 [0.77–0.89], p = 0.1791). For Group 3, S-Detect presented higher specificity

TABLE 1 | Clinical information and pathological results of the patients.

Clinical information	
Age (year)	
Median (25% - 75% quartiles)	47.5 (38.00 - 56.00)
Tumor Size (cm)	
Median (25% - 75% quartiles)	1.50 (1.00 - 2.20)
Histories of benign disease	
No	654
Papillary tumors	2
Fibroma	68
Atypical hyperplasia	33
Family histories	
No	748
Yes	9
Menopause	
No	561
Yes	196
Pathologic findings	
Benign	460
Fibroma	205
Adenosis	173
Papillary tumors	43
Sclerosing adenopathy	9
Inflammatory lesions	19
Phyllodes tumor	11
Malignant	297
Invasive ductal carcinoma	213
Invasive lobular carcinoma	7
In situ ductal carcinoma	41
Mucinous carcinoma	8
Solid papillary carcinoma	6
Micro-papillary carcinoma	2
Encapsulated papillary carcinoma	1
Adenoid-cystic carcinoma	3
Neuroendocrine carcinoma	3
tubular carcinoma	3
Malignant phyllodes tumor	6
Lymphoma	3
Leukemia	1

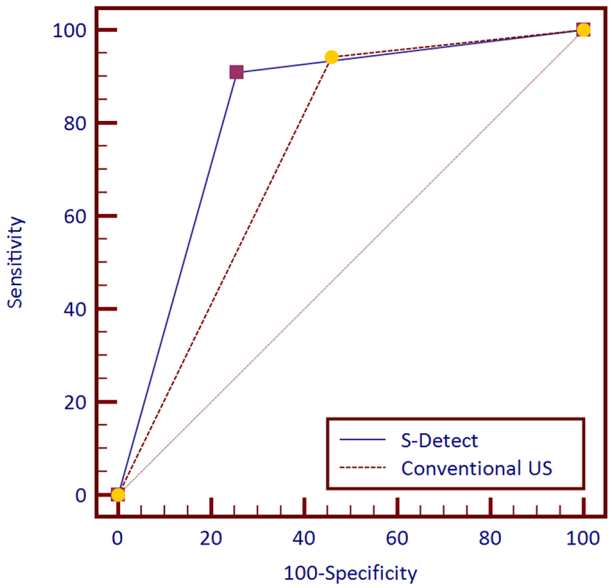

FIGURE 2 | Receiver operating characteristic (ROC) curves of S-Detect and the conventional ultrasound (US) for 757 patients.

than the conventional US, but the sensitivity showed no difference (p[Sp] = 0.016; p[Se] = 0.25). The AUC value of S-Detect was significantly higher than that of the conventional US (0.85 [0.76–0.92] vs. 0.68 [0.58–0.78], p = 0.0014). For Group 4, S-Detect had lower sensitivity and higher specificity than the conventional US (p[Sp] = 0.0001; p[Se] = 0.035), and it also presented a higher AUC value (0.75 [0.69–0.80] vs. 0.66 [0.60–0.72], p = 0.0038). In all groups, S-Detect presented higher specificity than the conventional US, and it also had higher AUC values.

The diagnostic performances of S-Detect and conventional US among the groups were also compared. For the performances of S-Detect in different groups, Group 1, 2, and 3 presented a significantly higher AUC value than Group 4, and others have no differences (0.89 [0.84–0.93], 0.84 [0.77–0.89], 0.85 [0.76–0.92], and 0.75 [0.69–0.80], respectively; p [1 vs. 4] < 0.0001, p [2 vs. 4] = 0.0165, p [3 vs. 4] = 0.0156). Specifically, both S-Detect of Groups 1 and 2 had higher specificity than that of Group 4 (83.87% [77.12%–89.28%], 80.81% [71.66%–88.03%], and 59.59% [51.16%–48.53%], respectively; p [1 vs. 4] < 0.0001, p [2 vs. 4] = 0.0004). For the performances of conventional US in different groups, Groups 1 and 2 had a significantly higher AUC value than Groups 3 and 4 (p [1 vs. 3] = 0.0107, p [1 vs. 4] < 0.0001, p [2 vs. 3] = 0.0036, p [2 vs. 4] < 0.0001). The comparisons in sensitivity, specificity, and AUC values among the four groups are shown in **Table 3**.

TABLE 2 | The diagnostic performances of S-Detect™, conventional US, and combining diagnosis.

x	Sensitivity (%)	Specificity (%)	PPV (%)	NPV (%)	PLR	NLR	AUC
Conventional US[1]	94.28 (90.99–96.63)	54.13 (51.42–60.29)	55.89 (51.42–60.29)	93.61 (89.96–96.23)	2.00 (1.81–2.22)	0.11 (0.07–0.17)	0.74 (0.70–0.77)
S-Detect[1]	91.91 (87.05–93.92)	74.35 (70.10–78.28)	69.59 (64.74–74.13)	92.68 (89.53–95.12)	3.54 (3.02–4.16)	0.12 (0.08–0.18)	0.83 (0.80–0.85)
Elastograohy + S-Detect[2]	88.94 (83.99–92.78)	73.93 (68.60–78.78)	70.96 (65.17–76.28)	90.32 (85.94–93.70)	3.41 (2.81–4.15)	0.15 (0.10–0.22)	0.87 (0.84–0.90)

PPV, positive predictive value; NPV, negative predictive value; PLR, positive likelihood ratio; NLR, negative likelihood ratio; AUC, area under the receiver operating characteristics; US, ultrasound.

[1]*Results for 757 patients.*

[2]*Results for 521 patients.*

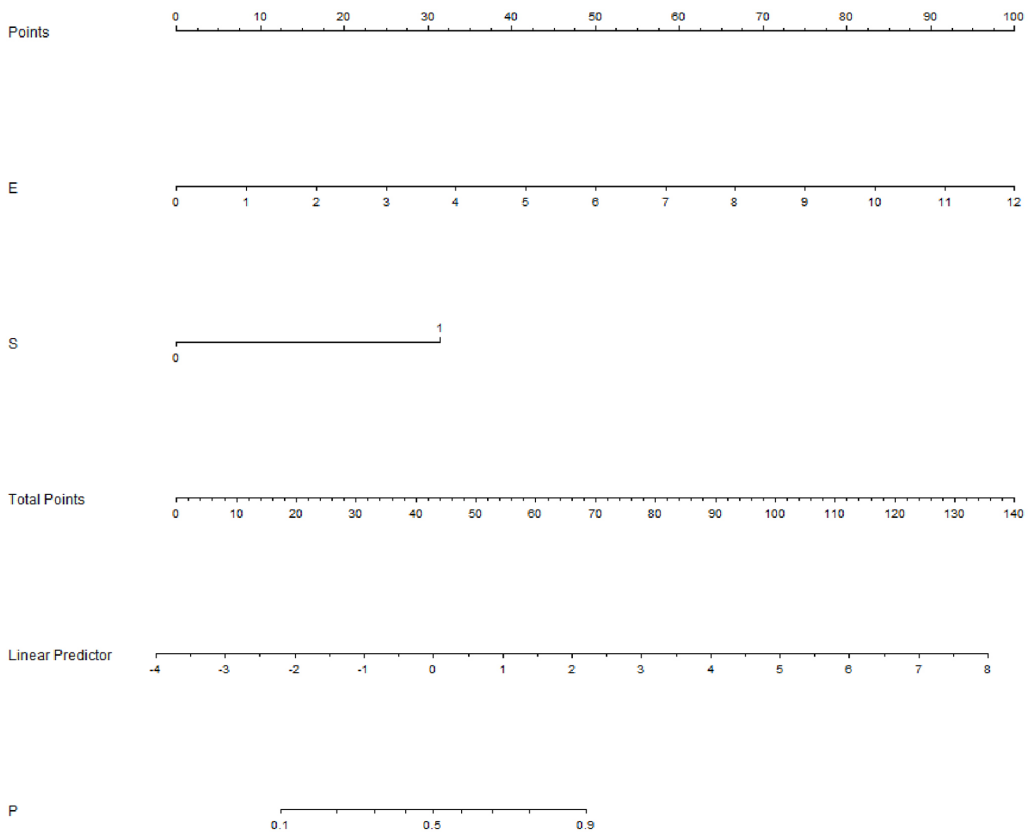

FIGURE 3 | Nomogram of combined diagnosis. E, elastography; strain ratio (SR) value; S, S-Detect result; P, predictive percentage.

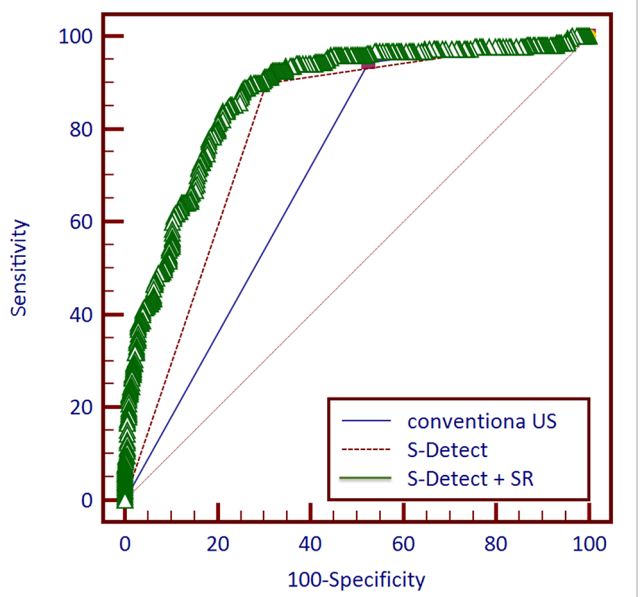

FIGURE 4 | Receiver operating characteristic (ROC) curves of three methods and combined diagnosis for 521 patients.

DISCUSSION

US has enjoyed great popularity in China as one of the most essential imaging methods for detecting breast cancer. It usually presents very high sensitivity but relatively low specificity (8). The low specificity and PPV of breast US causing high recall rate and unnecessary biopsies in breast screening have been major problems in the clinical utilization of US (33, 34). Efforts have been made to conquer this problem by applying other US modalities in addition to the grayscale US. In this multicenter study, we investigated the value of CAD and elastography in strengthening the diagnostic performance of US for the asymptomatic breast lesions detected by opportunistic screening US. The recruited patients in this study underwent breast US screening and were recalled for the diagnostic US. With the addition of S-Detect and the combination of S-Detect™ and elastography, the performance of US can be significantly enhanced, especially the specificity and PPV. These US techniques are promising in further clinical promotion for breast imaging, as an important adjunct to the routine US in detecting and diagnosing breast cancer.

In recent years, several self-developed or commercialized CAD systems for breast US based on DL methods have been developed and shown good performance in the detection, segmentation, and diagnosis of breast lesions (35, 36). S-

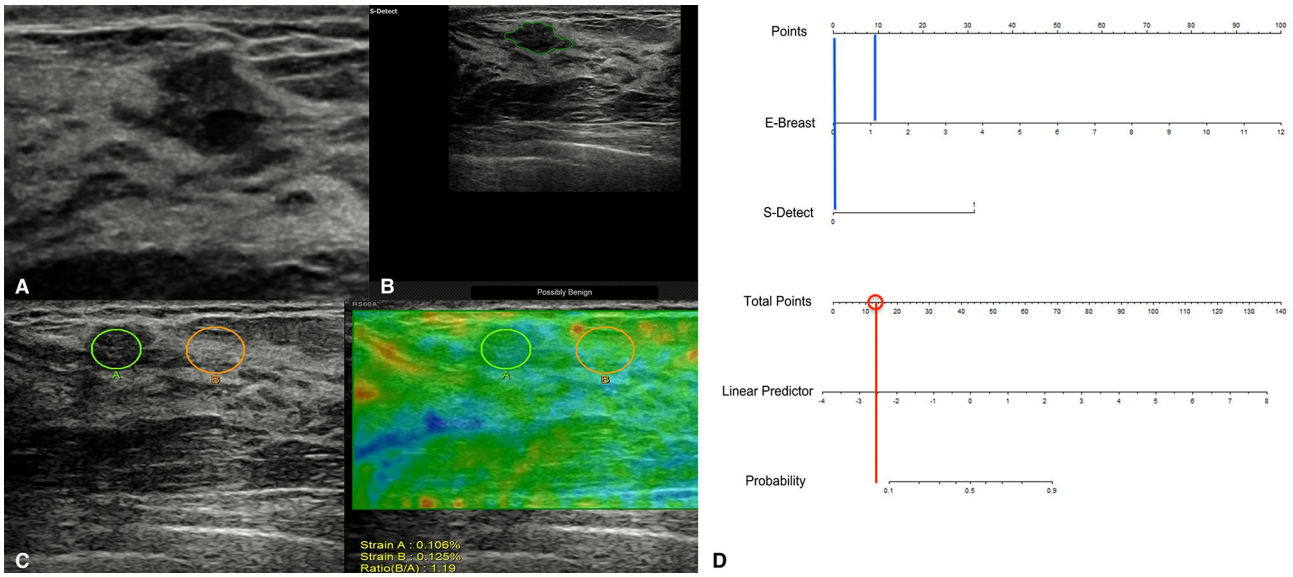

FIGURE 5 | A typical case of a 45-year-old patient with a breast lesion detected and classified as BI-RADS 4a by screening ultrasound (US) (**A**; grayscale of the US). S-Detect classified it as possibly benign **(B)**, and its strain ratio (SR) was 1.19 **(C)**. According to the nomogram, the point for SR result was near 10, and the point for S-Detect was 0 (blue vertical lines), thus acquiring a total score of 10 for the lesion and a predictive percentage of less than 0.1 **(D)**. The pathological result for the lesion was adenosis.

Detect™ is one of the DL-based CAD systems, constructed on convolutional neural networks (CNN) and trained by a large number of images of breast masses. Free from impact from handcrafted features, the CAD system can make segmentation and dichotomic classification of breast lesions automatically. According to previous studies from 2016 to 2019 about S-Detect™, the commercial CAD system presented outstanding accuracy and specificity in classifying breast lesions, thus holding potentials in enhancing the diagnostic performance of human readers (17–20). In this study, the higher AUC value and specificity of S-Detect™ compared with the conventional US were also verified (AUC, 0.799; specificity, 0.695), similar to previous reports, which also revealed an increment in specificity (0.78–0.90) and AUC value (0.80–0.92). The sensitivity was still maintained at a relatively high level, without statistical decrease. With the use of S-Detect™, unnecessary biopsies can be effectively reduced for those asymptomatic screening breast lesions.

In a common clinical situation, radiologists make a diagnosis of breast lesions by integrating clinical information and comprehensive imaging information. For those patients with typical clinical manifestations, such as severe pain, nipple discharge, and fast-growing nodules, the lesions might be upgraded by radiologists. In terms of the asymptomatic US screening-detected breast lesions, based on the results of our study, we can safely conclude that S-Detect™ is a reliable method in downgrading possibly benign lesions and avoiding unnecessary biopsies, which can be further applied in US screening.

The role of elastography has been established in recent years as an essential assisting method for breast US. A combination of elastography and the conventional US could benefit the diagnosis of breast lesions by improving specificity without lowering sensitivity (37, 38). In this study, we combined the CAD technique and elastography to further enhance the diagnostic performance of US for asymptomatic breast nodules. The combined diagnosis presented higher accuracy and specificity, compared with a single use of S-Detect™ and the conventional US, without lowering sensitivity. Moreover, both S-Detect™ and strain elastography (E-breast) can make objective assessments of breast lesions, independent of the conventional US diagnosis process. The two methods can play a complementary role for each other in collecting diagnostic information of breast nodules. In view of the results of this study, the combination of elastography and S-Detect™ has a significant clinical value in improving the specificity and overall performance of US in classifying the asymptomatic breast lesions, which in turn can reduce unnecessary biopsies for those US-screening-detected lesions. The easy access of the two built-in US techniques may also further facilitate their integration into US operating routine, without increasing workload.

We also compared the diagnostic performances in different groups of medical centers in this study. Based on the results, we can conclude that in most cases, S-Detect presents higher specificity and overall performances than the conventional US, which further validates its feasibility in diagnosing breast lesions. Additionally, due to its considerable accuracy in different regions of China, S-Detect's stability can be recognized in this multicenter study, and it is promising for further clinical promotion. However, significant differences in the AUC values of S-Detect of different regions were detected between groups. These centers also had different performances of conventional

TABLE 3 | The diagnostic performances of S-Detect™ and conventional US in the four groups.

Group	Test	Sensitivity (%)	Specificity (%)	PPV (%)	NPV (%)	PLR	NLR	AUC
Group 1	S-Detect	93.75 (86.01–97.94)	83.87[2] (77.12–89.28)	75.00 (65.34–83.12)	96.30 (91.57–98.79)	5.81 (4.04–8.36)	0.07 (0.03–0.17)	0.89[1] (0.84–0.93)
	Conventional US	95.00 (87.69–98.62)	66.45[4] (58.43–73.83)	59.38 (50.34–67.96)	96.26 (90.70–98.97)	2.83 (2.26–3.55)	0.08 (0.03–0.20)	0.81[3] (0.75–0.86)
Group 2	S-Detect	86.30 (76.25–93.23)	80.81[2] (71.66–88.03)	76.83 (66.20–85.44)	88.89 (80.51–94.54)	4.50 (2.97–6.81)	0.17 (0.09–0.30)	0.84[1] (0.77–0.89)
	Conventional US	100.00[5] (95.07–100.00)	58.59[4] (48.24–68.40)	64.04 (54.51–72.81)	100.00 (93.84–100.00)	2.41 (1.91–3.05)	0.00	0.79[3] (0.72–0.85)
Group 3	S-Detect	96.87 (83.78–99.92)	72.88 (59.73–83.64)	65.96 (50.69–79.14)	97.73 (87.98–99.94)	3.57 (2.34–5.45)	0.04 (0.01–0.30)	0.85[1] (0.76–0.92)
	Conventional US	87.50 (71.01–96.49)	49.15 (35.89–62.50)	48.28 (34.96–61.78)	87.88 (71.80–96.60)	1.72 (1.30–2.28)	0.25 (0.10–0.66)	0.68 (0.58–0.78)
Group 4	S-Detect	90.18 (83.11–94.99)	59.59 (51.16–48.53)	63.13 (55.15–67.62)	88.78 (80.80–94.26)	2.23 (1.82–2.74)	0.16 (0.09–0.29)	0.75 (0.69–0.80)
	Conventional US	92.86 (86.41–96.87)	40.14 (32.15–48.53)	54.17 (46.84–94.70)	88.06 (77.82–94.70)	1.55 (1.35–1.79)	0.18 (0.09–0.36)	0.66 (0.60–0.72)

PPV, positive predictive value; NPV, negative predictive value; PLR, positive likelihood ratio; NLR, negative likelihood ratio; AUC, area under the receiver operating characteristics; US, ultrasound.

[1]AUC value of S-Detect: p (1 vs. 4) < 0.0001, p (2 vs. 4) = 0.0165, p (3 vs. 4) = 0.0157.

[2]Specificity of S-Detect: p (1 vs. 4) < 0.0001, p (2 vs. 4) = 0.0003.

[3]AUC value of the conventional US: p (1 vs. 3) = 0.0107, p (1 vs. 4) < 0.0001, p (2 vs. 3) = 0.0036, p (2 vs. 4) < 0.0001.

[4]Specificity of the conventional US: p (1 vs. 3) = 0.020, p (1 vs. 4) < 0.0001, p (2 vs. 4) = 0.0048).

[5]Sensitivity of the conventional US: p (2 vs. 3) = 0.0023, p (2 vs. 4) = 0.0048.

US. For the centers with better performances of human readers, S-Detect also exhibited higher diagnostic accuracy. This issue was not previously reported in other single-center studies of S-Detect. It might be suggested that the training of US operators in the application of CAD is still essential. In the medical centers with better-trained US operators, more standard acquisition of US imaging for the CAD analysis can be realized, thus realizing the better performance of S-Detect.

There existed several limitations in this study. Firstly, the cases included are suspicious lesions found by US. The proportion of invasive ductal carcinoma is relatively high, and further studies are required to evaluate the value of the methods in diagnosing *in situ* ductal carcinoma. Also, we did not take the results of mammography into consideration in this study. The clinical information of the patients could also be included in further studies to construct a more comprehensive diagnostic model.

CONCLUSION

S-Detect™, a CAD system for breast US, presented a good diagnostic performance in classifying asymptomatic breast lesions detected by opportunistic screening, with a higher overall AUC value and specificity than the conventional US. After the results and strain elastography were combined, both of which could provide objective imaging information for breast nodules, the overall performance and specificity could be further improved. Characterized by the aid for screening US in enhancing diagnostic efficacy and reducing unnecessary biopsies, S-Detect™ and its combination with elastography can be further utilized clinically.

DATA AVAILABILITY STATEMENT

The data analyzed in this study is subject to the following licenses/restrictions: the datasets are available from the corresponding author on reasonable request. Requests to access these datasets should be directed to zqlpumch@126.com.

ETHICS STATEMENT

The studies involving human participants were reviewed and approved by the Institutional review board of Peking Union Medical College Hospital. The patients/participants provided their written informed consent to participate in this study.

AUTHOR CONTRIBUTIONS

QlZ, YJ, CZ, and MX contributed to the conception and design of the study. MX, XY, JD, LC, FG, MW, LL, QC, WC, JG, QL, QZh, JL, and QlZ organized the database. CZ and MX performed the statistical analysis. CZ wrote the first draft of

the manuscript. LM and MX wrote sections of the manuscript. QlZ revised the manuscript. All authors contributed to manuscript revision and read and approved the submitted version.

FUNDING

This work was funded by the CAMS Innovation Fund for Medical Sciences (CIFMS) (2020-I2M-C&T-B-033).

REFERENCES

1. Li T, Mello-Thoms C, Brennan PC. Descriptive Epidemiology of Breast Cancer in China: Incidence, Mortality, Survival and Prevalence. *Breast Cancer Res Treat* (2016) 159:395–406. doi: 10.1007/s10549-016-3947-0
2. Rajaram N, Mariapun S, Eriksson M, Tapia J, Kwan PY, Ho WK, et al. Differences in Mammographic Density Between Asian and Caucasian Populations: A Comparative Analysis. *Breast Cancer Res Treat* (2017) 161:353–62. doi: 10.1007/s10549-016-4054-y
3. Independent UK Panel on Breast Cancer Screening. The Benefits and Harms of Breast Cancer Screening: An Independent Review. *Lancet* (2012) 380:1778–86. doi: 10.1016/S0140-6736(12)61611-0
4. Berg WA. Current Status of Supplemental Screening in Dense Breasts. *J Clin Oncol* (2016) 34:1840–3. doi: 10.1200/JCO.2015.65.8674
5. Shen S, Zhou Y, Xu Y, Zhang B, Duan X, Huang R, et al. A Multi-Centre Randomised Trial Comparing Ultrasound vs Mammography for Screening Breast Cancer in High-Risk Chinese Women. *Br J Cancer* (2015) 112:998–1004. doi: 10.1038/bjc.2015.33
6. Pan B, Yao R, Zhu QL, Wang CJ, You SS, Zhang J, et al. Clinicopathological Characteristics and Long-Term Prognosis of Screening Detected Non-Palpable Breast Cancer by Ultrasound in Hospital-Based Chinese Population (2001-2014). *Oncotarget* (2016) 7:76840–51. doi: 10.18632/oncotarget.12319
7. Qiang SS-JS. Current Status and Suitable Mode Evaluation of Breast Carcinoma Screening in Chinese Women. *Med J Peking Union Med Coll Hosp* (2018) 9:298–302. doi: 10.3969/j.issn.1674-9081.2018.04.00
8. Berg WA, Blume JD, Cormack JB, Mendelson EB. Training the ACRIN 6666 Investigators and Effects of Feedback on Breast Ultrasound Interpretive Performance and Agreement in BI-RADS Ultrasound Feature Analysis. *AJR Am J Roentgenol* (2012) 199:224–35. doi: 10.2214/AJR.11.7324
9. Berg WA, Bandos AI, Mendelson EB, Lehrer D, Jong RA, Pisano ED. Ultrasound as the Primary Screening Test for Breast Cancer: Analysis From ACRIN 6666. *JNCI: J Natl Cancer Institute* (2015) 108:djv367. doi: 10.1093/jnci/djv367
10. Calas MJG, Almeida RMVR, Gutfilen B, Pereira WCA. Interobserver Concordance in the BI-RADS Classification of Breast Ultrasound Exams. *Clinics (Sao Paulo)* (2012) 67:185–9. doi: 10.6061/clinics/2012(02)16
11. Lee YJ, Choi SY, Kim KS, Yang PS. Variability in Observer Performance Between Faculty Members and Residents Using Breast Imaging Reporting and Data System (BI-RADS)-Ultrasound, Fifth Edition (2013). *Iran J Radiol* (2016) 13:e28281. doi: 10.5812/iranjradiol.28281
12. Dromain C, Boyer B, Ferré R, Canale S, Delaloge S, Balleyguier C. Computed-Aided Diagnosis (CAD) in the Detection of Breast Cancer. *Eur J Radiol* (2013) 82:417–23. doi: 10.1016/j.ejrad.2012.03.005
13. Chan HP, Samala RK, Hadjiiski LM. CAD and AI for Breast Cancer-Recent Development and Challenges. *Br J Radiol* (2020) 93:20190580. doi: 10.1259/bjr.20190580
14. Munir K, Elahi H, Ayub A, Frezza F, Rizzi A. Cancer Diagnosis Using Deep Learning: A Bibliographic Review. *Cancers (Basel)* (2019) 11:1235. doi: 10.3390/cancers11091235
15. Sheth D, Giger ML. Artificial Intelligence in the Interpretation of Breast Cancer on MRI. *J Magn Reson Imaging* (2020) 51:1310–24. doi: 10.1002/jmri.26878
16. Chen CM, Chou YH, Han KC, Hung GS, Tiu CM, Chiou HJ, et al. Breast Lesions on Sonograms: Computer-Aided Diagnosis With Nearly Setting-Independent Features and Artificial Neural Networks. *Radiology* (2003) 226:504–14. doi: 10.1148/radiol.2262011843
17. Cho E, Kim EK, Song MK, Yoon JH. Application of Computer-Aided Diagnosis on Breast Ultrasonography: Evaluation of Diagnostic Performances and Agreement of Radiologists According to Different Levels of Experience. *J Ultrasound Med* (2018) 37:209–16. doi: 10.1002/jum.14332
18. Di Segni M, de Soccio V, Cantisani V, Bonito G, Rubini A, Di Segni G, et al. Automated Classification of Focal Breast Lesions According to S-Detect: Validation and Role as a Clinical and Teaching Tool. *J Ultrasound* (2018) 21:105–18. doi: 10.1007/s40477-018-0297-2
19. Kim K, Song MK, Kim EK, Yoon JH. Clinical Application of S-Detect to Breast Masses on Ultrasonography: A Study Evaluating the Diagnostic Performance and Agreement With a Dedicated Breast Radiologist. *Ultrasonography* (2017) 36:3–9. doi: 10.14366/usg.16012
20. Zhao C, Xiao M, Jiang Y, Liu H, Wang M, Wang H, et al. Feasibility of Computer-Assisted Diagnosis for Breast Ultrasound: The Results of the Diagnostic Performance of S-Detect From a Single Center in China. *Cancer Manag Res* (2019) 11:921–30. doi: 10.2147/CMAR.S190966
21. Zhao C, Xiao M, Li J, Zhang J, Liu H, Wang M, et al. Diagnostic Value of Breast Lesions Between Deep Learning-Based Computer-Aided Diagnosis System and Experienced Radiologists: Comparison the Performance Between Symptomatic and Asymptomatic Patients. *Front Oncol* (2020) 10:1070. doi: 10.3389/fonc.2020.01070
22. Barr RG, Nakashima K, Amy D, Cosgrove D, Farrokh A, Schafer F, et al. WFUMB Guidelines and Recommendations for Clinical Use of Ultrasound Elastography: Part 2: Breast. *Ultrasound Med Biol* (2015) 41:1148–60. doi: 10.1016/j.ultrasmedbio.2015.03.008
23. Thittai AK, Yamal JM, Ophir J. Small Breast Lesion Classification Performance Using the Normalized Axial-Shear Strain Area Feature. *Ultrasound Med Biol* (2013) 39:543–8. doi: 10.1016/j.ultrasmedbio.2012.10.011
24. Thittai AK, Galaz B, Ophir J. On the Advantages of Imaging the Axial-Shear Strain Component of the Total Shear Strain in Breast Tumors. *Ultrasound Med Biol* (2012) 38:2031–7. doi: 10.1016/j.ultrasmedbio.2012.06.011
25. Carlsen JF, Ewertsen C, Lönn L, Nielsen MB. Strain Elastography Ultrasound: An Overview With Emphasis on Breast Cancer Diagnosis. *Diagnostics (Basel)* (2013) 3:117–25. doi: 10.3390/diagnostics3010117
26. Itoh A, Ueno E, Tohno E, Kamma H, Takahashi H, Shiina T, et al. Breast Disease: Clinical Application of US Elastography for Diagnosis. *Radiology* (2006) 239:341–50. doi: 10.1148/radiol.2391041676
27. Magny SJ, Shikhman R, Keppke AL. *Breast Imaging Reporting and Data System, StatPearls, StatPearls PublishingCopyright © 2021*. Treasure Island (FL: StatPearls Publishing LLC. (2021).
28. Lee SH, Chung J, Choi HY, Choi SH, Ryu EB, Ko KH, et al. Evaluation of Screening US-Detected Breast Masses by Combined Use of Elastography and Color Doppler US With B-Mode US in Women With Dense Breasts: A Multicenter Prospective Study. *Radiology* (2017) 285:660–9. doi: 10.1148/radiol.2017162424
29. DeLong ER, DeLong DM, Clarke-Pearson DL. Comparing the Areas Under Two or More Correlated Receiver Operating Characteristic Curves: A Nonparametric Approach. *Biometrics* (1988) 44:837–45. doi: 10.2307/2531595
30. Fan L, Strasser-Weippl K, Li J-J, St Louis J, Finkelstein DM, Yu K-D, et al. Breast Cancer in China. *Lancet Oncol* (2014) 15:e279–89. doi: 10.1016/S1470-2045(13)70567-9
31. Hanley JA, McNeil BJ. A Method of Comparing the Areas Under Receiver Operating Characteristic Curves Derived From the Same Cases. *Radiology* (1983) 148:839–43. doi: 10.1148/radiology.148.3.6878708
32. Magos L, Lentner C. *Geigy Scientific Tables, Vol. 1. Units of Measurement. Body Fluids. Composition of the Body. Nutrition. 1981, 298 Pp. Vol. 2. Introduction to Statistics. Statistical Tables. Mathematical Formulae. 1982, 241 Pp. Vol. 3. Physical Chemistry. Composition of the Blood. Haematology. Human Somatometric Data. 1984, 359 Pp. Vol. 4. Biochemistry. Metabolism of Xenobiotics. Inborn Error of Metabolism. Pharmacogenetics and Ecogenetics. 1986, 330 Pp*. Ciba-Geigy, Basel, £ 12.50 each volume: Distributed in UK by Farrand Press, Wiley Online Library (1987).

33. Nothacker M, Duda V, Hahn M, Warm M, Degenhardt F, Madjar H, et al. Early Detection of Breast Cancer: Benefits and Risks of Supplemental Breast Ultrasound in Asymptomatic Women With Mammographically Dense Breast Tissue. *A Syst Rev BMC Cancer* (2009) 9:335. doi: 10.1186/1471-2407-9-335
34. Sprague BL, Stout NK, Schechter C, van Ravesteyn NT, Cevik M, Alagoz O, et al. Benefits, Harms, and Cost-Effectiveness of Supplemental Ultrasonography Screening for Women With Dense Breasts. *Ann Intern Med* (2015) 162:157–66. doi: 10.7326/M14-0692
35. Moon WK, Lee YW, Ke HH, Lee SH, Huang CS, Chang RF. Computer-Aided Diagnosis of Breast Ultrasound Images Using Ensemble Learning From Convolutional Neural Networks. *Comput Methods Programs BioMed* (2020) 190:105361. doi: 10.1016/j.cmpb.2020.105361
36. Zhang E, Seiler S, Chen M, Lu W, Gu X. BIRADS Features-Oriented Semi-Supervised Deep Learning for Breast Ultrasound Computer-Aided Diagnosis. *Phys Med Biol* (2020) 190:125005. doi: 10.1088/1361-6560/ab7e7d
37. Berg WA, Cosgrove DO, Doré CJ, Schäfer FK, Svensson WE, Hooley RJ, et al. Shear-Wave Elastography Improves the Specificity of Breast US: The BE1 Multinational Study of 939 Masses. *Radiology* (2012) 262:435–49. doi: 10.1148/radiol.11110640
38. Stachs A, Hartmann S, Stubert J, Dieterich M, Martin A, Kundt G, et al. Differentiating Between Malignant and Benign Breast Masses: Factors Limiting Sonoelastographic Strain Ratio. *Ultraschall Med* (2013) 34:131–6. doi: 10.1148/radiol.11110640

Conflict of Interest: The authors declare that the research was conducted in the absence of any commercial or financial relationships that could be construed as a potential conflict of interest.

Publisher's Note: All claims expressed in this article are solely those of the authors and do not necessarily represent those of their affiliated organizations, or those of the publisher, the editors and the reviewers. Any product that may be evaluated in this article, or claim that may be made by its manufacturer, is not guaranteed or endorsed by the publisher.

frontiers in Oncology

ORIGINAL RESEARCH
published: 21 March 2022
doi: 10.3389/fonc.2022.861151

Association Between Vascular Index Measured *via* Superb Microvascular Imaging and Molecular Subtype of Breast Cancer

Xiao-Yan Zhang[1], Si-Man Cai[1], Li Zhang[1], Qing-Li Zhu[1], Qiang Sun[2], Yu-Xin Jiang[1], Hong-Yan Wang[1†] and Jian-Chu Li[1*†]*

[1] Department of Diagnostic Ultrasound, Peking Union Medical College Hospital, Chinese Academy of Medical Sciences, Beijing, China, [2] Department of Breast Surgery, Peking Union Medical College Hospital, Chinese Academy of Medical Sciences, Beijing, China

OPEN ACCESS

Edited by:
Abhishek Mahajan, Tata Memorial Hospital, India

Reviewed by:
Sven Kurbel, Josip Juraj Strossmayer University of Osijek, Croatia
Abidin Kılınçer, Selçuk University, Turkey
Sungbin Park, Chung-Ang University Hospital, South Korea
Matteo Ghilli, Pisana University Hospital, Italy

***Correspondence:**
Hong-Yan Wang
whychina@126.com
Jian-Chu Li
jianchu.li@163.com

†These authors have contributed equally to this work

Specialty section:
This article was submitted to Cancer Imaging and Image-directed Interventions, a section of the journal Frontiers in Oncology

Received: *24 January 2022*
Accepted: *21 February 2022*
Published: *21 March 2022*

Citation:
Zhang X-Y, Cai S-M, Zhang L, Zhu Q-L, Sun Q, Jiang Y-X, Wang H-Y and Li J-C (2022) Association Between Vascular Index Measured via Superb Microvascular Imaging and Molecular Subtype of Breast Cancer. Front. Oncol. 12:861151. doi: 10.3389/fonc.2022.861151

Background: To determine whether vascular index (VI; defined as the ratio of Doppler signal pixels to pixels in the total lesion) measured *via* superb microvascular imaging in breast cancer correlates with immunohistochemically defined subtype and is able to predict molecular subtypes.

Methods: This prospective study involved 225 patients with 225 mass-type invasive breast cancers (mean size 2.6 ± 1.4 cm, range 0.4~5.9 cm) who underwent ultrasound and superb microvascular imaging (SMI) at Peking Union Medical College Hospital before breast surgery from December 2016 to June 2018. The correlations between primary tumor VI measured *via* SMI, clinicopathological findings, and molecular subtype were analyzed. The performance of VI for prediction of molecular subtypes in invasive breast cancer was investigated.

Results: The median VI of the 225 tumors was 7.3% (4.2%~11.8%) (range 0%~54.4%). Among the subtypes of the 225 tumors, 41 (18.2%) were luminal A, 91 (40.4%) were luminal B human epidermal growth factor receptor-2 (HER-2)-negative, 26 (11.6%) were luminal B HER-2-positive, 17 (7.6%) were HER-2-positive, and 50 (22.2%) were triple-negative, and the corresponding median VI values were 5.9% (2.6%~11.6%) (range 0%~47.1%), 7.3 (4.4%~10.5%) (range 0%~29.5%), 6.3% (3.9%~11.3%) (range 0.6%~22.2%), 8.2% (4.9%~15.6%) (range 0.9%~54.4%), and 9.2% (5.1%~15.3%) (range 0.7%~32.9%), respectively. Estrogen receptor (ER) negativity, higher tumor grade, and higher Ki-67 index (≥20%) were significantly associated with a higher VI value. Tumor size, ER status, and Ki-67 index were shown to independently influence VI. A cutoff value of 4.1% yielded 79.9% sensitivity and 41.5% specificity with an area under the receiver operating characteristic curve (AUC) of 0.58 for predicting that a tumor was of the luminal A subtype. A cutoff value of 16.4% yielded 30.0% sensitivity and 90.3% specificity with an AUC of 0.60 for predicting a triple-negative subtype.

Conclusions: VI, as a quantitative index obtained by SMI examination, could reflect histologic vascular changes in invasive breast cancer and was found to be higher in more biologically aggressive breast tumors. VI shows a certain degree of correlation with the molecular subtype of invasive breast cancer and plays a limited role in predicting the luminal A with high sensitivity and triple-negative subtype with high specificity.

Keywords: breast cancer, molecular subtype, ultrasonography, superb microvascular imaging, vascular index

INTRODUCTION

Breast cancer is the cancer type with the highest prevalence and the second highest cancer-related premature mortality rate among women worldwide (1). According to the 12th St. Gallen International Expert Consensus, breast cancer is categorized into five subtypes: luminal A, luminal B human epidermal growth factor receptor-2 (HER-2)-positive, luminal B HER-2-negative, HER-2-enriched, and triple-negative based on the expression status of the estrogen receptor (ER), progesterone receptor (PR), HER-2-positive, and Ki-67 index (2). Owing to the different molecular classifications, along with tumor size, tumor grade, and nodal status, breast cancer is a heterogeneous disease in biological behavior and prognosis (3). ER/PR-positive cancers are usually low grade and less aggressive. Luminal A and B cancers account for approximately 70% of breast cancers with positive hormone receptors. Generally speaking, luminal A cancers are low grade with the best prognosis among all subtypes. Luminal B cancers tend to be higher grade and have a worse prognosis than luminal A. HER-2 overexpression is associated with aggressive clinical course and poor prognosis (4). Triple-negative breast cancers (TNBCs), which accounted for about 15%–20% of breast cancers (5), are in general high grade and associated with a poor prognosis (6).

The formation of neovascularization and the increase of blood flow are the basis of cancer cell growth. Tumors cannot exceed 2 mm^3 without vascular support (7). Angiogenesis in breast cancer is a well-established driver of cancer aggressiveness, therapy resistance, and poor prognosis (8, 9). Color Doppler ultrasound (US) imaging is the primary noninvasive modality for the vasculature evaluation of breast lesions. High-grade tumors usually have abundant vasculature, while low-grade tumors may have no demonstrable vascularization on Doppler US (10). Superb microvascular imaging (SMI; Canon Medical Systems) is a novel feasible microflow imaging technique applying multidimensional wall filtering systems that could improve sensitivity for low-flow tiny vessels and quantitatively assess tumor vascularity *via* measuring vascular index (VI) without the injection of contrast agents. VI was defined as the ratio of Doppler signal pixels to pixels in the total lesion measured *via* SMI. VI measured *via* SMI was a highly reproducible and objective quantitative parameter to estimate the degree of vascularity in breast lesions (11). Increased microvessel proliferation, an indicator of angiogenesis, was significantly correlated with negative ER status and basal-like phenotype in breast cancer (12–15). Previous studies showed that VI values of malignant breast lesions were significantly higher than those in benign breast lesions, and the combination of VI values with conventional B-mode US can enhance the diagnostic performance in differentiating benign from malignant breast masses (11, 16–19). However, the correlation between VI measured by SMI and the molecular subtypes in invasive breast cancer and the performance of VI for prediction of molecular subtypes in invasive breast cancer has not been investigated.

Therefore, the purpose of this study was to determine 1) whether a correlation exists between VI measured *via* SMI and the molecular subtype of invasive breast cancer defined by the St. Gallen International Expert Consensus and 2) whether VI could predict the molecular subtype of the invasive breast cancer.

Abbreviations: TNBCs, triple-negative breast cancers; ER, estrogen receptor; PR, progesterone receptor; HER-2, human epidermal growth factor receptor-2; FISH, fluorescence *in situ* hybridization; IDC, invasive ductal carcinoma; MVD, microvessel density; PPV, positive predictive value; NPV, negative predictive value; ACC, accuracy; AUC, area under the curve.

MATERIALS AND METHODS

Patients

The institutional review board approved this prospective study, and all patients provided a written informed consent. From December 2016 to June 2018, 482 consecutive female patients with 490 breast lesions who were referred to our hospital underwent US and SMI. Of these patients, 262 were malignant breast lesions. The following inclusion criteria were applied: 1) female patients older than 18 years of age; 2) patients for whom US and SMI screening were performed; 3) lesion size <6 cm (no more than the maximum scope of the probe display); 4) the pathological type was invasive breast cancer. The exclusion criteria were as follows: 1) lesions larger than the probe because the US parameter would be shielded; 2) Patients who received treatment like biopsy, surgery, or neoadjuvant chemotherapy were excluded because these treatments may have altered the blood supply of the breast lesions; 3) Pregnant women were excluded because breast parenchymal changes can also alter the blood flow to the targeted lesions. All patients underwent excision biopsy and were histopathologically examined. A total of 225 patients were finally included; the study flowchart is shown in **Figure 1**. The final pathologic results were considered the diagnostic gold standard. The clinical features of the patients were recorded.

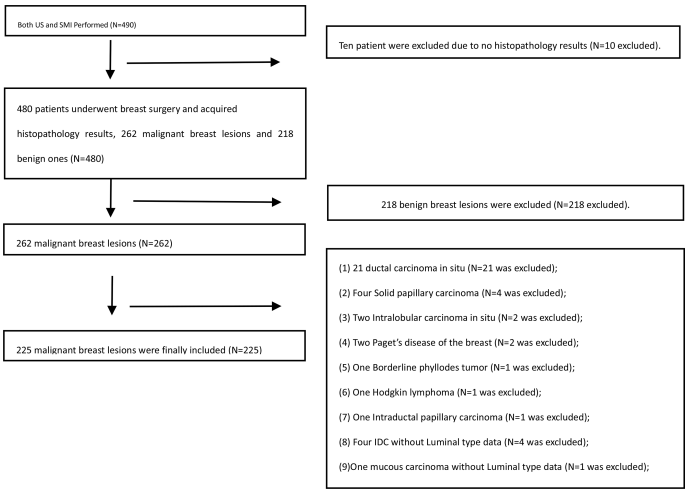

FIGURE 1 | Flowchart of patient selection and inclusion in the study.

Ultrasound and Superb Microvascular Imaging Examination

All lesions were detected using the US Aplio 500 (L14-5, Aplio 500, Canon Medical Systems Corporation, Tokyo, Japan) that could perform US and SMI examination. One radiologist (HW with >15 years of ultrasonic work experience and 2 months of experience in SMI) conducted US and SMI examinations. First, US images of the lesions were obtained, including B-mode and color Doppler images. The tumor size, shape, echogenicity, margin, presence of architectural distortion, acoustic shadowing, microcalcifications, and vascularity were evaluated by conventional US. After conventional US, SMI images were obtained by the same radiologists. SMI examination was performed using color mode. The parameters of the SMI were set to a low-velocity range (1.2~1.6 cm/s) to visualize extremely low-velocity flow with good resolution and a high frame rate with minimal flash artifacts (frame rate, 25~30/s; pulse repetition frequency, 15.4~20.2 kHz; dynamic range, 21 dB). The range of depth was adjusted to 2.5~6 cm according to lesion size, and the detectable width of the linear probe was 6 cm. Three-dimensional (3-D) SMI vasculature volume could be reconstructed from 2-D SMI images scanned using 2-D linear transducers. The 3-D SMI was used as a qualitative guidance to identify the 2-D SMI plane with the most abundant vasculature. The VI (%) was automatically calculated by manually tracing the boundary of the breast lesion on the 2-D SMI image with the most abundant vasculature by a radiologist three times and then averaged. The total inspection time was about 15–20 min.

Molecular Classification of Groups

ER, PR, and HER-2 levels were evaluated using immunohistochemistry (IHC). The Allred scoring system was used to assess ER and PR with a score of more than 2 points being considered positive (20). HER-2 expression was defined as positive when membrane 3+ and a 2+ were analyzed using fluorescence *in situ* hybridization (FISH) to determine a positive or negative status. In addition, Ki67 expression of 14% or more was considered positive, and Ki-67 index was stratified into three groups: "low" (<14%),"intermediate" (14%–20%), and "high" (≥20%) (21, 22). Molecular subtypes identified by St. Gallen International Expert Consensus (2) were as follows:

1. Luminal A: ER-positive and/or PR-positive, HER-2-negative, Ki-67 low (<14%);
2. Luminal B HER-2-negative: ER-positive and/or PR-positive, HER-2-negative, and Ki-67 high (≥14%);
3. Luminal B HER-2-positive: ER-positive and/or PR-positive, HER-2-positive, and any Ki-67 index;
4. HER-2-positive: ER-negative, PR-negative, and HER-2-positive;
5. Triple-negative: ER-negative, PR-negative, and HER-2-negative.

TNM Stage

TNM staging, published by the American Joint Committee on Cancer, uses both clinical and pathologic information of tumor size (T), status of regional lymph nodes (N), and distant metastases (M). The staging combines these factors and stratifies the disease into one of 5 stages (0, I, II, III, and IV) (23).

Nuclear Grade

Modified Bloom Richardson grading system was used for grading the tumors as grades 1, 2, and 3 (24).

Statistical Analysis

Kolmogorov–Smirnov test was used to test the normality of quantitative data. The quantitative data of normal distribution were expressed in means and standard deviations, and *t* test was used for the comparison between the two groups. The non-normality quantitative data were expressed in median (P25~P75), and the Mann–Whitney U rank sum test was used for the comparison between the two groups. The qualitative data were presented as

frequencies. The correlations between the VI of the breast cancer and the clinical, pathological, and immunohistochemical data were evaluated using the Mann–Whitney U rank sum test (two variables), the Kruskal–Wallis test (three or more nominal variables), linear-by-linear association test (three or more ordered variables), and linear regression. Multiple regression analysis was used to determine the clinicopathological and immunohistochemical variables that were independently associated with VI (The VI values were transformed into logarithm). The significant difference in median VI among the five subgroups was calculated using single-factor analysis of variance and a multiple comparison test for parametric data with Bonferroni correction. Receiver operating characteristic (ROC) curve analysis was performed to examine which subgroups could be differentiated from the others on the basis of VI. The diagnostic performance of the optimal cutoff value for differentiating one subgroup from the others was also determined by ROC analysis. All statistical analyses were conducted using SPSS software version 20.0 (IBM, Armonk, NY, USA). Differences with $P < 0.05$ were considered statistically significant.

RESULTS

A total of 482 patients with 490 breast lesions were screened by US and SMI. The final analysis included 225 patients with invasive breast cancers (mean age: 51.3 ± 12.2 years, range 23~83 years). The mean size of the invasive tumors was 2.6 ± 1.4 cm (range 0.4~5.9 cm). The histological classifications of the cancers were as follows: invasive ductal carcinoma (IDC; 210 patients, 93.3%), invasive lobular carcinoma (4 patients, 1.8%), and other specified cancers (11 patients, 4.9%; six mucinous carcinomas, two invasive solid papillary carcinoma, one micro invasive solid papillary carcinoma, one invasive encapsulated papillary carcinoma plus IDC, one sarcoma). The molecular subtypes of the 225 tumors were luminal A in 41 patients (18.2%), luminal B HER-2-negative in 91 patients (40.4%), luminal B HER-2-positive in 26 patients (11.6%), HER-2-positive in 17 patients (7.6%), and triple-negative in 50 patients (22.2%). The clinicopathological findings and results of univariate regression analysis for the 225 breast cancers are summarized in **Table 1**.

TABLE 1 | Correlations between clinicopathological and vascular index (VI) values of breast cancers.

	Number	VI (%)M (25%~75%)	*Z*	*P* value
Size(cm)			-0.819	0.413
≤2	94	7.7 (4.0~13.4)		
>2	131	7.0 (4.4~11.3)		
ER status			-2.361	**0.018**
Positive	158	6.7 (4.0~10.8)		
Negative	67	8.8 (5.1~18.2)		
PR status			-1.835	0.066
Positive	134	6.6 (3.9~10.8)		
Negative	91	8.2 (4.4~14.2)		
HER-2 status			-0.516	0.606
Negative	181	7.4 (4.3~12.1)		
Positive	44	6.7 (4.1~11.6)		
Ki-67 index (%)			-1.650	0.099
<14	45	5.9 (2.7~11.3)		
≥14	180	7.6 (4.4-12.4)		
Ki-67 index (%)			5.563	0.062
<14	45	5.9 (2.7~11.3)		
14~20	20	6.8 (2.6~9.3)		
≥20	160	7.7 (4.5~12.7)		
Ki-67 index (%)			-2.322	**0.020**
<20	65	6.2 (2.7~10.8)		
≥20	160	7.7 (4.5~12.7)		
Histology				
Invasive ductal carcinoma	210	7.5 (4.3~12.1)	2.931	0.231
Invasive lobular carcinoma	4	5.4 (1.5~12.0)		
Others	11	4.8 (1.4~9.5)		
Nuclear grade			6.792	**0.034**
1	32	5.3 (1.8~9.6)		
2	101	7.3 (4.3~12.4)		
3	92	8.2 (4.5~13.7)		
Axillary lymph node metastasis			-0.009	0.992
Absent	138	7.6 (3.8~13.3)		
Present	87	7.0 (4.7~10.6)		
Stage			2.646	0.449
I	66	8.5 (4.1~13.8)		
II	137	7.0 (4.3~11.4)		
III	21	6.5 (4.6~11.8)		
IV	1	11.7		

VI (%)M (25%~75%), Vascular index (%) Median (25%~75%); ER, estrogen receptor; HER-2, human epidermal growth factor receptor-2.
The difference is statistically significant in bold.

ER negativity (Z = -2.166, P = 0.031), higher nuclear grade (Z = 6.792, P = 0.034), and higher Ki-67 index (≥20%) (Z = -2.322, P = 0.020) were significantly associated with higher VI value, whereas the tumor size, PR status, HER-2 status, histology, axillary lymph node metastasis, and TNM stage were not associated with VI value significantly (**Table 1**). VI decreased with the increase of tumor size of the infiltrative breast cancer. The median VI values were 5.9% (2.6%~11.6%), 7.3% (4.4%~10.5%), 6.3% (3.9%~11.3%), 8.2% (4.9%~15.6%), and 9.2% (5.1%~15.3%) for the luminal A, luminal B HER-2-negative, luminal B HER-2-positive, HER-2-positive, and triple-negative subgroups, respectively (**Table 2**). The VI did not differ significantly among the five subgroups (F = 1.855, P = 0.119).

Multiple regression analysis was performed to select independent clinicopathological variables associated with VI in all patients with primary invasive breast cancer. The variables entered into the multivariate models included tumor size (≤2 cm vs. >2 cm), ER status, and Ki-67 expression. Backward regression analysis showed that tumor size, ER status, and Ki-67 index independently influenced VI (**Table 3**).

The median VI was 5.9% (2.6%~11.6%) (range 0%~47.1%) for luminal A tumors (n = 41, 18.2%) and 7.4% (4.2%~11.7%) (range 0~54.4%) for non-luminal A tumors (n = 184, 81.8%) (P = 0.1059). A cutoff VI of 4.1% yielded a sensitivity of 79.9% [95% confidence interval (95% CI), 73.4%~85.4%], a specificity of 41.5% (95% CI, 26.3%~57.9%), positive predictive value (PPV) of 86.0% (95% CI, 82.4%~88.9%), negative predictive value (NPV) of 31.5% (95% CI, 22.4%~42.2%), an accuracy of 72.9%, and an AUC of 0.58 (95% CI, 0.51~0.65) for differentiation of luminal A from non-luminal A subtypes (Z = 1.507, P = 0.0315). The positive likelihood ratio was 2.065 (95% CI, 0.9~1.6) (**Table 4**).

The median VI was 8.2% (4.9%–15.6%) (range 0.9%~54.4%) for HER-2-positive tumors (n = 17, 7.6%) and 7.3% (4.2%~11.7%) (range 0~47.1%) for non-HER-2-positive tumors (n = 208, 92.4%) (P = 0.5052). A cutoff VI of 5.3% yielded a sensitivity of 76.5% (95% CI, 50.1%–93.2%), a specificity of 37.0% (95% CI, 30.4%~44.0%), PPV of 9.0% (95% CI, 7.0%~11.6%), NPV of 95.1% (95% CI, 88.9%~97.9%), an accuracy of 40%, and an AUC of 0.55 (95% CI, 0.48~0.62) for prediction of HER-2-positive tumors (Z = 0.659, P = 0.5099). The positive likelihood ratio was 1.214 (95% CI, 0.9~1.6).

The median VI was 9.2% (5.1%~15.3%) (range 0.7%~32.9%) for triple-negative tumors (n = 50, 22.2%) and 6.8% (4.1%–10.9%) (range 0%~54.4%) for non-triple-negative tumors (n = 175, 77.8%) (P = 0.0298). A cutoff VI of 16.4% yielded a sensitivity of 30.0% (95% CI, 17.9%~44.1%), a specificity of 90.3% (95% CI, 84.9%~94.24%), PPV of 46.9% (95% CI, 32.2%~62.1%), NPV of 81.9% (78.9%~84.5%), an accuracy of 76.9%, and an AUC of 0.60 (95% CI, 0.533–0.665) for prediction of triple-negative tumors (Z = 2.151, P = 0.0315). The positive likelihood ratio was 3.093 (95% CI, 1.7~5.7).

DISCUSSION

The major findings of the present study were as follows: 1) VI shows a certain degree of correlation with the molecular subtype in invasive breast cancer; 2) ER negativity, higher tumor grade, and higher Ki-67 index (≥20%) were significantly associated with a higher VI value; (3) Tumor size, ER status, and Ki-67 index were shown to independently influence VI; (4) VI was of value in predicting the luminal A with high sensitivity and PPV and triple-negative type with high specificity and NPV.

Recent studies confirmed the predictive value of microvascular imaging features in the differentiation of breast tumors; malignant breast tumors have a higher VI than benign tumors, and VI could help distinguish malignant from benign breast tumors (16, 17, 19, 25). Accurately assessing the blood flow status in tumor can provide a basis for judging the malignancy of tumors. Tumor angiogenesis is variable according to the hormone receptor status and molecular subtype of breast cancer (26). The 3-D power Doppler sonographic vascular features are associated with the molecular subtypes and tumor grades in breast cancer; differences in 3-D power Doppler vascular features among subtypes of IDCs are attributed to the ER status (27). Malignant masses negative for ER or positive for Ki67 had higher microvessel density (MVD) (17). VI was significantly correlated with MVD (17, 28). Our results showed that ER negativity, higher nuclear grade, and higher Ki-67 index (≥20%) were significantly associated with higher VI value in invasive breast tumors, as reported in literature (17). It may be because ER inhibits tumor angiogenesis pathway resulting in decreased tumor vascular proliferation and perfusion. Ki-67 is a nuclear protein being associated with cellular proliferation. Ki-67 plays an important role in the process of cell proliferation and has a positive correlation with vascular endothelial growth factor (VEGF), which could promote angiogenesis. This also causes a mass to grow faster and increase in size with a higher degree. In the condition of high expression of Ki-67, the proliferating cells are accompanied by new blood vessels,

TABLE 2 | VI in different molecular subgroups of breast cancer.

Subgroup	Number (%)	VI (%)	
		M (25%~75%)	Range
Luminal A	41 (18.2)	5.9 (2.6~11.6)	0~47.1
Luminal B HER-2-negative	91 (40.4)	7.3 (4.4~10.5)	0~29.5
Luminal B HER-2-positive	26 (11.6)	6.3 (3.9~11.3)	0.6~22.2
HER-2-positive	17 (7.6)	8.2 (4.9~15.6)	0.9~54.4
Triple-negative	50 (22.2)	9.2 (5.1~15.3)	0.7~32.9
Total	225 (100)	7.3 (4.2~11.8)	0~54.4

Single-factor analysis of variance and Bonferroni correction showed no significant differences among the five subgroups (F = 1.855; P = 0.119) and any two subgroups (P > 0.05). VI (%)M (25%~75%), Vascular index (%) Median (25%~75%); ER, estrogen receptor; HER-2, human epidermal growth factor receptor-2.

TABLE 3 | Multiple regression analysis showing the effect of different characteristics on VI.

Factor	Favorable	Unfavorable	*P* value	β	t value	Lower 0.95	Upper 0.95
ER	Positive	Negative	**0.046**	-0.288	-2.007	-0.571	-0.005
Ki-67	<20%	≥20%	**0.035**	0.355	2.120	0.025	0.684
Size	>2cm	≤2cm	**0.023**	-0.306	-2.287	-0.570	-0.042

ER, estrogen receptor.

with the blood vessel density increasing, resulting in a rich blood flow, a high color Doppler flow imaging (CDFI) grade, and a higher VI (29). A mass with diameter >2 cm is positively correlated with high Ki-67 (30), thus the more tumor vasculature. However, VI is defined as the ratio of Doppler signal pixels to pixels in the total lesion, so in the present study, VI decreased with the increase of tumor size of the infiltrative breast cancer.

VI was not significantly correlated with all the molecular subtypes of invasive breast cancer, this may be due to that one of the most important limitations in this study was that ER, PR, and HER-2 levels were evaluated using IHC. We know very well that this determination represents a surrogate and cannot establish the intrinsic subtype of any given cancer while the correct correlation should have been assessed by genomics (31), with discordance rates between IHC-based markers and gene-based assays as high as 30% (32). Another reason may be due to the high heterogeneity of vasculature in invasive breast cancer, and there is considerable vasculature overlap among different molecular subtypes in invasive breast cancer. The luminal A tumors had lower VI values compared to non-luminal A tumors in the present study, consistent with the study that reported that the luminal A subtype was composed of masses with low vascularity (33) (**Figure 2**). Furthermore, vascular features including the number of vascular trees, total vessel length, number of bifurcations, and

TABLE 4 | Diagnostic performance of VI for luminal A, triple-negative, and HER-2-positive invasive breast cancers.

Molecular subtype	Cut point	Sensitivity (95% CI)	Specificity (95% CI)	PPV (95% CI)	NPV (95% CI)	ACC	AUC (95% CI)
Luminal A	4.1%	79.9% (73.4%~85.4%)	41.5% (26.3%~57.9%)	86.0% (82.4%~88.9%)	31.5% (22.4%~42.2%)	72.9%	0.58 (0.51~0.65)
Triple-negative	16.4%	30.0% (17.9%~44.1%)	90.3% (84.9%~94.24%)	46.9% (32.2%~62.1%)	81.9% (78.9%~84.5%)	76.9%	0.60 (0.53 ~ 0.67)
HER-2	5.3%	76.5% (50.1%~93.2%)	37.0% (30.4%~44.0%)	9.0% (7.0%~11.6%)	95.1% (88.9%~97.9%)	40.0%	0.55 (0.48~0.62)

HER-2, human epidermal growth factor receptor-2.

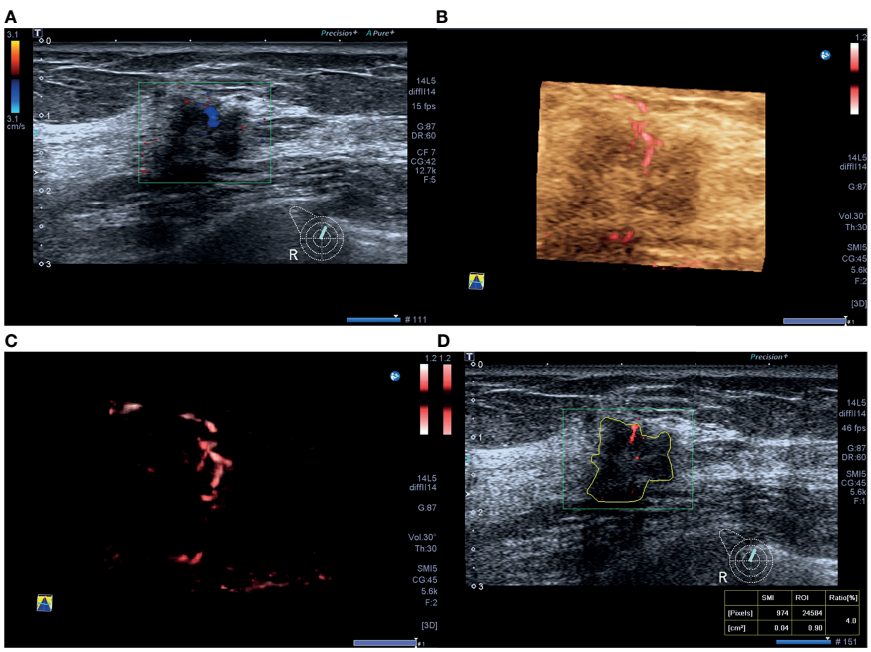

FIGURE 2 | A 46-year-old woman with luminal A invasive ductal cancer [1.7 cm, ER 90%, PR 95%, HER-2(-), Ki-67 10%, nuclear grade 1, T1N0M0]. **(A)** Color Doppler flow imaging image shows linear blood flow signals. **(B, C)** Smart three-dimensional superb microvascular imaging reveals linear blood flow. **(D)** Vascular index was measured on the plane containing the most abundant vasculature with a value of 4.0%.

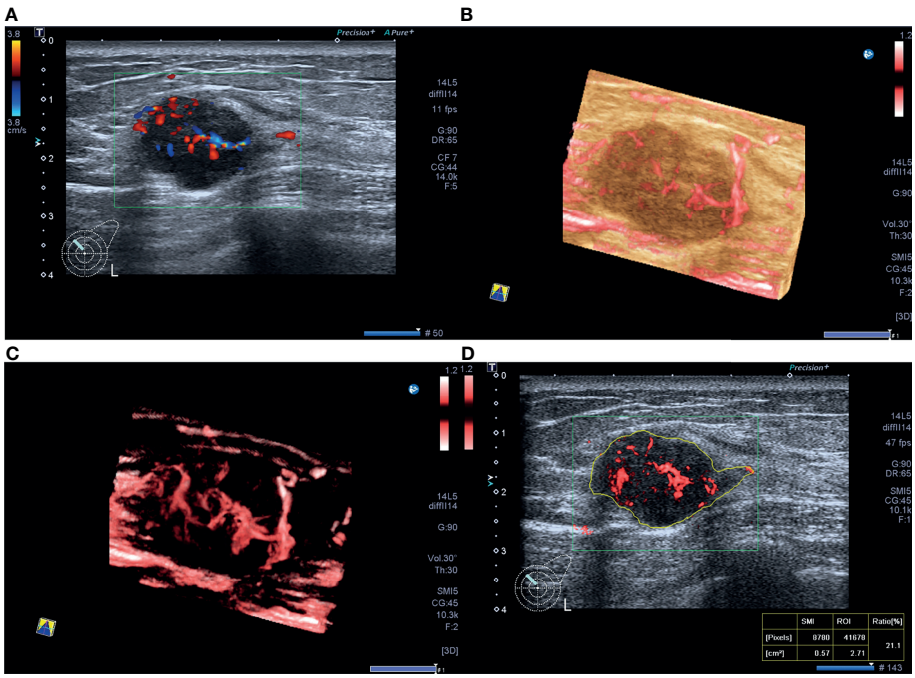

FIGURE 3 | A 40-year-old woman with triple-negative invasive ductal cancer [2.3 cm, ER (-), PR (-), HER-2(-), Ki-67 95%, nuclear grade 2, T2N1M0]. **(A)** Color Doppler flow image shows abundant and disordered blood flow signals. **(B, C)** Smart three-dimensional superb microvascular imaging reveals detailed and abundant vascular architecture with crab claw-like blood flow. **(D)** Vascular index was measured on the plane containing the most abundant vasculature with a value of 21.1%.

vessel-to-volume ratio in luminal type were significantly lower compared to HER-2-enriched or triple-negative types (27). HER-2-enriched cancers more commonly present as Adler grades 2 and 3 on ultrasonography (73.3%) (34). Here, 30.0% TNBCs had abundant blood supply on SMI images in the present study (**Figure 3**), consistent with the previous reports that 32.9%–43.4% TNBCs showed hypervascularity or Adler grades 2 and 3 on color Doppler flow imaging (34, 35). VI had good performance in predicting luminal A type with high sensitivity and PPV and triple-negative type with high specificity and NPV in the present study.

The present study has a few limitations. First, this study included a limited number of patients. Thus, VI value did not reflect the vascularity of all the invasive breast tumors. Second, VI value did not reflect the overall vascularity of the breast lesion. Since the measurements of VI were obtained on a 2-D SMI plane with the abundant vasculature although under the guidance of 3-D SMI, it was impossible to quantify the total volumetric vascularity of the lesion.

CONCLUSIONS

In conclusion, VI, as a quantitative index obtained by SMI examination, could reflect histologic vascular changes in invasive breast cancer and was found to be higher in more biologically aggressive breast tumors. VI shows a certain degree of correlation with the molecular subtype in invasive breast cancer and plays a limited role in predicting the luminal A and triple-negative subtype.

DATA AVAILABILITY STATEMENT

The original contributions presented in the study are included in the article/supplementary material. Further inquiries can be directed to the corresponding authors.

ETHICS STATEMENT

The Ethics Committee of Peking Union Medical College Hospital approved this prospective study. All patients were aware of the examination process and provided written informed consent. There is no identifiable patient information. The patients/participants provided their written informed consent to participate in this study.

AUTHOR CONTRIBUTIONS

Conceptualization, HW; Data curation, XZ, SC, and LZ; Formal analysis, XZ and HW; Investigation, HW; Resources, HW, QZ, JL, QS, and YJ; Writing original draft, XZ. All authors contributed to the article and approved the submitted version.

FUNDING

This work is supported by the Beijing Natural Science Foundation (7202156) and the Teaching Reform Project of Peking Union Medical College (10023201900113).

REFERENCES

1. DeSantis CE, Ma J, Gaudet MM, Newman LA, Miller KD, Goding Sauer A, et al. Breast Cancer Statistics, 2019. *CA Cancer J Clin* (2019) 69(6):438–51. doi: 10.3322/caac.21583
2. Goldhirsch A, Wood WC, Coates AS, Gelber RD, Thurlimann B, Senn HJ, et al. Strategies for Subtypes–Dealing With the Diversity of Breast Cancer: Highlights of the St. Gallen International Expert Consensus on the Primary Therapy of Early Breast Cancer 2011. *Ann Oncol* (2011) 22(8):1736–47. doi: 10.1093/annonc/mdr304
3. Eliyatkin N, Yalcin E, Zengel B, Aktas S, Vardar E. Molecular Classification of Breast Carcinoma: From Traditional, Old-Fashioned Way to A New Age, and A New Way. *J Breast Health* (2015) 11(2):59–66. doi: 10.5152/tjbh.2015.1669
4. Bedard PL, Cardoso F, Piccart-Gebhart MJ. Stemming Resistance to HER-2 Targeted Therapy. *J Mammary Gland Biol Neoplasia* (2009) 14(1):55–66. doi: 10.1007/s10911-009-9116-x
5. Kohler BA, Sherman RL, Howlader N, Jemal A, Ryerson AB, Henry KA, et al. Annual Report to the Nation on the Status of Cancer, 1975-2011, Featuring Incidence of Breast Cancer Subtypes by Race/Ethnicity, Poverty, and State. *J Natl Cancer Inst* (2015) 107(6):djv048. doi: 10.1093/jnci/djv048
6. Yam C, Mani SA , Moulder SL. Targeting the Molecular Subtypes of Triple Negative Breast Cancer: Understanding the Diversity to Progress the Field. *Oncologist* (2017) 22(9):1086–93. doi: 10.1634/theoncologist.2017-0095
7. Folkman J. Tumor Angiogenesis: Therapeutic Implications. *N Engl J Med* (1971) 285(21):1182–6. doi: 10.1056/NEJM197111182852108
8. Semenza GL. HIF-1 Mediates Metabolic Responses to Intratumoral Hypoxia and Oncogenic Mutations. *J Clin Invest* (2013) 123(9):3664–71. doi: 10.1172/JCI67230
9. Fu X, Pereira R, De Angelis C, Veeraraghavan J, Nanda S, Qin L, et al. FOXA1 Upregulation Promotes Enhancer and Transcriptional Reprogramming in Endocrine-Resistant Breast Cancer. *Proc Natl Acad Sci U S A* (2019) 116 (52):26823–34. doi: 10.1073/pnas.1911584116
10. Busilacchi P, Draghi F, Preda L, Ferranti C. Has Color Doppler a Role in the Evaluation of Mammary Lesions? *J Ultrasound* (2012) 15(2):93–8. doi: 10.1016/j.jus.2012.02.007
11. Lee EJ, Chang YW, Oh E, Hwang J, Kim HJ, Hong SS. Reproducibility and Diagnostic Performance of the Vascular Index of Superb Microvascular Imaging in Real-Time Breast Ultrasonography for Evaluating Breast Masses. *Ultrasonography* (2021) 40(3):398–406. doi: 10.14366/usg.20153
12. Stefansson IM, Salvesen HB, Akslen LA. Vascular Proliferation is Important for Clinical Progress of Endometrial Cancer. *Cancer Res* (2006) 66(6):3303–9. doi: 10.1158/0008-5472.CAN-05-1163
13. Bujor IS, Cioca A, Ceausu RA, Veaceslav F, Nica C, Cimpean AM, et al. Evaluation of Vascular Proliferation in Molecular Subtypes of Breast Cancer. *In Vivo* (2018) 32(1):79–83. doi: 10.21873/invivo.11207
14. Kruger K, Stefansson IM, Collett K, Arnes JB, Aas T, Akslen LA. Microvessel Proliferation by Co-Expression of Endothelial Nestin and Ki-67 is Associated With a Basal-Like Phenotype and Aggressive Features in Breast Cancer. *Breast* (2013) 22(3):282–8. doi: 10.1016/j.breast.2012.07.008
15. Foulkes WD, Brunet JS, Stefansson IM, Straume O, Chappuis PO, Begin LR, et al. The Prognostic Implication of the Basal-Like (Cyclin E High/P27 Low/P53+/Glomeruloid-Microvascular-Proliferation+) Phenotype of BRCA1-Related Breast Cancer. *Cancer Res* (2004) 64(3):830–5. doi: 10.1158/0008-5472.CAN-03-2970
16. Zhang XY, Zhang L, Li N, Zhu QL, Li JC, Sun Q, et al. Vascular Index Measured by Smart 3-D Superb Microvascular Imaging can Help to Differentiate Malignant and Benign Breast Lesion. *Cancer Manag Res* (2019) 11:5481–7. doi: 10.2147/CMAR.S203376
17. Park AY, Kwon M, Woo OH, Cho KR, Park EK, Cha SH, et al. A Prospective Study on the Value of Ultrasound Microflow Assessment to Distinguish Malignant From Benign Solid Breast Masses: Association Between Ultrasound Parameters and Histologic Microvessel Densities. *Korean J Radiol* (2019) 20 (5):759–72. doi: 10.3348/kjr.2018.0515
18. Lee EJ, Chang YW. Combination of Quantitative Parameters of Shear Wave Elastography and Superb Microvascular Imaging to Evaluate Breast Masses. *Korean J Radiol* (2020) 21(9):1045–54. doi: 10.3348/kjr.2019.0765
19. Chae EY, Yoon GY, Cha JH, Shin HJ, Choi WJ, Kim HH. Added Value of the Vascular Index on Superb Microvascular Imaging for the Evaluation of Breast Masses: Comparison With Grayscale Ultrasound. *J Ultrasound Med* (2021) 40 (4):715–23. doi: 10.1002/jum.15441
20. Hammond ME, Hayes DF, Dowsett M, Allred DC, Hagerty KL, Badve S, et al. American Society of Clinical Oncology/College of American Pathologists Guideline Recommendations for Immunohistochemical Testing of Estrogen and Progesterone Receptors in Breast Cancer (Unabridged Version). *Arch Pathol Lab Med* (2010) 134(7):e48–72. doi: 10.5858/134.7.e48
21. Goldhirsch A, Winer EP, Coates AS, Gelber RD, Piccart-Gebhart M, Thurlimann B, et al. Personalizing the Treatment of Women With Early Breast Cancer: Highlights of the St Gallen International Expert Consensus on the Primary Therapy of Early Breast Cancer 2013. *Ann Oncol* (2013) 24 (9):2206–23. doi: 10.1093/annonc/mdt303
22. Maisonneuve P, Disalvatore D, Rotmensz N, Curigliano G, Colleoni M, Dellapasqua S, et al. Proposed New Clinicopathological Surrogate Definitions of Luminal A and Luminal B (HER2-Negative) Intrinsic Breast Cancer Subtypes. *Breast Cancer Res* (2014) 16(3):R65. doi: 10.1186/bcr3679
23. Weiss A, Chavez-MacGregor M, Lichtensztajn DY, Yi M, Tadros A, Hortobagyi GN, et al. Validation Study of the American Joint Committee on Cancer Eighth Edition Prognostic Stage Compared With the Anatomic Stage in Breast Cancer. *JAMA Oncol* (2018) 4(2):203–9. doi: 10.1001/jamaoncol.2017.4298
24. Elston CW, Ellis IO. Pathological Prognostic Factors in Breast Cancer. I. The Value of Histological Grade in Breast Cancer: Experience From a Large Study With Long-Term Follow-Up. *Histopathology* (1991) 19(5):403–10. doi: 10.1111/j.1365-2559.1991.tb00229.x
25. Uysal E, Ozturk M, Kilincer A, Koplay M. Comparison of the Effectiveness of Shear Wave Elastography and Superb Microvascular Imaging in the Evaluation of Breast Masses. *Ultrasound Q* (2021) 37(2):191–7. doi: 10.1097/RUQ.0000000000000562
26. Yang WT, Tse GM, Lam PK, Metreweli C, Chang J. Correlation Between Color Power Doppler Sonographic Measurement of Breast Tumor Vasculature and Immunohistochemical Analysis of Microvessel Density for the Quantitation of Angiogenesis. *J Ultrasound Med* (2002) 21(11):1227–35. doi: 10.7863/jum.2002.21.11.1227
27. Chang YC, Huang YS, Huang CS, Chen JH, Chang RF. Intrinsic Subtypes and Tumor Grades in Breast Cancer are Associated With Distinct 3-D Power Doppler Sonographic Vascular Features. *Eur J Radiol* (2014) 83(8):1368–74. doi: 10.1016/j.ejrad.2014.05.005
28. Kim S, Lee HJ, Ko KH, Park AY, Koh J, Jung HK. New Doppler Imaging Technique for Assessing Angiogenesis in Breast Tumors: Correlation With Immunohistochemically Analyzed Microvessels Density. *Acta Radiol* (2018) 59(12):1414–21. doi: 10.1177/0284185118769690
29. Seo SH, Kim KH, Oh SH, Choi Y, Ahn KJ, Lee JY, et al. Ki-67 Labeling Index as a Prognostic Marker in Advanced Stomach Cancer. *Ann Surg Treat Res* (2019) 96(1):27–33. doi: 10.4174/astr.2019.96.1.27
30. Amornsiripanitch N, Nguyen VT, Rahbar H, Hippe DS, Gadi VK, Rendi MH, et al. Diffusion-Weighted MRI Characteristics Associated With Prognostic Pathological Factors and Recurrence Risk in Invasive ER +/HER2- Breast Cancers. *J Magn Reson Imaging* (2018) 48(1):226–36. doi: 10.1002/jmri.25909
31. Perou CM, Sorlie T, Eisen MB, van de Rijn M, Jeffrey SS, Rees CA, et al. Molecular Portraits of Human Breast Tumours. *Nature* (2000) 406 (6797):747–52. doi: 10.1038/35021093
32. Prat A, Pineda E, Adamo B, Galvan P, Fernandez A, Gaba L, et al. Clinical Implications of the Intrinsic Molecular Subtypes of Breast Cancer. *Breast* (2015) 24(Suppl 2):S26–35. doi: 10.1016/j.breast.2015.07.008
33. Huang J, Lin Q, Cui C, Fei J, Su X, Li L, et al. Correlation Between Imaging Features and Molecular Subtypes of Breast Cancer in Young Women (</=30 Years Old). *Jpn J Radiol* (2020) 38(11):1062–74. doi: 10.1007/s11604-020-01001-8
34. Wu T, Li J, Wang D, Leng X, Zhang L, Li Z, et al. Identification of a Correlation Between the Sonographic Appearance and Molecular Subtype of Invasive Breast Cancer: A Review of 311 Cases. *Clin Imaging* (2019) 53:179–85. doi: 10.1016/j.clinimag.2018.10.020
35. Li B, Zhao X, Dai SC, Cheng W. Associations Between Mammography and Ultrasound Imaging Features and Molecular Characteristics of Triple-

Negative Breast Cancer. *Asian Pac J Cancer Prev* (2014) 15(8):3555–9. doi: 10.7314/APJCP.2014.15.8.3555

Conflict of Interest: The authors declare that the research was conducted in the absence of any commercial or financial relationships that could be constructed as a potential conflict of interest.

Publisher's Note: All claims expressed in this article are solely those of the authors and do not necessarily represent those of their affiliated organizations, or those of the publisher, the editors and the reviewers. Any product that may be evaluated in this article, or claim that may be made by its manufacturer, is not guaranteed or endorsed by the publisher.

frontiers in Oncology

CASE REPORT
published: 22 March 2022
doi: 10.3389/fonc.2022.855028

Case Report: Mucocele-Like Tumor of the Breast Associated With Ductal Carcinoma *In Situ*

Ying Jiang[1], *Li Chai*[1], *Dandan Dong*[2], *Aamer Rasheed Chughtai*[3] *and Weifang Kong*[1]*

[1] *Department of Radiology, Sichuan Academy of Medical Sciences and Sichuan Provincial People's Hospital, Chengdu, China,* [2] *Department of Pathology, Sichuan Academy of Medical Sciences and Sichuan Provincial People's Hospital, Chengdu, China,* [3] *Section of Thoracic Imaging, Cleveland Clinic Health System, Cleveland, OH, United States*

Mucocele-like tumor of the breast is histologically characterized as mucin-containing cysts with mucin leaking to the stroma. It could be associated with atypical ductal hyperplasia (ADH), ductal carcinoma *in situ* (DCIS), and invasive ductal carcinoma (IDC). We report a case of mucocele-like tumor of the breast associated with DCIS confirmed by paraffin section. We review the literature and discuss the imaging features, pathology, and clinical management of the lesion. These lesions demonstrate characteristic imaging features, and we especially highlight the MR characteristics, as they have not been well documented. Performing a diagnostic fine-needle aspiration cytology (FNAC) of mucocele-like tumor carries a risk of tumor underestimation; therefore, excision for all mucocele-like tumors is suggested to be the best approach. However, some recent reports recommend close follow-up for patients with low-risk factors who have mucocele-like tumor without atypia on FNAC.

Keywords: mucocele-like tumor, breast, ductal carcinoma *in situ*, case report, imaging

OPEN ACCESS

Edited by:
Abhishek Mahajan, Tata Memorial Hospital, India

Reviewed by:
Fatemeh Derakhshan, Memorial Sloan Kettering Cancer Center, United States
Nebu Abraham George, Regional Cancer Center Thiruvananthapuram, India
Mangala Bopagoda, University of Kelaniya, Sri Lanka

***Correspondence:**
Weifang Kong
ongweifang@med.uestc.edu.cn

Specialty section:
This article was submitted to Cancer Imaging and Image-directed Interventions, a section of the journal Frontiers in Oncology

Received: *14 January 2022*
Accepted: *22 February 2022*
Published: *22 March 2022*

Citation:
Jiang Y, Chai L, Dong D, Chughtai AR and Kong W (2022) Case Report: Mucocele-Like Tumor of the Breast Associated With Ductal Carcinoma In Situ. Front. Oncol. 12:855028. doi: 10.3389/fonc.2022.855028

INTRODUCTION

Mucocele-like tumor of the breast was first described by Rosen in 1986 as mucin containing cysts with extravasated mucin in the stroma (1). Mucocele-like tumor associated with atypical ductal hyperplasia (ADH), ductal carcinoma *in situ* (DCIS), and invasive ductal carcinoma (IDC) were reported subsequently (2–4). In this report, we present imaging features, pathology findings, and clinical management of a 42-year-old woman diagnosed with mucocele-like tumor associated with DCIS. This report aims to illustrate these features and especially highlight the MR characteristics, as these have not been well described previously.

CASE PRESENTATION

A 42-year-old woman accidentally felt a mass in her right breast 2 years ago. The following ultrasound examination reported bilateral cystic dilatation of the ducts (categorized as BI-RADS 2), and routine follow-up was recommended. Two years later, the patient returned to our center right after a heterogeneous irregular mass was revealed on her routine ultrasound follow-up.

Physical examination revealed a 2-cm moderately mobile mass in the right breast with ill-defined margins. Mammography was performed, which demonstrated an irregular high-density mass with microlobulated margin (**Figure 1**). Scattered calcifications were observed in both breasts, but no calcification was found within the lesion. Ultrasound in our center confirmed the presence of a heterogeneous irregular mass with circumscribed margins in the upper outer quadrant of the right breast. Furthermore, the patient underwent an enhanced breast MR examination. The lesion was lobular and showed high signal intensity on T2-weighted sequence, which seemed like clustered cystic lesions. Following Gadolinium enhancement, the lesion showed persistent slight peripheral enhancement but no internal enhancement in all phases.

A fine-needle aspiration cytology (FNAC) was obtained, which showed mucocele-like tumor with ADH, and surgical excision was recommended. A partial right mastectomy was then performed. The frozen section showed mucocele-like tumor with atypical intraductal proliferative lesion and microcalcification. A definitive categorization required evaluation of the entire specimen. Paraffin section demonstrated multiple enlarged cystic ducts containing mucinous secretion and extravasated mucin in the stroma (**Figure 2**). Most of the ducts were lined by flat or columnar epithelium cells, and some micropapillary structures were present. In a few areas, we noticed neoplastic proliferations of epithelial cells with cytological atypia. These atypical ductal proliferations were multiple (homogeneous involvement of more than two ducts) and >2 mm in size. The proliferation foci were composed of monomorphic cells with low-grade cytological atypia, locally growing in micropapillae and cribriform. Microcalcifications were also noted within the enlarged ducts. The tumor measured 2 cm in total size (including the mucin-filled ducts without atypical proliferations), and the resection margins were negative. As for immunohistochemical staining, ER (+), PR (+), HER2-negative (focally weak positive), and Ki67 (positive expression rate 1%) immunohistochemistry stains for markers of myoepithelial cells (SMA, CK5/6, Calponin, and P63) confirmed the presence of myoepithelial cells at the outer layer of the ducts. According to the WHO Classification of Tumors of the Breast (1), the diagnosis of mucocele-like tumor associated with low-grade DCIS was established.

In this case, neither radiotherapy nor chemotherapy was indicated because the foci of intraductal carcinoma were not extensive, and the carcinoma did not involve the margins. According to the China Anti-cancer Association breast cancer diagnosis and treatment guideline and criterion (2), mammography and ultrasound were recommended for follow-up. The initial short-term follow-up interval is 3 months in the first 2 years. Assuming stability during this period, the follow-up interval could be increased to 6 months during the third to the fifth year. Again, assuming stability, the follow-up interval could be increased to 1 year for the remainder of her life. An ultrasound follow-up was

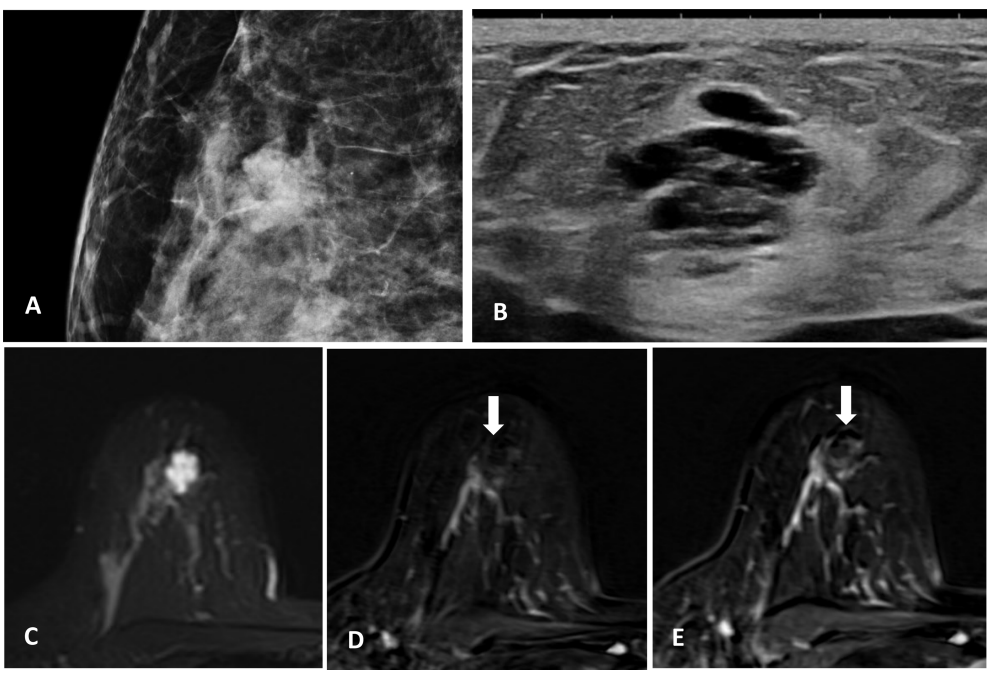

FIGURE 1 | **(A)** Irregular high-density mass with microlobulated margins on mammography, no calcification within the lesion. **(B)** Heterogeneous irregular mass with circumscribed margins on ultrasound. **(C)** MR T2-weighted sequence, the lesion is lobular and shows high signal intensity. **(D, E)** MR-enhanced T1-weighted sequence (immediately after contrast injection and about 6 min delay), the lesion shows persistent slight enhancement at the periphery with no internal enhancement.

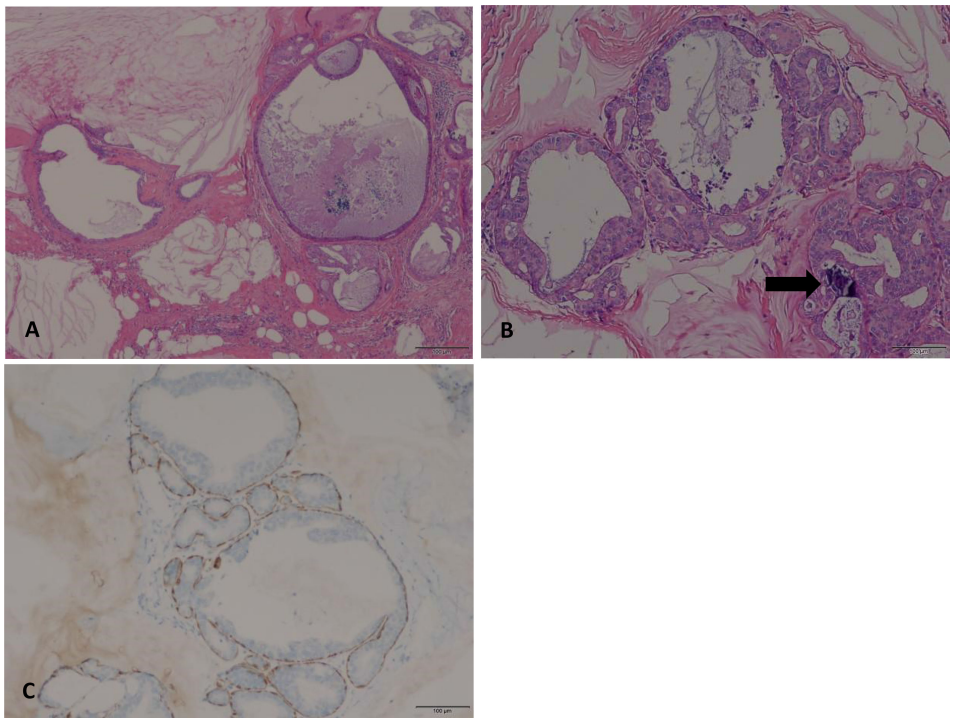

FIGURE 2 | **(A)** Multiple cystic enlarged ducts containing mucinous secretion and extravasated mucin in the stroma (HE, original magnification, 40×). **(B)** Multifocal neoplastic proliferation of epithelial cells (>2mm in size) with low-grade cytological atypia. Microcalcifications are also noted within the enlarged ducts (arrow) (HE, original magnification, 100×). **(C)** Myoepithelial cells at the outer layer of the duct were stained with P63 (original magnification, 100×).

done 3 months after the surgery, and no tumor recurrence was found.

DISCUSSION

Mucocele-like tumor is defined as mucin-containing cysts, and the extravasated mucin is commonly present in the stroma. It was first described by Rosen in 1986 as a benign lesion at first (3). In the years that followed, subsequent studies reported mucocele-like tumor associated with ADH, DCIS, and IDC (4–7), indicating that it has a potential for malignancy. Thus, Weaver et al. (8, 9) concluded that mucocele-like tumor and mucinous carcinoma may represent the two ends of pathological spectrum of mucocele-like lesions of the breast.

Recent reports (10, 11) have reached a common consensus that microcalcifications secreted by mucin were the most characteristic finding on mammography. In our case, the lesion appears as a lobulated mass on mammography. We could not observe any calcification within the lesion, even though the photomicrograph suggests that microcalcifications are present. Perhaps, the microcalcifications are too subtle to be detected on routine mammograms. It must be noted here that mammography findings of mucocele-like tumor are nonspecific, especially when there is lack of calcifications (12). It is therefore challenging to diagnose mucocele-like tumor correctly based on mammography features alone. On ultrasound, previous reports suggest that mucocele-like tumors usually manifest as grouped cysts with or without hyperechoic spots (13). The imaging and pathological features in this case demonstrate aggregated clustered cysts, which is consistent with previous studies.

To our knowledge, the MR features of mucocele-like tumor have not been well documented. This case has several MR features. One of the features is the lobular shape, which is consistent with its histological feature of multiple cystic enlarged ducts. Another feature is persistent slight enhancement at the periphery, which could be explained by the gradual movement of contrast medium into the mucin. These features are similar to those of mucinous carcinomas reported previously. Due to the similar histological structure, we hypothesize that the whole spectrum of mucocele-like lesions could have identical characteristics on MRI. This hypothesis still needs to be verified by more cases.

Although there are several MR features of mucocele-like tumor as mentioned above, mucocele-like tumor still needs to be differentiated from other lesions on imaging. The differential diagnosis includes fibroadenoma, pure cyst, and invasive carcinoma of no special type. Sometimes, it would be difficult to identify mucocele-like tumor and fibroadenoma on MRI, especially myxoid fibroadenoma. Both lesions could be lobular, show high signal intensity on T2 weighted sequence, and have persistent enhancement, but fibroadenoma is more likely to be round or oval in shape with a circumscribed margin.

Furthermore, in a typical fibroadenoma, calcifications are mainly coarse or "popcorn-like" on mammography, and it has a homogeneous echo-texture on ultrasound (14). A pure cyst is easy to distinguish; it is mostly round or oval in shape with circumscribed margins and does not enhance after contrast injection on MRI. As for invasive carcinoma of no special type, calcifications are usually suspicious on mammography, and the margins are not well-circumscribed. Invasive carcinoma of no special type usually enhances fast on initial phase and has a wash-out kinetic curve (15).

Management of mucocele-like tumor is still not standardized. It is difficult to identify mucocele-like tumor correctly by FNAC because of tumor heterogeneity. Moreover, there is possibility of the presence of ADH, DCIS, or IDC. This case was diagnosed with mucocele-like tumor with ADH by FNAC but upgraded to mucocele-like tumor with DCIS after surgical excision. Previous investigations reported the upgrading rates of mucocele-like tumor on FNAC range from 4% to 30% (16, 17). The potential for upgrading led to recommendations for excision of all mucocele-like tumors. However, recent studies showed that the upgrading rate of mucocele-like tumor without atypia on FNAC is relatively low (<5%). Close clinical and radiological follow-up may be a safe alternative to immediate surgical excision for these patients with low risk factors (18).

DATA AVAILABILITY STATEMENT

The original contributions presented in the study are included in the article/supplementary material. Further inquiries can be directed to the corresponding author.

ETHICS STATEMENT

Written informed consent was obtained from the individual for the publication of any potentially identifiable images or data included in this article.

AUTHOR CONTRIBUTIONS

YJ: writing and editing of the manuscript and review of final submission. LC and DD: collection of data, figure preparation, and review of final submission. AC: editing of the manuscript and review of final submission. WK: collection of data, editing of the manuscript, figure preparation, and review of final submission. All authors contributed to the article and approved the submitted version.

REFERENCES

1. Sunil RL, Ian OE, Stuart JS, Tan PH, Van de Vijver MJ. *WHO Classification of Tumors of the Breast. 4th ed*. France: The International Agency for Research on Cancer (2012). p. 88–94.
2. China Anti-Cancer Association and Committee of Breast Cancer Society. China Anti-Cancer Association Breast Cancer Diagnosis and Treatment Guideline and Criterion. *China Oncol* (2021) 31(10):954–1040. doi: 10.19401/j.cnki.1007-3639.2021.10.013
3. Rosen PP. Mucocele-Like Tumors of the Breast. *Am J Surg Pathol* (1986) 10 (7):464–9. doi: 10.1097/00000478-198607000-00003
4. Ro JY, Sneige N, Sahin AA, Silva EG, del Junco GW, Ayala AG, et al. Mucocele-Like Tumor of the Breast Associated With Atypical Ductal Hyperplasia or Mucinous Carcinoma. A Clinicopathologic Study of Seven Cases. *Arch Pathol Lab Med* (1991) 115(2):137–40. doi: 10.1016/S0960-9776(96)90057-0
5. Kulka J, Davies JD. Mucocoele-Like Tumours: More Associations and Possibly Ductal Carcinoma in Situ? *Histopathology* (2010) 22(5):511–2. doi: 10.1111/j.1365-2559.1993.tb00170.x
6. Fisher CJ, Millis RR. A Mucocoele-Like Tumour of the Breast Associated With Both Atypical Ductal Hyperplasia and Mucoid Carcinoma. *Histopathology* (2010) 21(1):69–71. doi: 10.1111/j.1365-2559.1992.tb00345.x
7. Lee JS, Kim HS, Jung J, Lee MC. Mucocele-Like Tumor of the Breast Associated With Ductal Carcinoma in Situ and Mucinous Carcinoma : A Case Report. *J Korean Med Sci* (2001) 16(4):516–8. doi: 10.3346/jkms.2001.16.4.516
8. Weaver MG, Abdul-Karim FW, Al-Kaisi N. Mucocele-Like Tumor of the Breast. A Pathologic Continuum. *Pathol Res Proc* (1993) 189:873–6. doi: 10.1016/S0344-0338(11)81097-6
9. Hamele-Bena D. Mammary Mucocele-Like Lesions. Benign and Malignant. *Am J Surg Pathol* (1996) 20(9):1081–5. doi: 10.1097/00000478-199609000-00005
10. Glazebrook K, Reynolds C. Original Report. Mucocele-Like Tumors of the Breast: Mammographic and Sonographic Appearances. *Am J Roentgenol* (2003) 180(4):949–54. doi: 10.2214/ajr.180.4.1800949
11. Kim JY, Han BK, Choe YH, Ko Y-H. Benign and Malignant Mucocele-Like Tumors of the Breast: Mammographic and Sonographic Appearances. *Ajr Am J Roentgenol* (2005) 185(5):1310–6. doi: 10.2214/AJR.04.0925
12. Farshid G, Pieterse S, Tan PH, Van de Vijver MJ, Tan PH, Robinson J. Mucocele-Like Lesions of the Breast: A Benign Cause for Indeterminate or Suspicious Mammographic Microcalcifications. *Breast J* (2015) 11(1):15–22. doi: 10.1111/j.1075-122X.2005.21437.x
13. Sun MK, Kim HH, Kang DK, Shin HJ, Cho N, Park JM, et al. Mucocele-Like Tumors of the Breast as Cystic Lesions: Sonographic-Pathologic Correlation. *Ajr Am J Roentgenol* (2011) 196(6):1424–30. doi: 10.2214/AJR.10.5028
14. Houssami N, Cheung MN, Dixon JM. Fibroadenoma of the Breast. *Med J Aust* (2001) 174(4):185–8. doi: 10.5694/j.1326-5377.2001.tb143215.x
15. Orel SG, Schnall MD. MR Imaging of the Breast for the Detection, Diagnosis, and Staging of Breast Cancer. *Radiology* (2001) 220(1):13–30. doi: 10.1148/radiology.220.1.r01jl3113
16. Rakha EA, Shaaban AM, Haider SA, Jenkins J, Menon S, Johnson C, et al. Outcome of Pure Mucocele-Like Lesions Diagnosed on Breast Core Biopsy. *Histopathology* (2013) 62(6):894–8. doi: 10.1111/his.12081
17. Carder PJ, Murphy CE, Liston JC. Surgical Excision is Warranted Following a Core Biopsy Diagnosis of Mucocoele-Like Lesion of the Breast. *Histopathology* (2010) 45(2):148–54. doi: 10.1111/j.1365-2559.2004.01920.x
18. Zhang G, Ataya D, Lebda PL, Calhoun BC. Mucocele-Like Lesions Diagnosed on Breast Core Biopsy: Low Risk of Upgrade and Subsequent Carcinoma. *Breast J* (2017) 24(3):314–8. doi: 10.1111/tbj.12929

Conflict of Interest: The authors declare that the research was conducted in the absence of any commercial or financial relationships that could be construed as a potential conflict of interest.

frontiers in Oncology

REVIEW
published: 28 March 2022
doi: 10.3389/fonc.2022.818812

Sentinel Lymph Node Biopsy Mapped With Carbon Nanoparticle Suspensions in Patients With Breast Cancer: A Systematic Review and Meta-Analysis

Yan Jiang[1], Jiayang Li[2], Baolin Chen[1], Yuxiang Bao[1], Chengmin Luo[1], Yi Luo[1], Taolang Li[1], Junyuan Lv[1] and Xiaoming Cheng[1]**

[1] Breast and Thyroid Surgery, Department of General Surgery, The Affiliated Hospital of Zunyi Medical University, Zunyi, China, [2] Drug Clinical Trial Institution, The Affiliated Hospital of Zunyi Medical University, Zunyi, China

OPEN ACCESS

Edited by:
Abhishek Mahajan,
Tata Memorial Hospital, India

Reviewed by:
Stephanie Kacerovsky-Strobl,
Medical University of Vienna, Austria
Zhenggui Du,
Sichuan University, China

***Correspondence:**
Junyuan Lv
junyuanlv@zmu.edu.cn
Xiaoming Cheng
cxm1688@sina.com

Specialty section:
This article was submitted to Cancer Imaging and Image-directed Interventions, a section of the journal Frontiers in Oncology

Received: 20 November 2021
Accepted: 21 February 2022
Published: 28 March 2022

Citation:
Jiang Y, Li J, Chen B, Bao Y, Luo C, Luo Y, Li T, Lv J and Cheng X (2022) Sentinel Lymph Node Biopsy Mapped With Carbon Nanoparticle Suspensions in Patients With Breast Cancer: A Systematic Review and Meta-Analysis. Front. Oncol. 12:818812. doi: 10.3389/fonc.2022.818812

Background: The mapping method represents a crucial factor affecting the rate of sentinel lymph node detection in breast cancer. We carried out this meta-analysis to assess the clinical utility of carbon nanoparticle suspensions (CNSs) in guiding sentinel lymph node biopsy (SLNB) for breast cancer patients.

Methods: Electronic databases, which comprised the China National Knowledge Infrastructure, the Wanfang electronic database, the Cochrane Library, EMBASE, and PubMed, were explored to identify relevant studies from database inception to July 2021 that studied the detection rate of CNSs-guided SLNB. A meta-analysis was performed to generate pooled sensitivity, specificity, positive likelihood ratio (PLR), negative likelihood ratio (NLR), a summary receiver operator characteristic curve (SROC), and a diagnostic odds ratio (DOR).

Results: A total of 33 publications that enrolled 2,171 patients were analyzed. The pooled sensitivity, specificity, PLR, and NLR were 0.93 (95% CI: 0.91–0.95, I^2 = 0.0%), 0.99 (95% CI: 0.98–0.99, I^2 = 56.5%), 42.85 (95% CI: 29.73–61.77, I^2 = 47.0%), and 0.09 (95% CI: 0.07–0.11, I^2 = 0.0%), respectively. The area under the curve (AUC) of the SROC curve was 0.98. There were no significant differences when analyzed based on the dose and site of CNS injection. There was significant publication bias among the included publications based on Deeks' funnel plot [Slope (Bias) = –7.35, P = 0.00]. Nonetheless, the sensitivity analysis identified the results to be reliable and stable.

Conclusion: This meta-analysis highlights the accuracy and feasibility of using CNSs for SLNB in patients with breast cancer. Clinically, the identification and predictive values of CNSs as an optimal tracer for SLNB remains undisputed.

Keywords: meta-analysis, diagnosis, sentinel lymph node biopsy, carbon nanoparticle suspensions, breast cancer

INTRODUCTION

The modern era of breast cancer surgery is progressing towards the direction of minimally invasive treatment. Previously, axillary lymph node dissection (ALND) represented an indispensable treatment component for breast cancer. However, the current standard of care for axillary staging is SLNB. The sentinel lymph node refers to the first axillary lymph node draining the tumor site and may potentially harbor metastatic deposits (1). SLNB is mainly determined by evaluating the SLN status to determine whether ALND is required. SLNB allows for careful selection of patients who are candidates for ALND. SLNB is as effective as ALNB but has the benefits of lower postoperative complications such as arm lymphedema and sensory loss (2–5). The mapping method is a crucial factor that determines the positive and negative detection rates of SLNB in breast cancer. SLNB techniques incorporate the use of either blue dye (BD) or radioisotopes (RI) (6). The RI method requires specialized equipment, authorized radiation protection areas, and nuclear medicine licensing, thus limiting the widespread use of this approach. BD, on the other hand, is a cost-effective method for SLNB but possesses a lower detection rate (7).

The past decade has seen a surge in research in the field of nanomaterials and nanotechnology. Several novel diagnostic and therapeutic techniques in the field of medicine have begun to incorporate nanobiotechnology. CNSs is a 150 nm nanoparticle lymphatic tracer made up of polymeric carbon granules and has been approved for clinical usage by the Chinese Food and Drug Administration (CFDA). CNSs selectively populate the lymphatic system (diameter: 120–500 nm) over the vascular system (diameter: 20–50 nm), given its permeability and molecular size (8). CNSs have received substantial attention over the recent years, especially with regards to their postulated benefits in lymphatic mapping. Thus, the aim of our analysis was to assess the effectiveness of CNSs for SLN mapping in breast cancer.

MATERIALS AND METHODS

Literature Search

A systematic literature search was carried out on the China National Knowledge Infrastructure, the Wanfang electronic database, the Cochrane Library, EMBASE, and PubMed to extract all related papers present from database inception until July 2021. The medical subject heading (MESH) terms used were as follows: breast neoplasm, breast carcinoma, breast tumor, breast cancer, carbon nanoparticle, nano-carbon, carbon nanoparticles suspensions, CNSs, sentinel lymph node biopsy, and SLNB.

Inclusion and Exclusion Criteria

The inclusion criteria were as follows:

1. Patients with breast cancer who had clinically negative lymph nodes.
2. The concurrent use of CNSs and other modalities for SLNB mapping.
3. The availability of diagnostic method and clinicopathological data.
4. The SLNB as the main study topic.
5. The reported primary data were sufficient to calculate totals of true negative (TN), false negative (FN), false positive (FP), and true positive (TP).

The exclusion criteria were as follows:

1. Letters, editorials, review articles, and case reports.
2. Overlapping information between studies.

Data Extraction and Quality Assessment

All studies were reviewed by two independent reviewers in order to extract the relevant data. A third reviewer was consulted to reach a consensus in case of a disagreement. A datasheet containing the following information was compiled: year of publication, author, age, dose of CNSs, injection site, TN, FN, FP, and TP values. The Quality Assessment of Diagnostic Accuracy Studies (QUADAS-2) protocols were referenced for quality assessment of the selected studies (9). These guidelines evaluate the degree of biases in the included studies across four major domains that included flow and timing, reference standard, index test, and patient selection. The highest possible score is 14, which indicates high study quality.

Statistical Analysis

The STATA version 15.1 (Stata Corporation, College Station, Texas, USA) and Meta-Disc version 1.4 Software (XI Cochrane Colloquium; Barcelona, Spain) was utilized for this meta-analysis. The degree of heterogeneity among the studies was estimated using I^2, while heterogeneity itself was assessed with the Chi-square-based Q statistic test. Heterogeneity was interpreted as being statistically significant when I^2 >50% or P <0.05. The fixed-effect model (Mantel–Haenszel) was used in cases of no study heterogeneity. In cases where there was study heterogeneity, a random-effect model (DerSimonian and Laird) was implemented.

Study sensitivity, specificity, PLR, NLR, and DOR were evaluated using a bivariate meta-analysis model. A suitable statistical analysis model was first used to calculate the estimates with the corresponding 95% CI. The AUC and SROC of these models were also determined. A higher diagnostic effect was recognized in results that had an AUC closer to 1.0. Publication bias was determined with the Deek test for funnel plot asymmetry.

RESULTS

Characteristics of Identified Studies

We extracted 277 potentially relevant publications. Of these, 131 duplicates were removed, and 61 were deemed irrelevant based on screening titles and abstracts. A total of 85 remaining full-text articles were then scrutinized for eligibility (**Figure 1**). Another 52 articles were additionally excluded: 7 articles were excluded due to duplicate use of the same data, 7 articles were summary

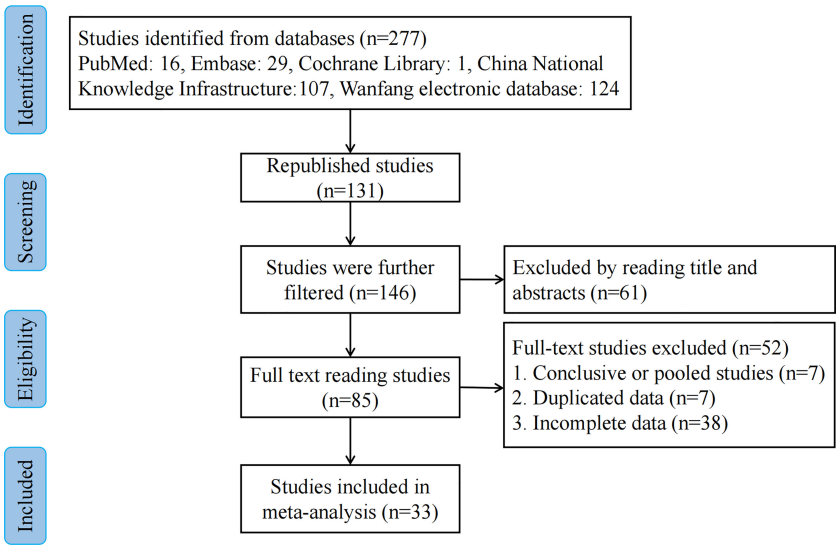

FIGURE 1 | Flowchart of the study selection process.

and summary data, while 38 articles contained incomplete data. Finally, 33 studies (10–42) including 2,171 patients were included in our meta-analysis. The amount of CNSs injected ranged from 0.2 to 2 ml. Peritumoral CNSs injection for SLNB was used in 3 studies, subareolar CNSs injection was used in 15 studies, and both peritumoral and subareolar CNSs injection were used in 14 studies. **Table 1** depicts the characteristics of the identified papers.

Diagnostic Accuracy

Figures 2–6 demonstrate the forest plot of sensitivity, specificity, PLR, NLR, and DOR for CNS in SLNB. The overall pooled sensitivity and specificity of all studies were 0.93 (95% CI: 0.91–0.95, I^2 = 0.0%) and 0.99 (95% CI: 0.98–0.99, I^2 = 56.5%). The overall pooled PLR and NLR were 42.85 (95% CI: 29.73–61.77, I^2 = 47.0%) and 0.09 (95% CI: 0.07–0.11, I^2 = 0.0%), respectively. The pooled DOR was 530.19 (95% CI: 314.70–893.22, I^2 = 0.0%). The SROC curve demonstrated an AUC of 0.98, which indicated excellent diagnostic accuracy (**Figure 7**). Additionally, the left upper quadrant (LUQ) in the likelihood ratio scatter diagram was occupied by summary PLR and NLR, indicating that CNSs was useful in improving the diagnostic accuracy of SLNB in breast cancer (**Figure 8**).

There is controversy over the optimal dose and site of injection for the tracking agents. We compared the combined sensitivity and specificity of SLNB according to different CNSs doses (**Table 2**). For the studies that used a less than or equal to 1 ml injection of CNSs, the combined sensitivity was 0.93 (95% CI: 0.91–0.95, I^2 = 0.0%) and specificity was 0.98 (95% CI: 0.97–0.99, I^2 = 63.0%) (**Figure S1**). For the studies that used a 2 ml injection of CNSs, the combined sensitivity and specificity was 0.93 (95% CI: 0.87–0.97, I^2 = 0.0%) and 0.99 (95% CI: 0.97–1.00, I^2 = 9.3%) (**Figure S2**). The results suggested that the diagnostic value of CNSs was not dose-dependent over the range of doses tested.

We further compared the effect of different injection sites, peritumoral or subareolar, on the SLNB (**Table 2**). The pooled sensitivity for studies that used subareolar injection was 0.93 (95% CI: 0.89–0.95, I^2 = 0.0%), while in studies using peritumoral and mixed injection, the pooled sensitivity was 0.94 (95% CI: 0.85–0.98, I^2 = 0.0%) and 0.93 (95% CI: 0.90–0.96, I^2 = 0.0%). The combined specificity for studies using subareolar, peritumoral and mixed injection was 0.99 (95% CI: 0.98–1.00, I^2 = 37.5%), 0.98 (95% CI: 0.93–0.99, I^2 = 50.6%) and 0.99 (95% CI: 0.97–0.99, I^2 = 71.2%), respectively. All groups were not significantly different from each other (**Figures S3–5**).

Publication Bias and Sensitivity Analysis

All studies harbored significant publication bias, as indicated by the Deeks' funnel plot [Slope (Bias) = −7.35, P = 0.00; **Figure 9**]. Nonetheless, the sensitivity analysis showed that the results were reliable and stable (**Table S1**).

DISCUSSION

SLNB was first reported in cutaneous melanoma by Morton et al. in 1992 (43). The SLNB concept was soon accepted for use in patients with breast cancer and led to better, less debilitating, axillary management (44). Both ALND and SLNB are not significantly different in terms of patient survival and tumor recurrence, thus further popularizing the widespread use of SLNB. SLNB carries the significant benefits of lower morbidity, especially with regards to arm lymphedema, paresthesia, and overall dysfunction (2–5). Currently, SLNB represents the standard surgical approach for axillary management in early breast cancer.

The mapping method is a decisive factor that determines the identification rate of SLN in breast cancer. RI technetium-99m was first used for SLNB mapping in 1993, followed by the use of

TABLE 1 | Detailed characteristics and QUADAS scores of the included study.

Study	Year	No. of patients	Age (years)	Dose of CNSs (ml)	Injection site	TP	FP	FN	TN	QUADAS
Liu et al. (10)	2019	59	51.5 ± 9.7	1 ml	Peritumoral	15	1	2	41	12
Wu et al. (11)	2019	46	53.63 ± 8.57	2 ml	Mixed	15	0	1	30	12
Xia et al. (12)	2019	86	51.37 ± 5.23	1 ml	Mixed	25	0	1	60	12
Gao et al. (13)	2018	58	47.2 ± 15.1	2 ml	Mixed	24	0	2	32	12
Li et al. (14)	2018	47	43.25 ± 10.15	2 ml	Subareolar	15	0	1	31	12
Wang et al. (15)	2018	77	NA	0.6 ml	Mixed	20	0	1	56	12
Qi et al. (16)	2018	52	50.2 ± 9.5	1 ml	Mixed	16	0	1	35	12
Zhang et al. (17)	2018	91	NA	1 ml	Subareolar	47	0	2	42	12
Yang et al. (18)	2018	136	50.9 ± 10.8	1 ml	Mixed	55	0	4	77	12
Zou et al. (19)	2017	86	NA	0.5 ml	Mixed	23	0	2	60	12
Wang et al. (20)	2017	77	NA	0.5 ml	Subareolar	28	0	1	48	12
Wang et al. (21)	2017	53	NA	0.6 ml	Mixed	12	0	1	40	12
Yue et al. (22)	2017	50	NA	0.4 ml	Subareolar	22	0	2	26	12
Zhang et al. (23)	2017	140	NA	NA	Mixed	20	0	2	118	12
Kong et al. (24)	2016	56	57.2 ± 11.1	2 ml	Subareolar	15	2	1	38	11
Sang et al. (25)	2016	42	NA	1 ml	NA	17	0	3	22	12
Kong et al. (26)	2016	63	NA	0.2–0.5 ml	Mixed	13	8	1	41	12
Huang et al. (27)	2016	83	NA	1 ml	Subareolar	16	1	2	64	12
Liu et al. (28)	2016	83	NA	NA	Subareolar	24	0	3	56	12
Chen et al. (29)	2015	50	42.39 ± 3.1	1 ml	Mixed	9	2	0	39	12
Wu et al. (30)	2015	49	NA	1 ml	Peritumoral	20	2	1	27	12
Mai et al. (31)	2015	43	NA	1 ml	Mixed	19	0	2	22	12
Wang et al. (32)	2015	41	NA	0.8 ml	Subareolar	16	3	1	21	12
Tu et al. (33)	2015	58	52.5 ± 13.1	0.5 ml	Subareolar	15	0	1	42	12
Guan et al. (34)	2015	87	NA	1 ml	Subareolar	31	0	2	54	12
Wu et al. (35)	2015	83	NA	NA	Subareolar	24	0	3	56	12
Lei et al. (36)	2014	56	NA	1 ml	Mixed	20	0	1	35	11
Ge et al. (37)	2013	88	NA	0.5 ml	Peritumoral	37	0	2	49	12
Gao et al. (38)	2013	34	NA	0.4 ml	Subareolar	14	0	2	19	11
Zhou et al. (39)	2012	74	NA	1 ml	Mixed	29	0	2	43	11
Chen et al. (40)	2012	44	NA	2 ml	Subareolar	22	0	2	20	12
Yang et al. (41)	2011	40	NA	2 ml	Subareolar	11	0	1	28	12
Li et al. (42)	2008	38	NA	2 ml	Subareolar	13	0	1	24	12

TP, true positive; FP, false positive; FN, false negative; TN, true negative; NA, not available; Mixed, the injection site is subareolar and peritumoral; QUADAS, quality assessment of diagnostic accuracy studies.

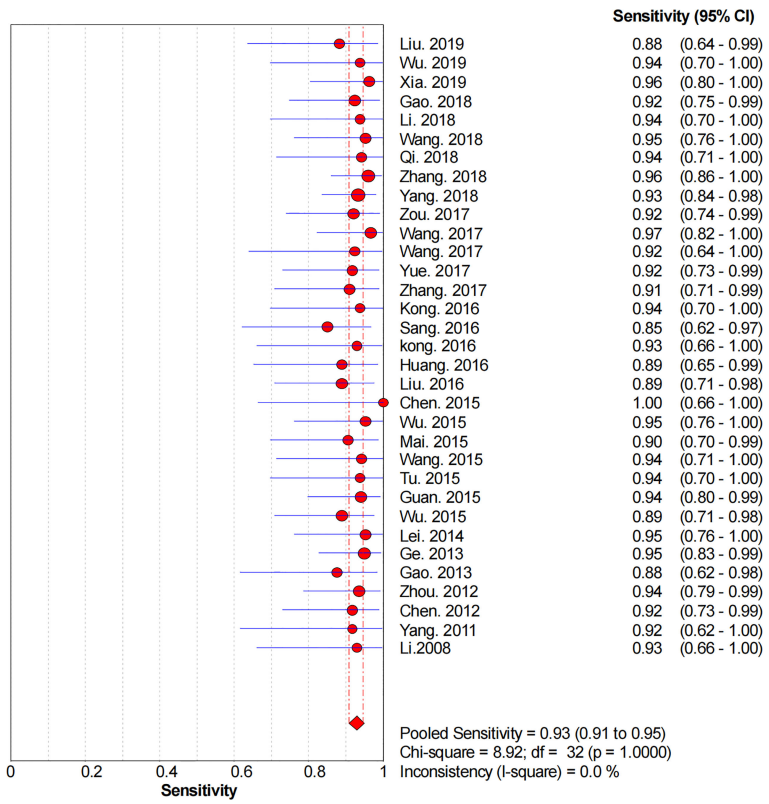

FIGURE 2 | Forest plot of pooled sensitivity of the diagnosis value of CNSs in SLNB of breast cancer. 95% CI, 95% confidence interval.

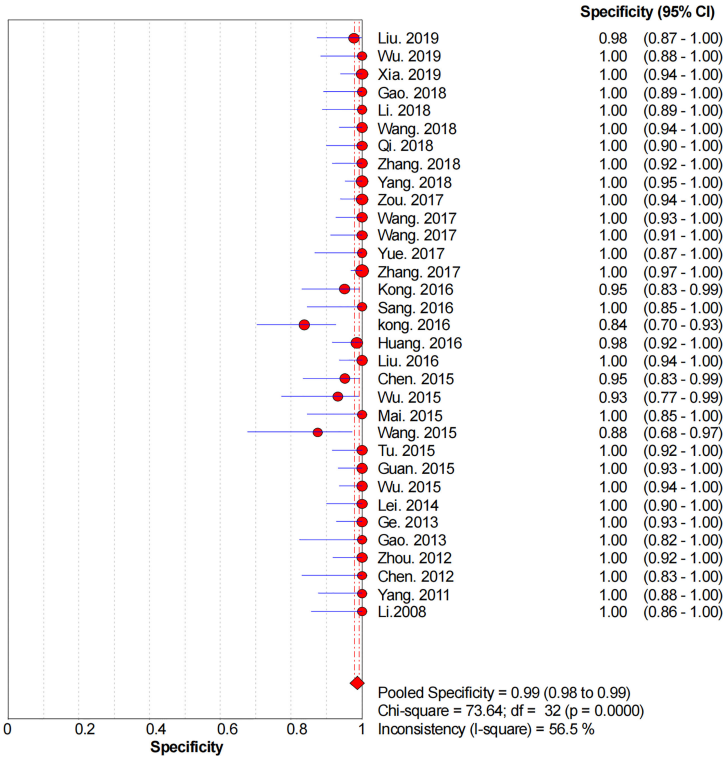

FIGURE 3 | Forest plot of pooled specificity of the diagnosis value of CNSs in SLNB of breast cancer. 95% CI, 95% confidence interval.

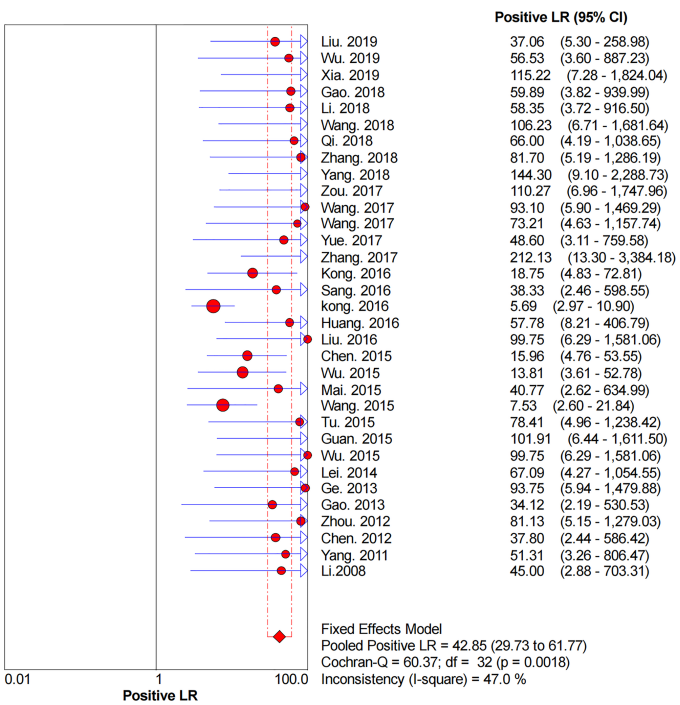

FIGURE 4 | Forest plot of pooled PLR of the diagnosis value of CNSs in SLNB of breast cancer. 95% CI, 95% confidence interval; PLR, positive likelihood ratio.

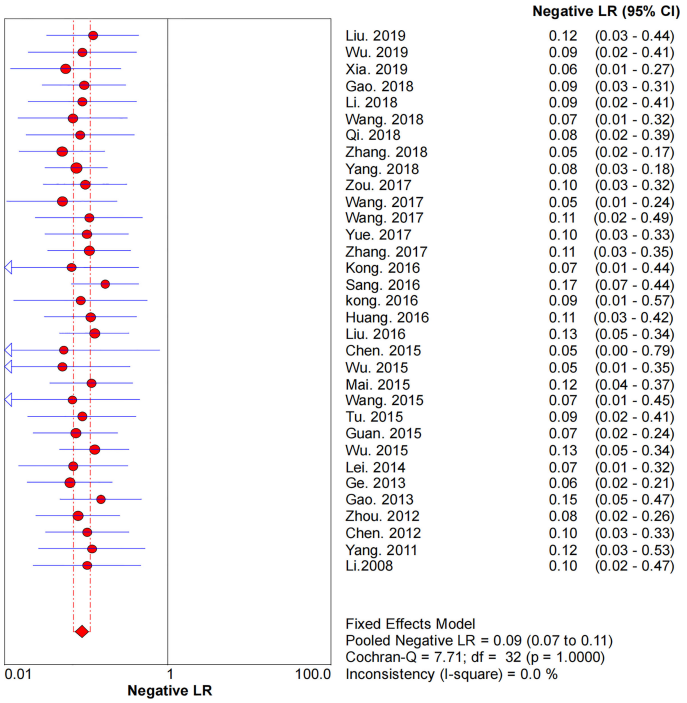

FIGURE 5 | Forest plot of pooled NLR of the diagnosis value of CNSs in SLNB of breast cancer. 95% CI, 95% confidence interval; NLR, negative likelihood ratio.

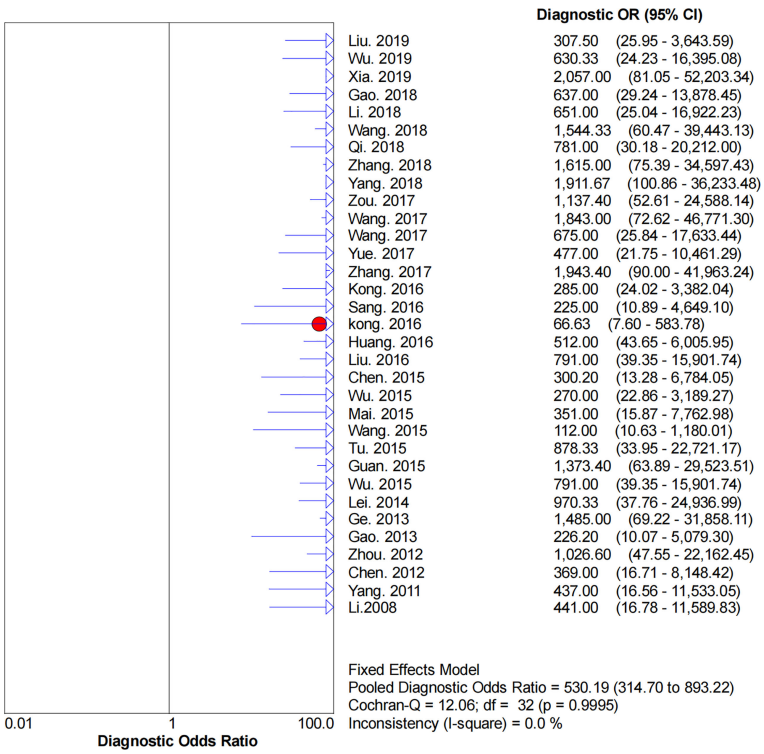

FIGURE 6 | Forest plot of pooled DOR of the diagnosis value of CNSs in SLNB of breast cancer. 95% CI, 95% confidence interval. DOR, diagnostic odds ratio.

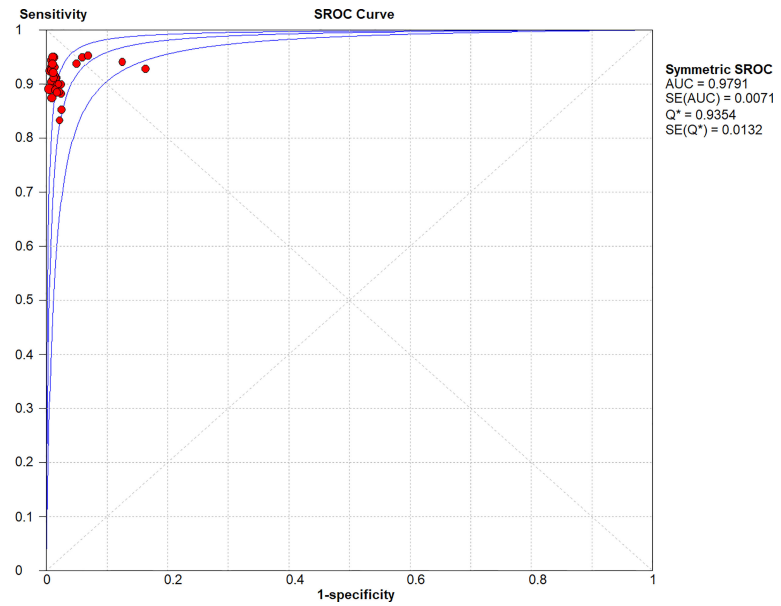

FIGURE 7 | Symmetric SROC curve of the diagnosis value of CNSs in SLNB of breast cancer. SROC, summary receiver operating characteristic curve; AUC, the area under the receiver-operator characteristic curve.

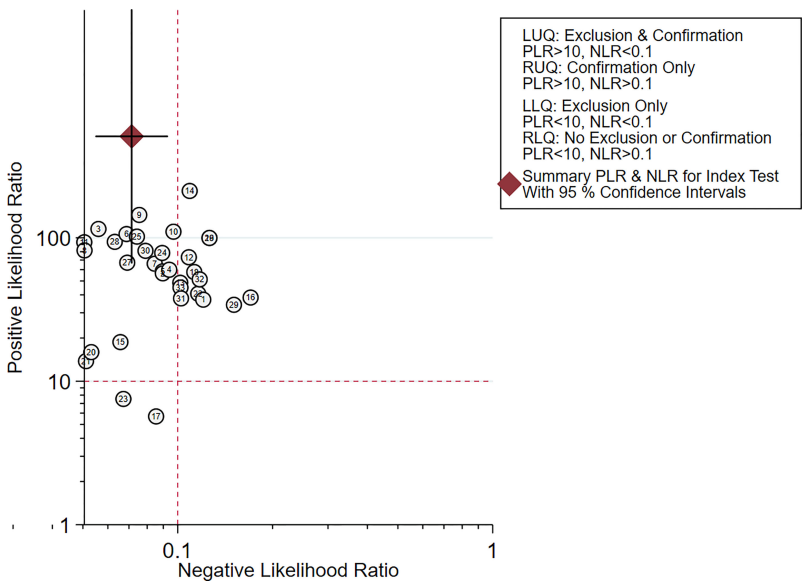

FIGURE 8 | Scattergram of the PLR and NLR of the diagnosis value of CNSs in SLNB of breast cancer. PLR, positive likelihood ratio; NLR, negative likelihood ratio; LLQ, left lower quadrant; LUQ, left upper quadrant; RLQ, right lower quadrant; RUQ, right upper quadrant.

blue dye (44, 45). The NSABP B-32 trial found that a combination of BD and radiocolloid resulted in a 97.1% detection rate for SNLB, compared with a 70.2% for BD and 89.4% for radiocolloid when used alone (46). Similar findings were noted in the ALMANAC study that demonstrated that a combination of isotope and BD had a 96.1% detection rate, but the use of either isotope or BD alone was 85.6% (47). Therefore, the method of combining BD and RI is currently regarded as the gold standard. Nevertheless, there are also disadvantages associated with this approach, namely, BD allergic reactions, the need for highly specialized nuclear medicine units, and the risk of radiation exposure to healthcare professionals and

TABLE 2 | Subgroup analysis was performed based on Carbon Nanoparticle injection doses and site.

Subgroup	Sensitivity	Specificity	PLR	NLR	DOR
Dose of CNSs (ml)					
≤1 ml	0.93 (0.91–0.95)	0.98 (0.97–0.99)	39.09 (20.01–76.36)	0.08 (0.06–0.11)	510.16 (275.17–945.81)
2 ml	0.93 (0.87–0.97)	0.99 (0.97–1.00)	40.30 (16.24–100.03)	0.09 (0.05–0.16)	458.56 (145.49–1,445.35)
Injection site					
Subareolar	0.93 (0.89–0.95)	0.99 (0.98–1.00)	43.53 (24.56–77.14)	0.09 (0.07–0.13)	521.22 (244.10–1,112.97)
Peritumoral	0.94 (0.85–0.98)	0.98 (0.93–0.99)	31.93 (11.15–91.39)	0.08 (0.03–0.17)	476.71 (109.29–2,079.27)
Mixed	0.93 (0.90–0.96)	0.99 (0.97–0.99)	53.40 (18.17–156.95)	0.08 (0.06–0.12)	591.05 (252.32–1,384.52)

PLR, positive likelihood ratio; NLR, negative likelihood ratio; DOR, diagnostic odds ratio; CNSs, carbon nanoparticles suspensions; Mixed, the injection site is subareolar and peritumoral.

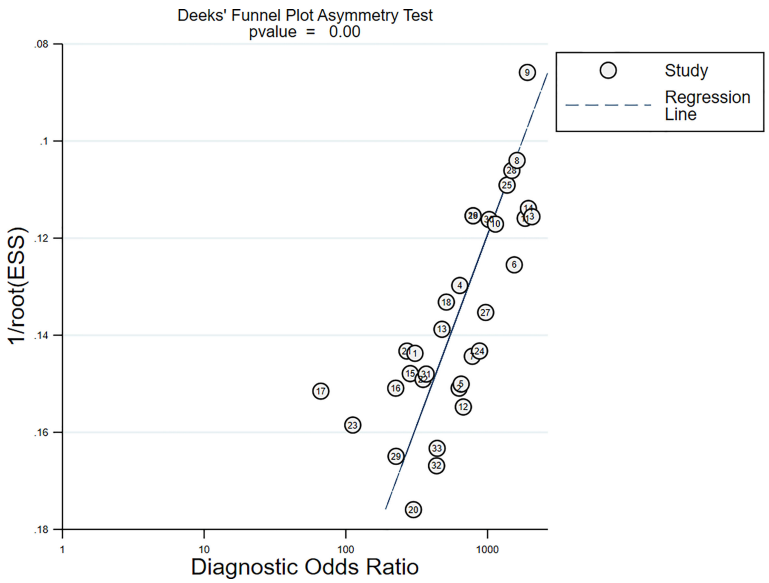

FIGURE 9 | Deeks' funnel plot for publication bias test.

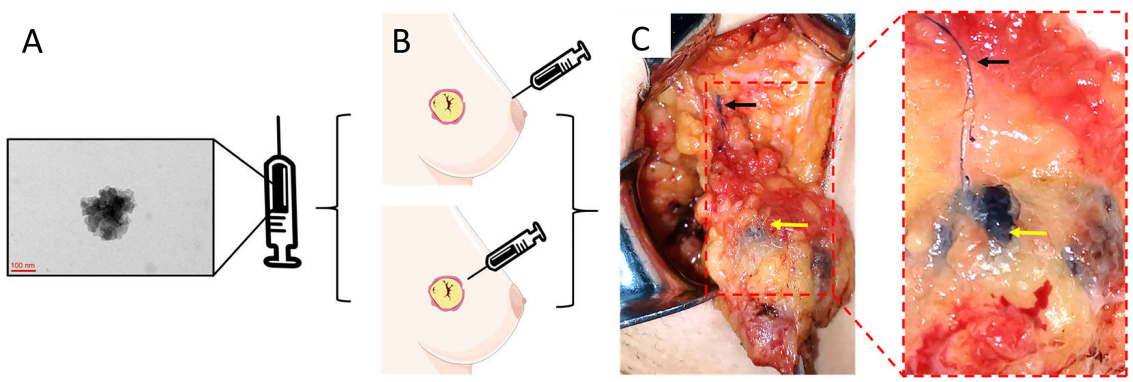

FIGURE 10 | The specific operation steps of CNSs as lymphatic tracer in SLNB. **(A)** The morphology of CNSs; **(B)** Injection site of CNSs; **(C)** Color rendering of CNSs in SLNB (Black arrow: Lymphatic vessel; Yellow arrow: Lymph node). **(A)** is the image of CNSs under transmission electron microscopy. Republished with permission of SAGE Publications, Inc., from Liu X, Chang S, Jiang XL, Huang P, Yuan ZT. Identifying parathyroid glands with carbon nanoparticle suspension does not help protect parathyroid function in thyroid surgery: a prospective, randomized control clinical study. Surg Innov (2016) 23(4):381–9. doi: 10.1177/1553350615624787. © The Author(s) 2016; permission conveyed through Copyright Clearance Center, Inc (49).

patients. New methods of lymphatic mapping that offer equal accuracy without the risks of allergies or irradiation are currently being trialed. A network meta-analysis showed that in contrast to using BD alone, superparamagnetic iron oxide nanoparticles or indocyanine green fluorescence alone are superior. The use of these novel agents alone is even comparable to the standard dual-modality technique. However, their use still mandates specialized equipment that may not be widely available (48).

CNSs is a new method that requires no specialized medical facilities for SLNB. This meta-analysis aimed to evaluate the diagnostic performance of CNSs for SLNB in breast cancer. The pooled sensitivity, specificity, and AUC of the SROC were 0.93, 0.99, and 0.98, respectively. The pooled DOR, a diagnostic performance index that takes into consideration specificity and sensitivity, in the current analysis was 530.19. Higher DOR values indicate a stronger discriminating power. The results suggest CNSs could be utilized to identify true positive patients with SLN metastases while also ruling out false negatives.

The optimal dose and injection site of CNSs for SLNB is controversial. The most regularly used doses are 1 and 2 ml. In the 33 studies analyzed, the volume of CNSs varied from 0.2 to 2 ml (**Table 1**). Subgroup analysis highlighted that there was no difference in specificity or sensitivity between the studies that used ≤1 ml versus 2 ml injections of CNSs (**Table 2**), which indicated that 1 ml volume of CNSs is sufficient. In this meta-analysis, peritumoral CNSs injection for SLNB was used in 3 studies, subareolar CNSs injection was used in 15 studies, and 14 studies were used in both approaches. No significant difference in the sensitivity and specificity of SLNB was detected between studies using peritumoral and subareolar CNSs injection. Therefore, both peritumoral and subareolar are appropriate injection sites for SLNB with CNSs (**Figure 10**) (49).

In terms of adverse effects, none of the 2,171 included patients in this analysis developed a local inflammatory response, fat or skin necrosis, or an anaphylactic reaction. Nevertheless, the use of CNSs does have some limitations, with skin staining being the most frequently encountered side effect of CNSs (18, 35). This complication appears to be linked to the depth of injection based on our empirical observations. Therefore, a subcutaneous injection should be used instead of an intradermal injection. Another disadvantage of CNSs is that they cannot be seen through the skin and fatty tissue, therefore possessing lower visualization clarity compared to a fluorescent tracer (e.g., indocyanine green). Interestingly, a recent study suggests that CNSs have not only been employed as lymph node tracers but may also be useful as a carrier for antitumor therapy (50).

Conclusions

This meta-analysis highlights the accuracy and feasibility of using CNSs for SLNB mapping in breast cancer patients. The CNSs mapping method would be especially helpful in institutions without access to fluorescence imaging systems or RI. CNSs may be incorporated in a wide range of clinical applications, namely, theranostics and in breast cancer therapy.

DATA AVAILABILITY STATEMENT

The original contributions presented in the study are included in the article/**Supplementary Material**. Further inquiries can be directed to the corresponding authors.

AUTHOR CONTRIBUTIONS

All authors read and approved the final manuscript prior to submission. YJ, JiL, BC, YB, CL, YL, and TL: data curation, software, writing—original draft. JuL and XC: supervision, writing—review and editing. All authors listed have made a substantial, direct, and intellectual contribution to the work and approved it for publication.

FUNDING

This study was supported by the National Natural Science Foundation of China (No. 81860715) and the Doctor Foundation of Affiliated Hospital of Zunyi Medical University (No. 201712).

SUPPLEMENTARY MATERIAL

The Supplementary Material for this article can be found online at: https://www.frontiersin.org/articles/10.3389/fonc.2022.818812/full#supplementary-material

REFERENCES

1. Cabanas RM. An Approach for the Treatment of Penile Carcinoma. *Cancer* (1977) 39(2):456–66. doi: 10.1002/1097-0142(197702)39:2<456::aid-cncr2820390214>3.0.co;2-i
2. Krag DN, Anderson SJ, Julian TB, Brown AM, Harlow SP, Costantino JP, et al. Sentinel-Lymph-Node Resection Compared With Conventional Axillary-Lymph-Node Dissection in Clinically Node-Negative Patients With Breast Cancer: Overall Survival Findings From the NSABP B-32 Randomised Phase 3 Trial. *Lancet Oncol* (2010) 11(10):927–33. doi: 10.1016/s1470-2045(10)70207-2
3. Ashikaga T, Krag DN, Land SR, Julian TB, Anderson SJ, Brown AM, et al. Morbidity Results From the NSABP B-32 Trial Comparing Sentinel Lymph Node Dissection Versus Axillary Dissection. *J Surg Oncol* (2010) 102(2):111–8. doi: 10.1002/jso.21535
4. Mansel RE, Fallowfield L, Kissin M, Goyal A, Newcombe RG, Dixon JM, et al. Randomized Multicenter Trial of Sentinel Node Biopsy Versus Standard Axillary Treatment in Operable Breast Cancer: The ALMANAC Trial. *J Natl Cancer Inst* (2006) 98(9):599–609. doi: 10.1093/jnci/djj158
5. Giuliano AE, Ballman KV, McCall L, Beitsch PD, Brennan MB, Kelemen PR, et al. Effect of Axillary Dissection vs No Axillary Dissection on 10-Year Overall Survival Among Women With Invasive Breast Cancer and Sentinel Node Metastasis: The ACOSOG Z0011 (Alliance) Randomized Clinical Trial. *JAMA* (2017) 318(10):918–26. doi: 10.1001/jama.2017.11470
6. Benson JR, della Rovere GQ. Management of the Axilla in Women With Breast Cancer. *Lancet Oncol* (2007) 8(4):331–48. doi: 10.1016/s1470-2045(07)70103-1

7. Yang J, Xu L, Liu P, Du Z, Chen J, Liang F, et al. Accuracy of Sentinel Lymph Node Biopsy in Breast Cancer: Pitfalls in the Application of Single Tracers. *Cancer Manag Res* (2020) 12:3045–51. doi: 10.2147/CMAR.S244806
8. Modugno G, Menard-Moyon C, Prato M, Bianco A. Carbon Nanomaterials Combined With Metal Nanoparticles for Theranostic Applications. *Br J Pharmacol* (2015) 172(4):975–91. doi: 10.1111/bph.12984
9. Whiting PF, Rutjes AW, Westwood ME, Mallett S, Deeks JJ, Reitsma JB, et al. QUADAS-2: A Revised Tool for the Quality Assessment of Diagnostic Accuracy Studies. *Ann Intern Med* (2011) 155(8):529–36. doi: 10.7326/0003-4819-155-8-201110180-00009
10. Liu XM, Bao GQ, Qiu B, Fan D, Tang H, Yang XJ, et al. Application of Nano-Carbon Suspension in Tracing Sentinel Lymph Node in the Diagnosis and Treatment of Early Breast Cancer. *Oncol Prog* (2019) 17(18):2134–6. doi: 10.11877/j.issn.1672-1535.2019.17.18.08
11. Wu PY, Chen YJ. Application Study of Nano-Carbon Staining Method in Sentinel Lymph Node Biopsy of Early Breast Cancer. *China Modern Med* (2019) 26(25):82–5. doi: 10.3969/j.issn.1674-4721.2019.25.024
12. Xia GH, Cao B, Yang Y, Tang J, Zhu JY. Application of Carbon Nanoparticles and Methylene Blue in Sentinel Lymph Node Biopsy of Breast Cancer. *Clin Educ Gen Pract* (2019) 17(6):554–5. doi: 10.13558/j.cnki.issn1672-3686.2019.06.024
13. Gao HY, Dai JB, Xue J. Carbon Nanoparticle Suspension With Methy Blue Injection in Sentinel Lymph Node Biopsy for Breast Cancer Patients. *J Chin Oncol* (2018) 24(9):892–5. doi: 10.11735/j.issn.1671-170X.2018.09.B010
14. Li DH, Kong Y. Application Value of Nano-Carbon and Methylene Blue in Sentinel Lymph Node Biopsy of Breast Cancer. *J Prev Med Chin PLA* (2018) 36(5):689–90. doi: 10.13704/j.cnki.jyyx.2018.05.039
15. Wang M, Yao F. Carbon Nanoparticle Suspension in Sentinel Lymph Node Biopsy in Patients With Breast Cancer. *J Chin Pract Diagn Ther* (2018) 32(4):358–61. doi: 10.13507/j.issn.1674-3474.2018.04.015
16. Qi X. *The Clinical Value of the Use of Carbon Nanoparticle Suspension Injection for Sentinel Lymph Node Biopsy in Breast Cancer. [Master's Thesis]*. Jilin, China: Jilin University (2018).
17. Yang SX, Wei WS, Jiang QH, Zhou YF, Qu W, Tu JH, et al. Analysis of 246 Sentinel Lymph Node Biopsies of Patients With Clinical Primary Breast Cancer by Application of Carbon Nanoparticle Suspension. *J Obstet Gynaecol Res* (2018) 44(6):1150–7. doi: 10.1111/jog.13635
18. Zhang L, Huang Y, Yang C, Zhu T, Lin Y, Gao H, et al. Application of a Carbon Nanoparticle Suspension for Sentinel Lymph Node Mapping in Patients With Early Breast Cancer: A Retrospective Cohort Study. *World J Surg Oncol* (2018) 16(1):112. doi: 10.1186/s12957-018-1414-6
19. Zou WW, Bai Y, Wang XL, Cheng K, Sun HG, Wu MM, et al. Comparison Between Indocyanine Green Fluorescence Imaging Plus Methylene Blue and Plus Carbon Nanoparticles Suspension Injection for Sentinel Lymph Node Biopsy in Breast Cancer Patients. *J Pract Med* (2017) 33(11):1857–60. doi: 10.3969/j.issn.1006-5725.2017.11.036
20. Wang XW. *Application of Nano-Carbon and Methylene Blue in Sentinel Lymph Node Biopsy of Breast Cancer. [Master's Thesis]*. Beijing, China: Peking Union Medical College (2017). doi: 10.7666/d.Y3277830
21. Wang L, Chen X, Zhao CG, Peng Q, Chen L, Yu HJ. Application of Nano-Carbon to the Sentinel Lymph Node Biopsy for Breast Cancer. *Chin J Clin Oncol Rehabil* (2017) 24(1):49–51. doi: 10.13455/j.cnki.cjcor.2017.01.14
22. Yue J, Pei J, Ren M, Zhang JJ, Yang F, Zhang ZS, et al. Application of Fluorescence Combined With Nano-Carbon in Sentinel Lymph Node Biopsy of Breast Cancer. *Acta Universitatis Medicinalis Anhui* (2017) 52(2):236–9. doi: 10.19405/j.cnki.issn1000-1492.2017.02.019
23. Zhang JW. *Comparison of the Value of Methylene Blue and Carbon Nano Partical Suspension in Sentinel Lymph Node Biopsy of Breast Cancer. [Master's Thesis]*. Shenyang, China: China Medical University (2017).
24. Kong ZH, Huang YF, Li JJ, Mo CS, Liang LC. Comparison of Nano-Carbon and Methylene Blue Tracer in Axillary Sentinel Lymph Node Biopsy of Breast Cancer. *Guangxi Med J* (2016) 38(6):852–3+8. doi: 10.11675/j.issn.0253-4304.2016.06.28
25. Sang JH. *Clinical Observation of Methylene Blue Combined With Carbon Nano-Tracers of Early Breast Cancer SLNB. [Master's Thesis]*. Zhengzhou, China: Zhengzhou University (2016).
26. Kong C, Xia Q, Yu H, Zhang CJ. A Clinical Comparative Study Between Carbon Nanoparticles and Methylene-Blue for the Application of Sentinel Lymph Node Biopsy in Early Breast Cancer. *Med Philosophy (B)* (2016) 37(3):26–8+85. doi: 10.12014/j.issn.1002-0772.2016.03b.08
27. Huang K, Zeng Y. Feasibility of Applying Nano-Carbon in Sentinel Lymph Node Biopsy in Early Breast Cancer. *IMHGN* (2016) 22(20):3097–9. doi: 10.3760/cma.j.issn.1007-1245.2016.20.013
28. Liu B, Li F, Wang SL, Zhang FF, Long HL. Study on the Application of Nano-Carbon Sentinel Lymph Node Biopsy in Patients With Early Breast Cancer Under Color Doppler Ultrasonography. *Psychologist* (2016) 22(35):176–8.
29. Chen PZ. Clinical Study of Nano-Carbon Tracer in Sentinel Lymph Node Biopsy of Breast Cancer. *Strait Pharm J* (2015) 27(12):186–7. doi: 10.3969/j.issn.1006-3765.2015.12.100
30. Wu Y, Zhou Y, Yang GS, Liu X, Huang H. Application Anulysis of Carbon Nanoparticles Suspension in Sentinel Lymph Node Biopsy for Breast Cancer. *J Clin Surg* (2015) 23(7):511–3. doi: 10.3969/j.issn.1005-6483.2015.07.013
31. Mai F. *Clinical Comparison Between Carbon Nanoparticles and Methylene Blue Staining on Sentinel Lymph Lymph Node Biopsy for Breast Cancer. [Master's Thesis]*. Dalian, China: Dalian Medical University (2015).
32. Wang LC, Li LJ, Li YQ, Li XQ, Gao YF, Li JY, et al. Application Value of Carbon Nanoparticle in Axillary Sentinel Lymph Node Biopsy for Breast Cancer. *Hubei J TCM* (2015) 37(2):19–20.
33. Tu JH, Zhang H, Lu YH, Wang S, Ling LJ. Feasibility of Nanogate Carbon as Agent for Sentinel Lymph Node Biospy in Early Breast Cancer Patients. *Chin J Exp Surg* (2015) 32(12):3147–50. doi: 10.3760/cma.j.issn.1001-9030.2015.12.073
34. Guan HT, Ma XB, Diao Y, Shan CY, Zhao Y, Min WL, et al. Sentinel Lymph Node Biopsy in Breast Cancer Patients by Using Nanometer Carbon Suspension Liquid. *J North Sichuan Med Coll* (2015) 30(4):439–41+446. doi: 10.3969/j.issn.1005-3697.2015.04.04
35. Wu XF, Lin QZ, Chen G, Lu JP, Zeng Y, Chen X, et al. Sentinel Lymph Node Detection Using Carbon Nanoparticles in Patients With Early Breast Cancer. *PloS One* (2015) 10(8). doi: 10.1371/journal.pone.0135714
36. Lei SG, Yu XF, Xie CW, Ji MY, Liu QM. Application of Carbon Nanoparficle in the Axillary Sentinel Lymph Node Biopsy for Breast Cancer. *Chin J Postgrad Med* (2014) 37(26):1–3. doi: 10.3760/cma.j.issn.1673-4904.2014.26.001
37. Ge J, Yan B, Cao XC. Comparison of Sentinel Lymph Node Detection by Methylene Blue and Carbon Nanoparticle Suspension Injection in Early Breast Cancer. *Chin J Oncol* (2013) 41(8):828–9. doi: 10.3969/j.issn.0253-9896.2013.08.032
38. Gao W, Guo WB. Application of Carbon Nanoparticle Suspension Injection Into the Mammary Gland in the Sentinel Lymph Node Biopsy for Breast Cancer. *Pract Pharm And Clin Remedies* (2013) 16(3):187–9. doi: 10.3969/j.issn.1673-0070.2013.03.003
39. Zhou Y, Du CH, Chen ZM, Li Y, Lin QM, Wang QT. Comparison Between Carbon Nanoparticles and Methylene Blue on the Sentinel Lymph Node Biopsy for Breast Cancer. *Lingnan Modern Clinics Surg* (2012) 12(2):118–20. doi: 10.3969/j.issn.1009-976X.2012.02.012
40. Chen ZY, Hu XC, Wang HJ, Liu DS, Hong W. Application of Nano-Carbon Suspension Injection in Sentinel Lymph Node Biopsy of Middle and Early Stage Breast Cancer. *Inner Mongol J Tradit Chin Med* (2012) 31(18):78–9. doi: 10.3969/j.issn.1006-0979.2012.18.092
41. Yang LJ, Li Z. Clinical Research of Sentinel Lymph Nodes Biopsy in Breast Cancer by Methylene Blue and Nanometres Carbon Suspension Liquid. *Modern Med Health* (2011) 27(15):2255–6.
42. Li X, Duan XQ. Comparative Study of Methylene Blue, Isosulfide Blue and Nano-Carbon Suspension in Sentinel Lymph Node Biopsy of Breast Cancer. *J Qiqihar Med Coll* (2008) 29(9):1051–3. doi: 10.3969/j.issn.1002-1256.2008.09.013
43. Morton DL, Wen DR, Wong JH, Economou JS, Cagle LA, Storm FK, et al. Technical Details of Intraoperative Lymphatic Mapping for Early Stage Melanoma. *Arch Surg* (1992) 127(4):392–9. doi: 10.1001/archsurg.1992.01420040034005

44. Giuliano AE, Kirgan DM, Guenther JM, Morton DL. Lymphatic Mapping and Sentinel Lymphadenectomy for Breast Cancer. *Ann Surg* (1994) 220(3):391–401. doi: 10.1097/00000658-199409000-00015
45. Krag DN, Weaver DL, Alex JC, Fairbank JT. Surgical Resection and Radiolocalization of the Sentinel Lymph Node in Breast Cancer Using a Gamma Probe. *Surg Oncol* (1993) 2(6):335–40. doi: 10.1016/0960-7404(93)90064-6
46. Krag DN, Anderson SJ, Julian TB, Brown AM, Harlow SP, Ashikaga T, et al. Technical Outcomes of Sentinel-Lymph-Node Resection and Conventional Axillary-Lymph-Node Dissection in Patients With Clinically Node-Negative Breast Cancer: Results From the NSABP B-32 Randomised Phase III Trial. *Lancet Oncol* (2007) 8(10):881–8. doi: 10.1016/s1470-2045(07)70278-4
47. Goyal A, Newcombe RG, Chhabra A, Mansel RE. Factors Affecting Failed Localisation and False-Negative Rates of Sentinel Node Biopsy in Breast Cancer–Results of the ALMANAC Validation Phase. *Breast Cancer Res Treat* (2006) 99(2):203–8. doi: 10.1007/s10549-006-9192-1
48. Mok CW, Tan SM, Zheng Q, Shi L. Network Meta-Analysis of Novel and Conventional Sentinel Lymph Node Biopsy Techniques in Breast Cancer. *BJS Open* (2019) 3(4):445–52. doi: 10.1002/bjs5.50157
49. Liu X, Chang S, Jiang XL, Huang P, Yuan ZT. Identifying Parathyroid Glands With Carbon Nanoparticle Suspension Does Not Help Protect Parathyroid Function in Thyroid Surgery: A Prospective, Randomized Control Clinical Study. *Surg Innov* (2016) 23(4):381–9. doi: 10.1177/1553350615624787
50. Xie P, Yang ST, Huang Y, Zeng C, Xin Q, Zeng G, et al. Carbon Nanoparticles-Fe(II) Complex for Efficient Tumor Inhibition With Low Toxicity by Amplifying Oxidative Stress. *ACS Appl Mater Interf* (2020) 12(26):29094–102. doi: 10.1021/acsami.0c07617

Conflict of Interest: The authors declare that the research was conducted in the absence of any commercial or financial relationships that could be construed as a potential conflict of interest.

Publisher's Note: All claims expressed in this article are solely those of the authors and do not necessarily represent those of their affiliated organizations, or those of the publisher, the editors and the reviewers. Any product that may be evaluated in this article, or claim that may be made by its manufacturer, is not guaranteed or endorsed by the publisher.

frontiers | Frontiers in Oncology

ORIGINAL RESEARCH
published: 07 April 2022
doi: 10.3389/fonc.2022.868164

Development and External Validation of a Simple-To-Use Dynamic Nomogram for Predicting Breast Malignancy Based on Ultrasound Morphometric Features: A Retrospective Multicenter Study

Qingling Zhang[1], Qinglu Zhang[2], Taixia Liu[3], Tingting Bao[1], Qingqing Li[1] and You Yang[1]*

[1] Depatment of Ultrasonography, The First Affiliated Hospital of Wannan Medical College, Wuhu, China, [2] Department of Ultrasonography, Shandong Provincial Third Hospital Affiliated to Cheeloo College of Medicine, Shandong University, Jinan, China, [3] Department of Ultrasonography, Linyi People's Hospital, Linyi, China

OPEN ACCESS

Edited by:
Kenji Suzuki,
Tokyo Institute of Technology, Japan

Reviewed by:
Jun Lyu,
First Affiliated Hospital of Jinan University, China
Mauro Giuseppe Mastropasqua,
University of Bari Medical School, Italy

****Correspondence:***
Qingling Zhang
qingling.go@gmail.com

Specialty section:
This article was submitted to Cancer Imaging and Image-directed Interventions, a section of the journal Frontiers in Oncology

Received: *02 February 2022*
Accepted: *14 March 2022*
Published: *07 April 2022*

Citation:
Zhang Q, Zhang Q, Liu T, Bao T, Li Q and Yang Y (2022) Development and External Validation of a Simple-To-Use Dynamic Nomogram for Predicting Breast Malignancy Based on Ultrasound Morphometric Features: A Retrospective Multicenter Study. Front. Oncol. 12:868164. doi: 10.3389/fonc.2022.868164

Background: With advances in high-throughput computational mining techniques, various quantitative predictive models that are based on ultrasound have been developed. However, the lack of reproducibility and interpretability have hampered clinical use. In this study, we aimed at developing and validating an interpretable and simple-to-use US nomogram that is based on quantitative morphometric features for the prediction of breast malignancy.

Methods: Successive 917 patients with histologically confirmed breast lesions were included in this retrospective multicentric study and assigned to one training cohort and two external validation cohorts. Morphometric features were extracted from grayscale US images. After feature selection and validation of regression assumptions, a dynamic nomogram with a web-based calculator was developed. The performance of the nomogram was assessed with respect to calibration, discrimination, and clinical usefulness.

Results: Through feature selection, three morphometric features were identified as being the most optimal for predicting malignancy, and all regression assumptions of the prediction model were met. Combining all these predictors, the nomogram demonstrated a good discriminative performance in the training cohort and in the two external validation cohorts with AUCs of 0.885, 0.907, and 0.927, respectively. In addition, calibration and decision curves analyses showed good calibration and clinical usefulness.

Conclusions: By incorporating US morphometric features, we constructed an interpretable and easy-to-use dynamic nomogram for quantifying the probability of breast malignancy. The developed nomogram has good generalization abilities, which may fit into clinical practice and serve as a potential tool to guide personalized treatment.

Our findings show that quantitative morphometric features from different ultrasound machines and systems can be used as imaging surrogate biomarkers for the development of robust and reproducible quantitative ultrasound dynamic models in breast cancer research.

Keywords: breast cancer, models, quantitative imaging, nomogram, morphometrics, ultrasound

INTRODUCTION

Globally, breast cancer is the leading cause of cancer-associated death in women (1). Effective screening approaches have the ability to reduce cancer-related mortality rates (2, 3). Due to its safety and wide availability, US examination is recommended as a supplemental screening tool for women of all ages (4). In asymptomatic women, the ability of US to detect breast cancer is comparable to that of mammography (5–7). Over the years, a structured reporting and classification system has been widely adopted for qualitatively describing breast US findings in routine clinical practice (e.g., ACR BI-RADS) (8). However, image interpretation for the traditional structured classification is generally subjective and is possibly affected by radiologists' experience (9–11). Moreover, predictions of malignancies by the classification system are not always precise, and there are significant differences between hospitals. As reported in the literature, BI-RADS category 4 lesions have a broad range of malignancy rates (3-94%) (12). Thus, the US capacity for detecting breast malignancy still needs to be upgraded considerably.

In the precision medicine context, quantitated methods provide the unique potential for making breast cancer screening more rapid and accurate using artificial intelligence and machine learning algorithms (13). Many studies are evaluating the applicability of US prediction models that are based on quantitated methods (e.g., radiomics) (14–17). These models have been developed to mine high-throughput quantitative image features fusing image pixels and morphology through machine learning methods to improve cancer diagnosis and prognosis (18). However, to varying degrees, reproducibility of quantification features derived from image pixels is sensitive to image preprocessing (19), particularly for US technology, which has the distinct inherent characteristic of operator- and device-dependent, not to mention that such pixel-based features often lack interpretability (20). This may lead to limitations in usability for real end-users, impeding their large-scale clinical applications.

Morphometrics, which are associated with tumor histological findings (21), refers to the quantified assessment of shape variations of organisms and their covariations with other variables. Unlike image pixel-based features, morphometric features characterize the shape and contour of lesions and are nearly independent of the different system settings and US machines (22). We hypothesized that a set of quantified morphological features are related to malignant breast lesions and may, therefore, act as independent predictive markers, without the involvement of pixels-based features. We tested this hypothesis and further build an interpretable and simple-to-use US nomogram for predicting breast malignancy.

MATERIALS AND METHODS

Study Population

In this multicenter retrospective study, patients were recruited from three tertiary medical centers; The First Affiliated Hospital of Wannan Medical College in Anhui Province (Center A), Shandong Provincial Third Hospital Affiliated to Cheeloo College of Medicine, Shandong University (Center B), and Linyi People's Hospital in Shandong Province (Center C). The training cohort for nomogram development was obtained from among the patients at Center A between January 2020 and September 2021 while the external validation cohorts were derived from Centers B and C between January 2021 and September 2021.

All consecutive female patients with US findings of breast lesions who fulfilled the inclusion/exclusion criteria were enrolled. The inclusion criteria were: i. The definitive pathological diagnosis was available from the breast lesion, either by biopsy or surgery; ii. US examination performed before biopsy or surgery; and iii. Breast lesions classified as BI-RADS US category 4 or 5 according to the second edition of the ACR BI-RADS US atlas. The exclusion criteria were: i. Indeterminate pathological results (difficult to distinguish between "benign" and "malignant"), ii. Incomplete clinical information, iii. Patients administered with radiotherapy or chemotherapy before US examination, and iv. Patients whose longest diameter of the lesion was beyond the display range of the US transducer. For patients with more than one lesion, only the lesion with confirmed pathological diagnosis was included for quantitative analysis.

The First Affiliated Hospital of Wannan Medical College Review Board, Shandong Provincial Third Hospital Review Board and Linyi People's Hospital Review Board approved this retrospective study. Patient consent was waived due to the use of retrospective, de-identified information from the image database.

Ultrasound Examination

Five different high-resolution US scanners equipped with a linear array transducer, including Esaote Mylab 90 (Genova, Italy) with a 4-13 MHz transducer, Siemens Acuson S3000 (IL, USA) with a 4-9 MHz transducer, Philips IU22 (PA, USA) with a 3-12 MHz transducer, Philips EPIQ5 (PA, USA) with a 5-12 MHz transducer, and Mindray Resona 7T (SZ, China) with 5-14 MHz transducer were used in this study.

All lesions were examined by 7 sonographers who had over 5 years of experience in breast US scanning. Parameters were adjusted to optimize image quality, then, the grey-scale image of the longest diameter section of target lesions was documented in the JPG format for further quantification analysis.

Outcome Measures

The outcome was the definitive histopathologic diagnosis by biopsy or surgery. Pathological results were reported independently by the pathologist of the participating hospitals and grouped into malignant and benign lesions. Histological processing was performed in the accredited Department of Pathology and conducted using a standardized procedure to ensure reproducibility.

Data Quality Control

Imaging and clinical data were collected by an independent investigator from respective hospitals. A radiologist with more than eight years of experience in breast US reviewed the results of data collecting and further confirmed the final datasets according to the inclusion/exclusion criteria. These data were anonymized and randomly attached with a number ID. Images of benign and malignant lesions from the training cohort were mixed and stored in a single folder for quantification analysis, so were those from the validation cohorts.

Morphometric analyses of images were independently performed by three sonographers who were not involved in data collection. Three identical lap-tops with 1920 × 1280 resolution were used, and each image was magnified by the delineate process so that the lesion occupied at least half of the display area. Lesions from the training cohort were measured by sonographer QL, while those from the validation cohorts were respectively measured by sonographers TB and YY. All the sonographers had 4 years of work experience in breast US. At the beginning of the study, they were uniformly trained on the use of the image quantification software. In addition, they were blinded to the clinical information and pathologic results as well as on the ratios of malignant to benign lesions.

Morphometric Feature Extraction

Image morphometric analysis was performed using the ImageJ software (https://imagej.nih.gov/ij, version 1.52p, NIH, USA). First, grey-scale US images of all target lesions were exported from the machines and imported into the ImageJ software. For each lesion, only one image was extracted. Next, using the Set Scale function of the Analyze Tab menu in ImageJ, lesion sizes were calibrated according to depth bar on each US image to obtain the actual size value. Finally, the contour of each lesion was manually delineated as the region of interest (ROI).

After delineating the ROI of lesions, thirteen morphometric features were automatically calculated and extracted: (1) Perimeter, the length of the outside boundary of the ROI; (2) Bounding Rectangle Width (BRW), the width of the smallest rectangle enclosing the ROI; (3) Bounding Rectangle Height (BRH), the height of the smallest rectangle enclosing the ROI; (4) Major Axis (MaA), the primary axis of the best fitting ellipse to the ROI; (5) Minor Axis (MiA), the secondary axis of the best fitting ellipse to the ROI; (6) Angle, the angle between the Major Axis and a line parallel to the x-axis of the US image, its range is 0 -180 degrees; (7) Circularity, a morphological feature that can mathematically indicate the degree of similarity to a perfect circle, taking into consideration the smoothness of the perimeter. This means that circularity is a measure of both lesion shape and roughness, the further away from a perfectly round and smooth circle, the lower the circularity value of the target lesion; (8) Axis Ratio (AR), the ratio of Major Axis and Minor Axis; (9) Roundness (Round), a value of 1.0 indicates a perfect circle. It is similar to circularity but is insensitive to irregular borders along the perimeter of the target lesion, also takes into consideration the major axis of the best fit ellipse; (10) Solidity, the ratio of contour area to its convex hull area, describes the extent to which a target lesion morphology is convex or concave. As lesion morphology becomes rough, the solidity value approaches zero. Conversely, very smooth, rounded lesions have solidity values that approach one; (11) Feret Diameter (FD), the longest distance between any two points along the ROI boundary, also known as a maximum caliper; (12) Min Feret (MinF), the minimum caliper diameter; (13) Feret Angle (FA), the angle between the Feret Diameter and a line parallel to the x-axis of the US image, its range is 0 -180 degrees. **Figure 1** shows illustrations of all the morphometric features.

Assessment of Intra- and Inter-Rater Reliability

Based on the calculated sample size (23), 80 lesions from the training cohorts were randomly selected to assess intra- and inter-rater reliability. Using the same procedure, the original assessor QL and another assessor TB performed the second measurements, three weeks after the first one.

Feature Selection

Feature selection was performed on the training cohort. A two-step feature selection procedure was used to generate optimal feature subsets. First, the features were ranked by the wrapper method *Boruta* algorithm (24). *Boruta* assesses if the importance of each individual feature is significantly higher than the importance of a random feature by iteratively fitting the Random Forest algorithm until all predictor features are classified as "confirmed," "tentative," or "rejected". Features "confirmed" by *Boruta* were deemed available for further analyses. Second, if two features are highly correlated among themselves, they provide redundant information in regards to the outcome, so a filter method that is based on Spearman's correlation was conducted to further reduce the dimensionality. A correlation matrix was created with all the *Boruta* "confirmed" features. Highly correlated features (Spearman's correlation coefficients > 0.75) were identified and removed, after which the final selected features were used to construct the nomogram.

Development of the Nomogram

Data from the training cohort was used to develop the nomogram. First, univariate and multivariate logistic regression analyses were performed to determine the independent predictor of breast malignancy. Candidate factors included results from feature selection and patient age. Non-linear relationships between continuous predictors and malignancy risk were assessed, and continuous predictors with significant non-linearity were transformed into categorical variables using restricted cubic splines (RCS) with three

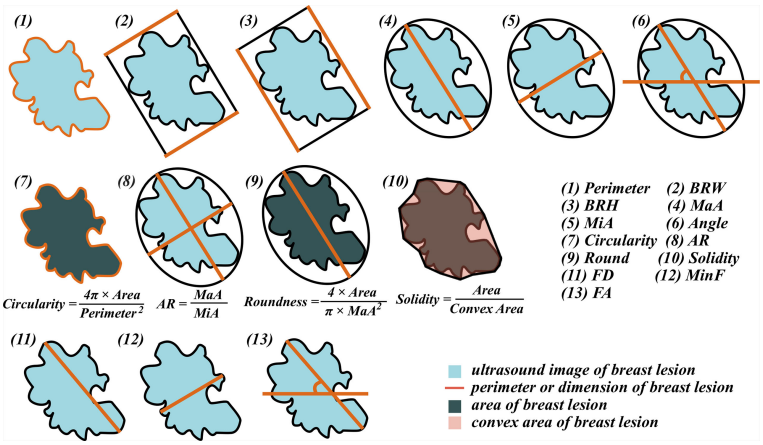

FIGURE 1 | Illustrations of the morphometric features.

knots (25). Factors with p value < 0.2 in univariable analyses were entered in multivariable analyses, which were conducted using stepwise logistic regression with backward elimination at an α level of 0.05.

Basic assumptions that must be met for logistic regression model include linearity between each predictor and outcome, absence of high multicollinearity among predictors, and no strongly influential outliers. To ensure that all logistic regression assumptions were valid, multicollinearity and influential outliers were also assessed. Multicollinearity was estimated by variance inflation factor (VIF), VIF values greater than 4 were an indication of multicollinearity problems (26). Influential outliers were checked by visualizing Cook's distance (27) and standardized residuals, cases with Cook's distance of ≥ 0.05 or standardized residuals of ≥3 (28) were considered to be outliers that had unduly large influences on the results. Therefore, they were further analyzed to determine whether they could be excluded from the model.

Finally, based on findings from the above logistic regression analysis, a web-based interactive nomogram was formulated.

Validation of the Nomogram

Internal and external validations were used to measure the nomogram's performance. The training cohort was used for internal validation while the two validation cohorts were used for external validation.

Performance was assessed using tests for discrimination, calibration, and clinical usefulness. The discriminative capacity was evaluated *via* receiver operating characteristic (ROC) curve analysis and measured by the area under the receiver operating characteristic curve (AUC). Calibration performance was visually assessed using a calibration plot (29), representing the agreement between observed outcomes and predicted probabilities. The Hosmer–Lemeshow test (30) was performed to assess goodness-of-fit. Finally, decision curve analysis (31, 32) was used to evaluate the clinical benefit of the nomogram by quantifying net benefits at different threshold probabilities.

Data Analysis

All data analyses and plots were performed and established using R Studio software (R version 4.0.2). The reported statistical significance levels were all two-sided, with p value < 0.05 being the threshold for significance, unless otherwise indicated.

Normality of distributions of continuous variables was assessed using the Shapiro–Wilk test. Continuous variables are expressed as medians and ranges, while categorical variables are shown as numbers and percentages. Comparisons between groups were performed using the Chi-square test for categorical variables, while the Wilcoxon test or Student's t-test were used for continuous variables.

Sample size estimation for reliability analysis was performed using "ICC Sample Size" in R. Inter-rater and intro-rater reliability was calculated using a single-rating, absolute-agreement, 2-way random-effects correlation coefficients (ICCs, model A,1). Reliability was classified as excellent (ICC > 0.90), good (ICC = 0.76–0.90), moderate (ICC = 0.51–0.75), or poor (ICC < 0.50) (33).

Feature selection was performed using "*Boruta*" in R. Correlations between any two morphological features were measured by Spearman rank correlation coefficient while "ggcorrplot" in R was used for visualization of the correlation matrix. The 3D scatter plots were produced using "plotly" in R.

The "glm" function in R was used to fit the multivariate logistic regression model. Regression diagnostics were used to assess the validity of the model, RCS analyses were performed using the "rms" package, multicollinearity was tested by calculating VIF using the "car" package, while influential outliers were graphly inspected by Cook's distance using the "broom" package. The "rms" and "DynNom" packages were used to develop the nomogram and the web-based calculator, respectively.

Performance evaluation, including visualizations of ROC, Calibration, and DCA, were generated with R packages "ggplot2", "Caret" and "rmda". The "pROC" package was used to measure AUCs and conduct the Delong test, while the "ResourceSelection" package was used for the Hosmer–Lemeshow test.

RESULTS

Basic Information

The flow chart of the study population is presented in **Figure 2**. In total, 917 breast lesions from 917 women were assessed in the study. The final histopathological diagnoses revealed 502 (54.74%) benign and 415 (45.26%) malignant lesions. The training cohort had 520 patients, the external validation cohort from Center B (cohort 1) had 191 patients, while the external validation cohort from Center C (cohort 2) had 206 patients. **Table 1** presents an overview of demographics and baseline characteristics for these study cohorts. While the cohorts did not show significant differences in patients' age and maximum diameters of lesions, there were significant differences with regards to proportions of benign and malignant lesions among the cohorts. As shown in **Table 1**, the predominant histology of malignant lesions for each cohort was invasive ductal carcinoma, the majority of benign lesions in this study had a breast tumor histology described as fibroadenoma, followed by mammary adenosis.

Morphometric Features

All of the morphometric feature data are available on GitHub (see *Data Availability*). **Figure 3** shows the findings obtained

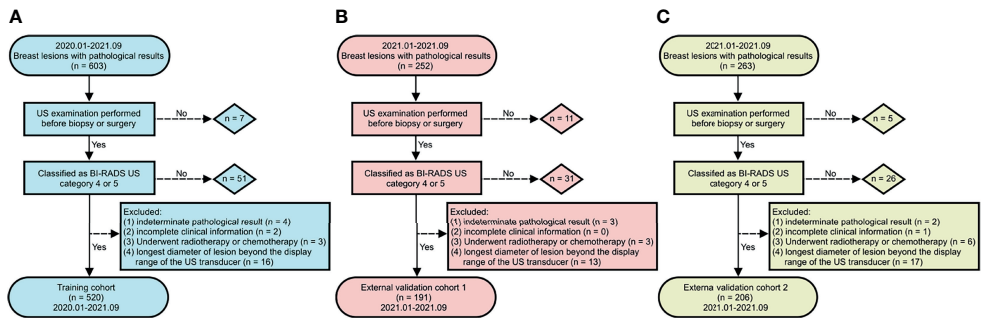

FIGURE 2 | Flow chart of study population. **(A)** training cohort, **(B)** external validation cohort 1, and **(C)** external validation cohort 2.

TABLE 1 | Comparisons of patient demographics and baseline characteristics in the training and validation cohorts.

	Training Cohort (n = 520)	External Validation Cohorts		*P*-value
		Cohort 1 (n = 191)	Cohort 2 (n = 206)	
Age, years (Md (IQR))	51.5 (44.0, 58.0)	52.0 (45.0, 60.0)	54.0 (46.0, 58.0)	0.430
Maximum diameter (n,%)				0.786
<10 mm	34 (6.54)	15 (7.85)	9 (4.37)	
10-20 mm	201 (38.65)	71 (37.17)	77 (37.38)	
20-30 mm	150 (28.85)	59 (30.89)	68 (33.01)	
≥30 mm	135 (25.96)	46 (24.09)	52 (25.24)	
Pathological outcome (n,%)				0.010
Benign lesions	295 (56.73)	113 (59.16)	94 (45.63)	
Malignant lesions	225 (43.27)	78 (40.84)	112 (54.37)	
Histologic subtypes (n,%), Benign				
Fibroadenoma	135 (25.96)	52 (27.23)	44 (21.36)	
Mammary adenosis	97 (18.65)	42 (21.99)	41 (19.90)	
Intraductal papilloma	53 (10.19)	17 (8.90)	7 (3.40)	
Mastitis	8 (1.54)	2 (1.05)	2 (0.97)	
Benign phyllodes tumor	2 (0.38)	0 (0.00)	0 (0.00)	
Histologic subtype (n,%), Malignant				
Invasive ductal carcinoma	192 (36.92)	75 (39.27)	102 (49.51)	
Ductal carcinoma in situ	22 (4.23)	2 (1.05)	4 (1.94)	
Mucous carcinoma	6 (1.15)	0 (0.0)	2 (0.97)	
Invasive lobular carcinoma	3 (0.58%)	1 (0.52)	2 (0.97)	
Solid papillary carcinoma	2 (0.38%)	0 (0.0)	1 (0.49)	

from preliminary analysis of morphometric features in the training cohort. Apart from Angle and FA, the other morphometric features were significantly different between benign and malignant groups. Perimeter, BRW, BRH, MaA, MiA, Round, FD, and MinF values of benign lesions were significantly lower than those of malignant lesions ($p < 0.001$), while Circularity, AR, and Solidity were significantly higher than those of malignant lesions ($p < 0.001$). Morphometric features of the validation cohorts are presented in **Supplementary Figures 1, 2**, respectively.

Reliability of Morphological Feature Measurements

Inter- and intra-rater reliability of measurement as estimated by the ICC was good or excellent for all morphometric features, apart from inter-rater reliability of Circularity, which was moderate. The ICCs for all morphological features are shown in **Supplement Material Page 6, 7**.

Feature Selection

Figure 4 shows the feature selection results. The *Boruta* algorithm and Spearman's correlation analysis identified 3 features as important and less correlated variables. The results are presented by interactive three-dimensional scatter plots (https://chart-studio.plotly.com/~qingling.go/5/#plot). The selected features were Solidity, AR, and MiA, which were then fed into the nomogram as inputs.

Development of the Nomogram

Univariate and Multivariate Analyses

We used restricted cubic splines to flexibly model and visualize the associations between age and morphometric features with malignancy risk (**Figure 5**). Since all these variables showed non-linear relationships with malignancy risk, we transformed them into categorical variables. The points where odds ratio (OR) ≈ 1.00 were chosen as the cutoff value according to the trend and knots position of the RCS curve; more importantly, these cut points showed the best performance in the following model fit test. As shown in **Figure 5**, for age < 51 years, malignancy risk gradually increased with age, while above 51 years, the risk was relatively flat, reaching the highest at around 59 years and gradually decreasing thereafter. When AR < 1.75 or Solidity < 0.92, malignancy risk decreased sharply and then leveled off. Regarding the strong inverted-U-shaped relationship between MiA and malignancy risk, the plot showed a substantial increase in the risk, which was highest at around 16, and decreased thereafter. After multiple comparisons of model fits, we found that the model with MiA cutoff at 11 and 25 can achieve the smallest Akaike information criterion (AIC), suggesting the best model fit.

Table 2 shows the results of univariate and multivariate analyses in the training cohorts. Morphometric features (AR, MiA, Solidity, and age) of patients were all identified as independent predictors for breast malignancy (all $p < 0.05$).

Logistics Regression Diagnostics

(1) Nonlinear relationships. Nonlinear relationships between predictors and pathological outcomes were resolved by RCS analyses. (2) Multicollinearity. All VIF values are below the threshold value of 2 (Age, VIF = 1.02; AR, VIF = 1.04, MiA, VIF = 1.23, Solidity, VIF = 1.20), indicating the absence of collinearity among predictors. (3) Influential outliers. As shown in **Supplementary Figures 3, 4**, no outliers were identified by Cook's distance or standardized residuals. The above findings indicate that all logistic regression assumptions for our model were met.

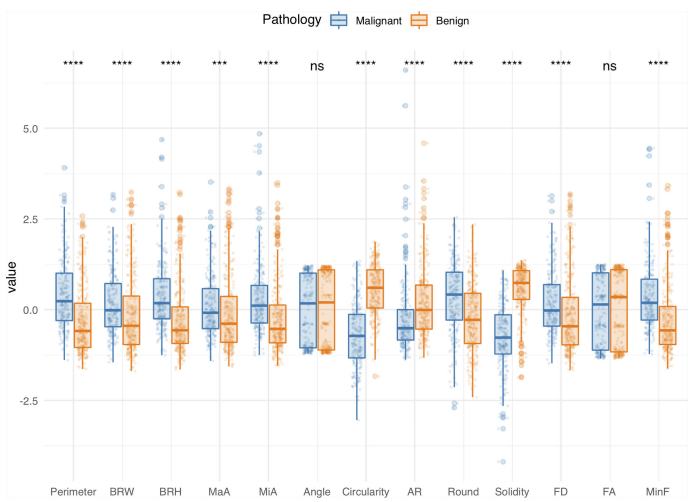

FIGURE 3 | Comparisons of morphological features between benign and malignant groups in the training cohort. Boxplots grouped by pathology show median (horizontal bars), IQR (boxes), and 95% CI (whiskers). Raw data points for each group are shown at the bottom of each box plot. Data were normalized and centered by Z-score transformation to appear on the same scale. Statistical analysis was performed using the Wilcoxon rank-sum test (all features except Round) and Student's t test (Round). ***$p < 0.001$, ****$p < 0.0001$, ns, not significant.

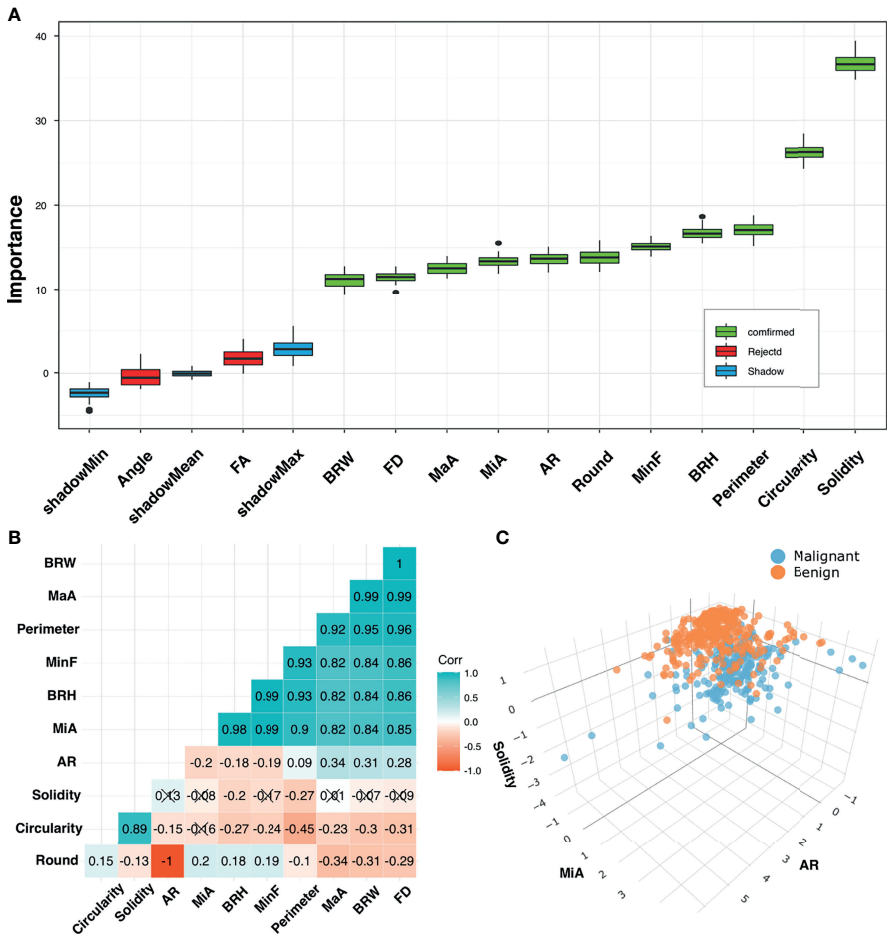

FIGURE 4 | Feature selection. **(A)** Selection of relevant morphometric features for discrimination between benign and malignant groups in the training cohort using the *Boruta* algorithm. Boxplots of features were sorted by increasing importance according to Z-scores. Blue boxes (Shadow) correspond to minimal, mean, and maximal importance, calculated from randomly permuted features. **(B)** Correlation matrix plot shows pairwise positively stronger correlations (blue) or negatively stronger correlations (red). Non-significant correlations ($p > 0.05$) are marked with a cross. **(C)** 3D scatter plots for final selected feature combinations displaying separations of benign and malignant groups.

Nomogram and Web-Based Calculator

Figure 6A shows the nomogram for predicting breast malignancy based on independent risk factors, including US morphometric features AR, MiA, and Solidity. Based on the above nomogram, we established an online risk calculator to facilitate the use of the nomogram by clinicians, which can be freely accessed at https://qingling.shinyapps.io/DynNomapp/ (**Figure 6B**). Using quantitative values of lesion morphological features, the calculator can individually predict the risk of breast malignancy. For instance, for patients aged > 51 years whose AR ≤ 1.75, MiA 11-25 and Solidity ≤ 0.92, the risk probability of malignancy was approximately 91.5% (95% CI 86.0–94.9%).

Validation of the Nomogram

Discrimination

The AUCs of the nomogram in the training and validation cohorts were 0.885, 0.907, and 0.927, respectively (**Figure 7A**). There were no significant differences in AUCs between any two cohorts (DeLong test, $p > 0.05$ for each comparison, **Supplementary Table 2**). Therefore, our nomogram performed well in all the training and validation cohorts.

Calibration

Calibration curves of the nomogram are close to the diagonal line in the training and validation cohorts, demonstrating that the predictive probability has good agreement with observed outcomes (**Figure 7B**). The Hosmer–Lemeshow test yielded a non-significant statistic ($p = 0.94$), indicating a good fit.

Clinical Utility

DCA curves of the training and validation cohorts revealed clinical usefulness of the nomogram (**Figure 7C**). From this figure, it can be seen that in all the training and validation cohorts, the nomogram has a higher net benefit than both "treat all" and "treat none" across the range of threshold probabilities 10-90%, indicating that the nomogram was clinically useful, that is, the nomogram would

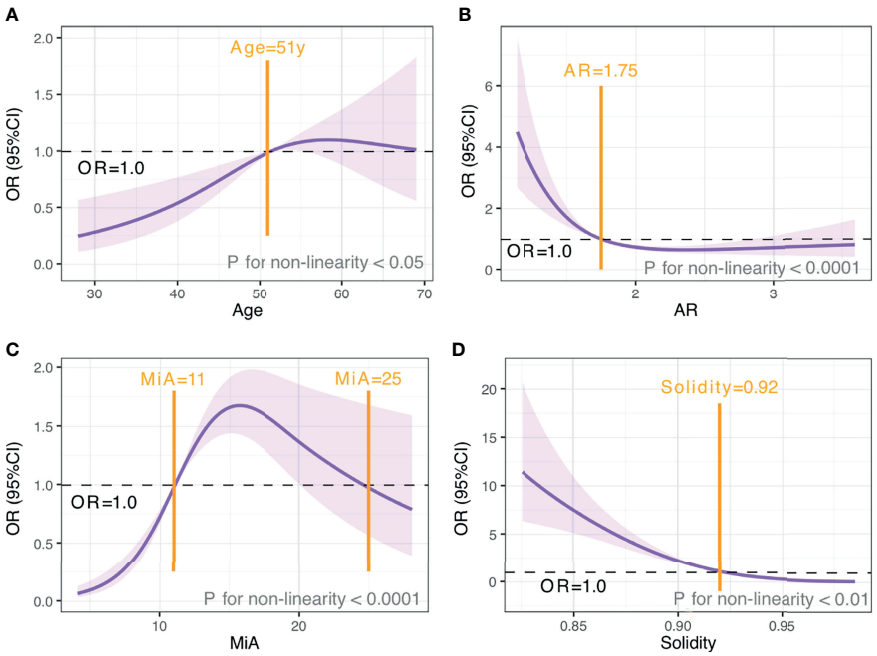

FIGURE 5 | The relationship between age and morphometric features with malignancy risk. OR and 95% CI for age **(A)**, AR **(B),** MiA **(C)**, and Solidity **(D).** The analyses used restricted cubic splines. Purple shaded areas, 95% CIs. Black horizontal dotted line, OR=1.00. Yellow vertical solid line, cut-off value.

TABLE 2 | Results of univariate and multivariate analyses for breast malignancy in the training group.

	Univariate analysis			Multivariate analysis		
	OR	**95%CI**	***P*-value**	**OR**	**95%CI**	***P*-value**
Age						
>51	Ref.			Ref.		
≤51	0.61	0.43~0.87	0.006	0.618	0.38~0.99	0.048
AR						
>1.75	Ref.			Ref.		
≤1.75	2.37	1.66~3.38	<0.001	2.01	1.24~3.26	0.005
MiA						
<11	Ref.			Ref.		
11-25	3.24	2.24~4.68	<0.001	3.83	2.32~6.46	< 0.001
≥25	1.95	0.78~4.89	0.156	8.02	2.65~23.83	< 0.001
Solidity						
>0.92	Ref.			Ref.		
≤0.92	20.28	12.83~32.06	<0.001	25.81	15.47~44.80	< 0.001

Factors associated with dependent variables with p < 0.2 in univariate analysis were entered into the logistic backward step-wise multivariate model.

improve patient outcome irrespective of patient or doctor preference for a reasonable threshold probability.

DISCUSSION

In this retrospective multicenter study of 917 patients with breast lesions, we analyzed US morphometric features and developed a simple-to-use nomogram for predicting cancer. The newly developed nomogram performed well, and its predictive value was validated using data from other hospitals in a different geographic region. Our nomogram has three ultrasonic morphometric features that are easy to generate using ImageJ software and that radiologists can easily understand and interpret. The nomogram can adapt to different ultrasonic instruments and settings, and it has a high generalization ability and practicality. To make the nomogram user-friendly, we have availed it as a free web-based calculator. Consequently, the nomogram developed in this study will potentially be a valuable tool in clinical practices.

As precision medicine advances, the nomogram, which can provide an individual patient with a quantitative risk assessment

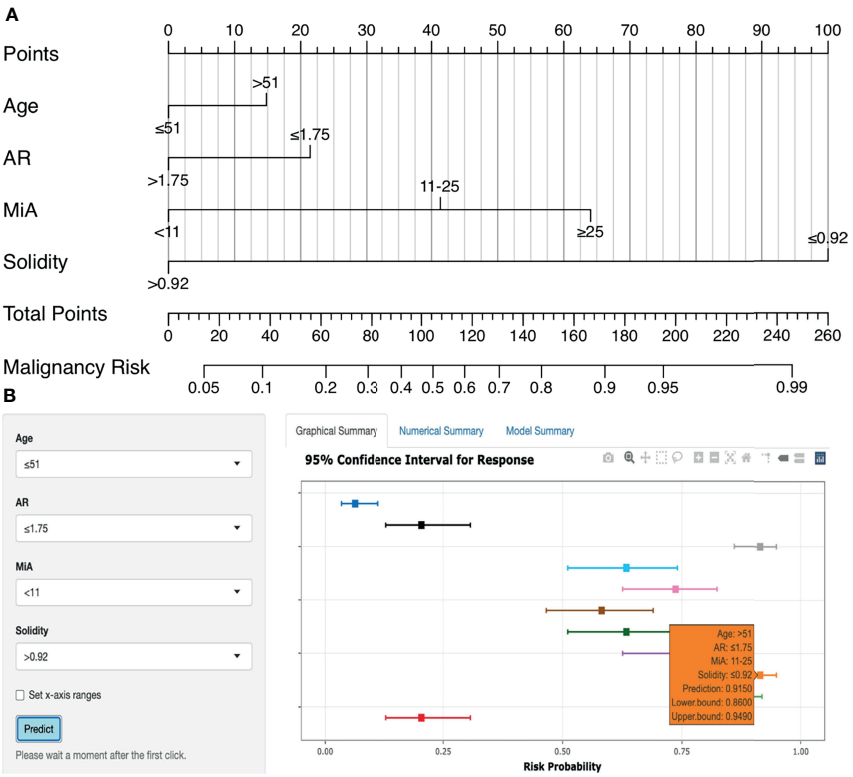

FIGURE 6 | Nomogram and online risk calculator. **(A)** Nomogram based on US morphometric features. Applications of the nomogram were exemplified in **Supplementary Figure 5**. **(B)** The online calculator application version of the nomogram.

of a particular outcome by a graphical interface, has been proposed as a simple and reliable means to improve disease prediction or prognosis (34, 35). Several US-based nomograms for predicting cancer risk or prognosis have been reported in the literature; all of these nomograms demonstrated high predictive performance with AUC = 0.747–0.951. Some of the nomograms were based on subjective evaluations using qualitative descriptors (e.g., spiculated, rounded, microcalcification, etc.), which are highly dependent on the level of expertise and experience and can suffer from a large intra- and inter-observer variability (36–39). However, other nomograms were based on quantitative methods such as radiomics, which can objectively describe tumor phenotypes using numerical features extracted from radiological images (14–16). These features, which are mainly related to tumor size, shape, texture, and intensity, provide a comprehensive tumor characterization. In this scenario, quantitative evaluation of US images is a natural consequence of the path towards personalized medicine.

The present study is based on quantitative features, and the performance of our nomogram was very comparable to that of the preceding studies, with a few notable differences. The first difference is that we only used the morphometric features to construct the nomogram, which was due to the following reasons. As a diagnostic or prognostic tool, a nomogram must be practical and generalizable in clinical settings. However, the reproducibility of quantitative features based on image pixels, including textural features, intensity-based features, and wavelet-based features, is affected by image preprocessing to variable degrees (19, 40, 41). Recently, Lee SE et al. found that the radiomics of textural features differed depending on the type of US machine (42). Previous literature has also associated the measurement of textural parameters with nonlinear variations in ultrasonic system settings such as time-gain compensation, total gain, and focal depth (43). Overall, these studies consistently indicated that due to variations in acquisition modes, parameter selections, or implementation procedures, the features derived from the pixel gray-level statistics in terms of intensity and spatial distribution have greater variability, particularly for US technique, which is more operator- and system-dependent. In contrast, the morphometric features characterize the shape and contour of a lesion and are essentially independent of the system settings and machines (22, 44). More importantly, the morphologic traits of breast cancer are associated with histological findings (21, 45, 46), which can provide valuable information for deriving robust multidisciplinary models (47). In this study, we found that most of the morphometric features differed significantly between benign and malignant groups, and the contributions of the selected features to the prediction model were as follows: Solidity > Circularity > Minor Axis. These results confirmed the association between ultrasonography morphologic features and histopathological findings.

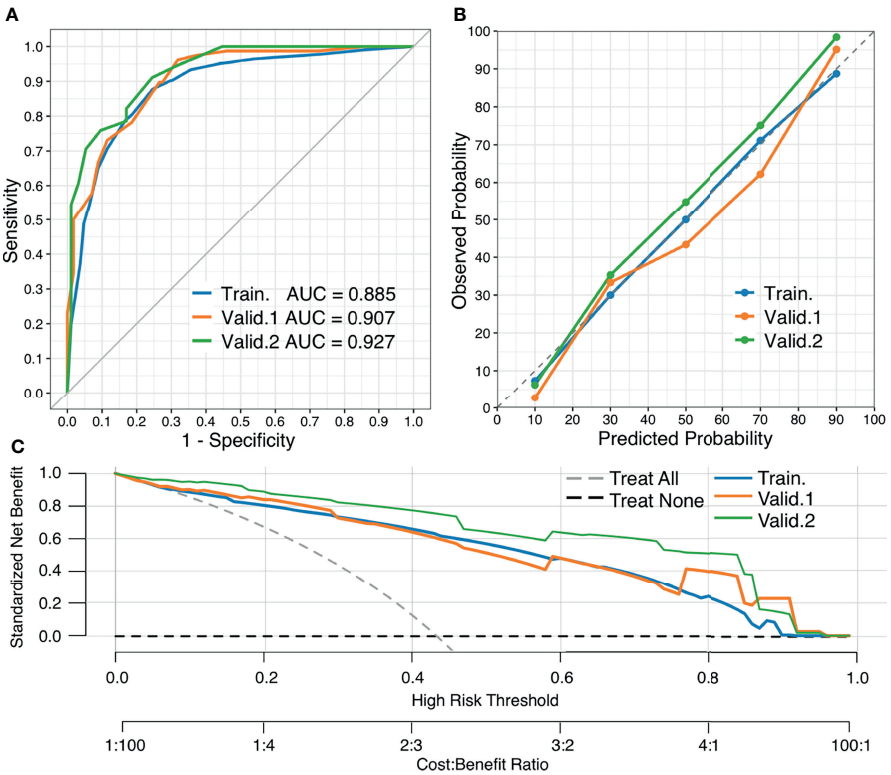

FIGURE 7 | Performance of the nomogram. **(A)** ROC curves of the nomogram in the training and external validation cohorts, respectively. **(B)** Calibration curves of the nomogram, which depict calibration of the nomogram in terms of agreement between the predicted risk of breast malignancy and observed outcomes. The diagonal dotted line denotes a perfect prediction, the closer the calibration curve fit is to the diagonal line, the better the predictive accuracy of the nomogram. **(C)** DCA curves of the nomogram. The gray and black dotted lines represent the hypothesis that all patients had a diagnosis of breast malignancy ("treat all") and that no patients had a diagnosis of breast malignancy ("treat none"), respectively. X-axis indicates the threshold probability for pathological outcomes while the Y-axis indicates the standardized net benefit for a given threshold probability.

The second difference is that in previous studies, the images from the US were almost entirely collected in one specific US machine and system (14–16), whereas in this study, the training and validation data were both pooled from different US machines and systems. Moreover, the US transducers used for imaging had different transmission frequencies, which is more congruent with the actual clinical settings and a significant strength of this study. The results with the external validation cohorts strengthened the predictive potential of the model, increasing our confidence in the robustness and generality of the novel nomogram. Furthermore, we built a web-based calculator with user-friendly digital interfaces to display the nomogram, which makes risk assessment easier. The user inputs the details of the lesion on the web page, and the probability of breast malignancy is calculated automatically for the patient.

Finally, when compared to other quantification-based nomograms (14–17), the predictor variables in our nomogram are easily accessed and interpreted. In general, lack of interpretability is one of the major barriers to successful translation of predictive models from research to clinical practice, particularly for data-driven precision medicine (20). From a clinical perspective, interpretability is critical for winning the trust of physicians, developing a robust decision-making system, and overcoming regulatory concerns (48). For example, it is difficult for radiomics practitioners to interpret first-order entropy or grey level co-occurrence matrix features and to assign biological meaning to them (49). Physicians must be able to interpret the nomogram model and identify the predictors separately for rejected and accepted outcomes, and decide on the subsequent treatment protocols (50). The morphometric features in our nomogram are relatively non-abstract and can be considered an extension of the analytical thinking of a radiologist. This assists radiologists in understanding the decision process of the nomogram and facilitates doctor–patient communication. Furthermore, the morphometric features are relatively easy to retrieve *via* the interactive freeware ImageJ, without the need to run scripts from the command line.

This study has several limitations that are worth mentioning. First, this was a retrospective study, which had inherent biases. Therefore, larger, high-quality prospective studies should be conducted in the future. Second, the distribution of pathological subtypes of breast cancer included in this study was unbalanced, especially for the specific pathological types such as mucinous or

medullary breast cancer. In addition, the sample size was relatively small and the specific pathological types had different histological substrates that manifest as different imaging features on US (51, 52), which may have resulted in bias. Third, large dimension lesions were not included in this study, which could have caused spectrum bias in patient selection. Finally, accurate segmentation is necessary for extracting quantitative features from a tumor (53). Although the features extracted using manual segmentation in this study showed high inter-observer and intra-observer reliability, the process was relatively time-consuming when compared to automatic segmentation. These limitations highlight the need for additional research to potentially improve model performance.

CONCLUSIONS

In this multicentric study, we developed an interpretable and simple-to-use dynamic nomogram to quantify the probability of breast malignancy based on US morphometrics. The nomogram demonstrated good discrimination performance between malignant and benign lesions, as well as good calibration and clinical usefulness. Moreover, the nomogram showed high generalization capabilities, suggesting that it may be used in clinical practice as a tool to guide personalized treatment. Our findings show that quantitative morphometric features from different ultrasound machines and systems can be used as imaging surrogate biomarkers for the development of robust and reproducible quantitative ultrasound dynamic models in breast cancer research.

DATA AVAILABILITY STATEMENT

The datasets presented in this study can be found in online repositories. The names of the repository/repositories and accession number(s) can be found below: https://github.com/QinglingGo/BUS-Morphometric-Datasets.

ETHICS STATEMENT

The First Affiliated Hospital of Wannan Medical College Review Board, Shandong Provincial Third Hospital Review Board and Linyi People's Hospital Review Board approved this retrospective study. Written informed consent was waived due to the use of retrospective, de-identified information from the image database.

AUTHOR CONTRIBUTIONS

QinglingZ: conceptualization, data curation, supervision, data analysis, and writing (original draft). QingluZ and TL: data curation, interpretation, and writing (review and editing). TB, QL, and YY: US morphometric data collection. All authors contributed to the article and approved the submitted version.

ACKNOWLEDGMENTS

The authors thank all the member staff at the Departments of Ultrasonography for their kind contribution and support while conducting the study.

SUPPLEMENTARY MATERIAL

The Supplementary Material for this article can be found online at: https://www.frontiersin.org/articles/10.3389/fonc.2022.868164/full#supplementary-material

REFERENCES

1. Sung H, Ferlay J, Siegel RL, Laversanne M, Soerjomataram I, Jemal A, et al. Global Cancer Statistics 2020: Globocan Estimates of Incidence and Mortality Worldwide for 36 Cancers in 185 Countries. *CA Cancer J Clin* (2021) 71 (3):209–49. doi: 10.3322/caac.21660
2. Basu P, Ponti A, Anttila A, Ronco G, Senore C, Vale DB, et al. Status of Implementation and Organization of Cancer Screening in the European Union Member States-Summary Results From the Second European Screening Report. *Int J Cancer* (2018) 142(1):44–56. doi: 10.1002/ijc.31043
3. Hogben RK. Screening for Breast Cancer in England: A Review. *Curr Opin Obstet Gynecol* (2008) 20(6):545–9. doi: 10.1097/GCO.0b013e3283186fab
4. Evans A, Trimboli RM, Athanasiou A, Balleyguier C, Baltzer PA, Bick U, et al. Breast Ultrasound: Recommendations for Information to Women and Referring Physicians by the European Society of Breast Imaging. *Insights Imaging* (2018) 9(4):449–61. doi: 10.1007/s13244-018-0636-z
5. Pan B, Yao R, Zhu QL, Wang CJ, You SS, Zhang J, et al. Clinicopathological Characteristics and Long-Term Prognosis of Screening Detected Non-Palpable Breast Cancer by Ultrasound in Hospital-Based Chinese Population (2001-2014). *Oncotarget* (2016) 7(47):76840–51. doi: 10.18632/oncotarget.12319
6. Berg WA, Bandos AI, Mendelson EB, Lehrer D, Jong RA, Pisano ED. Ultrasound as the Primary Screening Test for Breast Cancer: Analysis From Acrin 6666. *J Natl Cancer Inst* (2016) 108(4):djv367. doi: 10.1093/jnci/djv367
7. Bozzini A, Nicosia L, Pruneri G, Maisonneuve P, Meneghetti L, Renne G, et al. Clinical Performance of Contrast-Enhanced Spectral Mammography in Pre-Surgical Evaluation of Breast Malignant Lesions in Dense Breasts: A Single Center Study. *Breast Cancer Res Treat* (2020) 184(3):723–31. doi: 10.1007/s10549-020-05881-2
8. Mendelson EB, Böhm-Vélez M, Berg WA, D'Orsi CJ, Sickles EA, et al. ACR BI-RADS©Ultrasound. In: *ACR BI-RADS©Atlas, Breast Imaging Reporting and Data System*. Reston, VA: American College of Radiology (2013).
9. Zou X, Wang J, Lan X, Lin Q, Han F, Liu L, et al. Assessment of Diagnostic Accuracy and Efficiency of Categories 4 and 5 of the Second Edition of the Bi-Rads Ultrasound Lexicon in Diagnosing Breast Lesions. *Ultrasound Med Biol* (2016) 42(9):2065–71. doi: 10.1016/j.ultrasmedbio.2016.04.020
10. Stavros AT, Freitas AG, deMello GGN, Barke L, McDonald D, Kaske T, et al. Ultrasound Positive Predictive Values by Bi-Rads Categories 3-5 for Solid Masses: An Independent Reader Study. *Eur Radiol* (2017) 27(10):4307–15. doi: 10.1007/s00330-017-4835-7
11. Spinelli Varella MA, Teixeira da Cruz J, Rauber A, Varella IS, Fleck JF, Moreira LF. Role of Bi-Rads Ultrasound Subcategories 4a to 4c in Predicting Breast Cancer. *Clin Breast Cancer* (2018) 18(4):e507–e11. doi: 10.1016/j.clbc.2017.09.002
12. Kim YR, Kim HS, Kim HW. Are Irregular Hypoechoic Breast Masses on Ultrasound Always Malignancies?: A Pictorial Essay. *Korean J Radiol* (2015) 16(6):1266–75. doi: 10.3348/kjr.2015.16.6.1266

13. Nicosia L, Addante F, Bozzini AC, Latronico A, Montesano M, Meneghetti L, et al. Evaluation of Computer-Aided Diagnosis in Breast Ultrasonography: Improvement in Diagnostic Performance of Inexperienced Radiologists. *Clin Imaging* (2022) 82:150–5. doi: 10.1016/j.clinimag.2021.11.006
14. Luo WQ, Huang QX, Huang XW, Hu HT, Zeng FQ, Wang W. Predicting Breast Cancer in Breast Imaging Reporting and Data System (Bi-Rads) Ultrasound Category 4 or 5 Lesions: A Nomogram Combining Radiomics and Bi-Rads. *Sci Rep* (2019) 9(1):11921. doi: 10.1038/s41598-019-48488-4
15. Qiu X, Jiang Y, Zhao Q, Yan C, Huang M, Jiang T. Could Ultrasound-Based Radiomics Noninvasively Predict Axillary Lymph Node Metastasis in Breast Cancer? *J Ultrasound Med* (2020) 39(10):1897–905. doi: 10.1002/jum.15294
16. Xiong L, Chen H, Tang X, Chen B, Jiang X, Liu L, et al. Ultrasound-Based Radiomics Analysis for Predicting Disease-Free Survival of Invasive Breast Cancer. *Front Oncol* (2021) 11:621993. doi: 10.3389/fonc.2021.621993
17. Zha HL, Zong M, Liu XP, Pan JZ, Wang H, Gong HY, et al. Preoperative Ultrasound-Based Radiomics Score Can Improve the Accuracy of the Memorial Sloan Kettering Cancer Center Nomogram for Predicting Sentinel Lymph Node Metastasis in Breast Cancer. *Eur J Radiol* (2021) 135:109512. doi: 10.1016/j.ejrad.2020.109512
18. Lambin P, Leijenaar RTH, Deist TM, Peerlings J, de Jong EEC, van Timmeren J, et al. Radiomics: The Bridge Between Medical Imaging and Personalized Medicine. *Nat Rev Clin Oncol* (2017) 14(12):749–62. doi: 10.1038/nrclinonc.2017.141
19. Traverso A, Wee L, Dekker A, Gillies R. Repeatability and Reproducibility of Radiomic Features: A Systematic Review. *Int J Radiat Oncol Biol Phys* (2018) 102(4):1143–58. doi: 10.1016/j.ijrobp.2018.05.053
20. Vuong D, Tanadini-Lang S, Wu Z, Marks R, Unkelbach J, Hillinger S, et al. Radiomics Feature Activation Maps as a New Tool for Signature Interpretability. *Front Oncol* (2020) 10:578895. doi: 10.3389/fonc.2020.578895
21. Kim SH, Seo BK, Lee J, Kim SJ, Cho KR, Lee KY, et al. Correlation of Ultrasound Findings With Histology, Tumor Grade, and Biological Markers in Breast Cancer. *Acta Oncol* (2008) 47(8):1531–8. doi: 10.1080/02841860801971413
22. El-Azizy ARM, Salaheldien M, Rushdi MA, Gewefel H, Mahmoud AM. Morphological Characterization of Breast Tumors Using Conventional B-Mode Ultrasound Images. *Annu Int Conf IEEE Eng Med Biol Soc* (2019) 2019:6620–3. doi: 10.1109/EMBC.2019.8857438
23. Zou GY. Sample Size Formulas for Estimating Intraclass Correlation Coefficients With Precision and Assurance. *Stat Med* (2012) 31(29):3972–81. doi: 10.1002/sim.5466
24. Kursa MB, Rudnicki WR. Feature Selection With the *Boruta* Package. *J Stat Softw* (2010) 36(11):1–13. doi: 10.18637/jss.v036.i11
25. Durrleman S, Simon R. Flexible Regression Models With Cubic Splines. *Stat Med* (1989) 8(5):551–61. doi: 10.1002/sim.4780080504
26. Kirshner JJ, Heckler CE, Janelsins MC, Dakhil SR, Hopkins JO, Coles C, et al. Prevention of Pegfilgrastim-Induced Bone Pain: A Phase Iii Double-Blind Placebo-Controlled Randomized Clinical Trial of the University of Rochester Cancer Center Clinical Community Oncology Program Research Base. *J Clin Oncol* (2012) 30(16):1974–9. doi: 10.1200/JCO.2011.37.8364
27. Cook RD. Detection of Influential Observation in Linear Regression. *Technometrics* (1977) 19(1):15–8. doi: 10.1080/00401706.1977.10489493
28. Sorge RE, Mapplebeck JC, Rosen S, Beggs S, Taves S, Alexander JK, et al. Different Immune Cells Mediate Mechanical Pain Hypersensitivity in Male and Female Mice. *Nat Neurosci* (2015) 18(8):1081–3. doi: 10.1038/nn.4053
29. Steyerberg EW, Vickers AJ, Cook NR, Gerds T, Gonen M, Obuchowski N, et al. Assessing the Performance of Prediction Models: A Framework for Traditional and Novel Measures. *Epidemiology* (2010) 21(1):128–38. doi: 10.1097/EDE.0b013e3181c30fb2
30. Hosmer DW, Lemeshow S. Goodness-Of-Fit Tests for the Multiple Logistic Regression Model. *Commun Stat-Theor M* (1980) 9(10):1043–69. doi: 10.1080/03610928008827941
31. Vickers AJ, Elkin EB. Decision Curve Analysis: A Novel Method for Evaluating Prediction Models. *Med Decis Making* (2006) 26(6):565–74. doi: 10.1177/0272989X06295361
32. Vickers AJ, van Calster B, Steyerberg EW. A Simple, Step-By-Step Guide to Interpreting Decision Curve Analysis. *Diagn Progn Res* (2019) 3:18. doi: 10.1186/s41512-019-0064-7
33. Koo TK, Li MY. A Guideline of Selecting and Reporting Intraclass Correlation Coefficients for Reliability Research. *J Chiropr Med* (2016) 15(2):155–63. doi: 10.1016/j.jcm.2016.02.012
34. Balachandran VP, Gonen M, Smith JJ, DeMatteo RP. Nomograms in Oncology: More Than Meets the Eye. *Lancet Oncol* (2015) 16(4):173–80. doi: 10.1016/S1470-2045(14)71116-7
35. Martinez-Perez C, Turnbull AK, Ekatah GE, Arthur LM, Sims AH, Thomas JS, et al. Current Treatment Trends and the Need for Better Predictive Tools in the Management of Ductal Carcinoma in Situ of the Breast. *Cancer Treat Rev* (2017) 55:163–72. doi: 10.1016/j.ctrv.2017.03.009
36. Zhou P, Jin C, Lu J, Xu L, Zhu X, Lian Q, et al. Modified Model for Diagnosing Breast Imaging Reporting and Data System Category 3 to 5 Breast Lesions: Retrospective Analysis and Nomogram Development. *J Ultrasound Med* (2021) 40(1):151–61. doi: 10.1002/jum.15385
37. Niu Z, Tian JW, Ran HT, Ren WD, Chang C, Yuan JJ, et al. Risk-Predicted Dual Nomograms Consisting of Clinical and Ultrasound Factors for Downgrading Bi-Rads Category 4a Breast Lesions - a Multiple Centre Study. *J Cancer* (2021) 12(1):292–304. doi: 10.7150/jca.51302
38. Liang T, Cong S, Yi Z, Liu J, Huang C, Shen J, et al. Ultrasound-Based Nomogram for Distinguishing Malignant Tumors From Nodular Sclerosing Adenoses in Solid Breast Lesions. *J Ultrasound Med* (2021) 40(10):2189–200. doi: 10.1002/jum.15612
39. Yang Y, Hu Y, Shen S, Jiang X, Gu R, Wang H, et al. A New Nomogram for Predicting the Malignant Diagnosis of Breast Imaging Reporting and Data System (Bi-Rads) Ultrasonography Category 4a Lesions in Women With Dense Breast Tissue in the Diagnostic Setting. *Quant Imaging Med Surg* (2021) 11(7):3005–17. doi: 10.21037/qims-20-1203
40. Yip SS, Aerts HJ. Applications and Limitations of Radiomics. *Phys Med Biol* (2016) 61(13):R150–66. doi: 10.1088/0031-9155/61/13/R150
41. Pesapane F, Rotili A, Agazzi GM, Botta F, Raimondi S, Penco S, et al. Recent Radiomics Advancements in Breast Cancer: Lessons and Pitfalls for the Next Future. *Curr Oncol* (2021) 28(4):2351–72. doi: 10.3390/curroncol28040217
42. Lee SE, Han K, Kwak JY, Lee E, Kim EK. Radiomics of Us Texture Features in Differential Diagnosis Between Triple-Negative Breast Cancer and Fibroadenoma. *Sci Rep* (2018) 8(1):13546. doi: 10.1038/s41598-018-31906-4
43. Alvarenga AV, Infantosi A, Pereira W, Azevedo C. Morphometric and Texture Parameters in Distinguishing Breast Tumours on Ultrasound Images. In: R Magjarevic, JH Nagel, editors. *World Congress on Medical Physics and Biomedical Engineering*. Berlin: IFMBE Proceedings (2006). p. 2272–5. doi: 10.1007/978-3-540-36841-0_573
44. Wu WJ, Moon WK. Ultrasound Breast Tumor Image Computer-Aided Diagnosis With Texture and Morphological Features. *Acad Radiol* (2008) 15(7):873–80. doi: 10.1016/j.acra.2008.01.010
45. Malherbe K, Bresser P. Association Between Ultrasound Morphologic Features and Histopathological Findings of Lobular Carcinoma. *J Med Radiat Sci* (2019) 66(3):177–83. doi: 10.1002/jmrs.336
46. Wang H, Zhan W, Chen W, Li Y, Chen X, Shen K. Sonography With Vertical Orientation Feature Predicts Worse Disease Outcome in Triple Negative Breast Cancer. *Breast* (2020) 49:33–40. doi: 10.1016/j.breast.2019.10.006
47. Tot T. The Role of Large-Format Histopathology in Assessing Subgross Morphological Prognostic Parameters: A Single Institution Report of 1000 Consecutive Breast Cancer Cases. *Int J Breast Cancer* (2012) 2012:395415. doi: 10.1155/2012/395415
48. Naik N, Madani A, Esteva A, Keskar NS, Press MF, Ruderman D, et al. Deep Learning-Enabled Breast Cancer Hormonal Receptor Status Determination From Base-Level H&E Stains. *Nat Commun* (2020) 11(1):5727. doi: 10.1038/s41467-020-19334-3
49. Parekh VS, Jacobs MA. Deep Learning and Radiomics in Precision Medicine. *Expert Rev Precis Med Drug Dev* (2019) 4(2):59–72. doi: 10.1080/23808993.2019.1585805
50. Das D, Ito J, Kadowaki T, Tsuda K. An Interpretable Machine Learning Model for Diagnosis of Alzheimer's Disease. *PeerJ* (2019) 7:e6543. doi: 10.7717/peerj.6543
51. Pintican R, Duma M, Chiorean A, Fetica B, Badan M, Bura V, et al. Mucinous Versus Medullary Breast Carcinoma: Mammography, Ultrasound, and Mri Findings. *Clin Radiol* (2020) 75(7):483–96. doi: 10.1016/j.crad.2019.12.024
52. Chaudhry AR, El Khoury M, Gotra A, Eslami Z, Omeroglu A, Omeroglu-Altinel G, et al. Imaging Features of Pure and Mixed Forms of Mucinous Breast Carcinoma With Histopathological Correlation. *Br J Radiol* (2019) 92 (1095):20180810. doi: 10.1259/bjr.20180810

53. Thawani R, McLane M, Beig N, Ghose S, Prasanna P, Velcheti V, et al. Radiomics and Radiogenomics in Lung Cancer: A Review for the Clinician. *Lung Cancer* (2018) 115:34–41. doi: 10.1016/j.lungcan.2017.10.015

Conflict of Interest: The authors declare that the research was conducted in the absence of any commercial or financial relationships that could be construed as a potential conflict of interest.

Publisher's Note: All claims expressed in this article are solely those of the authors and do not necessarily represent those of their affiliated organizations, or those of the publisher, the editors and the reviewers. Any product that may be evaluated in this article, or claim that may be made by its manufacturer, is not guaranteed or endorsed by the publisher.

frontiers | Frontiers in Oncology

ORIGINAL RESEARCH
published: 24 May 2022
doi: 10.3389/fonc.2022.906501

Combined Use of Shear Wave Elastography, Microvascular Doppler Ultrasound Technique, and BI-RADS for the Differentiation of Benign and Malignant Breast Masses

Bin Wang[1], Yu-Yuan Chen[1], Si Yang[1], Zhen-Wen Chen[1], Jia Luo[1], Xin-Wu Cui[2], Christoph F. Dietrich[3] and Ai-jiao Yi[1]**

[1] Department of Medical Ultrasound, Yueyang Central Hospital, Yueyang, China, [2] Department of Medical Ultrasound, Tongji Hospital, Tongji Medical College, Huazhong University of Science and Technology, Wuhan, China, [3] Department Allgemeine Innere Medizin, Kliniken Hirslanden Beau Site, Salem und Permanence, Bern, Switzerland

OPEN ACCESS

Edited by:
Abhishek Mahajan,
Clatterbridge Cancer Centre NHS Foundation Trust, United Kingdom

Reviewed by:
Sung Bin Park,
Chung-Ang University Hospital, South Korea
Ayşegül Altunkeser,
University of Health Sciences (Turkey), Turkey

***Correspondence:**
Xin-Wu Cui
cuixinwu@live.cn
Ai-Jiao Yi
938186822@163.com

Specialty section:
This article was submitted to Cancer Imaging and Image-directed Interventions, a section of the journal Frontiers in Oncology

Received: 28 March 2022
Accepted: 25 April 2022
Published: 24 May 2022

Citation:
Wang B, Chen Y-Y, Yang S, Chen Z-W, Luo J, Cui X-W, Dietrich CF and Yi A-j (2022) Combined Use of Shear Wave Elastography, Microvascular Doppler Ultrasound Technique, and BI-RADS for the Differentiation of Benign and Malignant Breast Masses. Front. Oncol. 12:906501. doi: 10.3389/fonc.2022.906501

Objective: To evaluate the value of the combined use of Breast Imaging Reporting and Data System (BI-RADS), qualitative shear wave elastography (SWE), and AngioPLUS microvascular Doppler ultrasound technique (AP) for distinguishing benign and malignant breast masses.

Materials and Methods: A total of 210 pathologically confirmed breast lesions in 210 patients were reviewed using BI-RADS, qualitative SWE, and AP. The sensitivity, specificity, negative predictive value (NPV), positive predictive value (PPV), accuracy, and area under the receiver operating characteristic curve (AUC) of BI-RADS and the combination of qualitative SWE and/or AP with BI-RADS were compared, respectively.

Results: Compared with using BI-RADS alone, the use of combined qualitative SWE and/or AP with BI-RADS had higher AUC values ($P < 0.001$). Besides this, the combination of qualitative SWE and AP with BI-RADS had the best diagnostic performance for differentiating between benign and malignant masses. When AP and SWE were combined with BI-RADS, 49/76 benign masses were downgraded from BI-RADS category 4a into BI-RADS category 3, while no benign masses were upgraded from BI-RADS category 3 into BI-RADS category 4a. Three sub-centimeter malignant masses were downgraded from BI-RADS category 4a into BI-RADS category 3, while three malignant masses remain in BI-RADS category 3 due to a benign manifestation in both AP and qualitative SWE. Moreover, 5/6 of them were sub-centimeter masses, and 4/6 of them were intraductal carcinoma. The sensitivity, specificity, PPV, NPV, accuracy, and AUC were 91.0%, 81.1%, 69.3%, 95.1%, 84.3%, and 0.861 (95% confidence interval, 0.806–0.916; $P < 0.001$), respectively. Compared with BI-RADS alone, the sensitivity slightly decreased, while the specificity, PPV, NPV, and accuracy were significantly improved.

Conclusion: Combination of qualitative SWE and AP with BI-RADS improved the diagnostic performance in differentiating benign from malignant breast lesions, which is helpful for avoiding unnecessary biopsies. However, we should be careful about the downgrading of sub-centimeter BI-RADS 4a category lesions.

Keywords: breast mass, ultrasound, shear wave elastography, Angio PLUS, Breast Imaging Reporting and Data System

INTRODUCTION

Breast cancer is the leading cause in the morbidity and mortality of women all over the world. In recent years, the incidence of breast cancer has been increasing (1, 2). Breast ultrasound gives real-time results, is convenient, is of a low cost, and is non-radiative; thus, it has been a crucial tool for screening of breast lesions. The fifth edition of the Breast Imaging Reporting and Data System (BI-RADS) was widely used to standardize the risk evaluation of breast lesions (3). However, there was a highly variable rate of breast cancer and a high rate of benign lesions (61.2%) (4) in BI-RADS category 4, which might cause unnecessary biopsies.

Some studies showed that breast cancer was highly related to the angiogenesis of microvessels (5). Microvessels are essential to the growth, invasion, and survival of breast tumors. Furthermore, the microvascular architecture in benign tumors was markedly different from that of the malignant ones (6). Currently, color Doppler flow imaging (CDFI), power Doppler imaging (PDI), contrast-enhanced ultrasound (CEUS), and dynamic contrast-enhanced magnetic resonance imaging (CE-MRI) are widely used to detect vascularity in breast tumors (7–9). CDFI is the most widely used method, which is noninvasive and simple to operate, and it can provide some vascularity characteristics which suggest malignancy, such as hypervascularity, central or penetrating vessels, and a branching or disordered morphology (5, 10, 11). Compared with CDFI, PDI has an advantage in the detection of low-velocity vessels and allows one to observe blood vessels in real time. However, CDFI was limited in evaluating vessels <0.2 mm in diameter, PDI has low sensitivity in the detection of microvessels, and the differences of vascularity between malignant and benign lesions had great overlaps (12, 13), which impacted their differentiation ability compared with other invasive methods, such as CEUS and CE-MRI (14).

Angio PLUS microvascular Doppler ultrasound technique (AP) is an innovative Doppler ultrasound technique (Aixplorer, Supersonic Imaging, France). AP relies on two key pillars to achieve unfocused or plane waves and 3D wall filtering. Plane or unfocused waves are sent into the body at the maximum allowed pulse repetition, and all pixels of the explored tissue can be reconstructed from a single unfocused insonification with a significantly higher sampling rate than in classical CDFI. Thus, AP can increase the imaging sensitivity and resolution to get a better detection of microvessels (15, 16).

Shear wave elastography (SWE) is a technique that can assess tissue stiffness by using acoustic radiation to induce mechanical vibration. The SWE images are displayed in a real-time color overlay box with different colors to indicate the speed of the shear wave (in meters per second, m/s) or the degree of tissue stiffness (Young's modulus; in kilopascal, kPa) in each pixel. The stiffness of a tissue can be assessed by a quantitative measurement or a qualitative map. Previous studies have found that a quantitative measurement or a qualitative map is useful in the diagnosis of breast lesions, and it had been proven to be a reproducible technique (17–19).

To our best knowledge, there was no study on the combined use of SWE and AP with BI-RADS for the differentiation of benign and malignant breast masses. The purpose of this study was to compare the diagnostic efficiency of AP, SWE, and the combined use of SWE and/or AP with BI-RADS for breast lesions. We attempt to find optimal methods to differentiate benign breast lesions from malignant ones.

MATERIALS AND METHODS

This prospective study was approved by the ethics committee of our institution.

Patients

From August 2018 to July 2019, a total of 210 patients with solid breast masses were recruited. The inclusion criteria were patients aged 18 years or older with at least a solid mass detected on the B-mode ultrasound, and the pathology of all the breast masses was confirmed *via* ultrasound-guided core needle biopsy and/or surgery in 1 month according to standard clinical protocols. People were excluded if lactating or pregnant, had a previous needle biopsy, or had any treatment of the same lesions. When one patient had multiple lesions, the most suspicious lesion was included.

Ultrasound Examination

All ultrasound examinations, including grayscale ultrasound, CDFI, AP, and SWE were performed with a high-frequency transducer (L15-4 or L10-5 Aixplorer, Supersonic Imaging, France).

Bilateral breast ultrasound was performed. When a target lesion was detected, the general characteristics were observed. The B-mode features of the lesion were clearly depicted, including the shape, margin, orientation, echo pattern, posterior features, calcifications, and associated features. Each lesion was classified as either category 3 (probably benign), 4a (low suspicion for malignancy), 4b (moderate suspicion for malignancy), 4c (high suspicion for malignancy), or 5 (highly

suggestive of malignancy) according to the fifth edition of BI-RADS (3).

Two orthogonal planes containing the richest vascularity of each lesion were scanned with CDFI and AP. The following settings were used for the CDFI examination: the color velocity scale was adjusted at 3 cm/s, and the color gain was adjusted adequately as the background noise was just suppressed. The region of interest included the whole masses and the breast tissue surrounding the lesion for at least 3 mm. For those large breast masses (>40 mm) that were not single-screen included, we observed the lesions in different planes to cover all the masses and the surrounding areas.

In terms of the setting for AP, gain settings were tuned to the optimum degree without color noise for each imaging. During the examination of CDFI and AP, the patients were asked to hold their breath for a while, and no pressure was applied through the transducer to prevent the vessels from collapsing (12).

After the AP imaging, SWE imaging was obtained by the following recommendations: SWE imaging examination was induced by the transducer without pressure. The region of interest included the whole lesion and breast tissue surrounding the lesion for at least 3 mm. The stiffness range of the color map was from blue to red (0–180 kPa). The standard SWE imaging was obtained with several seconds of immobilization.

All sonographic scanning was performed by the same investigator who had more than 20 years of experience in breast ultrasound and 2 years of experience in AP and SWE.

Imaging Analysis

The imaging data were analyzed by two radiologists (about 10 years of experience in breast ultrasound and 2 years of experience in AP and SWE) who were blinded to the pathological results. The third investigator evaluated the lesions when a disagreement occurred. Pathology was considered to be a golden standard.

The morphologic and distribution features detected on AP were divided into five patterns according to the shape of the vascular networks: (1) non-vascular pattern, which was due to a lack of vessels; (2) a linear or curvilinear pattern, with a single or a few straight or slightly curved vessels without crossing which were found inside the lesion; (3) a treelike pattern, which consisted of proportioned microvessels branching within the lesions; (4) a root hair-like pattern, which was dominated by a twist and a chaotic arrangement, and the irregular vessels within the lesions had less than two enlarged and twisted vessels surrounding the lesion; and (5) a crab claw-like pattern, which was characterized by radial vessels and with small speculated vessels commonly seen in the peripheral region (**Figure 1**).

As for the qualitative SWE features, we used seven color patterns in this study (20): (1) no finding: no difference is observed at the margin of or inside the lesion with the color around the lesion (homogeneously blue); (2) vertical stripes pattern: a color is observed at the margin of or inside the lesion, which differs from the color around the lesion. The differing color extends beyond the lesion and continues vertically in cords on the cutaneous side and/or the thoracic wall; (3) spots pattern: colored areas are visible above and/or below the lesion; and (4) rim of stiffness pattern: a localized colored area appears at the margin of the lesion and creates a continuous closed circle; (5) colored lesion pattern: colored areas are heterogeneously visible inside the lesion; (6) void center pattern: There is a lack of SWE signal inside the lesion. The rest of the SWE Box fills correctly; and (7) horseshoe pattern: a localized colored area appears at the margin of the lesion and creates an open circle (**Figure 2**).

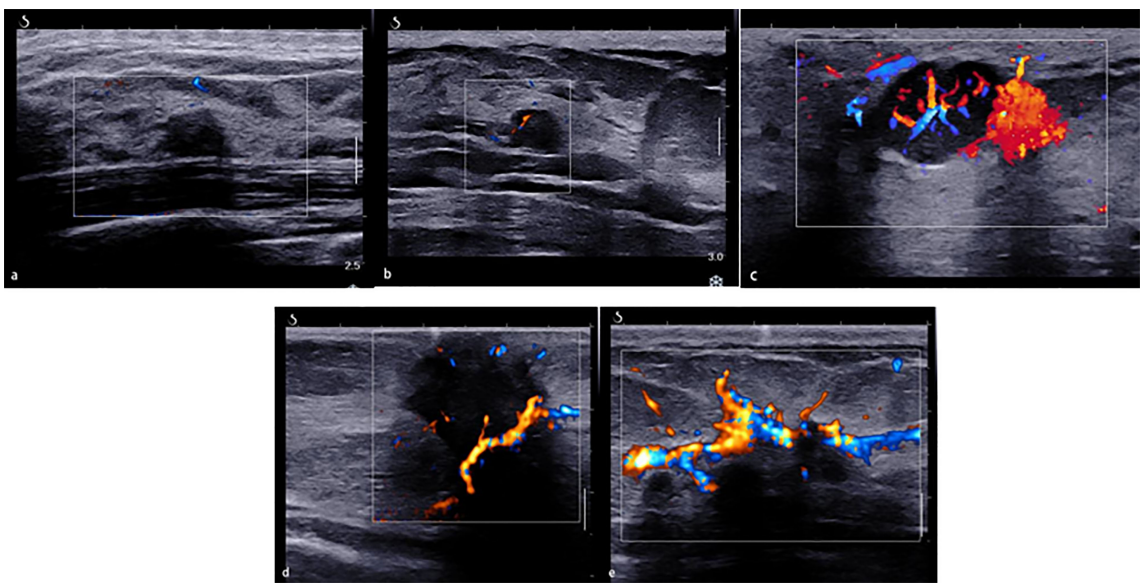

FIGURE 1 | The morphologic and distribution features of Angio PLUS. **(A)** Non-vascular pattern. **(B)** A linear or curvilinear pattern. **(C)** A treelike pattern. **(D)** A root hair-like pattern. **(E)** A crab claw-like pattern.

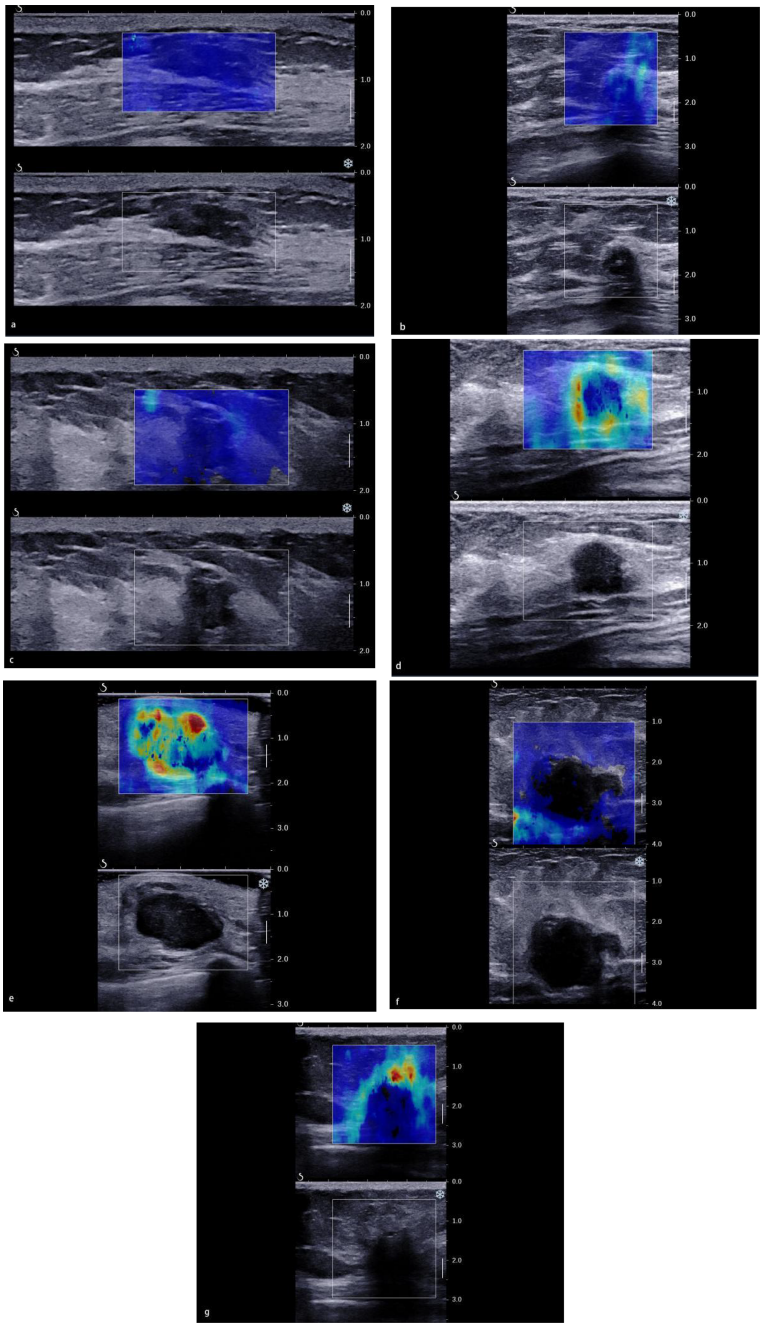

FIGURE 2 | The color pattern features of shear wave elastography. **(A)** No finding. **(B)** Vertical stripes pattern. **(C)** Spots pattern. **(D)** Rim of stiffness pattern. **(E)** Colored lesion pattern. **(F)** Void center pattern. **(G)** Horseshoe pattern.

Statistical Analysis

According to the final pathological results, the sensitivity, specificity, positive predictive value (PPV), negative predictive value (NPV), accuracy, and area under the receiver operating characteristic curve (AUC) of BI-RADS and the combination of BI-RADS, qualitative SWE, and AP were calculated and compared, respectively. A *P*-value <0.05 was considered statistically significant. SPSS 22.0 was used for all statistical analysis.

RESULTS

Pathological Findings

Of the 210 enrolled breast lesion cases (**Figure 3**), histopathologically, 67 (67/210) lesions were malignant, and 143 (143/210) lesions were benign (**Table 1**). Finally, 70 (33.3%) lesions were assigned to BI-RADS category 3, of which 3 (4.3%) were malignant. A total of 140 lesions were assigned to

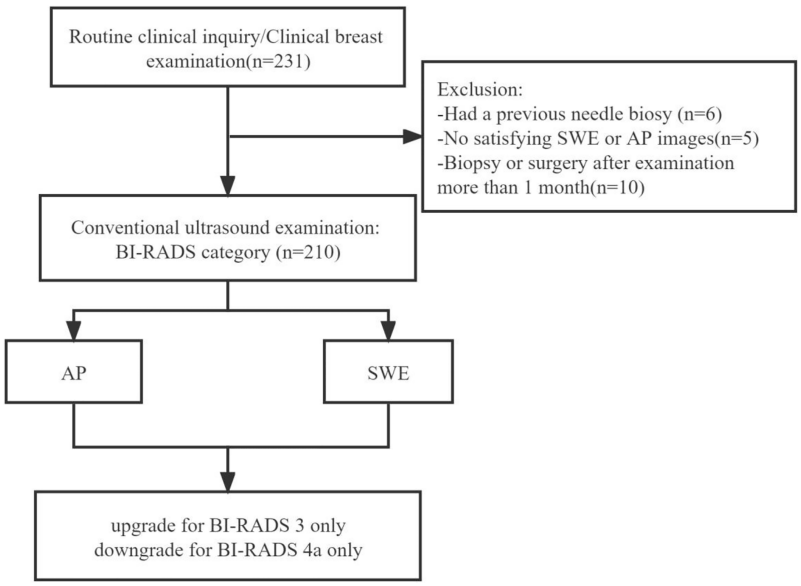

FIGURE 3 | Flow chart for the selection of breast lesions.

BI-RADS categories 4 and 5 (4a, 68 lesions; 4b, 32 lesions; 4c, 35 lesions; and 5, 5 lesions), and the confirmed malignant rates for 4a, 4b, 4c, and 5 were 10.3, 56, 97, and 100%, respectively.

Reclassification for BI-RADS Category 3 and 4a Lesions

In this study, the modified BI-RADS category combining SWE or/and AP with ultrasound (US) was only for BI-RADS categories 3 and 4a. When combining AP with BI-RADS, the morphologic and distribution features of BI-RADS category 4a manifested a non-vascular pattern, a linear or curvilinear pattern, and a treelike pattern which were downgraded into BI-RADS category 3. The morphologic and distribution features of BI-RADS category 3, which manifested a root hair-like pattern and a claw-like pattern, were upgraded into BI-RADS category 4a. When combining SWE with BI-RADS alone, the qualitative SWE features of BI-RADS category 4a showed no finding, vertical stripes, and spots above/below, which were downgraded to BI-RADS category 3. The qualitative SWE features of BI-RADS category 3 showed rim of stiffness, horse shoe, void center, and colored lesion, which were upgraded to BI-RADS 4a category (**Table 2**). When combining SWE and AP with BI-RADS, BI-RADS 4a category was downgraded into BI-RADS 3 category with the morphologic and distribution features that manifested a non-vascular pattern, linear or curvilinear pattern, and treelike pattern, and the qualitative SWE features showed no finding, vertical stripes, and spots above/below, while BI-RADS 3 category was upgraded into BI-RADS 4a category with the morphologic and distribution features manifested as root hair-like pattern and claw-like pattern, and the qualitative SWE features showed rim of stiffness, horse shoe, void center, and colored lesion.

TABLE 1 | Pathology of 210 breast lesions.

Pathology result	Number of lesions
Benign	143
Fibroadenoma	98
Fibrocystic mastopathy	29
Benign phyllodes tumor	2
Mastitis	9
Breast abscess	3
Intraductal papilloma	2
Malignant	67
Invasive ductal carcinoma	47
Intraductal carcinoma	11
Invasive lobular carcinoma	5
Papillary carcinoma	2
Mucinous carcinoma	2

Diagnostic Performance of BI-RADS, BI-RADS + AP, and BI-RADS + SWE and the Combination of SWE and AP With BI-RADS

BI-RADS category 3 was regarded as benign, while BI-RADS categories 4a, 4b, 4c, and 5 were regarded as malignant. The AUC of B-mode US with BI-RADS was 0.712 [95% confidence interval (CI), 0.643–0.781]. The sensitivity, specificity, PPV, NPV, and accuracy were 95.5, 46.9, 45.7, 95.7, and 62.4%, respectively. The sensitivity, specificity, PPV, NPV, and accuracy of AP alone were 59.7, 87.4, 69.0, 82.2, and 78.6%, respectively. The sensitivity, specificity, PPV, NPV, and accuracy of SWE alone were 83.6, 79, 65.1, 91.1, and 80.5%, respectively (**Table 3**). When AP was combined with BI-RADS, 89.7% (61/68) of BI-RADS 4a lesions were downgraded into BI-RADS 3, including 9.8% (6/61)

TABLE 2 | Comparison of qualitative SWE and AP features between benign and malignant lesions with pathological results.

	Benign	Malignant	*P*
Age[a]	44 (37–49)	53 (47–49)	<0.001
Size (mm)[a]	12 (9–18)	20 (13–28)	<0.001
AP[b]			<0.001
Non-vascular pattern	44	4	
Linear or curvilinear pattern	73	19	
Treelike pattern	9	1	
Root hair-like pattern	10	13	
Crab claw-like pattern	7	30	
SWE[b]			<0.001
No finding	84	9	
Vertical stripes pattern	15	1	
Spots pattern	14	1	
Rim of stiffness pattern	21	31	
Colored lesion pattern	6	15	
Void center pattern	1	3	
Horseshoe pattern	2	7	

[a]*Data are expressed as median (interquartile range).*
[b]*Data are expressed as numbers.*
AP, Angio PLaneWave UltraSensitive ultrasound imaging; SWE, shear wave elastography.

malignant lesions. The AUC of BI-RADS and AP was 0.828 (95% CI, 0.767–0.889). The sensitivity, specificity, PPV, NPV, and accuracy were 86.6, 79.0, 65.9, 92.6, and 81.4%, respectively. When SWE was combined with BI-RADS, the sensitivity was reduced from 95.5 to 91%, while the specificity increased from 46.9 to 74.1%. Four malignant breast masses were downgraded from BI-RADS category 4a into BI-RADS 3 category, and one malignant breast mass was upgraded from BI-RADS category 3 into BI-RADS category 4a. The AUC of BI-RADS and SWE was 0.826 (95% CI, 0.767–0.885). The sensitivity, specificity, PPV, NPV, and accuracy were 91.0, 74.1, 62.2, 94.6, and 79.5%, respectively. When AP and SWE were combined with BI-RADS, 49/76 (64.5%) benign masses were downgraded into BI-RADS category 3, while no benign masses were upgraded from BI-RADS category 3 into BI-RADS category 4a. Three sub-centimeter malignant masses were downgraded into BI-RADS category 3, and three malignant masses remain in BI-RADS category 3 due to benign manifestation in both AP and qualitative SWE—5/6 of them were sub-centimeter masses, and 4/6 of them were intraductal carcinoma. Compared with BI-RADS alone, the diagnostic performance of the combination of AP and qualitative SWE improved. The AUC was increased from 0.712 (95% CI, 0.643–0.781) to 0.861 (95% CI, 0.806–0.916) ($P < 0.001$) (**Figure 4**), and the sensitivity slightly decreased, while the specificity, PPV, NPV, and accuracy were increased from 46.9, 45.7, and 62.4% to 81.1, 69.3, and 84.3%, respectively (**Table 4**).

DISCUSSION

Our studies found that qualitative SWE can provide extra stiffness information of breast masses, AP can depict the morphologic and distribution features of microvessels, and the combination of qualitative SWE and AP with BI-RADS could significantly improve the diagnostic specificity to avoid unnecessary biopsy.

The American College of Radiology (ACR) BI-RADS lexicon mainly focused on morphology, which is widely used in ultrasound examination. This system could improve the reproducibility and reliability of cancer risk assessment (21, 22), and it has high sensitivity but with a low PPV with a substantial number of false-positive findings that cause unnecessary biopsies, which is the major limitation (13, 14). In this study, the sensitivity and specificity of using BI-RADS alone were 95.5 and 46.9%, respectively.

According to the 2013 ACR BI-RADS guideline, vascularity is one of the associated features. It is classified into 3 types in CDFI or PDI, including absent, internal vascularity, and vessels in rim. However, angiogenesis plays a critical role in tumor development and metastasis. Therefore, it is important to use vascularity as a diagnostic feature. However, microvessel detection was limited in CDFI or PDI, and AP can display more internal small vessels.

There were a few studies on morphologic and distribution features in differentiating benign breast lesions from malignant ones. Feng et al. (23) found that breast lesions with a centrally distributed branching or chaotic vessels were informative signs of breast malignancy. Chang et al. (24) found morphologic and tortuous features of microvessels in 3D power Doppler ultrasound, which was useful in distinguishing benign from malignant lesions. Xiao et al. (25) found that malignant lesions always showed penetrating vessels and spiculated or radial vessels in the peripheral regions, displaying root hair-like or crab claw-like patterns, whereas benign lesions mainly showed peripheral annular, non-vascular, linear, and treelike patterns.

In this study, we observed the morphologic and distribution features of AP in breast lesions. It was consistent with Xiao's study, but we found that there was an overlap between benign and malignant breast lesions, especially between inflammatory lesions and malignant breast lesions. Furthermore, since vascularity is an important factor for tumor differentiation, and AP performed well in vascular detection, in our study, we tried to combine AP with BI-RADS. When the morphologic and distribution features in AP were used alone, the sensitivity was reduced from 95.5 to 59.7%, while the specificity increased from 46.9 to 87.4%. Furthermore, 40.3% (27/67) malignant lesions were manifested in a non-vascular or linear pattern. It may be

TABLE 3 | Diagnostic performance of Breast Imaging Reporting and Data System, shear wave elastography, and AngioPLUS microvascular Doppler ultrasound technique in distinguishing malignant from benign lesions.

	Sensitivity (%)	Specificity (%)	Positive predictive value (%)	Negative predictive value (%)	Accuracy (%)
BI-RADS	95.5	46.9	45.7	95.7	62.4
AP	59.7	87.4	69	82.2	78.6
SWE	83.6	79.0	65.1	91.1	80.5

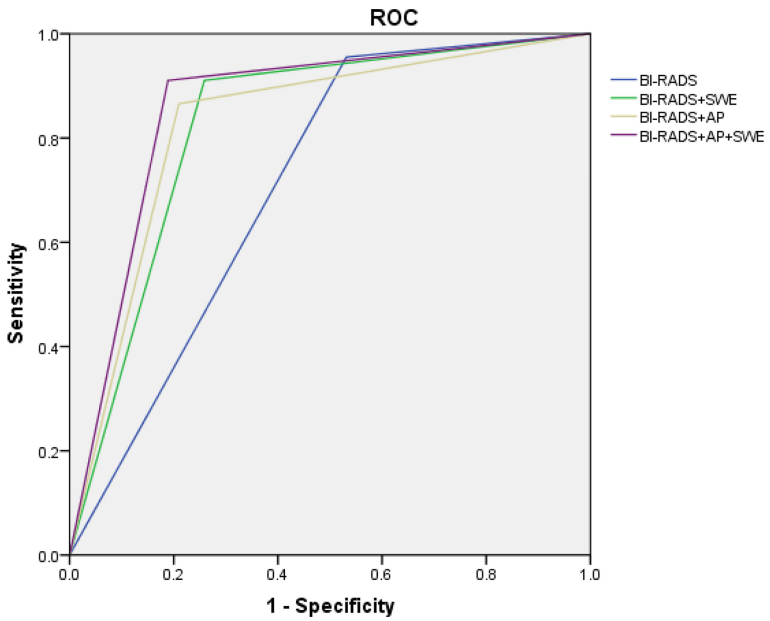

FIGURE 4 | ROC of Breast Imaging Reporting and Data System alone and combined qualitative shear wave elastography and/or AngioPLUS microvascular Doppler ultrasound technique. ROC, receiver operating characteristic; AUC, area under the ROC curve.

because the vascular velocity of some microvessels was lower than the threshold for AP, and some ductal carcinoma *in situ* or invasive cancers manifested low blood perfusion (26), which also indicates that the angiogenesis in malignant breast tumors was heterogeneous (27).

When AP was combined with BI-RADS, 6/61 malignant lesions were missed. All these 6 malignant lesions manifested a non-vascular or linear pattern. The final pathological results of these lesions were different grades of intraductal carcinoma or mucinous carcinoma: two were high-grade intraductal carcinoma, two were intermediate-grade intraductal carcinoma, one was low-grade intraductal carcinoma, which may be related to that part of intraductal carcinomas where there is a lack of blood supply, and two intraductal carcinoma were located at a depth of over 20 mm. The maximal diameter of one lesion was 5 mm, so AP could not depict a complete vascular caliber. What is more, one benign lesion was upgraded from BI-RADS 3 to BI-RADS 4a category because the morphologic and distribution features of AP manifested a claw-like pattern. Therefore, it was useful but insufficient to consider morphologic and distribution features as the only diagnostic feature in the interpretation.

In recent years, there were many studies on the differentiation of benign and malignant breast lesions with elastography. Lin et al. (20) found that malignant breast lesions mainly manifested rim of stiffness pattern, colored lesion pattern, void center pattern, and horseshoe pattern with qualitative SWE, while benign breast lesions mainly manifested no finding, vertical stripes pattern, and spots pattern, which were consistent with our study.

When SWE was combined with BI-RADS, four malignant breast lesions were missed. All these masses showed no finding with qualitative SWE, and 2/4 of these lesions were high-grade intraductal carcinoma, 1/4 of these was intermediate-grade intraductal carcinoma, 1/4 of these was invasive ductal carcinoma, and 3/4 of these lesions were sub-centimeter masses. Intraductal carcinoma is a precancerous lesion with a complicated pathological entity, so the lack of morphologic changes was difficult to be

TABLE 4 | Diagnostic performance of the combined qualitative parameters of shear wave elastography (SWE) or/and AngioPLUS microvascular Doppler ultrasound technique (AP) with Breast Imaging Reporting and Data System (BI-RADS) in distinguishing malignant from benign lesions.

	Sensitivity (%)	Specificity (%)	Positive predictive value (%)	Negative predictive value (%)	Accuracy (%)	Area under the receiver operating characteristic curve (95%CI)	p^a
BI-RADS	95.5 (64/67)	46.9	45.7	95.7	62.4	71.2 (0.643–0.781)	–
BI-RADS + AP	86.6 (58/67)	79	65.9	92.6	81.4	82.8 (0.767–0.889)	<0.001
BI-RADS + SWE	91.0 (61/67)	74.1	62.2	94.6	79.5	82.6 (0.767–0.885)	<0.001
BI-RADS + AP + SWE	91.0 (61/67)	81.1	69.3	95.1	84.3	86.1 (0.806–0.916)	<0.001

Data are expressed as percentage (numbers).

[a]*Comparison of the diagnostic performance between BI-RADS alone with the combination of the qualitative SWE and/or AP with BI-RADS.*

detected by ultrasound (28), and the stiffness may be lower than that of invasive carcinoma, which caused the no-finding manifestation of qualitative SWE. In addition, 1 malignant breast mass manifested a horseshoe pattern and was upgraded into BI-RADS category 4a. The final pathology result was invasive ductal carcinoma, and the maximum diameter of the lesion was 9 mm. Therefore, SWE features were useful for differentiation between benign and malignant lesions, and compared with AP, 4 sub-centimeter malignant lesions manifested malignant qualitative SWE features earlier than the malignant morphologic and distribution features of AP. However, 4 malignant breast lesions were downgraded into BI-RADS category 3, which was recommended with a short-time follow-up. Thus, it is insufficient to use SWE alone to differentiate benign from malignant breast lesions.

There was a study (29) which reported that the combination of the quantitative values of SWE and the vascular index in SMI could significantly improve the accuracy and specificity, but the sensitivity decreased slightly, which was consistent with this study. However, the ultrasound system of a previous study is different with this study, and the cutoff values of quantitative SWE and vascular index for differentiating benign from malignant breast masses may be varied in different ultrasound systems. The SWE technique of this study had been widely used and recognized in official clinical guidelines (20, 30). This study first found that the combination of qualitative SWE and AP with BI-RADS had an added value. When we combined SWE and AP with BI-RADS to modify the original BI-RADS category, we found that 64.5% of benign BI-RADS category 4a masses were downgraded into BI-RADS category 3 (**Figure 5**).

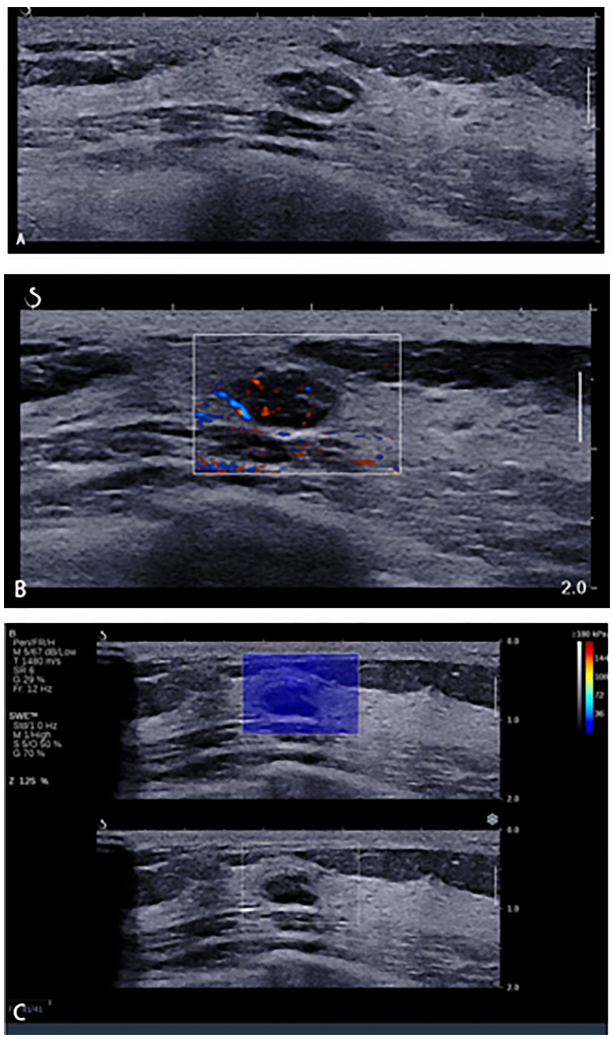

FIGURE 5 | A 45-year-old woman with breast lesions. **(A)** Conventional B-mode ultrasound revealed a 10 × 6-mm round, hypoechoic lesion with a clear margin in the right breast, which was categorized as Breast Imaging Reporting and Data System (BI-RADS) 4a. **(B)** The morphologic and distribution features of the microvessels in AngioPLUS microvascular Doppler ultrasound technique (AP) followed a linear pattern. **(C)** The qualitative shear wave elastography (SWE) feature showed no finding. Considering the benign manifestation both in AP and qualitative SWE, the final category was downgraded into BI-RADS 3. The ultrasound-guided biopsy revealed the lesion as fibroadenoma.

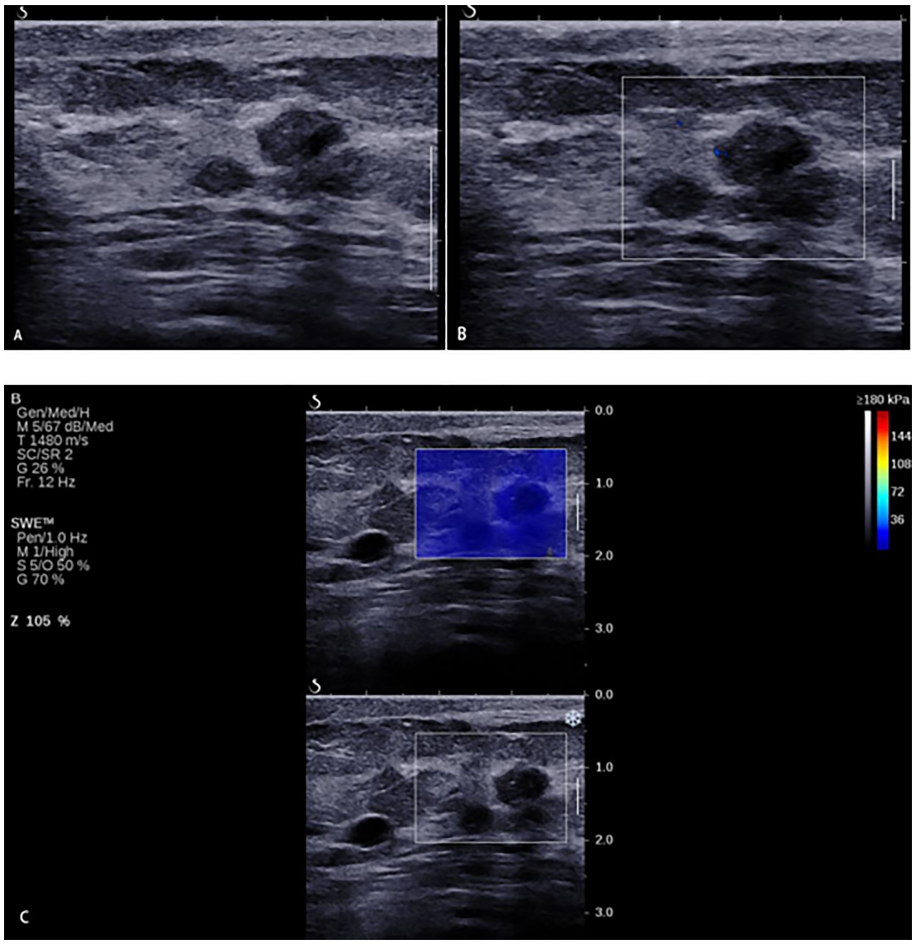

FIGURE 6 | A 33-year-old woman with breast lesions. **(A)** The conventional B-mode ultrasound revealed an 8 × 7-mm round, hypoechoic lesion with unclear margin in the right breast, which was categorized as Breast Imaging Reporting and Data System (BI-RADS) 4a. **(B)** The morphologic and distribution features of the microvessels in AngioPLUS microvascular Doppler ultrasound technique followed a linear pattern. **(C)** The qualitative shear wave elastography (SWE) feature showed no finding. Considering the benign manifestation both in AP and qualitative SWE, the final category was downgraded into BI-RADS 3. The ultrasound-guided biopsy revealed the lesion as intermediate-grade intraductal carcinoma.

The diagnostic specificity was significantly improved, thus avoiding a lot of unnecessary biopsies. However, 6 malignant masses were misdiagnosed due to benign manifestation in both AP and qualitative SWE; 5/6 of them were sub-centimeter, and 4/6 of them were intraductal carcinoma (**Figure 6**). For some sub-centimeter intraductal carcinoma masses, AP and SWE cannot detect obvious malignant features, which may be caused by heterogeneous angiogenesis or a small collagen fiber area. Thus, we should be careful in downgrading sub-centimeter BI-RADS category 4a lesions, and especially for sub-centimeter intraductal carcinoma masses, mammography and MRI can be combined if necessary.

There were several limitations in this study. First, it was a preliminary study in one center with a small sample. Second, some final pathology results of the patients were not available, which may have caused a selection bias of enrollment. Third, the time span was short, and the pathological categories were limited.

CONCLUSION

In conclusion, the morphologic and distribution features of microvessels in AP and the stiffness information in SWE were useful in the differential diagnosis of benign and malignant lesions. The combination of qualitative SWE and AP with BI-RADS could improve specificity, thus avoiding unnecessary biopsy. However, we should be careful when downgrading sub-centimeter BI-RADS category 4a lesions.

DATA AVAILABILITY STATEMENT

The datasets presented in this article are not readily available because the raw dataset contain the information of the enrolled patients. Requests to access the datasets should be directed to Xin-wu Cui (cuixinwu@live.cn).

ETHICS STATEMENT

The studies involving human participants were reviewed and approved by the ethics committee of Yueyang Central Hospital. The patients/participants provided their written informed consent to participate in this study.

AUTHOR CONTRIBUTIONS

Conception and design: BW, AY, X-WC, and CD. Drafting of the article: BW, Y-YC, and SY. Critical revision of the article for important intellectual content: BW, JL, and Z-WC. All authors contributed to the article and approved the submitted version.

FUNDING

This work was supported by the National Natural Science Foundation of China (numbers 82071953 and 21878237) and the Science and Technology Department of Hunan Province (number 2020SK52705).

REFERENCES

1. Mohey N, Hassan TA. Value of Mammography and Combined Greyscale Ultrasound and Ultrasound Elastography 251 in the Differentiation of Solid Breast Lesions. *Egyptian J Radiol Nucl Med* (2014) 45:253–61. doi: 10.1016/j.ejrnm.2013.11.002
2. Siegel R, Naishadham D, Jemal A. Cancer Statistics. *CA Cancer J Clin* (2013) 63:11–30. doi: 10.3322/caac.21166
3. Spak DA, Plaxco JS, Santiago L, Dryden MJ, Dogan BE. BI-RADS((R)) Fifth Edition: A Summary of Changes. *Diagn Interv Imaging* (2017) 98:179–90. doi: 10.1016/j.diii.2017.01.001
4. Elverici E, Barça AN, Aktaş H, Özsoy A, Zengin B, Çavuşoğlu M, et al. Nonpalpable BI-RADS 4 Breast Lesions: Sonographic Findings and Pathology Correlation. *Diagn Interv Radiol* (2015) 21:189–94. doi: 10.5152/dir.2014.14103
5. Giuseppetti GM, Baldassarre S, Marconi E. Color Doppler Sonography. *Eur J Radiol* (1998) 27(Suppl 2):S254–8. doi: 10.1016/S0720-048X(98)00076-X
6. Liu H, Jiang Y, Dai Q, Zhu Q, Wang L, Lu J. Peripheral Enhancement of Breast Cancers on Contrast-Enhanced Ultrasound: Correlation With Microvessel Density and Vascular Endothelial Growth Factor Expression. *Ultrasound Med Biol* (2014) 40:293–9. doi: 10.1016/j.ultrasmedbio.2013.10.004
7. Wang Y, Dan HJ, Fan JH, Wen SB. Evaluation of the Correlation Between Colour Power Doppler Flow Imaging and Vascular Endothelial Growth Factor in Breast Cancer. *J Int Med Res* (2010) 38:1077–83. doi: 10.1177/147323001003800335
8. Shen ZY, Hu B, Wu MF. Correlation Between Blood Flow Signal of Color Flow Imaging and Nottingham Prognostic Index in Patients With Breast Carcinoma. *Breast Care (Basel)* (2012) 7:126–30. doi: 10.1159/000337766
9. Bitencourt AGV, Lima ENP, Chojniak R, Marques EF, Souza JA, Andrade WP, et al. Multiparametric Evaluation of Breast Lesions Using PET-MRI: Initial Results and Future Perspectives. *Med (Baltimore)* (2014) 93:e115. doi: 10.1097/MD.0000000000000115
10. Kook SH, Park HW, Lee YR, Lee YU, Pae WK, Park YL. Evaluation of Solid Breast Lesions With Power Doppler Sonography. *J Clin Ultrasound* (1999) 27:231–7. doi: 10.1002/(SICI)1097-0096(199906)27:5<231::AID-JCU2>3.0.CO;2-P
11. Schroeder RJ, Bostanjoglo M, Rademaker J, Maeurer J, Felix R. Role of Power Doppler Techniques and Ultrasound Contrast Enhancement in the Differential Diagnosis of Focal Breast Lesions. *Eur Radiol* (2003) 13:68–79. doi: 10.1007/s00330-002-1413-3
12. Raza S, Baum JK. Solid Breast Lesions: Evaluation With Power Doppler Us. *Radiology* (1997) 203(1):164–8. doi: 10.1148/radiology.203.1.9122386
13. Wright IA, Pugh ND, Lyons K, Webster DJ, Mansel RE. Power Doppler in Breast Tumours: A Comparison With Conventional Colour Doppler Imaging. *Eur J Ultrasound* (1998) 7(3):175–81. doi: 10.1016/S0929-8266(98)00040-8
14. Heywang-Köbrunner SH, Schreer I, Heindel W, Katalinic A. Imaging Studies for the Early Detection of Breast Cancer. *Dtsch Arztebl Int* (2008) 105:541–7. doi: 10.3238/arztebl.2008.0541
15. *Aixplorer White Paper, Supersonic Imaging, Angio PL.U.S Ultrasound Imaging*. Available at: https://www.supersonicimagine.com/Aixplorer-MACH2/TECHNOLOGY, 2021.9.17
16. Liu H, Liao Q, Wang Y, Hu Y, Zhu Q, Wang L, et al. A New Tool for Diagnosing Parathyroid Lesions: Angio Plus Ultrasound Imaging. *J Thorac Dis* (2019) 11(11):4829–34. doi: 10.21037/jtd.2019.11.29
17. Cosgrove DO, Berg WA, Doré CJ, Skyba DM, Henry JP, Gay J, et al. Shear Wave Elastography for Breast Masses is Highly Reproducible. *Eur Radiol* (2012) 22(5):1023–32. doi: 10.1007/s00330-011-2340-y
18. Berg WA, Cosgrove DO, Doré CJ, Schäfer FK, Svensson WE, Hooley RJ, et al. Shear-Wave Elastography Improves the Specificity of Breast US: The BE1 Multinational Study of 939 Masses. *Radiol* (2012) 262(2):435–49. doi: 10.1148/radiol.11110640
19. Gweon HM, Youk JH, Son EJ, Kim JA. Clinical Application of Qualitative Assessment for Breast Masses in Shear-Wave Elastography. *Eur J Radiol* (2013) 82(11):e680–5. doi: 10.1016/j.ejrad.2013.08.004
20. Lin X, Chang C, Wu C, Chen Q, Peng Y, Luo B, et al. Confirmed Value of Shear Wave Elastography for Ultrasound Characterization of Breast Masses Using a Conservative Approach in Chinese Women: A Large-Size Prospective Multicenter Trial. *Cancer Manage Res* (2018) 10:4447–58. doi: 10.2147/CMAR.S174690
21. Baker JA, Kornguth PJ, Soo MS, Walsh R, Mengoni P. Sonography of Solid Breast Lesions: Observer Variability of Lesion Description and Assessment. *AJR Am J Roentgenol* (1999) 172(6):1621–5. doi: 10.2214/ajr.172.6.10350302
22. Lazarus E, Mainiero MB, Schepps B, Koelliker SL, Livingston LS. BI-RADS Lexicon for US and Mammography: Interobserver Variability and Positive Predictive Value. *Radiol* (2006) 239(2):385–91. doi: 10.1148/radiol.2392042127
23. Yongfeng Z, Ping Z, Wengang L, Yang S, Shuangming T. Application of a Novel Microvascular Imaging Technique in Breast Lesion Evaluation. *Ultrasound Med Biol* (2016) 42:2097–105. doi: 10.1016/j.ultrasmedbio.2016.05.010
24. Chang YC, Huang YH, Huang CS, Chang RF. Vascular Morphology and Tortuosity Analysis of Breast Tumor Inside and Outside Contour by 3-D Power Doppler Ultrasound. *Ultrasound Med Biol* (2012) 38:1859–69. doi: 10.1016/j.ultrasmedbio.2012.06.010
25. Xiao XY, Chen X, Guan XF, Wu H, Qin W, Luo BM. Superb Microvascular Imaging in Diagnosis of Breast Lesions: A Comparative Study With Contrast-Enhanced Ultrasonographic Microvascular Imaging. *Br J Radiol* (2016) 89(1066):20160546. doi: 10.1259/bjr.20160546
26. Boetes C, Strijk SP, Holland R, Barentsz JO, van der Sluis RF, Ruijs JH. False-Negative MR Imaging of Malignant Breast Tumors. *Eur Radiol* (1997) 7(8):1231–4. doi: 10.1007/s003300050281
27. Mankoff DA, Dunnwald LK, Gralow JR, Ellis GK, Charlop A, Lawton TJ, et al. Blood Flow and Metabolism in Locally Advanced Breast Cancer: Relationship to Response to Therapy. *J Nucl Med* (2002) 43(4):500–9.
28. Soliman AA, Wojcinski S, Degenhardt F. The Effect of Accompanying *in Situ* Ductal Carcinoma on Accuracy of Measuring Malignant Breast Tumor Size

Using B-Mode Ultrasonography and Real-Time Sonoelastography. *Int J Breast Cancer* (2012) 2012:376032. doi: 10.1155/2012/376032
29. Lee EJ, Chang YW. Combination of Quantitative Parameters of Shear Wave Elastography and Superb Microvascular Imaging to Evaluate Breast Masses. *Korean J Radiol* (2020) 21(9):1045–54. doi: 10.3348/kjr.2019.0765
30. Xu HX, Yan K, Liu BJ, Liu WY, Tang LN, Zhou Q, et al. Guidelines and Recommendations on the Clinical Use of Shear Wave Elastography for Evaluating Thyroid Nodule1. *Clin Hemorheol Microcirc* (2019) 72(1):39–60. doi: 10.3233/CH-180452

Conflict of Interest: The authors declare that the research was conducted in the absence of any commercial or financial relationships that could be construed as a potential conflict of interest.

Publisher's Note: All claims expressed in this article are solely those of the authors and do not necessarily represent those of their affiliated organizations, or those of the publisher, the editors and the reviewers. Any product that may be evaluated in this article, or claim that may be made by its manufacturer, is not guaranteed or endorsed by the publisher.

frontiers | Frontiers in Oncology

ORIGINAL RESEARCH
published: 24 May 2022
doi: 10.3389/fonc.2022.868975

Contrast-Enhanced Cone-Beam Breast CT: An Analysis of Diagnostic Value in Predicting Breast Lesion With Rim Enhancement Malignancy

Xin Zhao, Jun Yang, Yang Zuo, Wei Kang, Hai Liao, Zhong-Tao Zheng and Dan-Ke Su *

Department of Radiology, Guangxi Medical University Cancer Hospital, Nanning, China

Background: The objective of the current study was to investigate the diagnostic value of contrast-enhanced cone-beam breast computed tomography (CE-CBBCT) for breast lesion with rim enhancement (RE).

Methods: All 36 patients were examined by non-contrast (NC-CBBCT) and contrast-enhanced CBBCT (CE-CBBCT) after contrast media (CM) injection. Qualitative morphological enhancement parameters and quantitative enhancement parameters were compared between malignant and benign groups. Multivariable logistic regression analysis was performed to identify independent factors that could predict breast lesion with RE malignancy. Receiver operating curve (ROC) was used to evaluate prediction performance.

Results: A total of 36 patients with 40 lesions underwent breast CE-CBBCT were enrolled. There were significant differences in most qualitative morphological enhancement parameters between the two groups. A multivariate logistic regression model showed that △standardized HU ($INR_{phase\ 2}$–INR_{preCM}) [odds ratio (OR) = 1.148, 95% CI = 1.034–1.276, p = 0.01] and △standardized HU ($RP_{phase\ 2}$ – $RP_{phase\ 1}$) (OR = 0.891, 95% CI = 0.814–0.976, p = 0.013) were independent indicators in predicting breast lesion with RE malignancy. △standardized HU ($INR_{phase\ 2}$ – INR_{preCM}) combined with △standardized HU ($RP_{phase\ 2}$ – $RP_{phase\ 1}$) showed significant larger area under the receiver operating curve (AUC) and higher sensitivity than each alone (p < 0.001, AUC = 0.932, sensitivity = 92.59%, specificity = 92.31%). The regression equation of the prediction model was as follows: Logit (p) = 0.351 + 0.138X × △standardized HU ($INR_{phase\ 2}$ – INR_{preCM}) – 0.115 × △standardized HU ($RP_{phase\ 2}$ – $RP_{phase\ 1}$).

Conclusion: With the observation of qualitative morphological enhancement parameters and the comparison of quantitative enhancement parameters of CBBCT, a reliable basis for the diagnostic accuracy in predicting breast lesion with RE could be provided. These conclusions should be verified in large, well-designed studies.

Keywords: contrast-enhanced cone-beam breast computed tomography, clustered rim enhancement, qualitative morphological enhancement parameters, quantitative enhancement parameters, diagnostic accuracy

OPEN ACCESS

Edited by:
Abhishek Mahajan, Clatterbridge Cancer Centre NHS Foundation Trust, United Kingdom

Reviewed by:
Guo-Jun Zhang, Xiang'an Hospital, Xiamen University, China
Ni He, Sun Yat-sen University Cancer Center, China

***Correspondence:**
Dan-Ke Su
sudanke33@sina.com

Specialty section:
This article was submitted to Cancer Imaging and Image-directed Interventions, a section of the journal Frontiers in Oncology

Received: *03 February 2022*
Accepted: *06 April 2022*
Published: *24 May 2022*

Citation:
Zhao X, Yang J, Zuo Y, Kang W, Liao H, Zheng Z-T and Su D-K (2022) Contrast-Enhanced Cone-Beam Breast CT: An Analysis of Diagnostic Value in Predicting Breast Lesion With Rim Enhancement Malignancy. Front. Oncol. 12:868975. doi: 10.3389/fonc.2022.868975

INTRODUCTION

Breast lesion with rim enhancement (RE) is a special type of lesion with more enhancement in the edge than in the central region of the lesion through dynamic enhanced magnetic resonance imaging (MRI) scanning. Previous studies (1, 2) have indicated that REs are highly suggestive of malignant lesion. However, in clinical practice, REs may also appear in some of those benign lesions and often partially overlap with the malignant lesions, thus affecting the accuracy of qualitative diagnosis of lesions. With the rapid development of imaging technology, cone-beam breast computed tomography (CBBCT), as a new dedicated breast CT imaging technology based on cone-beam X-ray and flat panel detector (3, 4), has opened a new chapter in breast imaging diagnosis. In particular, the diagnostic effectiveness of contrast-enhanced cone-beam breast computed tomography (CE-CBBCT) is close to MRI (5), providing a new direction for the diagnosis of breast diseases. In the current study, the diagnostic value of CE-CBBCT in predicting breast lesion with RE malignancy was investigated.

MATERIALS AND METHODS

Ethics Statement

This study was conducted in accordance with the Declaration of Helsinki and approved by the Institutional Review Board of Guangxi Medical University Cancer Hospital. Written informed consent was given by all participants for their clinical records to be used in this study.

Patients

Patients who received CE-CBBCT as standard of care from July 2019 to October 2019 were retrospectively reviewed

The inclusion criteria were as follows: (1) the affected breast was imaged before breast biopsy, lumpectomy, and chemoradiotherapy; (2) CE-CBBCT scan was performed, and mass lesions with RE was detected by radiologist in the affected breast; and (3) the malignancy of the mass lesion was proven by pathology after biopsy or surgery.

A total of 36 patients with 40 lesions underwent breast CE-CBBCT were enrolled.

CBBCT Scanning

CBBCT examinations were performed using a dedicated flat-panel breast CT system (Koning Breast CT, CBCT 1000, Koning Corporation). The CBBCT system has been approved by the Food and Drug Administration (FDA) and the National Food and Drug Administration of China for diagnostic breast imaging. The CBBCT examinations were performed with a constant tube voltage of 49 kVp and variable tube currents (between 50 and 160 mA) depending on breast size and density (4, 6). Tube current was automatically selected after an initial scout image acquisition and kept constant for pre- and post-contrast CBBCT imaging. The patients took prone position with their arms raising, keeping the breasts naturally pendant at the center of the imaging field. The position was not changed during the whole examination. After the initial pre-contrast CBBCT scanning, ioversol contrast media (CM) (320 mgI/ml) was injected intravenously with a dual-chamber power injector at the flowrate of 2 ml/s and at the dose of 1.5–2.0 ml/kg. Two separate post-contrast CBBCT scans were performed at 60 s (phase 1) and 110 s (phase 2) after the injection of CM.

Image and Data Analyses

Image analyses were performed by two breast radiologists who were highly experienced in breast imaging including CBBCT. Both radiologists were blinded to clinicopathological and other imaging modality findings. When the diagnosis was inconsistent, the final decision was based on the agreement of the two radiologists. Koning Breast CT Image Viewer workstation was used to observe the qualitative morphological enhancement parameters and measure the quantitative enhancement parameters. CBBCT intensity was measured in Hounsfield units (HUs). Qualitative morphological enhancement parameters were described based on MRI breast imaging reporting and data system (BI-RADS), including the overall shape of the rim enhancement, the situation of rim paries (outer margin of the rim paries, border of outer margin, inner margin of the rim paries, border of inner margin, and uniformity of the rim paries), and peripheral vascular signs. Quantitative enhancement parameters included were as follows. First is the maximum thickness difference of the rim paries: the coronal plane of the lesion in the phase 1 of CE-CBBCT was selected to measure the thickest and thinnest diameter of rim paries; then, the difference between the two was calculated. Second is the △standardized CT value (HU): regions of interest (ROI) were selected at the same positions in different phases (non-enhanced and two-phase enhanced scans) of the rim paries, the inner of the rim, and the fat for CT value measurement (ROI area was 2–5 mm^2). When selecting an ROI for CT value measurement, it should be noted that (1) the ROI of the rim paries is selected in the area where the rim paries was significantly enhanced in the enhanced scan image, and the ROI in the non-enhanced scan image should correspond with it; (2) the ROI of the inner of the rim is selected in the area where the inner of the rim was not enhanced or not obviously enhanced in the enhanced scan image, and the ROI in the non-enhanced scan image should correspond with it; (3) when selecting the ROI of the fat, glands, blood vessels, skin, and other structures should be avoided; and (4) the measurement is performed on the image of coronal section with a thickness of 0.27 mm. After measuring the CT value, referring to the calculation methods of the enhancement

Abbreviations: CE-CBBCT, contrast-enhanced cone-beam breast computed tomography; NC-CBBCT, non-contrast CBBCT; MRI, magnetic resonance imaging; HU, Hounsfield units; INR, the inner of the rim; RP, rim paries; CI, confidence interval; ORs, odds ratios; AUC, area under the receiver operating curve; ROC, receiver operating curve.

parameters of Liu et al. (7) and Uhlig et al. (8), △standardized HUs were calculated according to the following formula:

$$\text{Formula 1}: \Delta\text{standardized HU}\left(INR_{phase\ 1} - INR_{preCM}\right) = HU\left(INR_{phase\ 1} - INR_{preCM}\right) - HU\left(fat_{phase\ 1} - fat_{preCM}\right).$$

$$\text{Formula 2}: \Delta\text{standardized HU}\left(INR_{phase\ 2} - INR_{preCM}\right) = HU\left(INR_{phase\ 2} - INR_{preCM}\right) - HU\left(fat_{phase\ 2} - fat_{preCM}\right).$$

$$\text{Formula 3}: \Delta\text{standardized HU}\left(INR_{phase\ 2} - INR_{phase\ 1)}\right) = HU\left(INR_{phase\ 2} - INR_{phase\ 1}\right) - HU\left(fat_{phase\ 2} - fat_{phase\ 1}\right).$$

$$\text{Formula 4}: \Delta\text{standardized HU}\left(RP_{phase\ 1} - RP_{preCM}\right) = HU\left(RP_{phase\ 1} - RP_{preCM}\right) - HU\left(fat_{phase\ 1} - fat_{preCM}\right).$$

$$\text{Formula 5}: \Delta\text{standardized HU}\left(RP_{phase\ 2} - RP_{preCM}\right) = HU\left(RP_{phase\ 2} - RP_{preCM}\right) - HU\left(fat_{phase\ 2} - fat_{preCM}\right).$$

$$\text{Formula 6}: \Delta\text{standardized HU}\left(RP_{phase\ 2} - RP_{phase\ 1}\right) = HU\left(RP_{phase\ 2} - RP_{phase\ 1}\right) - HU\left(fat_{phase\ 2} - fat_{phase\ 1}\right).$$

Statistical Analysis

SPSS Version 25.0 (IBM, Armonk, NY, USA) was used. Continuous variables are presented as mean ± standard deviation (SD) as measure of dispersion. The normality assumption of continuous variables was tested *via* the Shapiro–Wilks test. Continuous variables that did not conform to normal distribution are expressed as quartiles, which were presented as median (P25, P75). Categorical variables are presented as absolute number and percent.

Qualitative morphological enhancement parameters between malignant and benign groups were compared by using χ^2 or Fisher's exact tests. Quantitative enhancement parameters between malignant and benign groups were compared by Student's t-test or Mann–Whitney U-tests. Those quantitative enhancement parameters with $p < 0.1$ in the univariate analysis were included in the multivariable logistic regression analysis using forward:LR to identify independent factors that could predict breast lesion with RE malignancy. Diagnostic accuracy was assessed lesion based *via* test sensitivity, specificity, and area under the receiver operating curve (AUC) separately for those quantitative enhancement parameters with $p < 0.05$ in the multivariable logistic regression analysis by calculating the receiver operating curve (ROC). A p value < 0.05 was considered significant.

RESULTS

Patient Characteristics

The clinicopathological data of the patients included are presented in **Table 1**. A total of 36 patients with 40 lesions fulfilled the inclusion criteria. NC-CBBCT, post-CM CE-CBBCT scans at 60 s (phase 1), and 110 s (phase 2) were performed in all patients. All patients were female. The age of the patients ranged from 35 to 64 years, and the median age was 46 years. A total of 13 benign lesions (6 were proliferative lesions with inflammation, 3 were purulent inflammation, 3 were plasma cell mastitis, and 1 was fibroadenoma) were found in 11 patients. A total of 27 malignant lesions (all of them were invasive ductal carcinoma: 3 were luminal A subtype, 6 were luminal B subtype, 11 were Her-2-positive subtype, and 7 were triple negative subtype) were found in 25 patients.

TABLE 1 | The clinicopathological data and molecular pathological subtypes of these patients.

	Malignant group (n = 25)	Benign group (n = 11)	*p*-value
Number of lesions (n)	27	13	
Age (years)	48.36 ± 6.775	43.36 ± 4.433	0.032
Menstrual status (n)			0.387
Non-menopause	18	10	
Menopause	7	1	
Gland type (n)			0.411
Non-compact	12	4	
compact	13	7	
Size of lesion (cm)	2.24 ± 0.93	1.60 ± 0.58	0.005

Data are shown as the mean ± SD or number of patients.

Radiation Dose

The radiation doses of the 36 patients enrolled in this study ranged from 15.3 to 22.7 mGy, with a mean dose of 17.73 ± 1.53 mGy.

Comparison of the Qualitative Morphological Enhancement Parameters Between Malignant and Benign Groups

Most of the malignant lesions with REs showed irregular shape, irregular/spicula outer margin of the rim paries, unsmooth and indefinite inner margin of the rim paries, uneven thickness of the rim paries, and positive peripheral vascular sign (**Figure 1**). Most of the benign lesions showed round/quasi-circular shape, smooth/lobulate outer margin of the rim paries, smooth and definite inner margin of the rim paries, and uniform thickness of the rim paries (**Figure 2**). There were significant differences in most signs between the two groups except for one (border of outer margin) (**Table 2**).

Univariate Analysis and Multivariable Logistic Regression Analysis of the Quantitative Enhancement Parameters

Those quantitative enhancement parameters including thickness difference of the rim paries, △standardized HU ($INR_{phase\ 1} - INR_{preCM}$), △standardized HU ($INR_{phase\ 2} - INR_{preCM}$), △standardized HU ($RP_{phase\ 1} - RP_{preCM}$), and △standardized HU ($RP_{phase\ 2} - RP_{phase\ 1}$) in malignant group were significantly higher than that in the benign group (**Table 3**).

The quantitative enhancement parameters with $p < 0.1$ in univariate analysis above were included in the multivariable

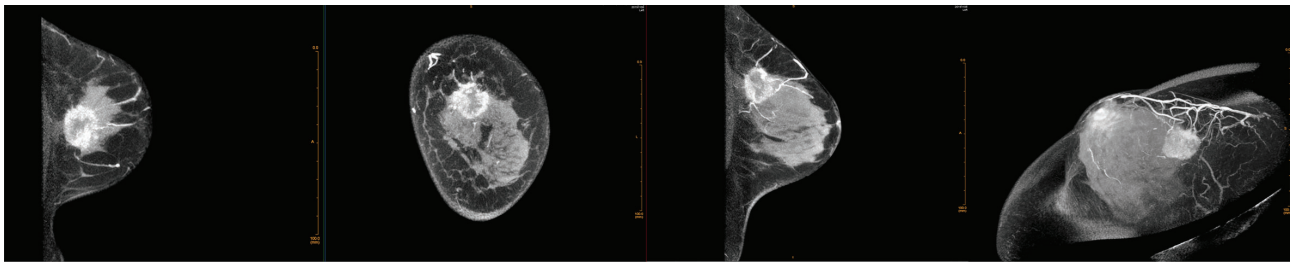

FIGURE 1 | Female, 48 years old, invasive ductal carcinoma in the left breast. **(A)** Transverse section. **(B)** Coronal section. **(C)** Median sagittal section. **(D)** MIP reconstruction images in phase 1 by CE-CBBCT. Those images showed an irregular rim-shaped enhanced mass with uneven thickness of rim paries, spicular outer margin of the rim paries, unsmooth and undefinite inner margin of the rim paries, and positive peripheral vascular signs (increased, thickened blood vessels around the mass and partially connected to it) in the upper quadrant of the left breast at about 12 o'clock. CE-CBBCT, contrast-enhanced CBBCT (CE-CBBCT); MIP, maximum intensity projection.

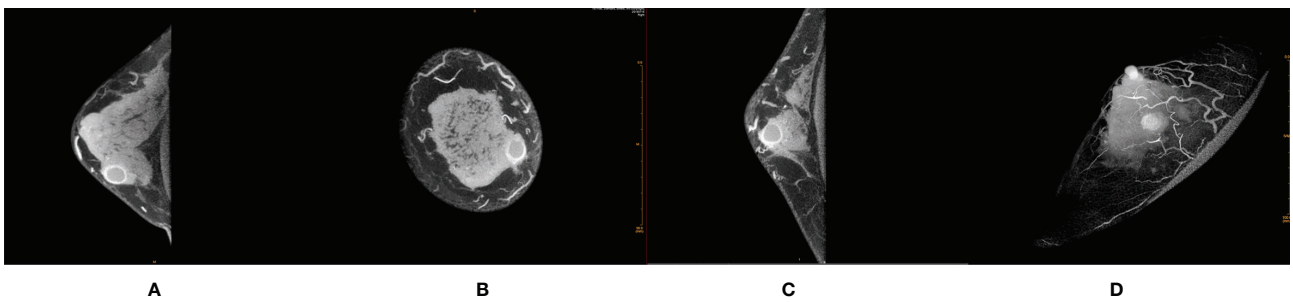

FIGURE 2 | Female, 32 years old, cystic fibrosis with inflammation in right breast. **(A)** Transverse section. **(B)** Coronal section. **(C)** Median sagittal section. **(D)** MIP reconstruction images in phase 1 by CE-CBBCT. Those image showed a circular rim-shaped enhanced mass with uniform thickness of rim paries, smooth and definite inner and outer margin of the rim paries, and negative peripheral vascular signs (without obvious increased and thickened blood vessels around the mass) in the inner and lower quadrant of the right breast at about 4 o'clock. CE-CBBCT, contrast-enhanced CBBCT (CE-CBBCT); MIP, maximum intensity projection.

logistic regression analysis to identify independent factors that could predict breast lesion with RE malignancy. Results showed that △standardized HU ($INR_{phase\ 2} - INR_{preCM}$) (OR = 1.148, 95% CI =1.034–1.276, $p = 0.01$) and △standardized HU ($RP_{phase\ 2} - RP_{phase\ 1}$) (OR = 0.891, 95% CI =0.814–0.976, $p = 0.013$) were independent indicators in predicting breast lesion with RE malignancy (**Table 4**).

Diagnostic Accuracy of the Enhancement Parameters

Both △standardized HU ($INR_{phase\ 2} - INR_{preCM}$) and △standardized HU ($RP_{phase\ 2} - RP_{phase\ 1}$) alone showed comparable AUC, sensitivity, and specificity for assessment of breast lesions malignancy. While △standardized HU ($INR_{phase\ 2} - INR_{preCM}$) combined with △standardized HU ($RP_{phase\ 2} - RP_{phase\ 1}$) showed significant larger AUC and higher sensitivity than each alone. The regression equation of the prediction model for combined both was as follows: Logit (p) = 0.351 + 0.138X × △standardized HU ($INR_{phase\ 2} - INR_{preCM}$) − 0.115 × △standardized HU ($RP_{phase\ 2} - RP_{phase\ 1}$) (**Table 5**).

DISCUSSION

REs may be found in both benign and malignant lesions. Most previous studies mainly focused on the differential diagnosis of RE in MRI technology, and most researchers believed that the post-CM morphological characteristics of lesions after scanning are vital basis for qualitative diagnosis (9–12). As a new type of equipment dedicated to breast imaging, CBBCT has the advantages including fast scanning speed and high image quality. It can obtain three-dimensional images with high spatial resolution and contrast from all directions and multiple perspectives without displacement and deformation. In addition, it has strong ability to display lesions of microcalcifications and soft tissue and to improve the detection of post-CM lesions and highlight their morphological characteristics after scanning (3, 5).

In the current study, the morphological enhancement parameters of breast lesions with REs by CE-CBBCT were analyzed, and the results indicated that there were significant differences in overall shape of the REs and the situation of rim paries (outer margin of the rim paries, border of outer margin,

TABLE 2 | Morphological enhancement signs of the breast lesions with rim enhancements by CE-CBBCT.

Morphological enhancement signs	Malignant group (n = 27)	Benign group (n = 13)	χ^2	*p*-value
Shape			9.548	0.002
Round/quasi-circular shape	11	12		
Irregular	16	1		
Outer margin of the rim paries			15.506	<0.001
Smooth/lobulate	7	12		
Irregular/spicular	20	1		
Border of outer margin			0.105	0.746
Clear	16	7		
Unclear	11	6		
Inner margin of the rim paries			13.713	<0.001
Smooth and definite	2	8		
Unsmooth and undefinite	25	5		
Border of inner margin			19.551	<0.001
Clear	5	12		
Unclear	22	1		
Uniformity of the rim paries			14.661	<0.001
Uniform thickness	0	6		
Uneven thickness	27	7		
Peripheral vascular signs			4.569	0.033
Positive	18	4		
Negative	9	9		

CE-CBBCT, contrast-enhanced cone-beam breast computed tomography.

inner margin of the rim paries, border of inner margin, and uniformity of the rim paries, and peripheral vascular signs) between malignant and benign lesions. These findings were consistent with the conclusions of most previous studies on the morphological characteristics of breast lesions with REs by MRI scanning (9–15). The difference in post-CM morphology between benign and malignant lesions with REs is mainly related to the difference in their biological behavior and pathological basis (16). The rim paries of benign lesions of which the growth rates are slow and uniform mostly consist of abscess wall, cyst wall with dilated duct wall, or inflammatory cell infiltration. Therefore, the corresponding imaging characteristics of the REs in benign lesions are mostly round/quasi-circular shape with smooth/lobulate outer margin and definite inner margin, and uniform thickness of their rim paries. The rim paries of malignant lesions of which the growth rates are fast and nonuniform consist of tumor cells that are high value added and heterogeneous. In addition, much vascular tumor angiogenesis around the tumor body are induced by endothelial growth factor (VEGF). Thus, the corresponding imaging characteristics of the REs in malignant lesions are mostly irregular shape with irregular/spicula outer margin, unsmooth and indefinite inner margin, uneven thickness of their rim paries, and positive peripheral vascular sign. The positive peripheral vascular sign is common. In this study, there was no significant difference between benign and malignant groups in the border of outer margin of the rim paries. The proportion of benign lesions with unclear border was equivalent to that with clear border of outer margin (6:7). A similar proportion was observed in malignant group (unclear border:clear border, 11:16). The proportion of benign lesions with blurred outer boundary was equivalent to that with clear outer boundary (6:7) to that of malignant group (11:16). This may be due to the fact that the benign group in the current study mainly consisted of inflammatory or benign lesions combined with inflammation, and the inflammatory edema or granulation tissue hyperplasia around the lesion caused by inflammation may be the reason for the unclear border of the outer margin of the rim paries between benign lesions and adjacent tissues.

In addition to the qualitative diagnosis of breast lesions by qualitative morphological enhancement parameters, the quantitative enhancement parameters of CE-CBBCT could reflect the hemodynamic characteristics of the lesions to a certain extent, so as to provide quantitative diagnostic basis for the identification of benign and malignant lesions. At present, there is no uniform standard for the time point setting of CE-CBBCT phases and the measurement methods of CE-CBBCT CT value in lesions all over the world (3, 5, 7, 8, 17). The traditional

TABLE 3 | Comparison of the quantitative enhancement parameters between malignant and benign groups by CE-CBBCT.

Parameters	Malignant group (n = 27)	Benign group (n = 13)	t or U	*p*-value
Maximum thickness difference of the rim paries (cm)	0.35 (0.2–0.7)	0.06 (0.04–0.07)	U = 37.500	<0.001
△standardized HU ($INR_{phase\ 1} - INR_{preCM}$) (Hu)	13.56 ± 17.26	0.37 ± 12.53	t = –2.455	0.019
△standardized HU ($INR_{phase\ 2} - INR_{preCM}$) (Hu)	23.24 ± 28.26	3.81 ± 14.52	t = –2.325	0.026
△standardized HU ($INR_{phase\ 2} - INR_{phase\ 1)}$) (Hu)	9.68 ± 22.05	3.44 ± 11.31	t = –0.957	0.345
△standardized HU ($RP_{phase\ 1} - RP_{preCM}$) (Hu)	85.9 ± 42.18	55.52 ± 34.14	t = 0.260	0.03
△standardized HU ($RP_{phase\ 2} - RP_{preCM}$) (Hu)	84.62 ± 41.43	75.08 ± 37	t = –0.705	0.485
△standardized HU ($RP_{phase\ 2} - RP_{phase\ 1}$) (Hu)	–1.27 ± 33.89	19.56 ± 16.22	t = 2.094	0.043

CE-CBBCT, contrast-enhanced cone-beam breast computed tomography; HU, ounsfifield Units; INR, the inner of the rim; RP, rim paries.

TABLE 4 | Multivariable logistic regression analysis to identify independent factors that could predict breast lesion with RE malignancy.

Parameters	Coefficient	Standard error	Wald value	*p*-value	OR (95%CI)
△standardized HU ($INR_{phase\ 2} - INR_{preCM}$) (Hu)	0.138	0.054	6.637	0.01	1.148 (1.034–1.276)
△ standardized HU ($RP_{phase\ 2} - RP_{phase\ 1}$) (Hu)	–0.115	0.047	6.107	0.013	0.891 (0.814–0.976)

RE, rim enhancement; HU, Hounsfield units; INR, the inner of the rim; RP, rim paries; CI, confidence interval; OR, odds ratios.

TABLE 5 | Summary of diagnostic accuracy of different parameters for predicting breast lesion with RE malignancy.

Modality	AUC	*p*-value	Cutoff	Youden's index	Sensitivity	Specificity
△standardized HU ($INR_{phase\ 2}$ − INR_{preCM}) (Hu)	0.732 (0.569–0.860)	0.026	≤−3.3	0.519	51.85%	100%
△standardized HU ($RP_{phase\ 2}$ − $RP_{phase\ 1}$) (Hu)	0.719 (0.555–0.850)	0.019	>14.4	0.405	48.15%	92.31%
△standardized HU ($INR_{phase\ 2}$ − INR_{preCM}) combined with △standardized HU ($RP_{phase\ 2}$ − $RP_{phase\ 1}$) (Hu)	0.932 (0.805–0.987)	<0.001	>0.537	0.849	92.59%	92.31%

RE, rim enhancement; HU, Hounsfifield Units; INR, the inner of the rim; RP, rim paries; AUC, area under the receiver-operating curve.

CT value is not suitable for cone-beam breast CT because the cone-line-beam imaging characteristics of cone-beam breast CT are different from those of conventional spiral CT. Our previous study (18) has shown that the stability of absolute CT value of CBBCT is lower than that of conventional spiral CT. Even in the same tissue of a breast, the corresponding absolute CT values of CBBCT in different positions of the breast differ. Therefore, in order to reduce the influence from the instability of absolute CT value, breast fat was used by researchers to standardize the CT value of CBBCT to get a △CT value in breast lesion (8). In this study, △CT value was used as the value of the density measurement for rim enhancement. Whether the relative CT value obtained by this method is more stable than the absolute CT value needs more experimental and theoretical confirmation in the future. Liu et al. (7) obtained the △CT value through calculation of the difference in CT value before and after injection of CM with single phase of post-CM scanning at 120 s. Uhlig et al. (8) obtained the △standardized CT value through calculation of the difference in CT value before and after injection of CM with two phases of post-CM scanning at 2 and 3 min, respectively. Referring to the calculation methods of the enhancement parameters of the two researchers above (7, 8), in the current study, with two phases of post-CM scanning at 60 and 110 s, respectively, a series of quantitative enhancement parameters by CE-CBBCT were obtained. In addition, the diagnostic value with different combinations of those quantitative enhancement parameters were compared to get the optimal diagnostic parameters. The results suggested that △standardized HU ($INR_{phase\ 2}$ − INR_{preCM}), as one of the parameters with differential diagnostic significance in multivariable logistic regression analysis, was higher in the malignant group than that in the benign group, indicating that the degree on enhancement of the inner rim in the malignant lesion was significantly higher than that in the benign lesion. These findings support the conclusion of some previous studies. In the study of Buadu et al. (19), REs were observed in nine cases of invasive cancer, of which seven cases were connective tissue in the central region but not necrotic components. The results of Liu et al. (20) showed that the microvascular density in the margin area of the malignant lesion was significantly higher than that in the central area, resulting in lower perfusion of CM in the central area than that in the margin area. This indicates that the appearance of REs in malignant tumors are related to the regional differences in distribution of tumor microvascular, resulting in delayed enhancement in the central region. The pathological basis of REs in benign lesions are mainly related to central liquefaction necrosis, mammary duct dilatation, or high degree of fibrous tissue hyperplasia, resulting in post-CM non-enhancement or low degree of enhancement in the central region (13). Our results also suggested that △standardized HU ($INR_{phase\ 2}$ − INR_{preCM}), as another one of the parameters with differential diagnostic significance in multivariable logistic regression analysis, is significantly lower in the malignant group than that in the benign group, which indicated that the degree of enhancement of RE in malignant lesion is lower in phase 2 than that in phase 1, and the degree of enhancement of RE in benign

lesion is gradually enhanced from phase 1 to 2. The results are consistent with the fact that outflow type is often found in malignant lesions and gradual increase type is often found in malignant lesions by MRI enhancement curve of time signal. However, whether the significance of types in MRI enhancement curve of time signal for the qualitative diagnosis of breast lesion is applicable to CE-CBBCT has not been reported at present, highlighting the need for further verification.

In terms of radiation dose control, it is worth mentioning that CBBCT could precisely control X-ray-related technical parameters such as tube voltage, tube current, and output power, and could adjust the scanning protocol individually according to the type, size, characteristics of breast glands, and the clinical requirements. In addition, during the examination, the system's self-shielding prevents the contralateral breast and other parts of the body from being exposed to radiation. Radiation dose of CBBCT reported in the literature varied (6, 21–24), with a minimum total radiation dose of 4 mGy and a maximum of 16.6 mGy. The variability in radiation doses may be related to X-ray technology-related factors, breast characteristics, and different scanning protocols (non-enhanced scan and non-enhanced scan combined with single- or multi-phase enhancement). At present, researchers have not reached consensus on scanning protocols in CE-CBBCT examinations. Regulatory agencies such as US Food and Drug Administration regulate the radiation dose of breast cancer screening (3 mGy per view) but does not set limit for breast cancer diagnostic workup. The standard-of-care procedure in the hospital takes one pre-contrast and two post-contrast scans to achieve preferable enhancement while keeping the radiation dose at a level safe for diagnostic patients. The total radiation dose of 36 patients enrolled ranged from 15.3 to 22.7 mGy, with a mean dose of 17.73 ± 1.53 mGy. According to the International Commission on Radiological Protection (ICRP) publication 103 (2007), the breast tissue effective dose weighting factor is 0.12. The effective dose level of this CE-CBBT exam is between 1.83 and 2.72 mSv, which is equivalent to 8–12 months of natural background radiation (25) and only 20% of a whole-body CT dose (26).

To the best of our knowledge, this is the first study investigating the diagnostic value of CE-CBBCT for breast lesion with RE using a combination of post-CM qualitative morphological enhancement parameters and quantitative enhancement parameters. The results were significant, and we hope they would provide a reference for future studies; nonetheless, the work has several limitations that may affect interpretation of the results. On the one hand, comparative study has not been performed between imaging findings and pathology. On the other hand, the sample size was relative small, and the few pathological types were covered. Therefore, in the future, the sample size should be further expanded, the pathological types should be increased, and the comparative study on pathological and imaging findings should be performed to improve the accuracy of the conclusions.

In conclusion, with the observation of qualitative morphological enhancement parameters and the comparison of quantitative enhancement parameters by CBBCT, a reliable basis for the diagnostic accuracy in predicting breast lesion with RE malignancy could be provided. However, these conclusions should be verified in large, well-designed studies.

DATA AVAILABILITY STATEMENT

The original contributions presented in the study are included in the article/supplementary material. Further inquiries can be directed to the corresponding author.

ETHICS STATEMENT

This study was conducted in accordance with the Declaration of Helsinki and approved by the Institutional Review Board of Guangxi Medical University Cancer Hospital. The patients/participants provided their written informed consent to participate in this study. Written informed consent was obtained from the individual(s) for the publication of any potentially identifiable images or data included in this article.

AUTHOR CONTRIBUTIONS

Designed the study: XZ and D-KS. Collected participants: JY and YZ. Analyzed the data: WK and HL. Statistical analyses: XZ and Z-TZ. Wrote the manuscript: XZ. All authors contributed to the article and approved the submitted version.

ACKNOWLEDGMENTS

This research was supported by National Natural Science Foundation (Grant No. 81971591, 81760517), Guangxi Clinical Research Center for Medical Imaging Construction (Grant No.Guike AD20238096), Guangxi Key Clinical Specialty (Medical imaging Department), Dominant Cultivation Discipline of Guangxi Medical University Cancer Hospital (Medical imaging Department).

REFERENCES

1. Uematsu T, Kasami M. High-Spatial-Resolution 3-T Breast MRI of Nonmasslike Enhancement Lesions: An Analysis of Their Features as Significant Predictors of Malignancy. *Am J Roentgenol* (2012) 198(5):1223–30. doi: 10.2214/AJR.11.7350
2. Tozaki M, Igarashi T, Fukuda K. Breast MRI Using the VIBE Sequence: Clustered Ring Enhancement in the Differential Diagnosis of Lesions Showing Non-Masslike Enhancement. *Am J Roentgenol* (2006) 187(2):313–21. doi: 10.2214/AJR.05.0881
3. Seifert P, Conover D, Zhang Y, Morgan R, Arieno A, Destounis S, et al. Evaluation of Malignant Breast Lesions in the Diagnostic Setting With Cone

Beam Breast Computed Tomography (Breast CT): Feasibility Study. *Breast J* (2014) 20(4) :364–74. doi: 10.1111/tbj.12285
4. Wienbeck S, Lotz J, Fischer U. Review of Clinical Studies and First Clinical Experiences With a Commercially Available Cone-Beam Breast CT in Europe. *Clin Imaging* (2017) 42:50–9. doi: 10.1016/j.clinimag.2016.11.011
5. Wienbeck S, Fischer U, Luftner-Nagel S, Lotz J, Uhlig J. Contrast-Enhanced Cone-Beam Breast-CT (CBBCT): Clinical Performance Compared to Mammography and MRI. *Eur Radiol* (2018) 28(9):3731–41. doi: 10.1007/s00330-018-5376-4
6. O'Connell A, Conover D, Zhang Y, Seifert P, Logan-Young W, Lin C, et al. Cone-Beam CT for Breast Imaging: Radiation Dose, Breast Coverage, and Image Quality. *Am J Roentgenol* (2010) 195(2): 496–509. doi: 10.2214/AJR.08.1017
7. Liu A, Ma Y, Yin L, Han P, Li H, Ye Z. Diagnostic Value of Contrast-Enhanced Cone Beam Breast CT in Dense Breast Lesions. *China Oncol* (2018) 28(11):807–12. doi: 10.19401/j.cnki.1007-3639.2018.11.002
8. Uhlig J, Fischer U, Surov A, Lotz J, Wienbeck S. Contrast-Enhanced Cone-Beam Breast-CT: Analysis of Optimal Acquisition Time for Discrimination of Breast Lesion Malignancy. *Eur J Radiol* (2018) 99:9–16. doi: 10.1016/j.ejrad.2017.12.003
9. Wedegärtner U, Bick U, Wörtler K, Rummeny E, Bongartz G. Differentiation Between Benign and Malignant Findings on MR-Mammography: Usefulness of Morphological Criteria. *Eur Radiol* (2001) 11(9):1645–50. doi: 10.1007/s003300100885
10. Schnall MD, Blume J, Bluemke DA, DeAngelis GA, DeBruhl N, Harms S, et al. Diagnostic Architectural and Dynamic Features at Breast MR Imaging: Multicenter Study. *Radiology* (2006) 238(1):42–53. doi: 10.1148/radiol.2381042117
11. Kang W, Zhong W, Su D. The Cone-Beam Breast Computed Tomography Characteristics of Breast Non-Mass Enhancement Lesions. *Acta Radiol* (2021) 62(10):1298–308. doi: 10.1177/0284185120963923
12. Kuhl CK, Schrading S, Bieling HB, Wardelmann E, Leutner CC, Koenig R, et al. MRI for Diagnosis of Pure Ductal Carcinoma in Situ: A Prospective Observational Study. *Lancet* (2007) 370(9586):485–92. doi: 10.1016/S0140-6736(07)61232-X
13. Yang J, Su D, Zhao X, Jin G, Huang X, Kang W, et al. The Diagnostic Value of Combining Dynamic Contrast Enhanced MRI and Diffusion Weighted Imaging in Breast Lesions With Peripheral Enhancement. *J Clin Radiol* (2016) 35(10):1490–4. doi: 10.13437/j.cnki.jcr.2016.10.011
14. Mei A, Hua J. Dynamic Contrast-Enhanced MR Imaging Manifestations of Breast Lesions With Peripheral Enhancement. *J Pract Radiol* (2011) 27(1):62–5. doi: 10.3969/j.issn.1002-1671.2011.01.016
15. Turnbull L, Brown S, Harvey I, Olivier C, Drew P, Napp V, et al. Comparative Effectiveness of MRI in Breast Cancer (COMICE) Trial: A Randomised Controlled Trial. *Lancet* (2010) 375(9714):563–71. doi: 10.1016/S0140-6736(09)62070-5
16. Wan W, Tao Xi, Gao X, Zhao D, Liu S, Xiao X, et al. Histopathologic Features of Rim Enhancement MRI for Breast Infiltrating Ductal Carcinoma. *Acad J OF Sec Militar Med Univ* (2010) 31(6):625–9. doi: 10.3724/SP.J.1008.2010.00625
17. Prionas ND, Lindfors KK, Ray S, Huang SY, Beckett LA, Monsky WL, et al. Contrast-Enhanced Dedicated Breast CT: Initial Clinical Experience. *Radiology* (2010) 256(3):714–23. doi: 10.1148/radiol.10092311
18. Zhao X, Su D, Kang W, Jin G, Liu L, Zheng Z, et al. Investigation of Breast CT Number in Asymptomatic Female: Characteristics of Cone Beam Breast CT Plain Scan. *J Pract Radiol* (2020) 36(9):1474–8. doi: 10.3969/j.issn.1002-1671.2020.09.030
19. Buadu LD, Murakami J, Murayama S, Hashiguchi N, Sakai S, Masuda K, et al. Breast Lesions: Correlation of Contrast Medium Enhancement Patterns on MR Images With Histopathologic Findings and Tumor Angiogenesis. *Radiology* (1996) 200(3):639–49. doi: 10.1148/radiology.200.3.8756
20. Liu P, Bao R, Niu Y, Yu Y. Angiogenesis and Dynamic Contrast Enhanced MRI of Benign and Malignant Breast Lesions: Preliminary Results. *Chin J Radiol* (2002) 36(11):967–72. doi: 10.3760/j.issn:1005-1201.2002.11.002.
21. O'Connell AM, Kawakyu-O'Connor D. Dedicated Cone-Beam Breast Computed Tomography and Diagnostic Mammography: Comparison of Radiation Dose, Patient Comfort, and Qualitative Review of Imaging Findings in BI-RADS 4 and 5 Lesions. *J Clin Imaging Sci* (2012) 2(1):1–8. doi: 10.4103/2156-7514.93274
22. He N, Wu Y, Kong Y, Lv N, Huang Z, Li S, et al. The Utility of Breast Cone-Beam Computed Tomography, Ultrasound, and Digital Mammography for Detecting Malignant Breast Tumors: A Prospective Study With 212 Patients. *Eur J Radiol* (2016) 85(2):392–403. doi: 10.1016/j.ejrad.2015.11.029
23. Wienbeck S, Uhlig J, Luftner-Nagel S, Zapf A, Surov A, Fintel E, et al. The Role of Cone-Beam Breast-CT for Breast Cancer Detection Relative to Breast Density. *Eur Radiol* (2017) 27(12):5185–95. doi: 10.1007/s00330-017-4911-z
24. Vedantham S, Shi L, Karellas A, O'Connell A, Conover D. Personalized Estimates of Radiation Dose From Dedicated Breast CT in a Diagnostic Population and Comparison With Diagnostic Mammography. *Phys Med Biol* (2013) 58(22):7921–36. doi: 10.1088/0031-9155/58/22/7921
25. Thurston J. NCRP Report No. 160: Ionizing Radiation Exposure of the Population of the United States. *Phys Med Biol* (2010) 55(20):6327.
26. Smith-Bindman R, Lipson J, Marcus R, Kim K, Mahesh M, Gould R, et al. Radiation Dose Associated With Common Computed Tomography Examinations and the Associated Lifetime Attributable Risk of Cancer. *Arch Intern Med* (2009) 169(22):2078–86. doi: 10.1001/archinternmed.2009.427

Conflict of Interest: The authors declare that the research was conducted in the absence of any commercial or financial relationships that could be construed as a potential conflict of interest.

frontiers | Frontiers in Oncology

ORIGINAL RESEARCH
published: 31 May 2022
doi: 10.3389/fonc.2022.858696

A Comprehensive Model for Diagnosis of Primary Breast Lymphoma Differentiated From Breast Cancer and Prognosis Evaluation of Surgical Treatment

*Yanan Li, Yan Zhang, Wei Wang, Chong Wei, Danqing Zhao and Wei Zhang**

Hematology Department, Peking Union Medical College Hospital, Beijing, China

OPEN ACCESS

Edited by:
Abhishek Mahajan, Clatterbridge Cancer Centre NHS Foundation Trust, United Kingdom

Reviewed by:
Pradipta Hande, Breach Candy Hospital Trust, India
Yun Qin, Sichuan University, China

***Correspondence:**
Wei Zhang
vv1223@vip.sina.com

Specialty section:
This article was submitted to Cancer Imaging and Image-directed Interventions, a section of the journal Frontiers in Oncology

Received: *11 February 2022*
Accepted: *19 April 2022*
Published: *31 May 2022*

Citation:
Li Y, Zhang Y, Wang W, Wei C, Zhao D and Zhang W (2022) A Comprehensive Model for Diagnosis of Primary Breast Lymphoma Differentiated From Breast Cancer and Prognosis Evaluation of Surgical Treatment. Front. Oncol. 12:858696. doi: 10.3389/fonc.2022.858696

Background: The objective of this work was to discriminate between primary breast lymphoma (PBL) and breast cancer by systematically analyzing clinical characteristics, laboratory examination results, ultrasound features, and mammography findings to establish a diagnostic model for PBL and to analyze the influence of surgical treatment on the prognosis of PBL patients.

Method: We analyzed 20 PBL and 70 breast cancer patients treated during the same period by comparing several characteristics: clinical features, such as age, tumor position, and breast complaints; laboratory examination findings, such as the lactate dehydrogenase (LDH) level, and imaging features such as the maximum diameter, shape, margins, aspect ratio, and calcification of the mass and axillary lymph node involvement. A diagnostic model was then developed using logistic regression analysis. The impact of surgery on the prognosis of PBL patients was assessed through Kaplan–Meier survival analysis.

Result: Breast cancer and PBL could be distinguished based on imaging features, including the maximum diameter, shape, margin, and calcification of the mass, and lymph node involvement ($P < 0.05$). There were no significant differences between PBL and breast cancer patients in terms of clinical features, or the LDH level. The area under the receiver operating characteristic curve was 0.821. The log-rank test showed that surgery had no significant influence on the prognosis of PBL patients.

Conclusion: Ultrasound and mammography are the most useful methods for detecting malignant breast tumors. Compared with breast cancer tumors, breast lymphoma tumors are larger with a more regular shape and less calcification and are often accompanied by axillary lymph node involvement. Patients with a breast malignancy should not undergo surgical excision without an accurate diagnosis.

Keywords: breast cancer, primary breast lymphoma, ultrasound, mammography, diagnosis

INTRODUCTION

Breast cancer has the highest incidence rate and second highest mortality rate in women. There are nearly 279,100 cases of the disease each year, with 42,690 patients dying from breast cancer annually in America (1). Primary breast lymphoma (PBL) is a relatively rare extranodal lymphoma of the breast that accounts for only 0.04%–0.5% of all breast malignancies (2). However, PBL generally exhibits early progression and a poor prognosis. Breast cancer and breast lymphoma are similar with respect to their clinical manifestations, performing as painless breast masses with poor mobility, and imaging examinations reveal nodules with low echo in ultrasound and solitary mass on mammography (3–5). In clinical practice, breast lymphoma is often misdiagnosed as breast cancer or other breast malignancies; however, the treatment of PBL is primarily immunochemotherapy rather than surgery. There are quite a few PBL patients who undergo surgical excision and then suffer from a poor quality of life and have no improvement in prognosis. To date, there is no systematic analysis of the difference between these two malignant cancer types. The purpose of this study was therefore to explore the difference in clinical manifestations and imaging findings between breast cancer and primary breast lymphoma and then to establish a clinical diagnostic model for breast lymphoma. Then, we compared the impact of surgery on the prognosis of primary breast lymphoma patients to provide a diagnostic reference for clinical diagnoses and to help these patients avoid unnecessary radical surgery.

MATERIALS AND METHODS

Patients

Our study included all of 20 patients with primary breast lymphoma and 70 patients with breast cancer treated at the same time in Peking Union Medical College Hospital during the period from 2000 to 2020. The inclusion criteria were as follows: 1) age ≥18 years, with a diagnosis of breast cancer or PBL by pathological examination and 2) pathological subtype of diffuse large B-cell lymphoma (DLBCL) for PBL patients and invasive carcinoma for breast cancer patients. The exclusion criteria were as follows: 1) incomplete imaging or laboratory examination data, including the absence of both ultrasound and mammography data, and 2) other types of breast tumors. Detailed patient information is shown in **Table 1**. All PBL patients were followed up *via* telephone until February 1, 2021. The follow-up rate was 90.0%, and the median follow-up time was 36.5 months.

Data Collection

General information was collected from the patients, including sex and age. Clinical manifestations included tumor position, breast-related complaints such as nipple retraction, bloody nipple discharge, and orange peel- or eczema-like skin changes. The main laboratory finding was the serum lactate dehydrogenase (LDH) level. Imaging examinations included color Doppler ultrasound and mammography. Ultrasonography acted as the main modality for assessing the following characteristics: the maximum diameter, shape, margin, and aspect ratio of the mass, and axillary lymph node involvement. We depended on mammography to identify mass calcification. The descriptions of imaging features were based on Breast Imaging Reporting & Data System (BI-RADS) Fifth Edition (2013) (6, 7). The mass shape was classified as 1) regular, including oval and round, or 2) irregular. The mass margin was classified as 1) circumscribed or 2) other, including obscured, microlobulated, indistinct, and spiculated. The aspect ratio was defined as ≥1 when the anteroposterior diameter of any section was greater than or equal to the transverse diameter; otherwise, it was defined as <1. Mass calcification was classified as 1) no or typically benign (rim, round) calcification or 2) suspicious morphology (amorphous, coarse heterogeneous, fine pleomorphic, and fine linear or fine linear branching) morphology.

The gold standard method for diagnosing breast malignancies was pathological examination. Tissues were observed after hematoxylin and eosin (H&E) staining, and the expression of cellular antigens, such as MUM1, Bcl-2, CD10, Bcl-6, CD79a, CD45, CD20, CD3, E-cadherin, ER, PR, and HER-2, was identified through immunohistochemistry (**Figure 1**). In our study, the surgical methods applied to treat breast cancer included classical radical mastectomy, modified radical mastectomy, simple mastectomy, and local mastectomy, excluding breast mass biopsy. The survival of PBL patients was evaluated by the overall survival (OS), defined as the time from the diagnosis of breast lymphoma to the date of death or the date when the follow-up endpoint was reached due to any cause, and progression-free survival (PFS), defined as the time from the beginning of treatment to the date of disease progression or the date when the follow-up endpoint was reached. Examinations of the recorded clinical data were performed by one person. Data verification and regular follow-up visits were used to avoid missing data.

Data Analysis

SPSS version 20 (IBM) was adopted to process all quantitative data, such as age, tumor site, LDH level, mass shape, mass margin, mass aspect ratio, mass calcification, and axillary lymph node involvement, into dichotomous/trichotomous variables. Then, the χ^2 test was used to analyze the differences between the PBL and breast cancer patients in terms of age, tumor location, LDH level, and imaging manifestations. T tests or Kolmogorov–Smirnov tests were used to analyze the differences in continuous variables, such as the maximum mass diameter and tumor growth. Taking the characteristics above as independent variables and the type of breast tumor as the dependent variable, bivariate forward stepwise logistic regression was performed. The Wald χ^2 test was used to estimate the regression parameters, and the likelihood ratio test was used to fit the whole model. Receiver operating characteristic (ROC) curves were used to evaluate the predictive ability of the logistic model. The Kaplan–Meier method was used to analyze the survival outcomes of PBL patients, and the log-rank test was used to calculate the influence of surgery on PFS and OS. All data

TABLE 1 | Clinical and image characteristics between breast cancer and primary breast lymphoma.

	Breast cancer (n = 70)	Primary breast lymphoma (n = 20)	Sig (χ^2 test)
Age			0.360
<50	27 (38.6%)	10 (50.0%)	
≥50	43 (61.4%)	10 (50.0%)	
Position			0.958
Left	33 (47.1%)	10 (50.0%)	
Right	34 (48.6%)	9 (45.0%)	
Both	3 (4.3%)	1 (5.0%)	
Breast complaints			1.000
Absence	64 (91.4%)	19 (95%)	
Presence	6 (8.6%)	1 (5.0%)	
LDH			0.410
Normal	64 (91.4%)	17 (85.0%)	
More than normal	6 (8.6%)	3 (15.0%)	
Shape			<0.001
Regular	4 (5.7%)	9 (45.0%)	
Irregular	66 (94.3%)	11 (55.0%)	
Margin			<0.001
Circumscribed	4 (5.7%)	8 (40%)	
Others	66 (94.3%)	12 (60%)	
Calcification			0.017
Absence	35 (50%)	16 (80%)	
Presence	35 (50%)	4 (20%)	
Aspect ratio			0.141
<1	51 (72.9%)	18 (90%)	
≥1	19 (27.1%)	2 (10%)	
Lymph node involved			0.007
Absence	48 (68.6%)	7 (35.0%)	
Presence	22 (31.4%)	13 (65.0%)	

were analyzed by SPSS 20.0 statistical software, and $P < 0.05$ was considered statistically significant.

RESULTS

All 20 patients with PBL in this study had DLBCL; among them, 60% had the germinal center B-cell (GCB) subtype and 40% had the non-GCB subtype. The distribution of BI-RADS categories for PBL patients was as follows: none was categories 0–2; category 3 was 4; category 4 was 13 (4 of category 4A, 7 of category 4B, and 2 of category 4C); and category 5 was 3. Unfortunately, 65% underwent surgery, and all 20 patients later underwent standard immunochemotherapy. All 70 patients with breast cancer were pathologically diagnosed with invasive carcinoma and underwent surgery excision. The distribution of BI-RADS categories for breast cancer was as follows: none was categories 0–2; category 3 was 1; category 4 was 45 (4 of category 4A, 12 of category 4B, and 29 of category 4C); and category 5 was 24. Other clinical and imaging characteristics of the patients are shown in **Table 1** and **Figures 2**, **3**.

Clinical characteristics such as age, tumor location, breast complaints, and LDH level did not differ significantly between

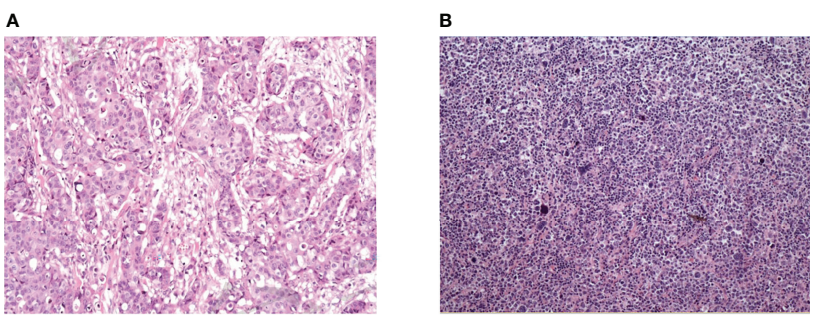

FIGURE 1 | Pathological results of breast cancer and primary breast lymphoma. **(A)** Female, 47, diffuse large B-cell lymphoma. Microscopically, large tumor cells were diffusely infiltrated and homogeneous in shape. Immunohistochemistry: CD20(++), PAX-5(+), CD5(+), Bcl-6(-), CD10(-), Mum-1(-), Ki-67(index 80%). **(B)** Female, 65, invasive breast cancer (non-specific, moderately differentiated), microscopically large tumor cells with invasive growth and acinar distribution, obvious atypia and mitotic visible. Immunohistochemistry: Her-2 (3+), CD10(-), PR(-), CgA(-), Syn(-), P53(+), Ki67 (index 70%).

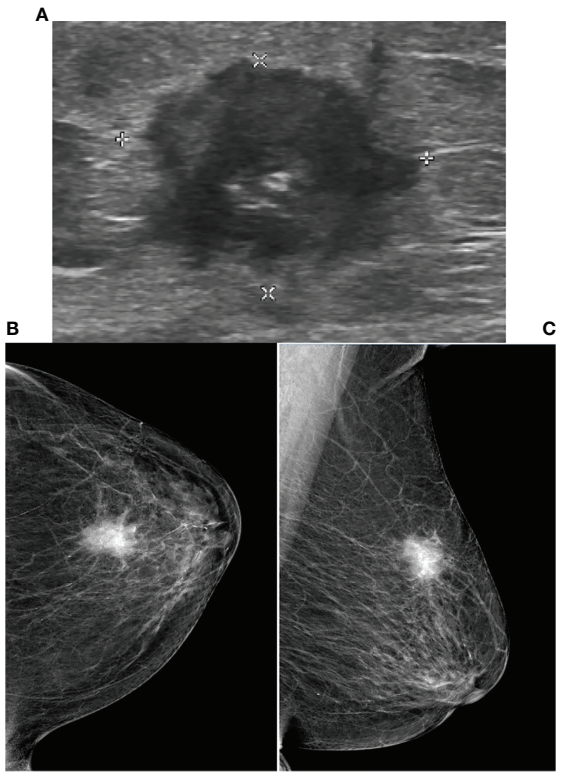

FIGURE 2 | Ultrasound and Mammography images for breast cancer. Legend: Female, 80, invasive carcinoma of left breast. **(A)** showed irregular heterogeneous echo in left breast, spiculated margins. The mammography of CC **(B)** and MLO **(C)** of left breast showed high-density mass, obscure margins, and clustered microcalcifications in the lesion.

the two groups. Among the imaging features, maximum mass diameter (P = 0.007), mass shape (P < 0.001), mass margin (P < 0.001), mass calcification (P = 0.017), and lymph node involvement (P = 0.007) were significantly different between the two groups (**Table 1** and **Supplemental Table 1**). These results indicate that it is difficult to distinguish PBL from breast cancer based on clinical manifestations and that this differentiation mainly depends on imaging examinations.

The dichotomous characteristics above were summarized in terms of predictive probability, and finally, three independent risk factors were chosen for inclusion in the logistic model, i.e., mass shape, mass calcification, and lymph node involvement (**Table 2**): Logit(P) = -0.573 + 2.748 × regular shape + 1.296 × no calcification - 1.744 × lymph node involvement. The likelihood ratio test of the above model yielded a statistically significant result (χ^2 = 27.815, P < 0.001). The Wald χ^2 test of each regression coefficient showed that the P values of mass shape, mass calcification, and lymph node involvement were less than 0.05. If P = 0.5 was chosen as the threshold, the predictive accuracy was as high as 84.4%, and the sensitivity, specificity, breast lymphoma predictive value, and breast cancer predictive value were 0.814, 0.650, 0.971, and 0.4, respectively. The area under the ROC curve was 0.821 (standard error = 0.053, 95% CI: 0.718–0.924) (**Figure 4**), indicating that the predictive accuracy of the model was high.

We then analyzed the impact of surgery on the prognosis of PBL patients. A total of 13 PBL patients (65%) underwent surgical treatment. **Figure 2** shows that surgery had no significant influence on the PFS or OS of these patients, suggesting that surgical treatment did not confer a better prognosis or longer survival time (**Figure 5**). The 10-year PFS and OS rates reached 71% and 87.5%, respectively. With the arrival of the rituximab era, the prognosis of PBL patients has been estimated to be better because of immunochemotherapy. Therefore, while it is not necessary for patients with PBL to undergo surgical treatment, it is vital for doctors to remain vigilant to avoid misdiagnosis.

DISCUSSION

Breast cancer has high incidence, and aggressive surgery can be used after early detection. However, primary breast lymphoma is rare, and its clinical manifestations are generally similar to those of breast cancer, so clinicians may misdiagnose breast lymphoma as breast cancer. However, the first-line treatment for breast lymphoma is immunochemotherapy rather than surgery (8). A multicenter study showed that mastectomy did not improve the prognosis of PBL patients, and the 5-year OS was 77.3% during the rituximab era (9). Therefore, early differential diagnosis is necessary for the selection of appropriate treatments and to improve quality of life. Although pathology is the gold standard to distinguish breast cancer from breast lymphoma, ultrasound and mammography are the most widely used detection methods in the clinic, playing an important role in the differential diagnosis of breast malignancies. Breast malignancies clinically manifest as palpable and painless masses with poor mobility, which may be accompanied by nipple invagination or discharge. Laboratory tests may show elevated LDH. Previous studies have summarized the ultrasonic characteristics of breast cancer, generally an irregular shape, irregular, spiculated, or microlobulated margins, low echo attenuation, micro/macro-calcification, and the presence of the retraction phenomenon. In contrast, primary breast lymphoma on mammography or ultrasound often shows isolated oval hypoechoic nodules with no obvious obscured margins (10). In addition, PBL has the general characteristics of lymphoma, exhibiting fast growth and a large tumor size. However, no research has systematically and quantitatively differentiated the clinical, laboratory, and imaging manifestations of these two types of cancer. In our research, we evaluated the differences in 10 features (**Table 1** and **Supplemental Table 1**) between the two tumor types and developed a model to differentiate primary breast lymphoma. Significant features with P < 0.05 (including mass maximum diameter, shape, margin, calcification, and lymph node involvement) were found to be primarily related to imaging findings according to the χ^2 test and t test. Moreover, lymphoma is more likely to invade and metastasize due to the

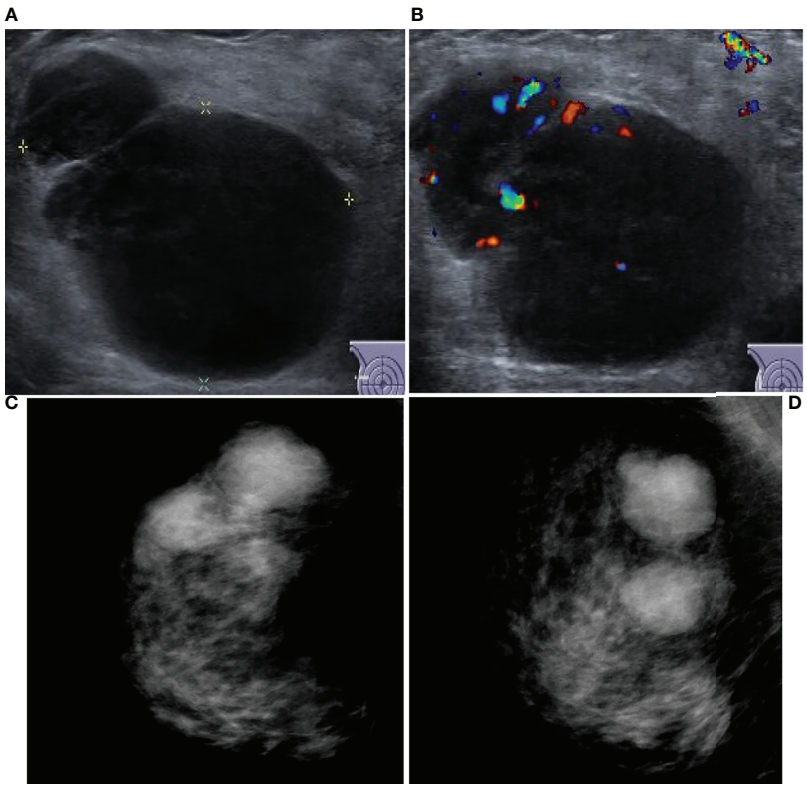

FIGURE 3 | Ultrasound and mammography images for PBL. Legend: Female, 49, right non-Hodgkin breast lymphoma. **(A)** shows irregular hypoecho in the right breast with circumscribed margins. **(B)** CDF1 shows abundant blood flow signals. Right breast mammography CC position **(C)** and MLO position **(D)** image showed high density mass, no micro/macro-calcification.

mutation of MYD88 or BCL6 genes and the action of multiple immune cells in the tumor microenvironment (11). There were more regular shapes for breast lymphoma, consistent with previous studies (12, 13). The calcification of breast cancer may be related to the mutation of HER2 or other intrinsic genes (14), or due to the acquisition of osteoblastic characteristics during the process of epithelial-to-mesenchymal transition (EMT), forming matrix vesicles and promoting calcification (15).

Our study is the first to summarize the differences between breast cancer and breast lymphoma and to fit a regression model combining clinical manifestations, laboratory tests, and ultrasound and mammography features, the most widely used modalities in clinical practice. Clinically, the results revealed that at diagnosis, breast lymphoma is typically large in size, with involvement of the surrounding lymph nodes, regular shapes, and no obvious calcification (**Figures 2**, **3**). The area under the ROC curve plotted by the prediction value fitted by logistic analysis was 0.821, supporting the differential diagnosis of breast lymphoma. Therefore, it is necessary for surgeons to perfect breast biopsy when imaging manifestation shows suspected malignancy as more than category 3 (16), rather than an arbitrary diagnosis and surgical resection.

Our research has some limitations, which should be mentioned. First, this was a retrospective study, and the sample size for breast lymphoma was small. Second, we did not analyze the differences in the equipment used between different hospitals. We look forward to performing systematic error correction between instruments and using larger-sample studies in future work.

In conclusion, conventional ultrasound and mammography are useful tools for distinguishing breast cancer from breast lymphoma. The distinguishing characteristics of breast

TABLE 2 | Logistic regression model analysis.

Variables	Regression coefficient	S.E	$\chi 2$	P value	OR
Shape	2.748	0.817	11.32	0.001	15.60
Calcification	1.296	0.671	3.73	0.05	3.66
Lymph node involvement	-1.744	0.659	7.00	0.008	0.18
constant	-0.573	0.738	0.60	0.437	0.56

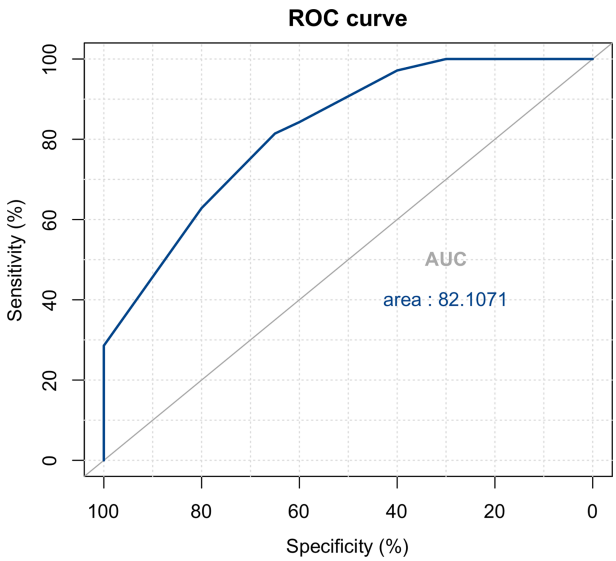

FIGURE 4 | ROC curve for the diagnostic logistic model.

lymphoma included mass maximum diameter, shape, margin,

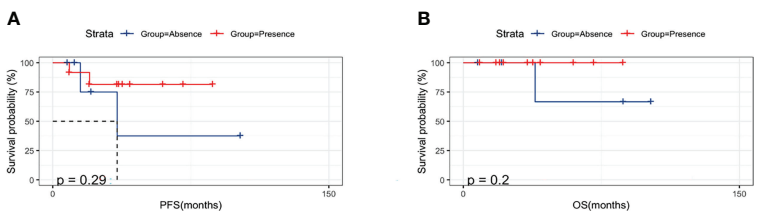

FIGURE 5 | Prognostic influence of operation on primary breast lymphoma.

calcification, and lymph node involvement, which are expected to be suggested for clinical differential diagnosis by breast surgeons.

DATA AVAILABILITY STATEMENT

The raw data supporting the conclusions of this article will be made available by the authors, without undue reservation.

ETHICS STATEMENT

'This study was reviewed and approved by the Institutional Review Board of Peking Union Medical College Hospital. Due to the retrospective nature of our research, a waiver of patients consent was obtained from the PUMCH Institutional Review Board. We guaranteed the anonymity and privacy of patient information and the accessed data conformed to the data and privacy regulations of Declaration of Helsinki.

AUTHOR CONTRIBUTIONS

YL contributed significantly to the data collection, examination, and analysis and wrote the manuscript. WZ contributed to the conception of the study and the revision of the manuscript. YZ contributed to the research design. WW performed the partial data analysis and was involved in the manuscript preparation. CW helped perform the analysis and provided constructive discussions. DZ helped collect the clinical data and revise the manuscript. All authors read and approved the final version of the manuscript.

SUPPLEMENTARY MATERIAL

The Supplementary Material for this article can be found online at: https://www.frontiersin.org/articles/10.3389/fonc.2022.858696/full#supplementary-material

REFERENCES

1. Gradishar WJ, Anderson BO, Abraham J, Aft R, Agnese D, Allison KH, et al. Breast Cancer, Version 3.2020, NCCN Clinical Practice Guidelines in Oncology. *J Natl Compr Canc Netw* (2020) 18(4):452–78. doi: 10.6004/jnccn.2020.0016
2. Picasso R, Tagliafico A, Calabrese M, Martinoli C, Pistoia F, Rossi A, et al. Primary and Secondary Breast Lymphoma: Focus on Epidemiology and Imaging Features. *Pathol Oncol Res* (2020) 26(3):1483–8. doi: 10.1007/s12253-019-00730-0
3. Libson S, Lippman M. A Review of Clinical Aspects of Breast Cancer. *Int Rev Psychiatry* (2014) 26(1):4–15. doi: 10.3109/09540261.2013.852971
4. Nicholson BT, Bhatti RM, Glassman L. Extranodal Lymphoma of the Breast. *Radiol Clin North Am* (2016) 54(4):711–26. doi: 10.1016/j.rcl.2016.03.005
5. Raj SD, Shurafa M, Shah Z, Raj KM, Fishman MDC, Dialani VM. Primary and Secondary Breast Lymphoma: Clinical, Pathologic, and Multimodality Imaging Review. *Radiographics* (2019) 39(3):610–25. doi: 10.1148/rg.2019180097
6. Rao AA, Feneis J, Lalonde C, Ojeda-Fournier H. A Pictorial Review of Changes in the BI-RADS Fifth Edition. *Radiographics* (2016) 36(3):623–39. doi: 10.1148/rg.2016150178
7. Spak DA, Plaxco JS, Santiago L, Dryden MJ, Dogan BE. BI-RADS(®) Fifth Edition: A Summary of Changes. *Diagn Interv Imaging* (2017) 98(3):179–90. doi: 10.1016/j.diii.2017.01.001
8. Lalani N, Winkfield KM, Soto DE, Yeap BY, Ng AK, Mauch PM, et al. Management and Outcomes of Women Diagnosed With Primary Breast Lymphoma: A Multi-Institution Experience. *Breast Cancer Res Treat* (2018) 169(1):197–202. doi: 10.1007/s10549-018-4671-8
9. Hu S, Song Y, Sun X, Su L, Zhang W, Jia J, et al. Primary Breast Diffuse Large B-Cell Lymphoma in the Rituximab Era: Therapeutic Strategies and Patterns of Failure. *Cancer Sci* (2018) 109(12):3943–52. doi: 10.1111/cas.13828
10. Lyou CY, Yang SK, Choe DH, Lee BH, Kim KH. Mammographic and Sonographic Findings of Primary Breast Lymphoma. *Clin Imaging* (2007) 31(4):234–8. doi: 10.1016/j.clinimag.2007.02.028
11. Shen R, Xu PP, Wang N, Yi HM, Dong L, Fu D, et al. Influence of Oncogenic Mutations and Tumor Microenvironment Alterations on Extranodal Invasion in Diffuse Large B-Cell Lymphoma. *Clin Transl Med* (2020) 10(7):e221. doi: 10.1002/ctm2.221
12. Talwalkar SS, Miranda RN, Valbuena JR, Routbort MJ, Martin AW, Medeiros LJ. Lymphomas Involving the Breast: A Study of 106 Cases Comparing Localized and Disseminated Neoplasms. *Am J Surg Pathol* (2008) 32(9):1299–309. doi: 10.1097/PAS.0b013e318165eb50
13. Wienbeck S, Meyer HJ, Uhlig J, Herzog A, Nemat S, Teifke A, et al. Radiological Imaging Characteristics of Intramammary Hematological Malignancies: Results From a German Multicenter Study. *Sci Rep* (2017) 7(1):7435. doi: 10.1038/s41598-017-07409-z
14. O'Grady S, Morgan MP. Microcalcifications in Breast Cancer: From Pathophysiology to Diagnosis and Prognosis. *Biochim Biophys Acta (BBA) - Rev Cancer* (2018) 1869(2):310–20. doi: 10.1016/j.bbcan.2018.04.006
15. Sharma T, Radosevich JA, Pachori G, Mandal CC. A Molecular sView of Pathological Microcalcification in Breast Cancer. *J Mammary Gland Biol Neoplasia* (2016) 21(1-2):25–40. doi: 10.1007/s10911-015-9349-9
16. Berg WA, Berg JM, Sickles EA, Burnside ES, Zuley ML, Rosenberg RD, et al. Cancer Yield and Patterns of Follow-Up for BI-RADS Category 3 After Screening Mammography Recall in the National Mammography Database. *Radiology* (2020) 296(1):32–41. doi: 10.1148/radiol.2020192641

Conflict of Interest: The authors declare that the research was conducted in the absence of any commercial or financial relationships that could be construed as a potential conflict of interest.

frontiers | Frontiers in Oncology

ORIGINAL RESEARCH
published: 30 June 2022
doi: 10.3389/fonc.2022.911790

Contribution of Diffusion-Weighted Imaging and ADC Values to Papillary Breast Lesions

Wenjie Lv[1†], *Dawen Zheng*[2†], *Wenbin Guan*[3] *and Ping Wu*[1*]

[1] Department of Breast Surgery, Xinhua Hospital Affiliated to Shanghai Jiao Tong University School of Medicine, Shanghai, China,
[2] Department of General Surgery, Xinhua Hospital Affiliated to Shanghai Jiao Tong University School of Medicine, Shanghai, China,
[3] Department of Pathology, Xinhua Hospital Affiliated to Shanghai Jiao Tong University School of Medicine, Shanghai, China

OPEN ACCESS

Edited by:
Abhishek Mahajan, Clatterbridge Cancer Centre NHS Foundation Trust, United Kingdom

Reviewed by:
Lian-Ming Wu, Shanghai Jiao Tong University, China
Fabrizio Urraro, University of Campania Luigi Vanvitelli, Italy
Hyunseok Seo, Korea Institute of Science and Technology, South Korea

***Correspondence:**
Ping Wu
breast_2022@163.com

[†]*These authors have contributed equally to this work and share first authorship*

Specialty section:
This article was submitted to Cancer Imaging and Image-directed Interventions, a section of the journal Frontiers in Oncology

Received: *03 April 2022*
Accepted: *31 May 2022*
Published: *30 June 2022*

Citation:
Lv W, Zheng D, Guan W and Wu P (2022) Contribution of Diffusion-Weighted Imaging and ADC Values to Papillary Breast Lesions. Front. Oncol. 12:911790. doi: 10.3389/fonc.2022.911790

This study aimed to evaluate the role of apparent diffusion coefficient (ADC) values obtained from diffusion-weighted imaging (DWI) in the differentiation of malignant from benign papillary breast lesions. The magnetic resonance imaging (MRI) data of 94 breast papillary lesions confirmed by pathology were retrospectively analyzed. The differences in ADC values of papillary lesions under different enhancements in MRI and different pathological types were investigated, and the ADC threshold was determined by the receiver operating characteristic curve for its potential diagnostic value. The mean ADC values in borderline and malignant lesions ($1.01 \pm 0.20 \times 10^{-3}$ mm^2/s) were significantly lower compared to benign lesions ($1.21 \pm 0.27 \times 10^{-3}$ mm^2/s) ($P < 0.05$). The optimal threshold of the ADC value could be 1.00×10^{-3} mm^2/s. The ADC values were statistically significant in differentiating between benign and malignant papillary lesions whether in mass or non-mass enhancement ($P < 0.05$). However, there were no statistical differences in the ADC values among borderline or any other histological subtypes of malignant lesions ($P > 0.05$). Measuring ADC values from DWI can be used to identify benign and malignant breast papillary lesions. The diagnostic performance of the ADC value in identifying benign and malignant breast lesions is not affected by the way of lesion enhancement. However, it shows no use for differential diagnosis among malignant lesion subtypes for now. The ADC value of 1.00×10^{-3} mm^2/s can be used as the most appropriate threshold for distinguishing between benign and malignant breast papillary lesions.

Keywords: diffusion-weighted imaging, apparent diffusion coefficient values, papillary breast lesions, magnetic resonance imaging, mass enhancement, non-mass enhancement, receiver operating characteristic curve

INTRODUCTION

Papillary breast lesions indicate a heterogeneous group of diseases including benign intraductal papilloma (IDP), borderline intraductal papilloma with atypical hyperplasia [intraductal papilloma with atypical ductal hyperplasia (ADH)], and malignant papillary lesions. Intraductal papilloma with ductal carcinoma *in situ* (intraductal papilloma with DCIS), papillary ductal carcinoma *in situ*

(papillary DCIS), encapsulated papillary carcinoma (EPC), solid papillary carcinoma (SPC), and invasive papillary carcinoma (IPC) fall into the third category (1). Papillary protrusions with a dendritic fibrovascular stroma represent the general histopathological feature of papillary breast lesions (2).

Magnetic resonance imaging (MRI) is widely applied in detecting papillary breast lesions as a prominently viable imaging modality. Due to the diversity of pathological subtypes, the variability among observational factors in MRI, such as morphology feature, enhancement mode, and time–signal intensity curve, and coupled with the absence of evidence from large samples or prospective studies (3–6), the imaging diagnostic criteria for papillary lesions have not been unified. Diffusion-weighted imaging (DWI) is emerging as a favorable alternative for deriving perfusion information to complement dynamic contrast-enhanced magnetic resonance imaging of the breast. By calculating the apparent diffusion coefficient (ADC), DWI, which is sensitive to water diffusion, can provide a quantitative analysis of both the cellularity and perfusion of tumors and has the potential to provide an evaluation of lesion characterization. Hyunseok Seo reports that a high-resolution ADC map and a DWI can be accurately obtained by using isotropic diffusion-weighted imaging while reducing the artifacts caused by the diffusion anisotropy, compared to diffusion-weighted echo-planar-imaging (7). More other studies have already proved DWI and ADC values as promising tools in breast lesion detection, prognostic assessment, and therapeutic response prediction (8–10).

However, fewer studies were capable of proving DWI's positive association with a diagnosis of breast papillary lesions, which contributed to the limited use of breast DWI in clinical practice. This retrospective study analyzes the mean ADC values observed from 94 different papillary breast lesions and aims to evaluate the role of ADC values in distinguishing malignant from benign lesions, especially in differentiating the histological subtypes of malignant lesions as well as in assessing the potential diagnostic contribution to papillary lesions in different enhancements.

MATERIALS AND METHOD

Data Collection

Clinical data were collected retrospectively on 69 female patients with papillary lesions who were admitted to our hospital from January 2021 to February 2022, with a total of 94 lesions. Among them, 51 cases were benign breast papillary lesions, all of which were IDP; 16 cases were borderline lesions, all of which were intraductal papilloma with ADH; and 27 cases were malignant lesions, including 13 cases of intraductal papilloma with DCIS, 3 cases of papillary DCIS, 1 case of EPC, 9 cases of SPC and 1 case of IPC. The inclusion criteria for this study were as follows: breast papillary lesions confirmed by postoperative pathology (one patient may have multiple lesions) and preoperative MRI examination was available from which the ADC values of the lesions corresponding to the postoperative pathology could be obtained on DWI. The exclusion criteria were as follows: lesions with non-high signal on DWI—namely, ADC values could not be obtained—and lesions with the coexistence of multiple pathological types, of which it was impossible to determine what kind of pathological type the ADC value belongs to.

MRI Examination

Imaging was performed on the same 3T MR unit (Philips Ingenia). All patients were in the prone position. The Philips MRI scanning sequence included the following: (1) cross-sectional T2WI, using two-dimensional fast spin-echo sequence, SPAIR fat suppression, and the following scanning parameters: TR/TE, 5,000/65 ms; slice thickness/slice interval, 4/1 mm; FOV, 37.2 cm; matrix, 465 × 381; (2) cross-sectional diffusion-weighted imaging DWI, using single-shot SE-EPI sequence, NEX = 1, SPIR + SSGR fat suppression, b = 0, 800 s/mm^2, and the following scanning parameters: TR/TE, 5,100/72 ms; layer thickness/layer spacing, 4/1 mm; FOV, 35 cm; matrix, 136 × 140; and (3) cross-sectional dynamic enhancement, three-dimensional gradient-echo sequence, and SPIR fat suppression. First, the plain scanned images were acquired and then collected by 4 to 5 consecutive phases without intervals after injecting the contrast agent (gadopentetate meglumine), followed by injection in the amount of 0.1 mmol/kg with a high-pressure syringe through the dorsal vein of the hand at a flow rate of 2.0 ml/s and then 15 ml of normal saline at the same flow rate. The scanning parameters were as follows: TR/TE, 4.2/2.1 ms; layer thickness/layer spacing, 1/0 mm; flip angle, 12°; FOV, 34 cm; and matrix, 407 × 404. Each scan lasted for 65 s. Imaging of all lesions was analyzed in consensus by two experienced breast radiologists. The solid area was selected at the layer with the largest diameter of the lesion to delineate the region of interest (ROI) on DWI corresponding to T2WI, dynamic enhancement, and subtraction images. The necrotic, cystic hemorrhagic parts of the lesion and where ROI was smaller than the range of the high signal area should be avoided as much as possible. The ADC value of the solid component of the lesion was measured on ADC maps.

Statistical Analysis

Statistical analysis was performed using IBM SPSS 26.0 (the mean ADC value was made for lesions whose ADC values were presented as a range). The statistical diagram was performed by GraphPad Prism 8.4. *T*-test or one-way analysis of variance was used to compare the quantitative variables between two groups and the Bonferroni method for multiple comparisons. The receiver operating characteristic (ROC) curves were constructed to obtain the area under the curve (AUC) and the optimal threshold of the ADC value with its sensitivity and specificity for potential diagnosis contribution to papillary lesions. *P*-value <0.05 was considered statistically significant.

RESULTS

Clinical Features

This study included a total of 94 papillary lesions of 69 patients ranging from 31 to 73 years old. The lesions were categorized as

mass and non-mass enhancement according to the BI-RADS fifth edition (11). Among them, 54 cases were mass lesions, while 40 cases were non-mass lesions; 35 cases were lesions with diameters <1 cm, while the others were with diameters ≥1 cm. The general features of benign, borderline, and malignant lesions are summarized in **Table 1**.

Comparison of Mean ADC Values in Benign, Borderline, and Malignant Papillary Lesions

The mean ADC values of benign, borderline, and malignant papillary lesions are shown in **Table 2**. The ADC values of benign papillary lesions ($1.21 \pm 0.27 \times 10^{-3}$ mm^2/s) were significantly higher than those of borderline and malignant papillary lesions ($1.03 \pm 0.19 \times 10^{-3}$ mm^2/s and $1.00 \pm 0.21 \times 10^{-3}$ mm^2/s) ($P < 0.05$), while the ADC values proved no significant difference between borderline lesions and malignant lesions ($P > 0.05$) (**Figure 1**).

In total, 13 cases of borderline papillary lesions were all intraductal papilloma with ADH, of which the mean ADC value was $1.03 \pm 0.19 \times 10^{-3}$ mm^2/s. Among malignant papillary lesions, the mean ADC value of 13 cases of intraductal papilloma with DCIS was $1.05 \pm 0.12 \times 10^{-3}$ mm^2/s, the mean ADC value of 3 cases of papillary DCIS was $1.08 \pm 0.49 \times 10^{-3}$ mm^2/s, there was only 1 case of EPC and IPC each, and the ADC values were 1.15×10^{-3} mm^2/s and 0.99×10^{-3} mm^2/s respectively. SPC had the lowest mean ADC value which was $0.89 \pm 0.21 \times 10^{-3}$ mm^2/s. However, there was no significant difference in the mean ADC values of borderline or any other malignant lesion subtypes ($P > 0.05$) (**Figure 2**). The MRI features of 3 different lesion subtypes are shown in **Figures 3–5**.

ROC Curves for Papillary Breast Lesions

Therefore, our study categorized borderline lesions and malignant lesions as one group. The mean ADC value in borderline and malignant lesions was significantly lower than that in benign lesions ($1.21 \pm 0.27 \times 10^{-3}$ *vs.* $1.01 \pm 0.20 \times 10^{-3}$ mm^2/s, $P < 0.05$), and the differences between the mean ADC values of the two categories were statistically significant whether in mass or non-mass enhancement ($P < 0.05$) (**Table 3**).

The ROC curves and AUC for papillary breast lesions with different subtypes are presented on **Figure 6**. The threshold of ADC value to differentiate benign papillary breast lesions from malignant was 1.00×10^{-3} mm^2/s (AUC, 0.728; sensitivity, 55.8%; specificity, 82.4%; $P < 0.05$). The threshold of the ADC value for mass lesions was 1.00×10^{-3} mm^2/s (AUC, 0.706; sensitivity, 63.2%; specificity, 74.3%; $P < 0.05$), while for the non-mass lesions this was 1.14×10^{-3} mm^2/s (AUC, 0.842; sensitivity, 70.8%; specificity, 87.5%; $P < 0.05$).

TABLE 1 | General features of benign, borderline, and malignant papillary breast lesions.

Groups	Benign	Borderline	Malignant	Total
Mean age (years old)	49.8	50.4	58.0	51.7
Number (cases)	51	16	27	94
Mass enhancement (cases)	35	7	12	54
Non-mass enhancement (cases)	16	9	15	40
Diameter, <1 cm (cases)	26	5	4	35
Diameter, ≥1 cm (cases)	25	11	23	59

TABLE 2 | Comparison of the mean apparent diffusion coefficient (ADC) values among benign, borderline, and malignant papillary breast lesions.

Papillary lesions	Number (cases)	Mean ADC values ($\times 10^{-3}$ mm^2/s)	*P*
Benign	51	1.21 ± 0.27	0.030[a]
Borderline	16	1.03 ± 0.19	1.000[b]
Malignant	27	1.00 ± 0.21	0.001[c]

[a]*Compared to borderline lesions.*
[b]*Compared to malignant lesions.*
[c]*Compared to benign lesions.*

DISCUSSION

Papillary breast lesions had drawn increasing attention in clinical practice recently. Benign intraductal papillomas are currently recognized as premalignant lesions. The World Health Organization (WHO) classification of papillary breast lesions suggests that the risk of subsequent invasive breast cancer development in central papillomas without epithelial atypia is believed to increase to two times that of the general population while to three times that of peripheral papillomas (1, 12). It is strongly recommended to closely follow up through imaging examination for such benign lesions in the long term.

DWI is an advanced MRI technique that can measure the mobility of water molecules diffusing in tissue, which is impacted by biophysical characteristics such as cell density, membrane

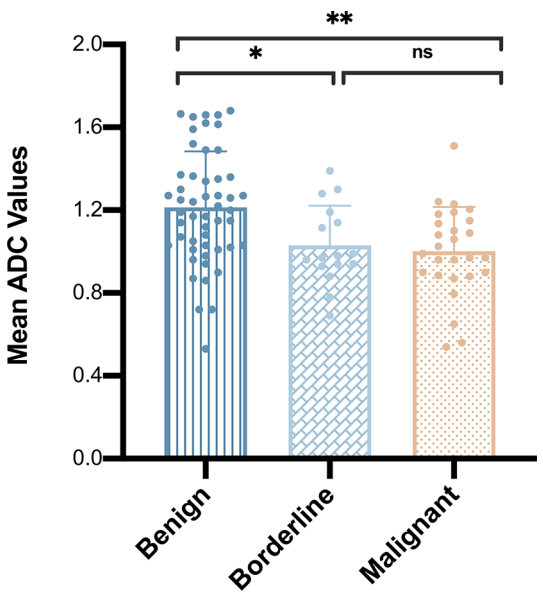

FIGURE 1 | Comparison of mean apparent diffusion coefficient values among benign, borderline, and malignant papillary breast lesions. *$P < 0.05$; **$P < 0.01$; ns, $P > 0.05$.

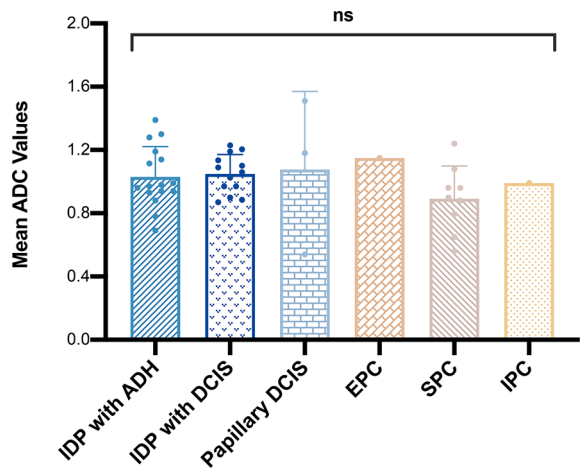

FIGURE 2 | Comparison of mean apparent diffusion coefficient values among different malignant papillary breast lesion subtypes. ns, $P > 0.05$.

integrity, and microstructure of the breast. DWI is now widely used as an important addition to standard breast MRI protocol to screen early breast cancer and potentially predict the response to and monitor the effect of neoadjuvant treatment over time (8, 13). The ADC derived from DWI that provides a quantitative measure of observed diffusion restriction can be used to distinguish between benign and malignant breast lesions. Numerous studies have demonstrated significantly lower ADC values in malignant *versus* benign lesions (14). The ADC values of benign and malignant papillary breast lesions in this research were consistent with previous studies. The mean ADC value of benign papillary lesions ($1.21 \pm 0.27 \times 10^{-3}$ mm^2/s) was significantly higher than borderline lesions ($1.03 \pm 0.19 \times 10^{-3}$ mm^2/s) and malignant lesions ($1.00 \pm 0.21 \times 10^{-3}$ mm^2/s) ($P < 0.05$, respectively). We suggest that ADC values can also be used to differentiate between benign and malignant papillary lesions.

In our study, we achieved the optimal threshold of ADC value as 1.00×10^{-3} mm^2/s through the ROC curve. The ADC value was the same as that what a meta-analysis based on 13,847 breast lesions concluded (15). Furthermore, this result from the meta-analysis was independent of Tesla strength, measure methods, and the choice of *b* values. In the study of Yildiz S et al. (16), the mean ADC values of benign and malignant papillary lesions were 1.339×10^{-3} and 0.744×10^{-3} mm^2/s, respectively, with a threshold of around 0.859×10^{-3} mm^2/s. The reason for the differences in results between the abovementioned research and our study lay in the fact that Yildiz S enrolled fewer papillary lesions (only 29 lesions), among which benign lesions took a big proportion (80%). Compared to his study, the ratio of benign and malignant lesions exhibited more reasonably in our research. We suggest that the optimal threshold of ADC value should be

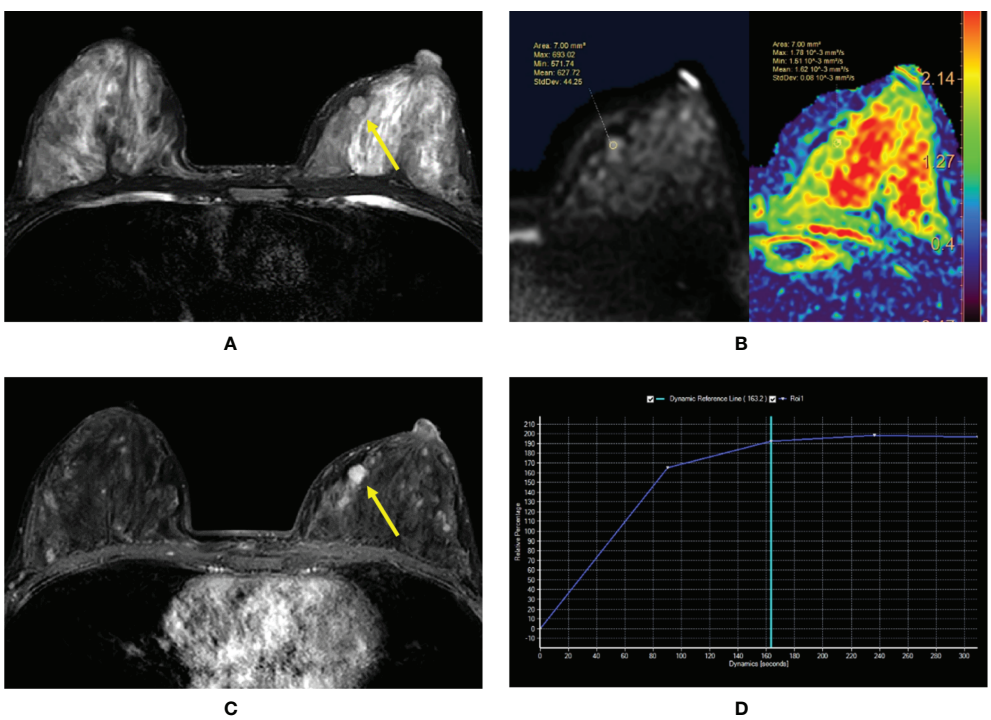

FIGURE 3 | **(A–D)** Intraductal papilloma in a 38-year-old woman. **(A)** T2-weighted image showing an isointensity signal mass lesion (yellow arrow) in the left breast. **(B)** Diffusion-weighted imaging showing a hyperintensity signal and apparent diffusion coefficient (ADC) map showing mean ADC = 1.62×10^{-3} mm^2/s. **(C)** Enhanced T1-weighted image showing a strong nodular enhancement (yellow arrow) with clear margins. **(D)** Time–signal intensity curve manifests as a rapid increase (initial phases) and a plateau type (delayed phases).

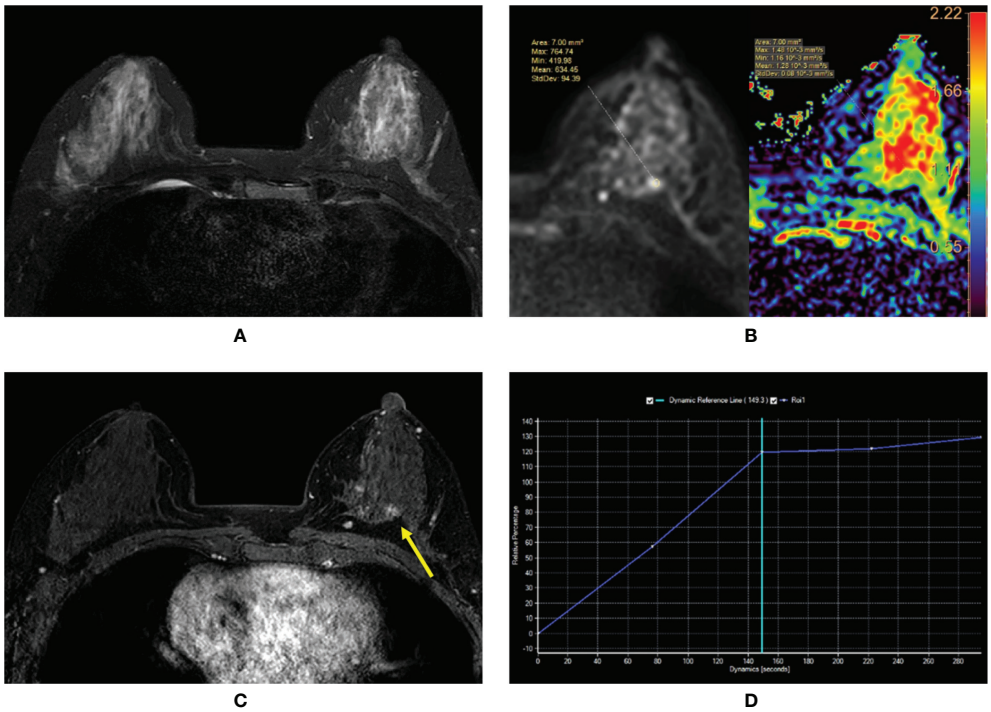

FIGURE 4 | **(A–D)** Intraductal papilloma with atypical ductal hyperplasia in a 43-year-old woman. **(A)** T2-weighted image showing an isointensity signal and unclear lesion in the left breast. **(B)** Diffusion-weighted imaging showing a hyperintensity signal and apparent diffusion coefficient (ADC) map showing mean ADC = 1.28 × 10^{-3} mm^2/s. **(C)** Enhanced T1-weighted image showing the nonhomogeneous enhancement of an irregular-shaped lesion with ill-defined margins (yellow arrow). **(D)** Time–signal intensity curve manifests as a rapid increase (initial phases) and a plateau type (delayed phases).

1.00 × 10^{-3} mm^2/s for discrimination of benign and malignant papillary lesions.

Papillary lesions of the breast represent diverse histological subtypes. Malignant lesion subtypes were difficult to distinguish through ADC values in our study ($P > 0.05$). Maric J et al. (17) also reported that there were no significant correlations between malignant lesion subtypes and ADC values. The highest ADC value of malignant pathology in our study attributed to EPC was 1.15 × 10^{-3} mm^2/s, which did not correspond to the study of Tang WJ et al. (18). The mean ADC value in his study was 0.876 × 10^{-3} mm^2/s based on 11 EPC lesions. SPC exhibited the lowest malignant pathology ADC values, which varied from 0.56 to 1.24 × 10^{-3} mm^2/s, and the mean ADC value was 0.89 ± 0.21 × 10^{-3} mm^2/s. The previous study (19) reported that the ADC values of SPC varied from 1.3 to 1.9 × 10^{-3} mm^2/s. Several potential factors might explain the disparities between the results. Malignant papillary lesions represented heterogeneous histological subtypes that show various cellularity and vascularization causing different degrees of diffusion. ROI placement in two studies also significantly influenced the ADC values measured in breast tumors (20). We suggest that the performance of ADC to distinguish among these subtypes might be variable, and presumably more studies with larger cohorts from multiple institutions might be needed or it might be helpful to apply ADC dataset to machine learning techniques for lesion classification.

ADH occurring within an intraductal papilloma considered as a borderline lesion deserves increasing attention clinically of late for the risk of subsequent invasive breast cancer development in such lesion is believed to be increased to 7.5× that of the general population. The WHO Working Group's classification of breast tumors defines atypical epithelial proliferation to be limited to <3 mm of extent as intraductal papilloma with ADH, whereas in intraductal papilloma with DCIS, it spanned ≥3 mm (21). There was no statistical significance of ADC value in differentiating between intraductal papilloma with ADH (1.03 ± 0.19 × 10^{-3} mm^2/s) and with DCIS (1.05 ± 0.12 × 10^{-3} mm^2/s) ($P > 0.05$) in our study. We presume that image examination such as MRI even with DWI is incapable of discriminating lesions of millimetric pathologic difference, especially between ADH and DCIS to date. We strongly recommend taking an active surgical procedure if any suspicious signs of ADH lesions are visible in MRI.

Correlations of ADC with discrimination of non-mass-like breast lesions had been inconsistent to date in conventional studies (22, 23). Wang LJ et al. (24) found that papilloma manifesting as non-mass enhancement (NME) could be due to the concomitant benign, atypical, and malignant proliferative

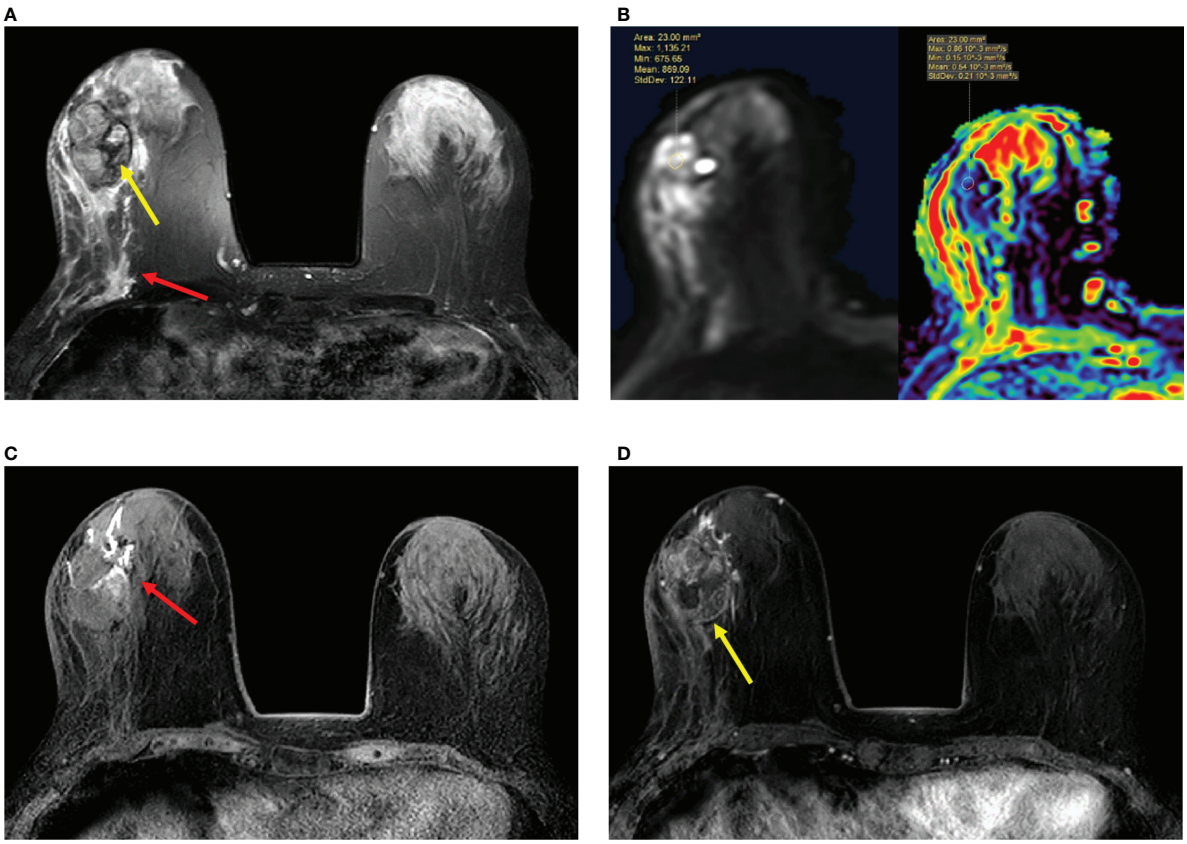

FIGURE 5 | **(A–D)** Papillary ductal carcinoma *in situ* in a 72-year-old woman. **(A)** T2-weighted image showing a hypointensity signal mass lesion (yellow arrow) and a large edema signal behind the mass (red arrow) in the left breast. **(B)** Diffusion-weighted imaging showing a hyperintensity signal mass lesion and apparent diffusion coefficient map showing mean ADC = 0.54 × 10^{-3} mm^2/s. **(C)** Plain T1-weighted image showing duct dilatation (red arrow) in front of the mass. **(D)** Enhanced T1-weighted image showing the nonhomogeneous enhancement of an irregular-shaped mass with ill-defined margins (yellow arrow). Time–signal intensity curve manifests as a slow increase (initial phases) and a persistent type (delayed phases).

lesions, and the ADC value showed no significant difference between benign and malignant NME papillary lesions. Our study demonstrated the diagnostic value of ADC to differentiate benign from malignant papillary lesions whether in mass enhancement or in non-mass enhancement. For the mass-enhanced lesions, the mean ADC values of benign and malignant lesions are 1.16 ± 0.28 × 10^{-3} and 0.97 ± 0.20 × 10^{-3} mm^2/s, respectively, with a threshold of 1.00 × 10^{-3} mm^2/s and diagnostic accuracy of 70.6%. For the non-mass-enhanced lesions, the mean ADC values of benign and malignant lesions are 1.34 ± 0.21 × 10^{-3} and 1.05 ± 0.21 × 10^{-3} mm^2/s, respectively, with a threshold of 1.14 × 10^{-3} mm^2/s and diagnostic accuracy of 84.2%. We confirm the positive association of ADC value with discrimination between benign and malignant lesions in both enhancements. The high performance of ADC will not be affected by the way lesions are enhanced.

In conclusion, the ADC value derived by DWI is capable of differentiating between malignant and benign papillary lesions. The optimal threshold of the ADC value can be 1.00 × 10^{-3} mm^2/s. The ADC value is statistically significant in differentiating between benign and malignant papillary lesions whether in mass

TABLE 3 | Comparison of mean apparent diffusion coefficient (ADC) values in different papillary breast lesion groups.

Groups	Mean ADC value (×10^{-3} mm^2/s)		P
	Benign	Borderline and malignant	
All lesions	1.21 ± 0.27 (*n* = 51)	1.01 ± 0.20 (*n* = 43)	0
Mass enhancement lesions	1.16 ± 0.28 (*n* = 35)	0.97 ± 0.20 (*n* = 19)	0.011
Non-mass enhancement lesions	1.34 ± 0.21 (*n* = 16)	1.05 ± 0.21 (*n* = 24)	0

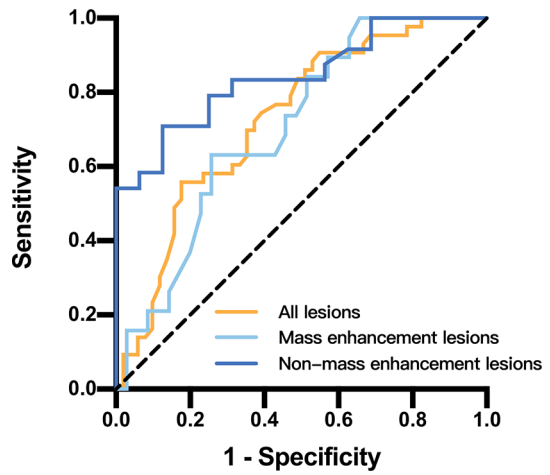

FIGURE 6 | Receiver operating characteristic curves and area under the curve for papillary breast lesions in different papillary breast lesion groups.

or non-mass enhancement. There is no statistical difference in the ADC value among histological subtypes of malignant lesions, and studies with larger patient groups are needed to assess the potential diagnostic performance. A surgical procedure should be performed at the first opportunity if any papillary lesion is diagnosed as a borderline lesion by MRI.

DATA AVAILABILITY STATEMENT

The raw data supporting the conclusions of this article will be made available by the authors without undue reservation.

ETHICS STATEMENT

Written informed consent was obtained from the individual(s) for the publication of any potentially identifiable images or data included in this article.

AUTHOR CONTRIBUTIONS

WL, DZ, and PW designed the study. WL and DZ collected the data and performed the statistical analysis. WL and DZ reviewed the MR images. WG reviewed the pathology findings. DZ drafted the manuscript. WL revised the manuscript. All authors contributed to the article and approved the submitted version.

REFERENCES

1. Tay TKY, Tan PH. Papillary Neoplasms of the Breast-Reviewing the Spectrum. *Mod Pathol* (2021) 34(6):1044–61. doi: 10.1038/s41379-020-00732-3
2. Kulka J, Madaras L, Floris G, Lax SF. Papillary Lesions of the Breast. *Virchows Arch* (2021) 480(1):65–84. doi: 10.1007/s00428-021-03182-7
3. Sarica O, Uluc F, Tasmali D. Magnetic Resonance Imaging Features of Papillary Breast Lesions. *Eur J Radiol* (2014) 83(3):524–30. doi: 10.1016/j.ejrad.2013.12.007
4. Eiada R, Chong J, Kulkarni S, Goldberg F, Muradali D. Papillary Lesions of the Breast: MRI, Ultrasound, and Mammographic Appearances. *AJR Am J Roentgenol* (2012) 198(2):264–71. doi: 10.2214/AJR.11.7922
5. Manganaro L, D'Ambrosio I, Gigli S, Di Pastena F, Giraldi G, Tardioli S, et al. Breast MRI in Patients With Unilateral Bloody and Serous-Bloody Nipple Discharge: A Comparison With Galactography. *BioMed Res Int* (2015) 806368. doi: 10.1155/2015/806368
6. Zhu Y, Zhang S, Liu P, Lu H, Xu Y, Yang WT. Solitary Intraductal Papillomas of the Breast: MRI Features and Differentiation From Small Invasive Ductal Carcinomas. *AJR Am J Roentgenol* (2012) 199(4):936–42. doi: 10.2214/AJR.12.8507
7. Seo H, Choi J, Oh C, Han Y, Park H. Isotropic Diffusion Weighting for Measurement of a High-Resolution Apparent Diffusion Coefficient Map Using a Single Radial Scan in MRI. *Phys Med Biol* (2014) 59(20):6289–303. doi: 10.1088/0031-9155/59/20/6289
8. Baltzer P, Mann RM, Iima M, Sigmund EE, Clauser P, Gilbert FJ, et al. Diffusion-Weighted Imaging of the Breast-a Consensus and Mission Statement From the EUSOBI International Breast Diffusion-Weighted Imaging Working Group. *Eur Radiol* (2020) 30(3):1436–50. doi: 10.1007/s00330-019-06510-3
9. Iima M, Honda M, Sigmund EE, Ohno Kishimoto A, Kataoka M, Togashi K. Diffusion MRI of the Breast: Current Status and Future Directions. *J Magn Reson Imag* (2020) 52(1):70–90. doi: 10.1002/jmri.26908
10. Mann RM, Cho N, Moy L. Breast MRI: State of the Art. *Radiology* (2019) 292(3):520–36. doi: 10.1148/radiol.2019182947
11. Spak DA, Plaxco JS, Santiago L, Dryden MJ, Dogan BE. BI-RADS((R)) Fifth Edition: A Summary of Changes. *Diagn Interv Imag* (2017) 98(3):179–90. doi: 10.1016/j.diii.2017.01.001
12. Tan PH, Ellis I, Allison K, Brogi E, Fox SB, Lakhani S, et al. The 2019 World Health Organization Classification of Tumours of the Breast. *Histopathology* (2020) 77(2):181–5. doi: 10.1111/his.14091
13. Newitt DC, Zhang Z, Gibbs JE, Partridge SC, Chenevert TL, Rosen MA, et al. Test-Retest Repeatability and Reproducibility of ADC Measures by Breast DWI: Results From the ACRIN 6698 Trial. *J Magn Reson Imag* (2019) 49(6):1617–28. doi: 10.1002/jmri.26539
14. Partridge SC, Nissan N, Rahbar H, Kitsch AE, Sigmund EE. Diffusion-Weighted Breast MRI: Clinical Applications and Emerging Techniques. *J Magn Reson Imag* (2017) 45(2):337–55. doi: 10.1002/jmri.25479
15. Surov AA-O, Meyer HJ, Wienke A. Can Apparent Diffusion Coefficient (ADC) Distinguish Breast Cancer From Benign Breast Findings? A Meta-Analysis Based on 13 847 Lesions. *BMC Cancer* (2019) 19(1):955. doi: 10.1186/s12885-019-6201-4
16. Yildiz S, Toprak H, Ersoy YE, Malya FU, Bakan AA, Aralasmak A, et al. Contribution of Diffusion-Weighted Imaging to Dynamic Contrast-Enhanced MRI in the Characterization of Papillary Breast Lesions. *Breast J* (2018) 24(2):176–9. doi: 10.1111/tbj.12861
17. Maric J, Boban J, Ivkovic-Kapicl T, Djilas D, Vucaj-Cirilovic V, Bogdanovic-Stojanovic D. Differentiation of Breast Lesions and Distinguishing Their Histological Subtypes Using Diffusion-Weighted Imaging and ADC Values. *Front Oncol* (2020) 10:332. doi: 10.3389/fonc.2020.00332
18. Tang WJ, Liang YS, Yan J, Hu Y, Sun ML, Liu GS, et al. Magnetic Resonance Imaging (MRI) Phenotypes May Provide Additional Information for Risk Stratification for Encapsulated Papillary Carcinoma of the Breast. *Cancer Manag Res* (2020) 12:11751–60. doi: 10.2147/CMAR.S277980
19. Zhang L, Zhuang L, Shi C, Miao Y, Zhang W, Song Q, et al. A Pilot Evaluation of Magnetic Resonance Imaging Characteristics Seen With Solid Papillary

Carcinomas of the Breast in 4 Patients. *BMC Cancer* (2017) 17(1):525. doi: 10.1186/s12885-017-3518-8

20. Bickel H, Pinker K, Polanec S, Magometschnigg H, Wengert G, Spick C, et al. Diffusion-Weighted Imaging of Breast Lesions: Region-Of-Interest Placement and Different ADC Parameters Influence Apparent Diffusion Coefficient Values. *Eur Radiol* (2017) 27(5):1883–92. doi: 10.1007/s00330-016-4564-3
21. Tan PH, Schnitt SJ, van de Vijver MJ, Ellis IO, Lakhani SR. Papillary and Neuroendocrine Breast Lesions: The WHO Stance. *Histopathology* (2015) 66 (6):761–70. doi: 10.1111/his.12463
22. Imamura T, Isomoto I, Sueyoshi E, Yano H, Uga T, Abe K, et al. Diagnostic Performance of ADC for Non-Mass-Like Breast Lesions on MR Imaging. *Magn Reson Med Sci* (2010) 9(4):217–25. doi: 10.2463/mrms.9.217
23. Cheng L, Bai Y, Zhang J, Liu M, Li X, Zhang A, et al. Optimization of Apparent Diffusion Coefficient Measured by Diffusion-Weighted MRI for Diagnosis of Breast Lesions Presenting as Mass and non-Mass-Like Enhancement. *Tumour Biol* (2013) 34(3):1537–45. doi: 10.1007/s13277-013-0682-6
24. Wang LJ, Wu P, Li XX, Luo R, Wang DB, Guan WB. Magnetic Resonance Imaging Features for Differentiating Breast Papilloma With High-Risk or Malignant Lesions From Benign Papilloma: A Retrospective Study on 158 Patients. *World J Surg Oncol* (2018) 16(1):234. doi: 10.1186/s12957-018-1537-9

Conflict of Interest: The authors declare that the research was conducted in the absence of any commercial or financial relationships that could be construed as a potential conflict of interest.

The reviewer L-MW declared a shared parent affiliation with the authors to the handling editor at the time of review.

frontiers | Frontiers in Oncology

TYPE Review
PUBLISHED 16 February 2023
DOI 10.3389/fonc.2022.926396

OPEN ACCESS

EDITED BY
Mangesh A. Thorat,
Guy's and St Thomas' NHS Foundation Trust, United Kingdom

REVIEWED BY
Javier Del Riego,
Instituto de Investigación e Innovación Parc Taulí (I3PT), Spain
Elizabeth M. Nichols,
University of Maryland Medical Center, United States

*CORRESPONDENCE
Meenakshi Thakur
thakurmh@tmc.gov.in

SPECIALTY SECTION
This article was submitted to Breast Cancer, a section of the journal Frontiers in Oncology

RECEIVED 22 April 2022
ACCEPTED 21 November 2022
PUBLISHED 16 February 2023

CITATION
Majithia J, Haria P, Popat P, Katdare A, Chouhan S, Gala KB, Kulkarni S and Thakur M (2023) Fat necrosis: A consultant's conundrum.
Front. Oncol. 12:926396.
doi: 10.3389/fonc.2022.926396

Fat necrosis: A consultant's conundrum

Jinita Majithia, Purvi Haria, Palak Popat, Aparna Katdare, Sonal Chouhan, Kunal Bharat Gala, Suyash Kulkarni and Meenakshi Thakur*

Radiology Department, Tata Memorial Hospital, Mumbai, India

Fat necrosis of the breast is a benign non-suppurative inflammation of the adipose tissue and often mimics breast cancers, posing a diagnostic challenge for the clinician and radiologist. It has a myriad of appearances on different imaging techniques, ranging from the pathognomic oil cyst and benign dystrophic calcifications to indeterminate focal asymmetries, architectural distortions, and masses. A combination of different modalities can assist a radiologist in reaching a logical conclusion to avoid unnecessary interventions. The aim of this review article was to provide a comprehensive literature on the various imaging appearances of fat necrosis in the breast. Although a purely benign entity, the imaging appearances on mammography, contrast-enhanced mammography, ultrasound, and magnetic resonance imaging can be quite misleading, especially in post-therapy breasts. The purpose is to provide a comprehensive and all-inclusive review on fat necrosis with a proposed algorithm allowing a systematic approach to diagnosis.

KEYWORDS

fat necrosis, breast imaging, radiology, mammography, ultrasonography

Introduction

Fat necrosis of the breast is a benign non-suppurative inflammation of the adipose tissue (1). It often mimics breast cancer and poses a diagnostic challenge for the clinician and radiologist. In the majority of cases, imaging provides conclusive evidence of its benignity; however, in a small percentage of cases, histological sampling becomes necessary to exclude malignancy, owing to its close semblance on imaging.

The breast parenchyma, which is composed of adipose, epithelial, and stromal tissues, is enveloped by skin and subcutaneous tissue. Adipose tissue forms the majority of the bulk of the breast volume, and the amount of adipose tissue varies throughout the reproductive life of a woman. An injury to the adipose tissue results in fat necrosis.

This review article aims to discuss and illustrate the spectrum of appearances of fat necrosis using different imaging techniques. In this article, we also review the literature on the clinical features and etiopathogenesis relevant to a radiologist. The purpose is to provide

a comprehensive and all-inclusive review on fat necrosis with a proposed algorithm allowing a systematic approach to diagnosis.

Pathophysiology

The most common stimulus for fat necrosis is hypoxia, leading to ischemia. The fragmentation of adipose cells following ischemic damage leads to the formation of intracellular vacuoles filled with necrotic lipid material. Fibroblasts, multinucleated giant cells, and lipid-laden or foamy histiocytes ("fat-filled macrophages" or "foam cells") along with enucleated adipocytes begin to accumulate (2). Damage to adipose cells also releases lipase in the interstitium which leads to triglyceride breakdown and the release of fatty acids. When unresolved, this leads to a cavity formation due to liquefactive necrosis, also known as membranous fat necrosis. Simultaneous fibrinogen secretion in the interstitium from the damaged blood vessels is followed by conversion to active fibrin catalyzed by thrombin (3), which is key to the development of fibrosis. Thus, loculated necrotic fat within the cystic cavity eventually gets surrounded by dense fibrous tissue. Sometimes, the negatively charged fatty acids bind to the positively charged calcium ions in a process called saponification (4), which leads to the development of calcification within the fat necrosis.

Irreversible cell injury is of two types: apoptosis and necrosis. In the breast, both these processes prevail. The intensity of initial insult determines which process will predominate which in turn determines the clinical presentation, the radiological appearance, and the histological finding (2). The greater the necrotic component, the greater the inflammation and the worse the clinical condition (3). Thus, a close correlation exists between the clinical age of the lesion, radiological appearances, and expected gross and histological findings in breast fat necrosis. All of these vary based on the time lapse from an inciting event.

Etiology

The common etiological factors leading to breast fat necrosis include trauma (accidental or iatrogenic), radiotherapy, systemic anticoagulation therapy like warfarin, infection, and idiopathic disease. The most common cause is accidental trauma accounting for 21%–70% of all cases of fat necrosis (2). Seat-belt injury is the most common type of blunt accidental trauma. Iatrogenic causes of trauma include interventions like cyst aspirations, incisional or excisional biopsies, and vacuum-assisted biopsies (VAB). Idiopathic fat necrosis of the breast is common in fatty pendulous breasts of middle-aged women (5).

Various surgeries, including but not limited to lumpectomy, breast conservative surgery (BCS), mastectomy, reduction mammoplasty, implant removal, and breast reconstruction, increase the risk of fat necrosis in the breast. A recent study by Dolan et al., comparing the imaging and biopsy results after breast surgery, found that the rate of fat necrosis after oncoplastic BCS was 7% as confirmed by pathology (6). Fat necrosis in the flap following reconstruction surgeries occurs due to ischemia from inadequate arterial inflow or poor venous outflow and is dependent on the type of flap (pedicled tissue flap *vs*. free fat flap), the surgeon's experience, and the administration of adjuvant radiation. Nakada et al. reported a 39% incidence of fat necrosis following pedicled tissue flap and almost 100% following free dermal fat flaps. Furthermore, symptomatic fat necrosis also showed a lower incidence following pedicled tissue flaps (2.9%) as compared with the free flaps (25%) (7). A confounding factor associated with fat necrosis following free flaps was smoking, and often the surgeons required patients to quit smoking at least 8 weeks prior to surgery (8–10). Fat grafting, which is used as a cosmetic procedure following BCS, involves harvesting fat from one part of the body and injecting it at the site that needs correction of the contour deformity. This leads to random diffusion and neovascularization of the grafted fat globules leading to fat necrosis. The incidence of fat necrosis following fat grafting varies from 2% to 18% (11).

Alone or following BCS, radiotherapy is an independent risk factor for the development of fat necrosis secondary to inflammation (12). The observation that recurrences tend to occur commonly at or near the previous lumpectomy site has led to the widespread use of accelerated partial breast irradiation (APBI) which delivers a larger dose per fraction over a shorter period of time to a targeted portion of the breast, i.e., the tumor bed, instead of the entire breast just like in whole-breast radiation (13). Brachytherapy, which can be used by itself as a form of APBI, is of two types: intracavitary and interstitial. Interstitial brachytherapy is delivered using hollow needles implanted in the tumor bed with radioactive pellets inserted through them at the time of radiotherapy (14). There is some evidence that interstitial brachytherapy causes additional trauma to the breast parenchyma from the implanted needles and, thus, leads to a higher incidence of fat necrosis. A similar incidence of symptomatic and asymptomatic fat necrosis has been reported following conventional WBI and APBI brachytherapy; however, it is greatly influenced by the volume of the irradiated breast as well as the strength and duration of irradiation (15). Different studies have reported a variable crude incidence of fat necrosis following radiation therapy in early-stage breast cancer. Wazer et al. found that the crude incidence for clinically evident fat necrosis was 27% (16). Garsa et al. studied 238 breasts in 236 women and reported that the crude incidence of fat necrosis was 17.6% and the rate of symptomatic fat necrosis was 10.1% (13). The median time to the development of fat necrosis following radiation to the breast was found to be 12.7 months (average range 3–42 months) by Rahimi et al. (17).

Clinical features

Fat necrosis is more often than not asymptomatic and diagnosed incidentally on imaging. The clinical findings do not normally vary according to the etiology of fat necrosis and are neither specific nor sensitive. Palpable lumps of fat necrosis may present as indolent nodular and mobile masses with smooth margins or as hard fixed irregular masses. Associated features like induration, ecchymosis, erythema, nipple retraction, skin retraction or dimpling, and lymphadenopathy may be present. More than 50% of symptomatic fat necrosis has clinical features of malignancy such as hard mass, nipple retraction, and skin tethering (18). Lesions developing following trauma are usually at or near the site of trauma, and when no relevant history is found, the lesions were most commonly located in the upper outer quadrant (18). Fat necrosis in obese women with pendulous breasts was commonly seen in the superficial and subareolar tissues (5).

Imaging

The imaging modalities for the diagnosis of fat necrosis in the breast include mammography (MMG), ultrasound (USG), and magnetic resonance imaging (MRI). The emerging newer technique of contrast-enhanced mammography (CEM) aids in the diagnosis of fat necrosis in disputed cases and, along with MRI, serves as a road map for targeted biopsies.

Mammography

Mammography, digital mammography (DM), or digital breast tomosynthesis (DBT) plays a pivotal role in the imaging of fat necrosis especially in clinically suspicious symptomatic women above the age of 40 years and in post-therapy cases. In fact, in a postoperative and post-therapy breast, a regular annual follow-up mammogram is the gold standard for imaging surveillance (19). It should be borne in mind, however, that a normal mammogram does not rule out an underlying pathology especially in dense breasts due to the overlap of lesions by glandular parenchyma. In such cases, USG is performed as a complementary investigation tool.

The appearance of fat necrosis on mammogram is in concordance with the stage of evolution of fat necrosis and ranges from focal asymmetries, architectural distortions, mass-forming solid lesions, cystic lesions, oil cysts, and calcifications. Early lesions develop hemorrhagic foci or areas of indurated fat with trabecular edema and can appear as focal asymmetry on MMG (12). Occasionally, like in post-traumatic cases, a hematoma formation is seen which evolves into a seroma, both appearing as small isodense mass-forming lesions on MMG. Some lesions develop a central cavity with liquified and necrotic contents called membranous fat necrosis also appearing as isodense lesions on MMG.

A loculated necrotic fat-containing cavity called an oil cyst appears as a radiolucent lesion on MMG, owing to the internal fat component, with a thin dense peripheral rim of fibrosis. Oil cysts are pathognomic of fat necrosis and are the second most prevalent finding on MMG after dystrophic calcifications, accounting for 27% of the cases (20). The fibrous rim of an oil cyst may calcify over time forming a thin dense rim of calcification, formerly called as "egg-shell calcification." The rim calcification does not develop entirely at the same time with inception as small foci of calcification, leading to curvilinear or arc-like calcification and eventually progressing into a complete rim. Thus, in the early stages, the small foci of calcification in the wall of an oil cyst appear similar to fine microcalcifications and need differentiation from the disease process (Supplementary Figures 1, 2). In certain instances, when the oil cysts are not purely fat-containing and have fat–fluid or fat–blood levels within, ultrasound serves as a problem-solving tool. With the incomplete replacement of fat and associated intense fibrotic reaction surrounding the oil cyst, thickened irregular walls may develop around the residual necrotic fat, giving a spiculated appearance on MMG, mimicking cancer (12). MMG is usually sufficient for the diagnosis of oil cysts, warranting no further investigation or follow-up; however, it is important to note that oil cysts may occasionally be occult on MMG, especially when overlapped by normal fatty and fibroglandular breast parenchyma and get diagnosed on USG or MRI. Supplementary Table 1 summarizes the key points of oil cysts.

An intermediate to late presentation of fat necrosis on MMG is focal asymmetry or architectural distortion. DBT is most useful in such cases to decrease the confounding effect of overlapping breast tissue. The underlying pathophysiology is the presence of varying amounts of inflammatory changes and areas of fibrosis interspersed with radiolucent necrotic fat. These are usually not clinically palpable and, in the majority of cases, are diagnosed solely on imaging. A post-surgical scar may appear as an area of architectural distortion with overlying contour deformity and skin thickening or nipple retraction at the site of surgery, features that may also mimic recurrence (Supplementary Figure 3). The identification of interspersed fat within an asymmetry can increase the confidence levels for benignity; however, existing fat within the breast can be engulfed by an evolving malignant process and must be viewed with suspicion and evaluated further, either with DBT, CEM, or MRI, and further histological confirmation as required (21).

Calcification is one of the most common findings following lumpectomy and radiation and also the most important imaging biomarker for local recurrence (22). With a rising trend toward breast conservation, there has been a learning curve with the imaging evaluation of post-therapy calcifications, to be able to

adequately differentiate benign calcifications of fat necrosis from malignant microcalcifications of residual or recurrent disease (23). It is observed that the median time for the development of benign calcifications is much earlier than malignant calcifications. Günhan-Bilgen et al. (24), Giess et al. (23), and Chang Sen et al. (25) reported that the median times for the development of benign calcifications were 24, 23, and 27 months, respectively, and for malignant calcifications, the median times were 52, 39, and 41 months, respectively. Therefore, a lower probability of malignancy is observed with early developing calcification (6–24 months) (23). The incidence of benign calcifications was also observed to be higher than malignant microcalcifications in post-therapy breasts (23, 24, 26). In the majority of cases, the calcifications of fat necrosis occur in and around the area of surgery, usually within the same quadrant (22, 27). Thus, calcifications observed elsewhere in the breast or in the contralateral breast should be addressed with caution (Supplementary Figure 4).

Calcifications representing recurrence commonly have an amorphous or fine pleomorphic morphology with segmental or regional distribution (28). Calcifications of early-stage fat necrosis may also appear fine and pleomorphic closely mimicking cancer; however, they show gradual coarsening with evolution into dystrophic calcifications (Supplementary Figure 5). Although not a ground rule, fine microcalcifications may be differentiated by the presence of fat-density radiolucent areas around and within the calcifications in fat necrosis, whereas the presence of high density associated with calcification is suggestive of recurrent disease (29). Unless unequivocally benign, all post-therapy calcifications should be viewed with caution. It is imperative to emphasize that suspicious-looking calcifications must undergo tissue diagnosis (Supplementary Figure 6).

The most common calcification in fat necrosis is dystrophic calcifications. These are larger than 1 mm, rough, and irregular and tend to coalesce to become larger. Calcifications within the irradiated breast are usually dystrophic with a typical benign appearance. They appear linear or round and coarse, within the irradiated field. The tubular appearance of these calcifications following brachytherapy is secondary to the fat necrosis developing along the implanted needle tract which on serial MMG shows classical interval coarsening (Supplementary Figure 7). The calcifications that develop in silicone granulomas or after autologous fat grafting are also coarse and dystrophic (Supplementary Figure 8). As mentioned, rim calcification in the wall of the oil cyst is also typically benign. The key points of calcifications in a post-therapy breast are summarized in Supplementary Table 2.

Ultrasonography

Ultrasound is a well-established, quick, and effective modality for imaging the breast for fat necrosis. The absence of hazardous radiation makes it the preferred investigation tool for symptomatic women less than 30 years of age as well as pregnant and lactating women. The sensitivity of USG is higher than mammograms especially in dense breasts of women less than 50 years of age (30, 31); however, MMG and USG are most effective when used in combination with the highest diagnostic accuracy when utilized together (31). Complemented with color Doppler and elastography, ultrasound is meritorious in differentiating benign fat necrosis from malignant lesions by allowing non-invasive characterization of tissue vascularity and stiffness, respectively. The absence of color flow on color Doppler hints toward the benignity of fat necrosis, but it is not reliable (32). On elastography, malignant lesions are expected to be hard, and benign lesions are presumed to be soft; however, a classic example of a confounding finding on elastography is the increased stiffness of benign lesions such as fibrosis and fat necrosis (33).

Fat necrosis on ultrasound may appear as solid or cystic masses. The solid masses of fat necrosis have well-circumscribed margins and may distort breast parenchyma. The cystic lesions may have clear contents, internal echoes, and fluid–debris levels or may appear as complex intracystic masses. The common appearances of oil cyst on USG include anechoic cystic lesions with posterior acoustic enhancement or anechoic lesions with posterior acoustic shadowing (34). The typical oil cysts on mammograms often appear as solid masses on USG (34) (Supplementary Figures 9, 10). An internal echogenic band, formed by the interface between lipid and serous/hemorrhagic fluid, that shifts its orientation with a change in patient position is a hallmark of oil cysts (34). With increasing complexity, internal echogenic mural nodules, thick septations, or calcifications may be seen (35). Conventionally, malignant hypoechoic masses are expected to demonstrate posterior acoustic shadowing; however, oil cysts, dystrophic calcifications, and focal architectural distortions of fat necrosis may also show dense posterior shadowing (36).

Increased echogenicity of surrounding breast parenchyma or subcutaneous fat is a reliable indicator of benignity (32). Fat necrosis, especially when precipitated from trauma, is superficial in location and appears as a hyperechoic mass with or without a small central hypoechoic focus (Supplementary Figures 11, 12). Only a small proportion, less than 0.8%, of hyperechoic masses represent malignancy (37). When situated deeper in the fibroglandular parenchyma of the breast, a hyperechoic mass needs to be viewed with caution and warrants differentiation from malignant lesions, such as lymphoma, leukemia, metastasis, intralobular carcinoma, or rarely intraductal carcinoma (37).

Contrast-enhanced mammography

CEM is a novel imaging modality developed as an adjunct to mammography to provide additional physiologic information

about local breast perfusion. An extensive search of the medical database revealed no publications describing or reviewing the appearance of fat necrosis on CEM. Very little literature was found on the benefits of CEM in the evaluation of mass-forming lesions, calcifications, or architectural distortions.

One of the common indications of CEM is a palpable mass in a postoperative breast. Mixed-density lesions on mammogram and ultrasound may need further characterization with CEM (Supplementary Figure 10). A heterogeneous area of intermixed fibroglandular and fatty tissue either shows no enhancement or shows thin uniform peripheral and/or septal enhancement (38). An oil cyst with a fibrous rim also shows thin uniform peripheral enhancement on CEM. For the assessment of calcifications, CEM may be beneficial in differentiating benign calcification of fat necrosis from suspicious microcalcifications by the absence of enhancement. The presence of enhancement supports the diagnosis of malignancy; however, the absence does not exclude it (39, 40). The interpretation of architectural distortion secondary to fat necrosis can be rather challenging on imaging. Although distortions are better evaluated on DBT, it is questionable whether it can obviate the need for biopsy owing to the low positive predictive value of DBT, especially when no ultrasound correlate is found (41). CEM can be of particular value in such cases as architectural distortion or focal asymmetry from fat necrosis usually does not demonstrate enhancement on CEM. A few benign causes of architectural distortions like a radial scar or complex sclerosing lesions, sclerosing adenosis, and post-surgical changes are close differentials. CEM may not always prove to be beneficial in equivocal cases for differentiating benign and malignant architectural distortions, and the paucity of data often compels the radiologist to consider biopsy in many cases of architectural distortion irrespective of demonstrable enhancement on CEM (42).

Magnetic resonance imaging

MRI has been a game changer in breast imaging owing to its high soft tissue resolution. It is not routinely required while evaluating breasts for fat necrosis; however, in some post-therapy complicated cases, when mammography and ultrasound findings are ambiguous and the clinical suspicion is high, the utility of MRI is justified.

The T1-weighted sequence (T1W) is one of the most important sequences for the diagnosis of fat necrosis. Demonstration of fat-containing lesions and tissue distortion in the operative bed (fat-engulfing scar tissue) on T1W sequence can significantly improve the diagnostic conviction even in the presence of suspicious enhancement or kinetics which can be misleading (43). Fat-saturated T1W images can confirm the fatty nature of the lesion. Diffusion-weighted imaging (DWI) with apparent coefficient of diffusion (ADC) map provides quantitative and qualitative data for differentiating postoperative fat necrosis from recurrence and improves the overall diagnostic accuracy of MRI breast (43, 44). Visualization of bright signal intensity in the postoperative bed with increasing *b*-values and low-signal intensity on the ADC map corresponds to recurrent disease (44). The kinetic curve assessment following dynamic post-contrast image acquisition may help in distinguishing benign from malignant causes of enhancement; however, it is non-specific and varies from slow and gradual to rapid enhancement (44).

Post-treatment or post-traumatic breasts with early-onset hemorrhage at the local site show a well-defined or an ill-defined mass or a focal asymmetry with altered signal intensity on different sequences. The signal intensity varies based on the age of blood, typically hyperintense on T1W images and hypointense on T2W images. No enhancement or mild peripheral enhancement can be seen on the post-contrast sequence (45). One of the most common MRI findings of fat necrosis is of an oil cyst, with a well-defined round to oval lesion with T1W and T2W hyperintense contents, following fat signal intensity on all sequences. Suppression of the signal on fat-saturated (FAT-SAT) T1 and short tau inversion recovery (STIR) images confirms the presence of fat within the lesion. The thin fibrous rim of an oil cyst shows subtle uniform enhancement (Supplementary Figures 13, 14). A signal drop in the rim of the oil cyst is suggestive of rim calcification. Fat necrosis showing decreased signal intensity on T1- and T2-weighted images can be a result of iron-containing siderophages (46, 47).

Architectural distortions occurring at or near the lumpectomy site under ideal circumstances would show signal intensity similar to fat on all sequences with adjacent parenchymal enhancement (48, 49). It can be quite a challenge to interpret architectural distortions, especially in the early postoperative phases because of the intense enhancement seen due to acute inflammation and edema. Mild mass-like enhancement is usually seen lasting for up to 18 months in the postoperative and post-radiation breast (50). A minimal or a small focal area of enhancement or thin linear homogeneous non-mass enhancement (NME) can be seen persisting for up to 5 years post-lumpectomy (51). Fibrosis, which is often identified in conjunction with fat necrosis, leads to the development of an irregular mass or architectural distortion and focal asymmetry with varying appearances on the T1W sequence (52). Multiple enhancement patterns of fibrosis are identified on MRI correlating with the stage of evolution of fat necrosis in a post-therapy breast. More recent lesions generally have an irregular contour with variable enhancement surrounding the lesion, whereas older lesions have markedly irregular margins, owing to fibrosis and retraction, and generally do not enhance (53) (Supplementary Figure 14). Fibrosis usually shows persistent or delayed plateau kinetics.

Certain patterns of enhancement are highly suspicious, like mass-like enhancement, nodular enhancement (more than 5 mm), and clumped or heterogeneous non-mass enhancement with segmental or regional distribution and suspicious kinetics (like rapid initial enhancement and washout), and should not be considered as benign fat necrosis.

Positron emission tomography/ computed tomography

The imaging features of fat necrosis on positron emission tomography/computed tomography (PET/CT) are all incidentally detected. ^{18}F-FDG PET/CT is not a routine recommendation for the detection of breast abnormalities and is primarily done for staging and metastatic evaluation. It cannot be emphasized enough that PET/CT is neither indicated nor recommended for recurrent disease evaluation in post-therapy breasts.

Fat necrosis shows no uptake on PET/CT; however, few studies have detected "false positive" cases demonstrating uptake on PET/CT (47, 54). The increased FDG uptake of fat necrosis can be attributed to the presence of locally increased metabolically active inflammatory cells reflecting hyperemia (2) (Supplementary Figure 15). Intense uptake in the setting of transverse rectus abdominis myocutaneous (TRAM) flap reconstruction is seen when the fat-rich tissue is damaged intraoperatively (55). Other benign conditions showing FDG uptake that may sometimes need differentiation from fat necrosis are acute and chronic inflammation.

Tissue diagnosis

Cases that are clinically and radiologically equivocal require confirmation with tissue diagnosis. Minimally invasive methods for tissue sampling are fine needle aspiration cytology (FNAC), core needle biopsy, and vacuum-assisted biopsy (VAB). The sensitivity and specificity of FNAC are 87% and 99%, respectively; however, it bears limitations such as inadequate sampling and repeated needling (2). Core needle biopsy has a higher sensitivity and diagnostic accuracy, almost comparable to surgical biopsy, and also allows immunohistochemistry testing of the tissue. The false-negative rate of core biopsy is 1.2% to 1.5% (56); thus, in a small proportion of cases when clinical suspicion is high, a surgical biopsy is recommended despite a negative core biopsy.

A spiculated dense mass on mammogram and a hypoechoic mass with angular margins and a taller-than-wide appearance on ultrasound in a post-therapy breast are suspicious features and warrant a tissue diagnosis. Amorphous or fine pleomorphic microcalcifications also require a histological sampling, compared with dystrophic and rim calcifications which are classically benign.

A summary of the different stages of fat necrosis is tabulated with its clinical and radiological features as well as its gross histopathological and microscopic features in Table 1.

Approach to the diagnosis of fat necrosis

Mammography has stood the test of time for imaging the breast in eligible women. It is the best and first investigation tool for most cases. The diagnostic accuracy of mammogram increases when combined with ultrasound (31). Ultrasound is the first investigation tool for women under 30 years of age (57). It is also the most common modality used for guided interventions. MRI is usually reserved for complicated cases when MMG and USG yield ambiguous results. However, MRI

TABLE 1 Clinical-Radiological-Pathological correlation with underlying pathology in Fat Necrosis.

Clinical	Stage	Radiological	Gross Pathological	Microscopic
Asymptomatic*I* Induration / Firmness/ Palpable Lump (tenderness+/-)	Early	Focal asymmetry or isodense mass-forming lesion	Haemorrhagic foci in the breast or areas of indurated fat. Bright yellow fat (Saponification)	Haemorrhage within fat with enucleated adipocytes,foamy histiocytes and multinucleated giantcells (due to phagocytosisof necrotic adioocvtes)
	Intermediate to Late	Isodenselesion corresponding to a cystic lesion	Cystic lesion filled with liquefied content	Cavity formation due to liquefactive necrosis, known as membranousfat necrosis
		Oil Cyst: Fat density lesion with well-defined margins Peripheral rim of calcification+/-	Cavitary lesion with firm/gritty walls and soft necrotic contents "membranousfat necrosis"	Loculated necrotic fat within a cyst surrounded by dense fibrous tissue. Egg-shell calcification +/-
		Micro or macrocalcification	Chalky white gritty areas (Calcification)	Specks or massesof dystrophic calcification± giant cell reaction
		!Asymmetry *I* Architectural distortion	Yellow-Grey firm areasof Fibrosis	Reactive inflammatory response,hemosiderin laden macrophages, areasof fibrosis and eventual scar formation

can be used as a frontline tool for imaging dense breasts, especially in young women less than 40 years of age (58).

The following flowcharts aspire to serve as a road map as an approach to various possible imaging appearances of fat necrosis in the post-therapy setting or a clinical setting of high suspicion for fat necrosis such as with a history of trauma, as depicted in Figure 1. The approach to calcifications in a post-therapy breast has also been depicted in a flowchart for ease of understanding in Figure 2 and for interpretation of various morphologies and distribution of calcifications.

Conclusion

Fat necrosis in the breast, albeit a benign entity, is a cause of concern for the clinician and often a cause of anxiety for the patient, and owing to its myriad of appearances on various imaging modalities, fat necrosis may be a cause of diagnostic dilemma for the radiologist. A radiologist should be conversant with the many typical and atypical features of fat necrosis and bear knowledge of the different evolution patterns enabling early diagnosis to circumvent unnecessary intervention. The overlap in imaging features of fat necrosis with breast cancer in a few cases makes it extremely difficult to reach a confident diagnosis based on imaging alone and often warrants histological sampling. Once diagnosed, fat necrosis requires no further attention or intervention as it bears no risk of malignant transformation.

With this comprehensive review article, one can attain information on the interplay of various imaging modalities such as MMG, USG, CEM, and MRI and their use in different permutations and combinations in a nutshell to aid in arriving at a logical conclusion for the diagnosis of fat necrosis. The one-of-

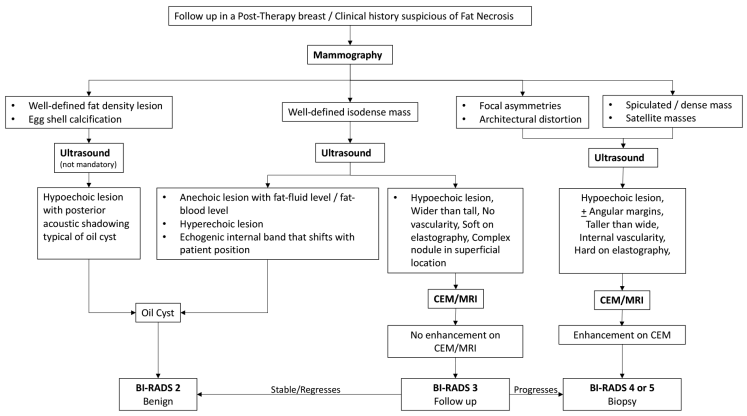

FIGURE 1
Algorithm for the approach to fat necrosis.

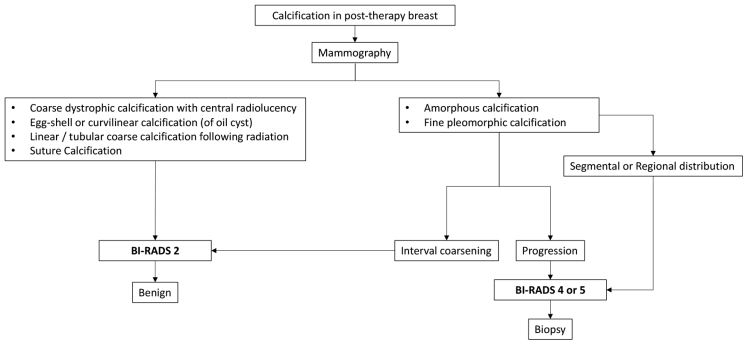

FIGURE 2
Algorithm for the approach to calcifications seen in fat necrosis.

a-kind tabulated information on the clinical–radiological–pathological correlation for different stages of fat necrosis makes it easy for a radiologist to better interpret the imaging findings based on the clinical presentation and expected cellular evolution. A visually stimulating flowchart for the approach to a post-therapy breast as well as calcifications allows one to become a clinical radiologist.

Author contributions

JM is the lead author of this review and has written and given the maximum contribution to the manuscript. PH has been a guide and mentor and has reviewed the content in-depth. PP, AK, and SC have helped by providing the images for the representative cases and by providing their valuable inputs. KB and SK have helped with the image-guided interventions of the representative cases. MT is the corresponding author and a source of inspiration and guidance for writing the manuscript. All authors contributed to the article and approved the submitted version.

Conflict of interest

The authors declare that the research was conducted in the absence of any commercial or financial relationships that could be construed as a potential conflict of interest.

Publisher's note

Supplementary material

The Supplementary Material for this article can be found online at: https://www.frontiersin.org/articles/10.3389/fonc.2022.926396/full#supplementary-material

References

1. Adair FE, Munzer JT. Fat necrosis of the female breast: report of one hundred test cases. *Am J Surg* (1947) 74:117–28. doi: 10.1016/0002-9610(47)90151-7

2. Tan PH, Lai LM, Carrington EV, Opaluwa AS, Ravikumar KH, Chetty N, et al. Fat necrosis of the breast–a review. *Breast.* (2006) 15(3):313–8. doi: 10.1016/j.breast.2005.07.003

3. Vasei N, Shishegar A, Ghalkhani F, Darvishi M. Fat necrosis in the breast: A systematic review of clinical. *Lipids Health Dis* (2019) 18(1):139. doi: 10.1186/s12944-019-1078-4

4. Pirahanchi Y, Sharma S. Biochemistry, lipase. In: *StatPearls*. Treasure Island (FL: StatPearls Publishing (2022).

5. Hogge JP, Robinson RE, Magnant CM, Zuurbier RA. The mammographic spectrum of fat necrosis of the breast. *Radiographics* (1995) 15(6):1347–56. doi: 10.1148/radiographics.15.6.8577961

6. Dolan R, Patel M, Weiler-Mithoff E, Mansell J, Stallard S, Doughty JC, et al. Imaging results following oncoplastic and standard breast conserving surgery. *Breast Care (Basel)* (2015) 10:325–9. doi: 10.1159/000437105

7. Nakada H, Inoue M, Furuya K, Watanabe H, Ikegame K, Nakayama Y, et al. Fat necrosis after breast-conserving oncoplastic surgery. *Breast Cancer* (2019) 26:125–30. doi: 10.1007/s12282-018-0901-5

8. Genova R, Garza RF. Breast fat necrosis. In: *StatPearls*. Treasure Island (FL: StatPearls Publishing (2022).

9. Hembd A, Teotia SS, Zhu H, Haddock NT. Optimizing perforator selection: A multivariable analysis of predictors for fat necrosis and abdominal morbidity in DIEP flap breast reconstruction. *PlastReconstr Surg* (2018) 142(3):583–92. doi: 10.1097/PRS.0000000000004631

10. Shechter S, Arad E, Inbal A, Friedman O, Gur E, Barnea Y. DIEP flap breast reconstruction complication rate in previously irradiated internal mammary nodes. *J ReconstrMicrosurg* (2018) 34(6):399–403. doi: 10.1055/s-0038-1625986

11. Delay E, Garson S, Tousson G, Sinna R. Fat injection to the breast: technique, results, and indications based on 880 procedures over 10 years. *AesthetSurg J* (2009) 29(5):360–76. doi: 10.1016/j.asj.2009.08.010

12. Beheshtian T, Olfatbakhsh A. A review on fat necrosis of the breast: The dilemma of differential diagnosis with cancer. *Arch Breast Cancer* (2015) 2:41–5. doi: 10.19187/abc.20152241-45

13. Garsa AA, Ferraro DJ, Dewees T, Margenthaler JA, Naughton M, Aft R, et al. Analysis of fat necrosis after adjuvant high-dose-rate interstitial brachytherapy for early-stage breast cancer. *Brachytherapy.* (2013) 12(2):99–106. doi: 10.1016/j.brachy.2012.04.005

14. Available at: https://www.cancer.org/cancer/breast-cancer/treatment/radiation-for-breast-cancer.html.

15. Lövey K, Fodor J, Major T, Szabó E, Orosz Z, Sulyok Z, et al. Fat necrosis after partial-breast irradiation with brachytherapy or electron irradiation versus standard whole-breast radiotherapy–4-year results of a randomized trial. *Int J Radiat Oncol Biol Phys* (2007) 69(3):724–31. doi: 10.1016/j.ijrobp.2007.03.055

16. Wazer DE, Lowther D, Boyle T, Ulin K, Neuschatz A, Ruthazer R, et al. Clinically evident fat necrosis in women treated with high-dose-rate brachytherapy alone for early-stage breast cancer. *Int J Radiat OncologyBiologyPhysics* (2001) 50 (1):107–11. doi: 10.1016/s0360-3016(00)01541-8

17. Rahimi A, Zhang Y, Kim DW, Morgan H, Hossain F, et al. Risk factors for fat necrosis after stereotactic partial breast irradiation for early-stage breast cancer in a phase 1 clinical trial. *Int J Radiat Oncol Biol Phys* (2020) 108(3):697–706. doi: 10.1016/j.ijrobp.2020.05.025

18. Hadfield G. Fat necrosis of the breast. *Br J Surg* (1930) 17:673–82.

19. Swinnen J, Keupers M, Soens J, Lavens M, Postema S, Van Ongeval C. Breast imaging surveillance after curative treatment for primary non-metastasised breast cancer in non-high-risk women: a systematic review. *Insights Imaging.* (2018) 9 (6):961–70. doi: 10.1007/s13244-018-0667-5

20. Weigel S, Heindel W, Heidrich J, Hense HW, Heidinger O. Digital mammography screening: sensitivity of the programme dependent on breast density. *EurRadiol* (2017) 27(7):2744–51. doi: 10.1007/s00330-016-4636-4

21. Freer PE, Wang JL, Rafferty EA. Digital breast tomosynthesis in the analysis of fat-containing lesions. *RadioGraphics* (2014) 34:343–58. doi: 10.1148/rg.342135082

22. Pinsky RW, Rebner M, Pierce LJ, Ben-David MA, Vicini F, Hunt KA, et al. Recurrent Cancer After Breast-Conserving Surgery with Radiation Therapy for Ductal Carcinoma in Situ: Mammographic Features, Method of Detection, and Stage of Recurrence. *Am J Roentgenol* (2007) 189:140–4. doi: 10.2214/AJR.06.1281

23. Giess CS, Keating DM, Osborne MP, Mester J, Rosenblatt R. Comparison of rate of development and rate of change for benign and malignant breast

calcifications at the lumpectomy bed. *AJR* (2000) 175:789–93. doi: 10.2214/ajr.175.3.1750789

24. Günhan-Bilgen I, Oktay A. Management of microcalcifications developing at the lumpectomy bed after conservative surgery and radiation therapy. *AJR Am J Roentgenol* (2007) 188(2):393–8. doi: 10.2214/AJR.06.0106

25. Chang Sen LQ, Ko A, Patel MM, Leung JWT. Time to development and imaging features of new calcifications in the treated breast after breast-conserving therapy. *Breast J* (2021) 27(10):761–7. doi: 10.1111/tbj.14277

26. Stomper PC, Recht A, Berenberg AL, Jochelson MS, Harris JR. Mammographic detection of the re- current cancer in the irradiated breast. *AJR* (1987) 148:39–43. doi: 10.2214/ajr.148.1.39

27. Liberman L, Van Zee KJ, Dershaw DD, Morris EA, Abramson AF, Samli B. Mammographic features of local recurrence in women who have undergone breast-conserving therapy for ductal carcinoma in situ. *AJR* (1997) 168:489–93. doi: 10.2214/ajr.168.2.9016233

28. Dershaw DD, Giess CS, McCormick B, Borgen P, Liberman L, Abramson AF, et al. Pat- terns of mammographically detected calcifications after breast-conserving therapy associated with tumor recurrence. *Cancer* (1997) 79:1355–61. doi: 10.1002/(sici)1097-0142(19970401)79:71355::aid-cncr13>3.0.co;2-z

29. Ramani SK, Rastogi A, Mahajan A, Nair N, Shet T, Thakur MH. Imaging of the treated breast post breast conservation surgery/oncoplasty: Pictorial review. *World J Radiol* (2017) 9(8):321–9. doi: 10.4329/wjr.v9.i8.321

30. Tan KP, Mohamad Azlan Z, Rumaisa MP, Siti AisyahMurni MR, Radhika S, Nurismah MI, et al. The comparative accuracy of ultrasound and mammography in the detection of breast cancer. *Med J Malaysia* (2014) 69(2):79–85.

31. Chen H-l, Zhou J-q, Chen Q, Deng Y-c. Comparison of the sensitivity of mammography, ultrasound, magnetic resonance imaging and combinations of these imaging modalities for the detection of small (≤2 cm) breast cancer. *Medicine* (2021) 100(26):e26531. doi: 10.1097/MD.0000000000026531

32. Upadhyaya VS, Uppoor R, Shetty L. Mammographic and sonographic features of fat necrosis of the breast. *Indian J Radiol Imaging* (2013) 23(4):366–72. doi: 10.4103/0971-3026.125619

33. Faruk T, Islam MK, Arefin S, Haq MZ. The journey of elastography: Background, current status and future possibilities in breast cancer diagnosis. *Clin Breast Cancer* (2015) 15(5):313–24. doi: 10.1016/j.clbc.2015.01.002

34. Soo MS, Kornguth PJ, Hertzberg BS. Fat necrosis in the breast: sonographic features. *Radiology* (1998) 206(1):261–9. doi: 10.1148/radiology.206.1.9423681

35. Berg WA, Sechtin AG, Marques H, Zhang Z. Cystic breast masses and the ACRIN 6666 experience. *Radiol Clin North Am* (2010) 48(5):931–87. doi: 10.1016/j.rcl.2010.06.007

36. Gaur1 S, Dialani1 V, Slanetz PJ, Eisenberg RL. Architectural distortion of the breast. *AJR* (2013) 201:W662–70. doi: 10.2214/AJR.12.10153

37. Adrada B, Wu Y, Yang W. Hyperechoic lesions of the breast: radiologic-histopathologic correlation. *Am J Roentgenol* (2013) 200(5):W518–30. doi: 10.2214/AJR.12.9263

38. Garibotto NL, Chan JKK, Taylor D. Appearance of fat necrosis on contrast-enhanced spectral mammography. *BMJ Case Rep CP* (2022) 15:e246231. doi: 10.1136/bcr-2021-246231

39. Cheung YC, Juan YH, Lin YC, Lo YF, Tsai HP, Ueng SH, et al. Dual-energy contrast-enhanced spectral mammography: Enhancement analysis on BI-RADS 4 non-mass microcalcifications in screened women. *PloS One* (2016) 11(9):e0162740. doi: 10.1371/journal.pone.0162740

40. Houben IP, Vanwetswinkel S, Kalia V, Thywissen T, Nelemans PJ, Heuts EM, et al. Contrast-enhanced spectral mammography in the evaluation of breast suspicious calcifications: diagnostic accuracy and impact on surgical management. *Acta Radiol* (2019) 60(9):1110–7. doi: 10.1177/0284185118822639

41. Durand MA, Wang S, Hooley RJ, Raghu M, Philpotts LE. Tomosynthesis-detected architectural distortion: management algorithm with radiologic-pathologic correlation. *RadioGraphics* (2016) 36(2):311–21. doi: 10.1148/rg.2016150093

42. Perry H, Phillips J, Dialani V, Slanetz PJ, Fein-Zachary VJ, Karimova EJ, et al. Contrast-enhanced mammography: A systematic guide to interpretation and reporting. *AJR* (2019) 212:222–31. doi: 10.2214/AJR.17.19265

43. Mansour SM, Behairy N. Residual breast cancer or post-operative changes: Can diffusion weighted magnetic resonance imaging solve the case? *Egyptian J Radiol Nucl Med* (2015) 46(1):225–34. doi: 10.1016/j.ejrnm.2014.11.017

44. Woodhams R, Ramadan S, Stanwell P, Sakamoto S, Hata H, Ozaki M, et al. Diffusion-weighted imaging of the breast: principles and clinical applications. *Radiographics* (2011) 31(4):1059–84. doi: 10.1148/rg.314105160

45. Dhillon GS, Bell N, Ginat DT, Levit A, Destounis S, O'Connell A. Breast MR imaging: What the radiologist needs to know. *J Clin Imaging Sci* (2011) 1:48. doi: 10.4103/2156-7514.85655

46. Ayyappan AP, Crystal P, Torabi A, Foley BJ, Fornage BD. Imaging of fat-containing lesions of the breast: a pictorial essay. *J Clin Ultrasound* (2013) 41:424–33. doi: 10.1002/jcu.22070

47. Akkas BE, UcmakVural G. Fat necrosis may mimic local recurrence of breast cancer in FDG PET/CT. *Rev Esp Med Nucl Imagen Mol* (2013) 32(2):105–6. doi: 10.1016/j.remn.2012.06.006

48. Daly CP, Jaeger B, Sill DS. Variable appearances of fat necrosis on breast MRI. *AJR Am J Roentgenol* (2008) 191(5):1374–80. doi: 10.2214/AJR.07.4051

49. Taboada JL, Stephens TW, Krishnamurthy S, Brandt KR, Whitman GJ. The many faces of fat necrosis in the breast. *AJR Am J Roentgenol* (2009) 192(3):815–25. doi: 10.2214/AJR.08.1250

50. Heywang-Köbrunner SH, Schlegel A, Beck R, Wendt T, Kellner W, Lommatzsch B, et al. Contrast-enhanced MRI of the breast after limited surgery and radiation therapy. *J Comput Assist Tomogr* (1993) 17(6):891–900. doi: 10.1097/00004728-199311000-00009

51. Brennan S, Liberman L, Dershaw DD, Morris E. Breast MRI screening of women with a personal history of breast cancer. *AJR Am J Roentgenol* (2010) 195 (2):510–6. doi: 10.2214/AJR.09.3573

52. Drukteinis JS, Gombos EC, Raza S, Chikarmane SA, Swami A, Birdwell RL. MR imaging assessment of the breast after breast conservation therapy: Distinguishing benign from malignant lesions. *RadioGraphics* (2012) 32:219–34. doi: 10.1148/rg.321115016

53. Ganau S, Tortajada L, Escribano F, Andreu X, Sentís M. The great mimicker: fat necrosis of the breastmagnetic resonance mammography approach. *CurrProblDiagnRadiol* (2009) 38:189–97. doi: 10.1067/j.cpradiol.2009.01.001

54. Adejolu M, Huo L, Rohren E, Santiago L, Yang WT. False-positive lesions mimicking breast cancer on FDG PET and PET/CT. *Am J Roentgenol* (2012) 198 (3):W304–14. doi: 10.2214/AJR.11.7130

55. Dobbs NB, Latifi HR. Diffuse FDG uptake due to fat necrosis following transverse rectus abdominus myocutaneous (TRAM) flap reconstruction. *Clin Nucl Med* (2013) 38(8):652–4. doi: 10.1097/RLU.0b013e31828e9948

56. Parker SH, Burbank F, Jackman RJ, Aucreman CJ, Cardenosa G, Cink TM, et al. Percutaneous large-core breast biopsy: a multi-institutional study. *Radiology* (1994) 193(2):359–64. doi: 10.1148/radiology.193.2.7972743

57. The American College of Radiology *ACR practice parameter for the performance of a diagnostic breast ultrasound examination, revised 2021 (Resolution 30)* Available at: https://www.acr.org/-/media/ACR/Files/Practice-Parameters/US-Breast.pdf (Accessed September 2021).

58. Salem DS, Kamal RM, Mansour SM, Salah LA, Wessam R. Breast imaging in the young: the role of magnetic resonance imaging in breast cancer screening, diagnosis and follow-up. *J Thorac Dis* (2013) 5 Suppl 1(Suppl 1):S9–S18. doi: 10.3978/j.issn.2072-1439.2013.05.02

Frontiers in Oncology

Advances knowledge of carcinogenesis and tumor progression for better treatment and management

The third most-cited oncology journal, which highlights research in carcinogenesis and tumor progression, bridging the gap between basic research and applications to imrpove diagnosis, therapeutics and management strategies.

Discover the latest Research Topics

See more →

Frontiers

Avenue du Tribunal-Fédéral 34
1005 Lausanne, Switzerland
frontiersin.org

Contact us

+41 (0)21 510 17 00
frontiersin.org/about/contact